



AFRL-RQ-ED-TR-2015-0015

Multiscale Numerical Methods for Non-Equilibrium Plasma

David Bilyeu
Hai Le

Jean-Luc Cambier

Air Force Research Laboratory (AFMC)
AFRL/RQRS
1 Ara Drive
Edwards AFB, CA 93524-7013

August 2015

In-House Final Report

Approved for Public Release; distribution unlimited. PA No. 15583

STINFO COPY

**AIR FORCE RESEARCH LABORATORY
AEROSPACE SYSTEMS DIRECTORATE**

- STINFO COPY -
NOTICE AND SIGNATURE PAGE

Using Government drawings, specifications, or other data included in this document for any purpose other than Government procurement does not in any way obligate the U.S. Government. The fact that the Government formulated or supplied the drawings, specifications, or other data does not license the holder or any other person or corporation; or convey any rights or permission to manufacture, use, or sell any patented invention that may relate to them.

Qualified requestors may obtain copies of this report from the Defense Technical Information Center (DTIC) (<http://www.dtic.mil>).

AFRL-RQ-ED-TR-2015-0015 HAS BEEN REVIEWED AND IS APPROVED FOR PUBLICATION IN ACCORDANCE WITH ASSIGNED DISTRIBUTION STATEMENT.

FOR THE DIRECTOR:

//signed//

DAVID L. BILYEU
Program Manager

//signed//

LUKE C. DRAS, CAPT, USAF
Chief, In-Space Propulsion Branch

//signed//

Technical Advisor
Rocket Propulsion Division

This report is published in the interest of scientific and technical information exchange, and its publication does not constitute the Government's approval or disapproval of its ideas or findings.

REPORT DOCUMENTATION PAGE				Form Approved OMB No. 0704-0188	
<p>Public reporting burden for this collection of information is estimated to average 1 hour per response, including the time for reviewing instructions, searching existing data sources, gathering and maintaining the data needed, and completing and reviewing this collection of information. Send comments regarding this burden estimate or any other aspect of this collection of information, including suggestions for reducing this burden to Department of Defense, Washington Headquarters Services, Directorate for Information Operations and Reports (0704-0188), 1215 Jefferson Davis Highway, Suite 1204, Arlington, VA 22202-4302. Respondents should be aware that notwithstanding any other provision of law, no person shall be subject to any penalty for failing to comply with a collection of information if it does not display a currently valid OMB control number. PLEASE DO NOT RETURN YOUR FORM TO THE ABOVE ADDRESS.</p>					
1. REPORT DATE (DD-MM-YYYY) 10 Aug 2015		2. REPORT TYPE In-House Final Technical Report		3. DATES COVERED (From - To) 10 August 2010 - 12 May 2015	
4. TITLE AND SUBTITLE Multiscale Numerical Methods for Non-Equilibrium Plasma				5a. CONTRACT NUMBER In-house	
				5b. GRANT NUMBER	
				5c. PROGRAM ELEMENT NUMBER 61102F	
6. AUTHOR(S) David Bilyeu, Jean-Luc Cambier, and Hai Le				5d. PROJECT NUMBER	
				5e. TASK NUMBER	
				5f. WORK UNIT NUMBER Q0AE	
7. PERFORMING ORGANIZATION NAME(S) AND ADDRESS(ES) Air Force Research Laboratory (AFMC) AFRL/RQRS 1 Ara Dr. Edwards AFB CA 93524-7013				8. PERFORMING ORGANIZATION REPORT NO.	
9. SPONSORING / MONITORING AGENCY NAME(S) AND ADDRESS(ES) Air Force Research Laboratory (AFMC) AFRL/RQR 5 Pollux Drive Edwards AFB CA 93524-7048				10. SPONSOR/MONITOR'S ACRONYM(S)	
				11. SPONSOR/MONITOR'S REPORT NUMBER(S) AFRL-RQ-ED-TR-2015-0015	
12. DISTRIBUTION / AVAILABILITY STATEMENT Approved for public release; distribution unlimited.					
13. SUPPLEMENTARY NOTES PA No. 15583					
14. ABSTRACT <p>The goal of this research program consisted of developing a high-fidelity modeling capability for non-equilibrium plasma, including detailed collisional-radiative kinetics, and magneto-hydrodynamic physics. Through this research effort, we have successfully implemented and verified single fluid, magneto-hydrodynamic and multi-fluid models. The collisional-radiative kinetics were solved and coupled to the fluid, and a new, high-accuracy model for complexity reduction of the atomic collisional-radiative chemistry was developed and tested. This allows an efficient yet accurate way to model complex and realistic plasma chemistries – involving multiple ion stages and multiple species – coupled to the fluid dynamics. Extensions of the model to allow such time-accurate simulations in multi-dimensional configurations are currently being investigated. Such a capability is a significant step forward in high-fidelity plasma simulations, for various conditions of interest to the Air Force and the DoD, and is made possible by the preliminary R&D conducted under this Laboratory Research Independent Research.</p>					
15. SUBJECT TERMS Plasma physics; numerical methods and procedures; particle collisions; collisional radiative plasmas; computational fluid dynamics; kinetic theory; detonation waves; excitation; multi fluid plasmas; field reversed configuration; modeling; simulation; magnetic fields					
16. SECURITY CLASSIFICATION OF:			17. LIMITATION OF ABSTRACT	18. NUMBER OF PAGES	19a. NAME OF RESPONSIBLE PERSON
a. REPORT	b. ABSTRACT	c. THIS PAGE			David Bilyeu
Unclassified	Unclassified	Unclassified	SAR	615	19b. TELEPHONE NO (include area code) (661) 275-5707

This Page Intentionally Left Blank

TABLE OF CONTENTS

Summary Program Description	1
References	2
Appendix A: GPU-based flow simulation with detailed chemical kinetics	A-1
Appendix B: Complexity reduction of collisional radiative kinetics for atomic plasma	B-1
Appendix C: Modeling of Inelastic Collisions in a Multifluid Plasma: Excitation and Deexcitation	C-1
Appendix D: Hydrodynamic models for multicomponent plasmas with collisional-radiative kinetics	D-1
Combustion and Magnetohydrodynamic Processes in Advanced Pulse Detonation Rocket Engines	E-1

LIST OF SYMBOLS, ABBREVIATIONS AND ACRONYMS

(B)	Boltzmann
(U)	uniform
1T	single temperature
2T	two temperature
ADER	advection-diffusion-reaction
AFRL	Air Force Research Laboratory
AR	area ratio
ASDF	atomic state distribution function
BGK	Bhatnagar-Gross-Krook
CFD	computational fluid dynamics
CFL	Courant-Friedrichs-Lewy
CJ	Chapman-Jouget
COM	center of mass
CP	chamber piston
CR	collisional-radiative
DB	detailed balance
DDT	deflagration to detonation transition
DM	Deutsch-Märk
DoD	Department of Defense
EEDF	electron energy distribution function
<i>EK</i>	enhanced kinetic
ENO	essentially non-oscillatory
FD	finite difference
FFT	fast fourier transform

FRC	field reversed configuration
FWHM	full width half maximum
GPU	Graphics Processing Unit
HA	high amplitude
HF	high frequency
HO	high-order
ISP	specific impulse
LHS	left hand side
LPI	laser plasma interactions
LPP	laser produced plasmas
LRIR	Laboratory Research Independent Research
M&S	modeling and simulation
MFD	magneto-fluid-dynamics
MHD	magneto-hydrodynamic
MHD1T	single temperature magnetohydrodynamic
MHD2T	two temperature magnetohydrodynamic
MP3	third-order monotonicity preserving
MP5	fifth-order monotonicity preserving
MPI	message passing interface
MR	microscopic reversibility
NG	nozzle generator
ODE	ordinary differential equation
PAC	plasma assisted combustion
PAI	plasma assisted ignition
PDE	partial differential equation
PDRE	pulse detonation rocket engines

PDRIME	pulse detonation rocket-induced magnetohydrodynamic ejectors
PIC	particle in cell
R&D	research and development
RHS	right hand side
RIME	rocket induced magnetohydrodynamic ejector
RK	Runge-Kutta
RPA	radiation pressure acceleration
RT	radiation transport
RT	Rayleigh-Taylor
RTI	Rayleigh-Taylor instabilities
SH	Spitzer-Harm
SSTO	Single-Stage-to-Orbit
TMM	transfer-matrix method
TNSA	target normal sheath acceleration
TVD	total variation diminishing
UCLA	University California Los Angeles
USAF	United States Air Force
UTIAS	University of Toronto's Institute of Aerospace Studies
VDF	velocity distribution function
WENO	weighted essentially non-oscillatory
WKB	Wentzel-Kramers-Brillouin

1 Summary Program Description

The goal of this research program consisted of developing a high-fidelity modeling capability for non-equilibrium plasma, including detailed collisional-radiative kinetics, and magneto-hydrodynamic (MHD) physics. Through this research effort, we have successfully implemented and verified single-fluid, MHD, and multi-fluid models. The collisional-radiative (CR) kinetics were solved and coupled to the fluid, and a new high-accuracy model for complexity reduction of the atomic CR chemistry was developed and tested; this allows an efficient yet accurate way to model complex and realistic plasma chemistries – involving multiple ion stages and multiple species – *coupled* to the fluid dynamics. Extensions of the model to allow time-accurate simulations in multi-dimensional configurations are currently being investigated. Such a capability is a significant step forward in high-fidelity plasma simulations, for various conditions of interest to the Air Force and the DoD, and is made possible by the preliminary R&D conducted under this Laboratory Research Independent Research (LRIR). Furthermore, we have also been able to complete a rigorous derivation of a new model of CR kinetics for multi-fluid plasma, the results of which are presented in appendix C.

On a parallel effort, we have developed and tested a MHD version of the single-fluid code using several monotonicity-preserving (MP), high-order (HO) numerical schemes: WENO [1], ADER-WENO [2], and MP [3]. The results of these tests are part of dissertation work by L. Cole, included in this report. We have also tested the implementation of both CFD schemes and kinetics on Graphics Processing Units (GPUs), allowing massive parallelization for future large-scale studies; the results of this GPU optimization were published and are included in this report.

This LRIR effort, although at a very moderate level of funding, was thoroughly successful:

1. Several innovative models and numerical schemes were developed, verified and validated, against known analytical solutions, experiments (e.g. Schlieren and interferometric data from shock-tubes), and other codes. These include: a) a new level-grouping methodology to reduce the complexity of atomic CR kinetics and allow high-fidelity of large-scale simulations, and; b) a new multi-fluid CR kinetics model and derivation of improved coupling coefficients for mass, momentum and energy.
2. New modeling capabilities were created at AFRL with more detailed reproduction of physical phenomena of critical importance to a number of problems of interest to the USAF, and which are being incorporated into a general-purpose framework for future applications to real systems: a) high-order MHD models; b) multi-fluid models; c) CR-chemistry models; d) optimized GPU parallelization; e) laser-plasma interactions (LPI).
3. The LRIR funded the dissertation work of one graduate student (H. Le) and partially that of another student (L. Cole), who worked at AFRL and under the direction of the PI, Dr. J.-L. Cambier. This was a very effective interaction, multiplying the skills of experienced personnel with the raw enthusiasm of very junior researchers, and a highly efficient use of resources. It also provided a best-approach template for the collaboration between AFRL and a local university, UCLA, with future impact on other R&D programs.

The results of this R&D effort are provided herewith as a series of appendices, namely:

1. A journal article describing the optimization of kinetics on the GPU platform (although tested on chemical kinetics of combustion, the same procedure is applicable to CR kinetics

with relatively minor modifications).

2. A journal article describing the derivation of a higher-order level-grouping scheme, for future, more accurate simulations of multi-dimensional plasma with complex chemistry and composition.
3. A journal article describing a new model of multi-fluid collisional-radiative kinetics, and the derivation of new resistance and coupling coefficients, as well as a demonstration of their potential impact. This article is part I of a two part series, with the second one describing the model for ionization and recombination (in preparation).
4. The Ph.D. thesis of Hai Le (UCLA), who performed most of the work under the scope of this LRIR. The dissertation provides; a) a detailed description of the single-fluid model with detailed CR kinetics and validation; b) a description of the multi-fluid model and associated kinetics; c) a description of the newly implemented laser-plasma interaction modeling capability, with reproduction of non-linear (ponderomotive) forces.
5. The Ph. D. thesis of Lord Cole (UCLA), which contains a detailed description of the various numerical schemes studied, and applications to MHD modeling capability.

In conclusion, this LRIR effort has provided a number of advances in modeling capabilities for AFRL, which are currently being integrated into a new, state-of-the-art M&S platform for future large-scale studies. By itself this defines a successful program with direct transition into a 6.2 effort. Of equal importance, this LRIR provided the seeds for on-going and future research with even more significant impact and even greater advances, under the general scope of multi-dimensional, time-accurate MHD and multi-fluid plasma simulations with detailed atomic physics and radiative transport. This new level of modeling accuracy is currently being developed as a continuation of this effort, through the same (and extended) collaboration with UCLA, and is expected to provide revolutionary capabilities to AFRL.

References

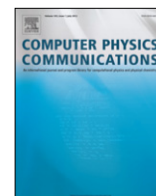
- [1] S. J. Osher and C.-W. Shu, “Weighted Essentially Non-Oscillatory,” *Journal of Computational Physics*, vol. 22, 1994.
- [2] V. A. Titarev and E. F. Toro, “ADER: Arbitrary High Order Godunov Approach,” *Journal of Computation Physics*, vol. 17, pp. 609–618, 2002.
- [3] A. Suresh and H. T. Huynh, “Accurate Monotonicity-Preserving Schemes with Runge-Kutta time Stepping,” *Journal of Computational Physics*, vol. 136, pp. 83–99, 1997.

Appendix A: GPU-based flow simulation with detailed chemical kinetics

Hai P. Le

Jean-Luc Cambier

Lord K. Cole



GPU-based flow simulation with detailed chemical kinetics

Hai P. Le^{a,*}, Jean-Luc Cambier^b, Lord K. Cole^a

^a Mechanical and Aerospace Engineering Department, University of California, Los Angeles, CA 90095-1597, United States

^b US Air Force Research Laboratory, Edwards AFB, CA 93524, United States

ARTICLE INFO

Article history:

Received 5 April 2012

Received in revised form

2 October 2012

Accepted 16 October 2012

Available online 23 October 2012

Keywords:

Computational fluid dynamics

GPU

Chemical kinetics

Finite volume

Cellular detonation

ABSTRACT

The current paper reports on the implementation of a numerical solver on the Graphic Processing Units (GPUs) to model reactive gas mixtures with detailed chemical kinetics. The solver incorporates high-order finite volume methods for solving the fluid dynamical equations coupled with stiff source terms. The chemical kinetics are solved implicitly via an operator-splitting method. We explored different approaches in implementing a fast kinetics solver on the GPU. The detail of the implementation is discussed in the paper. The solver is tested with two high-order shock capturing schemes: MP5 (Suresh and Huynh, 1997) [9] and ADERWENO (Titarev and Toro, 2005) [10]. Considering only the fluid dynamics calculation, the speed-up factors obtained are 30 for the MP5 scheme and 55 for ADERWENO scheme. For the fully-coupled solver, the performance gain depended on the size of the reaction mechanism. Two different examples of chemistry were explored. The first mechanism consisted of 9 species and 38 reactions, resulting in a speed-up factor up to 35. The second, larger mechanism, consisted of 36 species and 308 reactions, resulting in a speed-up factor of up to 40.

© 2012 Elsevier B.V. All rights reserved.

1. Introduction

Detail study of complex physical phenomena associated with high-speed fluid flow requires a deep understanding of the fundamental physics which involves many highly non-linear processes evolving in different spatial and temporal scales. Inevitably, the challenge of solving these problems is due to the coupling mechanism between these processes and what impact they have on the flow solution. For example, in combustion study, one has to pay close attention to the coupling between the fluid transport and chemical kinetics in order to characterize the combustion process. Computational Fluid Dynamics (CFD) techniques can be used to obtain a detailed flow solution which can be applied in practical applications. Although the mathematical formulation of the physics can be addressed in great detail, numerical simulation of high-speed fluid flow in a non-equilibrium environment is often limited by the computational power demanded for solving the governing equations. Modern CFD codes are designed to take advantage of high performance computing (HPC) platform to reduce run time. Unfortunately, the tradition HPC resources are very limited due to their cost and maintenance requirement. These limitations have accentuated a need for a compact and low-cost HPC solution where numerical solvers can be effectively implemented.

During the last eight years, the Graphic Processing Unit (GPU) has been introduced as a promising alternative to high-cost HPC

platforms. Within this period, the GPU has evolved into a highly capable and low-cost computing solution for scientific research. Fig. 1 illustrates the superiority of GPU over the traditional Central Processing Unit (CPU) in terms of floating point calculation. This is due to the fact that the GPU is designed for the highly parallel process of graphic rendering. Starting in 2008, the GPU began to support double precision calculation, which is necessary for scientific computing. The newest generation of NVIDIA GPUs called “Fermi” has been designed to enhance the performance on double precision calculation over the previous generations of NVIDIA GPUs. CUDA [1], which is currently the most popular programming environment for general purpose GPU computing, has undergone several development phases and reached a certain level of maturity, which is essential for the design of numerical solvers. Other alternatives such as OpenCL, DirectCompute, Stream, etc. have also began to mature which encourages new developments in scientific computing using GPU. Several attempts had been made in writing scientific codes on the GPU either by directly using CUDA or via some wrapper which calls the CUDA kernel functions, and promising results were obtained both in terms of performance and flexibility. Previous implementations of CFD codes on the GPU focused purely on solving the fluid dynamics using either finite volume [2,3] or finite element methods [4]. Recently, there have been a number of GPU-based implementations of multiphysics simulation. Of particular note are the extension to magnetohydrodynamics simulation by Wong et al. [5] and the automated preprocessor tool to model finite rate chemical kinetics by Linford et al. [6,7]. In all cases, the reported speed-ups show

* Corresponding author.

E-mail address: hai.le@ucla.edu (H.P. Le).

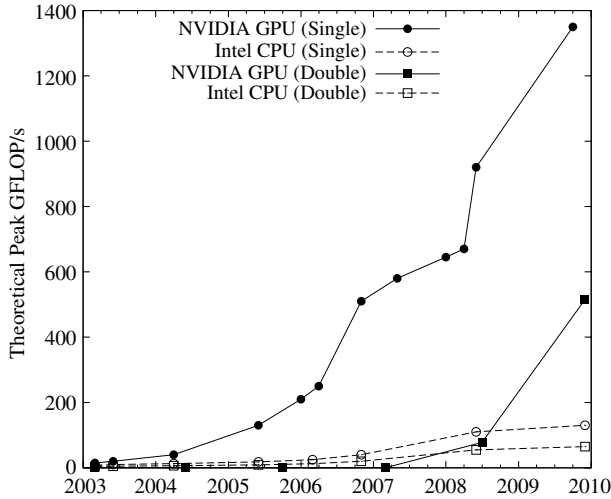


Fig. 1. Single and double precision floating point operation capability of GPU and CPU from 2003 to 2010.

Source: Adapted from Fig. 1 of NVIDIA [1].

promising performance results and clearly demonstrate that GPU is suitable for massively parallel scientific computing.

In this paper, we describe the detail code implementation of a numerical solver coupling the fluid dynamics with detailed chemical kinetics. Unlike previous attempts at adapting the GPU to numerical solver, we have placed our emphasis on the kinetics solver rather than the fluid dynamics. This is due to the fact that for the simulation of high-speed fluid flow, the computation is dominated by solving the kinetics. While the current implementation is only for chemical kinetics, it is easy to extend it to a more general kinetics (collision-radiative kinetics for plasma) since all the elementary processes for a plasma (excitation/de-excitation, ionization/recombination, etc.) can be represented by a chemical reaction with the rate computed *a priori* and tabulated as a function of temperature.

The rest of the paper is organized as follows. The governing equation and numerical formulation for both the fluid dynamics and chemical kinetics are described in Sections 2 and 3. Section 4 gives some background on GPU computing. The code implementation is detailed in Section 5, highlighting several optimization techniques for maximizing the performance of the solver. The results of several benchmark test cases both for non-reactive and reactive flow fields are presented in Section 6 as well as the performance results of the solver. Section 7 gives the conclusions and points out possible future works.

2. Governing equations

The flow is modeled as a mixture of gas species while neglecting viscous effects. The chemical reactions taken place between the gas components are to be modeled in great detail. The set of the Euler equations for a reactive gas mixture can be written as:

$$\frac{\partial Q}{\partial t} + \nabla \cdot \bar{F} = \dot{\Omega} \quad (1)$$

where Q and F are the vectors of conservative variables and inviscid fluxes, respectively. We assumed that there is no species diffusion and the gas is thermally equilibrium (i.e., all species have the same velocity and all the internal energy modes are at equilibrium). The right hand side (RHS) of Eq. (1) denotes the vector of source terms $\dot{\Omega}$, which are composed here of exchange terms due to chemical reactions. We solve the system (1) in a finite-volume

formulation, by applying Gauss's law to the divergence of the fluxes:

$$\frac{\partial Q}{\partial t} + \frac{1}{V} \oint_S F_n dS = \dot{\Omega} \quad (2)$$

where Q , F_n and $\dot{\Omega}$ now denote volume-averaged quantities, which can be written as:

$$Q = \begin{pmatrix} \rho_s \\ \vdots \\ \rho u_x \\ \rho u_y \\ \rho u_z \\ E \end{pmatrix}, \quad F_n = \begin{pmatrix} \rho_s u_n \\ \vdots \\ P n_x + \rho u_n u_x \\ P n_y + \rho u_n u_y \\ P n_z + \rho u_n u_z \\ u_n (P + E) \end{pmatrix}, \quad (3)$$

$$\dot{\Omega} = \begin{pmatrix} \dot{\omega}_s \\ \vdots \\ 0 \\ 0 \\ 0 \\ -\sum_s \dot{\omega}_s e_{0s} \end{pmatrix}$$

where u_n is the velocity vector normal to the interface and (n_x, n_y, n_z) is the corresponding unit vector. The total energy is the sum of the internal energies from each species and the total kinetic energy:

$$E = \sum_s \rho_s e_{is} + \frac{1}{2} \rho \bar{u}^2. \quad (4)$$

Since the species formation energies e_{0s} are not included in that definition, we must account for their change in the source term $\dot{\Omega}$. The convective terms and the source terms are solved independently of each other by making use of an operator-splitting technique.

$$\frac{\partial Q}{\partial t} = \left(\frac{\partial Q}{\partial t} \right)_{\text{conv}} + \left(\frac{\partial Q}{\partial t} \right)_{\text{chem}} = -\frac{1}{V} \oint_S F_n dS + \dot{\Omega}. \quad (5)$$

The equation of state (EOS) is that of an ideal gas, i.e. Dalton's law of partial pressures:

$$P = NRT = \sum_s \rho_s (R/M_s) T \quad (6)$$

where R is the Boltzmann constant (in J/mol · K) and M_s the species molar mass. The pressure can also be determined from the conserved variables, $\{\rho_s, \bar{m}, E\}$, where $\bar{m} = \rho \bar{u} = \sum_s \rho_s \bar{u}$, by:

$$P = (\gamma - 1) \left(E - \frac{\bar{m}^2}{2\rho^2} \right). \quad (7)$$

This formulation allows us to compute the pressure derivatives with respect to the conservative variables, needed for the flux Jacobian. Comparing (6) and (7), we find the expression for the effective ratio of specific heats γ :

$$\gamma = 1 + RT \frac{\sum_s \rho_s / M_s}{\rho \bar{e}_i} \quad \text{with } \rho \bar{e}_i = \sum_s \rho_s e_{is}. \quad (8)$$

Using

$$\left(\frac{\partial \gamma}{\partial \rho_s} \right)_{E, \bar{m}} = \frac{RT}{\rho \bar{e}_i} \left(\frac{1}{M_s} - \frac{e_{is}}{\bar{M} \bar{e}_i} \right) \quad (9)$$

with $\bar{M} = \rho/N$, we find (using the notation $P_{q_a} = \partial P / \partial q_a$):

$$P_{\rho_s} = (\gamma - 1) \frac{\bar{u}^2}{2} + \left(\frac{RT}{M_s} - \frac{RT}{\bar{M}} \frac{e_{is}}{\bar{e}_i} \right). \quad (10)$$

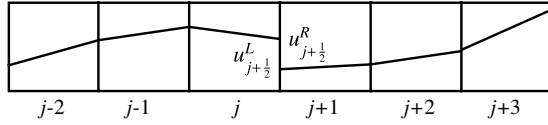


Fig. 2. Schematic of computational stencil for MP5 scheme with left and right states of an interface.

Note that $\sum_s \rho_s P_{\rho_s} \equiv (\gamma - 1) \bar{u}^2 / 2$. The other derivatives are:

$$P_{m_\alpha} = -(\gamma - 1) u_\alpha \quad \alpha = x, y, z \quad (11)$$

and

$$P_E = \gamma - 1. \quad (12)$$

The speed of sound is defined as

$$c^2 = \sum_s \hat{c}_s P_{\rho_s} + (h - \bar{u}^2) P_E = \gamma \frac{P}{\rho} \quad (13)$$

where $\hat{c}_s = \rho_s / \rho$ is the species mass fraction and

$$h = \frac{H}{\rho} = \frac{E + P}{\rho} \quad (14)$$

is the specific enthalpy.

3. Numerical formulation

3.1. Fluid dynamics

A dimensional splitting technique [8] is utilized for solving the convective part of the governing equations. In order to achieve high-order both in space and time, we employed a fifth-order Monotonicity-Preserving scheme (MP5) [9] for the reconstruction, and a third-order Runge–Kutta (RK3) for time integration. For the MP5 scheme, the reconstructed value of the left and right states of interface $j + \frac{1}{2}$ is given as (see Fig. 2):

$$u_{j+\frac{1}{2}}^L = \frac{1}{60} (2u_{j-2} - 13u_{j-1} + 47u_j + 27u_{j+1} - 3u_{j+2}) \quad (15a)$$

$$u_{j+\frac{1}{2}}^R = \frac{1}{60} (2u_{j+3} - 13u_{j+2} + 47u_{j+1} + 27u_j - 3u_{j-1}). \quad (15b)$$

The reconstructed values are then limited to avoid instability.

$$u_{j+\frac{1}{2}}^L \leftarrow \text{median} \left(u_{j+\frac{1}{2}}^L, u_j, u_{MP} \right) \quad (16)$$

where

$$u_{MP} = u_j + \min \text{mod} [u_{j+1} - u_j, \alpha (u_j - u_{j-1})] \quad (17)$$

with $\alpha = 2$.

In addition to the MP5 scheme, we also considered the Arbitrary Derivative Riemann Solver using the Weighted Essentially Non-Oscillatory reconstruction procedure, the so-called ADERWENO scheme [10]. At each interface of 1 one-dimensional stencil, we seek the solution of the generalized Riemann problem (GRP)

$$\partial_t Q + \partial_x F(Q) = 0 \quad (18)$$

with the following initial conditions

$$Q^{(k)}(x, 0) = \begin{cases} q_L^{(k)}(x) & \text{if } x < 0 \\ q_R^{(k)}(x) & \text{if } x > 0. \end{cases} \quad (19)$$

The solution of Eq. (18) can be expanded using the Taylor Series expansion in time.

$$Q(x_{j+1/2}, t + h) = Q(x_{j+1/2}, t) + \sum_{k=1}^{r-1} \frac{h^k}{k!} \frac{\partial^k}{\partial t^k} Q(x_{j+1/2}, t) \quad (20)$$

where all the temporal derivatives can be determined using the Cauchy–Kowalewski procedures [10]. The solution obtained in this form is high-order both in space and time, so no additional time stepping (i.e., multi-stage RK) is required. This provides certain advantages over the MP5 scheme since the overhead since the RK additional stages for high temporal order are no longer required. However, one disadvantage of the ADERWENO scheme is that the scheme is not guaranteed to be total variation diminishing (TVD) which might be an issue in the region of strong compression or expansion waves. It is worthwhile to mention that there are other formulations of ADER schemes available in the literature [11] which are proven to be TVD. Although such schemes have not been implemented, the core implementation of the solver described in this work can be used as the building blocks for other formulations of ADER schemes.

The interface fluxes are solved by employing the HLLC Riemann solver [12], which is given as

$$F_{j+1/2}^{\text{HLLC}} = \frac{b^+ F_R - b^- F_L}{b^+ - b^-} + \frac{b^+ b^-}{b^+ - b^-} \Delta Q_{j+1/2} \quad (21)$$

where

$$b^+ = \max(0, \hat{u}_n + \hat{c}, u_{nR} + c_R) \quad (22)$$

$$b^- = \min(0, \hat{u}_n - \hat{c}, u_{nL} - c_L). \quad (23)$$

3.2. Chemical kinetics

An elementary chemical reaction takes the form

$$\sum_s \nu'_s [X_s] \Leftrightarrow \sum_s \nu''_s [X_s] \quad (24)$$

where ν'_s and ν''_s are the molar stoichiometric coefficients of the reactants and products of each reaction. The forward rate can be expressed in modified Arrhenius form as:

$$K_{fr} = A_{fr} T^{\beta_r} \exp \left(-\frac{E_r}{RT} \right). \quad (25)$$

The backward reaction rate is calculated from the equilibrium constant, which is given as

$$K_e = \frac{K_{fr}}{K_{br}} = \left(\frac{P_a}{RT} \right)^{\sum_s \nu_s} \exp \left(\frac{-\Delta G^0}{RT} \right). \quad (26)$$

The species net production rate due to all reactions can then be determined from

$$\dot{\omega}_s = \sum_r M_s \nu_{rs} \left[K_{fr} \prod_s [X_s]^{\nu'_{rs}} - K_{br} \prod_s [X_s]^{\nu''_{rs}} \right] \quad (27)$$

where $\nu_{rs} = \nu''_{rs} - \nu'_{rs}$. By conservation of mass, sum of all the species production rates should be equal to zero which yields the following expression.

$$\sum_s \dot{\omega}_s = 0. \quad (28)$$

In order to solve for the change in the species concentration, one needs to know all the changes in the thermodynamics for each reaction as well as their rates (production/destruction). The backward rate for each reaction is calculated based on detail balancing. In practice, acceptable result can also be obtained using curve-fitting technique with the temperature as an input without the expense of calculating the equilibrium constant. In this work, we have computed the backward rates from the equilibrium constant.

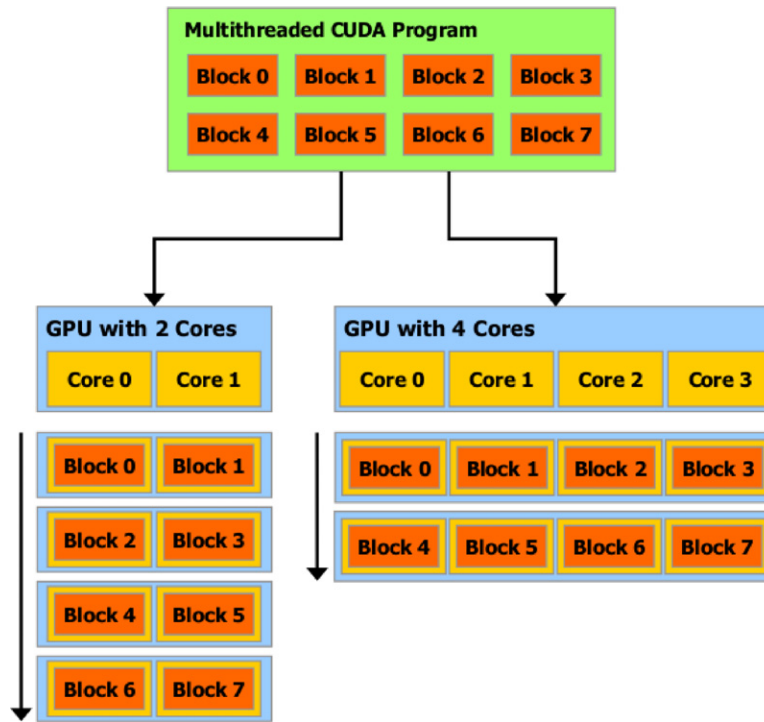


Fig. 3. Data parallelism in GPU [1].

The chemical kinetics, expressed in the form of an ODE, is solved using a point implicit solver to ensure stability. The formulation can be obtained by using a Taylor series expansion in time of the RHS

$$\frac{dQ}{dt} = \dot{\Omega}^{n+1} \quad (29)$$

$$\frac{dQ}{dt} = \dot{\Omega}^n + \Delta t \frac{\partial \dot{\Omega}^n}{\partial t}. \quad (30)$$

By applying chain rule to the time derivatives on the RHS, one could obtain

$$\left(I - \Delta t \frac{\partial \dot{\Omega}}{\partial Q} \right) \frac{dQ}{dt} = \dot{\Omega}. \quad (31)$$

As a linear system of equations, Eq. (31) can be solved using a variety of numerical methods. In the current work, a direct Gaussian elimination procedure is carried out in order to solve for the linear system of the chemical kinetics. It must be pointed out that the computational cost of the Gaussian elimination procedure scales as $(N_s)^3$ where N_s in this case is the number of species. For large/detailed kinetics, solving the system at every cell is clearly a computationally intensive task.

4. GPU computing

The GPU processes data in a Single-Instruction-Multiple-Thread (SIMT) manner. The instruction for executing on the GPU is called a kernel which is invoked from the host (CPU). The CUDA programming model consists of grid and thread block. A grid consists of multiple thread blocks and each thread block contains a number of threads. When a kernel is called, the scheduler unit on the device will automatically assign a group of thread blocks to the number of available streaming multi-processors (SM or GPU core) on the device. Once the SM has completed the calculation, it will be assigned another block. Since there is no communication between the thread blocks, the execution order is automatically optimized so GPU with more cores will perform the calculation faster, which is shown in Fig. 3.

The data parallelism is also inherent at the thread level. An instruction given to a thread block is handled by a SM which contains a number of streaming processors (SPs). All the threads within each block will be organized into groups of 32 threads called warps which are executed in a SIMT manner. The difference in the data parallelism between grid and thread block is that there is a synchronization mechanism for all the threads in a same block but not for all the blocks in the grid. It is therefore important to ensure that there is no data dependency between thread blocks.

5. Implementation

The overall implementation of the code can be divided into two parts: the fluid dynamics and kinetics. The fluid dynamics module is responsible for the advection calculation. The kinetics module, on the other hand, calculates the species consumption/production due to chemical reactions and ensures detail balance is satisfied. The overall flow chart of the program is shown in Fig. 4 (see also Fig. 5 for the flow chart of the fluid dynamics module). After all the flow variables have been initialized and transferred to the GPU, the entire calculation is performed on the device. There is no memory transfer between each iteration unless there is a need to output the flow solution. This effectively reduces the memory transfer time between iterations, which can be significant for large-scale problems. However, for calculation utilizing more than one GPU, it is unavoidable to transfer memory back to the host for boundary exchange (ghost cells).

5.1. Computational fluid dynamics

The parallelization is done by directly mapping the computational domain to a CUDA grid. The face values can be mapped the same way with a larger grid since the number of faces in each direction is always 1 greater than the number of cells in that direction. For a rectilinear grid, each CUDA thread can be associated with one cell/face inside the computational domain.

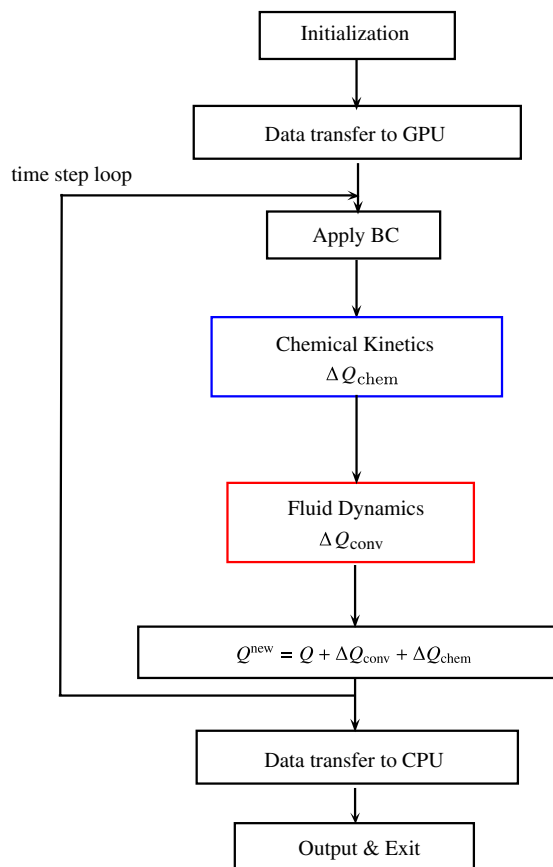


Fig. 4. The overall work flow of the program. The fluid dynamics calculation and chemical kinetics are done by several GPU kernels.

In order to maximize the memory access efficiency, the data for the whole domain is stored as one-dimensional arrays. The index of these arrays can be calculated from the dimensional indices and the variable index and vice versa. This is similar to the approach taken in [5]. Since all the data storage is one-dimensional, the domain can be decomposed into one-dimensional stencils of cell/face values where each stencil can be assigned to a CUDA block. Since the computational domain can be up to three-dimensional, one can split the stencil in different ways. However, it is desired to split the stencil so that all the elements of a stencil are located in contiguous memory space. For example, if i is the fastest varying index of a three-dimensional data array $A(i, j, k)$, the stencil is created by splitting the domain along the i direction. The directional indices (i, j, k) of a three-dimensional domain with lengths $IDIM$, $JDIM$ and $KDIM$ can be calculated from the thread index, as shown in the following CUDA code snippets:

```

int tid = blockIdx.x*blockDim.x+threadIdx.x;
int k = tid / (IDIM*JDIM);
int ij = tid % (IDIM*JDIM);
int j = ij / IDIM;
int i = ij % IDIM;

```

Since each stencil can be fitted into a block of threads, each component of the stencil is associated with a thread. Since all the threads within a block are accessing consecutive memory address, the access pattern is coalesced resulting in high memory bandwidth.

The calculation inside the CFD kernels requires a certain amount of memory which cannot be fitted in shared memory. This is because the size of the conservative variable vector is directly proportional to the number of species which can be quite large for a

reacting mixture. In addition, high-order reconstruction requires an interpolating stencil whose length is three or five computational cells depending on the order of the scheme. Hence, the shared memory was not found useful in this case. In the CFD calculation, the size of the thread block can have an impact on the performance of the kernel. It is usually recommended by the CUDA programming guide [1] to maximize the block occupancy to make up for the memory latency. Since the occupancy factor is proportional to the block size, a large block size would result in high occupancy. However, Volkov [13] has shown that in the case where there are multiple independent instructions in the kernel, it is more advantageous to make the block size smaller and utilize more registers to cover for the memory latency. Since each entry of the eigensystem can be constructed independently of the others, the kernel performs faster in the case of smaller block size. This is referred as Instruction-level Parallelism (ILP). This is the approach utilized in the CFD kernels to achieve high performance. One example is the construction of the eigensystem in the fluid solver. More information on how to optimize the performance of a kernel using ILP can be found in Volkov [13].

5.2. Chemical kinetics

The parallelization of the kinetics solver can greatly benefit from GPU acceleration. The problem can be described as a simple linear algebra problem $A \cdot x = b$ where A is the Jacobian matrix mentioned in Eq. (31). The solution of the system contains the change in molar concentration of all the species due to chemical reactions. It must be noted that the kinetics calculation is complex and the computation time depends on a variety of parameters such as domain size, number of species, number of reactions, etc. In the optimization study of the kinetics solver, we have neglected the effect of the number of reactions which is present in the rate calculation (i.e., construction of the Jacobian), so the focus can be placed on the matrix inversion algorithm where the system size (N_s) can be varied. In general, the construction of the Jacobian is also a time consuming process if one considers a large number of reactions, but case dependent optimization techniques can be applied, making generalization inefficient. Since the solver is designed to solve a general set of kinetics, the detail in the construction of the Jacobian is not discussed here, although in this work, we have also attempted to optimize the rate calculation. The efficiency of the rate calculation will be shown implicitly later in a comparison of two fully-coupled solutions using two different chemistry mechanisms.

The linear system $A \cdot x = b$ is solved using a Gaussian elimination algorithm, which is a sequential method. Since the kinetics in each computational cell are independent of other cells, one can parallelize the system on thread-per-cell basis. The Gaussian elimination process requires a considerable amount of memory access for read and write instructions to use and modify the values of the Jacobian. We investigated different approaches to maximize the performance of the kinetics solver. The first approach was to store the entire system for all cells on global memory. This is referred as the global memory approach. Although global memory is the slowest type of memory available on the device, coalesced memory access can result in high memory bandwidth close to the theoretical limit. The advantage of this approach lies in its simplicity. This is similar to the approach taken by Linford et al. [6, 7] for their implementation of the chemical kinetics kernel on the GPU. Since the global memory is the largest on the device, the restriction on the number of species can be relaxed. This is referred as the global memory (coalesced) approach throughout the text. A known issue of the Gaussian elimination is the significant accumulation of round-off error for large linear system, so double-precision is rapidly a necessity.

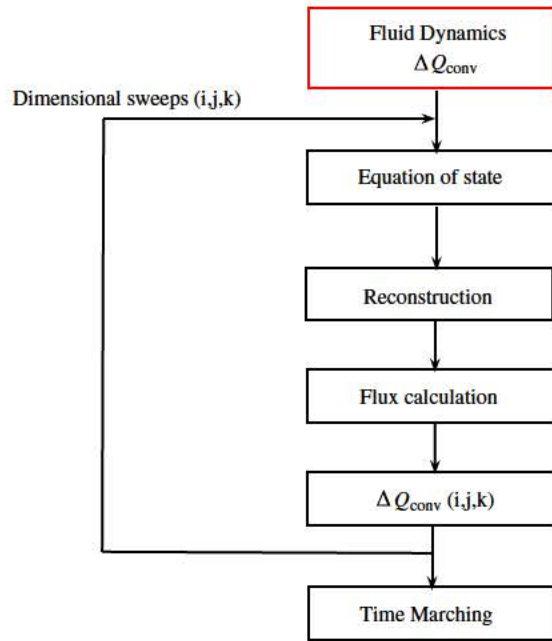


Fig. 5. Flow chart of the fluid dynamics calculation. The loop shown here represents the number of dimensions considered in the problem. For a three dimensional problem, one needs to sweep in all i , j and k directions.

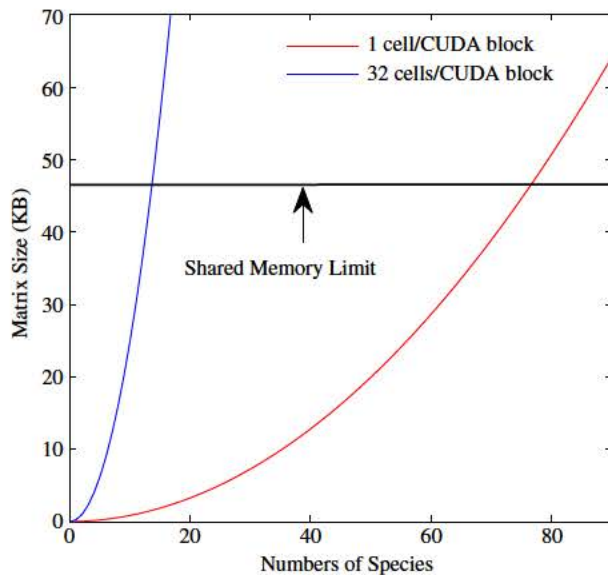


Fig. 6. Chemistry size limitation for storing the whole Jacobian matrix and the RHS vector on shared memory. Even when we only store 1 Jacobian per CUDA block, the maximum number of species is less than 13.

It is always recommended [1] to utilize shared memory whenever possible to reduce global memory traffic. In this case, solving the chemical system requires inverting a N_s -by- N_s matrix and the system needs to be solved at every computational cell. Storing the whole Jacobian and the RHS vector on shared memory is ideal in this particular case. Fig. 6 shows the memory requirement for storing the Jacobian and RHS on the typical shared memory (i.e., a Tesla C2050/2070 has 48 KB of shared memory per CUDA block). If we associated an entire thread block to the chemical system in a cell, the number of species is limited to 75. Storing more than 1 system per block decreases this limit further, which is the case for 1 thread per cell (32 threads block size). The approach of storing the entire system of one computational cell per block is referred as the shared memory (full storage pattern) approach.

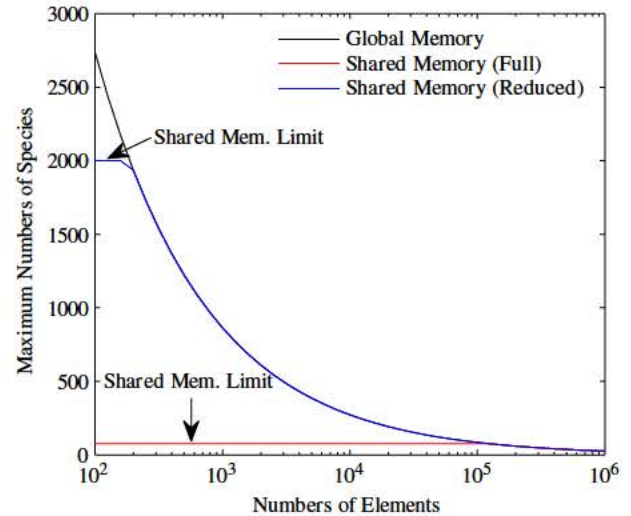


Fig. 7. Chemistry size limitation for storing only two rows of the Jacobian matrix on shared memory (reduced storage pattern). The number of species limit now is much higher than the previous approach (Fig. 6).



Fig. 8. Solution of the forward step problem using MP5 scheme with 600,000 cells.

In order to overcome the shared memory limit, we considered storing only two rows of the Jacobian in shared memory since the sequence of the elimination is done row-by-row. In this approach, referred as the shared memory (reduced storage pattern) approach, one needs to store values for the current row and the pivot row for each row elimination. Fig. 7 shows a comparison of the species limit for two approaches; the species limit for the reduced storage pattern is much higher than the full storage pattern. The draw-back of this approach, however, is that there are multiple memory transfers between global and shared memory, since we are required to copy back the values of each row after being eliminated. The parallelization is only effective when the calculation time dominates the global-shared memory transfer time (i.e., N_s is large). It will be shown later that this algorithm is only fast for linear systems with a large number of species. It must be noted that the shared memory approach stated in the remaining of paper will refer to the reduced storage pattern approach.

6. Results

6.1. Solver results

The first objective is to verify that the solver is correctly implemented using the CUDA kernels. For this purpose, we can compare the results with a pure-CPU version, but also compute a set of standard test cases. The first of those is a Mach 3 wind tunnel problem (a.k.a. the forward step problem) using the MP5 scheme, whose solution is shown in Fig. 8. This problem had been utilized by Woodward and Colella [14] to test a variety of numerical schemes. The whole domain is initialized with Mach-3 flow and reflective boundary conditions are enforced on the step and the upper part of the domain. The left and the right boundary conditions are set as in-flow and out-flow, respectively. Special attention is usually

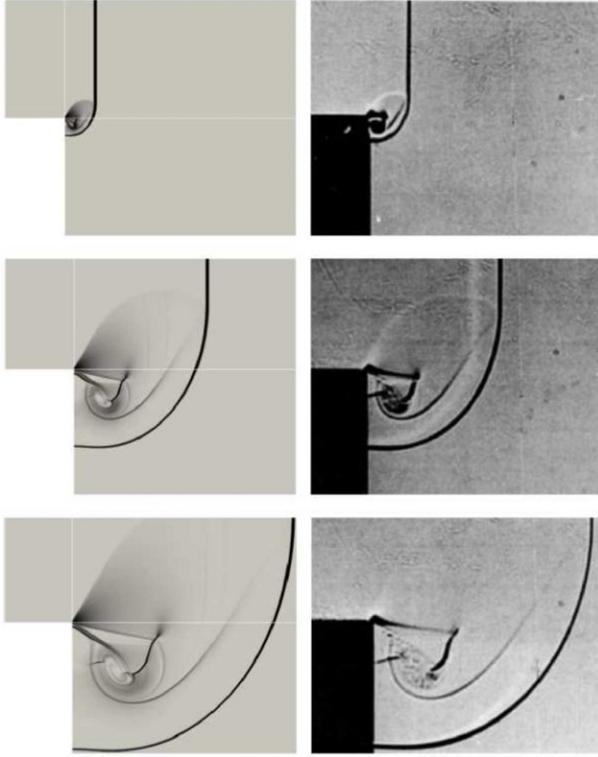


Fig. 9. Diffraction of a Mach 2.4 shock wave down a step using MP5 scheme with 27,000 cells. Comparison between numerical schlieren and experimental images.

required at the corner of the step since this is a singular point of the flow which can create numerical instabilities. Woodward and Colella treated this by assuming the flow near the corner is nearly steady. However, this artificial fix was not used in this simulation since we want to test the robustness of the solver in the case of strong shocks and how it handles the singularity in wall curvature, responsible for very strong expansion.

The second test involves a similar problem of a diffraction of a shock wave ($M = 2.4$) down a step [15]. The strong rarefaction at the corner of the step can cause a problem of negative density when performing the reconstruction. The problem is modeled here using 27,000 cells, and the numerical simulation is shown in pair with the experimental images in Fig. 9. The solver was able to reproduce the correct flow features with excellent accuracy.

We also modeled the Rayleigh–Taylor instability problem [16] (see Fig. 10). The problem is described as the acceleration of a heavy fluid into a light fluid driven by gravity. In this test case, the specific heat ratio is set to be a constant ($\gamma = 1.4$). For a rectangular domain of (0.25×1) , the initial conditions are given as follows:

$$\begin{aligned} \rho &= 2, & u &= 0, & v &= -0.025 \cos(8\pi x), \\ P &= 2y + 1 & \text{for } 0 \leq y \leq \frac{1}{2} \end{aligned} \quad (32)$$

$$\begin{aligned} \rho &= 1, & u &= 0, & v &= -0.025c \cos(8\pi x), \\ P &= y + \frac{3}{2} & \text{for } \frac{1}{2} \leq y \leq 1 \end{aligned} \quad (33)$$

where c is the speed of sound. The top and bottom boundaries are set as reflecting and the left and right boundaries are periodic. As the flow progresses, the shear layer starts to develop and the Kelvin–Helmholtz instabilities become more evident. A momentum and energy source is added to account for the gravitational effects. This source is relatively simple and contributes very little to the overall computational time. The performance of the fluid dynamics calculation is discussed in the next section of this report.

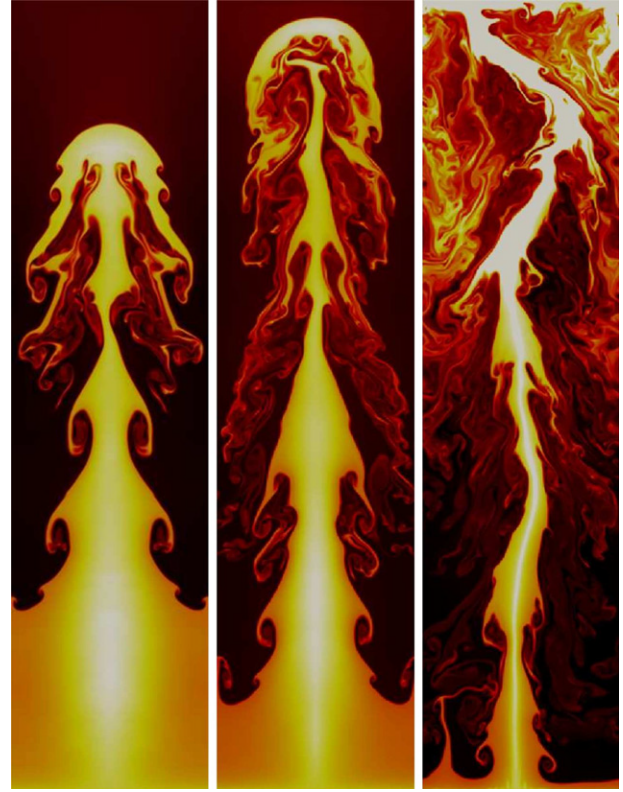


Fig. 10. Rayleigh–Taylor instability computed with the MP5 scheme with 640,000 cells.

We now turn the attention to the modeling of a reactive flow field. We simulated a spark-ignited detonation wave both in one- and two-dimension to demonstrate the capability of the solver. At a well-resolved scale, the detonation wave can be described as a strong shock wave supported by the heat release from a high-temperature flame behind an induction zone. Interesting features have been observed both in the 1-D and 2-D simulations, characterized by the coupling of the fluid dynamics and chemical kinetics. The study of flame-shock coupling is an on-going research topic [17] and certainly can be aided with GPU computing when the evolution of the detonation wave needs to be resolved at a very fine spatial scale.

The evolution of the pressure and temperature of a wall-spark ignited detonation is shown in Fig. 11. The chemical kinetics is modeled using the reduced H_2 –air mechanism which consists of 9 species gas mixture with 38 reactions. The mechanism used for the simulation is taken from the shock tube study by Jachimowski [18]. The computational domain is rectangular with a length of 20 cm and a height of 2 cm. The grid spacing in both directions is $50 \mu\text{m}$. The detonation cells, between the shock and the multiple triple points in transverse motion, are clearly seen. Fig. 12 illustrates the numerical soot film produced by recording the maximum density reached at each computation cell over the entire simulation time which is used to measure the cell structure. This well-known cellular structure has been observed both in experiments and numerical simulations. Various techniques in reproducing these images are discussed by Sharpe and Radulescu [19]. We will show in the next section how the superior performance of the GPU can enhance our ability in modeling reactive flows.

6.2. Performance results

Fig. 13 shows the performance of the solver for the simulation considering only the fluid dynamics aspect using the MP5 and the

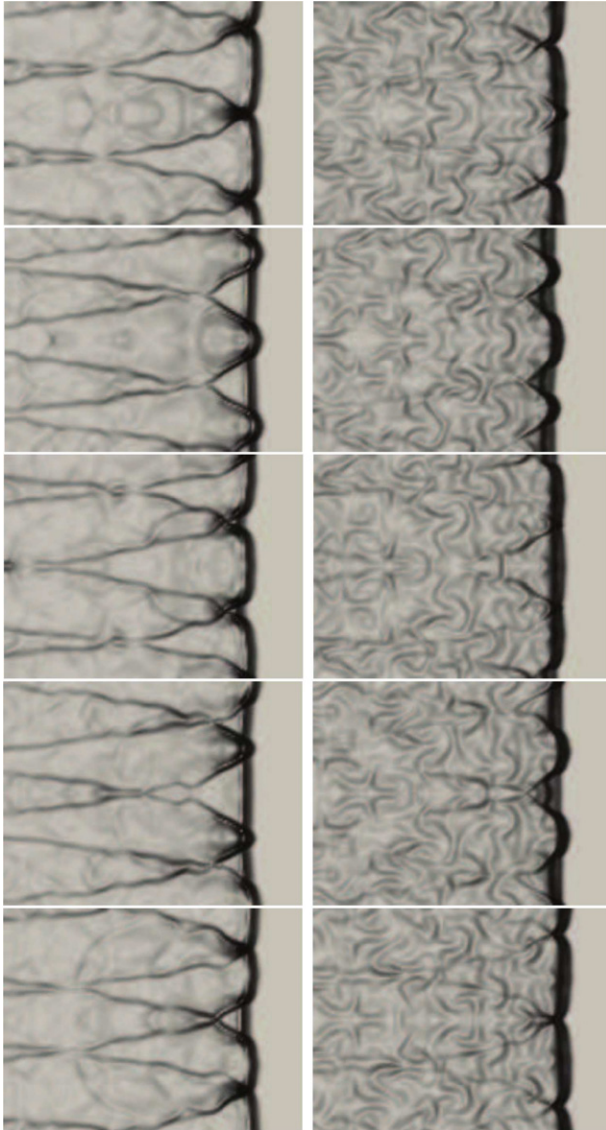


Fig. 11. Evolution of the pressure and temperature in a 2D detonation simulation.

ADERWENO schemes. All the comparisons reported in this paper are made between a Tesla C2070 GPU and an Intel Xeon X5650 CPU (single thread), both of which are using double precision calculation. Since the ADERWENO scheme only requires single-stage time integration, it is faster than the MP5 scheme. For the ADERWENO scheme, we can obtain almost 60 times speed-up for a large grid which is about twice faster than the MP5 scheme. The speed-ups obtained in both cases are very promising.

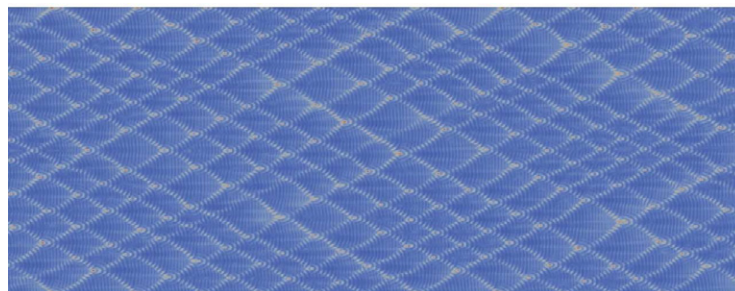


Fig. 12. Numerical soot film produced by recording the maximum density at each grid cell over the entire simulation.

The performance of the kinetics solver depends strongly on the memory access efficiency. Since the Gaussian elimination algorithm requires issuing a large amount of memory instructions (both *Read* and *Write*) to modify all the entries of the Jacobian, it is important to achieve high memory bandwidth while maintaining sufficient independent arithmetic operations to hide memory latency. The efficiency of the memory access scheme is very crucial in the case when the whole Jacobian is stored inside global memory (DRAM) which has much higher latency than shared memory. Fig. 14 illustrates the memory access efficiency of the GPU kernel performing the Gaussian elimination procedure. The figure shows that coalesced memory access results in much higher memory bandwidth comparing to the non-coalesced pattern for the same number of operations. The memory bandwidth obtained with this operation is approximately 80% of the theoretical peak limit of the device (144 GB/s for a Tesla C2050). Similar tests were performed for a species count ranging from 5 to 200. The results shown in Fig. 14 indicate that the global memory access pattern in the first approach (global memory) with coalesced memory access is very efficient. This access pattern is used consistently in the global memory approach stated in the remainder of the paper.

In the second approach, referred as the shared memory approach, we utilized shared memory to compensate for DRAM latency issues exhibited in the first approach. However, due to the memory intensive nature of the detailed chemical kinetics problem and the limitation of shared memory storage, there is a substantial amount of DRAM access required which cannot be avoided. The memory bottleneck introduces additional memory latency which can affect the performance of the kernel. Fig. 15 shows the performance of the kinetics solver only (i.e., without convective transport). Although the construction of the chemical Jacobian and source terms can also be a time intensive process, in the present study, we wish to focus on the more computational intensive process of solving the linear system and its scaling. Hence, the performance is measured by solving a number of linear systems $A \cdot x = b$ with different system sizes (N_s) and grid sizes (N_{cell}).

We described two different implementation approaches in our earlier discussion. The first approach is to store everything on global memory and try to achieve high memory bandwidth by coalesced memory reads. The second approach is to transfer memory to shared memory for each row elimination. Fig. 15 shows that the global memory approach outperforms the shared memory version in all cases. Since the shared memory approach requires additional memory transfers between each row elimination, it is only effective when N_s is large. It is shown in Fig. 15 that the algorithm is only effective when $N_s > 100$. In contrast, the performance of the global memory version depends strongly on the size of the grid. Since the parallelization is achieved across all the computational cells, solving a large number of systems makes it much more efficient. The global memory version seems to perform well in all cases. The speed-up obtained for the global memory is at least 30.

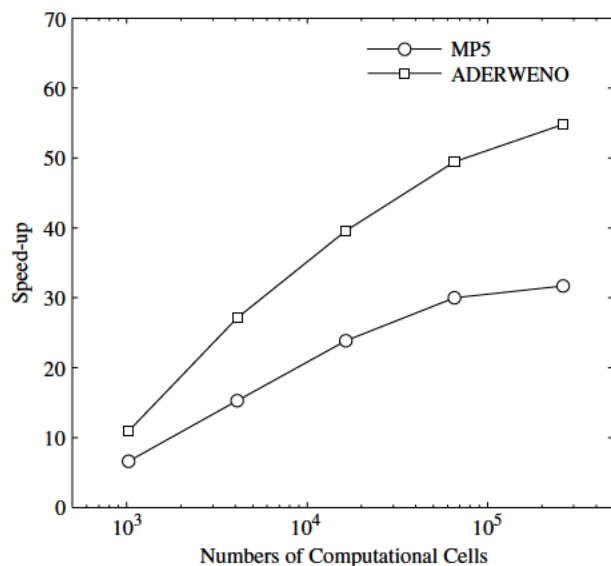


Fig. 13. Performance of the fluid dynamics simulation only (i.e., no chemical reactions). Comparison is made between two different schemes: MP5 and ADERWENO (both 5th order in space and 3rd order in time).

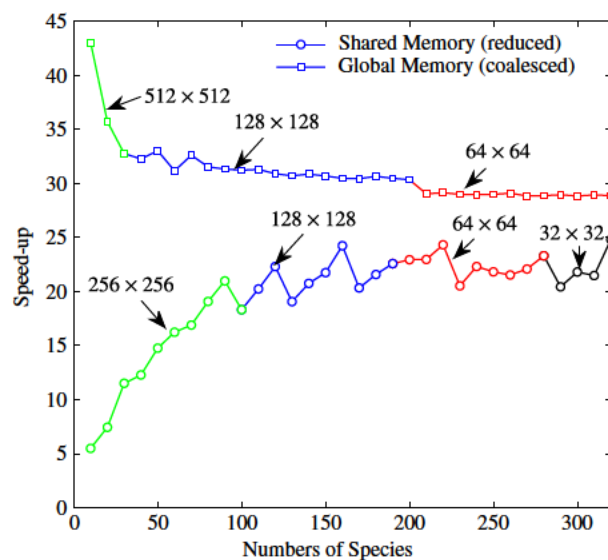


Fig. 15. Comparison of the speed-up factor obtained from the kinetics solver using both global memory (square line) and shared memory (circle line) approaches. Different colors indicate different grid sizes.

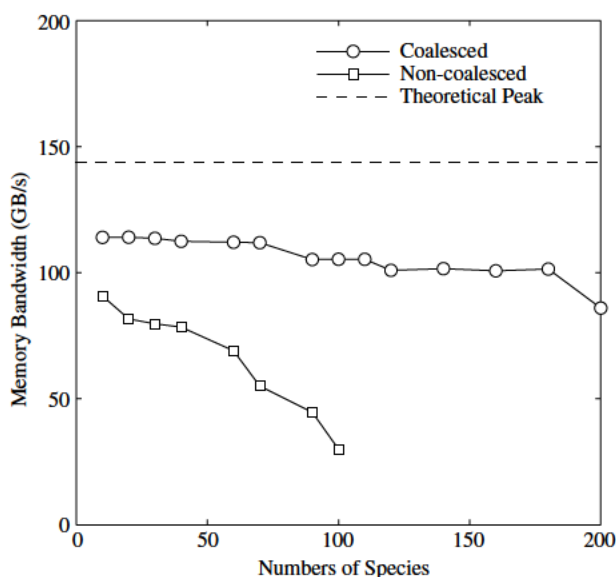


Fig. 14. Memory bandwidth of the kinetics solver measured on a Tesla C2050 for both coalesced and non-coalesced memory access. The memory bandwidth for both cases are compared with the theoretical bandwidth of a Tesla C2050 GPU to demonstrate the efficiency of the memory access scheme.

The speed-up obtained in the shared memory approach is approximately 20 for a species count ranging from 100 to 300.

Due to memory constraint, it became necessary for us to vary the grid size as the number of species increases. Thus, we were able to consider a 512×512 grid of cells for up to 25 species, then a 128×128 grid was possible up to 200 species, etc. The intense memory usage comes from the need to store a $N_s \times N_s$ Jacobian for each computational cell (e.g. this variable alone adds up to more than 5 GB of global memory for 200 species on the 128×128 grid). Some of the GPU's memory load can be alleviated by storing only the Jacobian for a segment of the domain; for example, a calculation of a 512×512 grid can be decomposed into 4 kernels, each of which performs calculation on a 512×128 grid. For this strategy to be effective, the decomposed domain must be sufficiently large, i.e. of the order of the number of streaming processors in the GPU, and the overhead for each kernel call is

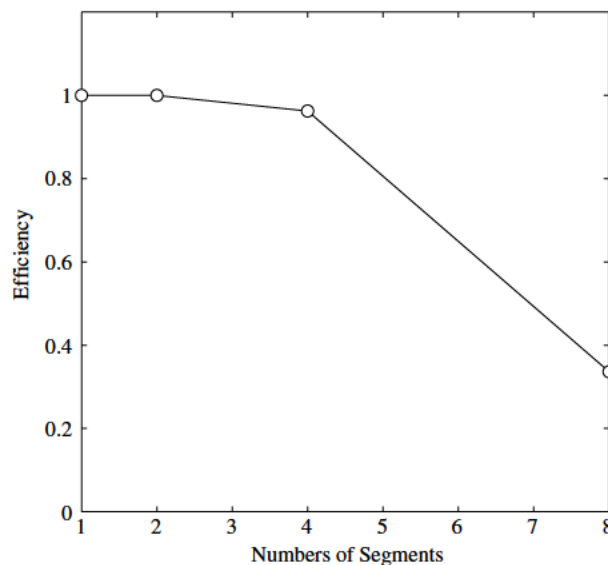


Fig. 16. Kinetics calculation of a 128×128 grid with 100 species. The calculation is done by decomposing the computational domain into numbers of segments (i.e., number of kernel calls).

small. The important of the domain size is highlighted in Fig. 16 where the calculation is performed for a grid with a fixed size of 128×128 with 100 species and varying number of segments. In this test case, the overhead due to the decomposition is negligible up to 4 segments. When the domain is further divided into 8 segments, the size of each segment gets smaller (2048 cells) and this strategy is no longer effective.

Fig. 17 shows the performance of the flow solver coupling with the chemical kinetics. The result shown in the plot is for a reduced H_2 -air mechanism consisting of 9 species and 38 reactions (both forward and backward). MP5 scheme is utilized in all cases. Although ADERWENO scheme has shown to be faster than MP5 in the case of convective transport, we do not expect to see significant difference in the performance because the computation time is dominated by chemical kinetics rather than convection. The overall performance is greatly dependent on the performance of the kinetics solver. It is clear that the global memory approach

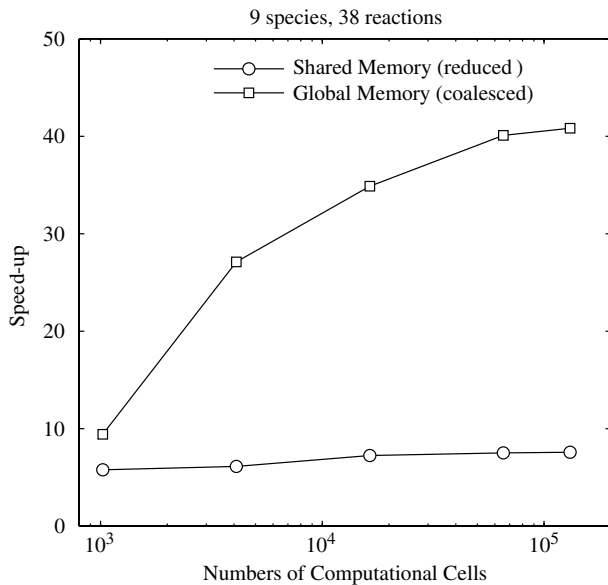


Fig. 17. Performance of the reactive flow solver for a 9-species gas with 38 reactions.

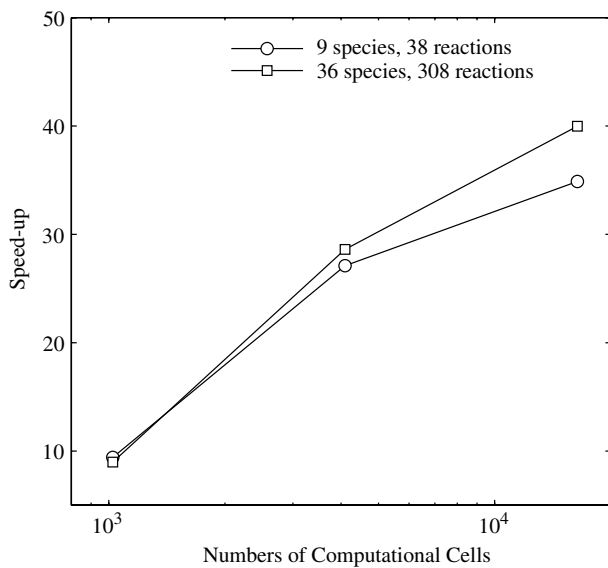


Fig. 18. Performance of the reactive flow solver for two different chemistry mechanisms (H_2 -air and CH_4 -air).

outperforms the shared memory approach. This is consistent with the results obtained earlier for the fluid dynamics and the kinetics separately. As the grid size increases, the speed-up factor obtained for the shared memory approach of the kinetics solver does not change rapidly. In contrast, the global memory approach results in a 40 times speed-up for a large grid.

We extend the simulation to model a larger mechanism of CH_4 -air detonation with 36 species and 308 reactions. The performance is compared with the previous result of H_2 -air detonation. Fig. 18 illustrates how the CH_4 -air detonation simulation achieves a greater speed-up than the H_2 -air detonation mainly because of better performance in the construction of the chemical kinetics Jacobian. This indicates that the performance of the rate calculation scales with the number of reactions; thus, we can expect better performance for a large number of reactions which makes it very attractive for CFD calculation of hypersonic flow and plasma where additional processes such as transitions between excited states of atoms and molecules need to be modeled.

7. Conclusion and future works

In the current paper, we described the implementation of a numerical solver for simulating chemically reacting flow on the GPU. The fluid dynamics is modeled using high-order shock-capturing schemes, and the chemical kinetics is solved using an implicit solver. Results of both the fluid dynamics and chemical kinetics are shown. Considering only the fluid dynamics, we obtained a speed-up of 30 and 55 times compared to the CPU version for the MP5 and ADERWENO scheme, respectively. For the chemical kinetics, we presented two different approaches on implementing the Gaussian elimination algorithm on the GPU. The best performance obtained by solving the kinetics problem ranges from 30 to 40 depending on the size of the reaction mechanism. When the fluid dynamics is coupled with the kinetics, we obtained a speed-up factor of 40 times for a 9-species gas mixture with 38 reactions. The solver is also tested with a larger mechanism (36 species, 308 reactions) and the performance obtained is faster than the small mechanism.

The current work can be extended in different ways. First, since the framework is performing well in shared memory architecture, it is possible to also extend it to distributed memory architecture utilizing Message Passing Interface (MPI). The extension permits using multi-GPU which is attracted for performing large-scale simulations. On the other hand, although the current simulation is done for chemically reacting flow, it is desired to extend it to simulate ionized gas (i.e. plasma) which requires modeling additional physical processes to characterize different excitation levels of the charged species (Collisional-Radiative kinetics). In addition, the governing equations also need to be extended to characterize the thermal non-equilibrium environment of the plasma. Given that the physics has been well established [20–22], the extension is certainly trivial.

Acknowledgment

The authors would like to thank Prof. Ann Karagozian of UCLA for countless support on performing simulation on the Hoffman2 GPU cluster.

References

- [1] NVIDIA Corporation, Compute Unified Device Architecture Programming Guide version 4.0, 2011.
- [2] T. Brandvik, G. Pullan, Acceleration of a 3D Euler Solver using Commodity Graphics Hardware, in: 46th AIAA Aerospace Sciences Meeting, AIAA paper 08-607.
- [3] E. Elsen, P. LeGresley, E. Darve, Large calculation of the flow over a hypersonic vehicle using a GPU, *J. Comput. Phys.* 227 (2008) 10148–10161.
- [4] A. Klockner, T. Warburton, J. Bridge, J. Hesthaven, Nodal discontinuous Galerkin methods on graphics processors, *J. Comput. Phys.* 228 (2009) 7863–7882.
- [5] H.-C. Wong, U.-H. Wong, X. Feng, Z. Tang, Efficient magnetohydrodynamic simulations on graphics processing units with CUDA, *Comput. Phys. Comm.* 182 (2011) 2132–2160.
- [6] J. Linford, J. Michalakes, M. Vachharjani, A. Sandu, Automatic generation of multi-core chemical kernels, *IEEE Transactions on Parallel and Distributed Systems* 22 (2011) 119–131 (Special Issue on High-Performance Computing with Accelerators).
- [7] J. Linford, J. Michalakes, M. Vachharjani, A. Sandu, Multi-core acceleration of chemical kinetics for modeling and simulation (2009).
- [8] E.F. Toro, *Riemann Solvers and Numerical Methods for Fluid Dynamics – A Practical Introduction*, second ed., Springer, 1999.
- [9] A. Suresh, H.T. Huynh, Accurate monotonicity-preserving schemes with Runge-Kutta time stepping, *J. Comput. Phys.* 136 (1997) 83–99.
- [10] V.A. Titarev, E.F. Toro, ADER schemes for three-dimensional nonlinear hyperbolic systems, *J. Comput. Phys.* 204 (2005) 715–736.
- [11] E.F. Toro, V.A. Titarev, TVD fluxes for the high-order ADER schemes, *Journal of Scientific Computing* 24 (2005) 285–309.
- [12] B. Einfeldt, C.D. Munz, P.L. Roe, B. Sjögren, On Godunov-type methods near low densities, *J. Comput. Phys.* 92 (1991) 273–295.
- [13] V. Volkov, Better performance at lower occupancy, in: GPU Technology Conference, 2010.
- [14] P. Woodward, P. Colella, The numerical simulation of two-dimensional fluid flow with strong shocks, *J. Comput. Phys.* 54 (1984) 115–173.

- [15] M. Van Dyke, *An Album of Fluid Motion*, Parabolic Press, Inc., 1989.
- [16] C.L. Gardner, J. Glimm, O. McBryan, R. Menikoff, D.H. Sharp, Q. Zhang, The dynamics of bubble growth for Rayleigh–Taylor unstable interfaces, *Phys. Fluids* 31 (1988) 447–465.
- [17] L.K. Cole, A.R. Karagozian, J.-L. Cambier, Stability of Flame-Shock Coupling in Detonation Waves: 1D Dynamics, *Combust. Sci. Technol.* 184 (10–11) (2012) 1502–1525.
- [18] C.J. Jachimowski, An analysis of combustion studies in shock expansion tunnels and reflected shock tunnels, Technical Report, NASA-TP-3224, 1992.
- [19] G.J. Sharpe, M.I. Radulescu, Statistical analysis of cellular detonation dynamics from numerical simulations: one-step chemistry, *Combust. Theory Model.* 15 (2011) 691–723.
- [20] M.G. Kapper, J.-L. Cambier, Ionizing shocks in argon. Part I: collisional-radiative model and steady-state structure, *J. Appl. Phys.* 109 (2011) 113308.
- [21] M.G. Kapper, J.-L. Cambier, Ionizing shocks in argon. Part II: transient and multi-dimensional effects, *J. Appl. Phys.* 109 (2011) 113309.
- [22] J.-L. Cambier, S. Moreau, Simulations of a molecular plasma in collisional-radiative nonequilibrium, AIAA paper 93-3196.

Appendix B:

Complexity reduction of collisional-radiative kinetics for atomic plasma

Hai P. Le

Ann R. Karagozian

Jean-Luc Cambier

Complexity reduction of collisional-radiative kinetics for atomic plasma

Hai P. Le,^{1,a)} Ann R. Karagozian,² and Jean-Luc Cambier^{3,b)}

¹ERC Inc., Edwards AFB, California 93524, USA

²Department of Mechanical and Aerospace Engineering, University of California, Los Angeles, California 90095, USA

³Air Force Research Laboratory, Edwards AFB, California 93524, USA

(Received 9 October 2013; accepted 3 December 2013; published online 23 December 2013)

Thermal non-equilibrium processes in partially ionized plasmas can be most accurately modeled by collisional-radiative kinetics. This level of detail is required for an accurate prediction of the plasma. However, the resultant system of equations can be prohibitively large, making multi-dimensional and unsteady simulations of non-equilibrium radiating plasma particularly challenging. In this paper, we present a scheme for model reduction of the collisional-radiative kinetics, by combining energy levels into groups and deriving the corresponding macroscopic rates for all transitions. Although level-grouping is a standard approach to this type of problem, we provide here a mechanism for achieving higher-order accuracy by accounting for the level distribution within a group. The accuracy and benefits of the scheme are demonstrated for the generic case of atomic hydrogen by comparison with the complete solution of the master rate equations and other methods. © 2013 AIP Publishing LLC. [<http://dx.doi.org/10.1063/1.4849417>]

I. INTRODUCTION

The ability to model plasma flows with non-equilibrium chemistry plays an important role in a number of applications including but not limited to plasma propulsion,¹ high-speed reentry flows,² plasma-assisted combustion and interpretation of laser diagnostics.³ In order to better understand the physical characteristics of the flow and the coupling with chemistry under the conditions of interests, one needs to accurately model all the non-equilibrium processes associated with the atoms and molecules (e.g., excitation, ionization, and dissociation) through collisional and radiative interactions.^{4–6} The most accurate treatment for these non-equilibrium plasmas requires a state-to-state approach,^{7–13} also referred to as collisional-radiative (CR) models, in which deviations from the equilibrium distribution of the internal states can be captured.

These CR models, although very accurate from a physics point of view, can be computationally very expensive due to the large number of internal states for which the number densities must be computed. For an atomic plasma, these states correspond to all the electronic excitation levels of the various neutral and ion species considered. For a molecular plasma, additional degrees of freedom such as the rotational and vibrational modes further increase the level of complexity. In addition, these molecular degrees of freedom are strongly coupled to the chemical reactions. For example, vibrational excitation facilitates dissociation or other endothermic reactions, and recombination can also favor the production of excited states. These models, derived from *ab initio* cross section databases for all elementary processes, can be applied to a wide range of plasma conditions and

offer more complete insight into the non-equilibrium effects. For example, a recent study of ionizing shocks in Argon by Kapper and Cambier^{10,11} demonstrated that this level of detail is needed for an accurate prediction of high-speed flows. In addition, the unsteady coupling of the hydrodynamics and CR kinetics leads to physical phenomena which can, in turn, provide additional information useful for model validation and/or experimental measurements of various parameters.

Due to the large computational workload involved in solving the CR master equations, simulations incorporating state-to-state kinetics have only been limited to zero- or one-dimension with a few exceptions of two-dimensional calculations.^{11,14,15} For example, the run-time for solving a set of rate equations for the CR kinetics of atomic hydrogen scales as the cubic power of the size of the atomic state distribution function (ASDF) when an implicit, backward-Euler method is employed. While better scaling laws could be obtained with iterative and more approximate schemes, their accuracy and stability for extremely stiff problems are still an issue. The development of very efficient and accurate schemes for CR kinetics is still an ongoing research topic which will be presented elsewhere; here, we discuss a different approach, consisting of lowering the complexity of the calculations by developing a reduced-order kinetic model suitable for multi-dimensional flow calculations while maintaining a sufficient level of detail required to accurately model the plasma. Several mechanism reduction schemes have been proposed in the literature with applications to various types of kinetics. Colonna *et al.*¹⁶ utilize a two-level distribution model to study nitrogen dissociation rates in recombining flows, in which all the vibrational levels except for the last level are modeled by a single energy equation with an assumption of a Boltzmann distribution, and the last vibrational level is modeled using state-to-state kinetics to take in account the non-equilibrium effects of the upper states. Magin *et al.*¹⁷ have

^{a)}Also at Department of Mechanical and Aerospace Engineering, University of California, Los Angeles, California 90095, USA.

^{b)}Author to whom correspondence should be addressed. Electronic mail: jean-luc.cambier@us.af.mil

developed a rovibrational collisional (RVC) coarse-grain model to characterize the internal energy excitation and dissociation processes of nitrogen flow behind a strong shock wave. The coarse-grain model is derived by lumping the rovibrational energy levels into groups, in which the population is described by a uniform distribution. Guy *et al.*¹⁸ proposed a multi-internal-temperatures models for a vibrationally non-equilibrium flow, in which the vibrational distribution is divided into two or three groups, each with its own vibrational temperature. Liu *et al.*,¹⁹ on the other hand, proposed a mechanism reduction to CR models based on the multi-group maximum entropy principle with the constraints being the macroscopic parameters.

In this paper, we examine several different level grouping schemes for the state-to-state kinetics of *atomic* electronic states. The first approach is similar to that of Magin *et al.*¹⁷ for the rovibrational collisional coarse-grain model and therefore is based on uniform (U) binning of the levels. The second approach here consists of grouping levels into groups with an assumed Boltzmann (B) distribution, allowing a higher-order description of the ASDF. In this case, the effective excitation temperatures are evolved in time by conserving a set of moments of the distribution function; the most obvious solution is to solve for number density and energy, similar to the approach by Guys *et al.*¹⁸ However, we will show that a different set of moment variables of the same order should be used, due to the specific nature of the ASDF.

The method developed here can be applied to a wide range of state-to-state kinetics models including the RVC^{13,17} and vibrational⁹ collisional (VC) models or the electronic collisional-radiative model.^{8,10–12,20} In the interest of simplicity, we consider here the CR model of atomic hydrogen, using classical models for the level energies and rates; the actual values of these parameters are unimportant here, as long as the structure of the ASDF is representative of the actual species, notably the geometric progression of the level energies of the ASDF and the stiffness ratio. The level grouping techniques are applied to reduce the cost of solving the full master equations and the results are compared with the reference solution computed from the full master equations.

The rest of the paper is organized as follows: we describe the state-to-state kinetics and numerical solution in Sec. II, while in Sec. III we describe the various mechanism reduction methods. We compare the results of the reduced-order models with the full set of master equations in Sec. IV and examine the issue of energy conservation in Sec. V. Finally, a summary is given in Sec. VI, while the derivation of the kinetic rates used in this study is given in Appendix.

II. COLLISIONAL-RADIATIVE MODEL

A. Definitions and rates

As mentioned above, we consider here the ASDF of atomic hydrogen coupled to electron impact excitation and ionization, and the reverse processes (respectively, deexcitation and recombination), as well as the radiative rates for line transitions in an optically thin approximation. Radiative

recombination is neglected and all radiation absorption is ignored, as is free-free (Bremsstrahlung) emission, since this does not directly affect the atomic level populations.²¹ The atomic states of the hydrogen atom are listed as a function of their principal quantum number (n) only, following the Bohr atomic model; the splitting of states with respect to orbital and spin numbers is ignored, and all states have a degeneracy $g_n = 2n^2$. The states number from $n = 1$ to ∞ and we consider a finite number of states $n = 1, \dots, M < \infty$ before reaching the ionization limit.²² In this simplified model, the energy of each state is given as $E_n = I_H(1 - 1/n^2)$, as measured from the ground state ($E_1 \equiv 0$), and we will denote by $I_n = I_H(1/n^2 - 1/M^2) \simeq I_H/n^2$ the energy required for ionization of level n .

The population density N_n is the number of atoms per unit volume of a state n . For a single bound-bound transition between states n and m ($m > n$) induced by electron-impact collisions, the rate of change of the population density is of the form

$$\frac{dN_n}{dt} = -\alpha_{(m|n)}^e N_n N_e + \beta_{(n|m)}^e N_m N_e. \quad (1)$$

Hereafter, we will use the convention of indexing the rates with the final state on the left, and the initial state on the right, i.e., $(f|i)$. The first term on the right of Eq. (1) describes the loss due to excitation from level n to m , as a result of collisions between free electrons (of number density N_e); the second term describes the gain due to collisional deexcitation from the state m , with number density N_m . Note that for the same transition between the levels n and m , we also have

$$\frac{dN_m}{dt} = +\alpha_{(m|n)}^e N_n N_e - \beta_{(n|m)}^e N_m N_e. \quad (2)$$

If there were only two states to consider, Eq. (1) would be the entire rate of change for level n , but since all transitions involving the state n must be counted, the rate of change for excitation and deexcitation alone involves summing up the right hand side over all levels $m \neq n$. At equilibrium (Boltzmann), the ratio of population densities is

$$\frac{N_m^*}{N_n^*} \equiv \mathcal{B}_{nm}(T_e) = \frac{g_m}{g_n} e^{-\Delta E_{nm}/kT_e}, \quad (3)$$

where $\Delta E_{nm} = E_m - E_n$ is the difference in level energies. For electron-impact processes, the rates α and β in Eqs. (1) and (2) are functions of T_e and are given by Eqs. (A9a) and (A9b) in Appendix. For low values of the energy gaps between levels ($\Delta E_{nm}/kT \ll 1$), both forward (α) and backward (β) rates become very large. This leads to a wide range of time scales as the number of levels is increased, and to a considerable stiffness in the system of equations. For example, Figure 1 demonstrates the increase in both the maximum eigenvalue (inverse time scale) and the spread of values, i.e., stiffness, as the plasma evolves as function of time. Additionally, Eqs. (A9a) and (A9b) show that the system is strongly diagonally dominant, in the sense that transitions with small changes in quantum number ($m - n \simeq 1$) have a

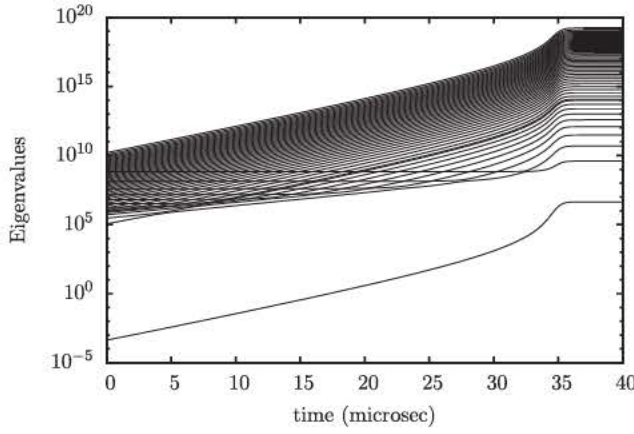


FIG. 1. Spectrum of eigenvalues of the CR system versus time, during constant T_e plasma evolution from a low temperature ASDF and low electron number density; as excitation and ionization proceed, the upper states and N_e increase, yielding a rapid growth of the characteristic frequencies.

higher rate than those with $m - n \gg 1$. In fact, a fairly good approximation here could be to consider a ladder process, i.e., transitions between neighboring states only, but this is not necessarily applicable to other atomic configurations, and this approximation is not used here.

For ionization and recombination processes, the rate of change of the population density for level n is

$$\frac{dN_n}{dt} = -\alpha_{(+|n)}^e N_n N_e + \beta_{(n|+)}^e N_+ N_e^2. \quad (4)$$

The first term on the right side is the loss due to ionization of that level by electron collisions (N_e), while the second term is due to the capture by an ion (N_+) of a free electron (one factor of N_e), in the presence of a second electron (leading to an N_e^2 dependence), required for energy conservation. The equilibrium for ionization and recombination (Saha) involves a different relation

$$\left(\frac{N_+ N_e}{N_n}\right)^* \equiv \mathcal{S}_n(T_e) = \frac{g_+}{g_n} 2 \left(\frac{2\pi m_e k T_e}{h^2}\right)^{3/2} e^{-I_n/kT_e}, \quad (5)$$

where g_+ is the degeneracy of the ion ground state (for atomic hydrogen, $g_+ \equiv 1$). Thus, we cannot assume that the equilibrium values are the same for both excitation/deexcitation and ionization/recombination processes. Usually, we can have Boltzmann equilibrium (3) without Saha equilibrium, but hardly the reverse, mostly because it takes more energy to ionize than to excite; for the upper states close to the ionization limit ($n \gg 1$), the difference is less significant.

Only the radiative transitions between atomic levels (“line,” or “bound-bound” emission) are considered here. For each bound-bound transition $m \rightarrow n$ ($m > n$), we have

$$\frac{dN_n}{dt} = +A_{(n|m)} N_m, \quad (6)$$

$$\frac{dN_m}{dt} = -A_{(n|m)} N_m. \quad (7)$$

B. Master equations

Once all the macroscopic rates are obtained, we can construct the master equations describing the collisional-radiative kinetics of all levels. In this study, we consider atomic hydrogen, which has only one ion state, and only electron collisions, which allows us to remove the superscript e in the rate definition hereafter. The rate of change of the population density of a level n is thus written as

$$\begin{aligned} \frac{dN_n}{dt} = & -\sum_{m>n} \alpha_{(m|n)} N_e N_n + \sum_{m>n} \beta_{(n|m)} N_e N_m + \sum_{m>n} A_{(n|m)} N_m \\ & + \sum_{m<n} \alpha_{(n|m)} N_e N_m - \sum_{m<n} \beta_{(m|n)} N_e N_n - \sum_{m<n} A_{(m|n)} N_n \\ & -\alpha_{(+|n)} N_e N_n + \beta_{(n|+)} N_+ N_e^2. \end{aligned} \quad (8)$$

Similarly, we can write another equation for the rate of change of the population density of the ions according to the rate of ionization or recombination

$$\frac{dN_+}{dt} = \sum_n \alpha_{(+|n)} N_e N_n - \sum_n \beta_{(n|+)} N_+ N_e^2. \quad (9)$$

Finally, the electron density is related to the ion density by the charge neutrality condition

$$N_e = \sum_q Z_q N_q. \quad (10)$$

We will compute the time evolution of a uniform plasma; if we assume a constant temperature bath, the conservation equations above constitute a complete set, but for constant-volume conditions with time variation of the temperature there is also conservation equation for the electron energy, which will be examined in more detail in Sec. V. The task of deriving a reduced model for the CR kinetics aims at modeling the shape of the ASDF at a lower computational cost compared to that required to solve the full master equations, while maintaining sufficient accuracy to capture the non-equilibrium effects. The most natural way to accomplish this is to partition the excited states into groups or “bins,” therefore reducing the number of variables in the system. Various assumptions can be made about the internal structure of each group, i.e., the distribution of states *within* the groups, and various approaches to solving the group-based variables can be devised.

C. Numerical solution

Examination of Eqs. (8) and (9) reveals that the full system of ODEs can be written in the following form:

$$\frac{dX_p}{dt} = -\mathbf{J}_p \cdot \mathbf{X}_p + \sum_q \mathbf{K}_{pq} X_q \quad \{p, q\} \in \{1, \dots, M, 1^+\}, \quad (11)$$

where X_p is the p -element of the vector of conserved variables for the set of master equations (8), $X_p \equiv N_p$ and \mathbf{J}_p , \mathbf{K}_{pq} are matrices built from summation over all possible transitions between levels, and are themselves functions of

X_p . Thus, the source term can generally be decomposed into a linear and non-linear terms. The system (11) can be solved using a variety of techniques. In this study, we have used a backward Euler scheme to avoid the stiffness of the CR kinetics. Expanding the general system (11)

$$dX_p = -(\mathbf{J}_p + d\mathbf{J}_p) \cdot (X_p + dX_p) + \sum_q (\mathbf{K}_{pq} + d\mathbf{K}_{pq})(X_q + dX_q) \quad (12)$$

and retaining 1st-order terms only, we obtain

$$\mathbf{A}_{pr} \cdot dX_r \simeq -\mathbf{J}_p \cdot X_p + \sum_q \mathbf{K}_{pq} \cdot X_q \quad (13)$$

with the Jacobian

$$\mathbf{A}_{pr} = (1 + \mathbf{J}_p)\delta_{pr} - \mathbf{K}_{pr} + X_p \left(\frac{\partial \mathbf{J}_p}{\partial X_r} \right) - \sum_q X_q \left(\frac{\partial \mathbf{K}_{pq}}{\partial X_r} \right). \quad (14)$$

For this implicit method, there is no stability restriction on the time step. For consistency, all the simulations shown in this paper utilized a constant time step. The same solution methodology is applied to the various cases of level groupings, where now some of the conserved variables in the set $\{X_p\}$ are summations over the levels within the groups/bins, while in the general case of non-isothermal plasma, it also includes the electron energy E_e .

III. LEVEL GROUPING STRATEGIES

A. Uniform grouping

Consider a group of M individual levels $i = \{n_0, \dots, n_{M-1}\}$, abbreviated as $i \in n$ and denote the group, or “bin” number by n ; hereafter, n, m, \dots are the group indices and i, j, \dots are level indices. This first approach to model reduction is essentially a zeroth-order approximation of the internal²³ distribution function, where only one moment variable, either the total number density of the group or the total excitation energy of the group, is required. The traditional choice is to conserve the total number density of the group, i.e., $\mathcal{N}_n = \sum_{i \in n} N_i$. Using Eq. (3), a Boltzmann approximation of the internal partition function \mathcal{Z}_n is obtained by²⁴

$$\mathcal{N}_n = N_{n_0} \sum_{i \in n} \frac{N_i}{N_{n_0}} \simeq \frac{N_{n_0}}{g_{n_0}} \underbrace{\sum_{i \in n} g_i e^{\Delta E_i/T_n}}_{\mathcal{Z}_n}, \quad (15)$$

where $\Delta E_i = E_i - E_{n_0}$ is the difference in energy between the level i and the first level of the group, n_0 . The approximation of a group with uniform internal distribution is equivalent to having a characteristic group temperature T_n approaching infinity, compared to the total energy width of the group, i.e.,

$$\mathcal{Z}_n \rightarrow g_n = \sum_{i \in n} g_i, \quad (16)$$

where g_n is the overall group degeneracy. The simplest model therefore consists of assuming all levels within the group to be distributed uniformly, i.e., weighted by the level degeneracy

$$N_i = \frac{g_i}{g_n} \mathcal{N}_n. \quad (17)$$

The rate equation for a group n is obtained by summing the master rate equations (8) and (9) for all the levels i within the group, and utilizing relation (15)

$$\begin{aligned} \frac{d\mathcal{N}_n}{dt} = & -N_e \mathcal{N}_n \left[\sum_{m>n} \sum_{i \in n} \frac{g_i}{g_n} \sum_{j \in m} \alpha_{(ji)} + \sum_{m<n} \sum_{i \in n} \frac{g_i}{g_n} \sum_{j \in m} \beta_{(ji)} \right] \\ & + N_e \mathcal{N}_m \left[\sum_{m<n} \sum_{i \in n} \sum_{j \in m} \frac{g_j}{g_m} \alpha_{(ij)} + \sum_{m>n} \sum_{i \in n} \sum_{j \in m} \frac{g_j}{g_m} \beta_{(ij)} \right] \\ & - \mathcal{N}_n \left[\sum_{m<n} \sum_{i \in n} \frac{g_i}{g_n} \sum_{j \in m} A_{(ji)} \right] + \mathcal{N}_m \left[\sum_{m>n} \sum_{i \in n} \sum_{j \in m} \frac{g_j}{g_m} A_{(ij)} \right] \\ & - N_e \mathcal{N}_n \left[\sum_{i \in n} \frac{g_i}{g_n} \alpha_{(+|i)} \right] + N_e^2 \mathcal{N}_+ \left[\sum_{i \in n} \beta_{(i|+)} \right]. \end{aligned} \quad (18)$$

Similarly for the ion state, one obtains

$$\frac{dN_+}{dt} = N_e \sum_n \mathcal{N}_n \left[\sum_{i \in n} \frac{g_i}{g_n} \alpha_{(+|i)} \right] - N_e^2 \mathcal{N}_+ \sum_n \left[\sum_{i \in n} \beta_{(i|+)} \right]. \quad (19)$$

The terms within brackets in Eqs. (18) and (19) contain *effective* rates for the groups, which can be pre-computed. For example, in the first term on the right-hand-side of Eq. (18)

$$\tilde{\alpha}_{(m|n)} = \sum_{i \in n} \frac{g_i}{g_n} \sum_{j \in m} \alpha_{(ji)}$$

is an effective excitation rate from group n to group m . Note that since this model does not require computing an excitation temperature T_n , all the effective transition rates between the groups can be expressed as a function of the kinetic temperature T_e only. It is important to emphasize that the grouping of levels is applied on the high energy states only; thus in any simulation we must choose a number of low-energy, “resolved” levels, as well as a variable number of groups combining the upper states. The number of discrete states, the number of groups and their widths are variable parameters of the model, whether we use uniform binning as above, or Boltzmann internal distributions, discussed below. In order to bound this parameter space (optimization is beyond the scope of the present work), we need to provide a reference solution, such that the population density of each level can be compared to the one reconstructed from the assumed internal distribution within each group. Figure 2 shows the evolution of the electron density computed from the master equations. This test corresponds to a strong ionization regime

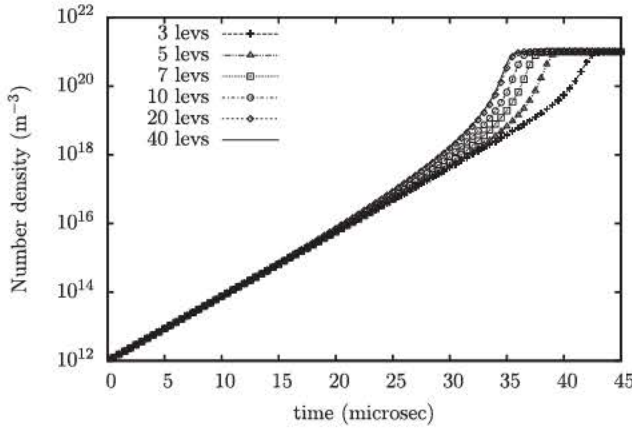


FIG. 2. Time evolution of the electron number density using different total number of atomic levels. The electron temperature is set at 3.0 eV.

and the time evolution of the ASDF shows an increasing population of the higher atomic levels while the electron density grows exponentially. It also demonstrates the effect of the number of levels included in the simulation, i.e., using a fewer number of atomic states has an impact on delaying the onset of the electron avalanche. This indicates that ionization from the high-energy states is an important process, and therefore the evolution of the upper states must be accurately captured. We could always increase the size of the ASDF to obtain higher accuracy, but with diminishing return; ultimately, the time-resolution of interest and the accuracy threshold dictate the number of levels required in a simulation. The mapping between the practical requirements and ASDF size is not a straightforward matter, but is an issue beyond the scope of this work. Convergence studies with respect to the size of the system showed that beyond 20 levels, there were no discernible differences in the results—see Figure 2. Thus, we chose our reference solution to be the one obtained for 20 levels, and all level-grouping models investigated here will be based on this extent of the ASDF.

B. Boltzmann grouping—Number and energy

Several assumptions can be made regarding a Boltzmann-like structure within the group. Panesi *et al.*¹² and Magin *et al.*²⁵ rely on the assumption that the population within a group follows a Boltzmann distribution at the kinetic temperature, i.e., in this case, $T_n \equiv T_e$. This approach is only valid if the rates of exchange between the levels within the group are much faster than the exchange rates with levels outside the group; otherwise, one could then assume that the entire ASDF is governed by T_e and is always in Boltzmann equilibrium. The validity of this assumption is highly questionable for atomic state populations.²⁶ Furthermore, when different collision partners must be considered, the kinetic temperature can be either that of the heavy particles or the electrons (e.g., electron-impact excitation and heavy impact quenching); in this case, choosing either one of the kinetic temperature can impact on the results.

In order to accurately describe the population of a group with a Boltzmann distribution, two moment variables of the

ASDF need to be conserved. The selection of these variables, however, can be arbitrary. Guy *et al.*¹⁸ conserved the total number density of the group and the average excitation energy; these, respectively, correspond to zeroth- and first-order moment variables, and would appear to be a natural choice. Consider the total number of states \mathcal{N}_n defined in Eq. (15) and the total energy within the bin $\mathcal{E}_n = \sum_{i \in n} E_i N_i$, for which we can write conservation equations, derived from Eq. (8)

$$\frac{d\mathcal{N}_n}{dt} = -N_e \mathcal{N}_n \left[\sum_{m>n} \sum_{i \in n} \frac{g_i e^{\Delta E_i/T_n}}{\mathcal{Z}_n} \sum_{j \in m} \alpha_{(j|i)} + \sum_{m<n} \sum_{i \in n} \frac{g_i e^{\Delta E_i/T_n}}{\mathcal{Z}_n} \sum_{j \in m} \beta_{(j|i)} \right] \dots \quad (20a)$$

$$\frac{d\mathcal{E}_n}{dt} = -N_e \mathcal{N}_n \left[\sum_{m>n} \sum_{i \in n} \frac{g_i e^{\Delta E_i/T_n}}{\mathcal{Z}_n} \sum_{j \in m} E_i \alpha_{(j|i)} + \sum_{m<n} \sum_{i \in n} \frac{g_i e^{\Delta E_i/T_n}}{\mathcal{Z}_n} \sum_{j \in m} E_i \beta_{(j|i)} \right] \dots \quad (20b)$$

For sake of brevity, we did not write the entire list of contributions in Eq. (20), which can be easily derived from Eq. (18) by generalizing the weighting factors g_i/g_n to $g_i e^{\Delta E_i/T_n}/\mathcal{Z}_n$, and similarly for other groups. By solving for total number and total energy of each group, according to Eqs. (20a) and (20b), we can guarantee direct conservation of both mass (total number of levels \mathcal{N}_n) and energy (\mathcal{E}_n). However, this approach presents some problems in determining the internal Boltzmann temperature, as will now be shown. First, let us define a total group/bin energy measured from the lower bound, i.e., $\Delta \mathcal{E}_n = \sum_{i \in n} (E_i - E_{n0}) N_i$; the rate of change of this shifted energy is still given by the right-hand-side of Eq. (20b). We can then write

$$\Delta \mathcal{E}_n = \frac{N_{n0}}{g_{n0}} \sum_{i \in n} g_i \Delta E_i e^{\Delta E_i/T_n} = \mathcal{N}_n \langle \Delta E \rangle_n, \quad (21)$$

where

$$\langle \Delta E \rangle_n = \frac{1}{\mathcal{Z}_n} \sum_{i \in n} g_i \Delta E_i e^{\Delta E_i/T_n} = T_n^2 \frac{d}{dT_n} \ln(\mathcal{Z}_n) \quad (22)$$

is the average group energy measured from the first internal level. Similarly, a specific heat at constant-volume can be determined, i.e.,

$$C_v(T_n) = \frac{d}{dT_n} \langle \Delta E \rangle_n = T_n^2 \left[\frac{\sum_{i \in n} g_i (\Delta E_i)^2 e^{\Delta E_i/T_n}}{\mathcal{Z}_n} - \langle \Delta E \rangle_n^2 \right] = T_n^2 \left[\langle \Delta E^2 \rangle_n - \langle \Delta E \rangle_n^2 \right]. \quad (23)$$

Since \mathcal{N}_n and \mathcal{E}_n are conserved variables, we obtain new values at each time level (k) and in order to compute the Boltzmann temperature T_n , we need to iterate the equation

$$\langle \Delta E \rangle_n(T_n^*) + C_v(T_n^*) \delta T_n^* = \frac{\Delta \mathcal{E}_n^{(k)}}{\mathcal{N}_n^{(k)}}, \quad (24)$$

where T_n^* is the running iterated value, until convergence ($\delta T_n^* \simeq 0$). However, the slope of the curve $\langle \Delta E \rangle_n(T_n)$ is extremely flat at low temperature, i.e., $C_v \rightarrow 0$. In fact, when $T_n \rightarrow 0$, to the leading order we have: $\mathcal{N}_n \simeq N_{n_0} o(1 + \epsilon)$, $\langle \Delta E \rangle_n \simeq o(\epsilon)$ and $C_v(T_n) \simeq o(\epsilon)$, where $\epsilon = e^{-\Delta E_1/T_n}$ is a small parameter. Therefore, during the iterations $\delta T_n^* = o(\epsilon)/o(\epsilon)$ and arbitrary temperature solutions can be obtained. Our studies showed that indeed, numerical instabilities prevent us from obtaining satisfactory solutions in many test cases. While it is possible to introduce limiters to prevent unphysical or improbable values and stop the iteration counters, this is not a satisfactory solution to the problem. We should also emphasize that the problem occurs when T_n is small, which does *not* imply that electronic levels are unpopulated, since we may very well have small *internal* group temperatures as a result of initial conditions or running iterations, but non-negligible overall electronic excitation ($\mathcal{N}_n \neq 0$).²⁷

C. Boltzmann grouping—Partitioning

In the approach above, we are dealing with two reduced variables \mathcal{N}_n and \mathcal{E}_n (or $\Delta \mathcal{E}_n$) which are both summations over the internal levels. An alternative may consist of keeping one of the level populations as a variable. Therefore, we could instead choose for each group n to conserve the population of the lowest level in that group N_{n_0} and \mathcal{N}_n , whose evolution is given by a form similar to Eq. (20a). To evaluate the Boltzmann temperature of the group, we now have at time step (k) , from Eq. (15):

$$\mathcal{N}_n^{(k)} = \frac{N_{n_0}^{(k)}}{g_{n_0}} \sum_{i \in n} g_i e^{-\Delta E_i/T_n} = \frac{N_{n_0}^{(k)}}{g_{n_0}} \mathcal{Z}_n(T_n^{(k)})$$

so that in order to evaluate the new bin temperature $T_n^{(k)}$ we need to solve

$$\mathcal{Z}_n(T_n^*) + \left(\frac{d\mathcal{Z}_n}{dT_n} \right) \delta T_n^* = \frac{\mathcal{N}_n^{(k)}}{N_{n_0}^{(k)}} g_{n_0} \quad (25)$$

until convergence. Using Eq. (22), this leads to

$$\delta T_n^* \simeq \frac{T_n^{*2}}{\mathcal{Z}_n(T_n^*) \langle \Delta E \rangle_n(T_n^*)} \left[\frac{\mathcal{N}_n^{(k)}}{N_{n_0}^{(k)}} g_{n_0} - \mathcal{Z}_n(T_n^*) \right], \quad (26)$$

where, again, the dependencies on temperature have been explicitly written. At low T_n , the denominator is $o(\epsilon)(1 + \epsilon)$ and the numerator is a difference between two terms of $o(1 + \epsilon)$. Therefore, the iterative procedure is again numerically unstable.

To attempt to alleviate this problem, we have examined yet another approach: for each group n we conserve the population of the lowest level in that group N_{n_0} and \mathcal{N}'_n , the total population of the *remaining* upper states n' of that group, such that $n = n_0 \cup n'$. This is an effective partitioning *within*

the group, which allows us to separate the variables, one of $o(1)$ and the other of $o(\epsilon)$. Clearly, we have now

$$\mathcal{N}'_n = \frac{N_{n_0}}{g_{n_0}} \underbrace{\sum_{i \in n'} g_i e^{-\Delta E_i/T_n}}_{\mathcal{Z}'_n} \quad \text{using} \quad N_i = \frac{\mathcal{N}'_n}{\mathcal{Z}'_n} g_i e^{-\Delta E_i/T_n}. \quad (27)$$

In order to evaluate the new temperature from the two conserved variables, we iterate on δT_n^* using a form similar to Eq. (25)

$$\mathcal{Z}'_n(T_n^*) + \left(\frac{d\mathcal{Z}'_n}{dT_n} \right) \delta T_n^* = \frac{\mathcal{N}'_n^{(k)}}{N_{n_0}^{(k)}} g_{n_0}. \quad (28)$$

However, it is easy to see that since $\frac{d}{dT} \mathcal{Z}' \equiv \frac{d}{dT} \mathcal{Z}$, we obtain a similar equation to Eq. (26):

$$\delta T_n^* \simeq \frac{T_n^{*2}}{\mathcal{Z}'_n(T_n^*) \langle \Delta E \rangle_n(T_n^*)} \left[\frac{\mathcal{N}'_n^{(k)}}{N_{n_0}^{(k)}} g_{n_0} - \mathcal{Z}'_n(T_n^*) \right].$$

In the same limit $T_n \rightarrow 0$, both numerators and denominators are of $o(\epsilon)$ and the temperature iterations are again unstable; this was verified through extensive tests under a variety of conditions and configurations. To avoid this systematic numerical problem, we must consider another way to evaluate the Boltzmann temperature inside each group.

Consider instead the following expansion of the partition function near the mean relative energy value $\overline{\Delta E}_n = \frac{1}{g_n} \sum_{i \in n} g_i \Delta E_i$. Defining $\delta_i \equiv \Delta E_i - \overline{\Delta E}_n$ as the shifted energy gap, we have

$$\begin{aligned} \mathcal{Z}_n(T_n) &= \sum_{i \in n} g_i e^{-\Delta E_i/T_n} = e^{-\overline{\Delta E}_n/T_n} \sum_{i \in n} g_i e^{-\delta_i/T_n} \\ &= e^{-\overline{\Delta E}_n/T_n} \sum_{i \in n} g_i \left[1 - \frac{\delta_i}{T_n} + \frac{1}{2} \frac{\delta_i^2}{T_n^2} + \dots \right] \\ &\simeq g_n e^{-\overline{\Delta E}_n/T_n} \left[1 + o(\langle \delta^2 \rangle / T_n^2) \right], \end{aligned} \quad (29)$$

where g_n is the total degeneracy see Eq. (16). Therefore, up to second-order in the approximate ratio of the bin width to the temperature, the partition function can be approximated by a single exponential function and the relation (29) can be inverted. If we use the (N_{n_0}, \mathcal{N}) pair of conserved variables, we have

$$\frac{\mathcal{N}'_n^{(k)}}{N_{n_0}^{(k)}} g_0 = \mathcal{Z}_n(T_n^{(k)}) \simeq g_n e^{-\overline{\Delta E}_n/T_n^{(k)}}. \quad (30)$$

However, the left-hand-side of Eq. (30) is $o(1 + \epsilon)$, and the right-hand-side should be as well. To see that this is the case, consider the first terms in the expansion of Eq. (29)²⁸

$$\mathcal{Z}_n(T_n) \simeq e^{-\overline{\Delta E}_n/T_n} \left[g_0 e^{-(\Delta E_0 - \overline{\Delta E}_n)/T_n} + g_1 e^{-(\Delta E_1 - \overline{\Delta E}_n)/T_n} + \dots \right].$$

Since $\overline{\Delta E} \simeq \Delta E_1$ and $\Delta E_0 \equiv 0$, the right-hand-side is $o(\epsilon)[o(1/\epsilon) + 1 + \dots] \simeq o(1 + \epsilon)$. Again, this is not a

desirable situation, since the evaluation of the group temperature T_n is of the form $1/\ln(1 + \epsilon)$, and is subject to significant errors. Furthermore, by computing the average gap $\overline{\Delta E}$ from the lower-bound of the energy bin, the requirement $\langle \delta \rangle \ll T_n$ may be hard to justify at low group temperature.

Instead, we can take advantage of the self-similar structure of the atomic spectrum (exact for hydrogen, approximate for other atoms) and the fact that the energy gaps become narrower as the level index increases. Thus, let us define the average energy counting from the first level *above* the lowest level, as obtained from \mathcal{Z}'_n , defined in Eq. (27)

$$\mathcal{Z}'_n = \sum_{i \in n'} g_i e^{\Delta E_i/T_n} = e^{\overline{\Delta E}'_n/T_n} \sum_{i > n_0} g_i e^{\delta'_i/T_n}. \quad (31)$$

By definition of the mean, the first-order term in the expansion of the exponential on the right-hand-side should be: $\sum_{i \in n'} g_i \delta'_i = 0$, where now $\delta'_i \equiv \Delta E_i - \overline{\Delta E}'_n$. This yields

$$\overline{\Delta E}'_n = \frac{1}{g'_n} \sum_{i \in n'} g_i \Delta E_i \quad \text{with} \quad g'_n = \sum_{i > n_0} g_i. \quad (32)$$

Therefore, $\overline{\Delta E}'$ differs from $\overline{\Delta E}$ only by a normalization factor, since $\Delta E_0 \equiv 0$. Note that $\overline{\Delta E}' > \Delta E_1$ and to *lowest-order*, $\mathcal{Z}'(T_n) \simeq g'_n e^{\overline{\Delta E}'_n/T_n} \simeq o(\epsilon)$. Using the conserved pair $(N_{n_0}, \mathcal{N}'_n)$, the group temperature is now estimated by

$$\frac{\mathcal{N}'_n(T_n)}{N_{n_0}} g_{n_0} = \mathcal{Z}'_n(T_n) \rightarrow T_n^{(k)} \simeq -\frac{\overline{\Delta E}'_n}{\ln \left[\frac{\mathcal{N}'_n g_{n_0}}{g'_n N_{n_0}} \right]} \simeq -\frac{1}{\ln(\epsilon)}. \quad (33)$$

This is now a stable computation when $\epsilon \rightarrow 0$. Furthermore, the approximation $\langle \delta \rangle \ll T_n$ is more justifiable since the largest value ($\delta_0 = E_{n_0} - \overline{\Delta E}$) is removed from the average.

We see that we now have the means to compute the internal group temperature from conserved variables without

risking fatal numerical errors; this is possible *only* by separating the lowest and upper levels within the group, i.e., by performing a sub-scale, internal partitioning of the group.²⁹ This is the approach used here for the last Boltzmann (hereafter denoted as B5) group we investigated, for which the appropriate pair of conserved variables to use is therefore $(N_{n_0}, \mathcal{N}'_n)$. Note that it is also possible to improve on the temperature evaluation by incorporating all higher-order terms into the definition of the total degeneracy, i.e.,

$$\mathcal{Z}'_n(T_n) = \tilde{g}'_n(T_n) e^{\overline{\Delta E}'_n/T_n} \rightarrow \frac{d\mathcal{Z}'_n}{dT_n} = \mathcal{Z}'_n(T_n) \cdot \left[\frac{\overline{\Delta E}'_n}{T_n^2} + \frac{d}{dT_n} \ln \tilde{g}'_n \right]. \quad (34)$$

If T_n^* is the running iteration, first evaluated by Eq. (33), successive estimates of $T_n^{(k)}$ are obtained, using Eq. (34), from:

$$T_n^{(k)} - T_n^* = \frac{\ln \mathcal{Z}'_n(T_n^{(k)}) - \ln \mathcal{Z}'_n(T_n^*)}{\left[\frac{d \ln \mathcal{Z}'_n}{dT_n} \right] (T_n^*)} \quad \text{where} \quad \mathcal{Z}'_n(T_n^{(k)}) = g_{n_0} \frac{\mathcal{N}'_n(T_n^{(k)})}{N_{n_0}^{(k)}}. \quad (35)$$

This iterative procedure can rapidly converge (as demonstrated in our tests) because we have an excellent approximation of the initial temperature from the lowest-order direct evaluation (33), and the $o(\epsilon)$ term has been factored as the leading term in the expansion. In other words, $\tilde{g}'_n(T_n)$ is a smooth function of temperature with a non-vanishing gradient, allowing gradient-descent iterations.

D. Boltzmann grouping—Effective rates

As before, the master equations are used to derive the conservation equations for the two new variables $(N_{n_0}, \mathcal{N}'_n)$, by setting $i = n_0$ for the first one, and summing over all levels $j \in n'$ in the second case. The latter yields the following:

$$\begin{aligned} \frac{d\mathcal{N}'_n}{dt} = & -N_e \mathcal{N}'_n \left[\sum_{m > n} \sum_{i \in n'} \frac{g_i e^{\Delta E_i/T_n}}{\mathcal{Z}'_n} \sum_{j \in m} \alpha_{(j|i)} + \sum_{m < n} \sum_{i \in n'} \frac{g_i e^{\Delta E_i/T_n}}{\mathcal{Z}'_n} \sum_{j \in m} \beta_{(j|i)} \right] \\ & + N_e \mathcal{N}_m \left[\sum_{m < n} \sum_{i \in n'} \sum_{j \in m} \frac{g_j e^{\Delta E_j/T_m}}{\mathcal{Z}_m} \alpha_{(i|j)} + \sum_{m > n} \sum_{i \in n'} \sum_{j \in m} \frac{g_j e^{\Delta E_j/T_m}}{\mathcal{Z}_m} \beta_{(i|j)} \right] \\ & - \mathcal{N}'_n \left[\sum_{m < n} \sum_{i \in n'} \frac{g_i e^{\Delta E_i/T_n}}{\mathcal{Z}'_n} \sum_{j \in m} A_{(j|i)} \right] + \mathcal{N}_m \left[\sum_{m > n} \sum_{i \in n'} \sum_{j \in m} \frac{g_j e^{\Delta E_j/T_m}}{\mathcal{Z}_m} A_{(i|j)} \right] \\ & - N_e \mathcal{N}'_n \left[\sum_{i \in n'} \frac{g_i e^{\Delta E_i/T_n}}{\mathcal{Z}'_n} \beta_{(n_0|i)} + \sum_{i \in n'} \frac{g_i e^{\Delta E_i/T_n}}{\mathcal{Z}'_n} A_{(n_0|i)} \right] - N_e \mathcal{N}'_n \left[\sum_{i \in n'} \frac{g_i e^{\Delta E_i/T_n}}{\mathcal{Z}'_n} \alpha_{(+|i)} \right] + N_e^2 N_+ \left[\sum_{i \in n'} \beta_{(i|+)} \right]. \quad (36) \end{aligned}$$

Note that we have used the total number $\mathcal{N}_m = N_{m_0} + \mathcal{N}'_m$ and the group total partition function $\mathcal{Z}_m = g_{m_0} + \mathcal{Z}'_m$ in the expressions on the right hand side, only as a way to group terms and lead to simpler expressions; the conserved

variables remain N_{m_0} and \mathcal{N}'_m . Equation (36) takes in account all the interactions between the groups, assuming the Boltzmann distribution approximation within each group. The effective rates for group transitions can be expressed

(and tabulated) as a function of two temperatures: the kinetic temperature T_e and the group excitation temperature T_n . Notice also that because of the bin-averaging, the effective radiative transition rates have also become temperature-dependent (T_n).

Similarly, the rate of change of the number density of the ground state of each group is

$$\begin{aligned} \frac{dN_{n_0}}{dt} = & -N_e N_{n_0} \left[\sum_{m>n} \sum_{j \in m} \alpha_{(j|n_0)} + \sum_{m<n} \sum_{j \in m} \beta_{(j|n_0)} \right] \\ & + N_e \mathcal{N}_m \left[\sum_{m<n} \sum_{j \in m} \frac{g_j e^{\Delta E_j/T_m}}{\mathcal{Z}_m} \alpha_{(n_0|j)} \right. \\ & + \left. \sum_{m>n} \sum_{j \in m} \frac{g_j e^{\Delta E_j/T_m}}{\mathcal{Z}_m} \beta_{(n_0|j)} \right] - N_{n_0} \left[\sum_{m<n} \sum_{j \in m} A_{(j|n_0)} \right] \\ & + \mathcal{N}_m \left[\sum_{m>n} \sum_{j \in m} \frac{g_j e^{\Delta E_j/T_m}}{\mathcal{Z}_m} A_{(n_0|j)} \right] \\ & + N_e \mathcal{N}'_n \left[\sum_{i \in n'} \frac{g_i e^{\Delta E_i/T_n}}{\mathcal{Z}'_n} \beta_{(n_0|i)} + \sum_{i \in n'} \frac{g_i e^{\Delta E_i/T_n}}{\mathcal{Z}'_n} A_{(n_0|i)} \right] \\ & - N_e N_{n_0} [\alpha_{(+|n_0)}] + N_e^2 N_+ [\beta_{(n_0|+)}]. \end{aligned} \quad (37)$$

Again, using the total number of levels $\mathcal{N}_m = N_{m_0} + \mathcal{N}'_m$ on the right-hand-side allows us to consider together transitions between lowest states at the boundaries of different groups ($N_{n_0} - N_{m_0}$), as well as the transitions with the excited sub-partitions ($N_{n_0} - \mathcal{N}'_m$) and simply the expressions. Since the ion is conserved here as an individual state, the rate of change of its number density remains the same but can be rewritten in terms of the group number densities

$$\begin{aligned} \frac{dN_+}{dt} = & N_e \sum_n \mathcal{N}_n \left[\sum_{i \in n} \frac{g_i e^{\Delta E_i/T_n}}{\mathcal{Z}_n} \alpha_{(+|i)} \right] \\ & - N_e^2 N_+ \left[\sum_n \sum_{i \in n} \beta_{(i|+)} \right]. \end{aligned} \quad (38)$$

Each term in brackets in Eqs. (36)–(38) is an effective rate for transfer between the group variables (N_{n_0}, \mathcal{N}'_n), $\forall n$. As mentioned in Sec. III A, both individual levels and groups (uniform or Boltzmann) are considered when solving the ASDF. The few individual states are the lowest in the energy scale, with the largest successive gaps, while the multitude of upper levels is distributed into a variable number of groups. This is justified on the basis of the kinetic rates (see the stiffness ratios of Figure 1), and as justification of the expansion (29).

IV. ACCURACY OF UNIFORM AND BOLTZMANN METHODS

A. Isothermal ionization test case

In the previous section, we have discussed several approaches to the level grouping strategy; these are summarized in Table I. This sequence of models was developed as a result of preliminary tests and the failure to obtain converged solutions for the group Boltzmann temperature T_n in many instances. Thus, we found that the *only* model which was

TABLE I. Summary of level grouping models investigated.

Model	Variables	Equations	T_n evaluation
U	\mathcal{N}_n	(18) and (19)	none
B1	$(\mathcal{N}_n, \mathcal{E}_n)$	(20a), (20b), and (38)	C_v unstable
B2	(N_{n_0}, \mathcal{N}_n)	(37) and (20a)	C_v unstable
B3	$(N_{n_0}, \mathcal{N}'_n)$	(37) and (36)	C_v unstable
B4	(N_{n_0}, \mathcal{N}_n)	(37) and (20a)	Eq. (29) unstable
B5	$(N_{n_0}, \mathcal{N}'_n)$	(37) and (36)	Eq. (31) stable

able to provide stable and satisfactory solutions for all test cases was model B5, using a sub-partition of the group into the ground level n_0 and the remainder, and the use of the form (31) for the partition function, which allowed us to factorize out the vanishingly small terms at low T_n . Therefore, considerations of the “equation of state” of the Boltzmann group dictated the correct approach to use here, and while all the models explored are listed in Table I, only the zeroth-order uniform binning described in Sec. III A and the B5 models are shown here and compared to the reference solution obtained from solving the full master equations; these are indicated as (U) and (B) models, respectively.

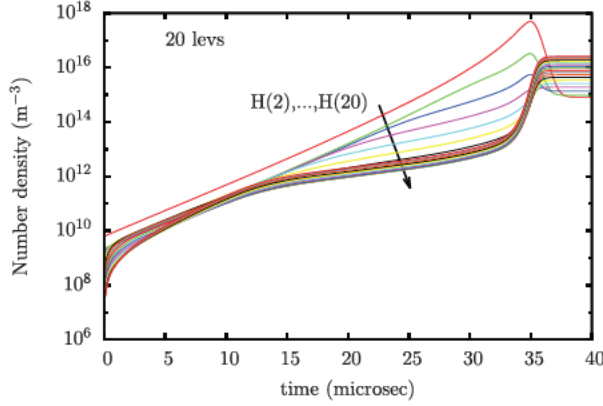
We conducted a large number of additional tests but for the sake of brevity, we are showing here the results of three representative cases: the initial conditions are summarized in Table II. For all the results shown in this section, a constant time step of 10^{-7} s had been used for the test cases in the ionization regime (cases 1 and 3), and a time step of 10^{-5} s was used for the recombination regime (case 2); the same backward-Euler scheme of Sec. II C was used throughout.

As indicated in Sec. III, the reference solution is based on the detailed kinetics for 20 atomic levels, while the group-based solutions will be based on a few low energy levels individually monitored, and with partitioning of the remaining upper states into a variable number of groups. The first test case is the iso-thermal relaxation in the excitation and ionization regime, i.e., the initial population of excited states and electron density is well below equilibrium.³⁰ This test case is the same as the one shown in Figure 2 for a variable number of electronic levels, solving for the full master equations (8) and (9). As the plasma relaxes towards equilibrium, an increasing number of electronic levels become populated and the electron number density grows exponentially, until an ionization cascade occurs. The rates increase very rapidly just before equilibrium, and the system becomes very stiff, as shown by the large spread of eigenvalues in Figure 1.

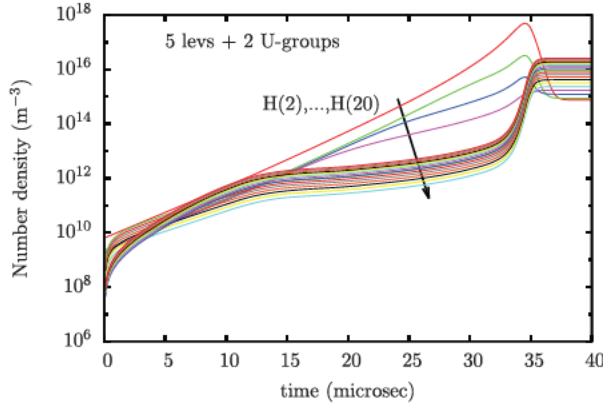
TABLE II. Initial conditions of test cases. For all cases, the total atomic density N_H is 10^{21} m^{-3} .

Case	T_e	x_e	N_+/N_H	N_n
1	3 eV	isothermal	10^{-9}	$(1 - x_e)N_H$ for $n = 1$ $10^{-20}N_H$ otherwise
2	1 eV	isothermal	Saha (3 eV)	Boltzmann (3 eV)
3	3 eV	isochoric	10^{-9}	$(1 - x_e)N_H$ for $n = 1$ $10^{-20}N_H$ otherwise

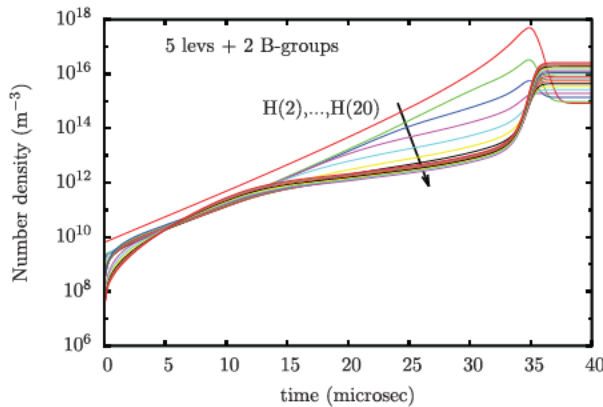
Figure 3 shows a comparison of the number densities of all the atomic states for the iso-thermal test case (1). In this simulation, the ground state and the first 4 excited states (1,...,5) are conserved as discrete levels while the remaining upper states (6,...,20) are partitioned into two groups, each of which has either a uniform or Boltzmann distribution. There are both significant and subtle differences in the traces



(a) Full solution with 20 levels.



(b) Solution with 5 levels and 2 Uniform groups



(c) Solution with 5 levels and 2 Boltzmann groups.

FIG. 3. Comparison of the time evolution of the excited states during the isothermal heating test case ($T_e = 3$ eV). From top to bottom: (a) full solution with 20 levels; (b) solution with 5 levels and 2 uniform groups; (c) solution with 5 levels and 2 Boltzmann groups. The first excited state $H(2)$ is the top curve, followed by the next higher level, etc.

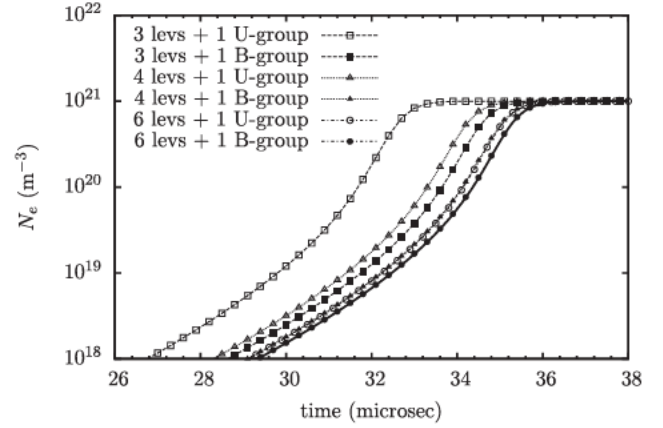


FIG. 4. Comparison between the solution obtained using both level grouping approaches. The solid line represents the full solution.

of the upper states. First, comparison of the uniform (Figure 3(b)) and Boltzmann (Figure 3(c)) grouping shows the influence of the assumed internal distribution, as the reconstructed levels of the groups are clearly separated in the uniform case. Second, comparison with the reference solution of Figure 3(a) shows that the Boltzmann groups are clearly more accurate. Slight differences remain in the very early stages of evolution³¹ below $1 \mu s$ for example and around $10 \mu s$.

The combined effect of the number of resolved lower levels and grouping strategy is shown in Figure 4. Generally speaking, one can clearly observe a dramatic improvement, for the same number of resolved levels, by switching from a uniform to Boltzmann group.³² By selecting the time of maximum rate of growth of the electron density as the approximate location of the avalanche ionization, we can measure the relative error in density. As shown in Table III, the error can be very substantial unless there is sufficient resolution of the ASDF kinetics, through the number of resolved lower levels and a higher-order (B) description of the groups. This is important when comparing, for example, with time-gated experimental results.

By conserving more discrete states and reducing the size of the upper state groups, the results are of course significantly improved. This is to be expected for ASDF kinetics, since the energy gaps are larger for the first levels, and grouping together these states would be less accurate, first by yielding excessive bin energy widths compared to mean energy and temperature scale violating the validity condition for the expansion (29) and also by disallowing

TABLE III. Relative error on electron density at peak rate of growth (approximately $33 \mu s$).

Method	Error (%)
3 levels + 1 U group	2618
3 levels + 1 B group	89.2
4 levels + 1 U group	165.8
4 levels + 1 B group	23.7
6 levels + 1 U group	20.9
6 levels + 1 B group	0.9

potential deviations from Boltzmann equilibrium in the most populated range of excited states.

There can of course be variations in the grouping strategy, but in all cases the general guidelines of keeping the *widths* of the groups small and the levels with the largest energy gaps as individual states are perfectly consistent with the objective of computational cost reduction, since the discrete lower energy states evolve more slowly and the upper states are numerous and have similar energy.³³

The relative accuracy of the grouping approaches can also be seen in Figure 5 where the ASDF is plotted at four different instances of time corresponding to $t = 10, 20, 30$, and $40 \mu\text{s}$. Both solutions with level grouping are obtained from using 3 atomic levels and 1 group of upper states. It is clearly seen that the Boltzmann group gives a more accurate representation of the upper states distribution during the heating process. We also showed in Figure 5 the results of a simplified model where it is assumed (see Sec. III B) that all groups have the same internal temperature, equal to the kinetic temperature, i.e., $T_b(n) \equiv T_e, \forall n$ (dashed line). This assumption is clearly violated, as shown in Figure 6, although the difference remains mostly confined to the upper states distribution. We should point out again that significant differences would be expected in a two-temperature kinetic system, i.e., including heavy-particle collisions.

We note also that the ASDF from the full solution indicates that the high lying states, starting from the third excited state, behave like a continuum state, although there appears to be two distinct sub-groups among the upper states, as can be seen most clearly at $t = 10 \mu\text{s}$. This suggests that the upper states are most effectively resolved by two groups or more, again confirming that relatively small widths of the groups are preferable, albeit at an increased computational expense. Figure 6 further illustrates this point by showing the evolution of the Boltzmann temperatures of the upper states, using here 4 discrete atomic states and partitioning the upper states into 3 groups. While the Boltzmann temperatures of the first two groups are close to each other, the temperature of the third group is slightly higher. This again confirms that the

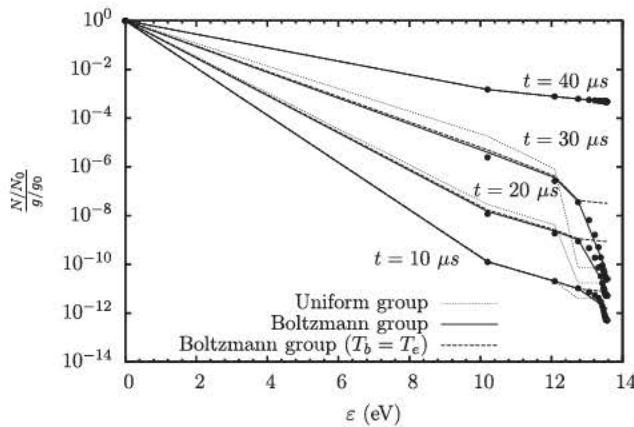


FIG. 5. The internal states population during the heating process at various times. The solid symbols are the full solution; the solid lines are the level grouping with Boltzmann distribution; the dotted lines are for level grouping with uniform distribution; dashed lines are for a simplified model with $T_b \equiv T_e$.

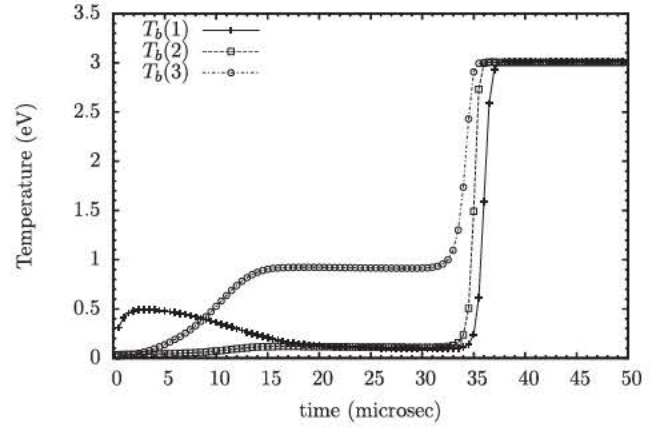


FIG. 6. Boltzmann temperature of the upper states.

upper states need to be resolved by at least 2 groups. When the system is near equilibrium, both approaches give similar results.

In these simulations, we have assumed that the plasma is optically thin to all the radiation from the line transitions. Spectral signatures being a major diagnostic tool for determining plasma conditions, it is important to know the CR kinetics in detail in order to match experimental data. Usually, this is accomplished by post-processing the numerical solution with a highly resolved spectral code including radiation transport (RT) if necessary with detailed computation of line shapes. This approach is accurate if the key parameters of such a spectral model, in particular N_e and T_e , are also very accurate. As discussed above and shown in Table III, our Boltzmann grouping procedure provides a significant improvement over conventional approaches, leading to a potentially much more accurate spectral signature prediction in transient and non-equilibrium plasma conditions. In addition, the ASDF solution is much closer to the true physical state, which may also lead to faster integration of the detailed CR kinetics with RT. These will be investigated in the future.

Accurate evaluation of the radiative emission is also important during the computation of flow dynamics, from simple reasons of power coupling, e.g., radiative cooling. Figure 7 shows the radiative losses due to bound-bound radiation from the upper states (5,...,20) to the first three atomic states (1, 2, 3) computed by grouping all the upper states together as a single group with a Boltzmann distribution. Although this is a somewhat coarse approximation to the ASDF, it is clear that the grouping scheme provides an excellent approximation to the radiative power. An accurate reproduction of the radiative spectrum depends inevitably on the reconstructed population of the atomic levels and, as can be seen by comparing the profiles in Figure 3, the agreement can be excellent.

B. Isothermal recombination test case

In this case, we performed a cooling test where the plasma is suddenly brought down from 3 eV to 1 eV. Thus, the simulation was run at a constant temperature ($T_e = 1 \text{ eV}$), while the initial conditions are the Boltzmann and Saha equilibrium values at 3 eV; these are exactly the conditions which would be obtained at the end of the first test case in

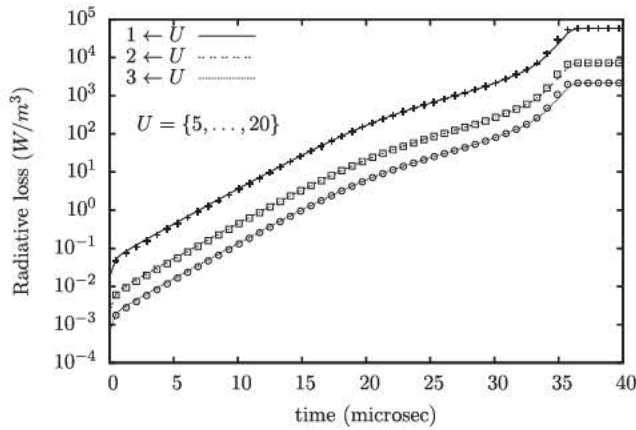


FIG. 7. Radiative loss due to bound-bound radiation from the upper states to the first 3 atomic states. The lines indicate the solution obtained from the full CR kinetics. The dots represent solution obtained with level grouping (5 levels + 1 group).

the absence of radiative losses. For all the simulations shown in this case, a constant time step of 10^{-5} s has been used.

In this case, the cooling process occurs very rapidly and the plasma is in a deexcitation and recombination regime; the ground state and the electron number densities are quickly adjusted to their new equilibrium values, as can be seen in Figure 8. Strictly speaking, since bound-bound radiation is assumed to be optically thin, the system cannot reach equilibrium. However, a quasi-equilibrium state is achieved at approximately 1 ms, after which the bound-bound radiation is the dominant *net* rate of change and the system continues to cool down at the radiative time scales. Note also that the uniform grouping is significantly less time-accurate than the Boltzmann method, as was already the case in the ionization regime—see Figure 4.

Figure 9 shows the evolution of the excited states as function of time for reference, uniform groups and Boltzmann groups. Once again, there is a noticeable discrepancy between the reference solution and the uniform bin model, especially concerning the red curve which crosses other levels during the relaxation process. This curve is the density of H(2), the first excited state, and is an effect of the

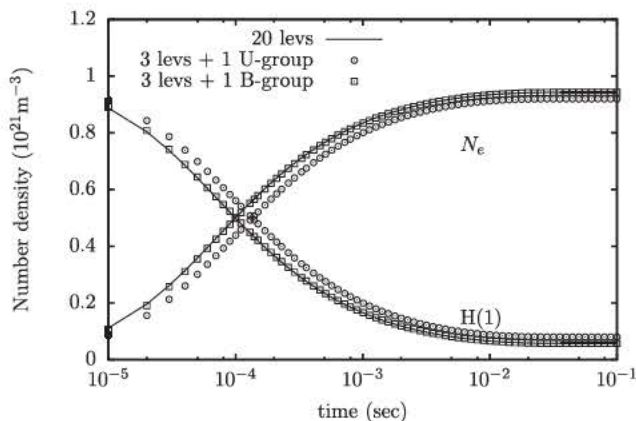
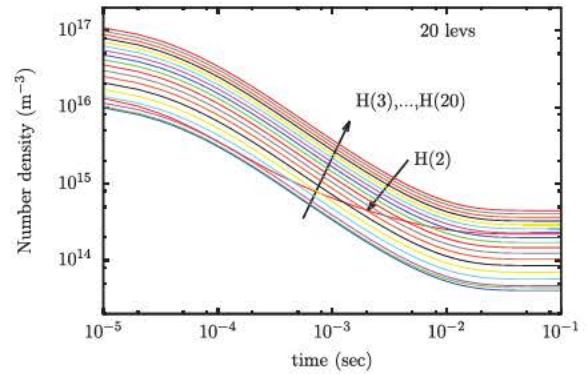
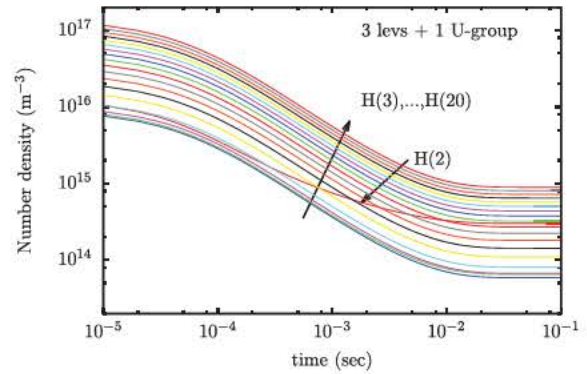


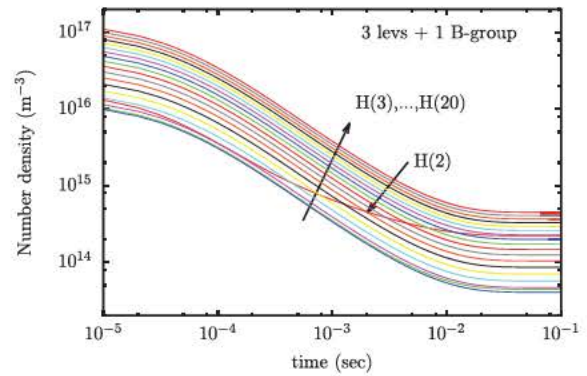
FIG. 8. Comparison of the time evolution of the ground state and the free electrons during the isothermal cooling process (3 eV \rightarrow 1 eV) using level grouping with uniform and Boltzmann distribution (3 levels + 1 group).



(a) Full solution with 20 levels.



(b) Solution with 3 levels and 1 Uniform group



(c) Solution with 3 levels and 1 Boltzmann group.

FIG. 9. Comparison of the time evolution of the excited states during the isothermal cooling test case (T_e 1 eV). From top to bottom: (a) full solution with 20 levels; (b) solution with 3 levels and 1 uniform group; (c) solution with 3 levels and 1 Boltzmann group. H(3) is the bottom curve, followed by the next higher level, etc.; the non conforming red curve is H(2). The higher population densities as the level index increases include the increase of the level degeneracy.

strong radiative decay of this state. Notice that the plot starts at $t = 10^{-5}$ s, i.e., the first implicit time step, but already the solution is far from the Boltzmann equilibrium which is the initial condition at $t = 0$, such that there is a population inversion with respect to H(2) for many upper states. Notice also that the time scale is logarithmic, and the processes considerably slow down as the electron density drops significantly. Because we are considering only electron impact collisions, the ASDF essentially becomes “frozen” in a quasi-static but

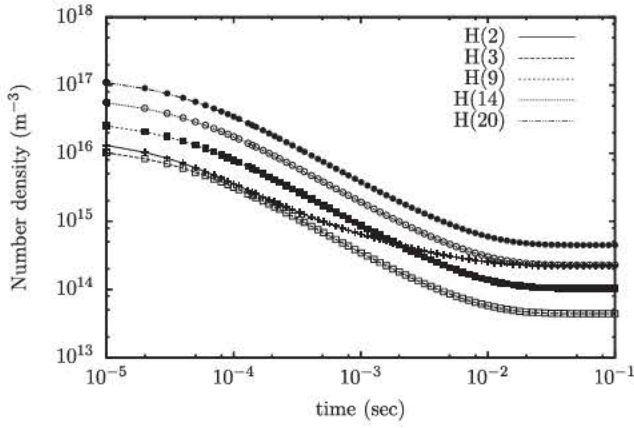


FIG. 10. Comparison of the time evolution of the excited states number densities during the isothermal cooling process. The lines are full solution. The dots represent solution obtained with level grouping (3 levels + 1 B group).

non-equilibrium state. If collisions by heavy particles were also considered, these would rapidly become the dominant process, leading to faster relaxation towards equilibrium. However, in some case of rapid plasma expansion, similar “frozen-in” non-equilibrium distribution functions of the ASDF could be obtained.

To better appreciate the accuracy of the Boltzmann grouping procedure, Figure 10 shows the evolution of several excited states compared to the exact solution and similarly to the “heating” (ionization) case, excellent agreement was obtained. In this simulation, the first 3 atomic states (1, 2, 3) are conserved as discrete levels and the upper states (4,...,20) are lumped into 1 Boltzmann group.

Finally, we show in Figure 11 the snapshots of the ASDF during the recombination. Contrary to the case of ionization, the upper states are not depleted but enhanced instead as expected, since the recombination proceeds preferentially onto the upper states. As a reflection of the observation made for Figure 10, the agreement is excellent for all atomic states.

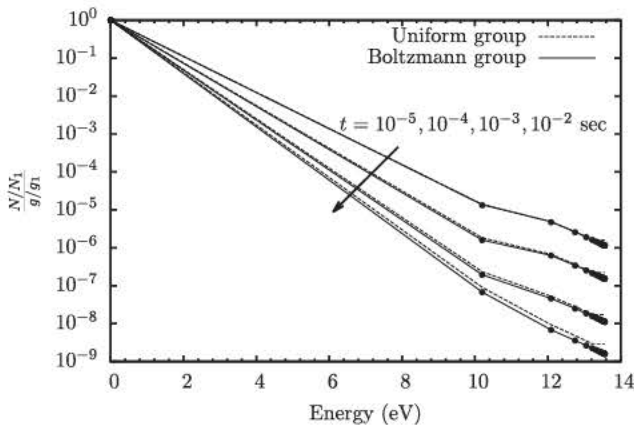


FIG. 11. Snapshots of the ASDF at several times during the cooling process. The dots represent the full solution. The solid lines are the solution obtained using the level grouping with Boltzmann distribution. The broken lines are the solution obtained using the level grouping with uniform distribution.

V. ENERGY CONSERVATION

A. Effective rates

The systems of equations (18) (19) and (36) (38) describe the complete evolution of the ASDF but for an isothermal plasma. In the more general case, the ASDF kinetics are coupled to the energy of the system; here, this includes only the total energy of the free electrons E_e . Thus for constant-volume or constant-pressure conditions, there must be an evolution equation for the energy or enthalpy (only constant-volume kinetics are considered here). We must then exert care that the formulation exactly conserves energy, i.e., that $E_e^{(k)} + \sum_n \mathcal{E}_n^{(k)}$ at any time level (k) remains the same within numerical round-off errors. If we were dealing with only electron-impact collisions, it would be sufficient to sum the energies of all levels using the new population densities at the end of the time step, compute the difference and assign the change to E_e . However, there are two obvious problems with this scenario: (a) when other collision partners must be accounted for, or when the electrons themselves are partitioned (e.g., for non-Maxwellian kinetics), one must be able to correctly apportion the changes in energy, e.g., to E_e and E_h (for heavy particles) and (b) for large time steps, there is no guarantee that the subsequent change in E_e is physically acceptable, i.e., $E_e^{(k)} = E_e^{(k-1)} + \delta E_e > 0$. We must therefore include an evolution equation for E_e (and another for E_h if heavy particle collisions are included), which must then be fully coupled, so that the Jacobian of the system (14) includes derivatives of the rates with respect to E_e , through the variation of T_e .

Energy conservation can be satisfied if the construction of the source term on the right-hand-side of the master equations also satisfies it. Thus, we must explicitly construct the energy source term from the master equations, as was already described briefly in Eq. (20). The same procedure is used, with the understanding that

$$\frac{dE_e}{dt} = - \sum_n \frac{d\mathcal{E}_n}{dt}.$$

Thus we can combine contributions as follows:

$$\begin{aligned} \frac{dE_e}{dt} = -N_e \mathcal{N}_n \left[\sum_{\substack{m>n \\ i \in n}} \frac{g_i e^{\Delta E_i/T_n}}{\mathcal{Z}_n} \sum_{j \in m} \Delta E_{ji} \alpha_{(j|i)} \right. \\ \left. + \sum_{\substack{m<n \\ i \in n}} \frac{g_i e^{\Delta E_i/T_n}}{\mathcal{Z}_n} \sum_{j \in m} \Delta E_{ji} \beta_{(j|i)} \right] \dots, \end{aligned} \quad (39)$$

where $\Delta E_{ji} = E_j - E_i$. Note that in the case of excitation from level $|i\rangle$, i.e., the first summation in Eq. (39), $\Delta E_{ji} > 0$, while $\Delta E_{ji} < 0$ in the second term for de-excitations from that level. We can then construct another set of effective rates, this time for the energy equation. Using the sub-partitioning of model B5, the rates derived from the first term on the right of Eq. (36) are

$$\tilde{\alpha}_{(m'|n')}^E = \left[\sum_{i \in n'} \frac{g_i e^{\Delta E_i / T_n}}{Z'_n} \sum_{j \in m'} \Delta E_{ji} \alpha_{(j|i)} \right], \quad (40a)$$

$$\tilde{\beta}_{(m'|n')}^E = \left[\sum_{i \in n'} \frac{g_i e^{\Delta E_i / T_n}}{Z'_n} \sum_{j \in m'} \Delta E_{ji} \beta_{(j|i)} \right]. \quad (40b)$$

These rates enter the evolution equation for E_e as

$$\frac{dE_e}{dt} = -N_e \mathcal{N}'_n \sum_{m > n} \tilde{\alpha}_{(m'|n')}^E - N_e \mathcal{N}'_n \sum_{m < n} \tilde{\beta}_{(m'|n')}^E + \dots \quad (41)$$

Note that the same formulation applies for uniform groups by taking the limit $T_n \rightarrow \infty$, and summing over the complete set $n = \{n_0, n'\}$. The rate of energy change can also be expressed as

$$\tilde{\alpha}_{(m'|n')}^E = \tilde{\alpha}_{(m'|n')} \cdot \bar{e}_{(m'|n')}, \quad (42)$$

where $\alpha_{(m'|n')}$ is of course given by the effective rate for the conserved number densities

$$\tilde{\alpha}_{(m'|n')} = \sum_{j \in m'} \sum_{i \in n'} \frac{g_i e^{\Delta E_i / T_n}}{Z'_n} \alpha_{(j|i)}.$$

Equation (42) defines an average energy $\bar{e}_{(m'|n')}$, transferred during excitation of levels of group n' to levels of group m' , which can be tabulated as function of the initial T_n and collisional (T_e) temperatures. This approach was successfully used, for example, for vibrational non-equilibrium.³⁴

B. Isochoric ionization test case

The third test case of Table II was designed to test for energy conservation. In this case, the energy loss and gain due to collisional processes are taken into account in the conservation equation for the electron energy. The evolution now proceeds at constant volume, and the electron temperature changes rapidly, as seen in Figure 12. The initial conditions are the same as those of the first test case, and the system is initially far below Boltzmann and Saha equilibrium. However, contrary to the isothermal case, the

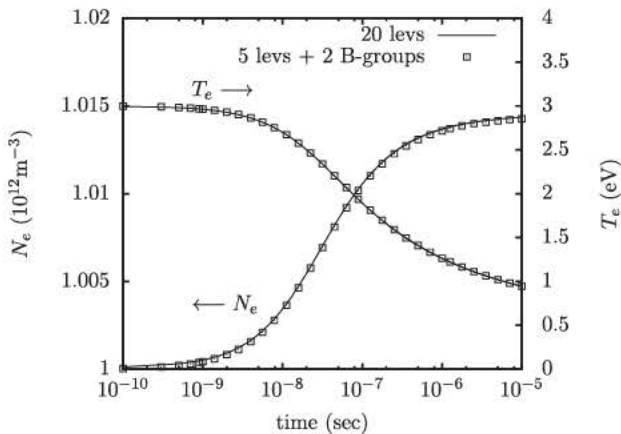


FIG. 12. N_e , T_e evolution in constant volume case.

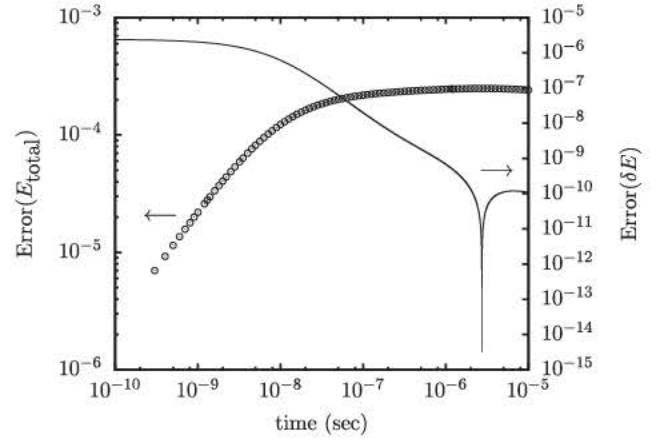


FIG. 13. Cumulative and instantaneous relative errors in energy conservation test case 3.

initial excitation and ionization processes deplete the electron energy and the system “freezes” rapidly, and the excited states remain at a low population density. If an external heating source was applied (e.g., Ohmic heating), the system would more closely resemble the isothermal test case, and the system would become stiff again. Here, we are mostly concerned with testing energy conservation and to simplify the analysis, the radiative rates were removed from the kinetics, so that no radiative energy losses were present.

We can monitor the error by comparing the values of E_e at the end of each time step with the total potential energy contained in the electronic states, by reconstruction of the level populations. Figure 13 shows both the accumulated error (symbols) and the one at each time step (solid line); this test was conducted with 5 resolved levels and 2 Boltzmann groups, and all computations were performed with a constant time step of 10^{-10} s, using the same backward-Euler integration scheme.³⁵

The error is certainly acceptable, but it is not commensurate with numerical round-off, which we would have expected if the scheme was exactly energy-conserving. By comparison, the cumulative error in energy was below 10^{-13} when solving the full master equations without level grouping.

While the exact solution consists of summing-up the contributions from each individual level, leading to the rate of change expressed by Eq. (20b). However, we are not using here the internal energy \mathcal{E}_n as a conserved variable, and we must be careful that the procedure be consistent with our definition, or *reconstruction* of the internal energy. The corrected procedure is described next.

C. Corrected energy rates

Consider for example the change in electron energy due to excitations and de-excitations, and let us examine first the case of uniform grouping.

$$\frac{dE_e}{dt} = - \sum_{m > n} \sum_n \tilde{\alpha}_{(m|n)}^E \mathcal{N}_n N_e + \sum_{m < n} \sum_n \tilde{\beta}_{(n|m)}^E \mathcal{N}_m N_e. \quad (43)$$

There are two formulations of the effective rates of energy transfer:

Formulation 1:

$$\tilde{\alpha}_{(m|n)}^E = \sum_{j \in m} \sum_{i \in n} \frac{g_i}{g_n} (E_j - E_i) \alpha_{(j|i)}, \quad (44a)$$

$$\tilde{\beta}_{(m|n)}^E = \sum_{j \in m} \sum_{i \in n} \frac{g_j}{g_m} (E_j - E_i) \beta_{(i|j)}. \quad (44b)$$

Formulation 2:

$$\tilde{\alpha}_{(m|n)}^E = (\tilde{E}_m - \tilde{E}_n) \sum_{j \in m} \sum_{i \in n} \frac{g_i}{g_n} \alpha_{(j|i)}, \quad (45a)$$

$$\tilde{\beta}_{(m|n)}^E = (\tilde{E}_m - \tilde{E}_n) \sum_{j \in m} \sum_{i \in n} \frac{g_j}{g_m} \beta_{(i|j)}, \quad (45b)$$

where $\tilde{E}_n = \sum_{i \in n} \frac{g_i}{g_n} E_i$ and similarly for \tilde{E}_m .

Only the second formulation is exactly energy-conserving. This is quite clear because in that case, the term on the right side of Eq. (45) is the product of the change in number density of the groups (dN_n/dt) and the difference in average group energy (\tilde{E}). Energy conservation follows from the definition of the total group energy $\mathcal{E}_n = \tilde{E}_n N_n$. Thus, the model assumptions *constrain* us to choose the appropriate formulation of the effective rates for energy change that is consistent with the definition of group energy.

Let us now examine the case of the Boltzmann grouping (B5), using the pair of conserved variables (N_{n0}, \mathcal{N}'_n) ; the rates of energy exchange must therefore be consistent with the electronic energy defined from these two variables, and with the equation of state used to describe the internal partition (i.e., T_n). We start with the conservation of the group energy

$$\begin{aligned} \frac{d\mathcal{E}_n}{dt} &= \frac{d}{dt} (N_{n0} E_{n0} + \mathcal{N}'_n \langle E \rangle_{n'}) \\ &= E_{n0} \frac{dN_{n0}}{dt} + \langle E \rangle_{n'} \frac{d\mathcal{N}'_n}{dt} + \mathcal{N}'_n \frac{d\langle E \rangle_{n'}}{dt}. \end{aligned} \quad (46)$$

Note that the averaging $\langle \rangle_{n'}$ is done for the remaining levels above the ground level n_0 of that group. We can write a similar equation for the total energy measured from the ground state of that group, i.e.,

$$\begin{aligned} \frac{d\Delta\mathcal{E}_n}{dt} &\equiv \sum_{i \in n} \Delta E_i \frac{dN_i}{dt} = \frac{d}{dt} (\mathcal{N}'_n \langle \Delta E \rangle_{n'}) \\ &= \langle \Delta E \rangle_{n'} \frac{d\mathcal{N}'_n}{dt} + \mathcal{N}'_n \frac{d\langle \Delta E \rangle_{n'}}{dt}. \end{aligned} \quad (47)$$

The first term in Eq. (47) describes the change in group energy from the global change in population of the group, i.e., $\langle E \rangle_n dN_n/dt$. The last term describes the change of the internal structure of the group as a result of the collisional transitions, since

$$\frac{d\langle \Delta E \rangle_{n'}}{dt} = \frac{1}{T_n^2} \left[\langle \Delta E^2 \rangle_{n'} - \langle \Delta E \rangle_{n'}^2 \right] \frac{dT_n}{dt} = C_{v,n'} \frac{dT_n}{dt}. \quad (48)$$

From Eq. (31),

$$\frac{d\mathcal{Z}'_n}{dt} = \frac{g_{n0}}{N_{n0}} \left[\frac{d\mathcal{N}'_n}{dt} - \frac{\mathcal{N}'_n}{N_{n0}} \frac{dN_{n0}}{dt} \right] = \mathcal{Z}'_n \left[\frac{\overline{\Delta E}_n}{T_n^2} + \frac{d \ln \tilde{g}'_n}{dT_n} \right] \frac{dT_n}{dt}. \quad (49)$$

Inserting into Eq. (47),

$$\mathcal{N}'_n \frac{d\langle \Delta E \rangle_{n'}}{dt} = \frac{C_{v,n'} T_n^2}{\left(\overline{\Delta E}'_n + T_n^2 \frac{d \ln \tilde{g}'_n}{dT_n} \right)} \left[\frac{d\mathcal{N}'_n}{dt} - \frac{\mathcal{N}'_n}{N_{n0}} \frac{dN_{n0}}{dt} \right]. \quad (50)$$

We can now combine with the other terms of Eq. (47) to obtain an expression which only depends on the rates of change of the conserved variables (N_{n0}, \mathcal{N}'_n) . Defining

$$\xi_{n'} = \frac{C_{v,n'} T_n^2}{\left(\overline{\Delta E}'_n + T_n^2 \frac{d \ln \tilde{g}'_n}{dT_n} \right)} \quad \text{and} \quad \omega_{n'} = \xi_{n'} \frac{\mathcal{N}'_n}{N_{n0}} \quad (51)$$

and adding the contribution from the ground state of the group, we obtain

$$\frac{d\mathcal{E}_n}{dt} = [E_{n0} - \omega_{n'}] \frac{dN_{n0}}{dt} + [E_{n0} + \langle \Delta E \rangle_{n'} + \xi_{n'}] \frac{d\mathcal{N}'_n}{dt}. \quad (52)$$

One can then identify the rates of change of the population density with the effective rates. Considering transitions between groups n and $m > n$, and using a similar expression for $d\mathcal{E}_m/dt$, we have

$$\begin{aligned} \tilde{\alpha}_{(m_0|n_0)}^E &= [E_{m_0} - \omega_{m'} - E_{n_0} + \omega_{n'}] \cdot \tilde{\alpha}_{(m_0|n_0)} \\ &\equiv \bar{e}_{(m_0|n_0)} \cdot \tilde{\alpha}_{(m_0|n_0)}, \end{aligned} \quad (53a)$$

$$\begin{aligned} \tilde{\alpha}_{(m'|n_0)}^E &= [E_{m_0} + \langle \Delta E \rangle_{m'} + \xi_{m'} - E_{n_0} + \omega_{n'}] \cdot \tilde{\alpha}_{(m'|n_0)} \\ &\equiv \bar{e}_{(m'|n_0)} \cdot \tilde{\alpha}_{(m'|n_0)}, \end{aligned} \quad (53b)$$

$$\begin{aligned} \tilde{\alpha}_{(m_0|n')}^E &= [E_{m_0} - \omega_{m'} - E_{n_0} - \langle \Delta E \rangle_{n'} - \xi_{n'}] \cdot \tilde{\alpha}_{(m_0|n')} \\ &\equiv \bar{e}_{(m_0|n')} \cdot \tilde{\alpha}_{(m_0|n')}, \end{aligned} \quad (53c)$$

$$\begin{aligned} \tilde{\alpha}_{(m'|n')}^E &= [E_{m_0} + \langle \Delta E \rangle_{m'} + \xi_{m'} - E_{n_0} - \langle \Delta E \rangle_{n'} - \xi_{n'}] \cdot \tilde{\alpha}_{(m'|n')} \\ &\equiv \bar{e}_{(m'|n')} \cdot \tilde{\alpha}_{(m'|n')}. \end{aligned} \quad (53d)$$

It is instructive to examine the limit of infinite Boltzmann temperatures; in this case,

$$\mathcal{Z}_{n'} \rightarrow g'_n, \quad C_{v,n'}, \xi_{n'}, \omega_{n'} \rightarrow 0 \quad \text{and} \quad \langle \Delta E \rangle_{n'} \rightarrow \overline{\Delta E}'_n$$

and similarly for m' . Equation (52) becomes

$$\begin{aligned} \frac{d\mathcal{E}_n}{dt} &= E_{n_0} \frac{dN_{n_0}}{dt} + \frac{\sum_{i \in n'} g_i E_i}{g_{n'}} \frac{dN_{n'}}{dt} = E_{n_0} \frac{dN_{n_0}}{dt} + \frac{\sum_{i \in n'} g_i E_i}{g_{n_0}} \frac{dN_{n_0}}{dt} \\ &= \frac{\sum_{i \in n} g_i E_i}{g_{n_0}} \frac{dN_{n_0}}{dt} = \tilde{E}_n \frac{dN_n}{dt}, \end{aligned} \quad (54)$$

where we have also used the fact that in that limit, $N_{n_0}/g_{n_0} = N_n/g_n$, and used the definition of the average group energy see Eq. (45). Since a similar equation is found for $d\mathcal{E}_m/dt$, the combination exactly yields Eq. (45). Thus, we have verified that by taking the limit $T_n, T_m \rightarrow \infty$, we recover the uniform group model.

For ionizations and recombinations, a similar procedure can be found. Considering the change in electron energy due to ionization and recombination from and to the group n , we have

$$\begin{aligned} \left(\frac{dE_e}{dt} \right)_n &= - \sum_{i \in n} \frac{dN_i}{dt} I_i = - \frac{d}{dt} [\langle I \rangle_n N_n] \\ &= -I_{n_0} \frac{dN_{n_0}}{dt} - \langle I \rangle_{n'} \frac{dN_{n'}}{dt} - N_{n'} \frac{d\langle I \rangle_{n'}}{dt}, \end{aligned} \quad (55)$$

where I_i is the ionization potential for level i and $\langle I \rangle_{n'}$ is the group ionization potential averaged over the sub-partition n' . Using $I_i = I_H - E_i = I_{n_0} - \Delta E_i$, it is easy to see that

$$\langle I \rangle_{n'} = I_{n_0} - \langle \Delta E \rangle_{n'} \quad \text{and} \quad \frac{d\langle I \rangle_{n'}}{dt} = -C_{v,n'}. \quad (56)$$

Equations (49) and (50) are still valid, and using again the definitions (51), we obtain the final form

$$\left(\frac{dE_e}{dt} \right)_n = -[I_{n_0} + \omega_{n'}] \frac{dN_{n_0}}{dt} - [I_{n_0} - \langle \Delta E \rangle_{n'} - \xi_{n'}] \frac{dN_{n'}}{dt}. \quad (57)$$

Note the similarity with Eq. (52). The effective rates are therefore

$$\tilde{\alpha}_{(+|n_0)}^E = [I_{n_0} + \omega_{n'}] \cdot \tilde{\alpha}_{(+|n_0)} \equiv \bar{e}_{(+|n_0)} \cdot \tilde{\alpha}_{(+|n_0)}, \quad (58a)$$

$$\tilde{\alpha}_{(+|n')}^E = [I_{n_0} - \langle \Delta E \rangle_{n'} - \xi_{n'}] \cdot \tilde{\alpha}_{(+|n')} \equiv \bar{e}_{(+|n')} \cdot \tilde{\alpha}_{(+|n')}. \quad (58b)$$

Examination of equations (53) and (58) reveals that the overall procedure consists of replacing the energy of the group's ground state n_0 and sub-partition n' by *effective energies* for the energy exchange

$$\tilde{E}_{n_0} = E_{n_0} - \omega_{n'} \quad \text{and} \quad \tilde{E}_{n'} = E_{n_0} + \langle \Delta E \rangle_{n'} + \xi_{n'}. \quad (59)$$

Thus, the effective rates of energy transfer become

$$\tilde{\alpha}_{(m_0|n_0)}^E = (\tilde{E}_{m_0} - \tilde{E}_{n_0}) \cdot \tilde{\alpha}_{(m_0|n_0)}, \quad (60a)$$

$$\tilde{\alpha}_{(m'|n_0)}^E = (\tilde{E}_{m'} - \tilde{E}_{n_0}) \cdot \tilde{\alpha}_{(m'|n_0)}, \quad (60b)$$

$$\tilde{\alpha}_{(m_0|n')}^E = (\tilde{E}_{m_0} - \tilde{E}_{n'}) \cdot \tilde{\alpha}_{(m_0|n')}, \quad (60c)$$

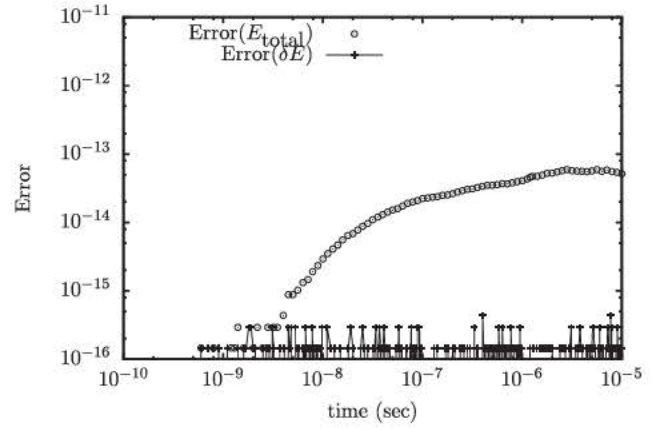


FIG. 14. Cumulative and instantaneous relative errors in energy conservation test case 3 with revised formulation.

$$\tilde{\alpha}_{(m'|n')}^E = (\tilde{E}_{m'} - \tilde{E}_{n'}) \cdot \tilde{\alpha}_{(m'|n')} \quad (60d)$$

and for ionization:

$$\tilde{\alpha}_{(+|n_0)}^E = (I_H - \tilde{E}_{n_0}) \cdot \tilde{\alpha}_{(+|n_0)}, \quad (61a)$$

$$\tilde{\alpha}_{(+|n')}^E = (I_H - \tilde{E}_{n'}) \cdot \tilde{\alpha}_{(+|n')}. \quad (61b)$$

The use of effective group energies³⁶ provides a straightforward approach, and the effective rates of energy transfer for *all* transitions (including de-excitations, recombination, and radiative transitions) can now be expressed in a simple form. Note that Eq. (61) is similar to the case of uniform grouping (45) and since we have already demonstrated that we can recover the uniform grouping case in the limit of infinite temperatures, we have achieved here a fully consistent model.

We are now left with the task of verifying energy conservation with this revised approach. Using the same test case (3), we now find a much smaller level of error, as can be seen from Figure 14 compare with Figure 13 that is the characteristic of the level of numerical round-off. Note that the cumulative error sums the absolute values of the stepwise error (L_1 norm), and is therefore a maximum bound. Figure 15 shows the effect of bin size on the relative error;

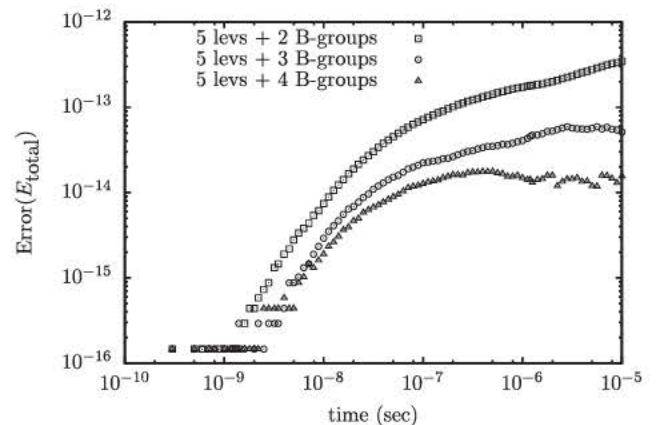


FIG. 15. Cumulative relative errors in energy conservation as function of group sizes; revised formulation.

this observation is similar to the one made regarding the accuracy of the ASDF – see Figure 5, i.e., smaller group widths are preferred. However, it is clear that even for one or two bins, the error on energy conservation remains very small.

VI. CONCLUDING REMARKS

In this paper, we described a model reduction mechanism for the collisional-radiative kinetics of the ASDF, by grouping electronic states into groups and deriving the corresponding macroscopic rates to take in account all the transitions. While level-grouping is a commonly used and necessary procedure when dealing with a very large number of atomic levels, as in high-temperature plasma,^{37,38} the procedure is commonly based on uniform grouping (i.e., simple average over the level degeneracies). A higher-order description of the internal structure of the groups was developed here by assuming a Boltzmann distribution of the levels within the group, with different temperatures for each group. This approach was shown here to have superior features to the uniform grouping procedure, as summarized below.

Numerical instabilities in the limit of low internal temperature led us to the design of this non-traditional approach. Instead of conserving the total energy of a group, we used a novel approach using conserved variables from a sub-partitioning of the group between the lowest level of that group (N_{n0}) and the remaining states (N'_n). Combined with an appropriate expansion of the sub-group partition function, this model was able to very rapidly determine the group temperatures in a stable and accurate fashion for all conditions, solving a problem that is particularly vexing for atomic collisional-radiative kinetics, due to the structure of the energy levels of atomic plasma.

The two grouping schemes (uniform and Boltzmann) were implemented on an electronic collisional-radiative model for atomic hydrogen and the results were compared with the full solution of the master equation on a large number of numerical tests, of which a representative sub-set was shown here. Both schemes showed agreement with the solution of the master equations and have excellent convergence properties. However, substantial accuracy improvements were obtained at minimal computational cost with the Boltzmann grouping. Detailed tests of energy conservation revealed the need for a revised approach to the construction of effective rates of energy transfer. This was made necessary because the total group energy was not part of the set of conserved variables, and consistency requirements led us to a new formulation involving effective level energies and average group energies between which energy exchange occurs. We derived this new formulation and showed that it was simple to implement, and consistent with the uniform grouping method.

For the case of atomic hydrogen studied here, it was sufficient to mix a few low-lying states with two Boltzmann groups for all the high energy states and be able to capture the correct ionization kinetics for all the states and the radiative spectrum. This significantly

reduces the computational cost associated with solving the kinetics and therefore can be applied in multidimensional and time-resolved flow calculations, with accurate coupling to radiative processes. The reduction schemes presented in this work could also be applied to other set of kinetics, e.g., rovibrational collisional and vibrational kinetics, although in this case the levels are distributed much more uniformly on the energy axis, in which case reduction schemes and group temperature determination are more straightforward. Future work includes a straightforward extension of the approach to non-hydrogenic and multi-stage ionization, as well as the application of more accurate and more efficient time integration schemes, currently under development. Further optimization of the scheme, such as dynamic re-partitioning, is also under exploration.

ACKNOWLEDGMENTS

We wish to acknowledge the support of the Air Force Office of Scientific Research (AFOSR), Grant No. 12RZ06COR (PM: Dr. F. Fahroo) for this work.

APPENDIX: COMPUTATION OF KINETIC RATES

The classical form of the cross-section for energy exchange between a free electron and the atom,⁶ leading to an excitation from level n to level $m > n$ is

$$\sigma_{nm}^e = (4\pi a_0^2) \frac{I_H^2(\varepsilon - E_{nm})}{E_{nm}\varepsilon^2} \cdot (3f_{nm}), \quad (\text{A1})$$

where a_0 is the Bohr radius, ε is the energy of the free electron, $\Delta E_{nm} = E_m - E_n$ is the energy gap between n and m and f_{nm} is the oscillator strength

$$f_{nm} = \frac{32}{3\pi\sqrt{3}} \frac{1}{n^5} \frac{1}{m^3} \frac{1}{\left(\frac{1}{n^2} - \frac{1}{m^2}\right)^3}. \quad (\text{A2})$$

The free electrons are assumed to follow an isotropic Maxwellian distribution $f_e(\varepsilon_e)$

$$f_e(\varepsilon_e)d\varepsilon_e = \frac{2}{\sqrt{\pi}(kT_e)^{3/2}} \varepsilon_e^{1/2} e^{-\varepsilon_e/kT_e} d\varepsilon_e, \quad (\text{A3})$$

where m_e is the electron mass, $\varepsilon_e = m_e v_e^2/2$ and T_e is the temperature. The rate of excitation is obtained by averaging over the distribution function

$$\alpha_{(m|n)}^e = \int_{E_{nm}}^{\infty} \sigma_{nm}^e(\varepsilon) v_e f(v_e) dv_e, \quad (\text{A4})$$

leading to

$$\alpha_{(m|n)}^e = (4\pi a_0^2) \bar{v}_e \left(\frac{I_H}{kT_e} \right)^2 (3f_{nm}) \psi_{nm}, \quad (\text{A5})$$

where

$$\bar{v}_e = \left(\frac{8kT_e}{\pi m_e} \right)^{1/2}, \quad \psi_{nm} = \frac{e^{-x_{nm}}}{x_{nm}} - E_1(x_{nm}), \quad \text{and} \\ E_1(x) = \int_x^\infty \frac{e^{-y}}{y} dy. \quad (\text{A6})$$

Here, \bar{v}_e is the mean thermal electron velocity, $x_{nm} = \Delta E_{nm}/kT_e$ and E_1 is the exponential integral. The reverse rate can be found from detailed balance

$$\beta_{(n|m)}^e = \frac{n^2}{m^2} e^{+x_{nm}} \cdot \alpha_{(m|n)}. \quad (\text{A7})$$

We use the low temperature approximation⁶ ($x_{nm} \gg 1$)

$$E_1(x) \simeq \frac{e^{-x}}{x} \left(1 - \frac{1}{x} \right), \quad (\text{A8})$$

in which case

$$\alpha_{(m|n)}^e \simeq \left[4\pi a_0^2 \cdot \frac{32}{\pi\sqrt{3}} \cdot \bar{v}_e \right] \frac{e^{-x_{nm}}}{n^5 m^3 (n^2 - m^2)^5}, \quad (\text{A9a})$$

$$\beta_{(n|m)}^e \simeq \left[4\pi a_0^2 \cdot \frac{32}{\pi\sqrt{3}} \cdot \bar{v}_e \right] \frac{1}{n^3 m^5 (n^2 - m^2)^5}. \quad (\text{A9b})$$

The factor in brackets is an upper bound, which is reached for the upper states when $x_{nm} \rightarrow 0$. Another scale is the factor I_H/kT_e in x_{nm} , which is effectively responsible for the stiffness. If that factor is very low (high temperatures), all rates are of the same order; at low temperatures, the exponential term dominates and the range of time scales is increased.

The cross-section for ionization by electron impact has a form similar to Eq. (A1), i.e.,

$$\sigma_n^e = (4\pi a_0^2) \frac{I_H^2 (\varepsilon - I_n)}{I_n \varepsilon^2}. \quad (\text{A10})$$

This leads to an ionization rate coefficient⁶

$$\alpha_{(+|n)}^e = (4\pi a_0^2) \bar{v}_e \left(\frac{I_H}{kT_e} \right)^2 \psi(x_n). \quad (\text{A11})$$

The final state $(+|)$ is an ionized state, i.e., where one electron initially bound to the atom has reached the ionization limit ($n = \infty$) and is part of a free continuum of states. Using the principle of detailed balance, the reverse (recombination) rate is

$$\beta_{(+|n)}^e \simeq \left[\frac{4}{\pi} \frac{a_0^2 h^3}{m_e^2 kT_e} \right] \left(\frac{I_H}{kT_e} \right)^2 n^2 \psi(x_n) e^{x_n}. \quad (\text{A12})$$

Using the same low temperature approximation (A8), we obtain⁶

$$\alpha_{(+|n)}^e \simeq (4\pi a_0^2) \left(\frac{8kT_e}{\pi m_e} \right)^{1/2} n^4 e^{-x_n}, \quad (\text{A13a})$$

$$\beta_{(n|+)}^e \simeq \left[\frac{4}{\pi} \frac{a_0^2 h^3}{m_e^2 kT_e} \right] n^6. \quad (\text{A13b})$$

The rates of radiative transitions between levels can also be obtained classically for the hydrogen atom.⁵ The spontaneous emission rates from an upper level m are

$$A_{(n|m)} = \left(\frac{8\pi^2 e^2}{m_e c^3} \right) \frac{g_n}{g_m} f_{nm} = \frac{1.6 \times 10^{10}}{m^3 n (m^2 - n^2)} \text{ s}^{-1}. \quad (\text{A14})$$

The expression on the right is for atomic hydrogen only.

¹R. G. Jahn, *Physics of Electric Propulsion* (Dover Publications, 2006).

²M. Capitelli, C. M. Ferreira, B. F. Gordiets, and A. I. Osipov, *Plasma Kinetics in Atmospheric Gases* (Springer, 2000).

³I. H. Hutchinson, *Principles of Plasma Diagnostics*, 2nd ed. (Cambridge University Press, 2005).

⁴W. G. Vincenti and C. H. Kruger, *Introduction to Physical Gas Dynamics* (Krieger Pub Co, 1975).

⁵M. Mitchner and C. H. Kruger, *Partially Ionized Gases*, 1st ed. (John Wiley and Sons, 1973).

⁶Y. B. Zel'dovich and Y. P. Raizer, *Physics of Shock Waves and High Temperature Hydrodynamic Phenomena*, 3rd ed. (Dover Publication, 2002).

⁷I. Armenise, M. Capitelli, R. Celiberto, G. Colonna, C. Gorse, and A. Lagani, "The effect of N+N₂ collisions on the non equilibrium vibrational distributions of nitrogen under reentry conditions," *Chem. Phys. Lett.* **227**, 157–163 (1994).

⁸A. Bultel, B. G. Cheron, A. Bourdon, O. Motapon, and I. F. Schneider, "Collisional radiative model in air for earth re entry problems," *Phys. Plasmas* **13**, 043502 (2006).

⁹C. O. Laux, L. Pierrot, and R. J. Gessman, "State to state modeling of a recombining nitrogen plasma experiment," *Chem. Phys.* **398**, 46–55 (2012).

¹⁰M. G. Kapper and J. L. Cambier, "Ionizing shocks in argon. Part I: Collisional radiative model and steady state structure," *J. Appl. Phys.* **109**, 113308 (2011).

¹¹M. G. Kapper and J. L. Cambier, "Ionizing shocks in argon. Part II: Transient and multi dimensional effects," *J. Appl. Phys.* **109**, 113309 (2011).

¹²M. Panesi, T. Magin, A. Bourdon, A. Bultel, and O. Chazot, "Electronic excitation of atoms and molecules for the FIRE II flight experiment," *J. Thermophys. Heat Transfer* **25**, 361–374 (2011).

¹³M. Panesi, R. L. Jaffe, D. W. Schwenke, and T. E. Magin, "Rovibrational internal energy transfer and dissociation of N₂(1Σg+) N(4S(u)) system in hypersonic flows," *J. Chem. Phys.* **138**, 044312 (2013).

¹⁴E. Josyula and W. Bailey, "Vibration dissociation coupling using master equations in nonequilibrium hypersonic blunt body flow," *J. Thermophys. Heat Transfer* **15**, 157–167 (2001).

¹⁵D. Giordano, V. Bellucci, G. Colonna, M. Capitelli, I. Armenise, and C. Bruno, "Vibrationally relaxing flow of N₂ past an infinite cylinder," *J. Thermophys. Heat Transfer* **11**, 27–35 (1997).

¹⁶G. Colonna, L. Pietanza, and M. Capitelli, "Recombination assisted nitrogen dissociation rates under nonequilibrium conditions," *J. Thermophys. Heat Transfer* **22**, 399–406 (2008).

¹⁷T. E. Magin, M. Panesi, A. Bourdon, R. L. Jaffe, and D. W. Schwenke, "Coarse grain model for internal energy excitation and dissociation of molecular nitrogen," *Chem. Phys.* **398**, 90–95 (2012).

¹⁸A. Guy, A. Bourdon, and M. Y. Perrin, "Consistent multi internal temperatures models for nonequilibrium nozzle flows," *Chem. Phys.* **420**, 15–24 (2013).

¹⁹Y. Liu, M. Vinokur, M. Panesi, and T. Magin, "A multi group maximum entropy model for thermo chemical non equilibrium," AIAA Paper 2010 4332, 2010.

²⁰J. Vlcek, "A collisional radiative model applicable to argon discharges over a wide range of conditions. I. Formulation and basic data," *J. Phys. D: Appl. Phys.* **22**, 623 (2000).

²¹Two of the test cases considered here are isothermal, i.e., T_e constant. The third test case has a variable T_e but is designed only to test energy conservation, and hence radiative energy losses would not serve this purpose.

²²Strictly speaking, the ionization limit I_H is attained for $n \rightarrow \infty$. In reality, the ionization potential is lowered as a result of interaction with the plasma (Debye shielding) and quantum uncertainty. In practice, the truncation is accomplished at a lower limit still; for the current purpose, details of this truncation procedure can be ignored. Suffice to say that the series extends to a number $n \sim M$, which can be considered large, e.g., $O(100)$.

²³That is, within the group.

²⁴For further ease of notation, the Boltzmann constant k is not explicitly written.

²⁵T. Magin, M. Panesi, A. Bourdon, R. Jaffe, and D. Schwenke, "Rovibrational internal energy excitation and dissociation of molecular nitrogen in hypersonic flows," AIAA Paper 2010 4336, 2010.

²⁶In a log plot, this model assumes that the slope within each "bin" is always the same, and is not related to the average slope determined by the difference between adjacent bins.

²⁷Note that this problem is particularly relevant to ASDF kinetics because of the geometric progression of the energy levels. By performing tests on a pseudo atom with equidistant energy levels, stability of the iterations was much improved, although not entirely eliminated for some conditions.

²⁸We have here temporarily simplified the notation ($g_0 \equiv g_{n_0}, g_1 \equiv g_{n_0+1}, \dots$).

²⁹This approach is a reflection of the self similar structure of the atomic levels.

³⁰Since we are considering electron collisions only, all test cases must start with an initial degree of ionization $x_e / 0$.

³¹This understandably so, since the ladder climbing process of the early evolution would be difficult to describe with grouping methods, even by 1st order approximation of the internal distribution within the groups.

³²By coincidence, the results of uniform binning for 6 resolved levels is right on top of the solution for a Boltzmann group with 4 lower levels.

³³Although the grouping techniques are formulated here for a general set of kinetics, the effectiveness of the grouping approach is problem specific. For other situations, e.g., ro vibrational states, a different strategy may be required than the one discussed here for atomic states.

³⁴J. L. Cambier and S. Moreau, "Simulations of a molecular plasma in collisional radiative nonequilibrium," AIAA Paper No. 93 3196; 24th AIAA Plasma Dynamics Conference, Orlando, FL, 1993.

³⁵Note that the scheme includes numerical errors resulting from the forward and backward sweeps of the Gaussian elimination procedure. However, this is negligible here, since we have used double precision.

³⁶Contrary to the uniform grouping case, we need to use two values, one for n_0 and one for n' , which reflects the additional degrees of freedom in the Boltzmann model.

³⁷H. A. Scott and S. B. Hansen, "Advances in NLTE modeling for integrated simulations," *High Energy Density Phys.* **6**, 39–47 (2010).

³⁸S. B. Hansen, J. Bauche, and C. Bauche Arnoult, "Superconfiguration widths and their effects on atomic models," *High Energy Density Phys.* **7**, 27–37 (2011).

This Page Intentionally Left Blank

Appendix C: Modeling of Inelastic Collisions in a Multifluid Plasma: Excitation and Deexcitation

Hai P. Le

Jean-Luc Cambier

Modeling of Inelastic Collisions in a Multifluid Plasma: Excitation and Deexcitation

Hai P. Le^{1, a)} and Jean-Luc Cambier^{2, b)}

¹⁾*Department of Mathematics, University of California, Los Angeles,
California 90095*

²⁾*Air Force Research Laboratory, Edwards AFB, California 93524*

(Dated: August 11, 2015)

We describe here a model for inelastic collisions for electronic excitation and deexcitation processes in a general, multifluid plasma. The model is derived from kinetic theory and applicable to any mixture and mass ratio. The principle of detailed balance is strictly enforced, and the model is consistent with all asymptotic limits. The results are verified with direct Monte Carlo calculations, and various numerical tests are conducted for the case of an electron-hydrogen two-fluid system, using a generic, semi-classical model of collision cross sections. We find that in some cases, the contribution of inelastic collisions to the momentum and thermal resistance coefficients is not negligible, in contrast to the assumptions of current multifluid models. This fundamental model is also applied to ionization and recombination processes, the studies on which are currently underway.

Keywords: Non-equilibrium plasma, collision, multifluid, Collisional-Radiative model

Approved for public release; distribution unlimited. PA Clearance 15342 Jun 24 2015

^{a)}hai.le@ucla.edu

^{b)}jean_luc.cambier@us.af.mil

Contents

I. Introduction	C-7
II. Rate Derivation	C-9
II-A. Transfer integral	C-9
II-B. Zeroth-order moment: number density	C-14
II-C. First-order moment: momentum density	C-16
II-D. Second-order moment: total energy density	C-19
III. Numerical Results	C-22
III-A. Reaction Rates	C-22
III-B. Momentum and Energy Exchange Rates	C-25
III-C. Verification	C-29
III-D. Zero-dimensional Calculations	C-30
IV. Concluding Remarks	C-33
Appendix A. Collision kinematics	C-35
Appendix B. Separation of variables	C-36
Appendix C. Atomic data and cross section models	C-38
Appendix D. Rate equations	C-39
References	C-41

List of Figures

- 1 Frame rotation and relative orientation of (a) \mathbf{w} and \mathbf{g} and (b) \mathbf{g} and \mathbf{g}' C-11

- 2 Multifluid reaction rates for electron-impact excitation/deexcitation collisions as a function of two temperatures. C-24

- 3 Multifluid reaction rates for electron-impact excitation/deexcitation collisions: lines with symbols correspond to different values of the drift temperature. C-25

- 4 Multifluid reaction rates for electron-impact excitation/deexcitation collisions: lines with symbols correspond to different values of the thermal temperature. C-26

- 5 Elastic momentum transfer cross section for electrons in atomic hydrogen computed with the DCS from equation (68). C-27

- 6 Comparison of the momentum exchange rates κ and thermal relaxation rates j due to elastic and inelastic collisions (excitation and deexcitation). C-30

- 7 Comparison of zeroth-order reaction rates with Monte Carlo integration of the full transfer integral C-30

- 8 Number density of excited states during a zero-dimensional chemistry test. C-32

- 9 Time evolution of the temperatures for several test cases with different initial drift velocities: solid line ($T_w = 0.01$ eV), dotted line ($T_w = 1$ eV), and dashed line ($T_w = 10$ eV). C-33

- 10 Time evolution of the temperatures for the case with (solid) and without (dashed) the exchange terms (momentum and energy) due to inelastic collisions. C-34

- 11 Time evolution of the temperatures for the case with (solid) and without (dashed) the exchange terms (momentum and energy) due to inelastic collisions. C-34

List of Tables

- 1 Initial conditions of 0D test cases. For all cases, the total atomic density n_t is 10^{20} m^{-3} . C-31

I. Introduction

Modeling of nonequilibrium processes in a low-temperature partially ionized plasma is of particular interest to a wide range of technical fields such as gas discharge, electric propulsion, spectroscopic and laser diagnostics, and material science¹⁻³. The complexity of the model is largely due to the characterization of various collisional and radiative processes, occurring at a wide range of spatial and temporal scales^{4,5}. Although the fundamental physical processes may be individually known, it is not always clear how their combination affects the overall operation, or at what level of detail this process needs to be modeled. The current state of the art for modeling detailed chemical kinetics of a low temperature plasma is the collisional-radiative (CR) model, first proposed by Bates et al. in 1962^{6,7}. CR models are now commonly used in studies of plasma discharge, plasma-assisted combustion, and hypersonics⁸⁻¹³. The advantage of a CR model is two-fold. First, strong deviations from equilibrium of the internal states can be captured accurately when CR models are employed. In addition, *ab initio* cross section data can be directly incorporated in the CR model, leading to a very accurate prediction of the thermochemical kinetics of the system.

There are, however, two issues with this modeling approach. The first arises from the complexity of the physical processes needed to be captured in the model. The required level of detail of the CR model is typically not known a priori and is possibly changing in a dynamical fashion as the system evolves in time. This can be resolved by coarse-graining techniques, which reduce the complexity of the kinetics to avoid solving a large system of equations¹⁴⁻¹⁶. The second issue comes from translational nonequilibrium, often found in a discharge, where we have both a bulk plasma (continuum) and a highly energetic component (kinetic), e.g., electrons emitted from the cathode. A proper treatment of this energetic beam-like component requires extending the solution of the CR kinetics to the so-called non-Maxwellian regime¹⁷⁻¹⁹. These simulations are typically very expensive and therefore limited to zero- or one-dimensional systems. In addition, space charge effects within the bulk plasma can also become important, requiring further separation, i.e., ions and electrons. A natural solution to this problem is to use a hybrid approach, decomposing the system into a continuum and a kinetic component²⁰. The continuum component can be solved by fluid equations, and the kinetic component by (for example) a particle method. Although the

idea seems quite intuitive, proper treatment of the coupling between the fluid and kinetic components is highly non-trivial. There appears to be no unique and consistent coupling methodology, and the choice is highly problem-dependent. This coupling issue is currently being addressed by many researchers and is outside of the scope of the current work.

We are concerned here with an alternative approach, the so-called multifluid model, which decomposes the plasma into several fluid components. For example, in a discharge configuration, one could have 4 different fluids, namely the neutrals, ions, bulk electrons, and the energetic electrons. The only required assumption is that collisions among particles within the same fluid are sufficiently fast to maintain a Maxwellian distribution. The validity of this assumption is not always well known. Nevertheless this approach is attractive, since it is much faster than a fully kinetic solver, and unambiguous since at the same time, the approach relies on kinetic theory for the treatment of coupling terms between different fluids. Furthermore, one can rely on fast implicit methods to solve these fluid equations and examine long time behavior of the system; this offers a big advantage over kinetic simulations, which are only suitable for problems with short time scales. Multifluid models are commonly used in simulations of astrophysical plasmas (see for example^{21,22}).

The most classical work in multifluid plasma modeling is due to Braginskii²³, who derived fluid equations for a fully ionized plasma, using a Chapman-Enskog closure. Braginskii's work has been successively refined by several authors, with particular emphases on improving the transport coefficients and/or including interaction with neutral species^{24–27}. Burgers, on the other hand, presents a rather general framework for the modeling of elastic collisions²⁸. These include both neutral collisions and charged particle collisions; the methodology is applicable for a general system of moment equations beyond the standard five-moment model. Burgers also introduces a simplified model for reactive collisions using a Bhatnagar-Gross-Krook (BGK) collision operator.

In the current work, we present a self-consistent model for inelastic collisions within the multifluid framework. The model is derived from kinetic theory and obeys the principle of detailed balance (DB), which we show to be an essential property to ensure that the system approaches the correct equilibrium limit. We focus on characterizing the exchange source terms due to collision, namely mass, momentum and energy exchanges (the hydrodynamics

and transport fluxes can be added following²³ when considering a non-uniform plasma). We will show that in most cases none of these terms can be neglected, and they have complex dependencies to microscopic quantities of the interaction, e.g., multiply-differentiated cross sections. We present the general description of the collision kinematics and derive the exchange terms for the case of excitation and deexcitation processes. Although we are mostly interested here in electron-impact collisions and atomic transitions, we keep the formulation as general as possible, such that the application to other species and chemistry (e.g. proton-impact, molecular vibrational transitions, charge-exchange, etc.) is a straight-forward extension. The case of ionization and recombination, and other three-body processes, is currently under examination, using the same basic formulation presented here.

The rest of the paper is organized as follows. The derivation of the exchange source terms is given in Sec. II, by first introducing the description of the transfer integral, and then presenting the derivation of the exchange rates in the following subsections. In Sec. III, we show the numerical evaluation of the multifluid rates, verify the results with Monte Carlo calculations, and perform zero-dimensional calculations utilizing the multifluid rates. Finally, conclusions and a summary of the present findings are given in Sec. IV. We also provide several appendices to elaborate on the derivation of the exchange source terms and the description of the numerical simulation.

II. Rate Derivation

A. Transfer integral

Let us consider an inelastic collision between two particles s and t , such that the particle t changes its internal state. The particles s and t are respectively the scattered and target in the laboratory frame of reference (LAB). The former will be identified as the electron and the target as the atom, but we will keep the general s, t notation until explicit assumptions and approximations are made, such as neglecting terms of the order of the mass ratio m_s/m_t for final expressions. Following Appendix A, the initial velocities are $\mathbf{v}_s, \mathbf{v}_t$, where $\mathbf{v} = \mathbf{u} + \mathbf{c}$ and \mathbf{u} is the fluid mean velocity in the LAB frame, and post-collision values are indicated by a prime, i.e.:

$$s(\mathbf{v}_s) + t(\mathbf{v}_t) \rightarrow s'(\mathbf{v}'_s) + t'(\mathbf{v}'_t) \quad (1)$$

We make here two assumptions: 1) the collision produces only two particles, which may or may not belong to the same fluids as the initial reactants, and 2) the masses of individual particles are the same before and after the collision, e.g. $m'_s \equiv m_s$, such that mass conservation is automatically obtained. Defining the energy transfer to and from the internal modes to be represented by $\Delta\varepsilon$, we have the following energy conservation constraint on the relative velocity \mathbf{g} where $\mathbf{g} = \mathbf{v}_s - \mathbf{v}_t$ (see Appendix A):

$$\mathbf{g}^2 = \mathbf{g}'^2 + \frac{2\Delta\varepsilon}{\mu} \quad (2)$$

For excitation, the transferred energy is a positive and fixed value $\Delta\varepsilon \equiv \varepsilon^*$, the energy gap between the levels, while for ionization it is a continuum of values: $\Delta\varepsilon \in [\varepsilon^*, \varepsilon]$, where $\varepsilon = \frac{1}{2}\mu\mathbf{g}^2$ is the available kinetic energy in the center-of-mass (COM) frame. In the limit $\Delta\varepsilon \rightarrow 0$, the collision is elastic. We will keep the same relations for the reverse process, for which the primed variables are post-collision and non-primed refer to pre-collision, such that for deexcitation, $\Delta\varepsilon = -\varepsilon^*$.

We can then define a transfer integral of the collision operator between the two species s and t ²⁸.

$$\Psi_{st} = n_s n_t \int d^3\mathbf{v}_s d^3\mathbf{v}_t f_s f_t g \int \psi d\omega(\mathbf{v}_s, \mathbf{v}_t; \mathbf{v}'_s, \mathbf{v}'_t) \quad (3)$$

where g is the magnitude of the relative velocity ($g = |\mathbf{g}|$), $d\omega$ is the differential cross section (DCS), and ψ is any moment variable exchanged during the collision. We now follow Appendix B, starting with the following transformations:

$$\mathbf{V}^* = \mathbf{V} - \mathbf{U} + \gamma \tilde{\mathbf{g}} \quad T^* = \frac{MT_s T_t}{m_s T_t + m_t T_s} \quad a^2 = \frac{2kT^*}{M} \quad (4a)$$

$$\tilde{\mathbf{g}} = \mathbf{g} - \mathbf{w} \quad \tilde{T} = \frac{m_s T_t + m_t T_s}{M} \quad \alpha^2 = \frac{2k\tilde{T}}{\mu} \quad (4b)$$

$$\text{and } \gamma = \frac{\mu(T_t - T_s)}{m_s T_t + m_t T_s} \quad (4c)$$

where the relative mean velocity $\mathbf{w} = \mathbf{u}_s - \mathbf{u}_t$. The product of the two Maxwellian distributions $f_s \cdot f_t$ is expressed in terms of the product of two other Maxwellians, $f_{V^*} \cdot f_{\tilde{g}}$, for the COM velocity and relative velocity respectively. Inserting (B.14–B.16) into (3), the transfer integral can be written as follows:

$$\Psi_{st} = n_s n_t \frac{1}{\pi^{\frac{3}{2}} a^3} \int d^3\mathbf{V}^* e^{-\mathbf{V}^{*2}/a^2} \cdot \frac{1}{\pi^{\frac{3}{2}} \alpha^3} \int d^3\mathbf{g} e^{-\tilde{\mathbf{g}}^2/\alpha^2} g \int \psi d\omega(\mathbf{g}; \mathbf{g}') \quad (5)$$

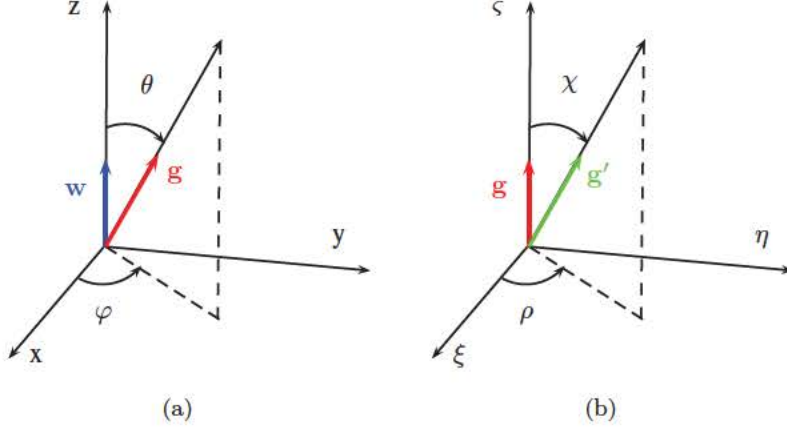


Figure 1. Frame rotation and relative orientation of (a) \mathbf{w} and \mathbf{g} and (b) \mathbf{g} and \mathbf{g}' .

Note that in the COM reference frame, the DCS only depends on the relative velocities, i.e., $d\omega(\mathbf{v}_s, \mathbf{v}_t; \mathbf{v}'_s, \mathbf{v}'_t) \equiv d\omega(\mathbf{g}; \mathbf{g}')$, and can be expressed as:

$$d\omega(\mathbf{g}; \mathbf{g}') = \sigma_{st}(g, \Omega') d\Omega' \quad (6)$$

where Ω' is the solid angle between the initial and final relative velocities, i.e., $d\Omega' = d\rho d\cos\chi$ with $\mathbf{g} \cdot \mathbf{g}' = gg' \cos\chi$. Without loss of generality, we can now choose a reference frame (LAB) such that the relative *mean* velocity \mathbf{w} is aligned with the $\hat{\mathbf{z}}$ axis, as shown in Figure 1. Thus, the unit vectors $\hat{\mathbf{g}}, \hat{\mathbf{g}}'$ are obtained by subsequent rotations of the $(\hat{\mathbf{x}}, \hat{\mathbf{y}}, \hat{\mathbf{z}})$ frame. Using the abbreviated notation $c_\varphi \equiv \cos\varphi$, $s_\varphi \equiv \sin\varphi$, etc, we define this rotation operator by the matrix:

$$R(\varphi, \theta) = \begin{pmatrix} c_\varphi c_\theta & -s_\varphi & c_\varphi s_\theta \\ s_\varphi c_\theta & c_\varphi & s_\varphi s_\theta \\ -s_\theta & 0 & c_\theta \end{pmatrix} \quad \text{and} \quad \hat{\mathbf{g}} = \frac{\mathbf{g}}{g} = R(\varphi, \theta) \cdot \hat{\mathbf{z}} = \begin{pmatrix} c_\varphi s_\theta \\ s_\varphi s_\theta \\ c_\theta \end{pmatrix} \quad (7)$$

Similarly, the post-collision relative velocity is rotated by the angles (ρ, χ) , such that $\hat{\mathbf{g}}' = R(\rho, \chi) \cdot \hat{\mathbf{g}}$.

Using $d^3\mathbf{g} = g^2 dg d\varphi dc_\theta$, and equation (6), the transfer integral can be written as:

$$\Psi_{st} = \frac{n_s n_t}{\pi^{\frac{3}{2}} \alpha^3} e^{-w^2/\alpha^2} \cdot \int d^3\mathbf{V}^* f_{V^*} \cdot \int dg g^3 e^{-g^2/\alpha^2} \cdot \int d\varphi dc_\theta e^{2gwc_\theta/\alpha^2} \int d\rho dc_\chi \psi \sigma_{st}(g, \Omega') \quad (8)$$

Let us now assume that the moment variable can be expanded in terms of powers of \mathbf{V}^* :

$$\psi = a + b\mathbf{V}^* + c\mathbf{V}^{*2} + \dots$$

where a, b, c, \dots are functions of the remaining velocity variables, and let us perform the integration over \mathbf{V}^* . Note that we have:

$$\int d^3\mathbf{V}^* f_{V^*} \equiv 1 \quad \int d^3\mathbf{V}^* \mathbf{V}^* f_{V^*} \equiv 0$$

the latter by reasons of symmetry. Thus, as long as ψ does not contain terms quadratic (or higher) in \mathbf{V}^* , a condition satisfied throughout this work, we can eliminate the integration over \mathbf{V}^* , keeping only the terms which are independent of \mathbf{V}^* . Also by symmetry, the DCS σ_{st} does not depend on the angle ρ , and we can write:

$$\sigma_{st}(g, \Omega') \equiv \bar{\sigma}_{st}(g) \cdot \mathcal{G}(g, \chi) \quad \text{s.t.} \quad \int d\rho \, dc_\chi \mathcal{G}(g, \chi) \equiv 1 \quad (9)$$

where \mathcal{G} is the angular-dependent DCS. More generally, we will define the averaging of any function ψ over the scattering angles as:

$$\langle \psi \rangle_{\Omega'} = 2\pi \int_{-1}^{+1} dc_\chi \psi \mathcal{G}(g, \chi) \quad (10)$$

A trivial integration over φ yields:

$$\Psi_{st} = \frac{2n_s n_t}{\pi^{\frac{1}{2}} \alpha^3} e^{-w^2/\alpha^2} \int dg g^3 e^{-g^2/\alpha^2} \bar{\sigma}_{st}(g) \cdot \int_{-1}^{+1} dc_\theta e^{2gwc_\theta/\alpha^2} \langle \psi \rangle_{\Omega'} \quad (11)$$

We now define the following, normalized energy variables,

$$z = \frac{\frac{1}{2}\mu g^2}{k\tilde{T}} \quad \lambda = \frac{\frac{1}{2}\mu w^2}{k\tilde{T}} \quad z^* = \max\left(0, \frac{\Delta\varepsilon}{k\tilde{T}}\right) \quad (12)$$

where \tilde{T} is defined in Appendix B. Using $g^3 dg \equiv 2\varepsilon d\varepsilon/\mu^2$ and a further change of variables, we finally obtain:

$$\Psi_{st} = n_s n_t \underbrace{\left(\frac{8k\tilde{T}}{\pi\mu}\right)^{\frac{1}{2}}}_{\bar{g}_{\tilde{T}}} e^{-\lambda} \int_{z^*}^{\infty} dz z e^{-z} \bar{\sigma}_{st}(z) \cdot \frac{1}{2} \int_{-1}^{+1} dc_\theta e^{2\sqrt{\lambda} z c_\theta} \cdot \langle \psi \rangle_{\Omega'} \quad (13)$$

with $\bar{g}_{\tilde{T}}$ a thermal velocity based on the average temperature \tilde{T} . Note that we have left the variable ψ undetermined, and since it could potentially depend on all integration variables

(z, χ, θ) , ψ must be kept inside all integrals. We will see what simplifications can be made next, depending on which moment variables we are integrating.

The lower limit of integration, z^* , is zero for elastic collisions or for exothermic reactions. Thus, equation (13) is a general formula, which applies equally to excitation ($z^* > 0$) and deexcitation ($z^* \equiv 0$)³⁸. Let us first consider an excitation collision:

$$s(\mathbf{v}_s) + t(E_\ell, \mathbf{v}_t) \rightarrow s(\mathbf{v}'_s) + t(E_u, \mathbf{v}'_t)$$

where ℓ and u denote the lower and upper energy states, respectively. We made here the assumption that both states (ℓ, u) belong to the same fluid, so that the particle indices (s, t) are kept the same, but this is not necessary. From eq. (2), energy conservation implies $\Delta\varepsilon = E_u - E_\ell > 0$. We can then define normalized energy variables for this case, x, x' and x^* :

$$x^* = \frac{\varepsilon^*}{kT} > 0; \quad x' \equiv x - x^* > 0 \quad (14)$$

Note that x (x') is the normalized kinetic energy of the initial (final) products of excitation respectively, and that x^* is the normalized energy threshold, always a positive quantity. For excitation, we can use (13) with the following identifications:

$$z \equiv x, \quad z^* \equiv x^*, \quad z' \equiv x', \quad \text{and} \quad n_t \equiv n_\ell \quad (15)$$

For a deexcitation collision, we have the reverse ($u \rightarrow \ell$), i.e. $\Delta\varepsilon < 0$:

$$s(\mathbf{v}_s) + t(E_u, \mathbf{v}_t) \rightarrow s(\mathbf{v}'_s) + t(E_\ell, \mathbf{v}'_t) \quad (16)$$

Equation (13) is again still valid, if we now make the following identifications:

$$z \equiv x', \quad z^* \equiv 0, \quad z' \equiv x, \quad \text{and} \quad n_t \equiv n_u \quad (17)$$

Therefore, in all cases the variable x always refers to the larger kinetic energy (before excitation or after deexcitation) and x' refers to the smaller value (after excitation or before deexcitation). We can therefore define two cases of (13):

$$\Psi_{s\ell}^\uparrow = n_s n_\ell \bar{g}_{\bar{T}} e^{-\lambda} \int_{x^*}^{\infty} dx x e^{-x} \bar{\sigma}_{s\ell}^\uparrow(x) \cdot \frac{1}{2} \int_{-1}^{+1} dc_\theta e^{2\sqrt{\lambda x} c_\theta} \cdot \langle \psi \rangle_{\Omega'} \quad (18a)$$

$$\Psi_{su}^\downarrow = n_s n_u \bar{g}_{\bar{T}} e^{-\lambda} \int_0^{\infty} dx' x' e^{-x'} \bar{\sigma}_{su}^\downarrow(x') \cdot \frac{1}{2} \int_{-1}^{+1} dc_\theta e^{2\sqrt{\lambda x'} c_\theta} \cdot \langle \psi \rangle_{\Omega'} \quad (18b)$$

where the superscripts \uparrow, \downarrow indicate excitation and deexcitation respectively (note the change of subscript from st to $s\ell$ for excitation, and su for deexcitation). It is worth pointing out that the averaging over the scattering angle, i.e., $\langle \psi \rangle_{\Omega'}$, has to be done with the corresponding angular-dependent DCS \mathcal{G} , e.g., $\langle \psi \rangle_{\Omega'} = 2\pi \int c_\chi \psi \mathcal{G}_{s\ell}^\uparrow$ for excitation. However, from time reversal we have $\mathcal{G}_{s\ell}^\uparrow = \mathcal{G}_{su}^\downarrow$, so for simplicity, we do not differentiate $\langle \psi \rangle$ between excitation and deexcitation. Note that the integration over the θ angle remains to be performed. If the moment variable ψ can be expanded in terms of power of $\cos \theta$, we can then define the following set of functions:

$$\zeta^{(k)}(\xi) = \mathcal{N}_k \int_{-1}^{+1} dy y^k e^{2\xi y} \quad (19)$$

where \mathcal{N}_k is a normalizing factor. In particular, we have:

$$\zeta^{(0)}(\xi) = \frac{1}{2} \int_{-1}^{+1} dy e^{2\xi y} = \frac{\sinh(2\xi)}{2\xi} \quad \text{s.t.:} \quad \lim_{\xi \rightarrow 0} \zeta^{(0)} = 1 \quad (20a)$$

$$\zeta^{(1)}(\xi) = \frac{3}{4\xi} \int_{-1}^{+1} dy y e^{2\xi y} = \frac{3}{4\xi^2} \left[\cosh(2\xi) - \frac{\sinh(2\xi)}{2\xi} \right] \quad \text{s.t.:} \quad \lim_{\xi \rightarrow 0} \zeta^{(1)} = 1 \quad (20b)$$

In the CR model, each internal state is treated as a pseudo-species, so the rate of change in number density for each state (n_ℓ, n_u) is taken into account separately. We can now examine the specific form taken by the transfer integral, according to the chosen moment variable, starting from (8), (13), or (18).

B. Zeroth-order moment: number density

The rate of change of the number density due to an inelastic collision of type (1) can be obtained by setting $\psi \equiv 1$ in (13), so the average over all the scattering angle is trivially removed:

$$\Gamma_{st} = n_s n_t \bar{g}_{\bar{T}} e^{-\lambda} \int_{z^*}^{\infty} dz z e^{-z} \bar{\sigma}_{st}(z) \cdot \frac{1}{2} \int_{-1}^{+1} dc_\theta e^{2\sqrt{\lambda} z c_\theta} \quad (21)$$

The integration over dc_θ yields the function $\zeta^{(0)}$ defined in eq. (20). We can now express the rates for transitions between two atomic levels ℓ, u , by making the appropriate substitutions for the energy variables. For the case of an excitation ($\ell \rightarrow u$), and according to eq. (15), we define the variable x as the normalized kinetic energy of the reactants (s, t) in the COM frame, prior to the collision: therefore in this case, $z \equiv x$, $z^* \equiv x^* > 0$ and $n_t \equiv n_\ell$. Thus,

$$\Gamma_{s\ell}^\uparrow = n_s n_\ell \bar{g}_{\bar{T}} e^{-\lambda} \int_{x^*}^{\infty} dx x e^{-x} \bar{\sigma}_{s\ell}^\uparrow(x) \zeta^{(0)}(\sqrt{\lambda} x) \quad (22)$$

For deexcitation ($u \rightarrow \ell$), the rate of change of number density follows from (17):

$$\Gamma_{su}^\downarrow = n_s n_u \bar{g}_{\bar{T}} e^{-\lambda} \int_0^\infty dx' x' e^{-x'} \bar{\sigma}_{su}^\downarrow(x') \zeta^{(0)}(\sqrt{\lambda x'}) \quad (23)$$

Both of these quantities are positive, hence the resultant rates equations are:

$$\frac{dn_\ell}{dt} = -\Gamma_{s\ell}^\uparrow = -\frac{dn_u}{dt} \quad \text{and} \quad \frac{dn_\ell}{dt} = +\Gamma_{su}^\downarrow = -\frac{dn_u}{dt}$$

In the case of electron-impact processes ($s \equiv e$), we can neglect terms of order m_e/M , and for an atomic transition between levels $\ell \rightarrow u$, we obtain:

$$\Gamma_{e\ell}^\uparrow = n_e n_\ell \bar{v}_e e^{-\lambda} \int_{x^*}^\infty dx x e^{-x} \bar{\sigma}_{e\ell}^\uparrow(x) \zeta^{(0)}(\sqrt{\lambda x}) \quad (24)$$

where $\bar{v}_e = \sqrt{\frac{8kT_e}{\pi m_e}}$. In the limit of thermal plasma where multifluid effects are weak, i.e. $\lambda \rightarrow 0$, we obtain:

$$\Gamma_{e\ell}^\uparrow = n_e n_\ell \bar{v}_e \int_{x^*}^\infty dx x e^{-x} \bar{\sigma}_{e\ell}^\uparrow(x) \quad (25)$$

which is *exactly* the expected result for a single-fluid plasma.

Using the Klein-Rosseland relation for detailed balance³⁰,

$$\bar{\sigma}_{s\ell}^\uparrow(x) x g_\ell = \bar{\sigma}_{su}^\downarrow(x') x' g_u \quad (26)$$

where g_ℓ, g_u are the degeneracies of the lower and upper atomic levels respectively, we can write the excitation rate as follows:

$$\Gamma_{s\ell}^\uparrow = n_s n_\ell \bar{g}_{\bar{T}} e^{-\lambda} \frac{g_u}{g_\ell} e^{-x^*} \int_0^\infty dx' x' e^{-x'} \zeta^{(0)}(\sqrt{\lambda(x^* + x')}) \bar{\sigma}_{su}^\downarrow(x') \quad (27)$$

One can then easily extract reaction rates, for example:

$$\Gamma_{s\ell}^\uparrow = \varpi_{s\ell}^\uparrow \cdot n_s n_\ell \quad (28a)$$

$$\Gamma_{su}^\downarrow = \varpi_{su}^\downarrow \cdot n_s n_u \quad (28b)$$

It is instructive to consider the ratio of these rates:

$$\frac{\varpi_{s\ell}^\uparrow}{\varpi_{su}^\downarrow} = \left[\frac{g_u}{g_\ell} e^{-x^*} \right] \cdot \frac{\int_0^\infty dx' x' e^{-x'} \zeta^{(0)}(\sqrt{\lambda(x^* + x')}) \bar{\sigma}_{su}^\downarrow(x')}{\int_0^\infty dx' x' e^{-x'} \zeta^{(0)}(\sqrt{\lambda x'}) \bar{\sigma}_{su}^\downarrow(x')} \quad (29)$$

The first term in brackets is the traditional Boltzmann equilibrium relation; the second term contains the correction due to the multifluid effects, and appears only through the $\zeta^{(0)}$

function (20-a). A Taylor expansion near $\lambda = 0$ yields (with an obvious definition of the Boltzmann function \mathcal{B}):

$$\begin{aligned} \frac{\varpi_{s\ell}^{\uparrow}}{\varpi_{su}^{\downarrow}} &= \left[\frac{g_u}{g_\ell} e^{-x^*} \right] \cdot \frac{\int_0^\infty dx' x' e^{-x'} \left[1 + \frac{2\lambda(x^*+x')}{3} \right] \bar{\sigma}_{su}^{\downarrow}(x')}{\int_0^\infty dx' x' e^{-x'} \left[1 + \frac{2\lambda x'}{3} \right] \bar{\sigma}_{su}^{\downarrow}(x')} \\ &\simeq \left[\mathcal{B}_{lu}(\tilde{T}) \right] \cdot \left(1 + \frac{2\lambda x^*}{3} + o(\lambda^2) \right) \end{aligned} \quad (30)$$

Thus, we recover the expression for Boltzmann equilibrium in the thermal (single-fluid) limit ($\lambda \rightarrow 0$). Note that the correction term increases with the energy threshold, i.e. transitions between high levels ($x^* \rightarrow 0$) will not be affected very much by the multifluid effects, while the impact will be stronger for excitation from low energy levels, with high energy gaps. For elastic collisions ($x^*=0$), the ratio of rates is exactly given by the ratio of degeneracies.

C. First-order moment: momentum density

Consider now the forward reaction (1) and the corresponding loss of momentum to the particles with velocity \mathbf{v}_s . The transfer variable in this case is $\psi = m_s \mathbf{v}_s$, and starting from equation (8), the contribution to the momentum equation is:

$$\mathbf{R}_s^- = -\frac{n_s n_t}{\pi^{\frac{3}{2}} \alpha^3} \cdot \int d^3 \mathbf{V}^* f_{V^*} \cdot \int dg g^3 e^{-g^2/\alpha^2} \bar{\sigma}_{st}(g) \cdot \int d\varphi dc_\theta e^{2gwc_\theta/\alpha^2} \langle m_s \mathbf{v}_s \rangle_{\Omega'} \quad (31)$$

Similarly, the gain in momentum is given by the production of *new* particles with velocity \mathbf{v}'_s :

$$\mathbf{R}_s^+ = +\frac{n_s n_t}{\pi^{\frac{3}{2}} \alpha^3} \cdot \int d^3 \mathbf{V}^* f_{V^*} \cdot \int dg g^3 e^{-g^2/\alpha^2} \bar{\sigma}_{st}(g) \cdot \int d\varphi dc_\theta e^{2gwc_\theta/\alpha^2} \langle m_s \mathbf{v}'_s \rangle_{\Omega'} \quad (32)$$

Using the relation:

$$m_s (\mathbf{v}_s - \mathbf{v}'_s) = \mu (\mathbf{g} - \mathbf{g}') \quad (33)$$

we verify that the integrand does not depend on \mathbf{V}^* and its integration is trivially removed. The *net* rate of change to the momentum density of species s is therefore:

$$\mathbf{R}_s = -\mu \frac{n_s n_t}{\pi^{\frac{3}{2}} \alpha^3} \cdot \int dg g^3 e^{-g^2/\alpha^2} \bar{\sigma}_{st}(g) \cdot \int d\varphi dc_\theta e^{2gwc_\theta/\alpha^2} \langle \mathbf{g} - \mathbf{g}' \rangle_{\Omega'} \quad (34)$$

Let us consider the last integral over the scattering angle. From Figure 1, the vectors \mathbf{g}, \mathbf{g}' in the rotated frame (ξ, η, ς) are:

$$\mathbf{g} = g \hat{\mathbf{g}} = g \cdot \begin{pmatrix} 0 \\ 0 \\ 1 \end{pmatrix}; \quad \mathbf{g}' = g' \cdot \hat{\mathbf{g}}' = g' \begin{pmatrix} c_\rho s_\chi \\ s_\rho s_\chi \\ c_\chi \end{pmatrix} \quad (35)$$

Therefore the integral yields:

$$\begin{aligned} \int d\Omega' (\mathbf{g} - \mathbf{g}') \mathcal{G}(g, \Omega') &= 2\pi g \int dc_\chi \mathcal{G}(g, \chi) \hat{\mathbf{g}} - 2\pi g' \int dc_\chi c_\chi \mathcal{G}(g, \chi) \hat{\mathbf{g}} \\ &= [g - g' \langle \cos \chi \rangle_{\Omega'}] \hat{\mathbf{g}} \end{aligned} \quad (36)$$

We must now express the unit vector $\hat{\mathbf{g}}$ in the initial $(\hat{\mathbf{x}}, \hat{\mathbf{y}}, \hat{\mathbf{z}})$ frame, which is given by (7); integration over the φ variable leaves only one component, $c_\theta \hat{\mathbf{w}}$, yielding:

$$\mathbf{R}_s = -\mu \hat{\mathbf{w}} \frac{2n_s n_t}{\pi^{\frac{1}{2}} \alpha^3} \cdot \int dg g^3 e^{-g^2/\alpha^2} \bar{\sigma}_{st}(g) \cdot \int dc_\theta c_\theta e^{2gwc_\theta/\alpha^2} [g - g' \langle \cos \chi \rangle_{\Omega'}] \quad (37)$$

Using (20) to replace the last integral and using the normalized variables (12) leads to:

$$\mathbf{R}_s = -\frac{2}{3} \mu \mathbf{w} n_s n_t \bar{g}_{\bar{T}} e^{-\lambda} \int_{z^*}^{\infty} dz z^{\frac{3}{2}} e^{-z} \bar{\sigma}_{st}(z) \zeta^{(1)}(\sqrt{\lambda} z) \left(\sqrt{z} - \sqrt{z'} \langle \cos \chi \rangle_{\Omega'} \right) \quad (38)$$

A similar (but of opposite sign) expression can be obtained for the species of type t , as a result of the identity $m_s(\mathbf{v}_t - \mathbf{v}'_t) = \mu(\mathbf{g}' - \mathbf{g})$.

We can now specify the type of collision. For an $\ell \rightarrow u$ excitation, we follow (15), to yield:

$$\mathbf{R}_s^\uparrow = -\frac{2}{3} \mu \mathbf{w} n_s n_\ell \bar{g}_{\bar{T}} e^{-\lambda} \int_{x^*}^{\infty} dx x^{\frac{3}{2}} e^{-x} \bar{\sigma}_{s\ell}^\uparrow(x) \zeta^{(1)}(\sqrt{\lambda} x) \left(\sqrt{x} - \sqrt{x'} \langle \cos \chi \rangle_{\Omega'} \right) \quad (39)$$

For deexcitation, we follow (17):

$$\mathbf{R}_s^\downarrow = -\frac{2}{3} \mu \mathbf{w} n_s n_u \bar{g}_{\bar{T}} e^{-\lambda} \int_0^{\infty} dx' (x')^{\frac{3}{2}} e^{-x'} \bar{\sigma}_{su}^\downarrow(x') \zeta^{(1)}(\sqrt{\lambda} x') \left(\sqrt{x'} - \sqrt{x} \langle \cos \chi \rangle_{\Omega'} \right) \quad (40)$$

Note that the expressions (39–40) are obtained in a frame where \mathbf{w} is aligned with the $\hat{\mathbf{z}}$ direction and corresponds to the change in momentum density along that direction. Thus, it is the component of a force *parallel* to \mathbf{w} , while all components in the transverse directions are zero, by reason of symmetry³⁹. The components in an arbitrary rest-frame must be obtained by projecting \mathbf{w} .

Since the force density is *approximately* proportional to \mathbf{w} , we can group all the other terms into the definition of a coefficient, such that

$$\mathbf{R}_s^\uparrow = -K_{s\ell}^\uparrow(\mathbf{u}_s - \mathbf{u}_t) \quad \mathbf{R}_t^\uparrow = +K_{s\ell}^\uparrow(\mathbf{u}_s - \mathbf{u}_t) \quad (41a)$$

$$\mathbf{R}_s^\downarrow = -K_{su}^\downarrow(\mathbf{u}_s - \mathbf{u}_t) \quad \mathbf{R}_t^\downarrow = +K_{su}^\downarrow(\mathbf{u}_s - \mathbf{u}_t) \quad (41b)$$

where $K_{s\ell}^\uparrow$ and K_{su}^\downarrow are known as resistance coefficients:

$$K_{s\ell}^\uparrow = \frac{2}{3} \mu n_s n_\ell \bar{g}_{\tilde{T}} e^{-\lambda} \int_{x^*}^{\infty} dx x^{\frac{3}{2}} e^{-x} \bar{\sigma}_{s\ell}^\uparrow(x) \zeta^{(1)}(\sqrt{\lambda x}) \left[\sqrt{x} - \sqrt{x'} \langle \cos \chi \rangle_{\Omega'} \right] \quad (42a)$$

$$K_{su}^\downarrow = \frac{2}{3} \mu n_s n_u \bar{g}_{\tilde{T}} e^{-\lambda} \int_0^{\infty} dx' (x')^{\frac{3}{2}} e^{-x'} \bar{\sigma}_{su}^\downarrow(x) \zeta^{(1)}(\sqrt{\lambda x'}) \left[\sqrt{x'} - \sqrt{x} \langle \cos \chi \rangle_{\Omega'} \right] \quad (42b)$$

It must be pointed out that when the collision is elastic, i.e., $x = x'$, we recover the expression of the momentum transfer cross section often used in transport calculation, i.e., $\sigma^m(x) \equiv \bar{\sigma}(1 - \langle \cos \chi \rangle)$ (see for example³²). In the limit of weak divergence of mean fluid velocities ($\lambda \rightarrow 0$) and isotropic scattering ($\mathcal{G}(\chi) = 1/4\pi$), we have:

$$K_{s\ell}^\uparrow \simeq \frac{2}{3} \mu n_s n_\ell \bar{g}_{\tilde{T}} \int_{x^*}^{\infty} dx x^2 \bar{\sigma}_{s\ell}^\uparrow(x) e^{-x} \quad (43)$$

Again, using the Klein-Rosseland relation, the excitation resistance coefficient can be written as:

$$K_{s\ell}^\uparrow = \left[\mathcal{B}_{\ell u}(\tilde{T}) \right] \frac{2}{3} \mu n_s n_\ell \bar{g}_{\tilde{T}} e^{-\lambda} \int_0^{\infty} dx' x' x^{\frac{1}{2}} e^{-x'} \zeta^{(1)}(\sqrt{\lambda(x)}) \bar{\sigma}_{su}^\downarrow(x') \left[\sqrt{x} - \sqrt{x'} \langle \cos \chi \rangle_{\Omega'} \right] \quad (44)$$

As in the case of the zero-th order moment, we define the momentum exchange rates by:

$$K_{s\ell}^\uparrow = \mu n_s n_\ell \kappa_{s\ell}^\uparrow \quad (45a)$$

$$K_{su}^\downarrow = \mu n_s n_u \kappa_{su}^\downarrow \quad (45b)$$

In the case of weak divergence of mean fluid velocities and isotropic scattering, the ratio of the rate coefficients for the forward and backward processes is approximately:

$$\frac{\kappa_{s\ell}^\uparrow}{\kappa_{su}^\downarrow} \simeq \left[\mathcal{B}_{\ell u}(\tilde{T}) \right] \cdot \frac{\int_0^{\infty} dx' e^{-x'} x' (x^* + x') \left[1 + \frac{2}{5} \lambda (x^* + x') \right] \bar{\sigma}_{su}^\downarrow(x')}{\int_0^{\infty} dx' e^{-x'} x'^2 \left[1 + \frac{2}{5} \lambda x' \right] \bar{\sigma}_{su}^\downarrow(x')} \quad (46)$$

Note that there is an additional contribution from high-order moment from the expansion.

This can be seen by further expanding the integrand of the numerator:

$$x' (x^* + x') \left[1 + \frac{2}{5} \lambda (x^* + x') \right] = x'^2 \left[1 + \frac{2}{5} \lambda x' \right] + x^* x' \left[1 + \frac{2}{5} \lambda (x^* + 2x') \right]$$

such that

$$\frac{\kappa_{s\ell}^\uparrow}{\kappa_{su}^\downarrow} \simeq \left[\mathcal{B}_{\ell u}(\tilde{T}) \right] \cdot \left[1 + x^* \frac{\int_0^\infty dx' e^{-x'} x' \left[1 + \frac{2}{5} \lambda (x^* + 2x') \right] \bar{\sigma}_{su}^\downarrow(x')}{\int_0^\infty dx' e^{-x'} x'^2 \left[1 + \frac{2}{5} \lambda x' \right] \bar{\sigma}_{su}^\downarrow(x')} \right] \quad (47)$$

Note that even as $\lambda \rightarrow 0$, the correction term does not vanish. Therefore, there is no equivalence between the resistance coefficients of the forward and backward processes in the limit $\lambda \rightarrow 0$. However, this is perfectly understandable; note that the correction is proportional to the energy threshold, and since kinetic energy must be removed from particle s in order to achieve excitation, but not for deexcitation, there must also be an imbalance in the momentum exchange rate. As expected, this imbalance vanishes for elastic collisions ($x^* \rightarrow 0$), and the rates are consistent with the detailed balance of the mass exchange. In all cases, detailed balance is enforced through relation (26) at the microscopic level.

D. Second-order moment: total energy density

The net rate of change of total energy of species s can be obtained by setting $\psi = \frac{1}{2} m_s (\mathbf{v}'_s - \mathbf{v}_s^2)$ into equation (11):

$$Q_s = \frac{n_s n_t}{\pi^{\frac{3}{2}} \alpha^3} \cdot \int d^3 \mathbf{V}^* f_{V^*} \int dg g^3 e^{-g^2/\alpha^2} \bar{\sigma}_{st}(g) \cdot \int d\varphi d\cos\theta e^{2gwc_\theta/\alpha^2} \left\langle \frac{1}{2} m_s (\mathbf{v}'_s - \mathbf{v}_s^2) \right\rangle_{\Omega'} \quad (48)$$

Using the transformation defined in Appendix B,

$$\frac{1}{2} m_s (\mathbf{v}'_s - \mathbf{v}_s^2) = \mu (\mathbf{g}' - \mathbf{g}) \cdot [\mathbf{V}^* + \mathbf{U} - \gamma(\mathbf{g} - \mathbf{w})] - \frac{m_t}{M} \Delta \varepsilon \quad (49)$$

The integration of the first term in the square bracket is zero since $\int d^3 \mathbf{V}^* \mathbf{V}^* f_{V^*} = 0$. One can easily see that the second term in brackets is simply $\mathbf{R}_s \cdot \mathbf{U}$ by comparing with (34). Similarly, the last term in (49) is identified as $-(m_t/M) \Delta \varepsilon \Gamma_{st}$. The third term in brackets involves the following dot product:

$$\begin{aligned} (\mathbf{g}' - \mathbf{g}) \cdot (\mathbf{g} - \mathbf{w}) &= \mathbf{g} \cdot \mathbf{g}' - \mathbf{w} \cdot \mathbf{g}' - g^2 + \mathbf{w} \cdot \mathbf{g} \\ &= gg' \cos \chi - wg'(\hat{\mathbf{g}}' \cdot \hat{\mathbf{w}}) - g^2 + wg \cos \theta \end{aligned} \quad (50)$$

We can now perform the averaging over the scattering angle; in particular, we have

$$\int d\Omega' \mathcal{G}(\chi) \hat{\mathbf{g}}' \cdot \hat{\mathbf{w}} = \langle \cos \chi \rangle_{\Omega'} \cos \theta$$

so that

$$\int d\Omega' \mathcal{G}(\chi) (\mathbf{g}' - \mathbf{g}) \cdot (\mathbf{g} - \mathbf{w}) = (g' \langle \cos \chi \rangle_{\Omega'} - g)(g - w \cos \theta) \quad (51)$$

Thus, we obtain, after integration over φ :

$$Q_s = \mathbf{U} \cdot \mathbf{R}_s - \frac{m_t}{M} \Delta \varepsilon \Gamma_{st} - \mu \gamma \frac{4n_s n_t}{\pi^{\frac{1}{2}} \alpha^3} e^{-\lambda} \int dg g^3 \bar{\sigma}_{st}(g) e^{-g^2/\alpha^2} \mathcal{I}_\theta \quad (52)$$

where the last angular integral is

$$\begin{aligned} \mathcal{I}_\theta &= \frac{1}{2} \int dc_\theta e^{2gwc_\theta/\alpha^2} (g' \langle c_\chi \rangle_{\Omega'} - g)(g - wc_\theta) \\ &= (g' \langle c_\chi \rangle_{\Omega'} - g) \left\{ g \frac{1}{2} \int dc_\theta e^{2gwc_\theta/\alpha^2} - \frac{w}{2} \int dc_\theta c_\theta e^{2gwc_\theta/\alpha^2} \right\} \\ &= (g' \langle c_\chi \rangle_{\Omega'} - g) g \left\{ \zeta^{(0)}(\sqrt{\lambda}z) - \frac{2}{3} \frac{w^2}{\alpha^2} \zeta^{(1)}(\sqrt{\lambda}z) \right\} \end{aligned} \quad (53)$$

Therefore, after the change of variables $g \rightarrow z$:

$$\begin{aligned} Q_s &= \mathbf{U} \cdot \mathbf{R}_s - \frac{m_t}{M} \Delta \varepsilon \Gamma_{st} \\ &\quad + \mu \gamma \frac{4n_s n_t}{\pi^{\frac{1}{2}} \alpha^3} e^{-\lambda} \frac{\alpha^6}{2} \int dz z^{\frac{3}{2}} e^{-z} \bar{\sigma}_{st}(z) \left(\sqrt{z} - \sqrt{z'} \langle \cos \chi \rangle_{\Omega'} \right) \left(\zeta^{(0)}(\sqrt{\lambda}z) - \frac{2\lambda}{3} \zeta^{(1)}(\sqrt{\lambda}z) \right) \end{aligned} \quad (54)$$

The factor in front of the integral can be re-arranged to yield:

$$\gamma n_s n_t \bar{g}_{\tilde{T}} e^{-\lambda} (2k\tilde{T})$$

Using the identity $\gamma(2k\tilde{T}) = \frac{2\mu}{M} k(T_t - T_s)$, the final result has a traditional form:

$$Q_s = \mathbf{U} \cdot \mathbf{R}_s - \frac{m_t}{M} \Delta \varepsilon \Gamma_{st} + J_{st} \frac{2\mu}{M} k(T_t - T_s) \quad (55)$$

with the thermal resistance coefficient defined as:

$$J_{st} = n_s n_t \bar{g}_{\tilde{T}} e^{-\lambda} \int dz z^{\frac{3}{2}} e^{-z} \bar{\sigma}_{st}(z) \left(\sqrt{z} - \sqrt{z'} \langle \cos \chi \rangle_{\Omega'} \right) \left(\zeta^{(0)}(\sqrt{\lambda}z) - \frac{2\lambda}{3} \zeta^{(1)}(\sqrt{\lambda}z) \right) \quad (56)$$

This result is general, and we can now make the usual substitutions for excitation:

$$Q_s^\dagger = \mathbf{U} \cdot \mathbf{R}_s^\dagger - \frac{m_t}{M} \varepsilon^* \Gamma_{s\ell}^\dagger + J_{s\ell}^\dagger \frac{2\mu}{M} k(T_t - T_s) \quad (57a)$$

$$J_{s\ell}^\dagger = n_s n_\ell \bar{g}_{\tilde{T}} e^{-\lambda} \int dx x^{\frac{3}{2}} e^{-x} \bar{\sigma}_{s\ell}^\dagger(x) \left(\sqrt{x} - \sqrt{x'} \langle \cos \chi \rangle_{\Omega'} \right) \left(\zeta^{(0)}(\sqrt{\lambda}x) - \frac{2\lambda}{3} \zeta^{(1)}(\sqrt{\lambda}x) \right) \quad (57b)$$

In the case of deexcitation, we can still use the general formula (54), except that in this case, $\Delta\varepsilon = -\varepsilon^*$. This can be seen if we start from eq. (48), which gives us:

$$\begin{aligned} Q_s^\downarrow = & -\mu \frac{n_s n_t}{\pi^{\frac{3}{2}} \alpha^3} e^{-\lambda} \int d^3 \mathbf{g}' g' \bar{\sigma}_{su}^\downarrow(g') e^{-g'^2/\alpha^2} e^{2g' w c_\theta / \alpha^2} \mathbf{U} \cdot \langle \mathbf{g}' - \mathbf{g} \rangle_{\Omega'} \\ & + \mu \gamma \frac{n_s n_t}{\pi^{\frac{3}{2}} \alpha^3} e^{-\lambda} \int d^3 \mathbf{g}' g' \bar{\sigma}_{su}^\downarrow(g') e^{-g'^2/\alpha^2} e^{2g' w c_\theta / \alpha^2} (\mathbf{g}' - \mathbf{g}) \cdot (\mathbf{g} - \mathbf{w}) \\ & + \frac{m_t}{M} \varepsilon^* \Gamma_{su}^\downarrow \end{aligned} \quad (58)$$

Again, one can easily recognize the standard formulae:

$$Q_s^\downarrow = \mathbf{U} \cdot \mathbf{R}_s^\downarrow + \frac{m_t}{M} \varepsilon^* \Gamma_{su}^\downarrow + J_{su}^\downarrow \frac{2\mu}{M} k(T_t - T_s) \quad (59a)$$

$$J_{su}^\downarrow = n_s n_u \bar{g}_{\bar{T}} e^{-\lambda} \int dx' (x')^{\frac{3}{2}} e^{-x'} \bar{\sigma}_{su}^\downarrow(x') \left(\sqrt{x'} - \sqrt{x} \langle \cos \chi \rangle_{\Omega'} \right) \left(\zeta^{(0)}(\sqrt{\lambda x'}) - \frac{2\lambda}{3} \zeta^{(1)}(\sqrt{\lambda x'}) \right) \quad (59b)$$

which could also be obtained directly from (55 - 56), with the usual substitutions (17).

We can also express the source term for particle t , using:

$$\begin{aligned} \frac{1}{2} m_t (\mathbf{v}_t'^2 - \mathbf{v}_t^2) &= \frac{1}{2} m_t \left(\left(\mathbf{V} - \frac{m_s}{M} \mathbf{g}' \right)^2 - \left(\mathbf{V} - \frac{m_s}{M} \mathbf{g} \right)^2 \right) \\ &= \frac{m_s}{2M} \mu (\mathbf{g}'^2 - \mathbf{g}^2) - \mu \mathbf{V} \cdot (\mathbf{g}' - \mathbf{g}) \\ &= -\mu (\mathbf{g}' - \mathbf{g}) \cdot [\mathbf{V}^* + \mathbf{U} - \gamma(\mathbf{g} - \mathbf{w})] - \frac{m_s}{M} \Delta\varepsilon \end{aligned} \quad (60)$$

Comparing with (49), we easily obtain (note the inversion of T_s and T_t in the last term):

$$Q_t^\uparrow = \mathbf{U} \cdot \mathbf{R}_t^\uparrow - \frac{m_s}{M} \varepsilon^* \Gamma_{sl}^\uparrow + J_{sl}^\uparrow \frac{2\mu}{M} k(T_s - T_t) \quad (61a)$$

$$Q_t^\downarrow = \mathbf{U} \cdot \mathbf{R}_t^\downarrow + \frac{m_s}{M} \varepsilon^* \Gamma_{su}^\downarrow + J_{su}^\downarrow \frac{2\mu}{M} k(T_s - T_t) \quad (61b)$$

with $\mathbf{R}_t^{\uparrow(\downarrow)} = -\mathbf{R}_s^{\uparrow(\downarrow)}$. Combining both s and t fluids, the only term remaining is the loss of energy equal to the energy gap between the levels, as expected. Note also that this energy loss is distributed to the respective fluids according to the ratio of masses, such that the lighter element receives the major contribution. This is also an expected result, similar to the energy exchange due to elastic collisions, and due to the kinematics of collision.

In the limits of near-single fluid ($\lambda \rightarrow 0$) and isotropic scattering, we have:

$$J_{sl}^\uparrow \simeq n_s n_\ell \bar{g}_{\bar{T}} \left(1 - \frac{2\lambda}{3} \right) \int_{x^*}^\infty dx x^2 \bar{\sigma}_{sl}^\uparrow(x) e^{-x} \quad (62)$$

The thermal relaxation rates can be extracted similarly:

$$J_{s\ell}^{\uparrow} = n_s n_{\ell} j_{s\ell}^{\uparrow} \quad (63a)$$

$$J_{su}^{\downarrow} = n_s n_u j_{su}^{\downarrow} \quad (63b)$$

The ratio of the thermal relaxation rates can be written as:

$$\frac{j_{s\ell}^{\uparrow}}{j_{su}^{\downarrow}} \simeq [\mathcal{B}_{\ell u}(\tilde{T})] \cdot \left[1 + x^* \frac{\int_0^{\infty} dx' e^{-x'} x' \left[1 - \frac{2}{3}\lambda + \frac{2}{3}\lambda(x^* + 2x') \right] \bar{\sigma}_{su}^{\downarrow}}{\int_0^{\infty} dx' e^{-x'} x'^2 \left[1 - \frac{2}{3}\lambda + \frac{2}{3}\lambda x' \right] \bar{\sigma}_{su}^{\downarrow}} \right] \quad (64)$$

Similar to the case of momentum transfer rates, the correction terms do not vanish when $\lambda \rightarrow 0$ due to contribution from high-order moments.

III. Numerical Results

In the following sections, we carry out a numerical evaluation and verification of the exchange rates derived in [IIB](#), [IIC](#) and [IID](#), for the case of free electrons interacting with hydrogen atoms; these processes include electron-neutral elastic collision and electron-impact excitation and deexcitation. Ionization and recombination are currently omitted and will be included in future work. For comparison purpose, we also show the exchange rates due to Coulomb collision, i.e., electron-hydrogen ion, which is the dominating elastic exchange mechanism for plasma with high ionization fraction.

The notations are slightly modified to better distinguish each type of interaction. We use superscripts (en) , (ei) and (xd) to denote electron-neutral, electron-ion (Coulomb), and excitation/deexcitation (as a whole) collisions, respectively. These grouped notations are useful, for example, when looking at the net momentum (or energy) transfer due to each type of collision. The symbols \uparrow, \downarrow are still retained to indicate individual excitation and deexcitation rates. For each transition between two atomic states, we use the convention of indexing the final state on the left, and the initial state on the right, i.e., $(f|i)$. For example, $\varpi_{(u|\ell)}^{\uparrow}$ is the forward excitation rate from ℓ to u , and $\varpi_{(\ell|u)}^{\downarrow}$ is the reverse process. The energy levels and cross sections models for atomic hydrogen are given in classical form and summarized in [Appendix C](#)

A. Reaction Rates

All the exchange rates (mass, momentum, energy) can be tabulated as a function of two parameters: the average thermal temperature \tilde{T} , defined in [appendix B](#), and a non-dimensional

parameter λ , defined in eq. (12), which corresponds to the relative mean kinetic energy. For convenience, we also define an equivalent drift temperature $T_w = \lambda \tilde{T}^{40}$, such that all the rates can be tabulated in terms of two temperatures. Since the mass ratio between the electron and the atom is very small ($m_e \ll M_H$), we can drop terms of order m_e/M and arrive at the following approximations: $\mu \simeq m_e$, $\tilde{T} \simeq T_e$, $T_w \simeq \lambda T_e$ and $\bar{g}_{\tilde{T}} \simeq \bar{v}_e = \sqrt{\frac{8kT_e}{\pi m_e}}$. Therefore, all the exchange rates for electron-induced collisions (both elastic and inelastic) can be numerically evaluated in terms of the electron temperature T_e and the drift temperature T_w .

Figure 2 shows example calculations of the zeroth-order reaction rates, defined in eqs. (22), (23) and (28), for electron-impact excitation and deexcitation between the first three atomic states of hydrogen. These rates exhibit a similar trend for the range of temperatures plotted here, that is, starting from low temperature, the rates first increase, reaching a plateau and then decrease as temperature further increases. The value at which the rate is maximum is very close to the threshold temperature of the transition. This trend holds both in the direction of increasing thermal T_e (x-axis) or drift temperatures T_w (y-axis).

It is clearly shown from Figure 2 that the reaction rates can be significantly different from the thermal limit when the relative mean velocity between two fluids is significant. In particular, one sees an increase of the reaction rate in the low temperature regime where T_e and T_w are small compared to the excitation temperature of the collision; this enhancement corresponds directly to the form of the cross sections. Therefore, one can expect that significant deviation from the thermal rate occurs when the mean kinetic energy is of the same order as the excitation temperature. This indicates that excitation and deexcitation among low energy states with large threshold energies are more sensitive to the multifluid effects. This is consistent with the prior statement we made when examining the ratio of forward and backward rates.

Figure 3 shows the forward and backward reaction rates of the first transition between the ground state and the first excited state as a function of the *thermal* temperature for several drift temperature values. Even at very low thermal temperature ($T_e \simeq 0.1$ eV), one can have significant excitation ($\varpi \simeq 10^{-14}$ m³/s) due to a high drift temperature. In addition, Figure 3 also shows that in the limit $\lambda \rightarrow 0$, the multifluid rate, as formulated here, converges to the expression for thermal limit, given in eq. (C.3), as expected. Figure 4 shows the reaction

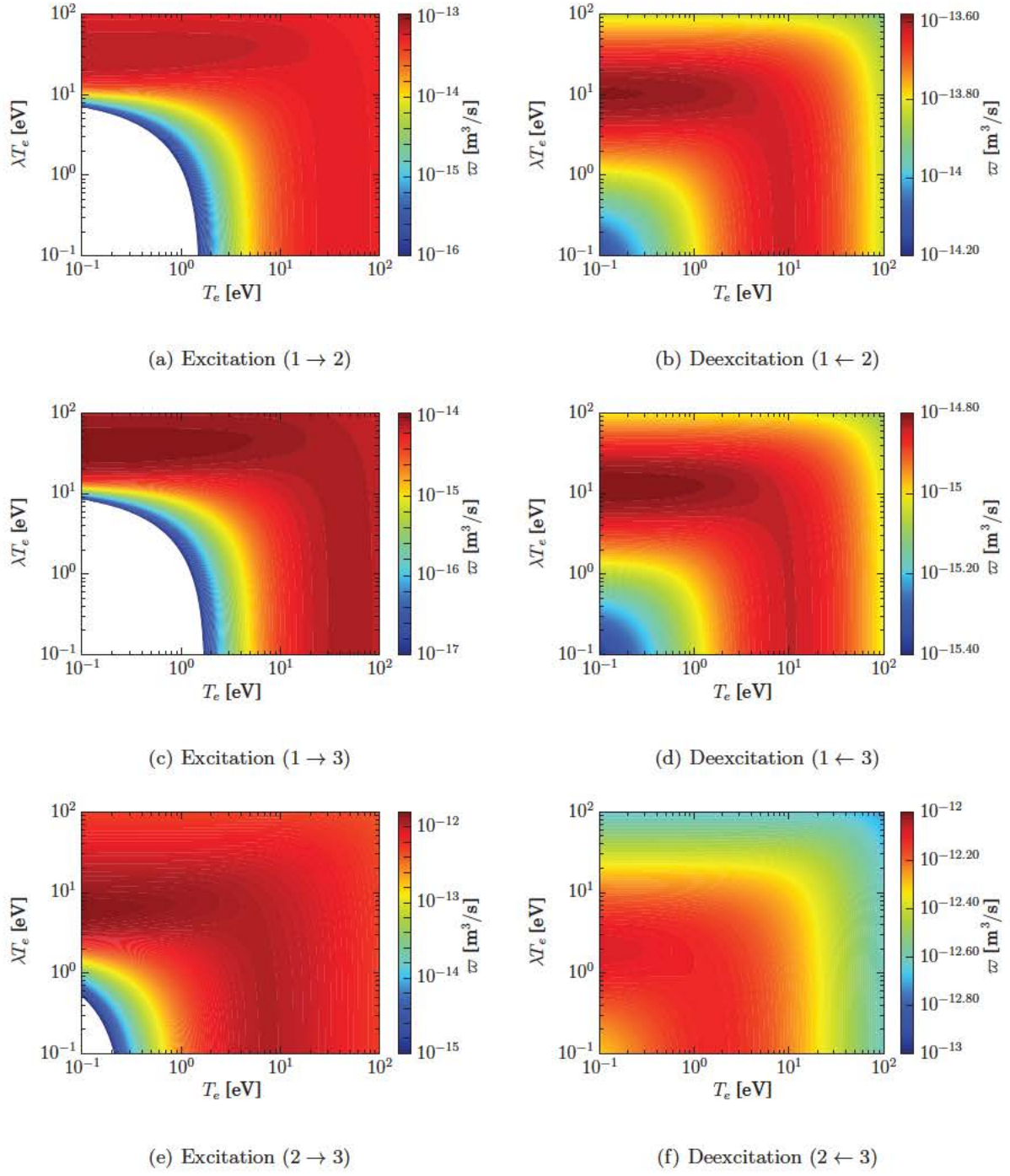


Figure 2. Multifluid reaction rates for electron-impact excitation/deexcitation collisions as a function of two temperatures.

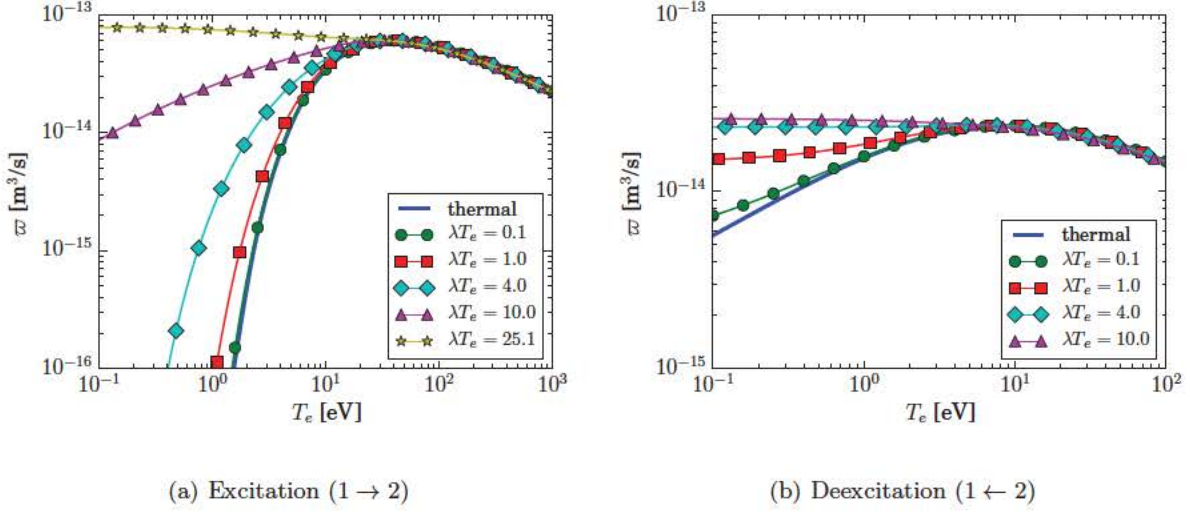


Figure 3. Multifluid reaction rates for electron-impact excitation/deexcitation collisions: lines with symbols correspond to different values of the drift temperature.

rates as a function of the *drift* temperature for several thermal temperature values; here we can identify a different asymptotic limit of the rate. In the limit $\lambda \rightarrow \infty$, the electron velocity distribution function approaches the form of a delta function centered at the relative mean velocity w , and the reaction rates approach the beam limit given by eq. (C.5). It must be noted that in the numerical integration of the multifluid rates, e.g., eq. (22), the energy grid x needs to be refined near the value of the the mean kinetic energy λ to avoid numerical error due to the integration over a delta function.

B. Momentum and Energy Exchange Rates

We now compute the momentum and energy exchange rates due to both excitation and deexcitation, and compare with those due to elastic collisions (electron-neutral and electron-ion). Recall from eq. (55) that the total energy transfer include three terms: the first term due to work done by friction in the COM reference frame, the second term due to thermal resistance (or thermal relaxation), and the last one due to heat release/absorption due to chemical reaction. There are three different rate coefficients associated with each of these processes, namely the momentum exchange rate κ , thermal relaxation rate j , and the reaction rate ϖ . In this section, we will focus on examining the momentum exchange and thermal relaxation rates. The expressions derived in IIC and IID can be readily used for the case

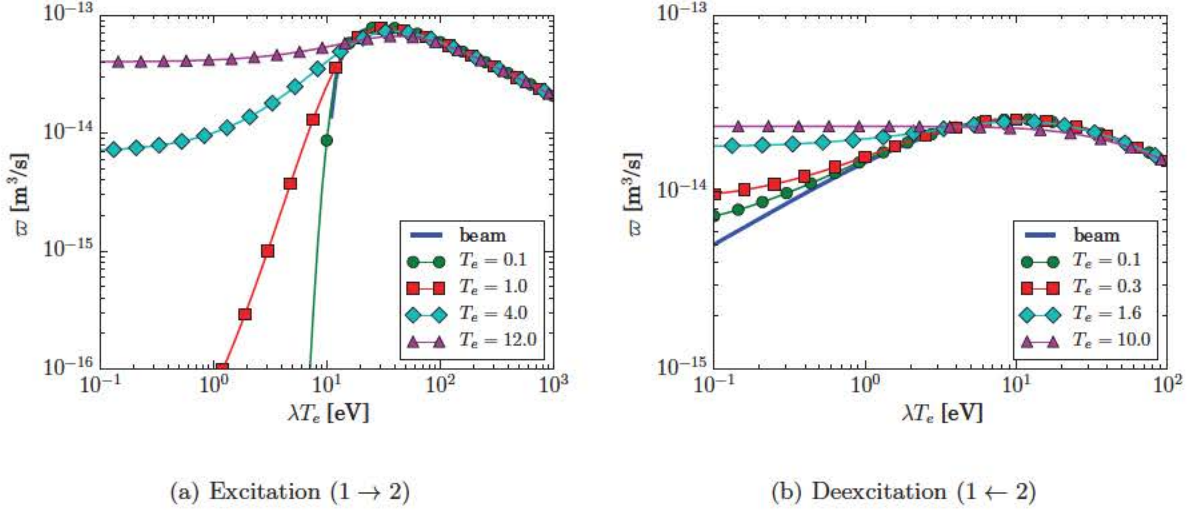


Figure 4. Multifluid reaction rates for electron-impact excitation/deexcitation collisions: lines with symbols correspond to different values of the thermal temperature.

of elastic collisions by simply setting $z^* = 0$ and $z' = z = x$. For example, in the case of electron-neutral (en) collision, we have:

$$\kappa^{(en)} = \frac{2}{3} \bar{v}_e e^{-\lambda} \int_0^\infty dx x^2 e^{-x} \bar{\sigma}^{(en)}(x) [1 - \langle \cos \chi \rangle_{\Omega'}] \zeta^{(1)}(\sqrt{\lambda x}) \quad (65a)$$

$$j^{(en)} = \bar{v}_e e^{-\lambda} \int_0^\infty dx x^2 e^{-x} \bar{\sigma}^{(en)}(x) [1 - \langle \cos \chi \rangle_{\Omega'}] \left[\zeta^{(0)}(\sqrt{\lambda x}) - \frac{2\lambda}{3} \zeta^{(1)}(\sqrt{\lambda x}) \right] \quad (65b)$$

It can be seen from the previous two equations that in order to compute the rate for the case of elastic collisions, we only need the so-called momentum transfer cross section $\sigma^{(en)m}(x) \equiv \bar{\sigma}^{(en)}(1 - \langle \cos \chi \rangle)$. These cross sections are available for a wide range of neutral species due to their extensive use in calculation of transport properties (see for example¹³). The electron-neutral collision cross section utilized in this work is taken from Bray and Stelbovics³⁴. For inelastic collisions, we need the full DCS, i.e., both $\bar{\sigma}(x)$ and $\mathcal{G}(x, \chi)$ in eq. (9) for each process. These cross sections are generally not available and analytical approximation is needed. For Coulomb collision, we use the analytical DCS from Rutherford's scattering formula with suitable cut-off based on the Debye length⁴, yielding a momentum transfer cross section of the form:

$$\sigma^{(ei)m} = \frac{e^4}{16\pi\epsilon_0^2\epsilon^2} \ln \Lambda \quad (66)$$

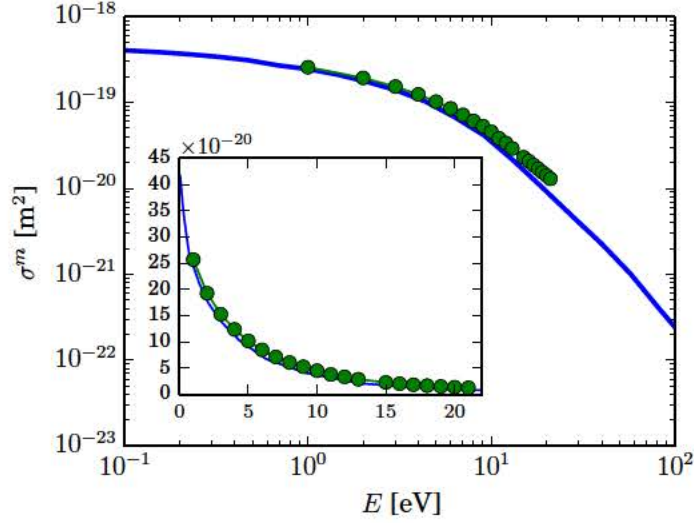


Figure 5. Elastic momentum transfer cross section for electrons in atomic hydrogen computed with the DCS from equation (68).

where $\ln \Lambda$ is the well-known Coulomb logarithm,

$$\Lambda = 1.24 \times 10^7 \left(\frac{T_e^3}{n_e} \right)^{1/2}$$

Typically, $\ln \Lambda \approx 5 - 20$; for convenience, we take a constant value of $\ln \Lambda = 5$ for all the plots shown here. In this case, the momentum exchange and thermal relaxation rates can be obtained in exact forms²⁸:

$$\kappa^{(ei)}(T_e, \lambda) = \frac{e^4 \ln \Lambda}{16\pi\epsilon_0^2 (kT_e)^2} \frac{1}{\lambda} \left[\frac{\text{erf}(\sqrt{\lambda})}{\sqrt{\lambda}} - \frac{2}{\sqrt{\pi}} e^{-\lambda} \right] \quad (67a)$$

$$j^{(ei)}(T_e, \lambda) = \frac{e^4 \ln \Lambda}{16\pi\epsilon_0^2 (kT_e)^2} \left[\frac{2}{\sqrt{\pi}} e^{-\lambda} \right] \quad (67b)$$

where erf is the typical error function.

Due to the lack of data of the DCS for inelastic processes, we have used an analytical Born scattering approximation for a Coulomb screened potential¹³, given by the following form:

$$\mathcal{G}(\varepsilon, \chi) = \frac{C}{(1 - h \cos \chi)^2}; \quad h = \frac{1}{1 + \frac{21.8}{\varepsilon}} \quad (68)$$

where C is a normalization constant such that $2\pi \int_{-1}^1 \mathcal{G}(\varepsilon, \chi) d\cos \chi = 1$. This angular-dependent DCS has been used to compute momentum transfer and thermal relaxation rates for both

electron-neutral and excitation/deexcitation collisions. We note here that the angular-dependent DCS's \mathcal{G} for excitation and deexcitation have to satisfy detailed balance³⁰:

$$\mathcal{G}_{(u|\ell)}^{\uparrow}(\varepsilon, \chi) = \mathcal{G}_{(\ell|u)}^{\downarrow}(\varepsilon', \chi) \quad (69)$$

The above condition implies that the probability for a deexcitation collision with an incident energy ε to have a scattering angle of χ is the same as that for an excitation collision with an incident energy $\varepsilon + \varepsilon^*$; therefore, one cannot independently specify both DCS's for the forward and backward processes. Figure 5 shows a comparison of the computed elastic momentum transfer cross sections to the result from a direct close-coupling calculation of Bray and Stelbovics³⁴; the agreement between the two is excellent. Using the angular-dependent DCS defined in eq. (68), the exchange rates, e.g., κ and j , can be computed for each bound-bound transition and summed over all transitions to yield the total rates:

$$K^{(xd)} = m_e \sum_{\ell} \sum_{u > \ell} \left(\kappa_{(u|\ell)}^{\uparrow} n_l n_e + \kappa_{(\ell|u)}^{\downarrow} n_u n_e \right) \quad (70a)$$

$$J^{(xd)} = \sum_{\ell} \sum_{u > \ell} \left(j_{(u|\ell)}^{\uparrow} n_l n_e + j_{(\ell|u)}^{\downarrow} n_u n_e \right) \quad (70b)$$

Based on the total frictional and thermal resistance coefficients, we can extract *average* momentum transfer and thermal relaxation rates for all excitation/deexcitation processes as follows:

$$K^{(xd)} = m_e n_e n_n \kappa^{(xd)} \quad (71a)$$

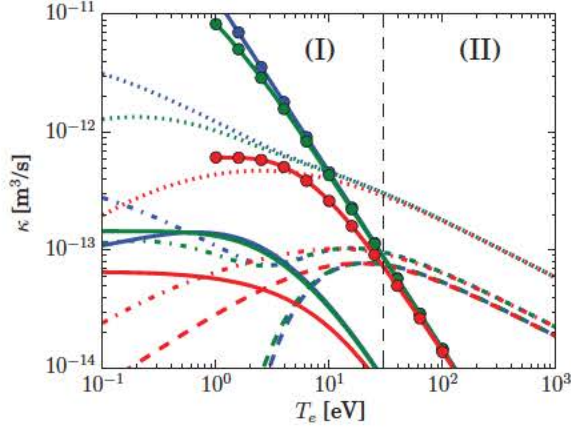
$$J^{(xd)} = n_e n_n j^{(xd)} \quad (71b)$$

where $n_n = \sum_k n_k$ is the total atomic number density (summation over levels). Note that according to our definitions, the exchange rates $\kappa^{(xd)}$ and $j^{(xd)}$ contain terms designating the population of the excited states, e.g., n_k/n_n . For comparison purpose, these average rates are calculated by assuming a Boltzmann distribution of the atomic states, i.e., $n_k = n_n \frac{g_k e^{-E_k/kT_B}}{\mathcal{Z}_n}$ and $\mathcal{Z}_n = \sum_{k \in n} g_k e^{-E_k/kT_B}$. One can see that in this case the population of the excited states is effectively replaced by a Boltzmann distribution characterized by a temperature T_B . This step is only done for the comparison shown below. In a CR calculation, the *detailed* population of the atomic states (equilibrium or not) is known and the exchange rates are computed for each transition as specified in eq. (70).

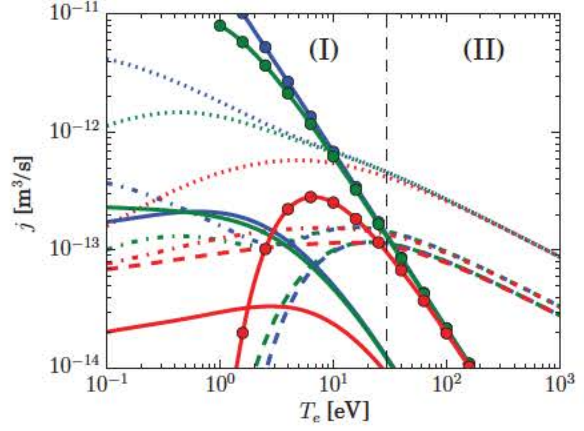
Figure 6 shows a comparison between the momentum exchange and thermal relaxation rates for three different processes: electron-neutral, electron-ion (Coulomb), and excitation/deexcitation collisions. For clarity, the rates due to Coulomb collision are only shown for value of $T_e > 1$ eV. Two important observations can be deduced from this plot. Firstly, when the atoms are cold, i.e., T_B is low, the inelastic exchange rates are much smaller than elastic ones. This is due to the fact that when T_B is low, only collisions between the ground state and a first few excited states are significant; the rates for these transitions are low compared to the others due to larger energy threshold. As the atoms are being excited and T_B increases, transitions among highly excited states become significant, leading to an overall increase in the total rates. These rates eventually exceed those due to elastic collisions as can be noticed in region (I) in Figure 6 for the dash-dotted and dotted lines. Secondly, the rates due to inelastic processes tends to have a slower drop-off at high temperature compared to the elastic rates, which suggests that at sufficiently high temperature, the main momentum and energy transfer mechanisms (region (II) in Figure 6) are due to inelastic collisions. Thus, we are led to the important conclusion that one *cannot* neglect momentum and energy transfer due to inelastic collisions. The only justification for neglecting these terms is when the atoms are cold and thermal temperature is low, but both of these conditions will not be realized in most practical systems.

C. Verification

The accuracy of the derived formulas of the exchange source terms are verified against direct evaluation of the full transfer integral (3) over six dimensional space using the Monte Carlo method. The procedure for the Monte Carlo integration is as follows: (1) sample different pair of particles (one atom and one electron) from two different Maxwellian distributions, (2) compute the exchange rate due to each sample pair, and (3) accumulate these rates. The sum of these rates will follow the correct probability distribution function of the samples. For brevity, we only show an example calculation of the zeroth-order reaction rate for an excitation and deexcitation from levels 2 and 5. Figure 7 shows a detailed comparison between the rate expressions obtained from eqs. (22) and (23) against Monte Carlo results with an excellent agreement. Similar agreement is obtained with other sampled transitions, giving us complete confidence in the accuracy of our derivation of the multifluid rates from

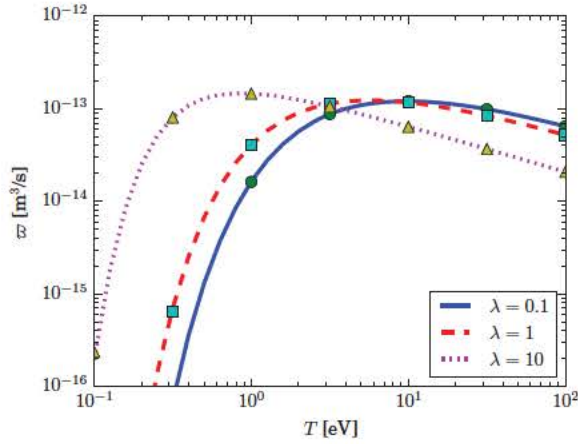


(a) Momentum exchange

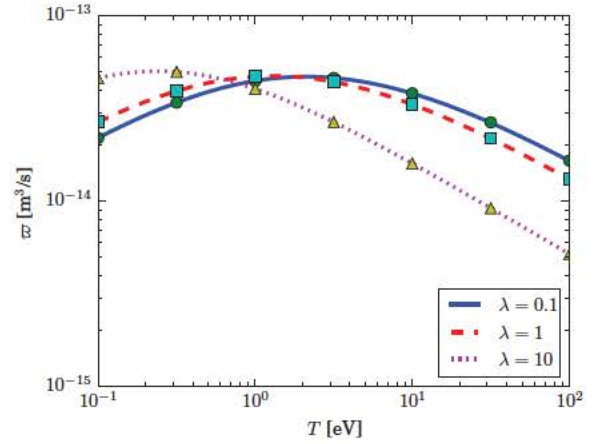


(b) Thermal relaxation

Figure 6. Comparison of the momentum exchange rates κ and thermal relaxation rates j due to elastic and inelastic collisions (excitation and deexcitation).



(a) Excitation ($2 \rightarrow 5$)



(b) Deexcitation ($2 \leftarrow 5$)

Figure 7. Comparison of zeroth-order reaction rates with Monte Carlo integration of the full transfer integral.

kinetic theory.

D. Zero-dimensional Calculations

We conducted zero-dimensional (0D) calculations for a constant-volume (isochoric) system to support our findings in sections III A and III B, which include the following: (1) reaction

	number density	temperature
atomic states	$n_i = 0.9n_t$ for $i = 1$ $n_i = 10^{-15}n_t$ otherwise	0.3 eV
electron	$n_e = 0.1n_t$	2 eV

Table I. Initial conditions of 0D test cases. For all cases, the total atomic density n_t is 10^{20} m^{-3} .

rates can be enhanced when the relative mean drift velocity is significant, and (2) momentum transfer and thermal relaxation due to inelastic collisions are non-negligible. The system contains hydrogen atoms and a small fraction of free electrons⁴¹. The governing equations are described in appendix D, and the resultant system of ordinary differential equations is solved using the Radau5 method of Hairer and Wanner³⁶, which is ideally suited for stiff problems.

The initial conditions for the number densities and temperatures of the atoms and free electrons are summarized in Table I. Initially, all the atoms are at the ground state (denoted by $i = 1$ in table I) with a translational temperature of 0.3 eV. The atoms are assumed to be at rest, i.e., their mean velocity is zero. The free electrons have a temperature of 2 eV, and their mean velocity is varied to demonstrate the multifluid effects. In all the test cases, we include the first 10 atomic levels of hydrogen according to the model described in Appendix C.

In the first test, we perform the calculation with various initial mean velocities of the electrons, or equivalently, the drift temperatures T_w . Figure 8 shows the time evolution of the number densities of the excited states during the isochoric heating process for two cases: $T_w = 0.01$ and 10 eV; the former corresponds to a single fluid calculation of a thermal bath with a warm electron population, and the latter corresponds to a situation where an electron beam is injected to the system. One can clearly see from Figure 8 that there is an enhancement to the excitation process, indicated by an early increase in the population of excited states, due to the presence of a non-zero mean velocity of the electrons. The same argument can be made from Figure 9, which shows the time evolution of the temperatures for three cases of different initial T_w . In this plot, the Boltzmann temperature T_B indicates the degree of excitation of the atom. It must be pointed out that the enhancement in excitation, how-

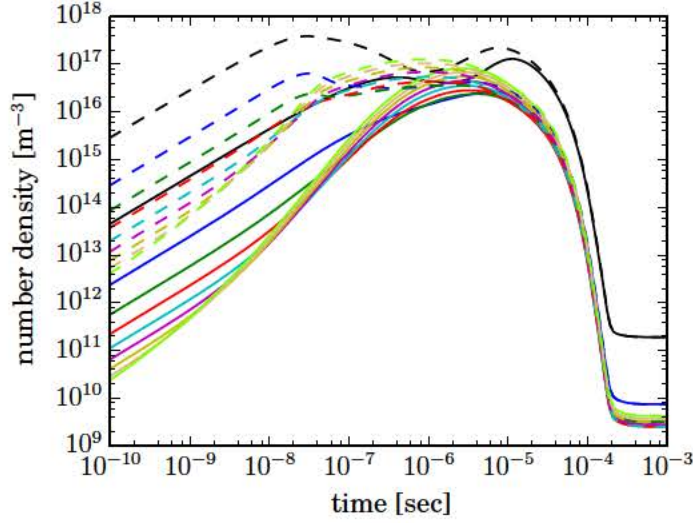


Figure 8. Number density of excited states during a zero-dimensional chemistry test.

ever, persists on the time scale of the momentum relaxation process, which is indicated by a drop in T_w at approximately 3×10^{-7} sec as shown in the bottom plot of Figure 9. After this time, the momentum of the electrons is completely absorbed by the atom, signifying a change to single fluid kinetics. In all the test cases, the excitation proceeds at a time scale much smaller than the resolution of the figures, i.e., T_B approximately goes from 0 to 0.7 eV in 10^{-9} sec. As mentioned before, when T_B is sufficiently large, the momentum exchange and thermal relaxation rates from inelastic collisions cannot be neglected.

In the second test, we specifically identify the effect of inelastic collisions. Figure 10 shows a comparison of the temperature evolution for two test cases, both with a very small initial drift temperature $T_w = 0.01$: the solid lines correspond the solution with both elastic and inelastic exchanges, and the dashed lines to the solution without inelastic exchanges. In this case, the friction is negligible since $T_w \approx 0$, and there are only thermal relaxation and heat release from reaction. It is clearly shown that inelastic collisions do contribute to the total energy transfer between the electrons and atoms, leading to a faster temperature equilibration $T_n - T_e - T_B$. It is interesting to point out here that while $T_e - T_B$ equilibration is due to the heat release/absorption term, $T_e - T_n$ equilibration is only due to the thermal relaxation term. Figure 10 indicates that there is a faster $T_e - T_n$ equilibration when inelastic thermal relaxation is included. This result is quite intriguing, since this effect is normally

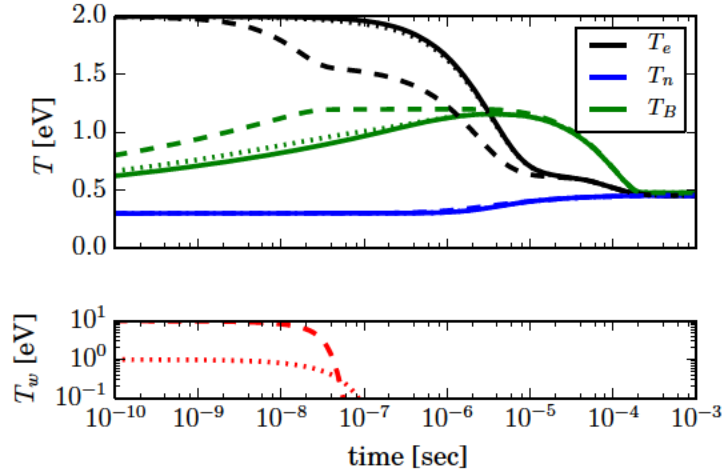


Figure 9. Time evolution of the temperatures for several test cases with different initial drift velocities: solid line ($T_w = 0.01$ eV), dotted line ($T_w = 1$ eV), and dashed line ($T_w = 10$ eV).

neglected in most of single fluid multi-temperature calculations.

Figure 11 shows the results for the same two test cases but now with an initial drift temperature $T_w = 10$ eV. One can make the same argument that inelastic collisions further enhance the temperature equilibration process. However, it is worthwhile to point out that during the time period $10^{-8} < t < 10^{-7}$, the electrons, although being decelerated due to friction, are also heated due to the work done by the same force (first term on the right hand side of eq. (D.5a)). This thermal heating term contains contribution from both elastic and inelastic collisions, which explains why the electron temperature drops faster towards equilibrium when inelastic exchanges are neglected. Finally we should emphasize that the thermal equilibrium between all components (T_B, T_e, T_n) can be obtained purely from inelastic collisions, as a result of properly accounting for detailed balance in our model; elastic collisions are not required to achieve equilibrium, but of course are needed to obtain the correct rate of relaxation.

IV. Concluding Remarks

We have presented a model for inelastic collisions for electronic excitation and deexcitation within the context of a multifluid description of a plasma. The model is rigorously derived

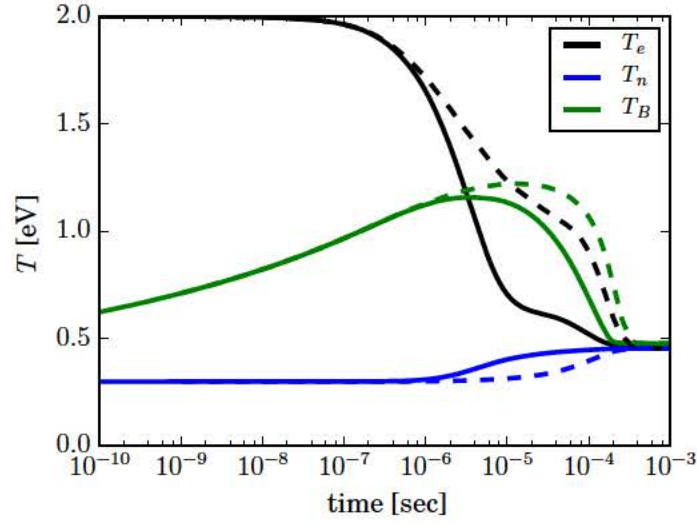


Figure 10. Time evolution of the temperatures for the case with (solid) and without (dashed) the exchange terms (momentum and energy) due to inelastic collisions.

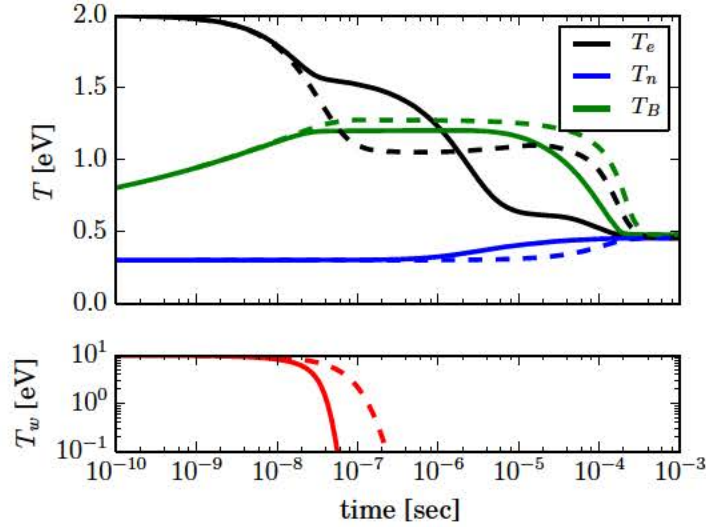


Figure 11. Time evolution of the temperatures for the case with (solid) and without (dashed) the exchange terms (momentum and energy) due to inelastic collisions.

from kinetic theory and is applicable to any multifluid plasma, irrespective of the mass ratio, and strictly obeys the detailed balance principle. The appropriate mass transfer rates and momentum and thermal resistance coefficients are derived, and are found to satisfy the

proper asymptotic limits, such that in the limit of vanishing energy gap, the well-known expressions for elastic collisions are recovered.

Numerical evaluations of the multifluid rates are carried out for a two-fluid electron-hydrogen plasma using Bohr model for the energy levels and semi-classical cross sections. Several numerical tests were performed in a virtual (zero-dimensional) test cell, and both the known thermal and beam limits were correctly recovered from the model. We also found that in some plasma conditions of interest, the contribution of the inelastic collisions to the resistance coefficients is significant, contrary to the usual assumptions made in current multifluid models.

Appendix A Collision kinematics

Let us consider an inelastic collision between two particles s and t , such that the post-collision particles can have modified internal states. The process is formally described as the relation

$$s(\mathbf{v}_s) + t(\mathbf{v}_t) \rightarrow s'(\mathbf{v}'_s) + t'(\mathbf{v}'_t) \quad (\text{A.1})$$

Note that only two particles are produced by the collision. The initial velocities are $\mathbf{v}_s, \mathbf{v}_t$. The mean fluid velocity is \mathbf{u} , such that $\mathbf{u} \equiv \langle \mathbf{v} \rangle \equiv \int d^3\mathbf{v} \mathbf{v} f(\mathbf{v})$ and a thermal velocity $\mathbf{c} = \mathbf{v} - \mathbf{u}$. By definition, we also have $\langle \mathbf{c} \rangle \equiv 0$.

The collision can be transformed to the center of mass (COM) reference frame, moving with velocity \mathbf{V} with respect to the LAB frame. Similarly, we can also define a mean velocity of this COM frame as \mathbf{U} . The subsequent Galilean transformations yield the following definitions:

$$\mathbf{V} = \frac{m_s \mathbf{v}_s + m_t \mathbf{v}_t}{M} \quad \mathbf{g} = \mathbf{v}_s - \mathbf{v}_t \quad (\text{A.2a})$$

$$\mathbf{U} = \frac{m_s \mathbf{u}_s + m_t \mathbf{u}_t}{M} \quad \mathbf{w} = \mathbf{u}_s - \mathbf{u}_t \quad (\text{A.2b})$$

where $M = m_s + m_t$. The inverse transformation yields:

$$\mathbf{v}_s = \mathbf{V} + \frac{m_t}{M} \mathbf{g} \quad \mathbf{u}_s = \mathbf{U} + \frac{m_t}{M} \mathbf{w} \quad (\text{A.3a})$$

$$\mathbf{v}_t = \mathbf{V} - \frac{m_s}{M} \mathbf{g} \quad \mathbf{u}_t = \mathbf{U} - \frac{m_s}{M} \mathbf{w} \quad (\text{A.3b})$$

Mass conservation imposes the relation $m_s + m_t = M = m'_s + m'_t$. For the case of two-body processes such as excitation of internal states, the masses are individually conserved, i.e.

$m'_s = m_s, m'_t = m_t$. Expressed in the COM frame, momentum and energy conservation yield, respectively:

$$M\mathbf{V} = M\mathbf{V}' \quad (\text{A.4a})$$

$$\frac{1}{2}M\mathbf{V}^2 + \frac{1}{2}\mu\mathbf{g}^2 = \frac{1}{2}M\mathbf{V}'^2 + \frac{1}{2}\mu\mathbf{g}'^2 + \Delta\varepsilon \quad (\text{A.4b})$$

where $\mu = m_s m_t / M$. Therefore, we have the following constraints:

$$\mathbf{V} = \mathbf{V}' \quad \text{and} \quad \mathbf{g}^2 = \mathbf{g}'^2 + \frac{2\Delta\varepsilon}{\mu} \quad (\text{A.5})$$

For an excitation between two atomic levels, the transferred energy is a fixed value $\Delta\varepsilon \equiv \varepsilon^* > 0$, the energy gap between levels. For a deexcitation, we use the same formulation as above (i.e. post-collision variables indicated by a prime), but in this case, $\Delta\varepsilon = -\varepsilon^* < 0$. In the limit $\Delta\varepsilon \rightarrow 0$, the collision is elastic.

Appendix B Separation of variables

Consider the Maxwellian velocity distribution functions (VDF) of each particle type, normalized to unity, e.g. (recall that $\mathbf{c} = \mathbf{v} - \mathbf{u}$):

$$f_s(\mathbf{v}_s) = \left(\frac{m_s}{2\pi k T_s} \right)^{\frac{3}{2}} \exp \left[-\frac{m_s \mathbf{c}_s^2}{2k T_s} \right] \quad (\text{B.1})$$

and similarly for f_t . The averaging over initial states will yield a product of these two distributions:

$$f_s(\mathbf{v}_s) f_t(\mathbf{v}_t) = \left(\frac{m_s}{2\pi k T_s} \right)^{\frac{3}{2}} \left(\frac{m_t}{2\pi k T_t} \right)^{\frac{3}{2}} \exp[\mathcal{A}] \quad (\text{B.2})$$

where the argument of the exponential function is, from (A.3):

$$\mathcal{A} = \frac{m_s}{2k T_s} \left[\mathbf{V} - \mathbf{U} + \frac{m_t}{M}(\mathbf{g} - \mathbf{w}) \right]^2 + \frac{m_t}{2k T_t} \left[\mathbf{V} - \mathbf{U} - \frac{m_s}{M}(\mathbf{g} - \mathbf{w}) \right]^2 \quad (\text{B.3})$$

Following Burgers²⁸, this expression can be simplified with an appropriate transformation of variables; since the basic procedure will be used elsewhere, we describe it below. First, we define the following variables

$$\beta_p = \frac{m_p}{2k T_p}, \quad \tilde{\mathbf{g}} = \mathbf{g} - \mathbf{w} \quad (\text{B.4})$$

such that

$$\begin{aligned}\mathcal{A} &= \beta_s \left[(\mathbf{V} - \mathbf{U}) + \frac{m_t}{M} \tilde{\mathbf{g}} \right]^2 + \beta_t \left[(\mathbf{V} - \mathbf{U}) - \frac{m_s}{M} \tilde{\mathbf{g}} \right]^2 \\ &= (\beta_s + \beta_t) (\mathbf{V} - \mathbf{U})^2 + \left[\beta_s \frac{m_t^2}{M^2} + \beta_t \frac{m_s^2}{M^2} \right] \tilde{\mathbf{g}}^2 + 2 \left[\beta_s \frac{m_t}{M} - \beta_t \frac{m_s}{M} \right] (\mathbf{V} - \mathbf{U}) \cdot \tilde{\mathbf{g}}\end{aligned}\quad (\text{B.5})$$

Let us define:

$$\mathbf{V}^* = \mathbf{V} - \mathbf{U} + \gamma \tilde{\mathbf{g}} \quad (\text{B.6})$$

and comparing the expression

$$(\beta_s + \beta_t) \mathbf{V}^{*2} = (\beta_s + \beta_t) (\mathbf{V} - \mathbf{U})^2 + (\beta_s + \beta_t) \gamma^2 \tilde{\mathbf{g}}^2 + 2\gamma (\beta_s + \beta_t) (\mathbf{V} - \mathbf{U}) \cdot \tilde{\mathbf{g}} \quad (\text{B.7})$$

with (B.5), we can choose the appropriate value of the coefficient γ to eliminate the dot product from \mathcal{A} :

$$\gamma = \frac{1}{\beta_s + \beta_t} \left(\beta_s \frac{m_t}{M} - \beta_t \frac{m_s}{M} \right) \quad (\text{B.8})$$

We then obtain complete separation of variables:

$$\mathcal{A} = (\beta_s + \beta_t) \mathbf{V}^{*2} + \left[\beta_s \frac{m_t^2}{M^2} + \beta_t \frac{m_s^2}{M^2} - \frac{1}{\beta_s + \beta_t} \left(\beta_s \frac{m_t}{M} - \beta_t \frac{m_s}{M} \right)^2 \right] \tilde{\mathbf{g}}^2 \quad (\text{B.9})$$

The term in brackets is easily simplified:

$$[\dots] = \frac{\beta_s \beta_t}{\beta_s + \beta_t} \quad (\text{B.10})$$

We can now define effective, average temperatures:

$$\beta_s + \beta_t = \frac{m_s}{2kT_s} + \frac{m_t}{2kT_t} = \frac{M}{2k} \frac{m_s T_t + m_t T_s}{M T_s T_t} \equiv \frac{M}{2kT^*} \quad (\text{B.11a})$$

$$\frac{\beta_s \beta_t}{\beta_s + \beta_t} = \frac{\mu}{2k} \frac{M}{T_s T_t} \frac{T_s T_t}{m_s T_t + m_t T_s} \equiv \frac{\mu}{2k\tilde{T}} \quad (\text{B.11b})$$

and γ becomes:

$$\gamma = \frac{\mu}{M} \frac{T_t - T_s}{\tilde{T}} = \mu \frac{T_t - T_s}{m_s T_t + m_t T_s} \quad (\text{B.12})$$

To summarize, we have performed the following change of variables:

$$\mathbf{V}^* = \mathbf{V} - \mathbf{U} + \mu \frac{T_t - T_s}{m_s T_t + m_t T_s} \tilde{\mathbf{g}} \quad \tilde{\mathbf{g}} = \mathbf{g} - \mathbf{w} \quad (\text{B.13a})$$

$$T^* = M \frac{T_s T_t}{m_s T_t + m_t T_s} \quad \tilde{T} = \frac{m_s T_t + m_t T_s}{M} \quad (\text{B.13b})$$

These are the same expressions found in²⁸ (pp. 45-46) (with an occasional change of naming convention) for which it is easy to verify that the Jacobian of the transformations is unity, i.e.

$$d^3\mathbf{v}_s d^3\mathbf{v}_t \equiv d^3\mathbf{V} d^3\mathbf{g} \equiv d^3\mathbf{V}^* d^3\tilde{\mathbf{g}} \quad (\text{B.14})$$

Furthermore, we note that:

$$\left(\frac{m_s}{2kT_s}\right)^{\frac{3}{2}} \left(\frac{m_t}{2kT_t}\right)^{\frac{3}{2}} \equiv (\beta_s\beta_t) = (\beta_s+\beta_t)^{\frac{3}{2}} \left(\frac{\beta_s\beta_t}{\beta_s+\beta_t}\right)^{\frac{3}{2}} \equiv \left(\frac{M}{2kT^*}\right)^{\frac{3}{2}} \left(\frac{\mu}{2k\tilde{T}}\right)^{\frac{3}{2}} \quad (\text{B.15})$$

The product of two distributions can now be written as:

$$f_s \cdot f_t = \left(\frac{M}{2\pi kT^*}\right)^{\frac{3}{2}} \exp\left[-\frac{M\mathbf{V}^{*2}}{2kT^*}\right] \cdot \left(\frac{\mu}{2\pi k\tilde{T}}\right)^{\frac{3}{2}} \exp\left[-\frac{\mu\tilde{\mathbf{g}}^2}{2k\tilde{T}}\right] \equiv f^*(\mathbf{V}^*) \cdot \tilde{f}(\tilde{\mathbf{g}}) \quad (\text{B.16})$$

All subsequent expressions can now be simplified with this separation of variables. For example, any operator \mathcal{O} that depends only on variables expressed in the COM frame $(\mathbf{g}, \mathbf{g}')$, we have:

$$\int d^3\mathbf{v}_s d^3\mathbf{v}_t f_s f_t \mathcal{O}(\mathbf{g}, \mathbf{g}') = \underbrace{\int d^3\mathbf{V}^* f^*(\mathbf{V}^*)}_{\equiv 1} \cdot \int d^3\tilde{\mathbf{g}} \tilde{f}(\tilde{\mathbf{g}}) \mathcal{O}(\mathbf{g}, \mathbf{g}') \quad (\text{B.17})$$

Note that this procedure applies equally well for elastic, excitation and deexcitation collisions, and that no approximations have been made on the mass ratio. Furthermore, since the averaging over initial states only involves the distribution functions for the s and t particles, we have not necessarily assumed that the final products s' and t' belong to the same fluid as the initial particles.

Appendix C Atomic data and cross section models

The atomic states of the Hydrogen atom are listed as a function of their principal quantum number (n) only, following the Bohr atomic model; the splitting of states with respect to orbital and spin numbers is ignored, and all states have a degeneracy $g_n = 2n^2$. The states number from $n = 1$ to ∞ and we consider a finite number of states $n = 1, \dots, M < \infty$ before reaching the ionization limit⁴². In this simplified model, the energy of each state is given as $E_n = I_H (1 - 1/n^2)$, as measured from the ground state ($E_1 \equiv 0$), and we will denote by $I_n = I_H (1/n^2 - 1/M^2) \simeq I_H/n^2$ the energy required for ionization of level n .

The classical form of the cross section for energy exchange between a free electron and the atom (Hydrogen) is used⁵. For an excitation collision from level ℓ to level $u > \ell$, the cross section takes the form:

$$\sigma_{(u|\ell)}^\uparrow(x) = (4\pi a_o^2)(3f_{\ell u}) \left(\frac{I_H}{kT_e} \right)^2 \frac{(x - x_{\ell u})}{x_{\ell u} x^2} \quad (\text{C.1})$$

where a_o is the Bohr radius, x is the nondimensional incident energy of the electron, $x_{\ell u} = (E_u - E_\ell)/kT_e$ is the energy gap between ℓ and u , and $f_{\ell u}$ is the oscillator strength:

$$f_{\ell u} = \frac{32}{3\pi\sqrt{3}} \frac{1}{\ell^5} \frac{1}{u^3} \frac{1}{\left(\frac{1}{\ell^2} - \frac{1}{u^2}\right)^3} \quad (\text{C.2})$$

In the thermal (single fluid) limit ($\lambda \rightarrow 0$), the reaction rate can be obtained in an exact form:

$$\varpi_{(u|\ell)}^\uparrow \simeq (4\pi a_o^2)(3f_{\ell u})\bar{v}_e \left(\frac{I_H}{kT_e} \right)^2 \psi_{\ell u} \quad (\text{C.3})$$

where

$$\bar{v}_e = \left(\frac{8kT_e}{\pi m_e} \right)^{\frac{1}{2}}, \quad \psi_{\ell u} = \frac{e^{-x_{\ell u}}}{x_{\ell u}} - E_1(x_{\ell u}) \quad \text{and} \quad E_1(x) = \int_x^\infty \frac{e^{-y}}{y} dy \quad (\text{C.4})$$

Here, \bar{v}_e is the mean thermal electron velocity and E_1 is the exponential integral. On the other hand, in the beam limit ($T_e \rightarrow 0$), the reaction rate takes the form:

$$\varpi_{(u|\ell)}^\uparrow \simeq \frac{\sqrt{\pi}}{2} \bar{v}_e \sigma_{(u|\ell)}^\uparrow(\lambda) = (4\pi a_o^2)(3f_{\ell u})\bar{v}_e \left(\frac{I_H}{kT_e} \right)^2 \phi_{\ell u} \quad (\text{C.5})$$

where

$$\phi_{\ell u} = \frac{\sqrt{\pi}}{2} \frac{(\lambda - x_{\ell u})}{x_{\ell u} \lambda^2} \quad (\text{C.6})$$

Appendix D Rate equations

We describe here the governing equations for the zero-dimensional simulation, which describe the time evolution of a constant-volume system during a thermochemical relaxation process.

The following system of rate equations is considered:

$$\frac{dn_e}{dt} = 0 \quad (\text{D.1a})$$

$$\frac{dn_i}{dt} = \Gamma_i^{(xd)} \quad (\text{D.1b})$$

$$\frac{d}{dt}(m_e n_e \mathbf{u}_e) = -(\mathbf{u}_e - \mathbf{u}_n)(K^{(en)} + K^{(xd)}) \quad (\text{D.1c})$$

$$\frac{d}{dt}(m_n n_n \mathbf{u}_n) = +(\mathbf{u}_e - \mathbf{u}_n)(K^{(en)} + K^{(xd)}) \quad (\text{D.1d})$$

$$\begin{aligned} \frac{dE_e}{dt} = & -\bar{\mathbf{u}} \cdot (\mathbf{u}_e - \mathbf{u}_n)(K^{(en)} + K^{(xd)}) \\ & - \frac{2m_e}{m_n} k(T_e - T_n)(J^{(en)} + J^{(xd)}) - \Xi^{(xd)} \end{aligned} \quad (\text{D.1e})$$

$$\begin{aligned} \frac{dE_n}{dt} = & +\bar{\mathbf{u}} \cdot (\mathbf{u}_e - \mathbf{u}_n)(K^{(en)} + K^{(xd)}) \\ & + \frac{2m_e}{m_n} k(T_e - T_n)(J^{(en)} + J^{(xd)}) \end{aligned} \quad (\text{D.1f})$$

where $n_n = \sum_{i \in n} n_i$ and $E_{e(n)}$ is the total energy of the fluid:

$$E_{e(n)} = \underbrace{\frac{3}{2} n_{e(n)} k T_{e(n)}}_{\varepsilon_{e(n)}} + \frac{1}{2} m_{e(n)} n_{e(n)} \mathbf{u}_{e(n)} \cdot \mathbf{u}_{e(n)} \quad (\text{D.2})$$

where $\varepsilon_{e(n)}$ is defined as the thermal energy of the fluid. The exchange source terms can be decomposed into two parts: elastic and inelastic collisions between the electrons and atoms. The momentum and energy exchange rates due to elastic and inelastic collisions are defined in eqs. (65) and (70). The remaining terms are:

$$\Gamma_i^{(xd)} = \sum_{u>i} \left[-n_i n_e \varpi_{(u|i)}^\uparrow + n_u n_e \varpi_{(i|u)}^\downarrow \right] + \sum_{\ell < i} \left[-n_i n_e \varpi_{(\ell|i)}^\downarrow + n_\ell n_e \varpi_{(i|\ell)}^\uparrow \right] \quad (\text{D.3})$$

$$\Xi^{(xd)} = \sum_{\ell} \sum_{u>\ell} \left[n_\ell n_e \varpi_{(u|\ell)}^\uparrow \varepsilon_{\ell u}^* - n_u n_e \varpi_{(\ell|u)}^\downarrow \varepsilon_{\ell u}^* \right] \quad (\text{D.4})$$

where $\varepsilon_{\ell u}^* = E_u - E_\ell$. Comparing eqs. (D.1c)-(D.1f) and (D.2), we can also write conservation equations for the thermal energies of electrons and atoms:

$$\begin{aligned} \frac{d\varepsilon_e}{dt} = & -m_e (\bar{\mathbf{u}} - \mathbf{u}_e) \cdot (\mathbf{u}_e - \mathbf{u}_n)(K^{(en)} + K^{(xd)}) \\ & - \frac{2m_e}{m_n} k(T_e - T_n)(J^{(en)} + J^{(xd)}) - \Xi^{(xd)} \end{aligned} \quad (\text{D.5a})$$

$$\begin{aligned} \frac{d\varepsilon_n}{dt} = & +m_e (\bar{\mathbf{u}} - \mathbf{u}_n) \cdot (\mathbf{u}_e - \mathbf{u}_n)(K^{(en)} + K^{(xd)}) \\ & + \frac{2m_e}{m_n} k(T_e - T_n)(J^{(en)} + J^{(xd)}) \end{aligned} \quad (\text{D.5b})$$

References

- ¹Y. P. Raizer, *Gas discharge physics*. Berlin: Springer, 1997.
- ²M. A. Lieberman, *Principles of plasma discharges and materials processing*. Wiley-Interscience, 2nd ed., 1994.
- ³R. G. Jahn, *Physics of electric propulsion*. Dover books on physics, Mineola, N.Y: Dover Publications, Inc, 2012.
- ⁴L. M. Biberman, V. S. Vorobev, and I. T. Yakubov, *Kinetics of Nonequilibrium Low-temperature Plasmas*. Springer Verlag, 1982.
- ⁵Y. B. Zeldovich and Y. B. Raizer, *Physics of shock waves and high-temperature hydrodynamic phenomena*. Dover Publications, 2002.
- ⁶D. R. Bates, A. E. Kingston, and R. W. P. McWhirter, “Recombination Between Electrons and Atomic Ions. I. Optically Thin Plasmas,” *Proceedings of the Royal Society A: Mathematical, Physical and Engineering Sciences*, vol. 267, pp. 297–312, May 1962.
- ⁷D. R. Bates, A. E. Kingston, and R. W. P. McWhirter, “Recombination between Electrons and Atomic Ions. II. Optically Thick Plasmas,” *Proceedings of the Royal Society A: Mathematical, Physical and Engineering Sciences*, vol. 270, pp. 155–167, Nov. 1962.
- ⁸J. Vlcek, “A collisional-radiative model applicable to argon discharges over a wide range of conditions. I. Formulation and basic data,” *Journal of Physics D: Applied Physics*, vol. 22, no. 5, pp. 623–631, 1989.
- ⁹J. Poggie, I. Adamovich, N. Bisek, and M. Nishihara, “Numerical simulation of nanosecond-pulse electrical discharges,” *Plasma Sources Science and Technology*, vol. 22, no. 1, p. 015001, 2013.
- ¹⁰M. Panesi, T. E. Magin, A. Bourdon, A. Bultel, and O. Chazot, “Electronic Excitation of Atoms and Molecules for the FIRE II Flight Experiment,” *Journal of Thermophysics and Heat Transfer*, vol. 25, no. 3, pp. 361–374, 2011.
- ¹¹M. G. Kapper and J.-L. Cambier, “Ionizing shocks in argon. Part I: Collisional-radiative model and steady-state structure,” *Journal of Applied Physics*, vol. 109, no. 11, p. 113308, 2011.
- ¹²M. G. Kapper and J.-L. Cambier, “Ionizing shocks in argon. Part II: Transient and multi-dimensional effects,” *Journal of Applied Physics*, vol. 109, no. 11, p. 113309, 2011.
- ¹³M. Capitelli, D. Bruno, and A. Laricchiuta, *Fundamental aspects of plasma chemical*

This Page Intentionally Left Blank

Appendix D:

Hydrodynamic models for multicomponent plasmas with collisional-radiative kinetics

Hai P. Le

UNIVERSITY OF CALIFORNIA

Los Angeles

Hydrodynamic models for multicomponent plasmas with collisional-radiative kinetics

A dissertation submitted in partial satisfaction
of the requirements for the degree
Doctor of Philosophy in Mechanical Engineering

by

Hai Phuoc Le

2014

Approved for public release; distribution unlimited. PA Clearance 14560 Nov 20 2014

© Copyright by
Hai Phuoc Le
2014

ABSTRACT OF THE DISSERTATION

**Hydrodynamic models for multicomponent
plasmas with collisional-radiative kinetics**

by

Hai Phuoc Le

Doctor of Philosophy in Mechanical Engineering

University of California, Los Angeles, 2014

Professor Ann R. Karagozian, Chair

Energy and space propulsion are two of the largest applied research areas requiring contributions from fundamental physical sciences, due to the growing world-wide demand in energy and continuing interests in expanding the frontier of deep space exploration. One of the common thrust areas in these two disciplines is plasma physics, the study of the motion of charged particles and their interaction with the electromagnetic field. The characterization of these plasma systems requires a comprehensive understanding of the physics of charged particles, collisional and radiative interactions among these particles, and how they interact with the electromagnetic field.

This dissertation presents some advances in the development of hydrodynamic models for plasma modeling and simulations in highly non-equilibrium conditions. Expressed in the form of conversation laws, these governing equations are solved by a finite volume discretization with a high-order reconstruction procedure and a multi-stage time integration method. High-fidelity collisional-radiative (CR) models are constructed by taking into account various elementary processes responsible for the excitation and ionization kinetics. The accuracy of the CR model

Distribution A: Approved for public release; distribution is unlimited. PA number 14560.

Approved for public release; distribution unlimited. PA Clearance 14560 Nov 20 2014

is benchmarked against different experimental shock tube data, and yields satisfactory agreement for a wide range of flow conditions. A mechanism reduction scheme, based on a level grouping approach, is derived to lower the complexity of the CR kinetics while maintaining sufficient accuracy to capture the non-equilibrium dynamics of the plasma kinetics. The method is shown to be more accurate and efficient than standard level grouping approach, and is suitable for multidimensional flow calculations.

Although the hydrodynamic or fluid approach offers a convenient way to model the system, it requires some assumptions on the time and length scales, which in some case might be violated. Fortunately, small deviations from these assumptions can still be captured by extending the fluid equations to multi-fluid equations, which characterize the plasma species (ions and electrons) via their own set of conservation laws. The extension of the CR model to the multi-fluid regime requires a new derivation for exchange source terms. A model for excitation and deexcitation collisions within the multi-fluid framework is derived, starting from kinetic theory, where the model obeys the principle of detailed balance. The multi-fluid equations developed in the current work are used to study ion acceleration in laser-plasma interaction. The role of the laser parameters and the mechanism of the acceleration are examined in detail, demonstrating the capabilities of this computational framework.

The dissertation of Hai Phuoc Le is approved.

Jean-Luc Cambier

Russel Caflisch

George Morales

Xiaolin Zhong

Ann R. Karagozian, Committee Chair

University of California, Los Angeles

2014

*This dissertation is lovingly dedicated to my mother, Mai Hoang, for everything
she has given to me and her unconditional love.*

TABLE OF CONTENTS

1	Introduction	1
1.1	Background	1
1.1.1	Plasma-assisted combustion	2
1.1.2	Re-entry physics	4
1.1.3	Laser-plasma interactions	6
1.2	Overview of plasma physics	9
1.2.1	Plasma kinetic equations	9
1.2.2	Modeling and simulations	12
1.3	Scope of present work	15
2	Hydrodynamic Equations	17
2.1	Introduction	17
2.2	Multi-fluid equations	19
2.2.1	Euler-Maxwell and Euler-Poisson systems	19
2.2.2	Time and length scales of multi-fluid equations	21
2.2.3	Generalized Ohm's law	23
2.3	Magnetohydrodynamics	25
2.4	Multi-temperature and chemically reactive hydrodynamics	29
3	Numerical Formulation	34
3.1	Introduction	34
3.2	Numerical methods	34
3.2.1	Finite volume methods	34

3.2.2	Hyperbolic solvers - Approximated Riemann solvers	36
3.2.3	High-order reconstruction	39
3.2.4	Hyperbolic solvers - Implicit time marching	42
3.2.5	Source term treatment	44
3.2.6	Diffusive transport	45
3.3	Benchmark problems	47
3.3.1	Euler equations	48
3.3.2	Multi-fluid equations	55
3.3.3	Diffusion processes	65
4	Collisional-Radiative Models for Atoms	73
4.1	Introduction	73
4.2	Thermal equilibrium	74
4.2.1	Maxwell distribution	75
4.2.2	Boltzmann distribution	76
4.2.3	Saha distribution	77
4.2.4	Planck distribution	78
4.3	Elementary processes and detailed balance	79
4.3.1	Collisional excitation/deexcitation	81
4.3.2	Collisional ionization/recombination	82
4.3.3	Radiative processes	83
4.3.4	Elastic processes	85
4.4	Rate equations	86
4.5	Physical models	87
4.5.1	Argon	87

4.5.2	Krypton	93
4.5.3	Xenon	96
4.5.4	Electron-neutral elastic collisions	98
4.6	Benchmark studies	102
4.6.1	Steady-state flows	102
4.6.2	Unsteady flows	115
5	Complexity Reduction of Collisional-Radiative Kinetics	119
5.1	Introduction	119
5.2	Collisional-Radiative model	122
5.2.1	Definitions and rates	122
5.2.2	Master equations	124
5.3	Level grouping strategies	126
5.3.1	Uniform grouping	126
5.3.2	Boltzmann grouping - number and energy	128
5.3.3	Boltzmann grouping - partitioning	131
5.3.4	Boltzmann grouping - effective rates	135
5.4	Accuracy of uniform and Boltzmann methods	138
5.4.1	Isothermal ionization test case	138
5.4.2	Isothermal recombination test case	146
5.5	Energy conservation	150
5.5.1	Isochoric ionization test case	153
5.5.2	Corrected energy rates	156
6	Modeling of Collisions in Multifluid Plasmas	162

6.1	Introduction	162
6.2	Transfer integral	163
6.3	Excitation/Deexcitation collisions	168
6.3.1	Zero th -order moment: number density	169
6.3.2	First-order moment: momentum density	171
6.3.3	Second-order moment: total energy density	174
6.4	Summary of results	177
7	Simulations of Laser-Plasma Interactions	178
7.1	Introduction	178
7.2	Electromagnetic wave propagation in plasmas	179
7.2.1	Electrodynamic equations	179
7.2.2	WKB approximation	183
7.2.3	Collisional absorption	184
7.2.4	Ponderomotive forces	186
7.3	Multi-fluid model for laser plasma interactions	188
7.4	Numerical solutions of the wave equations	192
7.4.1	Finite difference method	192
7.4.2	Transfer-matrix method	193
7.4.3	Benchmark problems	194
7.5	Ion acceleration via Ponderomotive forces	198
8	Conclusions and Future Directions	208
8.1	Achievements and contributions	208
8.2	Future directions	211

A	Eigensystems	213
A.1	2T Model	213
A.2	Maxwell's equations	216
B	Steady-state Flow Equations	218
C	Collision kinematics	220
C.1	Two-body processes	220
C.2	Three-body processes	224
D	Microscopic Detailed Balance	230
D.1	Collisional excitation and deexcitation	230
D.2	Collisional ionization and recombination	232
D.3	Line emission and absorption	234
D.4	Photoionization and radiative recombination	234
E	Derivation of the Ponderomotive Force for a Single Particle	236
	References	238

LIST OF FIGURES

1.1	Flame stabilization by plasma enhancement [15].	3
1.2	PDRIME concept: a) Overpressure at the nozzle exit launch a shock to enter the bypass tube, which slows and raises the temperature of the air stream inside the tube. Energy is extract from the flow (MHD power generation). b) During the blowdown, the nozzle pressure drops, and power is applied to accelerate compressed air in the bypass channel (MHD acceleration). [18, 19]	4
1.3	Physical phenomena occurred during planetary entry (courtesy of NASA).	6
1.4	Physical processes in typical laser-plasma interaction: (1) collisional absorption, instabilities, magnetic field generation; (2) resonance absorption, profile steepening, hot electrons generation; (3) heat transport, soft x-rays generation; (4) hard x-rays generation. Figure adapted from [38].	8
3.1	Schematic of computational stencil for MP5 and WENO schemes with left and right states of an interface.	41
3.2	Solution of the Woodward-Colella blast wave problem with 600 cells. Only part of the simulated domain is shown to illustrate the difference of two schemes.	49
3.3	Solution of the Shu-Osher problem with 300 cells. Only part of the simulated domain is shown to illustrate the difference of two schemes.	50
3.4	Solution of the forward step problem using MP5 scheme with 600,000 cells.	52

3.5	Diffraction of a Mach 2.4 shock wave down a step using MP5 scheme with 27,000 cells. Comparison between numerical schlieren (left) and experimental image (right).	53
3.6	Rayleigh-Taylor instability computed with the MP5 scheme using 640,000 cells.	54
3.7	Evolution of pressure and temperature in a 2D detonation simulation.	56
3.8	Numerical soot film produced by recording the maximum density at each grid cell over the entire simulation for a 2D detonation corresponding to figure 3.7.	57
3.9	Number density of the ions at the electron at different time and comparison of the time evolution of the ion current at the electrode with analytical solution of Lieberman [78]. Time is normalized by the ion plasma frequency, and velocity is normalized by the Bohm velocity $u_B = \sqrt{\frac{kT_e}{m_i}}$	58
3.10	Number density and velocity profile of the ions and the electric potential at steady-state condition. Velocity is normalized by the Bohm velocity $u_B = \sqrt{\frac{kT_e}{m_i}}$	60
3.11	Electric potential and velocity profile of the ions at steady-state condition with and without collisional drag. Velocity is normalized by the Bohm velocity $u_B = \sqrt{\frac{kT_e}{m_i}}$ and $\alpha = \frac{\lambda_D}{\lambda_i}$	61
3.12	Ion density of the ideal two-fluid Riemann problem	64
3.13	Transverse magnetic field of the ideal two-fluid Riemann problem	64
3.14	Numerical solution and error of the heat conduction problem with 100 cells using both explicit and implicit schemes. The explicit scheme is stable for $\Delta t \leq 10^{-6}$ while the implicit scheme is stable up to $\Delta t = 10^{-3}$	66

3.15	Temperature profile at $t = 100\tau_e$ for the hot spot relaxation by electron heat conduction. The solid line indicated the initial temperature.	68
3.16	Temperature profile for the hot spot simulation with and without laser heating.	70
3.17	Heat flux for the hot spot simulation with and without laser heating. The value of the heat flux is normalized by the freestream limit given by $q_f = p_e(kT_e/m_e)^{1/2}$	71
3.18	Steady profile of a shock propagation into a cold Nitrogen plasma (N^+, e) with (bottom) and without (top) electron heat conduction. Free stream conditions are $u_\infty = 7000$ m/s, $T_\infty = 273$ K, $n_\infty = 2.14 \times 10^{14}$ cm $^{-3}$. Solid lines are ion (black) and electron (red) temperatures. The dashed line is the number density. The x axis is adjusted so the shock starts at $x = 0$	72
4.1	Excitation cross sections from ground state to the 4s manifold due to electron-impact for Ar I taken from [102].	91
4.2	Ionization cross sections due to electron-impact for Ar I as computed by the Deutsch-Märk formalism	92
4.3	Excitation cross sections from ground state to the 5s manifold due to electron-impact for Kr I taken from [105].	96
4.4	Ionization cross sections due to electron-impact for Kr I as computed by the Deutsch-Märk formalism	97
4.5	Excitation cross sections from ground state to the 6s manifold due to electron-impact for Xe I taken from [105].	98
4.6	Ionization cross sections due to electron-impact for Xe I as computed from the work of Erwin and Kunc [108].	100

4.7	Momentum transfer cross sections for Argon, Krypton and Xenon. Solid lines are the results of McEachran <i>et al.</i> [104, 107]. Dashed lines are the results of Zatsarinny <i>et al.</i> [109].	101
4.8	Computed and experimental results of ionizing shock in Argon for case 1: $p_\infty = 5.14$ Torr, $T_\infty = 293.6$ K, $Ma = 15.9$. The values of the electron number density and the total mass density are normalized by the equilibrium values: $n_e^* = 1.69 \times 10^{17} \text{ cm}^{-3}$, $\rho^* = 8.4 \times 10^{-3} \text{ g/cm}^3$. Symbols represent experimental data for n_e and ρ from Glass and Liu [110].	104
4.9	Temperature profile of the electrons and heavy particles for case 1 from table 4.13.	105
4.10	The atomic state distribution function (ASDF) plotted at different locations of starting from the shock front utilizing the experimental condition from case 1 of table 4.13.	106
4.11	Electron number density and total density for $M_\infty = 16.1$ Ar shock corresponded to case 2 in table 4.13. The freestream conditions are: $p_\infty = 5.15$ Torr, $T_\infty = 295.9$ K. The values of the electron number density and the total mass density are normalized by the equilibrium values: $n_e^* = 1.83 \times 10^{17} \text{ cm}^{-3}$, $\rho^* = 0.87 \times 10^{-4} \text{ g/cm}^3$. Symbols represent experimental data for n_e and ρ from Glass and Liu [110].	107

4.12	Electron number density and total density for $M_\infty = 16.5$ Ar shock corresponded to case 3 in table 4.13. The freestream conditions are: $p_\infty = 5.12$ Torr, $T_\infty = 296.6$ K. The values of the electron number density and the total mass density are normalized by the equilibrium values: $n_e^* = 2.1 \times 10^{17} \text{ cm}^{-3}$, $\rho^* = 0.88 \times 10^{-4} \text{ g/cm}^3$. Symbols represent experimental data for n_e and ρ from Glass and Liu [110].	108
4.13	Electron number density and total density for $M_\infty = 13.0$ Ar shock corresponded to case 4 in table 4.13. The freestream conditions are: $p_\infty = 5.00$ Torr, $T_\infty = 296.6$ K. The values of the electron number density and the total mass density are normalized by the equilibrium values: $n_e^* = 5.62 \times 10^{16} \text{ cm}^{-3}$, $\rho^* = 0.62 \times 10^{-4} \text{ g/cm}^3$. Symbols represent experimental data for n_e and ρ from Glass and Liu [110].	109
4.14	Electron number density and total density for $M_\infty = 15.05$ Kr shock corresponded to case 1 in table 4.14. The freestream conditions are: $p_\infty = 5.15$ Torr, $T_\infty = 296.2$ K. The values of the electron number density and the total mass density are normalized by the equilibrium values: $n_e^* = 1.677 \times 10^{17} \text{ cm}^{-3}$, $\rho^* = 1.712 \times 10^{-4} \text{ g/cm}^3$. Symbols represent experimental data for n_e and ρ from Glass <i>et al.</i> [111].	111
4.15	Temperature profile of the electrons and heavy particles for case 1 from table 4.14.	112
4.16	The ASDF plotted at different locations of starting from the shock front utilizing the experimental conditions from case 1 of table 4.14.	112

4.17	Computed and experimental results of ionizing shock in Krypton for case 2: $p_\infty = 5.07$ Torr, $T_\infty = 295.4$ K, $Ma = 15.17$. The values of the electron number density and the total mass density are normalized by the equilibrium values: $n_e^* = 1.712 \times 10^{17} \text{ cm}^{-3}$, $\rho^* = 1.708 \times 10^{-4} \text{ g/cm}^3$. Symbols represent experimental data for n_e and ρ from Glass <i>et al.</i> [111].	113
4.18	Electron number density and heavy particle number density for $M_\infty = 13.1$ Xe shock. Symbols represent experimental data for n_e and n_h from Ezumi <i>et al.</i> [112]. The freestream conditions are: $p_\infty = 2.00$ Torr, $T_\infty = 300$ K.	114
4.19	Total mass density of ionizing shock in Argon for case 1 of table 4.13. Different lines correspond to the solutions at the different times, and the arrow indicates flow solutions as time increases. The symbols are the experimental data from the UTIAS experiment [110].	117
4.20	Electron number density of ionizing shock in Argon for case 1 of table 4.13. Different lines correspond to the solutions at different times. The symbols are the experimental data from the UTIAS experiment [110].	118
5.1	Time evolution of the electron number density using different total number of atomic levels. The electron temperature is set at 3.0 eV.	129
5.2	Comparison of the time evolution of the excited states during the isothermal heating test case ($T_e = 3$ eV). From top to bottom: (a) full solution with 20 levels; (b) solution with 5 levels and 2 Uniform groups; (c) solution with 5 levels and 2 Boltzmann groups. The first excited state - H(2) - is the top curve, followed by the next higher level, etc.	141
5.3	Comparison between the solution obtained using both level grouping approaches. The solid line represents the full solution.	142

5.4	The internal states population during the heating process at various times. The solid symbols are the full solution; the solid lines are the level grouping with Boltzmann distribution; the dotted lines are for level grouping with uniform distribution; dashed lines are for a simplified model with $T_b \equiv T_e$	143
5.5	Boltzmann temperature of the upper states	143
5.6	Radiative loss due to bound-bound radiation from the upper states to the first 3 atomic states. The lines indicate the solution obtained from the full CR kinetics. The dots represent solution obtained with level grouping (5 levels + 1 group).	145
5.7	Comparison of the time evolution of the ground state and the free electrons during the isothermal cooling process (3 eV \rightarrow 1 eV) using level grouping with Uniform and Boltzmann distribution (3 levels + 1 group).	147
5.8	Comparison of the time evolution of the excited states during the isothermal cooling test case ($T_e = 1$ eV). From top to bottom: (a) full solution with 20 levels; (b) solution with 3 levels and 1 Uniform group; (c) solution with 3 levels and 1 Boltzmann group. H(3) - is the bottom curve, followed by the next higher level, etc.; the non-conforming red curve is H(2).	148
5.9	Comparison of the time evolution of the excited states number densities during the isothermal cooling process (3 levels + 1 B group).	150
5.10	Snapshots of the ASDF at several times during the cooling process. The dots represent the full solution. The solid lines are the solution obtained using the level grouping with Boltzmann distribution. The broken lines are the solution obtained using the level grouping with uniform distribution.	151
5.11	N_e, T_e evolution in constant-volume case.	154

5.12	Cumulative and instantaneous relative errors in energy conservation - test case 3.	155
5.13	Cumulative and instantaneous relative errors in energy conservation - test case 3 - with revised formulation	161
5.14	Cumulative relative errors in energy conservation as function of group sizes; revised formulation.	161
6.1	Frame rotation and relative orientation of (a) \mathbf{w} and \mathbf{g} and (b) \mathbf{g} and \mathbf{g}' . The rotation operator matrix $R(\varphi, \theta)$ (or $R(\rho, \chi)$) is defined such that $\hat{\mathbf{g}} = R(\varphi, \theta) \cdot \hat{\mathbf{w}}$ and $\hat{\mathbf{g}}' = R(\rho, \chi) \cdot \hat{\mathbf{g}}$	167
7.1	Coordinate system of a one dimensional electromagnetic wave propagation where x is the direction of propagation: $\mathbf{E} = E(x)\hat{\mathbf{e}}_y$, $\mathbf{B} = B(x)\hat{\mathbf{e}}_z$, and $\mathbf{k} = k\hat{\mathbf{e}}_x$	182
7.2	Solution of the electric field for a linear density profile (shown by the black dotted line) computed using both TMM and FD methods. The solid black line is the exact solution given by the Airy function. The length is normalized by the laser wavelength	196
7.3	Ponderomotive force for a linear density profile. The numerical solution is obtained using the electric field computed in figure 7.2. The solution of Lindl and Kaw [136] is reproduced by omitting the term containing the magnetic field in the expression of the Maxwell stress tensor. The broken line is the solution obtained from the WKB approximation, i.e., equation (7.44).	197
7.4	Spatial profile of the electromagnetic wave intensity as it propagates into the plasma. The wave energy is completely absorbed near the critical surface.	198
7.5	Gaussian laser pulse with a maximum intensity of 10^{16} W/cm^2 . .	200

7.6	Ion number density (solid line) and the ponderomotive potential (dashed line) at four different times during the laser pulse. The ponderomotive potential is defined as $\epsilon_0(E^2 + c^2 B^2)$. The ion number density is normalized by the laser critical number density, and the potential is normalized by its value at the vacuum region. . .	202
7.7	Electrostatic field generated in the plasmas due to charge separation.	203
7.8	Ion velocity at various times after the laser pulse initiation.	204
7.9	Ion number density at (a) 20 ps, (b) 50 ps, and (c) 90 ps for both cases of negatively chirped and unchirped laser pulse. For the negatively chirped laser, the frequency is linearly decreased 25 % over the entire pulse duration.	205
7.10	Comparison of the ponderomotive potential for (a) negatively chirped and (b) unchirped laser. The ponderomotive potential is defined as $\epsilon_0(E^2 + c^2 B^2)$. The values of the potential are normalized by its value in the vacuum region.	207

LIST OF TABLES

4.1	Rate coefficients for collisional-radiative model	80
4.2	Lowest 31 levels of Ar I by energy.	88
4.3	Atom impact excitation parameters for allowed transitions for Ar- gon. χ_{nm}^* for allowed transitions from ground state of neutral Ar has been tuned to match the experimental induction length. . . .	89
4.4	Electron-impact ionization parameters as taken from [103].	90
4.5	Radii of Ar valence electron and reduced weighting factors for $\xi = 1$ as taken from [103].	91
4.6	Summary of the elementary cross sections used in the CR model for Argon	93
4.7	Lowest 31 levels of Kr I by energy.	94
4.8	Atom impact excitation parameters for allowed transitions for Kryp- ton.	95
4.9	Summary of the elementary cross sections used in the CR model for Krypton	97
4.10	Lowest 31 levels of Xe I by energy	99
4.11	Atom impact excitation parameters for allowed transitions for Xenon.	100
4.12	Summary of the elementary cross sections used in the CR model for Xenon	102
4.13	Summary of test conditions of the UTIAS experiments for ioniz- ing shock in Argon with the predicted thermal equilibrium flow properties. Data are taken from Glass and Liu [110].	103

4.14	Summary of test conditions of the UTIAS experiments for ionizing shocks in Krypton with the predicted thermal equilibrium flow properties. Data are taken from Glass <i>et al.</i> [111].	110
5.1	Summary of level-grouping models investigated.	138
5.2	Initial conditions of test cases. For all cases, the total atomic density N_H is 10^{21} m^{-3}	139
5.3	Relative error on electron density at peak rate of growth (approx. $33 \mu\text{sec}$).	140

ACKNOWLEDGMENTS

This dissertation would have not been possible without the continuous support and encouragement from many individuals. I would like to thank my advisor, Prof. Ann Karagozian, for her guidance, support, and inspiration throughout my graduate study. I am grateful for her flexibility in allowing me to tackle many problems of interests. She has always been responsive when I have questions. Her encouragement and great insights to the academia has helped guide me towards a career in teaching and research.

I am very fortunate to have met and worked with my AFRL mentor, Dr. Jean-Luc Cambier. I thank him for being very patient with me from the beginning, answering my never-ending questions, giving me countless opportunities to excel in my research, and sharing his knowledge in a wide range of topics. His passion for science has influenced me positively, and shaped me into who I am today. His attention to detail has had a significant impact on the quality of my research.

I would also like to acknowledge other members of my committee, who have contributed in one way or another to my research. In particular, I thank Prof. Morales for offering a solid foundation in plasma physics, Prof. Zhong for fundamental courses in gas dynamics and CFD, Prof. Smith for sharing his elegant course notes in chemical kinetics, and Prof. Caflisch for many positive comments about my research. I would also like to acknowledge Prof. Periklis Papadopoulos from SJSU for inspiring me to pursue graduate study, and giving me advices on choosing the topic of my research.

During the course of my graduate study, I have been privileged to work with an excellent team of researchers from AFRL. I thank Dr. Michael Kapper for his brief but valuable assistance in the start. His initial work on collisional-radiative cross section database has allowed me to immediately be proficient in doing CR modeling. I also thank Dr. Lord Cole for sharing his passion in coding and CFD.

Dr. David Bilyeu is gratefully acknowledged for scaring me away from the CESE method, hence keeping my focus on finite-volume method. I would also like to thank Drs. Rob Martin and Carl Lederman for many stimulating discussions on physics and math, and Dr. Justin Koo for making my time in the desert and at the lab much easier and enjoyable. Despite being the only one in the group without a PhD (according to Dr. Bilyeu's record as of June 2014), I am glad that I still have much fun working with all of you.

I would also like to thank various friends and classmates at UCLA: Ali, Ayaboe, Clifton, Dung, Giang, Kyle, Lauren, Levon, Patrick, San and many more. Thank you all for the fun times during group study, conferences, and get-together after school. A large portion of my weekends in the bay area was filled with joy in the company of friends: Chau, Dante, Freddy, Luong, Oanh and many others. I am grateful for the support and love of my companion and best friend, Diem. Thank you for being understanding and putting up with me through my bad times.

My accomplishment today would not have been successful without the support of my family. I thank my stepfather, Chuong Nguyen, for always being there when I needed. Most importantly, I thank my mother, Mai Hoang, for her sacrifice throughout the years to get me to where I am today. Her love is the main driver to get me through difficult times, and her support is the key foundation for my accomplishment.

This research was supported by the Air Force Office of Scientific Research (AFOSR) laboratory task 12RZ06COR (PM: Dr. Fariba Fahroo), ERC, Inc. under subcontracts RS111738 and RS131109, and the UCLA MAE Department graduate fellowship program.

VITA

2009	B.S. (Aerospace Engineering) San José State University, San José, CA
2009–2010	Research Assistant, ELORET Corp. NASA Ames Research Center, Moffett Field, CA
2011	M.S. (Aerospace Engineering) San José State University, San José, CA
2012	M.S. (Mechanical Engineering) University of California, Los Angeles, CA
2010–Present	Research Engineer, ERC Inc. Air Force Research Laboratory, Edwards AFB, CA

PUBLICATIONS

H.P. Le, A. Karagozian, J.-L. Cambier, Complexity Reduction of Collisional-Radiative Kinetics for Atomic Plasma, *Phys. Plasmas* 20, 123304 (2013).

H.P. Le, J.-L. Cambier, L. Cole, GPU-based Flow Simulation with Detailed Chemical Kinetics, *Computer Physics Communication* 184, 596-606 (2013).

H.P. Le, J.-L. Cambier. Development of a Flow Solver with Complex Kinetics on the Graphic Processing Units. AIAA paper 2012-721, 2012.

B. Cruden, **H.P. Le**, R. Martinez. Electron Density Measurement in Re-Entry Shocks for Lunar Return. AIAA paper 2011-3628, 2011.

B. Cruden, D. Prabhu, R. Martinez, **H.P. Le**, D. Bose, J. Grinstead. Absolute

Radiation Measurement in Venus and Mars Entry Conditions. AIAA paper 2010-4508, 2010.

CHAPTER 1

Introduction

1.1 Background

Plasma science is a multidisciplinary topic, with a wide spectrum of applications such as thermonuclear fusion [1], astrophysical plasmas [2], solar physics [3], electric propulsion thrusters [4], material processing [5], and many others. High temperature and collisionless plasmas have been studied extensively by Vlasov theory [6, 7]; these studies laid a foundation on the understanding of linear and quasi-linear phenomena occurred in a plasma, e.g., Landau damping, plasma instabilities, and collisionless shock [8, 9]. These phenomena are pertinent to the study of plasma waves in fusion devices or astrophysical phenomena, e.g., supernova, active galactic nucleus jets, etc.

Low temperature and partially ionized plasmas, on the other hand, have tremendous technological applications in manufacturing and material processing, miniaturized ion propulsion device [4], novel combustion devices [10], and re-entry physics [11]. These plasmas often exhibit strong deviation from thermal and chemical equilibrium, thus collisional and radiative kinetics play an important role in characterizing their dynamic behavior. For example, the interaction of the plasma with the radiation field is directly applicable to predicting and analysing thrusters' plume signature, radiative heat in hypersonic shock layer, and X-ray generation in laser-plasma interaction (LPI).

The challenges in exploring non-linear phenomena and the transport of par-

ticles and energy still remain, both of which would require theoretical, computational and experimental efforts. In the non-linear regime, one has to solve the full set of governing equations; this task is quite challenging, and can only be done by numerical calculations. Even so, the numerical methods themselves have limitations¹, and often cannot be used in a general scenario. In such cases, theoretical knowledge is required to give insights to the design of the numerical methods, and experimental verification (or code validation) is very essential to completely understand the physics of the problem. The abundance and complexity of plasma science can be seen in three representative technical application areas: plasma-assisted combustion, re-entry physics, and laser-plasma interactions.

1.1.1 Plasma-assisted combustion

Plasmas have long been of interest as a propellant candidate for spacecraft due to the ability to generate very high exhaust velocities, and thus very high specific impulse (ISP) as a consequence of electromagnetic and/or electrostatic acceleration [4]. Besides electric propulsion, plasma physics also finds use in chemical propulsion applications due to the unique advantage coming from the participation of the plasma species in the combustion processes and their interactions with the electromagnetic field. The existence of a plasma inside a combustion chamber can potentially be utilized for different purposes, whether to enhance the reaction kinetics or to be used for flow control [12, 13].

Recently, the concepts of plasma assisted combustion (PAC) and plasma assisted ignition (PAI) have drawn a lot of attention due to their potential for improving ignition reliability, enhancing flame stabilization and reducing pollutant emission [14, 15, 13]. These concepts have been proposed in a variety of combus-

¹This comes from both from a numerical and physical points of view. The numerical limitation lies in the deterministic or stochastic nature of the methods when dealing with high dimensional problems. The physical limitation simply comes from the fact that it is impossible to include physics at all scales so one must be aware of which physics can be included and/or missing from the model.

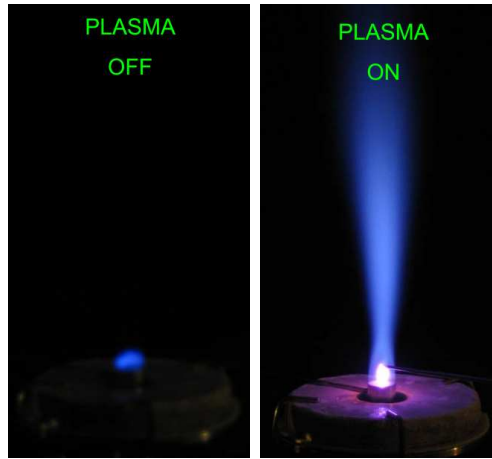


Figure 1.1: Flame stabilization by plasma enhancement [15].

tion devices including scramjets and gas turbine engines [16, 17]. The plasma, typically created by electric discharges, can deposit heat locally in the vicinity the flame, which quickly raises the gas temperature, and creates reactive radicals and excited species, which initiate chain reactions, therefore stabilizing the flame. Figure 1.1 illustrates the flame stabilization effects that can be seen by application of a nanosecond repetitively pulsed plasma [15].

Several concepts of propulsion systems have been proposed to take advantage of magnetohydrodynamic (MHD) phenomena. One example is the pulse detonation rocket-induced magnetohydrodynamic ejectors (PDRIME) concept, proposed by Cambier [18], from which MHD power is extracted from the unsteady nozzle flows within a pulse detonation rocket engines (PDRE) and applied in a bypass air stream to provide additional thrust. The schematic concept of PDRIME is illustrated in figure 1.2 showing the flow patterns for different stages of the cycle. Numerical simulations of the PDRIME, as well as other MHD-based cycle modification, were carried out by Zeineh *et al.* [19] showing potential increases in performance for many operating conditions. Technical challenges associated with the requirement for PDRIME operation were also revealed, which suggests further analysis and optimization study. The numerical simulations have proven

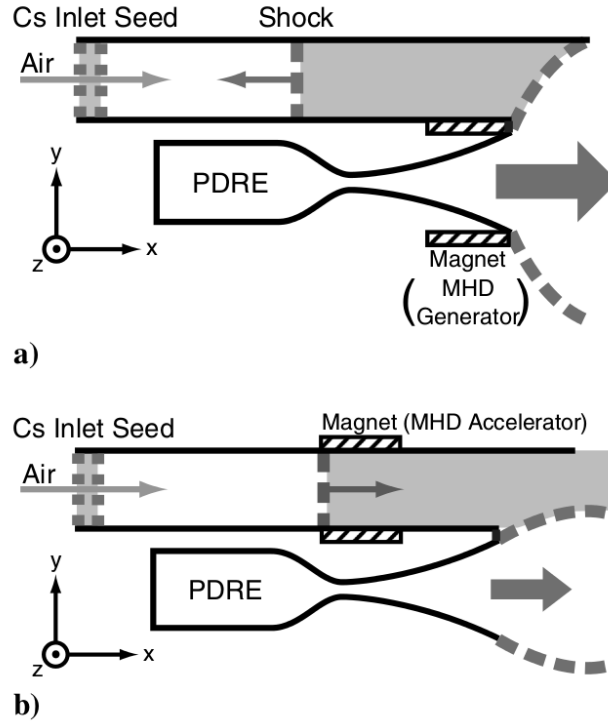


Figure 1.2: PDRIME concept: a) Overpressure at the nozzle exit launch a shock to enter the bypass tube, which slows and raises the temperature of the air stream inside the tube. Energy is extract from the flow (MHD power generation). b) During the blowdown, the nozzle pressure drops, and power is applied to accelerate compressed air in the bypass channel (MHD acceleration). [18, 19]

to be very useful in the preliminary evaluation of the PDRIME concept and its variants.

1.1.2 Re-entry physics

Re-entry plasmas are typically created due to a strong bow shock that forms in front of a vehicle such as the space shuttle when it enters the atmosphere. As the air passes through the shock, the kinetic energy is quickly converted to thermal energy, which for high re-entry Mach number, is sufficient to ionize the gas. Nonequilibrium phenomena such as chemical reactions and energy relaxation

processes are particularly relevant and extremely important (see figure 1.3), owing to the fact that the success of the flight mission depends on how accurately the flow field can be predicted in order to design adequate thermal protection system [20].

In high speed re-entry conditions, the convective time scales of the fluid can be of the same order of magnitude as the chemical and energy relaxation time scales. The processes of translational, rotational and vibrational relaxation as well as ionization of the gas thus must be taken into account for an accurate prediction of the flow field [21, 11]. In addition, at very high velocity and low density regime, the radiation from the gas becomes significant and can in turn interact with the plasma; one must then take in account radiation transport and kinetic processes involving the radiation field such as photo-excitation and photo-ionization must be included². In that case, the problem quickly becomes intractable and one must rely mostly on empirical flight data or simplified models. These simplified models are sometimes questionable and can not be used in a wide range of conditions.

In the past decade, experimental data from ground facilities for radiative heat spectra relevant to re-entry conditions for different atmospheric gas composition have become available, providing a useful set of validation data for physical models and chemical reaction rates used in current state-of-the-art computational fluid dynamics (CFD) tools [22, 23, 24, 25, 26]. These data have motivated a number of studies using high-fidelity collisional-radiative (CR) models [27, 28, 29] to benchmark against experimental data, e.g., radiative spectrum of shock-heated gas. The results from these studies are mixed: good agreement is obtained in some regions of the spectrum but poor agreement is reported in other regions. Moreover, the experimental spectrum also reveals additional features, e.g., contaminated species,

²In that case, one must solve the radiation transport equation in addition to the fluid equations. The radiation transport is a challenging problem in itself due to the hyper-dimensionality aspect of the governing equation. Typically, radiation transport is decoupled from the flow field and only used as a post-processing step [21]. In simple flow geometry, one can rely on approximation such as the tangent slab method to reduce the dimensionality of the problem.

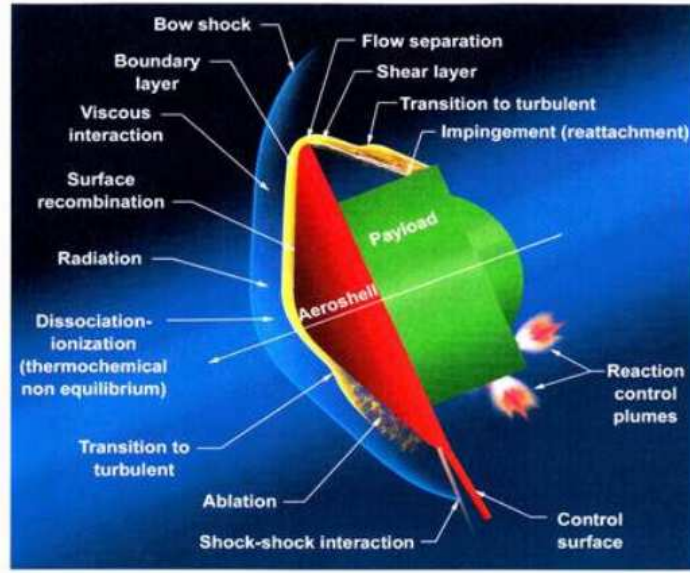


Figure 1.3: Physical phenomena occurred during planetary entry (courtesy of NASA).

continuum radiation, and high-lying transitions, all of which appear to be missing or inadequately understood from the numerical model. There are several reasons for the discrepancies: incomplete thermochemical rates, unsteady phenomena, and possibly experimental artifact. These problems are current being tackled with a better *ab initio* chemical database [30, 31], improved high-order and more efficient transport schemes[32, 33, 34, 35], as well as mechanism reduction [36, 37] for unsteady and multidimensional simulations.

1.1.3 Laser-plasma interactions

Lasers, among the greatest inventions of mankind, are devices which can produce electromagnetic radiation at a range of wavelengths at very high intensity. Due to their ability to deliver a large amount of energy at short duration, lasers have been used widely in a wide numbers of applications [38]. As a consequence, the physics of LPI has quickly become one of the fastest growing fields of research.

LPI has direct applications in inertial confinement fusion, particle accelerators, and medical imaging [39].

The physics of LPI can be quite complex, depending on both the laser configuration and the plasma condition. For example, while long-pulse lasers (nanosecond) have long been used for target heating in inertial fusion [40], ultra-short-pulse lasers (femtosecond), following the invention of chirped pulse amplification (CPA) in 1985, created an immense range of exotic phenomena (some of which are still not well understood), including particle acceleration, x-rays generation, and atomic physics [41]. Furthermore, while the interaction of a laser with an under-dense plasma results in different types of instabilities and particle acceleration, its interaction with an over-dense plasma can be utilized to create soft and hard x-rays (see figure 1.4 for an illustration).

It is worthwhile to highlight several aspects of the fundamental plasma physics, which contribute to the understanding of LPI. Firstly, the propagation of electromagnetic wave propagation in plasma directly relates to various instabilities as well as absorption mechanisms occurring in the corona layer of laser produced plasmas (LPP). Secondly, the self-consistent coupling of the plasma with the field gives rise to particle acceleration; this is a direct result of the Coulomb force from the electrostatic field induced in the plasma. Lastly, X-ray generation can be explained by collisions induced by the superthermal electrons generated in short-pulse LPI.

In the three research areas described above, several key processes can be identified to better model the plasma therein. The first one is based on a complete understanding of the CR processes and their coupling with the flow dynamics. The challenges associated with these studies are twofold. In the case of PAC, the combustion kinetics itself is a very complicated process, which comprises very detailed reaction mechanisms. Moreover, the existence of a plasma in a flame results in the generation of highly energetic excited species and reaction radicals;

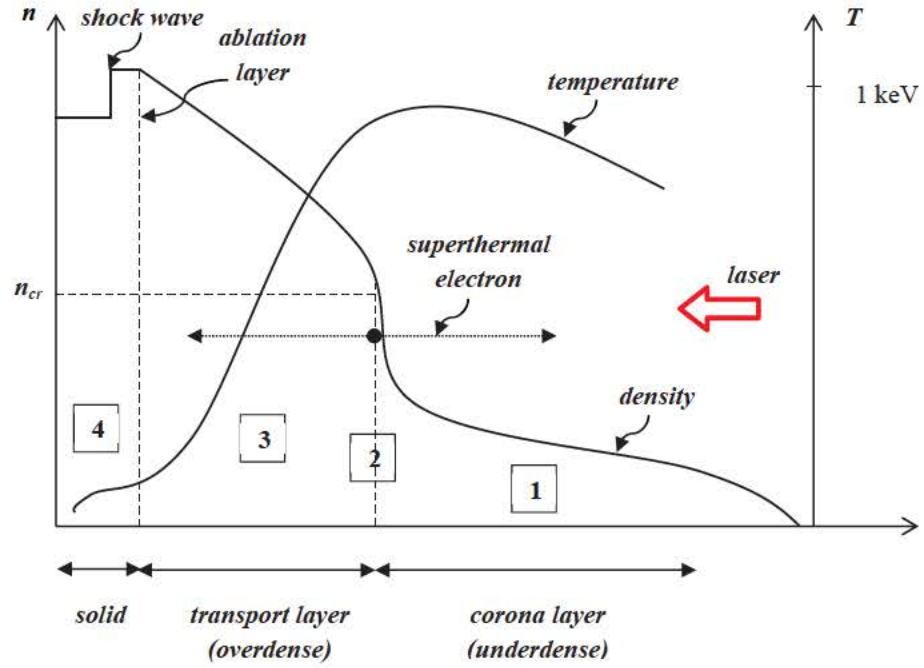


Figure 1.4: Physical processes in typical laser-plasma interaction: (1) collisional absorption, instabilities, magnetic field generation; (2) resonance absorption, profile steepening, hot electrons generation; (3) heat transport, soft x-rays generation; (4) hard x-rays generation. Figure adapted from [38].

these processes add more complexity to the overall kinetics of the system. In addition, the effects of species and thermal transport from both convection and diffusion processes, also introduce more couplings to the system. These effects are also relevant for applications in re-entry physics. Therefore, in order to accurately model such a complex system, one needs to understand different aspects of the plasmadynamics, the plasma chemical kinetics, and, more importantly, the coupling of the two.

On the other hand, typical plasma conditions found in LPI exhibit a high degree of translational non-equilibrium and charge separation between different species. These effects are most severe for ultra high intensity laser since relativistic electrons can be generated, which significantly alters the dynamics of the system. Moreover, the plasma evolution in these applications might span several physical regimes, from which multi-scale phenomena quickly arise. One must then be able to obtain a multi-scale description of the plasma; from a numerical modeling point of view, this is most computationally efficient with a hybrid model, i.e., combination of different numerical models at different regimes of interests. Some of these issues are addressed in this dissertation, specifically on the modeling of CR processes and non-equilibrium plasmas.

1.2 Overview of plasma physics

1.2.1 Plasma kinetic equations

Plasma flow can be modelled accurately at the microscopic level by the kinetic equation, which describes the evolution of the plasma *distribution function* in phase-space and Maxwell's equations, which describe the evolution of the electromagnetic field. In the simplest case of a single plasma component, the kinetic

equation for the distribution function takes the form:

$$\frac{\partial f}{\partial t} + \mathbf{v} \cdot \nabla_{\mathbf{x}} f + \mathbf{a} \cdot \nabla_{\mathbf{v}} f = \left(\frac{\partial f}{\partial t} \right)_{\text{CR}} \quad (1.1)$$

where $f \equiv f(\mathbf{x}, \mathbf{v}, t)$ is the distribution function in phase-space, and \mathbf{a} is the acceleration due to external force.

The terms on the left hand side (LHS) of the kinetic equation is denoted the streaming operator, and the term on the right hand side (RHS) is the collision operator responsible for all the exchange processes, including elastic (Coulomb) and inelastic collisions (i.e., CR kinetics). Without the RHS, equation (1.1) represent an advection equation in six-dimension so-called Vlasov equation. While the advection in configuration space is linear in nature, the advection in velocity space, as in the case of a plasma, can be non-linear due to the acceleration term \mathbf{a} . In the case of a plasma, \mathbf{a} represents the coupling terms between the plasma and the electromagnetic field, i.e., via the Coulomb and Lorentz forces $\mathbf{a} = \frac{q}{m} (\mathbf{E} + \mathbf{v} \times \mathbf{B})$. The electromagnetic field is governed by Maxwell's equations:

$$\nabla \times \mathbf{B} = \mu_0 \mathbf{j} + \mu_0 \epsilon_0 \frac{\partial \mathbf{E}}{\partial t} \quad (1.2)$$

$$\nabla \times \mathbf{E} = -\frac{\partial \mathbf{B}}{\partial t} \quad (1.3)$$

$$\nabla \cdot \mathbf{E} = \frac{\rho_q}{\epsilon_0} \quad (1.4)$$

$$\nabla \cdot \mathbf{B} = 0 \quad (1.5)$$

The non-linearity in the acceleration comes from the fact that an electric field can be induced from the plasma current, as can be seen in equation (1.2), and this field in turn acts on the plasma. Indeed, this closed loop system with constant feedback is the essential ingredient for particle-wave coupling, which in many cases results in instabilities or damping mechanisms [6].

The RHS of the kinetic equation (1.1) is quite complex, since it comprises of all the exchange processes due to collisional and radiative interactions. It is

well known that Coulomb collisions are generally the most important process in plasma; however, when the plasma is partially ionized or the energy transfer between the components is large enough to activate the large number of atomic transitions, inelastic collisions become significant and must be included. For example, inelastic collisions play an important role in the formation of field-reversed configuration (FRC) plasma [42], and internal energy excitation process in hypersonic shock layer.

One can see from equation (1.1) that a direct numerical solution (DNS) of the kinetic equation in 6-dimensional space with a complete detailed model of all the exchange processes is unrealistic and would require enormous computational resources. In addition, the plasma's chemical composition can add complexity to the system due to non-equilibrium effects between the components. In such cases, one needs to model each component separately (i.e., having one kinetic equation for each component).

Besides having to deal with the *curse of dimensionality* when directly solving the kinetic equation, the time scales associated with each component might be orders of magnitude different from the others, making the system extremely stiff. For example, electrons are much lighter than the heavy particles and therefore their transport occurs at a much shorter characteristic time scales. The interaction of the electrons with other species also gives rise to both the elastic and inelastic exchange processes, e.g., electron-impact excitation and ionization. The numerical solution of CR kinetics presents a huge challenge for traditional multi-scale methods due to the non-separation of time scales characteristics of the master equations; some of the issues and novel techniques devised to deal with these problems will be shown in this dissertation for the case of CR kinetics.

1.2.2 Modeling and simulations

Various methods had been derived in order to solve the kinetic equations, whether in simplified or the original form. The choice of the methods depends on the plasma collisionality and the ratios of length and time scales. These methods can be categorized as two main group of approaches: fluid based methods and kinetic methods.

The plasma fluid equations can be derived by taking a finite number of moments of the kinetic equation[43], and therefore obtaining a set of conservation laws for these moment variables. The most common model is the five-moment model, which results in the classical hydrodynamic equations, e.g., the Euler or Navier-Stokes equations. The fundamental issue with the moment approach is the closure problem, that is, each moment equation is always coupled to the next higher order moment variable, and the system cannot be completely closed without knowing the form of the distribution function. For example, in the energy equation, the coupling effect introduces the heat flux term, which is a high-order term; this term cannot be determined without the distribution function.

Two limiting cases can be identified where the fluid equations are valid. These are referred to as the *isothermal* and *inertial* (or *adiabatic*) regime. These regimes can be defined by comparing the characteristic velocity v_{char} to the thermal velocity of the plasma $v_T = \sqrt{\frac{kT}{m}}$. In the isothermal regime ($v_{\text{char}} \ll v_T$), the heat flux term in the energy equation dominates the inertial and collision terms, and temperature becomes spatially uniform. In the inertial regime ($v_{\text{char}} \gg v_T$), the heat flux terms can be neglected and the system can be closed at the energy equation.

Besides the two limiting cases where the fluid equations can be closed exactly, one can also perform an asymptotic expansion of the distribution function with a small parameter, i.e., $f = f^{(0)} + \epsilon f^{(1)} + \epsilon^2 f^{(2)} + \dots$, and deriving the fluid

equations by keeping only low-order terms of the distribution function. The most well-known closure scheme is the Chapman-Enskog method [44], first introduced for neutral gases, in which the distribution function is expanded with the small parameter being the ratio of the mean-free-path between collisions to the macroscopic length-scale so-called Knudsen number ($\epsilon = Kn$). Therefore, the scheme is only valid when the plasma is dominated by collisions (i.e., very similar to neutral gas), making the distribution function very close to a Maxwellian distribution function. For zeroth and first order Chapman-Enskog expansion, the resultant set of fluid equations are the Euler and Navier-Stokes equations. For second order expansion, the resultant system is the Burnett equations [45]. In 1965, Braginskii [46] derived the plasma fluid equations for electrons and ions with the Chapman-Enskog closure, the result of which, led to the well-known Braginskii equations for a two-fluid fully ionized plasma.

Another classical closure scheme is Grad's moment method [47]. Grad's method originally attempted to extend the validity of the fluid equations into the rarefied regime by conserving higher order moments (e.g., individual component of the full stress tensor) of the distribution function. Grad's closure is done based on the Hilbert expansion of the distribution function in Hermite polynomials. The resultant systems from this family of closure are the Grad 13-moment and 26-moment equations. One of the challenges associated with Grad's type equations is the lack of physical intuition of the moment variables, which imposes difficulties on boundary conditions.

Since moment equations can always be represented as a set of conservation laws, they can be solved by various efficient finite difference, finite volume, or finite element methods. In both closure approaches described above, the complication of modeling the exchange processes still remains, some of which are present in the current research, but the computational resource required for solving these equations are much more affordable. For example, in chemically reacting flow, the

exchange source terms (mass production/consumption) are often computed from a zeroth-order (Maxwellian) distribution, which is inconsistent with the Chapman-Enskog closure. A rigorous treatment of the exchange terms requires including high-order correction to the both chemical rates and the transport coefficient [48, 49].

The second approach, kinetic methods, aim at solving the distribution function f in equation (1.1) by means of either a deterministic or stochastic method. There have been various attempts in solving the kinetic equation directly in phase-space, but most of the simulations is only limited to 2D-2V (that is, two-dimensional in both physical and velocity space).

The most widely used plasma simulation method, introduced in the late 1950s, is the particle-in-cell (PIC) method [50], the most favorite choice for simulating collisionless plasma (i.e., solving the Vlasov equation). In PIC codes, the distribution function f is represented as a collection of pseudo-particles, i.e., the distribution function is discretized into Lagrangian points in phase-space. In that case, the distribution function is given by the superposition of these computational particles.

$$f(\mathbf{x}, \mathbf{v}, t) = \sum_p w_p \delta(\mathbf{v} - \mathbf{v}_p) S(\mathbf{x} - \mathbf{x}_p) \quad (1.6)$$

where w_p is the statistical weight³ and $S(\mathbf{x} - \mathbf{x}_p)$ is the shape function of the computational particle p .

The evolution of the distribution function is modelled by solving the equations of motion for these particles under the influence of the electromagnetic fields. These equations can be derived by introducing the expression (1.6) into the kinetic equation, and then taking the moment of the kinetic equations. A complete derivation is given by Lapenta [51] and will not be repeated here.

Neglecting relativistic effects, the resultant equations of motion for these pseudo

³the number of real particle each pseudo particle represents.

particles read:

$$\frac{d\mathbf{x}_p}{dt} = \mathbf{v}_p \quad (1.7)$$

$$\frac{d\mathbf{v}_p}{dt} = \frac{q}{m} (\mathbf{E} + \mathbf{v}_p \times \mathbf{B}) \quad (1.8)$$

These are the characteristic equations of the Vlasov system. Furthermore, these equations are coupled with Maxwell's equations for the evaluation of the electric and magnetic fields. The advantage of PIC method is that instead of solving the distribution function, one only needs to keep track of these computational particles and the complete distribution function can always be reassembled. However, similar to other particle-based methods for neutral gas, the PIC method has difficulties modeling dense and highly collisional plasmas due to statistical noise.

1.3 Scope of present work

In the previous sections, multiple approaches in the numerical modeling of non-equilibrium plasma were described, which revealed significant challenges in constructing a unified model for non-equilibrium plasma simulation. These challenges are associated with the hyper-dimensionality aspect, and the complexity and abundance of the physical processes embedded in the collisional operators.

In the current research, special attention is paid to the dynamics of collisional and radiative interactions in a plasma, and more importantly, the coupling between collisions and transport. The current work focuses on studying this coupling in plasma regimes, for which the dimensionality of the problem can be reduced. In particular, the research presented here is restricted to the hydrodynamic framework. The validity and variation of these hydrodynamic models will be discussed, and a self-consistent treatment of CR kinetics will be presented.

To summarize, the overall objective of this dissertation is to construct hydrodynamic models for non-equilibrium plasma flows with self-consistent treatment of

the exchange terms due to CR kinetics, and present a numerical model for solving these coupled sets of equations. The dissertation can be divided into three parts. In the first part, different hydrodynamic models for plasma flows are presented with emphasis on clarifying the assumptions of each model and their relation to one another. The multi-fluid equations, which constitutes by far the most general treatment of plasmadynamics within the hydrodynamic framework, will also be introduced. The high-order numerical methods used to solve these equations are also presented.

In the second part, the description of the CR model is introduced. The coupling of CR kinetics with fluid equations will be detailed for the case of an atomic plasma. The constructed CR model will be used to study in detail the dynamic of excitation and ionization, as well as their coupling with convection. A novel technique is derived to lower the complexity of CR kinetics while maintaining high accuracy; this technique can help making multidimensional calculation with CR kinetics feasible. In the last part, a self-consistent treatment of elastic and inelastic collisions in multi-fluid equations will be presented. The multi-fluid model is then used to study laser-plasma interaction phenomena.

CHAPTER 2

Hydrodynamic Equations

2.1 Introduction

In this chapter, the hydrodynamic equations for plasma flow in thermal non-equilibrium conditions are presented. It is worthwhile to go over the fundamental assumptions which suggest to the domain of validity of these models. We emphasize that here, the fluid is assumed to be sufficiently collisional that the *continuum hypothesis*¹ is satisfied. In the picture of neutral gas flow, this is characterized by a single unit-less parameter known as the Knudsen number Kn , defined as the ratio of collision mean free path to the characteristic length scale. In the limit of $Kn \ll 1$, the flow is said to be strongly collisional such that the translational degrees of freedom are in equilibrium, that is, they can be represented by a classical Maxwellian distribution function. Small perturbations from Maxwellian equilibrium of order Kn can be incorporated into the kinetic equations, which result in various transport phenomena, commonly seen in the Navier-Stokes equations [52, 44, 53].

While justification of the continuum hypothesis is fairly straight-forward in neutral gas flow, the situation gets quite complicated in plasma flows, mainly due to the stiff time scales introduced by the electrons and the coupling of the plasma to electrodynamic forces, e.g., electron-ion collision time, plasma frequency, gyrofrequency, etc. The implied consequence is that the system's degree of stiffness

¹This term is commonly used in fluid dynamics literature.

can no longer be characterized by a single parameter, and the hydrodynamic regime cannot be distinguished without further assumptions. Moreover, these fundamental time scales can also be evolved dynamically with the system, which allows the plasma to go from one regime to another. For examples, in ultra-high intensity LPI, while the plasma formation and interaction with a femtosecond laser pulse are commonly simulated with a kinetic code, the slower plasma expansion, on the other hand, can be simulated with a fluid code or a hybrid kinetic-fluid code. This dynamical stiffness creates significant challenges for numerical modeling and simulations.

It is therefore more convenient to define the assumptions of a particular hydrodynamic model in each section rather than listing all the assumptions at once. However, since we are working in the hydrodynamic framework, it is sufficient to say that at all time the velocity distribution function (VDF) of *each* plasma component can be characterized by a Maxwellian VDF. This is indeed a very crude approximation and needs further elaboration.

It must be assumed that the electromagnetic field is not strong enough to distort the distribution function. For the electrons, this assumption is quite hard to satisfy due to their high mobility. Fortunately enough, in a lot of cases, deviation from Maxwellian equilibrium can be localized in both physical and velocity space, that is to say, the electron VDF can be efficiently decomposed into an equilibrium and a non-equilibrium parts. This is typically done in laser fusion, where the electrons are divided into two populations: cold and hot (superthermal) electrons [40]. The “hot” electrons, typically represented by a fast tail in the VDF, can be extracted from a bulk Maxwellian VDF and treated using a kinetic method, while the “cold” population can be well characterized by a fluid approximation.

Therefore, the models presented in this work, despite being unable to capture kinetic effects, are still useful for a hybrid description of the plasma. It must be noted that, for a typical Chapman-Enskog expansion of the plasma VDF,

the electric and magnetic fields can affect the plasma transport properties, i.e., the transport coefficient is dependent of the field strength. These results can be found from classical transport theory, and will not be described here [46, 54, 55]. In this chapter, all the transport terms are omitted in the presentation of the fluid equations, except for electron heat conduction, since it is one of the main mechanisms for thermal transport in LPI applications [38]. This term is introduced in the multi-temperature model presented in section 2.4.

2.2 Multi-fluid equations

2.2.1 Euler-Maxwell and Euler-Poisson systems

Let us now consider the multi-fluid equation for a multicomponent plasma. The plasma described here can be partially ionized, so there is a neutral population among the charged species. In this section, s and t are defined to be a general species index, while n , i , and e are the used to refer to the neutral, ion, and electron populations, respectively, i.e., $s, t \in \{n, i, e\}$. For clarity in the presentation of the hydrodynamic framework, detailed treatment of the collision terms is omitted here, and their description is deferred for chapter 6. The elastic collision terms appearing in the momentum and energy equations are kept in general form. The inelastic terms are omitted in the current discussion.

The continuity equation for each plasma species follows conservation law:

$$\partial_t \rho_s + \nabla \cdot (\rho_s \mathbf{u}_s) = 0 \quad (2.1)$$

where the subscript s is used to distinguish between the given species properties from the total plasma properties. For example, \mathbf{u}_s is the average velocity of the species s , which is different from the mass averaged velocity, denoted as $\bar{\mathbf{u}}$. In the absence of chemical reactions, the RHS of equation (2.1) is zero. Since each species can have its own hydrodynamic velocity, its momentum can be separately

conserved. The conservation equation of the momentum can be written as:

$$\partial_t (\rho_s \mathbf{u}_s) + \nabla \cdot (\rho_s \mathbf{u}_s \mathbf{u}_s) + \nabla p_s = n_s q_s (\mathbf{E} + \mathbf{u}_s \times \mathbf{B}) + \sum_t \mathbf{R}_{st} \quad (2.2)$$

The first term on the RHS of equation (2.2) represents the electrodynamic forces acting on the plasma. This term is zero for the neutral population ($q_n = 0$). The second term comprises of momentum exchange due to collision with other populations. For example, the conservation equation for the electron momentum includes two terms representing collisions with neutral and ion populations: \mathbf{R}_{ei} and \mathbf{R}_{en} . In addition, momentum conservation implies:

$$\mathbf{R}_{st} + \mathbf{R}_{ts} = 0 \quad (2.3)$$

The conservation of thermal energy of each species can be written as:

$$\partial_t \varepsilon_s + \nabla \cdot (\varepsilon_s \mathbf{u}_s) + p_s \nabla \cdot \mathbf{u}_s = \sum_t Q_{st} \quad (2.4)$$

The RHS of equation (2.4) represents thermal relaxation effects due to elastic collisions (inelastic collisions are neglected here). Equation (2.4) can be combined with (2.2) to yield the conservation equation for the total energy of each species:

$$\partial_t E_s + \nabla \cdot [(E_s + p_s) \mathbf{u}_s] = \mathbf{j}_s \cdot \mathbf{E} + \sum_t (Q_{st} + \mathbf{R}_{st} \cdot \mathbf{u}_s) \quad (2.5)$$

where $E_s = \varepsilon_s + \frac{1}{2} \rho_s \mathbf{u}_s \cdot \mathbf{u}_s$. Similarly, conservation of energy implies the following relation to hold:

$$Q_{st} + \mathbf{R}_{st} \cdot \mathbf{u}_s + Q_{ts} + \mathbf{R}_{ts} \cdot \mathbf{u}_t = 0 \quad (2.6)$$

The fluid equations can be closed by specifying an equation of state, similar to that of an ideal gas:

$$p_s = n_s k T_s \quad (2.7)$$

where $n_s = \rho_s / m_s$. For an atomic plasma, the thermal energy is simply $\varepsilon_s = p_s / (\gamma_s - 1)$, where γ_s is the ratio of specific heat for the plasma.

The evolution of the electric and magnetic fields are governed by Maxwell's equations and will not be repeated here. In the case where the field is electrostatic, the electric field can be solved from Gauss's law, equation (1.4). It is more convenient to express the electric field in term of the electric potential, i.e., $\mathbf{E} = -\nabla\phi$, such that Gauss's law can be transformed to Poisson's equation:

$$\nabla^2\phi = \frac{e}{\epsilon_0}(n_e - Z_i n_i) \quad (2.8)$$

The Euler-Maxwell (or Euler-Poisson) system, equations (1.2)-(1.5) and (2.1)-(2.8) form a complete self-consistent model for a multicomponent plasma. These equations are referred to as comprising the multi-fluid plasma model.

2.2.2 Time and length scales of multi-fluid equations

Several fundamental time scales associated with the multi-fluid equations can be identified. These time scales are crucial in the design of the numerical methods for solving hyperbolic partial differential equations (PDEs) with source terms. Firstly, a thermal velocity for each species can be defined from the translational temperature, leading to a resultant time scale:

$$\tau_s = \frac{L}{v_{Ts}} \quad (2.9)$$

where v_{Ts} is the thermal speed of species s , i.e., $v_{Ts} = \sqrt{\frac{kT_s}{m_s}}$ and L is a characteristic length scale. The time scales associated with the electromagnetic forces are given in terms of the plasma frequency (inverse of time scale):

$$\omega_{ps} = \sqrt{\frac{n_s q_s^2}{\epsilon_0 m_s}} \quad (2.10)$$

and the gyrofrequency:

$$\omega_{cs} = \frac{q_s |\mathbf{B}|}{m_s} \quad (2.11)$$

In addition, when electromagnetic wave propagation must be considered, the light transit time becomes relevant:

$$\tau_c = \frac{L}{c} \quad (2.12)$$

where $c = 3 \times 10^8$ m/s is the speed of light. Lastly, the momentum and energy exchange processes between the species introduce relaxation time scales to the system. In a typical fully-ionized plasma, the scaling of these collisional frequencies is as follows [55]:

$$\nu_{ee} \sim T_e^{-3/2} \quad (2.13)$$

$$\nu_{ei} \sim Z_i \nu_{ee} \quad (2.14)$$

$$\nu_{ii} \sim Z_i^3 \sqrt{\frac{m_e}{m_i}} \nu_{ee} \quad (2.15)$$

$$\nu_{ei}^\varepsilon \sim Z_i \frac{m_e}{m_i} \nu_{ee} \quad (2.16)$$

where ν_{ei}^ε is the energy relaxation frequency between the ion and electron. This term scales as the mass ratio m_e/m_i and is much smaller compared to the momentum relaxation frequency ν_{ei} . In a typical plasma system, the electron plasma frequency ω_{pe} is the largest frequency in the system with the possible exception of low density and strongly magnetized plasma, where ω_{ce} can also become quite large.

Several length scales associated with the plasmadynamics characterized by the multi-fluid equations can be identified. The characteristic length scale corresponding to the plasma frequency is the Debye length, defined as follows:

$$\lambda_D = \sqrt{\frac{\epsilon_0 k T}{e^2 n_e}} \quad (2.17)$$

If the characteristic length scale of the system is much larger compared to the Debye length, the plasma can be approximated to be quasi-neutral. Similarly, the characteristic length scale corresponding to the gyro-motion of the particle due to

the magnetic field can be defined as:

$$r_{Ls} = \frac{v_{Ts}}{\omega_{cs}} \quad (2.18)$$

where r_{Ls} is known as the gyro-radius (or Larmor radius). If the plasma is collisional, one can also define a collision mean free path λ_s as follows:

$$\lambda_s = \frac{v_{Ts}}{\nu_s} \quad (2.19)$$

where ν_s is the collisional frequency of species s . Typically, it is more convenient to define the collision mean free path for each collision type, since the collision dynamics can be quite different from each other.

An important observation to be made about the multi-fluid equations, is that there is a large disparity in the time scales. The electrons, being very mobile and responsive to the electromagnetic fields, might be approximated in a quasi steady-state condition. Using this approximation, the electron momentum equation is reduced to the so-called generalized Ohm's law, which is derived in the next section.

2.2.3 Generalized Ohm's law

In order to simplify the derivation, let us consider for now a two-component fully ionized plasma consisting of ions and electrons with Coulomb interaction. The generalization to include an additional neutral population can be done, but with a more lengthy derivation since more collision terms need to be involved.

Starting from the electron momentum equation:

$$\partial_t (\rho_e \mathbf{u}_e) + \nabla \cdot (\rho_e \mathbf{u}_e \mathbf{u}_e) + \nabla p_e = -en_e (\mathbf{E} + \mathbf{u}_e \times \mathbf{B}) + \mathbf{R}_{ei} \quad (2.20)$$

the so-called *massless electron* assumption is utilized, i.e., the two inertial terms on the LHS of equation (2.20) are negligible compared to the other terms. Note that the collision term \mathbf{R}_{ei} can be expressed in terms of the collisional frequency,

i.e., $\mathbf{R}_{ei} = m_e n_e \nu_{ei} (\mathbf{u}_i - \mathbf{u}_e)$ [46]. Hence, equation (2.20) is reduced to:

$$\nabla p_e = -en_e (\mathbf{E} + \mathbf{u}_e \times \mathbf{B}) + m_e n_e \nu_{ei} (\mathbf{u}_i - \mathbf{u}_e) \quad (2.21)$$

In this case, the electron dynamics are given by a steady-state condition given by equation (2.21). In the limit of $m_e \rightarrow 0$, one also obtains:

$$\bar{\mathbf{u}} = \frac{\rho_i \mathbf{u}_i + \rho_e \mathbf{u}_e}{\rho_i + \rho_e} \simeq \mathbf{u}_i + o\left(\frac{m_e}{m_i}\right) \quad (2.22)$$

where $\bar{\mathbf{u}}$ is the mass averaged velocity of the plasma. From the definition of the total current density, one also obtains:

$$\mathbf{j} = Z_i e n_i \mathbf{u}_i - e n_e \mathbf{u}_e = e n_e (\bar{\mathbf{u}} - \mathbf{u}_e) + e (Z_i n_i - n_e) \bar{\mathbf{u}} \quad (2.23)$$

Let us now assume that the system is *close* to charge neutrality ($Z_i n_i - n_e \simeq 0$), such that the second term on the RHS of equation (2.23) is smaller compared to the first one, which leads to the following expression for the electron velocity:

$$\mathbf{u}_e \simeq \bar{\mathbf{u}} - \frac{\mathbf{j}}{e n_e} \quad (2.24)$$

Using expression (2.24), equation (2.21) can be brought into the form:

$$\mathbf{j} = \bar{\sigma} (\mathbf{E} + \bar{\mathbf{u}} \times \mathbf{B}) + \frac{\bar{\sigma}}{n_e e} \nabla p_e - \beta_e \mathbf{j} \times \hat{\mathbf{b}} \quad (2.25)$$

where

$$\bar{\sigma} = \frac{n_e e^2}{m_e \nu_{ei}} \quad (2.26)$$

$$\beta_e = \frac{\omega_{ce}}{\nu_{ei}} \quad (2.27)$$

$$\hat{\mathbf{b}} = \frac{\mathbf{B}}{|\mathbf{B}|} \quad (2.28)$$

Equation (2.25) is known as the generalized Ohm's Law. $\bar{\sigma}$ and β_e are the plasma conductivity and Hall parameter, respectively. The first term on the RHS of equation (2.25) is the conduction term, the second term is the electron diffusion, and the last term is the Hall term. Various MHD models can be derived starting from Ohm's law.

2.3 Magnetohydrodynamics

In this section, Ohm's law is utilized to derive the MHD equations. It is worthwhile to clarify that the MHD approximation corresponds to the assumption of a steady-state current given by Ohm's law, i.e., using equation (2.25) in place of the electron momentum equation. One can easily retain all the other equations in the multi-fluid systems and solve the system self-consistently. Those equations are commonly referred to as the multi-fluid MHD equations. In this study, the term multi-fluid is strictly reserved for the case where each plasma component including the electrons are conserved as a separate fluid, as previously shown in section 2.2.

Let us now look at the MHD equations in the single fluid limit, which implies that the momentum exchange is sufficiently fast such that one only needs to keep track of the total momentum of the bulk plasma². This needs not be the case for the energy equation, since the energy transfer rate is rather slow, e.g., see equation (2.16); this suggests a multi-temperature approach, which will be described in the next section. For simplicity, consider Ohm's law in the following form:

$$\mathbf{j} = \bar{\sigma}(\mathbf{E} + \mathbf{u} \times \mathbf{B}) \quad (2.29)$$

where the electron diffusion and the Hall terms were neglected. Also for clarity, we drop the bar in the expression of the plasma average velocity, i.e., $\bar{\mathbf{u}} \rightarrow \mathbf{u}$.

The continuity equation for the plasma is in its typical form of conservation law:

$$\partial_t \rho + \nabla \cdot (\rho \mathbf{u}) = 0 \quad (2.30)$$

where the convective speed is now \mathbf{u} , and ρ is the plasma total density. If chemical reactions and transport phenomena between the species (such as diffusion) are

²This condition is required for the single fluid approximation, i.e., all species have the same averaged velocity. In general, one only needs $\rho_e \mathbf{u}_e \ll \rho_i \mathbf{u}_i$; if the plasma mixture contains several ion species with different averaged velocity, a multi-fluid MHD description can be used.

important, equation (2.30) is replaced by a set of conservation equations for each species, convected at the same velocity. The chemical reactions are represented by a source term for each species equation, representing the rate of consumption or formation of the species. The difference between each species velocity and the bulk is given by the given species diffusion velocity. For brevity, only the total plasma density here is considered. The extension to multi-species for a chemically reactive plasma is given in the next section.

The total plasma momentum equation can be written as:

$$\partial_t (\rho \mathbf{u}) + \nabla \cdot (\rho \mathbf{u} \mathbf{u}) + \nabla p = \epsilon_0 \mathbf{E} (\nabla \cdot \mathbf{E}) + \mathbf{j} \times \mathbf{B} \quad (2.31)$$

where all the quantities now denote the properties of the bulk plasma instead of individual species.

Let us now introduce two further approximations. The first approximation corresponds to *charge neutrality* condition³, from which the first term on the RHS of (2.31) vanishes ($\nabla \cdot \mathbf{E} = 0$). This assumption is valid when the characteristic length of the domain is much larger than the Debye length, or equivalently, when the characteristic time is much slower than the plasma oscillation time. The second one is the *infinite speed of light* approximation. In this limit, the displacement current is negligible compared to the electric current and Ampere's law yields:

$$\nabla \times \mathbf{B} = \mu_0 \mathbf{j} \quad (2.32)$$

Inserting the expression above for \mathbf{j} into the total plasma momentum equation and with some vector calculus identities, one can obtain:

$$\partial_t (\rho \mathbf{u}) + \nabla \cdot (\rho \mathbf{u} \mathbf{u} + \mathbb{P}_B) + \nabla p = 0 \quad (2.33)$$

where $\mathbb{P}_B = \frac{1}{\mu_0} \left(\frac{1}{2} \mathbf{B} \cdot \mathbf{B} - \mathbf{B} \mathbf{B} \right)$ is known as the Maxwell stress tensor⁴. It is shown

³This approximation is now consistent with the assumption first made in arriving at equation (2.24).

⁴Here charge neutrality was assumed, so the effect of electric field does not show up in the expression of Maxwell stress tensor.

that the effect of the Lorentz force is now replaced by an equivalent magnetic pressure [56].

The conservation equation of the plasma total energy can be written as:

$$\partial_t E + \nabla \cdot [(E + p) \mathbf{u}] = \mathbf{j} \cdot \mathbf{E} \quad (2.34)$$

where Joule heating is the only coupling term remaining on the RHS. The conservation equation for the magnetic energy density [56] can be written as:

$$\partial_t \left(\frac{\mathbf{B} \cdot \mathbf{B}}{2\mu_0} \right) + \nabla \cdot \left(\frac{\mathbf{E} \times \mathbf{B}}{\mu_0} \right) = -\mathbf{j} \cdot \mathbf{E} \quad (2.35)$$

Taking a cross product of Ohm's law (2.29) with \mathbf{B} and substituting the expression of $\mathbf{E} \times \mathbf{B}$ back into equation (2.35), one obtains:

$$\partial_t \left(\frac{\mathbf{B} \cdot \mathbf{B}}{2\mu_0} \right) + \nabla \cdot \left(\frac{\mathbf{B} \cdot \mathbf{B}}{2\mu_0} \mathbf{u} \right) + \nabla \cdot (\mathbb{P}_B \cdot \mathbf{u}) - \nabla \cdot \left(\frac{1}{\mu_0 \bar{\sigma}} \nabla \cdot \mathbb{P}_B \right) = -\mathbf{j} \cdot \mathbf{E} \quad (2.36)$$

Combining equation (2.36) and (2.34) yields the conservation for the total plasma energy density including the magnetic field energy:

$$\partial_t E^* + \nabla \cdot [(E^* + p) \mathbf{u}] + \nabla \cdot (\mathbb{P}_B \cdot \mathbf{u}) = \nabla \cdot \left(\frac{1}{\mu_0 \bar{\sigma}} \nabla \cdot \mathbb{P}_B \right) \quad (2.37)$$

where $E^* = E + \frac{\mathbf{B} \cdot \mathbf{B}}{2\mu_0}$. The term on the RHS of equation (2.37) corresponds to the resistive diffusion of the magnetic field energy. The equation of state is that of ideal gas similar to equation (2.7):

$$p = nkT = (\gamma - 1)E \quad (2.38)$$

where $n = \rho/m$ is the number density of the gas.

Similarly, an equation for the evolution of the magnetic field can also be derived. Starting with Faraday's law of induction (1.3), Ohm's law can be used to express $\nabla \times \mathbf{E}$ in terms the current density and the magnetic field, which leads to:

$$\partial_t \mathbf{B} - \nabla \times (\mathbf{u} \times \mathbf{B}) = -\nabla \times \frac{1}{\bar{\sigma}} \mathbf{j} \quad (2.39)$$

Using Ampere's law (2.32) to relate the current density to the magnetic field and utilizing some vector calculus identities, one obtain an equation for the evolution of the magnetic field:

$$\partial_t \mathbf{B} - \nabla \times (\mathbf{u} \times \mathbf{B}) = -\nabla \times \left(\frac{1}{\mu \bar{\sigma}} \nabla \times \mathbf{B} \right) \quad (2.40)$$

Equations (2.30), (2.33), (2.37), (2.38) and (2.40) constitute a complete set for a standard resistive MHD model. In the limit of infinitely conducting plasma, i.e., $\bar{\sigma} \rightarrow \infty$, all the diffusion terms associated with the magnetic field vanish, and the ideal MHD equation is recovered. This point will be revisited in section 3.3.2.3 when we make comparison between the solution of the multi-fluid system and the MHD equation.

It must be noted that the effect of electron diffusion and Hall current has been left out in the expression of Ohm's law. In the first case, one can introduce an effective electric field $\hat{\mathbf{E}} = \mathbf{E} + \frac{\nabla p_e}{en_e}$ such that Ohm's law can be put in the form of (2.29). In the case when the Hall term is also included, Ohm's law can still be written in the same form where the scalar conductivity $\bar{\sigma}$ now becomes a conductivity tensor [57]. Introducing the expression of the effective electric field into generalized Ohm's law equation (2.25), one obtains:

$$\mathbf{j} + \beta_e \mathbf{j} \times \hat{\mathbf{b}} = \bar{\sigma} \hat{\mathbf{E}} \quad (2.41)$$

where $\hat{\mathbf{E}} = \mathbf{E} + \mathbf{u} \times \mathbf{B}$. Let us introduce a coordinate such that the magnetic field is aligned with the z -direction, i.e., $\mathbf{B} = |\mathbf{B}| \hat{\mathbf{e}}_z$. Ohm's law can be brought into the following form:

$$\begin{bmatrix} j_x \\ j_y \\ j_z \end{bmatrix} = \frac{\bar{\sigma}}{1 + \beta_e^2} \begin{bmatrix} 1 & -\beta_e & 0 \\ \beta_e & 1 & 0 \\ 0 & 0 & 1 + \beta_e^2 \end{bmatrix} \begin{bmatrix} \hat{E}_x \\ \hat{E}_y \\ \hat{E}_z \end{bmatrix} \quad (2.42)$$

One can see from equation (2.42) that in the limit of strongly magnetized plasma, the current parallel to the magnetic field is much stronger than the transverse currents.

2.4 Multi-temperature and chemically reactive hydrodynamics

When the chemical reaction time scale is of the same order of magnitude as the hydrodynamic time scale, one must take in account the species mass production/consumption and energy exchanges between different modes. The resultant set of equations is referred to as the multi-species multi-temperature model. These models are widely used in numerical simulations due to their high efficiency in multi-dimensional calculations [21].

The number of “temperature” variables included in the model is dictated by the underlying assumption of the energy transfer rate between different energy modes. For example, in an atomic plasma, due to the slow energy exchange rates between the heavy species and the electrons, an additional conservation equation for the electron energy is usually required, resulting in the so-called two-temperature (2T) plasma model.

In the case of a molecular plasma, due to additional degrees of freedom such as rotational and vibrational modes, one can write separate conservation equation for rotational and vibrational energies, leading to various multi-temperature models. The choice of partition between these energy modes is not trivial, and is highly condition dependent. In hypersonic plasma, a typical assumption is that the rotational modes is in equilibrium with the translational mode, and vibrational energy can be considered separately. High-fidelity kinetic models indicate that this assumption is questionable and indeed for high temperature and low pressure conditions, rotational and vibrational exchange can proceed at the same rate [58].

In this section, a 2T model for atomic plasma is presented, where the electron thermal energy is separated conserved from the total energy. In addition, chemical reactions are taken into account by extending the Euler equation to multiple species. For simplicity, only the single-fluid approximation is considered, and the

effects of the electromagnetic fields is omitted. The resultant system of equations is similar to the Euler equations for reactive neutral gas flow:

$$\partial_t \rho_s + \nabla \cdot (\rho_s \mathbf{u}) = m_s \dot{\omega}_s \quad (2.43)$$

$$\partial_t (\rho \mathbf{u}) + \nabla \cdot (\rho \mathbf{u} \mathbf{u}) + \nabla p = 0 \quad (2.44)$$

$$\partial_t E + \nabla [(E + p) \mathbf{u}] + \nabla \cdot \mathbf{q}_e = \dot{\omega}_{\varepsilon_e} + \dot{\omega}_{\varepsilon_h} \quad (2.45)$$

$$\partial_t \varepsilon_e + \nabla (\varepsilon_e \mathbf{u}) + p_e \nabla \cdot \mathbf{u} + \nabla \cdot \mathbf{q}_e = \dot{\omega}_{\varepsilon_e} \quad (2.46)$$

where the total energy of the plasma in this case is defined as:

$$E = \varepsilon_h + \varepsilon_e + \frac{1}{2} \rho \mathbf{u} \cdot \mathbf{u} \quad (2.47)$$

and

$$\varepsilon_h = \frac{p_h}{\gamma - 1} \quad (2.48)$$

$$\varepsilon_e = \frac{p_e}{\gamma_e - 1} \quad (2.49)$$

For the case of an atomic plasma, one simply takes $\gamma = \gamma_e = \frac{5}{3}$. The equation of state for a 2T plasma can be written as:

$$p = \sum_{s \neq e} n_s k T_h + n_e k T_e \quad (2.50)$$

$$p_e = n_e k T_e \quad (2.51)$$

The electron translational energy equation written in (2.46) is non-conservative due to the adiabatic heating term $p_e \nabla \cdot \mathbf{u}_e$. A conservative form of the equation can be obtained by defining an entropy-like variable $S_e \equiv \rho \hat{s}_e = \rho \frac{p_e}{\rho^{\gamma_e}}$ and rewriting the equation accordingly⁵:

$$\partial_t \left(\frac{p_e}{\rho^{\gamma_e-1}} \right) + \nabla \cdot \left(\frac{p_e \mathbf{u}}{\rho^{\gamma_e-1}} \right) = \frac{\gamma_e - 1}{\rho^{\gamma_e-1}} \left[\frac{\partial \varepsilon_e}{\partial t} + \nabla \cdot (\mathbf{u} \varepsilon_e) \right] + \frac{\gamma_e - 1}{\rho^{\gamma_e-1}} (p_e \nabla \cdot \mathbf{u}) \quad (2.52)$$

⁵This is similar to the approach taken in [59] but the electron entropy is defined in term of ρ instead of ρ_e . The advantage is that the entropy remains finite when the ionization fraction goes to zero ($\rho_e \rightarrow 0$) [60].

Using equation (2.46), we can obtain a conservation equation for the electron entropy:

$$\frac{\partial S_e}{\partial t} + \nabla \cdot (S_e \mathbf{u}) + \left(\frac{\gamma_e - 1}{\rho^{\gamma_e - 1}} \right) \nabla \cdot \mathbf{q}_e = \frac{\gamma_e - 1}{\rho^{\gamma_e - 1}} \dot{\omega}_{\varepsilon_e} \quad (2.53)$$

Note that the source term must be modified based on the definition of the new variable. The equation of state can be expressed in term of the electron entropy:

$$p = p_h + p_e = \rho^{\gamma_e - 1} S_e + \sum_{s \neq e} n_s k T_h \quad (2.54)$$

Similarly, we can rewrite the expression for the total energy in term of the electron entropy:

$$E = \frac{S_e \rho^{\gamma_e - 1}}{\gamma_e - 1} + \sum_{s \neq e} \rho_s \varepsilon_s + \frac{1}{2} \rho \mathbf{u} \cdot \mathbf{u} \quad (2.55)$$

It is important to mention that the source term on the RHS of the total energy equation (2.45) is non-zero, which, however, does not violate energy conservation. The reason for this is that the species heat of formation is not included in the definition of the total energy E . Therefore, the change of the energy when a new species is produced or destroyed has to be accounted for properly⁶. The choice of such a definition of the total energy is purely due to numerics. It was observed that for the simulation of flow containing species of high chemical energy, the linearization of the energy (or enthalpy), an important step in the finite volume method for solving non-linear PDEs, can introduce some error at the composition discontinuity if the heat of formation is included in the definition of E [61].

The term on the RHS of (2.43) corresponds the rate of change of each species due to chemical reaction. Consider a general reaction of the following type:



⁶One must take in account the rate of change of energy for the heavy particle and electron accordingly depending on a specific chemical process. For example, heavy-particle impact and electron impact excitations must be considered as two separate processes, since the energy exchange is taken from different conserved quantities.

the corresponding source term for species s due to this reaction can be written as:

$$\dot{\omega}_s = -k_f n_s n_t + k_b n_{s'} n_{t'} \quad (2.57)$$

where k_f denote the forward rate and k_b denote the backward rate of reaction (2.57). The most commonly used expression for the chemical reaction rate is the modified Arrhenius form:

$$k_f = A_f T^{\beta_f} \exp\left(-\frac{\delta E_f}{kT}\right) \quad (2.58)$$

where A , β , and δE are the three main parameters controlling the rate. It is important to note that the forward and the backward rates can always be related by the principle of detailed balance. In the single-fluid approximation, these two rates can be related by the so-called equilibrium constant:

$$k_{eq} = \frac{k_f}{k_b} \quad (2.59)$$

The principle of detailed balance for atomic collisional and radiative processes, resulting in a particular form of the equilibrium constant k_{eq} , will be described in detailed in chapter 4. In addition, it will also be shown in chapter 6 that expressions of the same type as equation (2.59) no longer hold for multi-fluid equations. A detail treatment of these terms will be described in chapter 4.

The electron heat conduction process is also included in both conservation equations for the total energy and electron entropy. This term is expressed as a divergence of the electron heat flux \mathbf{q}_e . The electron heat flux is usually expressed by Fourier's law of heat conduction:

$$\mathbf{q}_e = -\kappa_e \nabla T_e \quad (2.60)$$

where κ_e is the electron heat conductivity.

The most commonly used expression for the electron heat flux in fully ionized plasma is due to Spitzer-Harm (SH) [54], from which κ_e is determined from

Coulomb interaction. The SH expression yields $\mathbf{q}_e \sim \kappa_0 \nabla(T_e^{7/2})$ where κ_0 is a constant. This expression is used, for example, in calculation of target heating in inertial fusion. However, cautions must be exercised when using this formula, especially in the region where the temperature gradient is large. This issue is discussed in detail in chapter 7 for a numerical study of LPI using hydrodynamic equations.

CHAPTER 3

Numerical Formulation

3.1 Introduction

The numerical methods for solving the governing equations described in chapter 2 are presented in this chapter. Although the numerical methods are applicable for a general set of hyperbolic PDEs with source term, in this research we only focus on the multi-fluid equations and the 2T model for partially and fully ionized plasma describe in sections 2.2 and 2.4, respectively. The procedure for solving the MHD equations in section 2.3 can be performed with the same numerical approach. The relation between the solutions of the multi-fluid and MHD equation will be discussed later in this chapter.

3.2 Numerical methods

3.2.1 Finite volume methods

In the absence of viscous effects, the full set of governing equations can be written in the form of a hyperbolic system of PDEs with a source term vector:

$$\partial_t \mathbf{Q} + \nabla \cdot \overline{\overline{\mathbf{F}}} = \dot{\mathbf{\Omega}} \quad (3.1)$$

where \mathbf{Q} is the vector of conservative variables, $\overline{\overline{\mathbf{F}}}$ is the inviscid flux tensor, and $\dot{\mathbf{\Omega}}$ is the source term vector due to exchange processes and/or coupling forces. The diffusive term, i.e., electron heat conduction, can also be included in equation (3.1) using an expression of a diffusive flux tensor. This term is described separately

in section 3.2.6. For the fluid equations, $\mathbf{Q} = [\rho_s, \rho u_x, \rho u_y, \rho u_z, E, S_e]^T$, and for Maxwell's equations, $\mathbf{Q} = [E_x, E_y, E_z, B_x, B_y, B_z]^T$.

In this research framework, a finite volume method is developed to solve both of these equations, using a similar discretization procedure. For the sake of generality, the numerical methods are presented using the general form of the PDEs. Specific details regarding a particular set of equations will be mentioned where appropriate.

Equation (3.1) is solved using an operator splitting technique, where the changes in the conservative variables for each process are evaluated independently within a time step, and accumulated independently at the end of each time step. For example, at each time step n , the solution of the next time step $n + 1$ is computed as follows:

$$\Delta \mathbf{Q}_{\text{conv}} = \mathcal{L}_{\text{conv}}^{\Delta t} (\mathbf{Q}^n) - \mathbf{Q}^n \quad (3.2)$$

$$\Delta \mathbf{Q}_{\text{diff}} = \mathcal{L}_{\text{diff}}^{\Delta t} (\mathbf{Q}^n) - \mathbf{Q}^n \quad (3.3)$$

$$\Delta \mathbf{Q}_{\text{source}} = \mathcal{L}_{\text{source}}^{\Delta t} (\mathbf{Q}^n) - \mathbf{Q}^n \quad (3.4)$$

$$\mathbf{Q}^{n+1} = \mathbf{Q}^n + \Delta \mathbf{Q}_{\text{conv}} + \Delta \mathbf{Q}_{\text{diff}} + \Delta \mathbf{Q}_{\text{source}} \quad (3.5)$$

where $\mathcal{L}_{\text{conv}}$, $\mathcal{L}_{\text{diff}}$, $\mathcal{L}_{\text{source}}$ are the convective, diffusive, and source term operators, respectively, which advance the solution forward in time (so-called “propagators”).

The splitting scheme described above is a first order splitting scheme of $\mathcal{O}(\Delta t)$. High-order splitting schemes such as Strang splitting [62] can also be employed. For a convective-diffusive-reactive system, the splitting is as follows:

$$\mathbf{Q}^{n+1} = \mathcal{L}_{\text{source}}^{\Delta t/2} \mathcal{L}_{\text{diff}}^{\Delta t/2} \mathcal{L}_{\text{conv}}^{\Delta t} \mathcal{L}_{\text{diff}}^{\Delta t/2} \mathcal{L}_{\text{source}}^{\Delta t/2} (\mathbf{Q}) \quad (3.6)$$

where the splitting error is $\mathcal{O}(\Delta t^2)$. In the current research, only the first order splitting scheme is employed. The reason is due to its simplicity in implementation. Also, the source terms of these equations are very stiff, e.g.,

CR kinetics, which results in a small time scale restriction¹. Since local time-stepping is not used, all the operators are marched at the smallest time step introduced by these operators, making the splitting error of $\mathcal{O}(\Delta t_{\min})$ where $\Delta t_{\min} = \min(\Delta t_{\text{conv}}, \Delta t_{\text{diff}}, \Delta t_{\text{source}})$. A detailed analysis of high-order schemes and error estimate for time operator splitting approach can be found in the work of Duarte *et al.* [63].

The integral form of the governing equations suitable for finite-volume formulation can be obtained by integrating equation (3.1) over the control volume and using Gauss's law for the divergence of the flux.

$$\frac{d\mathbf{Q}}{dt} + \frac{1}{V} \sum_s \mathbf{F}_s A_s = \dot{\mathbf{\Omega}} \quad (3.7)$$

where \mathbf{F}_s is the numerical flux computed at each face and A_s is its surface area. Note that in equation (3.7), \mathbf{Q} and $\dot{\mathbf{\Omega}}$ denote volume averaged quantities. For the case of the Euler terms, the fluxes are computed by solving a Riemann problem at each face of the control volume.

3.2.2 Hyperbolic solvers - Approximated Riemann solvers

3.2.2.1 Semi-discrete approach

For simplicity, consider now a hyperbolic system of PDEs in one-dimensional of the form:

$$\partial_t \mathbf{Q} + \partial_x \mathbf{F}(\mathbf{Q}) = 0 \quad (3.8)$$

where the domain is discretized into a uniform grid with constant spacing Δx . The system (3.8) is classified as a hyperbolic system if the eigenvalues of the flux Jacobian, $\frac{\partial \mathbf{F}}{\partial \mathbf{Q}}$, are real, which is the case for the Euler equations and Maxwell's equations. Utilizing the standard finite volume approximation similar to equation

¹Even when implicit time integration is employed, accuracy constraint still introduces time step restriction.

(3.7), the spatial derivative in equation (3.8) is replaced by the expression of a numerical flux, yielding the following expression:

$$\frac{d\mathbf{Q}_i}{dt} = -\frac{1}{\Delta x} (\mathbf{F}_{i+1/2} - \mathbf{F}_{i-1/2}) \quad (3.9)$$

where $i \pm 1/2$ denote the left and right faces of cell i .

Equation (3.9) is known as the semi-discrete form of (3.8), where only the spatial terms had been discretized [64]. This approach converts the original system of PDEs to a coupled system of ordinary differential equations (ODEs). The advantage of the semi-discrete approach is that any time integration method can be utilized to solve equation (3.9), once the fluxes had been computed. In the current work, a third-order total variation diminishing (TVD) Runge-Kutta (RK) time integration is utilized. The resultant scheme is referred to as RK3:

$$\mathbf{Q}^{n+1/3} = \mathbf{Q}^n + \Delta t \mathcal{F}(\mathbf{Q}^n) \quad (3.10)$$

$$\mathbf{Q}^{n+2/3} = \frac{3}{4}\mathbf{Q}^n + \frac{1}{4}(\mathbf{Q}^{n+1/3} + \Delta t \mathcal{F}(\mathbf{Q}^{n+1/3})) \quad (3.11)$$

$$\mathbf{Q}^{n+1} = \frac{1}{3}\mathbf{Q}^n + \frac{2}{3}(\mathbf{Q}^{n+2/3} + \Delta t \mathcal{F}(\mathbf{Q}^{n+2/3})) \quad (3.12)$$

where $\mathcal{F}(\mathbf{Q})$ is now referred to the RHS of equation (3.9). Since RK3 is an explicit method, the time step must satisfy the Courant-Friedrichs-Lewy (CFL) condition:

$$\left[\max_i |\lambda_i^{\max}| \right] \frac{\Delta t}{\Delta x v} \leq 1 \quad (3.13)$$

where v is the CFL number, and λ_i^{\max} is the maximum eigenvalues of the flux Jacobian. In the case of Euler equations, $\lambda_i^{\max} = [|\mathbf{u}| + a]_i$ where a is the speed of sound. For Maxwell's equations, $\lambda_i^{\max} = c = 3 \times 10^8$.

3.2.2.2 Approximate Riemann solvers

In order to compute the flux term in equation (3.9), a Riemann problem needs to be solved at each face from the given left and right states. The exact solution of the Riemann problem can be computationally expensive and thus is not practical

for numerical calculation. The numerical framework in this research utilizes an approximate Riemann solver for the solution at the faces, that is, instead of solving (3.8), one can solve:

$$\partial_t \mathbf{Q} + \mathbf{A}(\mathbf{Q}) \partial_x \mathbf{Q} = 0 \quad (3.14)$$

where the flux Jacobian, $\mathbf{A} = \frac{\partial \mathbf{F}}{\partial \mathbf{Q}}$, is replaced by a constant matrix $\tilde{\mathbf{A}}$, which is determined from the left and right states of each face, i.e., $\tilde{\mathbf{A}} = \tilde{\mathbf{A}}(\mathbf{Q}^L, \mathbf{Q}^R)$.

The validity of the linearization process requires that the Jacobian \mathbf{A} be diagonalizable with real eigenvalues, i.e., $\mathbf{A} = \mathbf{R}\mathbf{\Lambda}\mathbf{L}$. The left and the right eigenvectors can be used to project equation (3.14) from the physical to characteristic space.

$$\frac{\partial(\mathbf{LQ})}{\partial t} + \mathbf{\Lambda} \frac{\partial(\mathbf{LQ})}{\partial x} = 0 \quad (3.15)$$

By introducing the characteristic variable $\mathbf{W} = \mathbf{LQ}$, equation (3.15) now becomes:

$$\frac{\partial \mathbf{W}}{\partial t} + \mathbf{\Lambda} \frac{\partial \mathbf{W}}{\partial x} = 0 \quad (3.16)$$

The original system of PDEs now has been linearized and decoupled from the original system resulting in a linear system of scalar hyperbolic PDEs. For the Euler equations, the linearization is carried out using Roe-averaging procedures:

$$\tilde{\rho} = \sqrt{\rho^L \rho^R} \quad (3.17)$$

$$\tilde{\mathbf{u}} = \frac{\sqrt{\rho^L} \mathbf{u}^L + \sqrt{\rho^R} \mathbf{u}^R}{\sqrt{\rho^L} + \sqrt{\rho^R}} \quad (3.18)$$

$$\tilde{h} = \frac{\sqrt{\rho^L} h^L + \sqrt{\rho^R} h^R}{\sqrt{\rho^L} + \sqrt{\rho^R}} \quad (3.19)$$

$$\tilde{s}_e = \frac{\sqrt{\rho^L} \hat{s}_e^L + \sqrt{\rho^R} \hat{s}_e^R}{\sqrt{\rho^L} + \sqrt{\rho^R}} \quad (3.20)$$

For Maxwell's equations, an arithmetic average of the field values is sufficient:

$$\tilde{\mathbf{E}} = \frac{\mathbf{E}^L + \mathbf{E}^R}{2} \quad (3.21)$$

$$\tilde{\mathbf{B}} = \frac{\mathbf{B}^L + \mathbf{B}^R}{2} \quad (3.22)$$

The eigensystems of both Euler and Maxwell's equations are given in appendix A.

The interface fluxes are solved by employing the Harten, Lax, vanLeer and Einfeldt (HLLE) Riemann solver [65], which is given as

$$\mathbf{f}_{i+1/2}^{\text{HLLE}} = \frac{b^+ \mathbf{f}_{i+1/2}^R - b^- \mathbf{f}_{i+1/2}^L}{b^+ - b^-} + \frac{b^+ b^-}{b^+ - b^-} \Delta \mathbf{W}_{j+1/2} \quad (3.23)$$

where

$$b^+ = \max(0, \tilde{u}_n + \tilde{a}, u_n^R + a^R) \quad (3.24)$$

$$b^- = \min(0, \tilde{u}_n - \tilde{a}, u_n^L - a^L) \quad (3.25)$$

where u_n denote the velocity normal to the face. It must be noted that the fluxes in equation (3.23) are expressed in characteristic form, i.e., $\mathbf{f}_{i+1/2} = \tilde{\mathbf{L}} \mathbf{F}_{i+1/2}$.

3.2.3 High-order reconstruction

3.2.3.1 Monitonicity-Preserving schemes

In order to achieve high-order spatial accuracy, a fifth-order Monotonicity-Preserving (MP5) scheme [66] is used for the reconstruction of the interface values. For non-linear equations, the reconstruction is performed on characteristic variables with the help of the eigenvectors. For a one dimensional stencil, the reconstructed value of the left and right states of interface $i + \frac{1}{2}$ is given as (see figure 3.1)

$$w_{i+\frac{1}{2}}^L = \frac{1}{60} (2w_{i-2} - 13w_{i-1} + 47w_i + 27w_{i+1} - 3w_{i+2}) \quad (3.26a)$$

$$w_{i+\frac{1}{2}}^R = \frac{1}{60} (2w_{i+3} - 13w_{i+2} + 47w_{i+1} + 27w_i - 3w_{i-1}) \quad (3.26b)$$

The reconstructed values are then limited to avoid instability.

$$w_{i+\frac{1}{2}}^L \leftarrow \text{median} \left(w_{i+\frac{1}{2}}^L, w_i, w_{\text{MP}} \right) \quad (3.27)$$

where

$$w_{\text{MP}} = w_i + \text{minmod} [w_{i+1} - w_i, \alpha (w_i - w_{i-1})] \quad (3.28)$$

with $\alpha = 2$. The minmod and median functions are defined as follows:

$$\text{minmod}(x, y) = \begin{cases} \text{sgn}(x) \min(|x|, |y|) & \text{if } xy > 0 \\ 0 & \text{otherwise} \end{cases} \quad (3.29)$$

$$\begin{aligned} \text{median}(x, y, z) &= x + \text{minmod}(y - x, z - x) \\ &= y + \text{minmod}(x - y, z - y) \\ &= x + \frac{1}{2} [\text{sgn}(y - x) + \text{sgn}(z - x)] \min(|y - x|, |z - x|) \end{aligned} \quad (3.30)$$

where $\text{sgn}(z)$ is the sign function.

The CFL condition of MP schemes depends on the value of α . In addition, the original MP5 scheme of Suresh and Huynh [66] also contains an additional accuracy-preserving constraint to avoid the loss of accuracy near the shock. The detail of the constraint procedure is discussed in their paper and will not be repeated here.

Another variant of the original MP5 scheme is a third order monotonicity-preserving (MP) scheme, known as MP3, which utilize a three point stencil [32]. The MP3 reconstruction starts with a parabolic interpolation:

$$w_{i+\frac{1}{2}}^L = \frac{1}{6} (2w_{i-1} + 5w_i - w_{i+1}) \quad (3.31)$$

$$w_{i+\frac{1}{2}}^R = \frac{1}{6} (2w_{i+2} + 5w_{i+1} - w_i) \quad (3.32)$$

The MP limiter in (3.27) and (3.28) is then applied to avoid instability in the solution containing discontinuity. The MP schemes have been determined to hold some CFL restriction based on the value of α . It is recommended to use a CFL number close to $1/(1 + \alpha)$ for a stable solution.

3.2.3.2 Weighted essentially non-oscillatory schemes

Weighted essentially non-oscillatory (WENO) schemes, developed by Liu *et al.* [67] and Jiang and Shu [68] are based on the essentially non-oscillatory (ENO)

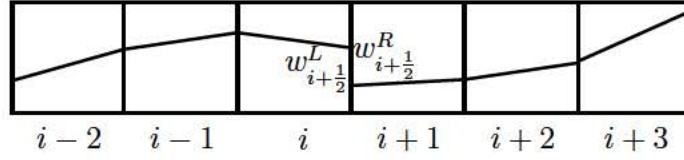


Figure 3.1: Schematic of computational stencil for MP5 and WENO schemes with left and right states of an interface.

schemes developed by Harten *et al.* [69] in the form of cell-averages. In WENO reconstruction, an adaptive-stencil approach is utilized, and the reconstructed values is a convex combination of all the stencils. The WENO schemes preserve the essentially non-oscillatory property of the original ENO scheme, but also improves the order of accuracy in the smooth part of the flow solution. A fifth-order scheme is implemented in the current work. For a one dimensional stencil similar to the one in figure 3.1, the reconstructed value of the left state of interface $i + 1/2$ is written as a weighted summation of three smaller stencils:

$$w_{i+1/2}^L = \omega_1 w^{(1)} + \omega_2 w^{(2)} + \omega_3 w^{(3)} \quad (3.33)$$

The three stencil values are:

$$w^{(1)} = \frac{1}{3}w_{i-2} + \frac{7}{6}w_{i-1} + \frac{11}{6}w_i \quad (3.34)$$

$$w^{(2)} = -\frac{1}{6}w_{i-1} + \frac{5}{6}w_i + \frac{1}{3}w_{i+1} \quad (3.35)$$

$$w^{(3)} = \frac{1}{3}w_i + \frac{5}{6}w_{i+1} - \frac{1}{6}w_{i+2} \quad (3.36)$$

$$(3.37)$$

and the non-linear weight are designed to adapted to the smoothness of the stencil.

For a discontinuous stencil, the non-linear weight is reduced to zero:

$$\omega_i = \frac{\chi_i}{\sum_{n=1}^3 \chi_n} \quad (3.38)$$

$$\chi_i = \frac{C_i^r}{IS_i + \epsilon} \quad (3.39)$$

where $\epsilon = 10^{-7} - 10^{-5}$ is a small number to avoid division by zero. C_i^r is known as the optimal weight, given by:

$$C_1^r = \frac{1}{10} \quad (3.40)$$

$$C_2^r = \frac{6}{10} \quad (3.41)$$

$$C_3^r = \frac{3}{10} \quad (3.42)$$

and the smoothness indicator IS are:

$$IS_1 = \frac{13}{12} (w_{i-2} - 2w_{i-1} + w_i)^2 + \frac{1}{4} (w_{i-2} - 4w_{i-1} + 3w_i)^2 \quad (3.43)$$

$$IS_2 = \frac{13}{12} (w_{i-1} - 2w_i + w_{i+1})^2 + \frac{1}{4} (w_{i-1} - w_{i+1})^2 \quad (3.44)$$

$$IS_3 = \frac{13}{12} (w_i - 2w_{i+1} + w_{i+2})^2 + \frac{1}{4} (3w_i - 4w_{i+1} + w_{i+2})^2 \quad (3.45)$$

The reconstructed value of the right state can be found easily by symmetry. The stability of both MP and WENO is enhanced by RK3 time integration, yielding a fifth-order spatial accuracy (third order in the case of MP3).

3.2.4 Hyperbolic solvers - Implicit time marching

It was mentioned previously that the solution of the multi-fluid equations contains several time scales, which can be of different orders of magnitude. This is certainly the case for the electron due to the small mass ratio compared to the heavy species. The CFL time step restriction for the electrons is much more severe compared to the heavy species. It is therefore advantageous to be able to solve the electron fluid equation implicitly. A similar argument applies to the case of electromagnetic wave propagation in the Maxwell's equations. In this section, an implicit time stepping scheme is described within the finite volume approximation.

Consider now the discretized equation of (3.8):

$$\frac{\Delta \mathbf{Q}_i^n}{\Delta t} = \frac{1}{\Delta x} (\mathbf{F}_{i-1/2} - \mathbf{F}_{i+1/2}) \quad (3.46)$$

where $\Delta \mathbf{Q}_i^n = \mathbf{Q}_i^{n+1} - \mathbf{Q}_i^n$. In the explicit scheme, the RHS of equation (3.46) is evaluated at the current time step n . Let us define \mathcal{F}_i to be the explicit flux terms:

$$\mathcal{F}_i = \frac{\Delta t}{\Delta x} (\mathbf{F}_{i-1/2}^n - \mathbf{F}_{i+1/2}^n) \quad (3.47)$$

In order to facilitate an implicit time-stepping scheme, the numerical fluxes in equation (3.46) need to be evaluated at time level $n + \theta$. This can be done through the linearization approximation:

$$\mathbf{F}_{i\pm 1/2}^{n+\theta} = \mathbf{F}_{i\pm 1/2}^n + \theta \mathbf{A}(\mathbf{Q})(\Delta \mathbf{Q})_{i\pm 1/2} \quad (3.48)$$

The Jacobian can be split based on the sign of the eigenvalues, i.e., $\mathbf{A} = \mathbf{R}(\mathbf{\Lambda}^+ + \mathbf{\Lambda}^-)\mathbf{L} = \mathbf{A}^+ + \mathbf{A}^-$, where $\mathbf{\Lambda}^+$ contains all the positive eigenvalues and $\mathbf{\Lambda}^-$ contains all the negative ones. The flux linearization can be written as:

$$\mathbf{F}_{i+1/2}^{n+\theta} = \mathbf{F}_{i+1/2}^n + \theta \mathbf{A}_{i+1/2}^+(\Delta \mathbf{Q})_i + \theta \mathbf{A}_{i+1/2}^-(\Delta \mathbf{Q})_{i+1} \quad (3.49)$$

Similarly,

$$\mathbf{F}_{i-1/2}^{n+\theta} = \mathbf{F}_{i-1/2}^n + \theta \mathbf{A}_{i-1/2}^+(\Delta \mathbf{Q})_{i-1} + \theta \mathbf{A}_{i-1/2}^-(\Delta \mathbf{Q})_i \quad (3.50)$$

The discretized version of equation (3.46) becomes:

$$\begin{aligned} \left[-\eta \mathbf{A}_{i-1/2}^+ \right] \Delta \mathbf{Q}_{i-1} + \left[1 + \eta \mathbf{A}_{i+1/2}^+ - \eta \mathbf{A}_{i-1/2}^- \right] \Delta \mathbf{Q}_i \\ + \left[\eta \mathbf{A}_{i+1/2}^- \right] \Delta \mathbf{Q}_{i+1} = \mathcal{F}_i \end{aligned} \quad (3.51)$$

where $\eta = \frac{\theta \Delta t}{\Delta x}$. For stability, the LHS of (3.51) is reverted to first order approximation, the fully implicit system now can be written as:

$$\left[-\eta \mathbf{A}_{i-1}^+ \right] \Delta \mathbf{Q}_{i-1} + \left[1 + \eta \mathbf{A}_i^+ - \eta \mathbf{A}_i^- \right] \Delta \mathbf{Q}_i + \left[\eta \mathbf{A}_{i+1}^- \right] \Delta \mathbf{Q}_{i+1} = \mathcal{F}_i \quad (3.52)$$

It must be noted that for $\theta = 1/2$, the resultant scheme is the same as the Crank-Nicolson method. For $\theta = 1$, the scheme is the backward Euler method. System (3.52) is a block tridiagonal system with block size N , where N is the number of

conservative variables. Standard techniques like Gaussian elimination and back substitution can be applied to solve this system of equations. This is referred as the Thomas Block-Tridiagonal algorithm.

A similar approach can be used for 2-D equations, leading to a penta-diagonal system of $N \times N$ block matrices. The cost of inverting the matrix in that case is very large, and for the 3D case, directly inverting a septa-diagonal system is completely prohibitive. Another approach, which consumes less memory, and has a lower number of operations, is via the dimensional splitting technique, that is, a block-tridiagonal system is solved for each direction, and the change in the conservative variables can be successively refined by an iterative procedure. Detail of such an approach is discussed in [70]. It must be pointed out that since most of the problems considered in this work are highly transient, an iterative solution of equation (3.52) does not give any advantage over the Thomas algorithm.

3.2.5 Source term treatment

The source term is solved using a point-implicit solver. In general, we seek the solution of a system of ODEs written in the form:

$$\frac{d\mathbf{Q}}{dt} = \dot{\mathbf{\Omega}} \quad (3.53)$$

where \mathbf{Q} is the state variables, and \mathbf{S} is the source term vectors due to the kinetics or coupling terms with the electromagnetic forces, i.e., Lorentz force and Joule heating terms. For the CR kinetics, the system of ODEs is very stiff due to the multitude of the kinetics time scales involved in the a wide range of physical processes. An implicit time integration method is required to ensure the stability of the solution. The implicit formulation of the system can be obtained by expanding the source term vector via a Taylor series expansion about the current time step n .

$$\frac{d\mathbf{Q}^n}{dt} = \dot{\mathbf{\Omega}}^n + \frac{\partial \dot{\mathbf{\Omega}}^n}{\partial t} \Delta t \quad (3.54)$$

By using the chain rule on the time derivative of the source term vector, one can find

$$\frac{d\mathbf{Q}^n}{dt} = \dot{\mathbf{\Omega}}^n + \mathbf{J} \frac{d\mathbf{Q}^n}{dt} \Delta t \quad (3.55)$$

where \mathbf{J} is the Jacobian matrix written as:

$$\mathbf{J} = \frac{\partial \dot{\mathbf{\Omega}}}{\partial \mathbf{Q}} \quad (3.56)$$

By simple algebraic manipulation, one can obtain:

$$\Delta \mathbf{Q}^n = \Delta t (\mathbf{I} - \Delta t \mathbf{J})^{-1} \dot{\mathbf{\Omega}}^n \quad (3.57)$$

The solution of equation (3.57) gives the total change of the conservative variables due to the source term vector. Since the system is integrated implicitly, there is no restriction on the time step. The time step in this case is only restricted for accuracy purpose, i.e., for CR kinetics, the time step is limited by controlling the rate of change in the state population. For the electromagnetic coupling term in the two-fluid equation, the time step is set relative to the electron plasma frequency and the gyro-frequency.

As a linear system of equations, equation (3.57) can be solved using a variety of numerical methods. In the current work, a direct Gaussian elimination procedure is utilized to invert the system. It must be pointed out that the computational cost of the Gaussian elimination procedure scales as N^3 where N is the number of variables. For a large/detailed kinetics mechanism, i.e., many states, solving the system at every cell is clearly a computationally intensive task. For most of the simulations carried out in this dissertation, N is sufficiently small so that Gaussian elimination is the optimal choice.

3.2.6 Diffusive transport

A numerical method for solving the diffusive transport is described in this section. The method is used to solve the electron heat conduction equation. When

the plasma ionization fraction is sufficient, the electron heat conduction process can be very rapid, which suggests an implicit time marching scheme for stability requirement. Let us consider the heat conduction equation in 1d:

$$\begin{aligned}\partial_t E &= -\partial_x q \\ &= \partial_x (\kappa \partial_x T)\end{aligned}\tag{3.58}$$

where q is the heat flux, E is the energy and κ is the thermal conductivity. Using a finite volume approximation, the discretized form of equation (3.58) can be written as:

$$\Delta E_i^n = \frac{\Delta t}{\Delta x} (F_{i+1/2}^\kappa - F_{i-1/2}^\kappa)\tag{3.59}$$

where F^κ denotes the diffusive flux ($F^\kappa = -q$):

$$F_{i+1/2}^\kappa = \kappa_{i+1/2} f_{i+1/2}\tag{3.60}$$

$$f_{i+1/2} = \frac{1}{\Delta x} (T_{i+1} - T_i)\tag{3.61}$$

For the transport properties at the face, one can use a simple arithmetic average, i.e., $\kappa_{i+1/2} = \frac{\kappa_i + \kappa_{i+1}}{2}$. Let us now define the integrated diffusive flux, i.e., the RHS of equation (3.59) evaluated at the current time n , to be \mathcal{F}_i^κ , such that for an explicit time integration, one simple have $\Delta E_i = \mathcal{F}_i^\kappa$. For an implicit scheme, the fluxes can be linearized about the current time step n as follows:

$$F_{i\pm 1/2}^{\kappa, n+\theta} = F_{i\pm 1/2}^{\kappa, n} + \theta \delta F_{i\pm 1/2}^\kappa\tag{3.62}$$

where

$$\delta F_{i+1/2}^\kappa = \frac{\Delta E_i}{\rho_i c_{v,i}} \frac{\partial F_{i+1/2}^\kappa}{\partial T_i} + \frac{\Delta E_{i+1}}{\rho_{i+1} c_{v,i+1}} \frac{\partial F_{i+1/2}^\kappa}{\partial T_{i+1}}\tag{3.63}$$

Note that we have used chain rule to relate the energy derivatives to the temperature derivatives. From equation (3.60), one also has:

$$\frac{\partial F_{i+1/2}^\kappa}{\partial T_i} = -\frac{\kappa_{i+1/2}}{\Delta x} + \frac{\partial \kappa_i}{\partial T} \frac{f_{i+1/2}}{2}\tag{3.64}$$

$$\frac{\partial F_{i+1/2}^\kappa}{\partial T_{i+1}} = \frac{\kappa_{i+1/2}}{\Delta x} + \frac{\partial \kappa_{i+1}}{\partial T} \frac{f_{i+1/2}}{2}\tag{3.65}$$

The expression for $\delta F_{i-1/2}^\kappa$ can be found similarly. This leads to:

$$\begin{aligned} \Delta E_i = \mathcal{F}_i^\kappa + \frac{\theta \Delta t}{\Delta x} \left\{ \Delta E_i \frac{1}{\rho_i c_{v,i}} \left[-\frac{\kappa_{i+1/2}}{\Delta x} + \frac{1}{2} \frac{\partial \kappa_i}{\partial T} f_{i+1/2} \right] \right. \\ + \Delta E_{i+1} \frac{1}{\rho_{i+1} c_{v,i+1}} \left[\frac{\kappa_{i+1/2}}{\Delta x} + \frac{1}{2} \frac{\partial \kappa_{i+1}}{\partial T} f_{i+1/2} \right] \\ - \Delta E_{i-1} \frac{1}{\rho_{i-1} c_{v,i-1}} \left[-\frac{\kappa_{i-1/2}}{\Delta x} + \frac{1}{2} \frac{\partial \kappa_{i-1}}{\partial T} f_{i-1/2} \right] \\ \left. - \Delta E_i \frac{1}{\rho_i c_{v,i}} \left[\frac{\kappa_{i-1/2}}{\Delta x} + \frac{1}{2} \frac{\partial \kappa_i}{\partial T} f_{i-1/2} \right] \right\} \quad (3.66) \end{aligned}$$

The resultant system of equation is as follows:

$$A \Delta E_{i-1} + B \Delta E_i + C \Delta E_{i+1} = \mathcal{F}_i^\kappa \quad (3.67)$$

where

$$A = \frac{\eta}{\rho_{i-1} c_{v,i-1}} \left[-\frac{\kappa_{i-1/2}}{\Delta x} + \frac{1}{2} \frac{\partial \kappa_{i-1}}{\partial T} f_{i-1/2} \right] \quad (3.68)$$

$$B = 1 + \frac{\eta}{\rho_i c_{v,i}} \left[\frac{\kappa_{i+1/2}}{\Delta x} - \frac{1}{2} \frac{\partial \kappa_i}{\partial T} f_{i+1/2} \right] + \frac{\eta}{\rho_i c_{v,i}} \left[\frac{\kappa_{i-1/2}}{\Delta x} + \frac{1}{2} \frac{\partial \kappa_i}{\partial T} f_{i-1/2} \right] \quad (3.69)$$

$$C = \frac{\eta}{\rho_{i+1} c_{v,i+1}} \left[-\frac{\kappa_{i+1/2}}{\Delta x} - \frac{1}{2} \frac{\partial \kappa_{i+1}}{\partial T} f_{i+1/2} \right] \quad (3.70)$$

and $\eta = \frac{\theta \Delta t}{\Delta x}$. Similarly, $\theta = 1$ corresponds to Backward-Euler and $\theta = 1/2$ corresponds to Crank-Nicolson method. The resulting system of equation to be solved at each time step is a tridiagonal system, which can be solved efficiently with a Thomas algorithm. In the case of multi-dimensional diffusion, one can employ the similar approach of dimensional splitting described in the previous section.

3.3 Benchmark problems

In this section, a series of benchmark test cases is presented to validate the numerical method described in section 3.2. Although most of the simulations are limited to one-dimensional and a few two-dimensional test cases, the numerical method

can be easily generalized to three-dimensional, if the computational resource permits. The reason is because the current research puts emphasis on high-fidelity physical models associated with multiple couplings of the plasma, thus imposing a large requirement on the computer resource. As will be shown later, some of these models are not practical for multidimensional calculation, and a complexity reduction strategy must be formulated.

3.3.1 Euler equations

3.3.1.1 Blastwave problem

The first problem presented for the solution of the Euler equations is the Woodward-Colella blast wave problem [71]. This problem is designed to test the capability of the numerical scheme to handle interaction of strong shock waves. The problem is initialized with two strong shocks travelling past each other and reflected from the wall to expedite multiple interactions. The initial condition of the problem for a domain of $x \in (0, 1)$ is given as:

$$[\rho, u_x, p] = \begin{cases} [1, 0, 10^3] & \text{if } x < 0.1 \\ [1, 0, 10^{-3}] & \text{if } 0.1 \leq x \leq 0.8 \\ [1, 0, 10^2] & \text{if } x > 0.8 \end{cases} \quad (3.71)$$

Figure 3.2 shows the numerical solution of the blast wave problem with 600 cells at $t = 0.038$. The reference solution is computed using MP5 scheme with 5,000 cells. As shown in figure 3.2, the contact discontinuity is well-resolved for both MP5 and WENO scheme. The MP5 scheme performs slightly better in resolving the contact. It must be noted that artificial compression method can be used to enhance resolution in the near the discontinuity. Such a method was not applied here since we want the scheme to be robust and free of numerical parameters which are problem-dependent.

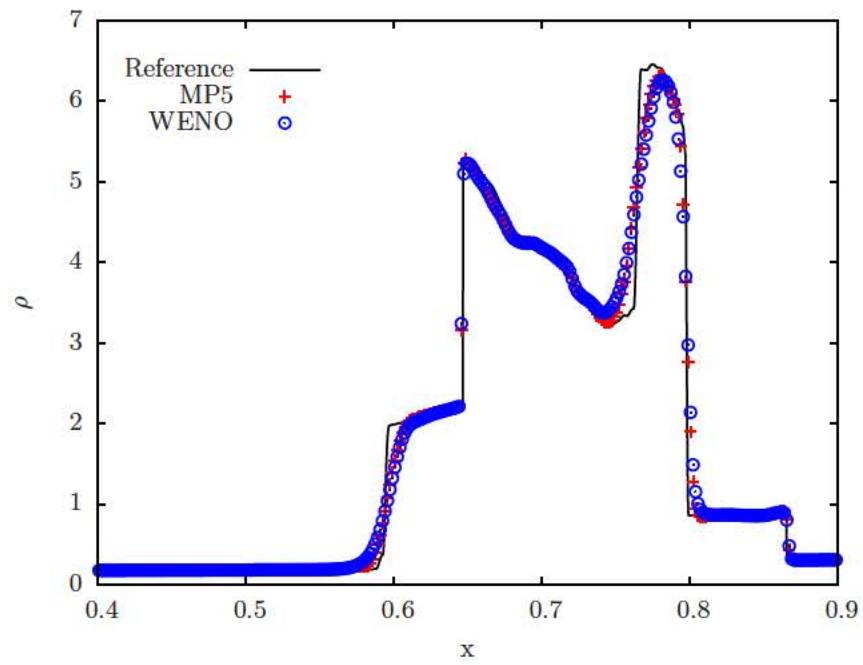


Figure 3.2: Solution of the Woodward-Colella blast wave problem with 600 cells. Only part of the simulated domain is shown to illustrate the difference of two schemes.

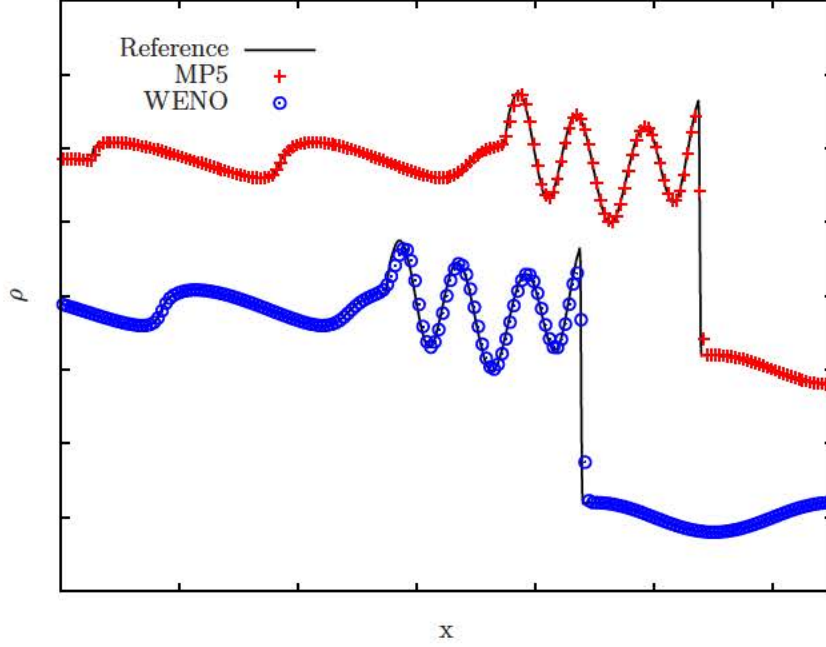


Figure 3.3: Solution of the Shu-Osher problem with 300 cells. Only part of the simulated domain is shown to illustrate the difference of two schemes.

3.3.1.2 Shu-Osher problem

The next test case is the Shu-Osher problem, which models the interaction of a moving shock wave with an entropy disturbance. This problem can be used to test the capability of the scheme to resolve complex flow structure with instability. The initial condition for the problem is given for a domain of $x \in [-1, 1]$ as follows:

$$[\rho, u_x, p] = \begin{cases} [3.857, 2.629, 10.333] & \text{if } x < -0.8 \\ [1 + 0.2 \sin(5\pi x), 0, 1] & \text{if } x \geq -0.8 \end{cases} \quad (3.72)$$

Figures 3.3 shows the density plot of the solution using 300 cells at $t = 0.36$. The reference solution is computed using the MP5 scheme with 1600 cells. The solution obtained with both MP5 and WENO schemes shows that complex flow features such as local maximum and minimum density can be efficiently resolved in high-resolution.

3.3.1.3 Forward step problem

Results of two-dimensional test cases are now presented. From the one-dimensional test cases, we learn that MP5 provides slightly better results than WENO in resolving the discontinuity and entropy waves. However, the CFL restriction of the MP5 scheme is more severe than that of the WENO scheme. Therefore, WENO scheme is slightly at more advantage in terms time step requirement, but the MP5 scheme generally yields better solution. For brevity, only the solution computed using the MP5 scheme is presented.

The first two-dimensional test problem is the forward step problem, also known as the Emery problem, or the Mach-3 wind tunnel problem. The problem consists of uniform flow of Mach-3 past a step. The step and upper part boundaries of the domain is set to be reflective. For the left and the right boundaries, simple extrapolation is sufficient. An interesting feature of this problem is located at the corner of the step. Numerical error generated in this region can create a so-called numerical boundary layer which can affect the structure of the flow. A treatment of this problem was given by Woodward and Colella [72], and is not used here.

Figures 3.4 shows the solution of forward step problem with 600,000 computational cells using the MP5 scheme. The WENO solution of this problem, although not shown here, yields similar results but slightly more diffusive notably in the Kelvin-Helmholtz instability occurring near the top of the domain. This is consistent with the observation from the 1D simulations.

3.3.1.4 Backward step problem

The next test involves a similar problem of a diffraction of a shock wave ($M = 2.4$) down a step [73]. The strong rarefaction at the corner of the step can cause a problem of negative density when performing the reconstruction. The problem is modeled here using 27,000 cells, and the numerical simulation is shown along

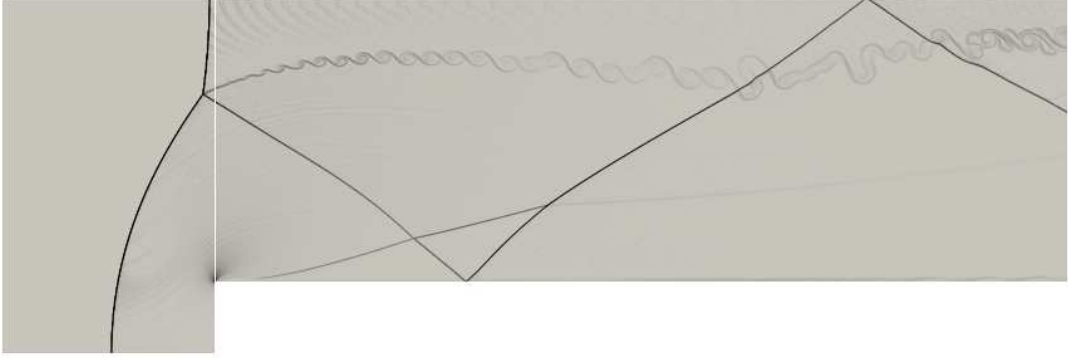


Figure 3.4: Solution of the forward step problem using MP5 scheme with 600,000 cells.

with the experimental images in figure 3.5. The solver was able to reproduce the correct flow features with excellent accuracy.

3.3.1.5 Rayleigh-Taylor instabilities

The Rayleigh-Taylor instability problem [74] is simulated in this section. The problem is described as the acceleration of a heavy fluid into a light fluid driven by gravity. In this test case, the specific heat ratio is set to be a constant ($\gamma = 1.4$). For a rectangular domain of (0.25×1) , the initial conditions are given as follows:

$$\rho = 2, u = 0, v = -0.025 \cos(8\pi x), p = 2y + 1 \text{ for } 0 \leq y \leq \frac{1}{2} \quad (3.73)$$

$$\rho = 1, u = 0, v = -0.025a \cos(8\pi x), p = y + \frac{3}{2} \text{ for } \frac{1}{2} \leq y \leq 1 \quad (3.74)$$

where a is the speed of sound. The top and bottom boundaries are set as reflecting and the left and right boundaries are periodic. As the flow progresses, the shear layer starts to develop and the Kelvin-Helmholtz instabilities become more evident, as can be seen in figure 3.6. A momentum and energy source terms are added to account for the gravitational effects.

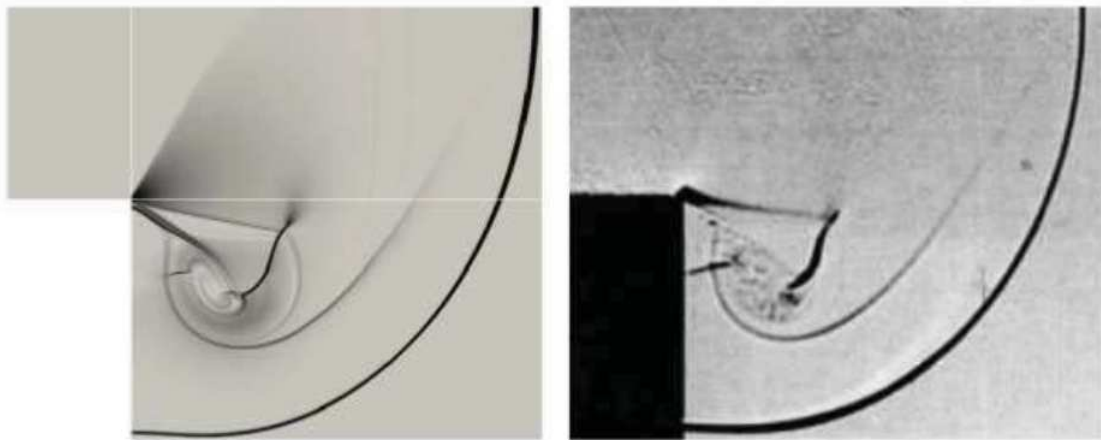


Figure 3.5: Diffraction of a Mach 2.4 shock wave down a step using MP5 scheme with 27,000 cells. Comparison between numerical schlieren (left) and experimental image (right).

3.3.1.6 Two-dimensional detonation

Modeling of a reactive flow field is now considered. A spark-ignited detonation wave both in one- and two-dimension is simulated to demonstrate the capability of the solver. Only the two-dimensional results are shown here. At a well-resolved scale, the detonation wave can be described as a strong shock wave supported by the heat release from a high-temperature flame behind an induction zone. Interesting features have been observed both in the 1-D and 2-D simulations, characterized by the coupling of the fluid dynamics and chemical kinetics. The study of flame-shock coupling dynamics in one-dimension is described in [75].

The evolution of the pressure and temperature of a wall-spark ignited detonation is shown in Figure 3.7. The chemical kinetics is modeled using the reduced H_2 –air mechanism which consists of 9 species gas mixture with 38 reactions. The mechanism used for the simulation is taken from the shock tube study by Jachimowski [76]. The computational domain is rectangular with a length of 20 cm and a height of 2 cm. The grid spacing in both directions is $50\ \mu\text{m}$.

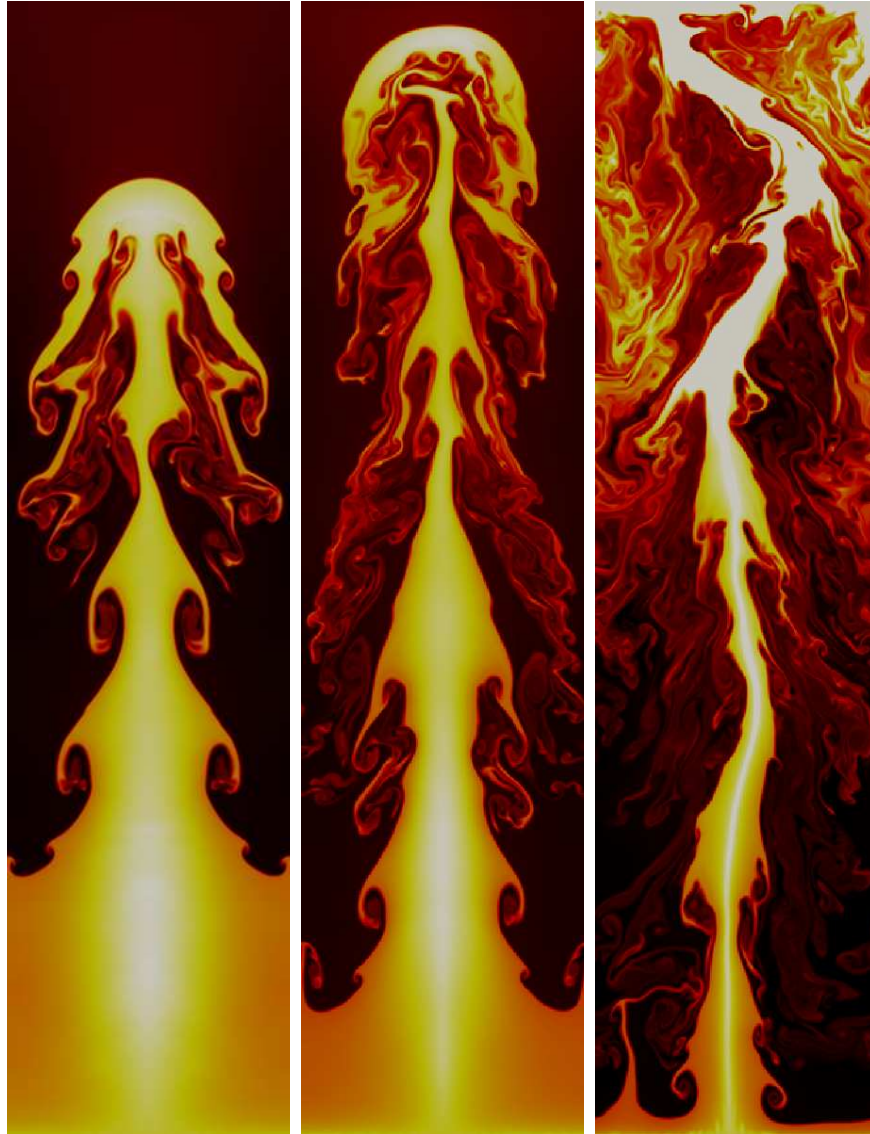


Figure 3.6: Rayleigh-Taylor instability computed with the MP5 scheme using 640,000 cells.

The detonation cells, between the shock and multiple triple points in transverse motion, is clearly seen. Figure 3.8 illustrates the numerical soot film produced by recording the maximum density reached at each computation cell over the entire simulation time which is used to measure the cell structure. This well-known cellular structure has been observed both in experiments and numerical simulations. Various techniques in reproducing these images are discussed by Sharpe and Radulescu [77].

3.3.2 Multi-fluid equations

In this section, several test cases of the multi-fluid equations are described. Before getting into the solution of the full multi-fluid model, the first two test cases model a sheath problem utilizing a simple model for the electron fluids. In these test cases, the electrons are assumed to be in Boltzmann equilibrium with the electrostatic field. At any time, the electron density can be expressed as:

$$n_e = n_0 e^{-(\phi - \phi_0)/kT_e} \quad (3.75)$$

where n_0 is a reference number density value and ϕ_0 is a corresponding reference potential. In this case, we solve a non-linear Poisson equation for the electric field:

$$\nabla^2 \phi = -\frac{e}{\epsilon_0} n_i Z_i + \frac{e}{\epsilon_0} n_0 e^{-(\phi - \phi_0)/kT_e} \quad (3.76)$$

This approximation is used to simulate both a transient and steady-state sheath problem.

3.3.2.1 Transient sheath

For the transient sheath problem, the reference plasma condition is $n_0 = 10^{-14} m^{-3}$, $T_i = 0.025$ eV and $T_e = 1$ eV. This corresponds to an ion plasma frequency, $\omega_{pi} = 2.086 \times 10^{-6}$ rad/sec, and a Debye length $\lambda_D = 74.3$ mm as defined in equation (2.17). The transient sheath problem is computed on 1D domain of

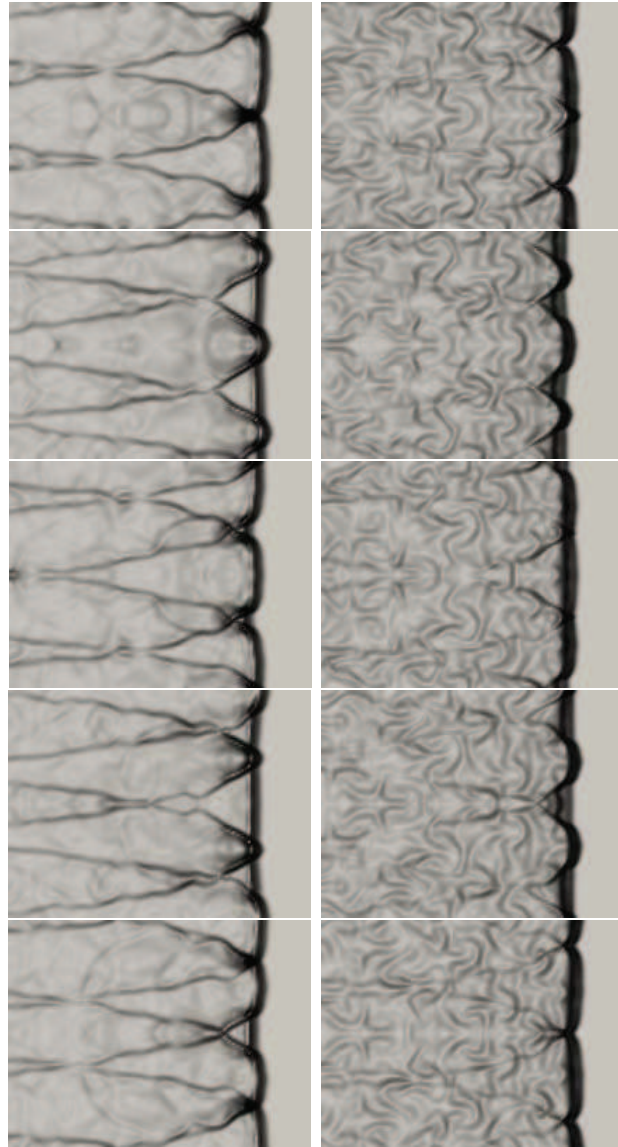


Figure 3.7: Evolution of pressure and temperature in a 2D detonation simulation.

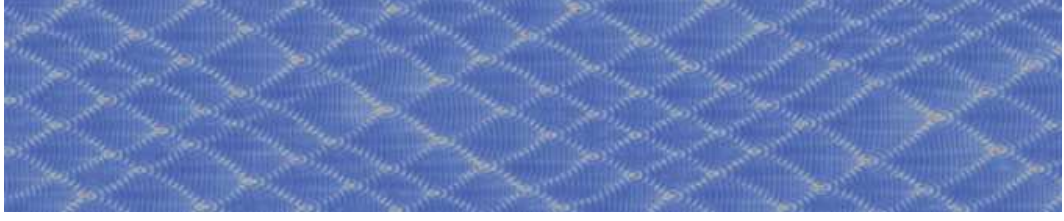


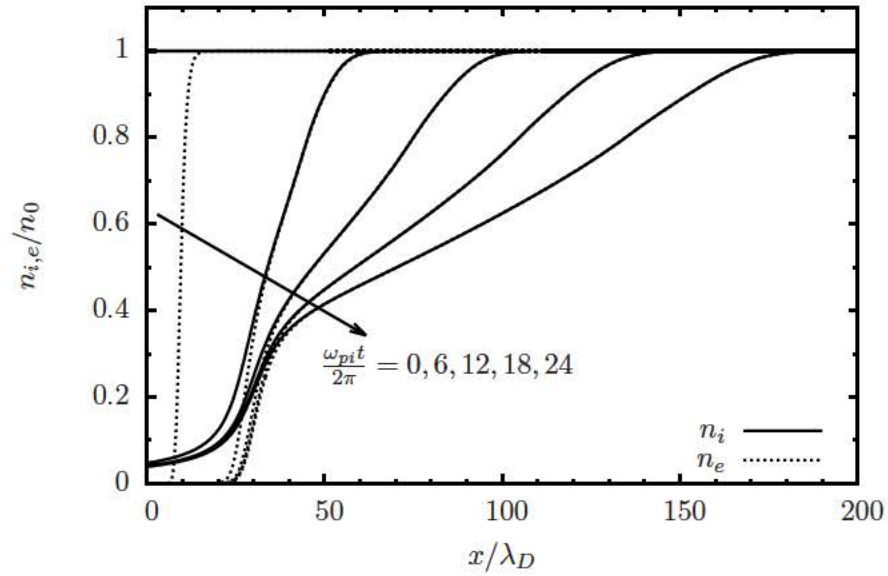
Figure 3.8: Numerical soot film produced by recording the maximum density at each grid cell over the entire simulation for a 2D detonation corresponding to figure 3.7.

$L = 200\lambda_D$. Initially, the domain is filled with ions at rest with number density $n_i = n_0$. At $t = 0$, the electric field is introduced, by setting the electric potential to -50 V at $x = 0$, and 0 V at $x = L$. The electrons are assumed to be in Boltzmann equilibrium. For the ions, the full Euler equations are solved using the WENO scheme. The solution of the electric field is determined from the solution of equation (3.76).

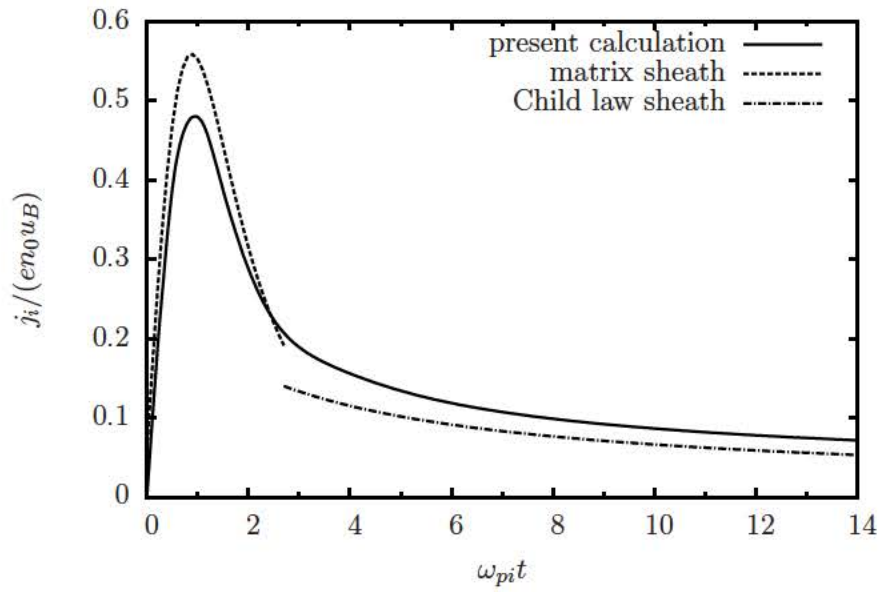
In this simulation, the ion boundary conditions are treated by simple extrapolation. Figure 3.9 shows the profile of the ion and electrons number densities at different instances of time, as well as the time history of the ion current collected at the electrode. The numerical solution of the ion current are compared and in good agreement to the analytical results of Lieberman [78].

3.3.2.2 Steady sheath

The reference plasma condition of the steady sheath is similar to that of the transient sheath simulation. The solution is computed on a 1D domain of $L = 100\lambda_D$. In order to obtain a steady-state sheath, the ion loss to the wall is made up by introducing a ionizing source term $\omega_I = n_e z$ where $z = \frac{n_i u_i|_{x=0}}{\int n_e dx}$. The steady-state is achieved when the ionization rate z has reach a steady value, i.e., the ion loss is exactly balanced by ionizing source and therefore the sheath reaches



(a) Ion and electron number densities



(b) Ion current

Figure 3.9: Number density of the ions at the electron at different time and comparison of the time evolution of the ion current at the electrode with analytical solution of Lieberman [78]. Time is normalized by the ion plasma frequency, and velocity is normalized by the Bohm velocity $u_B = \sqrt{\frac{kT_e}{m_i}}$.

an equilibrium state. In this problem, the electrons are also assumed to be in Boltzmann equilibrium, and the ion fluid equation is solved using WENO scheme. Figure 3.10 shows the spatial profile of the ions number density, velocity and the electric potential at the steady-state condition.

In addition, we also computed a steady-state sheath with a collisional friction force. This acts as a source term on the momentum equation of the ions, which is written as follows:

$$f_i = -\frac{|u_i|}{\lambda_i} \rho_i u_i \quad (3.77)$$

where λ_i is the ion mean-free-path. One also has a corresponding heating term due to the work done by the friction force. Figure 3.11 shows the electric potential as well as the ion velocity with collisional drag term. For the collisional case, the sheath thickness slightly increases, and the ion velocity at the electrode are lower than the collisionless case. This indicates that the ions while moving to the electrode experiences a drag force, resulting in a thicker sheath.

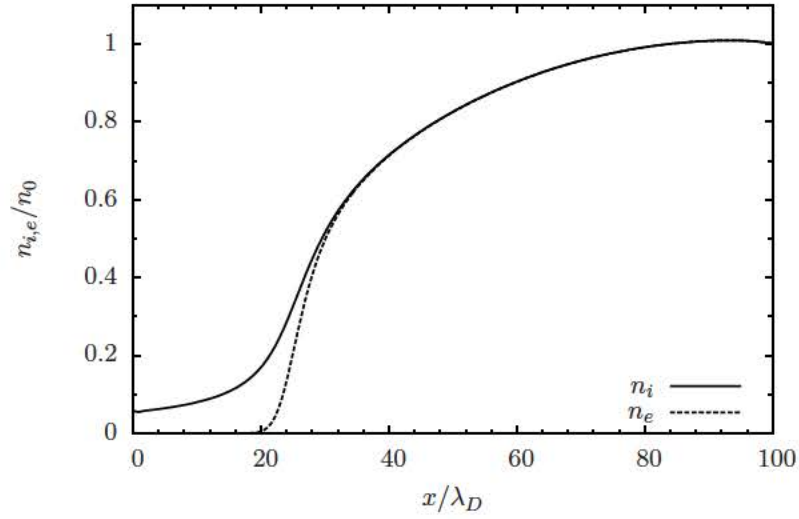
3.3.2.3 Generalized Brio-Wu problem

This is a generalization of the standard Brio-Wu problem often used to benchmark MHD codes. The MHD approximation corresponds to the use of Ohm's law in deriving a steady-state current density, which was derived in section 2.3. In the case of a fully-ionized plasma, Ohn's law can be written as:

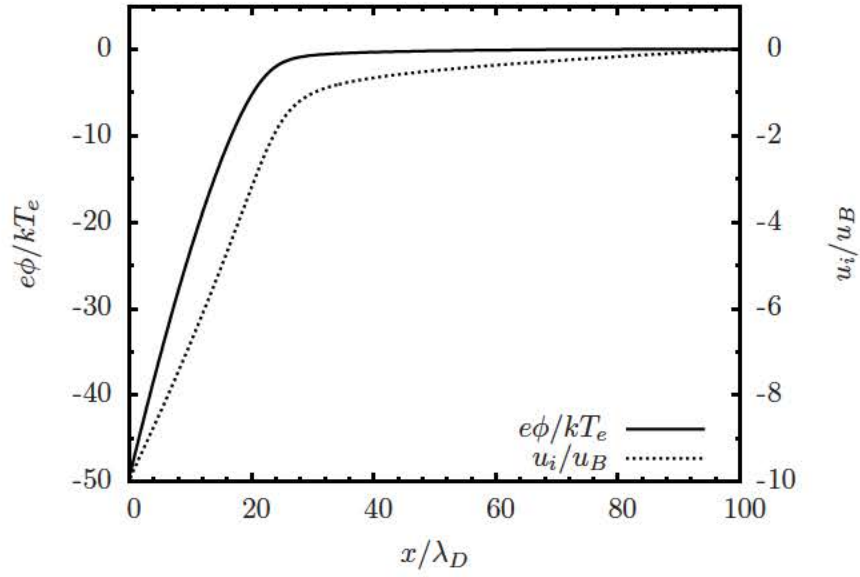
$$\mathbf{E} + \mathbf{u} \times \mathbf{B} = \frac{1}{en_e} (\mathbf{j} \times \mathbf{B} - \nabla p_e + \mathbf{R}_{ei}) \quad (3.78)$$

The ideal MHD limit simply means $\mathbf{E} + \mathbf{u} \times \mathbf{B} \simeq 0$, i.e., all the terms on the RHS are small. One can derive a scaling relation such that ideal MHD condition is satisfied. Following the work of Freidberg [79], the sufficient conditions for ideal MHD are (1) small Larmor radius, and (2) weak collisionality². The Larmor radii

²The collisionality should be weak enough for diffusion to be neglected but still strong enough to satisfy hydrodynamic theory.

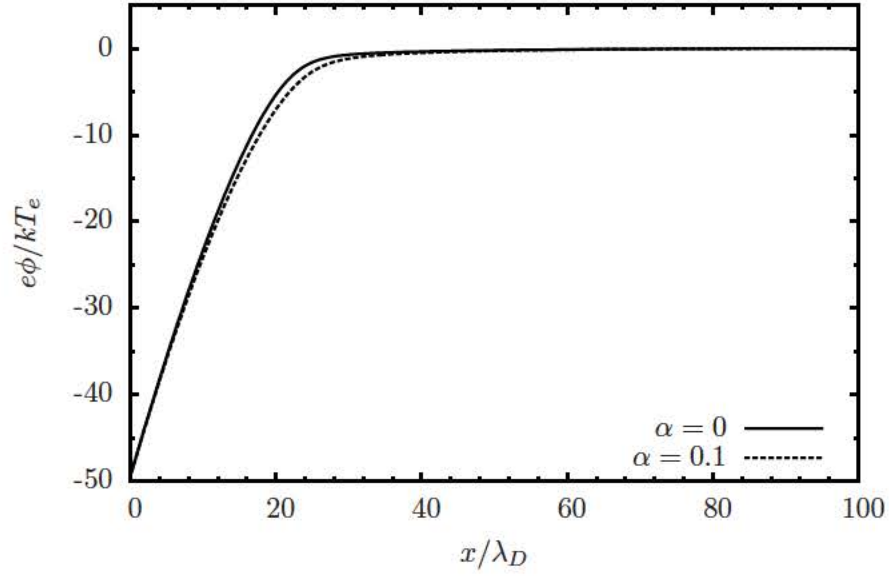


(a) Ion and electron number densities

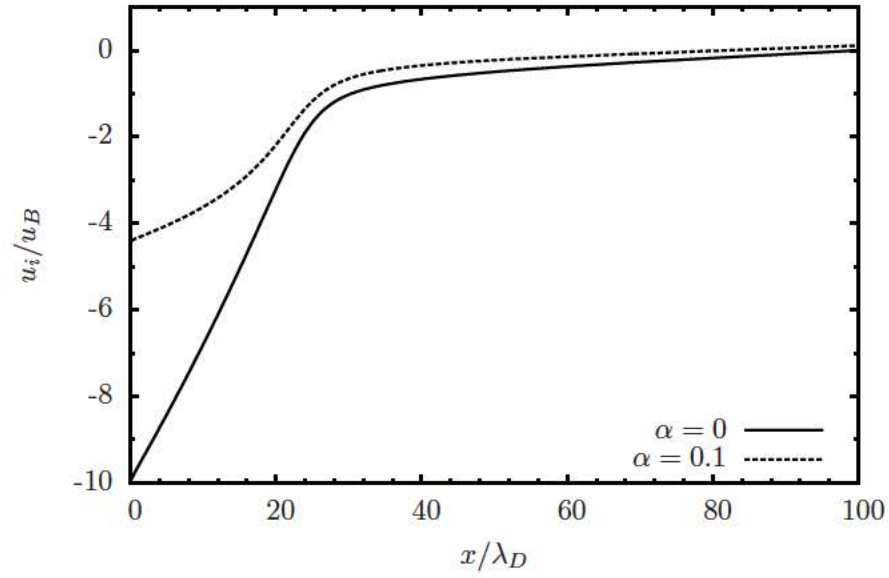


(b) Ion velocity and electric potential

Figure 3.10: Number density and velocity profile of the ions and the electric potential at steady-state condition. Velocity is normalized by the Bohm velocity $u_B = \sqrt{\frac{kT_e}{m_i}}$.



(a) Electric potential



(b) Ion velocity

Figure 3.11: Electric potential and velocity profile of the ions at steady-state condition with and without collisional drag. Velocity is normalized by the Bohm velocity $u_B = \sqrt{\frac{kT_e}{m_i}}$ and $\alpha = \frac{\lambda_D}{\lambda_i}$.

for the ion and electron, defined in equation (2.18), are related as:

$$\frac{r_{Le}}{r_{Li}} \simeq Z_i \sqrt{m_e/m_i} \quad (3.79)$$

where we have assumed $T_i \simeq T_e$. Therefore, we expect that the two-fluid model produces results comparable to the ideal MHD solution at the correct asymptotic limit, that is, in the limit of small electron-ion mass ratio, infinite speed of light, charge neutrality, strongly conducting and large magnetic field. The first three assumptions come from the general MHD approximation.

Strictly speaking, we do not expect an exact agreement between the two-fluid solution and the ideal MHD solution due to the following reasons. Firstly, the two-fluid solution can still capture some electron inertial effects and electromagnetic wave propagation; these physics are missing from the ideal MHD model. Secondly, the numerical solution utilizing the MHD model can vary depends on the numerical formulation of the governing equations, and this is purely a numerical artifact. For example, Thompson et al [80] reproduced the solution of the Brio-Wu problem using two different formulations of the magneto-fluid-dynamics (MFD) equations³ and the results are slightly different from each other.

The initial conditions of the ideal two-fluid electromagnetic shock problem is given by Shumlak and Loverich [81]. In this simulation we assumed a mass ratio $m_i/m_e = 1836$, constant of adiabatic index $\gamma = 5/3$, and set $\epsilon_0, \mu_0, c = 1$. Coulomb collisions are neglected in this simulation such that resistive effects can be neglected. The shock is created by a initial discontinuity in the middle of the

³The MFD equations still assume massless electrons but they contain EM wave propagation and charge separation.

domain as follows:

$$\begin{aligned}
\begin{bmatrix} \rho_i \\ u_i^{x,y,z} \\ p_i \\ \rho_e \\ u_e^{x,y,z} \\ p_e \\ B^x \\ B^y \\ B^z \\ E^{x,y,z} \end{bmatrix} &= \begin{bmatrix} 1 \\ 0 \\ 5 \times 10^{-5} \\ m_e/m_i \\ 0 \\ 5 \times 10^{-5} \\ 0.75 \times 10^{-2} \\ 1 \times 10^{-2} \\ 0 \\ 0 \end{bmatrix} \quad \text{for } x < 0; \\
\begin{bmatrix} \rho_i \\ u_i^{x,y,z} \\ p_i \\ \rho_e \\ u_e^{x,y,z} \\ p_e \\ B^x \\ B^y \\ B^z \\ E^{x,y,z} \end{bmatrix} &= \begin{bmatrix} 0.125 \\ 0 \\ 5 \times 10^{-6} \\ 0.125m_e/m_i \\ 0 \\ 5 \times 10^{-6} \\ 0.75 \times 10^{-2} \\ -1 \times 10^{-2} \\ 0 \\ 0 \end{bmatrix} \quad \text{for } x > 0
\end{aligned} \tag{3.80}$$

Figure 3.12 shows the ion density for several values of the Larmor radius in addition to the MHD solution of the same problem. WENO schemes are used to solve the fluid and Maxwell's equations for all the test cases here. It was shown that in the limit of $r_{Li} \rightarrow 0$ (or r_{Le}), the solution of the two-fluid equation converges to the MHD solution. Same argument can be made about the solution of the transverse magnetic field as shown in figure 3.13.

Two observations were made about the solution of the collisionless two-fluid system. Firstly, it is important that the spatial accuracy of the numerical schemes for solving the fluid and Maxwell's equation is consistent; inconsistency causes the solution to be diffusive. Secondly, since the source term is solved implicitly, a time step restriction is imposed for purposes of accuracy. Typically, in the source term corresponding to the Lorentz force and Joule heating, the time step size is chosen relative to ω_{pe} . All the solutions shown in figure 3.12 correspond to a time step size of $0.1\omega_{pe}$ which is the smallest time step in the system. The solution obtained with a larger time step is more diffusive. These simulations show that the multi-fluid system retains all the correct asymptotic limit of MHD approximation, and

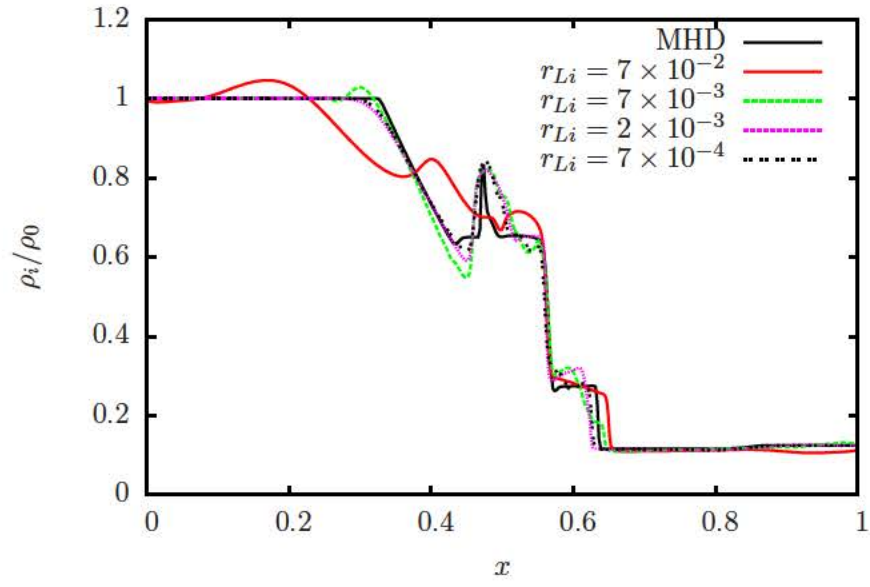


Figure 3.12: Ion density of the ideal two-fluid Riemann problem

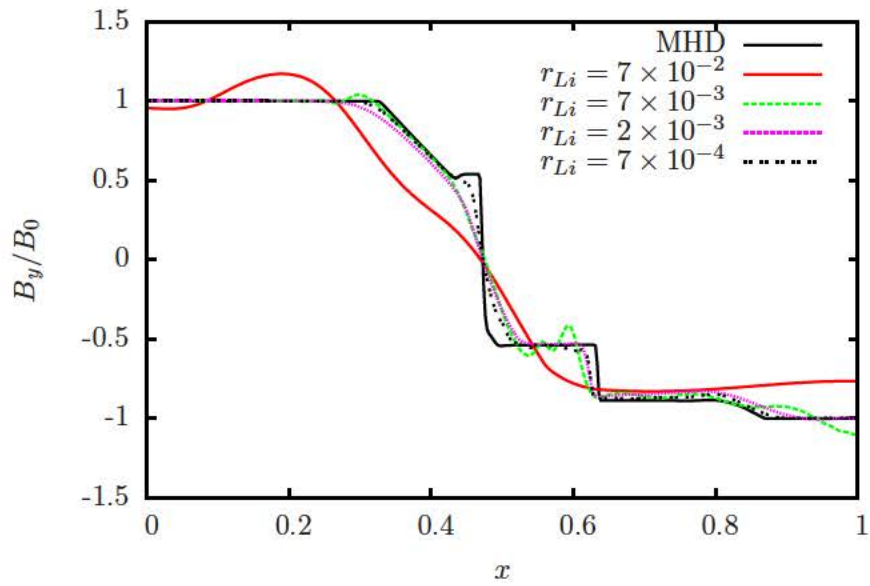


Figure 3.13: Transverse magnetic field of the ideal two-fluid Riemann problem

also includes additional physics of electromagnetic wave propagation and charge separation. However, in the MHD limit, the two-fluid system becomes stiff and the time-step restriction (for accuracy purpose) is quite severe.

3.3.3 Diffusion processes

3.3.3.1 Travelling thermal wave problem

In this section, a one-dimensional travelling heat wave problem is simulated. The problem is representative of the electron thermal transport process in LPI problem. The model equation reads:

$$\partial_t T = \partial_x (\lambda_0 T^\alpha \partial_x T) \quad (3.81)$$

with the following initial and boundary conditions:

$$T(0, t) = \left[\frac{\alpha D}{\lambda_0} (x_1 + Dt) \right]^{1/\alpha} \quad (3.82)$$

$$T(x, 0) = \left[\frac{\alpha D}{\lambda_0} (x_1 - x) \right]^{1/\alpha}; \quad 0 < x \leq x_1 \quad (3.83)$$

$$T(x, 0) = 0 \quad \text{otherwise} \quad (3.84)$$

The exact solution for this problem reads:

$$T(x, t) = \left[\frac{\alpha D}{\lambda_0} (Dt + x_1 - x) \right]^{1/\alpha}; \quad x \leq x_1 + Dt \quad (3.85)$$

Figure 3.14 shows the solution of the model problem for $x_1 = 0$, $\lambda_0 = 0.5$, $D = 5$ and $\alpha = 2$ at $t = 0.1$. In this case, the explicit time step corresponds to 10^{-6} . The implicit scheme allows a time step of three orders of magnitude larger than that required for the explicit scheme while the error for the two cases are of the same order of magnitude. This indicates the robustness of the implicit scheme in handling larger time step, which is a desired properties, since transport phenomena can be stiff, e.g., the electron heat conduction process, and the coupling with convection can lift the stiffness ratio of the system.

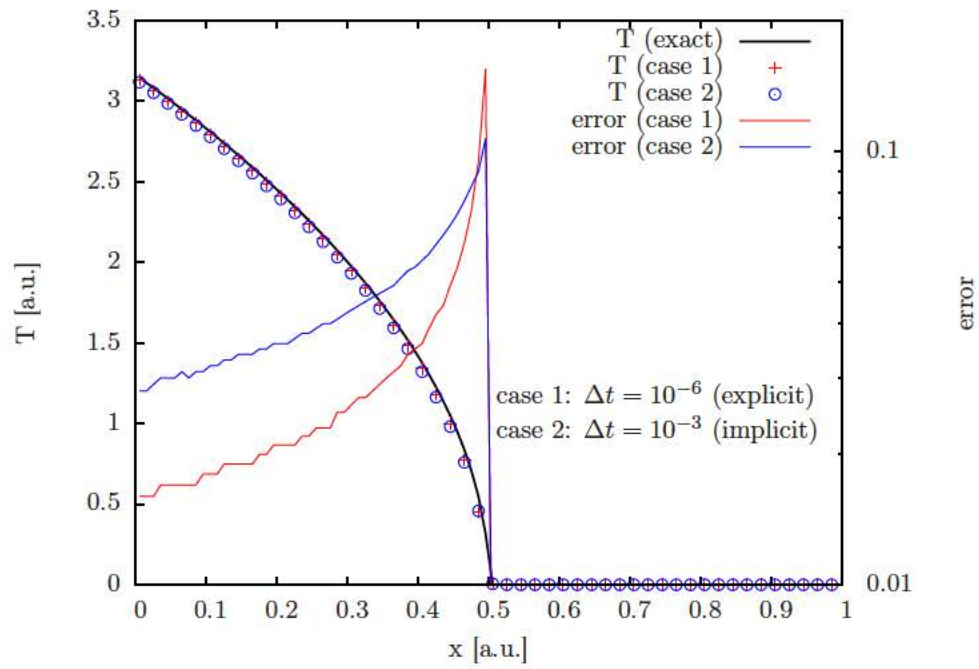


Figure 3.14: Numerical solution and error of the heat conduction problem with 100 cells using both explicit and implicit schemes. The explicit scheme is stable for $\Delta t \leq 10^{-6}$ while the implicit scheme is stable up to $\Delta t = 10^{-3}$.

3.3.3.2 Laser produced plasmas with hot spot

In this section, we simulate the heat transport process of a laser produced plasma hot spot. Convection is neglected here. This problem was simulated using Fokker-Planck and PIC models by Batishchev [82] to study non-local heat transport theory. Generally speaking, non-local effects becomes important when the temperature gradient length scale is of the same order as the collision mean free path. In such case, the electron energy distribution function (EEDF) becomes non-Maxwellian and the classical (local) SH transport [54] breaks down. The current simulation is set up such that classical SH transport remains valid. There are two reference time and length scales, namely the electron collision time τ_e and mean free path λ_e .

$$\tau_e = \frac{3\sqrt{m_e}T_e^{3/2}}{4\sqrt{2\pi}e^4Z^2n_e\ln\Lambda} = 3.5 \times 10^5 \frac{T_e^{3/2}}{Zn_e\ln\Lambda} [\text{sec}] \quad (3.86)$$

$$\lambda_e = \frac{3T_e^2}{4\sqrt{2\pi}e^4Z^2n_e\ln\Lambda} = 1.5 \times 10^{12} \frac{T_e^2}{Zn_e\ln\Lambda} [\text{cm}] \quad (3.87)$$

$$(3.88)$$

where T_e is in eV , n_e is in cm^{-3} , and $\ln\Lambda$ is the Coulomb logarithm.

In the first test, we only consider the effect of thermal transport. The problem is initialized with a quasi-neutral plasma containing (Ar^+, e) with an initial electron temperature enhancement near the center. This condition is representative of plasma heating process due to laser absorption. The reference number density are $n_e = n_i = n_0 = 10^{16} \text{ cm}^{-3}$ and $T_0 = 10 \text{ eV}$. The domain length, L , is set to span $[-300\lambda_e, 300\lambda_e]$, and the initial electron temperature is assumed to be a spatial Gaussian profile:

$$T_e(x, t = 0) = T_0 + T_1 e^{-x^2/l^2} \quad (3.89)$$

where $l = 50\lambda_{ei}$ and $T_1 = 0.4T_0$. The electron heat flux from SH theory are

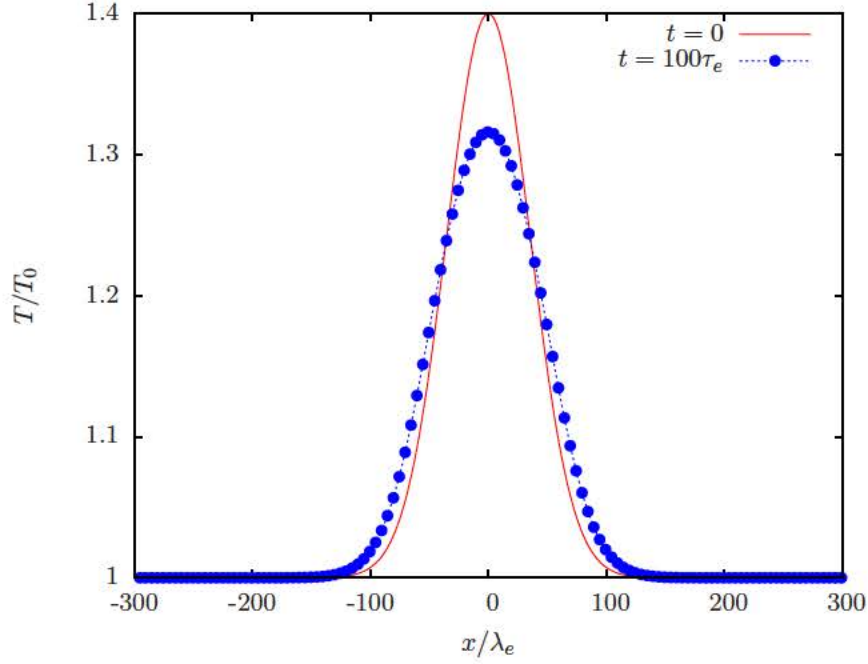


Figure 3.15: Temperature profile at $t = 100\tau_e$ for the hot spot relaxation by electron heat conduction. The solid line indicated the initial temperature.

written as:

$$\mathbf{q}_e = -\kappa_e \nabla T_e \quad (3.90)$$

where $\kappa_e = \gamma_0 n_e k^2 T_e \tau_e / m_e$ and γ_0 is a function depending weakly on ion charge Z . The values of γ_0 for different Z are given in [46, 83, 84]. Here we take $\gamma_0 = 3.16$. This is known as the classical SH transport. This result breaks down when $\frac{\lambda_e}{T/\nabla T}$ exceeds a value of approximately 10^{-2} [85]. Figure 3.15 shows the profile of the electron temperature at time $t = 100\tau_e$, at which the temperature starts diffusing outward. In the simulation, we also include Coulomb thermalization, but the final result shows very little dependence on this term. This is because the energy relaxation time scale between the ions and the electrons is much slower than the diffusive time scales, e.g., $\tau_e \sim (m_e/m_i)\tau_{ei}^E$.

In the second test, we consider laser absorption due to inverse Bremsstrahlung processes. The electron energy equation now includes an addition term due to the

absorption, and can be written as:

$$\partial_t E_e + \nabla \cdot \mathbf{q}_e = \alpha I \quad (3.91)$$

where α is the absorption coefficient due to collisional process, and I is the laser intensity. Here we assume I is only spatially dependent and takes the form:

$$I(x) = I_0 e^{-x^2/d^2} \quad (3.92)$$

where $I_0 = 10^{12} \text{ W/cm}^2$ and $d = 10\lambda_e$. The absorption coefficient is defined as follows:

$$\alpha = \frac{\nu}{c} \frac{\omega_{pe}^2}{\omega^2} \left(1 - \frac{\omega_{pe}^2}{\omega^2} \right)^{1/2} \quad (3.93)$$

where ν is the collisional frequency, ω is the laser frequency, and c is the speed of light.

Figure 3.16 shows the temperature profile at $t = 100\tau_e$ and a comparison with the former case where IB process was not included. When the laser absorption is taken into account, the electron temperature begins to rise, especially at the center of the hot spot. Figure 3.17 also shows a comparison of the thermal heat flux in both cases. The magnitude of the heat fluxes in both cases remains below 10% of the freestream limit $q_f = p_e(kT_e/m_e)^{1/2}$. SH results tend to break down when the heat-flux exceeds approximately 15% of the free-stream value.

3.3.3.3 Hypersonic shocks

We now simulate a 1D hypersonic plasma shock with electron heat conduction. This test is designed to test the coupling of the transport and convection in addition to thermalization via Coulomb collision. The shock is initiated by imposing a uniform flow with a wall on the right side of the domain. The freestream condition is a fully ionized plasma with (Ar^+, e) where $n_i = n_e = 2.14 \times 10^{14} \text{ cm}^{-3}$, $T_\infty = 273$, and $u_\infty = 7000 \text{ m/s}$. The fluid equations are solved with the MP5 scheme.

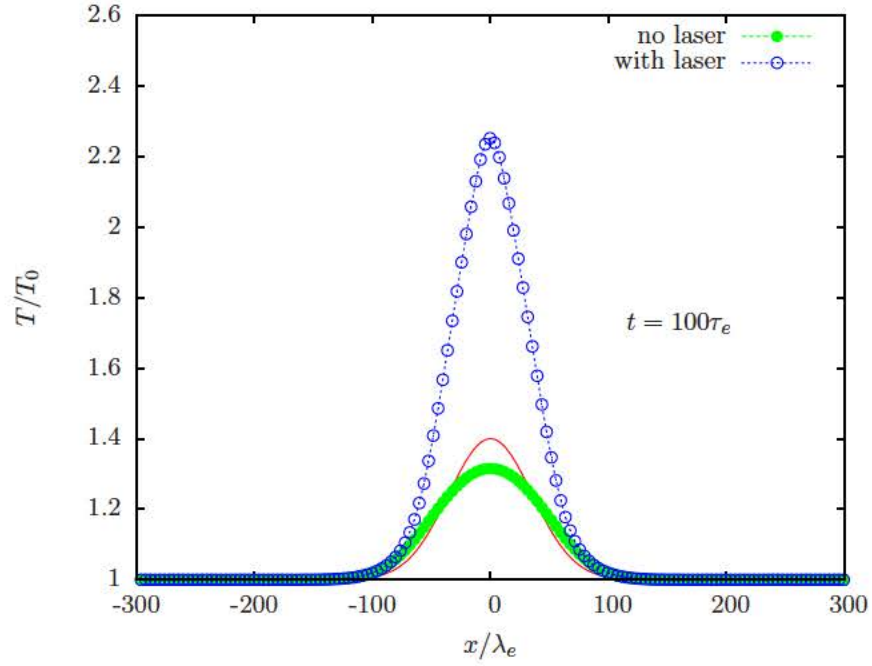


Figure 3.16: Temperature profile for the hot spot simulation with and without laser heating.

Figure 3.18 shows the results for a nitrogen plasma shock computed with and without heat conduction. For the case with heat conduction, the post shock temperature of the heavy particles is lower due to precursor conductive heating of the electron, effectively raising the speed of sound of the plasma ahead of the shock. In case of a partially ionized plasma, this precursor heating can yield interesting dynamics such as precursor excitation and radiation.

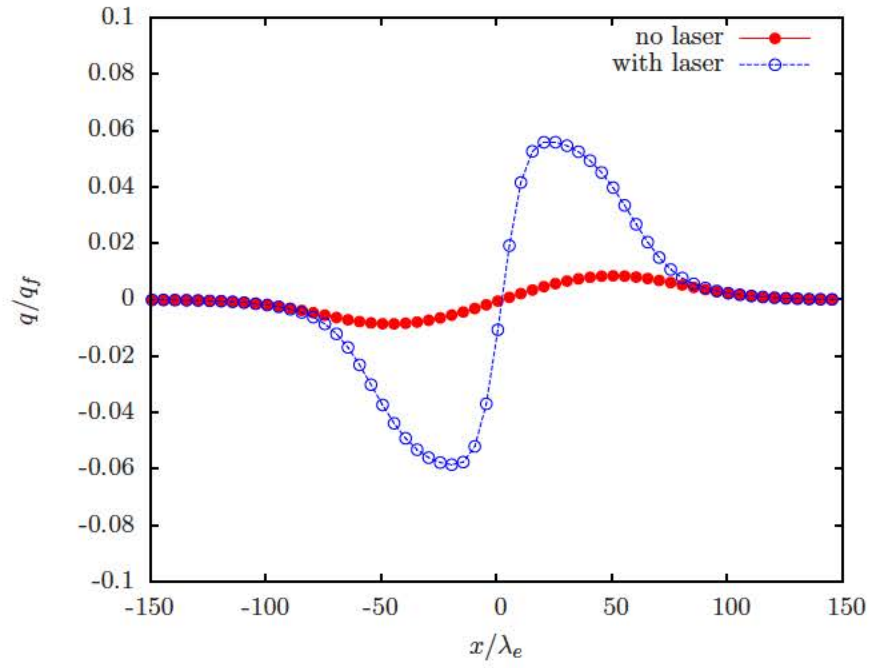


Figure 3.17: Heat flux for the hot spot simulation with and without laser heating. The value of the heat flux is normalized by the freestream limit given by $q_f = p_e(kT_e/m_e)^{1/2}$.

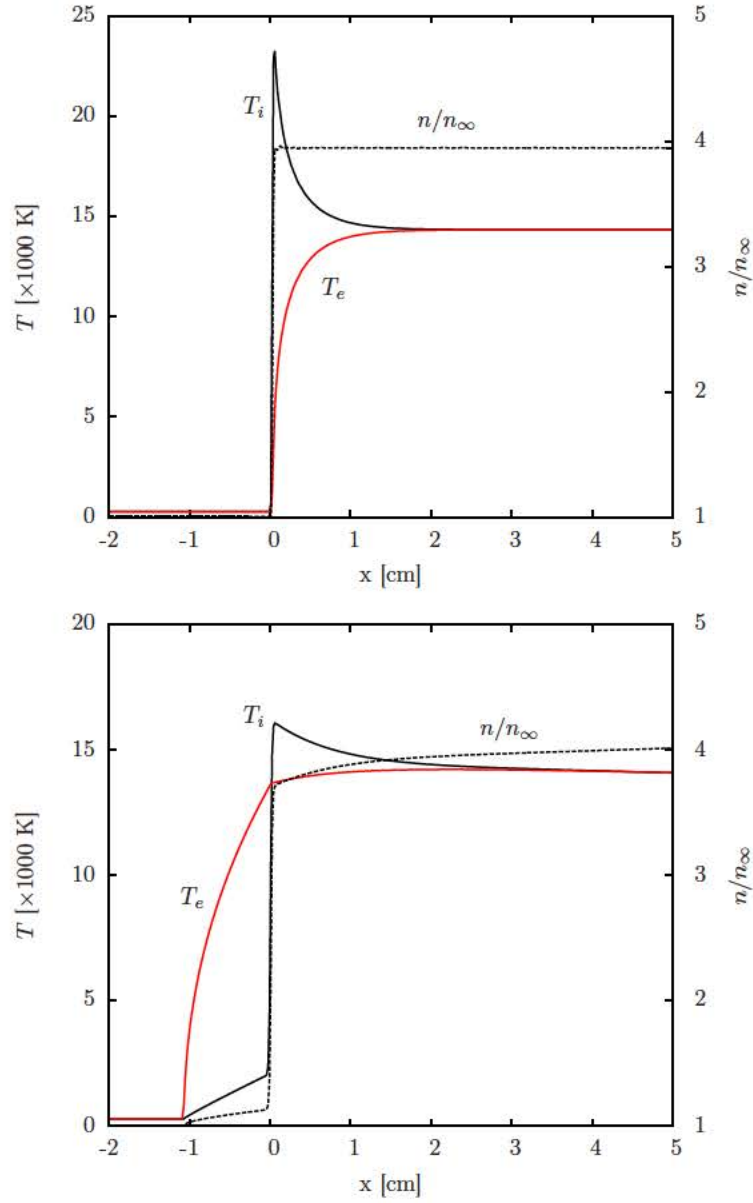


Figure 3.18: Steady profile of a shock propagation into a cold Nitrogen plasma (N^+, e) with (bottom) and without (top) electron heat conduction. Free stream conditions are $u_\infty = 7000$ m/s, $T_\infty = 273$ K, $n_\infty = 2.14 \times 10^{14}$ cm $^{-3}$. Solid lines are ion (black) and electron (red) temperatures. The dashed line is the number density. The x axis is adjusted so the shock starts at $x = 0$.

CHAPTER 4

Collisional-Radiative Models for Atoms

4.1 Introduction

This chapter goes over a detailed description of the CR models for an atomic plasma. Firstly, different thermal equilibrium distributions are derived, and the principle of detailed balance is discussed for various elementary processes implemented in the CR model. Due to the great complexity in the collection of inelastic processes which could occur in a plasma, we limit ourselves to discussing only several important inelastic processes occurring in an atomic plasma: collisional and radiative excitations/deexcitation, and ionization/recombination. A more complete description of these processes can be found in [86, 87, 88, 89, 83].

Secondly, we describe in detail the cross section models for Argon, Krypton, and Xenon for all the CR transitions. The model for Argon was previously developed by Kapper and Cambier [90] based on prior work of Vlcěk [91] and Bultel *et al.* [92] with mostly *ab initio* cross sections for electron-impact processes and semi-empirical model for atom-impact processes. Preliminary extensions to Krypton and Xenon were carried out by Magin and Kapper [93] with a software framework named Colorado. We extend their work by adding more *ab initio* cross sections for electron-impact processes, updating some of the old cross sections, and validating the models with available shock tube experimental data.

4.2 Thermal equilibrium

This section goes over various thermodynamic equilibrium distribution of gases and plasmas. Thermodynamic equilibrium of radiation field is also discussed, since it can play an important role in the inelastic exchange processes especially for very high temperature plasmas. It must be noted that thermodynamic equilibrium distributions can be determined from statistical thermodynamics and the principle of maximum entropy. In this section, we derive thermal equilibrium distributions using a different approach, that is, by considering the equilibrium reaction balance of different processes.

We start with the *principle of microscopic reversibility (MR)* which states that in thermal equilibrium, any reaction from a quantum state to another state is exactly counterbalanced by the reverse reaction. In the classical limit, i.e., the case from which the number of quantum states is much larger than number of particles, this leads to the following expression:

$$\begin{aligned} w(s, t \rightarrow s', t') N(s) N(t) G(s') G(t') \\ = w(s', t' \rightarrow s, t) N(s') N(t') G(s) G(t) \end{aligned} \quad (4.1)$$

where $w(s, t \rightarrow s', t')$ is the transition probability from states (s, t) to (s', t') , $N(s)$ is the number of particle of type s , and $G(s)$ is the total degeneracy. By introducing the elementary occupation number, $\eta(s) \equiv N(s)/G(s)$, and utilizing the quantum mechanical reciprocity relation, $w(s, t \rightarrow s', t') = w(s', t' \rightarrow s, t)$, one arrives at the following expression:

$$\eta(s)\eta(t) = \eta(s')\eta(t') \quad (4.2)$$

The validity of equation (4.2) depends solely on the validity of the quantum mechanical reciprocity relation, which is discussed in more detail by Oxenius [87] from a quantum mechanics point of view. In the scope of the current study, we assume that equation (4.2) is physically acceptable from which thermal equilibrium distribution can be derived. For simplicity, we assume that the system is

isotropic so all the angular variables do not appear in the formula of the distribution function.

4.2.1 Maxwell distribution

Consider an elastic collision between particles X and Y , from which an amount of energy, W , is transferred:

$$X(E) + Y(E') \Leftrightarrow X(E + W) + Y(E' - W) \quad (4.3)$$

where E and E' are the incident energy of particles X and Y , respectively. From the MR relation, equation (4.2), we have:

$$\eta_X(E)\eta_Y(E') = \eta_X(E + W)\eta_Y(E' - W) \quad (4.4)$$

which leads to:

$$\frac{\eta_X(E)}{\eta_X(E + W)} = \frac{\eta_Y(E' - W)}{\eta_Y(E')} = r(W) \quad (4.5)$$

The expression of $r(W)$ is introduced since the first and second terms of equation (4.5) cannot be a function of either E or E' . It can be proved that the solution of equation (4.5) is given by the following (see ref [87]):

$$r(W) = e^{\beta W} \quad (4.6)$$

$$\eta(E) = \zeta e^{-\beta E} \quad (4.7)$$

It is well known from statistical mechanics that $\beta = 1/kT$. The normalization constant ζ is :

$$\zeta = \frac{1}{g} n \lambda^3 \quad (4.8)$$

where g is the statistical weight, $n = N/V$ is the number density, and λ is the thermal de Broglie wavelength of the particle, i.e.:

$$\lambda = \frac{h}{(2\pi m k T)^{1/2}} \quad (4.9)$$

The total degeneracy of the particle $G(E)$ is:

$$G(E)dE = gV \frac{2^{5/2} \pi m^{3/2}}{h^3} E^{1/2} dE \quad (4.10)$$

Using (4.7) and (4.10), we can write the complete form of the Maxwell distribution function $f(E) \equiv N(E)/N$:

$$f(E)dE = \frac{2E^{1/2}}{\pi^{1/2}(kT)^{3/2}} e^{-E/kT} dE \quad (4.11)$$

where $f(E)$ is the normalized distribution function, i.e., $\int_0^\infty f(E)dE = 1$. It must be noted that the Maxwellian distribution function describes the translational states population in the classical limit, i.e., $\eta \ll 1$. When $\eta \rightarrow 1$, either Fermi-Dirac or Bose-Einstein statistics should be applied according to the particle type. This condition is relevant, for example, in low temperature and very dense electron gas found in inertial fusion problems where the electrons are characterized by Fermi-Dirac statistics. The case of Bose-Einstein statistics is relevant for the distribution of photons as will be shown later in this chapter.

4.2.2 Boltzmann distribution

The Boltzmann distribution can be derived by considering an inelastic collision where particle X with infinite mass at rest¹ is (de)excited from a bound electronic states by collision with particle M :

$$X(E_1) + M(E) \Leftrightarrow X(E_2) + M(E - \Delta E_{21}) \quad (4.12)$$

where E_1 , E_2 are the energy of the electronic bound states and $\Delta E_{21} = E_2 - E_1$ is the energy gap between the lower and upper levels. Utilizing the MR relation, it follows that:

$$\eta_X(E_1)\eta_M(E) = \eta_X(E_2)\eta_M(E - \Delta E_{21}) \quad (4.13)$$

¹This assumption allows us to neglect the translational degree of freedom of X and M .

Using the same argument as in the previous section, i.e., $\eta_M(E - \Delta E_{21})/\eta_M(E) = e^{\beta \Delta E_{21}}$ we can arrive at the following results:

$$\frac{n_2}{n_1} = \frac{g_2}{g_1} e^{-\Delta E_{21}/kT} \quad (4.14)$$

where g_1 and g_2 is the degeneracy weight of the excited states. This is the Boltzmann distribution for the bound excited states. It can also be written in the following form for any particular state i of particle X :

$$\frac{n_{i \in X}}{n_X} = \frac{g_i}{\mathcal{Z}_X} e^{-E_i/kT} \quad (4.15)$$

where $n_X = \sum_{i \in X} n_i$, and $\mathcal{Z}_X = \sum_{i \in X} g_i e^{-E_i/kT}$ is the electronic partition function of X .

4.2.3 Saha distribution

Let us now consider a collisional ionization and its reverse process, three-body recombination, as follows:

$$X(E_0) + M(E) \Leftrightarrow X^+(E_+) + M(E - I_0 - E') + e(E') \quad (4.16)$$

where $I_0 = E_+ - E_0$ is the ionization energy. Similarly, the MR relation gives:

$$\eta_X(E_0) \eta_M(E) = \eta_{X^+}(E_+) \eta_M(E - I_0 - E') \eta_e(E') \quad (4.17)$$

Similar to the previous section, this equation can be written in the form:

$$\frac{\eta_X(E_0)}{\eta_{X^+}(E_+) \eta_e(E')} = \frac{\eta_M(E - I_0 - E')}{\eta_M(E)} = r(I_0 + E') = e^{\beta(I_0 + E')} \quad (4.18)$$

It can be seen that the mean occupation number of the electron is independent of I_0 , i.e., $\eta_e(E') = \frac{1}{2} n_e \lambda_e^3 e^{-\beta E'}$, where λ_e is the thermal de Broglie wavelength of the electron given by equation (4.9). Substituting this expression back to equation (4.18), we obtain the Saha distribution:

$$\frac{n_e n_+}{n_0} = \frac{2g_+}{g_0} \lambda_e^{-3} e^{-I_0/kT} \quad (4.19)$$

Note that the factor of 2 appeared in the Saha distribution is due to the degeneracy weight of the electron spin.

Also, in this process we have also assumed that the atom and ion have infinite mass so that the center of mass (COM) is collocated with the atom and ion. If we were to include the finite electron mass effect, the thermal de Broglie wavelength needs to be computed using the reduced mass of the electron and ion, e.g., $\mu_{+e} = m_+m_e/(m_+ + m_e)$. If internal degrees of freedom of X and X^+ are taken into account, the Saha relation can be generalized:

$$\frac{n_e n_+}{n_0} = \frac{2\mathcal{Z}_+}{\mathcal{Z}_0} \lambda_e^{-3} e^{-I_0/kT} \quad (4.20)$$

where \mathcal{Z}_0 and \mathcal{Z}_+ are the partition functions of X and X^+ , respectively.

4.2.4 Planck distribution

We now consider an elementary balance of emission and absorption of photons by free particles M :

$$M(E) \Leftrightarrow M(E - h\nu) + p(\nu) \quad (4.21)$$

The MR needs to be modified since quantum effects must be taken into account for photons, which leads to the following relation:

$$\eta_M(E) (1 + \eta_p(\nu)) = \eta_M(E - h\nu) \eta_p(\nu) \quad (4.22)$$

Here the photons are treated as bosons, leading to the multiplicative factor of $1 + \eta_p(\nu)$ on the LHS. Hence, we arrive at a slightly different relation:

$$\frac{\eta_M(E - h\nu)}{\eta_M(E)} = \frac{1 + \eta_p(\nu)}{\eta_p(\nu)} = r(h\nu) = e^{\beta h\nu} \quad (4.23)$$

We can then express the mean occupation number of a photon state as follow:

$$\eta_p(\nu) = (e^{\beta h\nu} - 1)^{-1} \quad (4.24)$$

For photons, $G_p(\nu) = V8\pi\nu^2c^{-3}$, thus it leads to the expression of photon density per unit volume, aka Planck distribution:

$$n(\nu)d\nu = \frac{8\pi\nu^2}{c^3}(e^{h\nu/kT} - 1)^{-1}d\nu \quad (4.25)$$

By introducing the spectral radiance quantity $I_\nu = n(\nu)h\nu c/4\pi$, we can rewrite Planck's radiation law into its familiar form:

$$I_\nu(T) = \frac{2h\nu^3}{c^2}(e^{h\nu/kT} - 1)^{-1} \quad (4.26)$$

In the low temperature limit ($e^{h\nu/kT} \gg 1$), Planck's distribution is replaced with the so-called Wien approximation:

$$I_\nu^W(T) = \frac{2h\nu^3}{c^2}e^{-h\nu/kT} \quad (4.27)$$

On the other hand, in the high temperature limit ($e^{h\nu/kT} \ll 1$), Planck's distribution reduces to the Rayleigh-Jeans function:

$$I_\nu^{RJ}(T) = \frac{2kT\nu^2}{c^2} \quad (4.28)$$

4.3 Elementary processes and detailed balance

In the CR model, each electronic state of the atom is treated as a separate species. The time evolution of the species' number densities are determined by solving a set of rate equations, which includes all the relevant kinetic processes by means of collisional and radiative interactions. All the macroscopic rates are computed assuming a Maxwellian EEDF of the heavy particles or electrons.

For a given microscopic cross section, $\sigma(E)$, the macroscopic reaction rate is computed as follows:

$$k(T) = \frac{\bar{v}}{(kT)^2} \int_{E_0}^{\infty} \sigma(E)Ee^{-E/kT}dE \quad (4.29)$$

where E_0 is the threshold energy, and $\bar{v} = \left(\frac{8k_BT}{\pi\mu}\right)^{1/2}$ is the mean thermal velocity with μ being the reduced mass. The rates computed in this form are tabulated

Rate	
Coefficient	Process
$k_{(m n)}^{ex}$	collisional excitation by electrons ($n \rightarrow m$)
$k_{(m n)}^{hx}$	collisional excitation by ground state atoms ($n \rightarrow m$)
$k_{(n m)}^{ed}$	collisional de-excitation by electrons ($m \rightarrow n$)
$k_{(n m)}^{hd}$	collisional de-excitation by ground state atoms ($m \rightarrow n$)
k_n^{ei}, k_n^{hi}	collisional ionization
k_n^{er}, k_i^{hr}	three-body recombination
k_n^{pr}	radiative recombination
$A_{(m n)}$	transition probability/spontaneous emission (Einstein coefficient)
$\Lambda_{(m n)}$	bound-bound optical escape factor
Λ_n	bound-free optical escape factor
\bar{k}_{ei}	electron-ion elastic collisions
k_{en}	electron-neutral elastic collisions

Table 4.1: Rate coefficients for collisional-radiative model.

as a function of temperature. It must be noted that for recombination processes, the rates are functions of both the heavy and electron temperatures as will be described later in this chapter.

A summary of all the elementary processes responsible for the excitation and ionization kinetics in a low temperature plasma is presented in this section. The principle of detailed balance is discussed for each type of process, i.e., the relation of the forward and backward rates. In this section, we use Argon as an example, but the same formulation also holds for Krypton and Xenon. A summary of the rates coefficients' definitions is listed in table 4.1. For bound-bound transitions, we use the convention of indexing the rates with the final state on the left, and the initial state on the right, i.e., $(f|i)$.

4.3.1 Collisional excitation/deexcitation

A collisional excitation/deexcitation process of an atom can be due to impact with another atom or the electron. Consider an electron-impact excitation process and its reversed deexcitation process between levels n and m ($n < m$),



the rate of change of the population density of state n due to the collisional process is of the form:

$$\frac{dn_n}{dt} = -k_{(m|n)}^{ex} n_n n_e + k_{(n|m)}^{ed} n_m n_e \quad (4.31)$$

The first term on the RHS of equation (4.31) describes the loss due to excitation from level n to m , as a result of collisions of the free electron with the existing state n ; the second term describes the gain due to the collisional deexcitation induced by the free electron from state m . The total rate of change of the number density of level n can be determined by summing up the RHS of equation (4.31) for all levels $m \neq n$.

At equilibrium (“Boltzmann”), the ratio of the population densities of the lower and upper states are:

$$\frac{n_m^*}{n_n^*} \equiv \mathcal{B}_{nm}(T_e) = \frac{g_m}{g_n} e^{-\Delta E_{nm}/kT_e} \quad (4.32)$$

where $\Delta E_{nm} = E_m - E_n$. The rate of change of the number density at equilibrium is null, i.e., $\frac{dn_n^*}{dt} \simeq 0$, and therefore we obtain a relation for the forward and the backward rates:

$$\frac{k_{(m|n)}^{ex}}{k_{(n|m)}^{ed}} = \frac{g_m}{g_n} e^{-\Delta E_{nm}/kT_e} \quad (4.33)$$

Similarly for an atom-impact collisional excitation and its reverse process,



the rate of change of the population is written similar to equation (4.31) with n_e being replaced by n_{Ar} and the expression for the backward rate is the same as

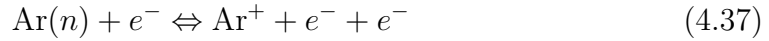
equation (4.33) with T_e being replaced by T_h :

$$\frac{dn_n}{dt} = -k_{(m|n)}^{hx} n_n n_{Ar} + k_{(n|m)}^{hd} n_m n_{Ar} \quad (4.35)$$

$$\frac{k_{(m|n)}^{hx}}{k_{(n|m)}^{hd}} = \frac{g_m}{g_n} e^{-\Delta E_{nm}/kT_h} \quad (4.36)$$

4.3.2 Collisional ionization/recombination

Consider an electron-impact ionization and recombination written as:



the rate of change of the number density of level n in this case is:

$$\frac{dn_n}{dt} = -k_n^{ei} n_n n_e + k_n^{er} n_+ n_e^2 \quad (4.38)$$

The first term on the RHS of equation (4.38) describes the loss due to ionization from level n , as a result of collisions of the free electrons with the existing state n ; The second term describes the gain due to the three-body recombination process induced by the free electrons from the ion state.

The equilibrium for ionization and recombination (“Saha”) involves a different relation:

$$\left(\frac{n_+ n_e}{n_n} \right)^* \equiv \mathcal{S}_n(T_e) = \frac{2g_+}{g_n} \left(\frac{2\pi m_e k T_e}{h^2} \right)^{3/2} e^{-I_n/kT_e} \quad (4.39)$$

Thus we cannot assume that the equilibrium values are the same for both excitation and ionization. Usually we can have Boltzmann equilibrium without Saha equilibrium, but hardly the reverse, mostly because it takes more energy to ionize than to excite; for the upper states close to the ionization limit ($n \gg 1$), the difference is less significant. Using the principle of detailed balance, the recombination rate is written as:

$$\frac{k_n^{ei}}{k_n^{er}} = \frac{2g_+}{g_n} \left(\frac{2\pi m_e k T_e}{h^2} \right)^{3/2} e^{-I_n/kT_e} \quad (4.40)$$

Similarly for an atom-impact collisional ionization and its reverse process,



The rate of change of the state population is written similar to equation (4.38) with n_e being replaced by n_{Ar} and the expression for the backward rate is the same as equation (4.40) with T_h in the exponential term:

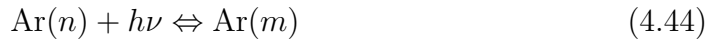
$$\frac{dn_n}{dt} = -k_n^{hi} n_n n_{\text{Ar}} + k_n^{hr} n_+ n_e n_{\text{Ar}} \quad (4.42)$$

$$\frac{k_n^{hi}}{k_n^{hr}} = \frac{2g_+}{g_n} \left(\frac{2\pi m_e k T_e}{h^2} \right)^{3/2} e^{-I_n/kT_h} \quad (4.43)$$

where I_n is the ionization potential of the excited state n . Note that the expression for the detailed balance includes the electron translational partition function, which is defined by the electron temperature T_e ; therefore, the recombination rate is a function of both T_e and T_h .

4.3.3 Radiative processes

Radiation can also play an important role in the excitation and ionization kinetics. Radiative transition rates between bound states, referred to as bound-bound transition, can be expressed in terms of the Einstein coefficient A . Consider a spontaneous absorption/emission process between level n and m



In order to calculate the rate of change in the population due to the forward process, one needs to know the intensity of the radiation field, which is governed by the radiation transport equation. A coupled solution of the CR kinetics with radiation transport, although of great interest, is beyond the scope of the current study. A simplified treatment can be made by using the so-called optical escape factor Λ , which gives a local approximation of the radiative losses. Since the

radiation mean free path can be significantly different for each process, the escape factors are defined for each specific process. The rate of change of the number density of a lower level n due to a bound-bound emission process, or line radiation from an upper level m , can be written as:

$$\frac{dn_n}{dt} = \Lambda_{(n|m)} A_{(n|m)} n_m \quad (4.45)$$

The spontaneous emission rates for this transition, $A_{(n|m)}$, is defined as:

$$A_{(n|m)} = \left(\frac{8\pi^2 e^2}{m_e c^3} \right) \frac{g_n}{g_m} f_{nm} \quad (4.46)$$

where f_{nm} is the oscillator strength of the transition.

Similarly for the photoionization and radiative recombination process,

$$\text{Ar}(n) + h\nu \Leftrightarrow \text{Ar}^+ + e^- \quad (4.47)$$

the rate of change of the population of level n , using the escape factor, is written as:

$$\frac{dn_n}{dt} = \Lambda_n k_n^{pr} n_+ n_e \quad (4.48)$$

In all the radiative transitions, $\Lambda = 0$ corresponds to the optically thick and $\Lambda = 1$ corresponds to the optically thin approximation. For the radiative recombination case, the electron energy production rate also needs to be computed and tabulated:

$$k'(T) = \frac{\bar{v}}{(kT)^2} \int_{E_0}^{\infty} \sigma(E) E^2 e^{-E/kT} dE \quad (4.49)$$

and the resultant rate of change of the electron thermal energy is as follows:

$$\frac{d\varepsilon_e}{dt} = -\Lambda_n k_n^{pr'} n_+ n_e \quad (4.50)$$

The use of the escape factor is convenient and computationally efficient. However, in very high-temperature plasma, the radiation field might have a stronger impact on the inelastic processes, and radiation transport must be taken into account. It is also important, for example, when the radiation mean free path is

comparable to the characteristic length scale of the flow. In such cases, detailed treatment of the radiative terms need to be considered, and the calculation can get very expensive (see [94] and [95]). Moreover, since the escape factor is defined locally, global effects cannot be captured, i.e., precursor effects in plasma shocks [96].

4.3.4 Elastic processes

In addition to the all the excitation and ionization processes, the current model also takes in account the effect of elastic collision between the the heavy particles and the electrons. These collisions are responsible to enforce the equilibrium between the translational energy of the electrons and the heavy particles. The energy transfer between the two components due to the elastic collisions is given as:

$$\frac{d\varepsilon_e}{dt} = -\frac{d\varepsilon_h}{dt} = \frac{2m_e}{m_{Ar}}n_en_n\frac{3}{2}k(T_h - T_e)k_{en} + \frac{2m_e}{m_{Ar}}n_en_+\frac{3}{2}k(T_h - T_e)\bar{k}_{ei} \quad (4.51)$$

where n_n and n_+ are the number densities of the neutral and ion species, respectively.

The first term on the RHS of equation (4.51) describes the energy transfer due to electron-neutral collision, the second term describes the energy transfer due to Coulomb collisions. The Coulomb collision can be computed from the energy-averaged properties [86]:

$$\bar{k}_{ei} = \bar{v}_e\sigma_{ei} \quad (4.52)$$

$$\sigma_{ei} = 5.58 \times 10^{-10} \frac{\ln \Lambda}{T_e^2} [m^2] \quad (4.53)$$

Free-free radiation had also been incorporated in the current model via Kramer's formula [83] for Bremsstrahlung emission. The rate of change of the electron energy is as follows:

$$\frac{d\varepsilon_e}{dt} = -\frac{16\pi^2}{3\sqrt{3}} \frac{\bar{v}_e Z_{\text{eff}}^2 e^6 \bar{g}}{m_e h (4\pi E_0 c)^3} n_+ n_e = -1.42 \times 10^{-40} Z_{\text{eff}}^2 T_e^{1/2} n_+ n_e [\text{J} \cdot \text{m}^{-3} \cdot \text{s}^{-1}] \quad (4.54)$$

where \bar{g} is the gaunt factor taken to be unity and Z_{eff} is the effective charge.

4.4 Rate equations

Once all the macroscopic rates are obtained, one can construct a system of rate equations, which computes the rate of change of the specie's number densities and the energies of the electrons and the heavy particles. These rate equations are summarized below:

Ground state and excited states

$$\begin{aligned} \frac{\partial n_k}{\partial t} = & \sum_{i < k} n_i (n_e k_{(k|i)}^{ex} + n_{\text{Ar}} k_{(k|i)}^{hx}) - \sum_{j < k} n_k (n_e k_{(j|k)}^{ed} + n_{\text{Ar}} k_{(j|k)}^{hd} + \Lambda_{(j|k)} A_{(j|k)}) \\ & - \sum_{j > k} n_k (n_e k_{(j|k)}^{ex} + n_{\text{Ar}} k_{(j|k)}^{hx}) + \sum_{i > k} n_i (n_e k_{(k|i)}^{ed} + n_{\text{Ar}} k_{(k|i)}^{hd} + \Lambda_{(k|i)} A_{(k|i)}) \\ & + n_+ n_e (n_{\text{Ar}} k_k^{hr} + n_e k_k^{er} + \Lambda_k k_k^{pr}) - n_k (n_e k_k^{ei} + n_{\text{Ar}} k_k^{hi}) \end{aligned} \quad (4.55)$$

Ion state

$$\frac{\partial n_+}{\partial t} = \sum_i n_i (n_e k_i^{ei} + n_{\text{Ar}} k_i^{hi}) - n_+ n_e \sum_i (n_{\text{Ar}} k_i^{hr} + n_e k_i^{er} + \Lambda_i k_i^{pr}) \quad (4.56)$$

Heavy particles energy

$$\frac{\partial \varepsilon_h}{\partial t} = n_{\text{Ar}} \sum_i \sum_{j > i} \Delta E_{ij} (n_j k_{(i|j)}^{hd} - n_i k_{(j|i)}^{hx}) + n_{\text{Ar}} \sum_i I_i (n_e n_+ k_i^{hr} - n_i k_i^{hi}) \quad (4.57)$$

$$- 3\rho_e n_n k (T_h - T_e) \frac{k_{en}}{m_{\text{Ar}}} - 3\rho_e n_+ k (T_h - T_e) \frac{\bar{k}_{ei}}{m_{\text{Ar}^+}} \quad (4.58)$$

Electron energy

$$\frac{\partial \varepsilon_e}{\partial t} = n_e \sum_i \sum_{j > i} \Delta E_{ij} (n_j k_{(i|j)}^{ed} - n_i k_{(j|i)}^{ex}) + n_e \sum_i I_i (n_e n_+ k_i^{er} - n_i k_i^{ei}) \quad (4.59)$$

$$- n_e n_+ \sum_i \Lambda_i k_i^{pr'} - n_+ n_e \frac{16\pi^2}{3\sqrt{3}} \frac{\bar{v}_e Z_{\text{eff}}^2 e^6 \bar{g}}{m_e h (4\pi\epsilon_0 c)^3} \quad (4.60)$$

$$+ 3\rho_e n_n k (T_h - T_e) \frac{k_{en}}{m_{\text{Ar}}} + 3\rho_e n_+ k (T_h - T_e) \frac{\bar{k}_{ei}}{m_{\text{Ar}^+}} \quad (4.61)$$

The electron number density is determined from charge neutrality, i.e., $n_e = \sum_s Z_s n_s$. Also, in the case where the mixture of gas consists of multiple chemical species, one also needs to take in account the collisional processes with all the heavy species. The expression for the atom-impact processes would need to be summed over all the heavy species.

4.5 Physical models

4.5.1 Argon

The CR model for Argon implemented in this study is based on the work of Vlcěk [91] and Bultel *et al.* [92], both of which, were specifically developed for Argon. Subsequently, Kapper and Cambier [90, 97] extended this model, and obtained a calibrated set of atom-impact excitation rates for Argon. Their CR model takes in account the ground state and the first 30 excited levels of neutral Argon obtained from the NIST database [98]. The electronic levels are split into two configurations based on the core angular momentum numbers, which yield two effective ionization potentials. The energy levels of all the excited states of Argon are listed in table 4.2.

For atom-impact excitation processes, the cross sections are computed from the semi-empirical Drawin's formula [99, 100]. For the low energy range considered in this study, the cross sections can be approximated by a linear function. For excitation from ground state ($1 \rightarrow m$), the cross sections take the form:

$$\sigma_{1m}^a = \chi_{1m}^* (E - \Delta E_{1m}) \quad (4.62)$$

where

$$\chi_{nm}^* = 4\pi a_0^2 \frac{(I_H)^2}{\Delta E_{nm}^3} \xi^2 f_{nm} \frac{2m_e}{m_H} \quad (4.63)$$

and f_{nm} is the oscillator strength of the transition ($n \rightarrow m$). The values of χ_{1m}^* in the current CR model were calibrated to obtain a satisfactory induction length (or

n	$E(n)$ [eV]	g_n	j_c	$n\ell[K]_J$	n	$E(n)$ [eV]	g_n	j_c	$n\ell[K]_J$
1	0	1	1.5	[Mg]3p ⁶	18	13.903	5	1.5	3d[3/2] ₂
2	11.548	5	1.5	4s[3/2] ₂	19	13.979	9	1.5	3d[7/2] ₄
3	11.624	3	1.5	4s[3/2] ₁	20	14.013	7	1.5	3d[7/2] ₃
4	11.723	1	0.5	4s'[1/2] ₀	21	14.063	5	1.5	3d[5/2] ₂
5	11.828	3	0.5	4s'[1/2] ₁	22	14.068	5	1.5	3d[3/2] ₁
6	12.907	3	1.5	4p[1/2] ₁	23	14.090	3	1.5	5s[3/2] ₂
7	13.076	7	1.5	4p[5/2] ₃	24	14.099	7	1.5	5s[5/2] ₃
8	13.095	5	1.5	4p[5/2] ₂	25	14.153	3	1.5	3d[3/2] ₁
9	13.153	3	1.5	4p[3/2] ₁	26	14.214	5	0.5	5s'[1/2] ₀
10	13.172	5	1.5	4p[3/2] ₂	27	14.234	5	0.5	3d'[5/2] ₂
11	13.273	1	1.5	4p[1/2] ₀	28	14.236	7	0.5	5s'[1/2] ₁
12	13.283	3	0.5	4p'[3/2] ₁	29	14.241	1	0.5	3d'[3/2] ₂
13	13.302	5	0.5	4p'[3/2] ₂	30	14.255	3	0.5	3d'[5/2] ₃
14	13.328	3	0.5	4p'[1/2] ₁	31	14.304	3	0.5	3d'[3/2] ₁
15	13.480	1	0.5	4p'[1/2] ₀	∞	15.760	4	1.5	[Mg]3p ⁵
16	13.845	1	1.5	3d[1/2] ₀	∞'	15.937	2	0.5	[Mg]3p ⁵
17	13.864	3	1.5	3d[1/2] ₁					

Table 4.2: Lowest 31 levels of Ar I by energy.

n	m	$\chi_{nm}^* [\text{m}^2/\text{eV}]$	n	m	$\chi_{nm}^* [\text{m}^2/\text{eV}]$
1	3	9.35×10^{-25}	2	3	1.79×10^{-24}
1	5	3.36×10^{-24}	2	4	4.80×10^{-26}
1	17	8.14×10^{-27}	2	5	4.80×10^{-26}
1	23	2.64×10^{-25}	3	4	4.80×10^{-26}
1	25	7.27×10^{-25}	3	5	4.80×10^{-26}
1	30	1.35×10^{-25}	4	5	1.79×10^{-24}
1	31	5.88×10^{-25}			

Table 4.3: Atom impact excitation parameters for allowed transitions for Argon. χ_{nm}^* for allowed transitions from ground state of neutral Ar has been tuned to match the experimental induction length.

relaxation length) compared to the experimentally observed values (see Kapper and Cambier[90] for more detail). The inner $3p^54s$ manifold transitions take the form:

$$\sigma_{nm}^a = \chi_{nm}^* \frac{E - \Delta E_{nm}}{\Delta E_{nm}^{2.26}} \quad (4.64)$$

where ΔE_{nm} is in eV. The resultant set of values are summarized in table 4.3.

The atom-impact ionization cross sections are less sensitive to the induction length. The ionization cross section from the ground state is taken from the work of Haugsjaa and Amme [101]:

$$\sigma_1^a(E) = 1.8 \times 10^{-25} (E - 15.760)^{1.3} [\text{m}^2], \quad (4.65)$$

where E is in eV. For all other levels, the cross sections are computed from Drawin's formula:

$$\sigma_n^a(E) = 4\pi a_0^2 \left(\frac{I_H}{I_n} \right)^2 \frac{m_{Ar}}{m_H} \xi^2 \frac{2m_e}{m_{Ar} + m_e} \frac{E/I_n - 1}{\left(1 + \frac{2m_e}{m_{Ar} + m_e} (E/I_n - 1) \right)^2}. \quad (4.66)$$

While the atom-impact processes have a significant effect on the overall induction length, the electron-impact processes have a dominated effect on the electron

Parameter for Eq. (4.68)	Valence electron shell			
	<i>s</i>	<i>p</i>	<i>d</i>	<i>f</i>
<i>a</i>	1.06	2	3/2	3/2
<i>b</i>	0.23	1	3	1
<i>c</i>	1	1	2/3	2/3
<i>d</i>	1	1	1	1

Table 4.4: Electron-impact ionization parameters as taken from [103].

avalanche. The cross sections for electron-impact excitation from ground state and 4s levels to all the levels below the 5p manifold are due to Zatsarinny and Bartschat [102]. Figure 4.1 shows the excitation cross sections due to electron-impact from the ground state to the 4s levels. The cross sections of Zatsarinny and Bartschat are obtained from from a semi-relativistic Breit-Pauli B-spline R-matrix calculation of e-Ar collisions. Drawin's formulas have been used for all other transitions.

The electron-impact ionization cross sections have been determined from the Deutsch-Märk (DM) formalism [103].

$$\sigma_i^e(E) = g_{nl}\pi r_{nl}^2 \xi_{nl} f_i(E) \quad (4.67)$$

where g_{nl} are the reduced weighting factors, r_{nl} are the radii of the valence electron, and

$$f_i(E) = d \frac{I_i}{E} \left(\frac{E/I_i - 1}{E/I_i + 1} \right)^a \times \left[b + c \left(1 - \frac{I_i}{2E} \right) \ln(2.7 + (E/I_i - 1)^{1/2}) \right] \quad (4.68)$$

The necessary parameters for equations (4.67) and (4.68) are given in Tables 4.4 and 4.5. The results of the ionization cross sections due to electron-impact collisions are shown in figure 4.2.

The Einstein coefficients for the all the bound-bound transitions are taken from the NIST database [98]. The radiative capture cross sections are determined

Valence electron shell, $n\ell$	$r_{n\ell}$ [\AA]	$g_{n\ell} \times I_{n\ell}$ [eV]
$4s$	2.49	7.40
$5s$	6.35	6.35
$4p$	3.40	31.00
$3d$	4.36	13.60

Table 4.5: Radii of Ar valence electron and reduced weighting factors for $\xi = 1$ as taken from [103].

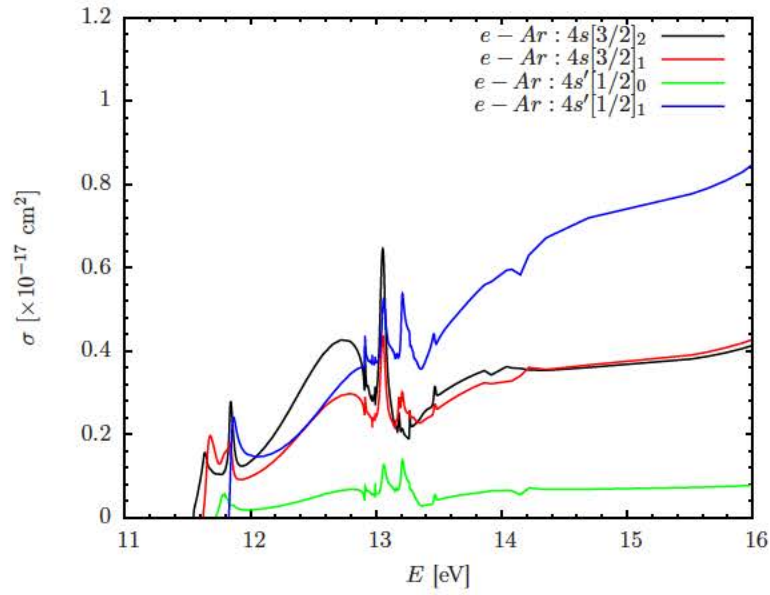


Figure 4.1: Excitation cross sections from ground state to the $4s$ manifold due to electron-impact for Ar I taken from [102].

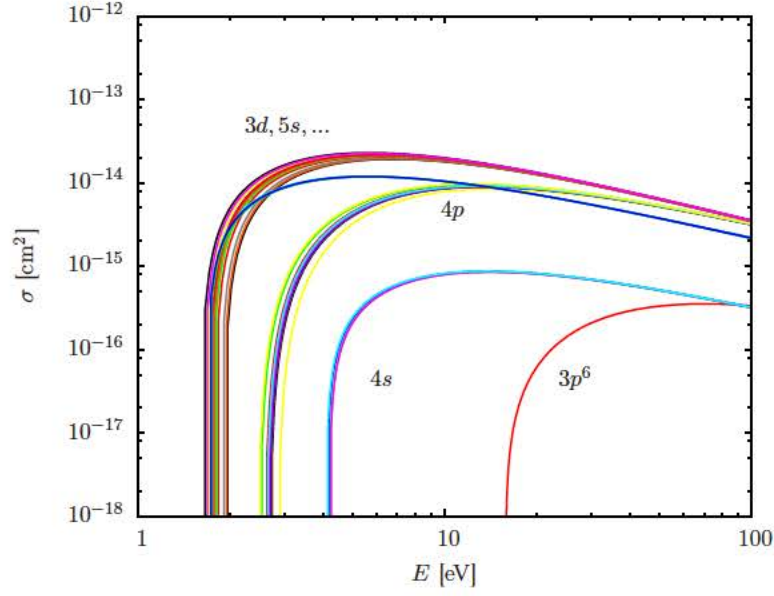


Figure 4.2: Ionization cross sections due to electron-impact for Ar I as computed by the Deutsch-Märk formalism

from detailed balance,

$$\sigma_n^c(\nu) = \frac{g_n}{g_+} \frac{h^2 \nu^2}{m_e^2 \nu_e^2 c^2} \sigma_n^\nu(\nu) \quad (4.69)$$

with the photoionization cross sections given by Vlcěk [91]. Utilizing the relation $h\nu = E + E_i$, the cross section associated with the ground state is given by

$$\sigma_1^\nu(E) = \frac{g_1}{g_+} \frac{(E + E_1)^2}{2Em_e c^2} \times \begin{cases} 3.5 \times 10^{-21} & 0 \leq E \leq 2I_H - E_1 \\ 2.8 \times 10^{-20} \left(\frac{I_H}{E + E_1} \right)^3 & E > 2I_H - E_1 \end{cases} \quad (4.70)$$

while all others are computed using

$$\sigma_i^\nu(E) = \gamma_i \frac{g_i}{g_+} \frac{(E + E_i)^2}{2Em_e c^2} 10^{-22} \times \begin{cases} 2 & 0 \leq E \leq 0.59I_H - E_1 \\ 7.91 \left(\frac{E_i}{I_H} \right)^{5/2} \left(\frac{I_H}{E + E_i} \right)^3 & E > 0.59I_H - E_i \end{cases} \quad (4.71)$$

The parameter γ_i takes the values 0.0763, 0.0458, 0.0305, and 0.0915 for $i = 2$,

Processes	Ref.
Atom-impact exc.	Drawin[99, 100, 92] (allowed trans.) Bultel[92] (others)
Atom-impact ion.	Haugsjaa[101] (ground state) Drawin[99, 100] (others)
Electron-impact exc.	Zatsarinny[102] (from ground state) Drawin[99, 100] (others)
Electron-impact ion.	Deutsch-Märk[103]
Line transition	NIST [98]
Photoionization	Vlcěk[91]
Bremsstrahlung emission	Kramer's formula[83]
Elastic collisions	McEachran[104]

Table 4.6: Summary of the elementary cross sections used in the CR model for Argon

3, 4, and 5, respectively. The cross sections for all the collisional and radiative transitions of Argon are summarized in table 4.6.

4.5.2 Krypton

In a similar fashion, the CR model for Krypton is constructed starting from the electronic levels taken from NIST database [98]. For brevity, only the first 31 excited states, ordered by increasing energy values, are shown in table 4.7.

Similarly to Argon, the atom-impact excitation cross sections for Krypton are computed from equation (4.62) with the linear dependence on energy. The values of χ_{nm}^* are listed in table 4.8. It must be noted that the excitation cross sections from the ground state were calibrated to obtain a reasonable agreement with the experimental induction length. The heavy particle impact ionization cross sections

n	$E(n)$ [eV]	g_n	j_c	$n\ell[K]_J$	n	$E(n)$ [eV]	g_n	j_c	$n\ell[K]_J$
1	0	1	1.5	[Zn]4p ⁶	18	12.144	5	0.5	5p'[3/2] ₂
2	9.915	5	1.5	5s[3/2] ₂	19	12.179	7	1.5	4d[7/2] ₃
3	10.032	3	1.5	5s[3/2] ₁	20	12.256	1	0.5	5p'[1/2] ₀
4	10.562	1	0.5	5s'[1/2] ₀	21	12.258	5	1.5	4d[5/2] ₂
5	10.644	3	0.5	5s'[1/2] ₁	22	12.284	7	1.5	4d[5/2] ₃
6	11.303	3	1.5	5p[1/2] ₁	23	12.352	5	1.5	6s[3/2] ₂
7	11.443	7	1.5	5p[5/2] ₃	24	12.355	3	1.5	4d[3/2] ₁
8	11.445	5	1.5	5p[5/2] ₂	25	12.385	3	1.5	6s[3/2] ₁
9	11.526	3	1.5	5p[3/2] ₁	26	12.756	3	1.5	6p[1/2] ₁
10	11.546	5	1.5	5p[3/2] ₂	27	12.785	7	1.5	6p[5/2] ₃
11	11.666	1	1.5	5p[1/2] ₀	28	12.785	5	1.5	6p[5/2] ₂
12	11.998	1	1.5	4d[1/2] ₀	29	12.803	5	0.5	4d'[3/2] ₂
13	12.037	3	1.5	4d[1/2] ₁	30	12.809	3	1.5	6p[3/2] ₁
14	12.100	3	0.5	5p'[3/2] ₁	31	12.815	5	1.5	6p[3/2] ₂
15	12.112	5	1.5	4d[3/2] ₂	∞	14.000	4	1.5	[Zn]4p ⁵
16	12.125	9	1.5	4d[7/2] ₄	∞'	14.665	2	0.5	[Zn]4p ⁵
17	12.140	3	0.5	5p'[1/2] ₁					

Table 4.7: Lowest 31 levels of Kr I by energy.

n	m	$\chi_{nm}^* [\text{m}^2/\text{eV}]$	n	m	$\chi_{nm}^* [\text{m}^2/\text{eV}]$
1	3	1.11×10^{-23}	3	9	7.01×10^{-22}
1	5	7.93×10^{-24}	3	10	3.68×10^{-22}
2	6	7.15×10^{-22}	3	11	2.44×10^{-22}
2	7	9.93×10^{-22}	3	14	1.20×10^{-23}
2	8	2.57×10^{-22}	4	12	1.09×10^{-21}
2	9	5.05×10^{-23}	4	13	1.15×10^{-21}
2	10	4.41×10^{-22}	5	12	5.96×10^{-22}
2	13	3.79×10^{-24}	5	13	4.22×10^{-22}
2	14	8.32×10^{-25}	5	14	1.26×10^{-21}
3	8	1.31×10^{-21}	5	15	2.36×10^{-22}

Table 4.8: Atom impact excitation parameters for allowed transitions for Krypton.

are computed from the Drawin's formula.

For electron-impact transitions, we have utilized the the cross sections from the work of Zatsarinny and Bartschat [105]. These cross sections are determined from a semi relativistic Breit-Pauli B-spline R-matrix calculation. Figure 4.3 show the cross sections for excitation to the $5s$ manifold. For all other transitions, Drawin's formula has been used systematically. The DM formula has been used for all the ionization cross sections. In particular, we have only considered the $5s$ sub-shell for computing ionization from the core. For the excited states, we have considered the electron in the valence shell. The results of the ionization cross sections due to electron-impact collisions computed with the DM formalism are shown in figure 4.4.

For the radiative combination rates, we have used the same form of the cross sections given by Vlcěk [91] for Argon where the coefficients are tuned to match with the radiative cooling slope from experimental data. The cross sections for all

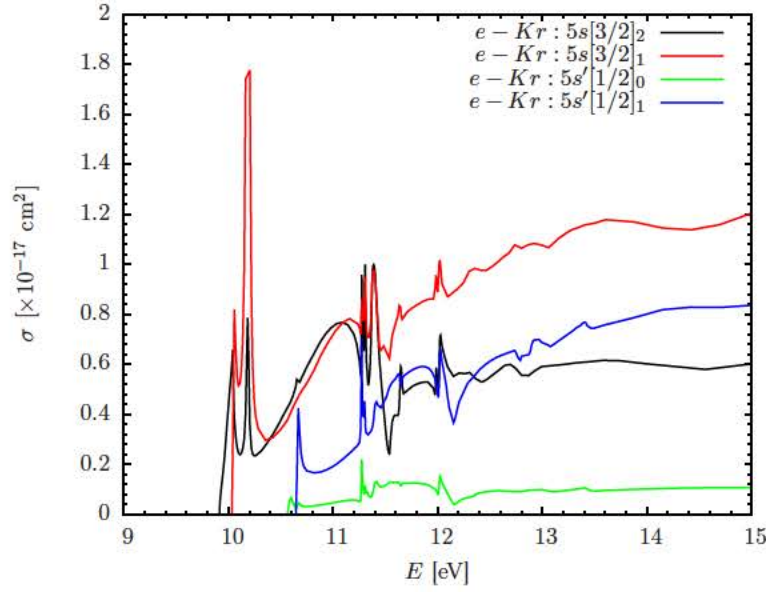


Figure 4.3: Excitation cross sections from ground state to the $5s$ manifold due to electron-impact for Kr I taken from [105].

the collisional and radiative transitions of Krypton are summarized in table 4.9.

4.5.3 Xenon

The CR model for Xenon is constructed similarly to Argon and Krypton. Table 4.10 lists the first 31 excited levels of Xenon ordered by increasing energy values. All the electronic energy of the excited states as well as the oscillator strength of the allowed transition are taken from the NIST database [98]. The effect of spin-orbit splitting of the ion due to different core angular momentum j_c is similar to those of Argon and Krypton.

The atom-impact processes including excitation and ionization have been computed from Drawin's formula. The values of χ_{nm}^* are provided in table 4.11. The electron-impact excitation cross sections from the ground state are computed by Zatsarinny and Bartschat using R-matrix calculation [105]. The excitation cross sections from the ground state to all the $6s$ levels are plotted in figure 4.5.

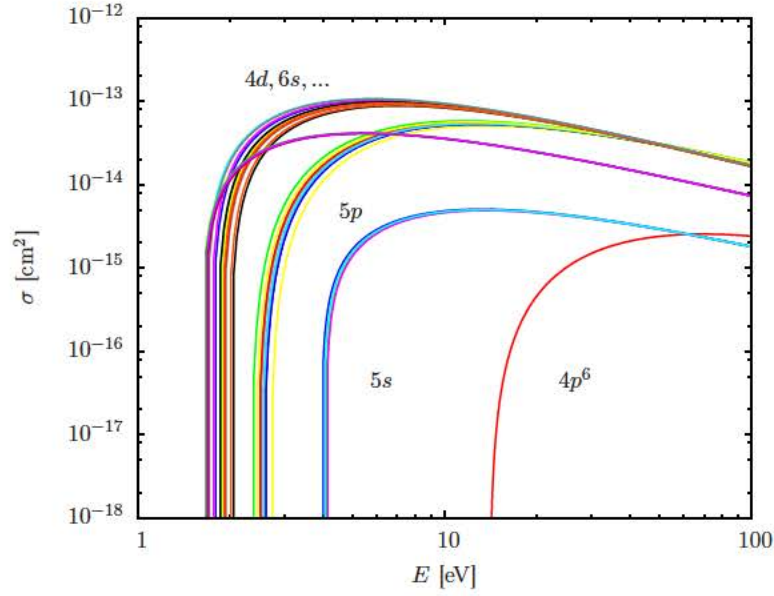


Figure 4.4: Ionization cross sections due to electron-impact for Kr I as computed by the Deutsch-Märk formalism

Processes	Ref.
Atom-impact exc.	Drawin[99, 100]
Atom-impact ion.	Drawin[99, 100]
Electron-impact exc.	Zatsarinny[105] (from ground state) Drawin[99, 100] (others)
Electron-impact ion.	Deutsch-Märk[103]
Line transition	NIST [98]
Photoionization	Modified Vlcěk[91]
Bremsstrahlung emission	Kramer's formula[83]
Elastic collisions	Mitroy[106] & McEachran[107]

Table 4.9: Summary of the elementary cross sections used in the CR model for Krypton

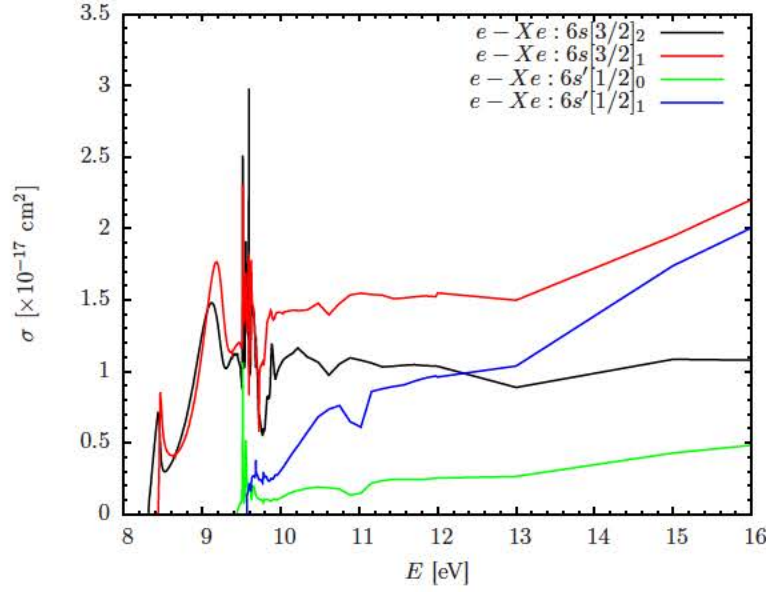


Figure 4.5: Excitation cross sections from ground state to the $6s$ manifold due to electron-impact for Xe I taken from [105].

For electron-impact ionization of the ground state, $6s$ and $6p$ levels, we used the cross sections of Erwin and Kunc [108], which are plotted in figure 4.6. For ionization from higher levels, DM formalism is used. Due to the lack of available cross sections for radiative combination, we have utilized the formula given by Vlcěk [91]. The cross sections for all the collisional and radiative transitions of Xenon are summarized in table 4.12.

4.5.4 Electron-neutral elastic collisions

The momentum transfer cross sections of elastic collisions with electrons for Argon, Krypton, and Xenon are taken from the works of McEachran [104, 107] and Mitroy [106]. The results of these cross sections are shown in figure 4.7. The comparison with the results of Zatsarinny *et al.* [109] are excellent for all cases.

n	$E(n)$ [eV]	g_n	j_c	$n\ell[K]_J$	n	$E(n)$ [eV]	g_n	j_c	$n\ell[K]_J$
1	0	1	1.5	[Cd]5p ⁶	18	10.220	7	1.5	5d[5/2] ₃
2	8.315	5	1.5	6s[3/2] ₂	19	10.401	3	1.5	5d[3/2] ₁
3	8.437	3	1.5	6s[3/2] ₁	20	10.562	5	1.5	7s[3/2] ₂
4	9.447	1	0.5	6s'[1/2] ₀	21	10.593	3	1.5	7s[3/2] ₁
5	9.570	3	0.5	6s'[1/2] ₁	22	10.902	3	1.5	7p[1/2] ₁
6	9.580	3	1.5	6p[1/2] ₁	23	10.954	5	1.5	7p[5/2] ₂
7	9.686	5	1.5	6p[5/2] ₂	24	10.958	3	0.5	6p'[3/2] ₁
8	9.721	7	1.5	6p[5/2] ₃	25	10.969	7	1.5	7p[5/2] ₃
9	9.789	3	1.5	6p[3/2] ₁	26	10.971	1	1.5	6d[1/2] ₀
10	9.821	5	1.5	6p[3/2] ₂	27	10.979	3	1.5	6d[1/2] ₁
11	9.890	1	1.5	5d[1/2] ₀	28	10.996	5	1.5	7p[3/2] ₂
12	9.917	3	1.5	5d[1/2] ₁	29	10.998	5	1.5	6d[3/2] ₂
13	9.933	1	1.5	6p[1/2] ₀	30	11.003	3	1.5	7p[3/2] ₁
14	9.943	9	1.5	5d[7/2] ₄	31	11.015	1	1.5	7p[1/2] ₀
15	9.959	5	1.5	5d[3/2] ₂	∞	12.130	4	1.5	[Cd]5p ⁵
16	10.039	7	1.5	5d[7/2] ₃	∞'	13.436	2	0.5	[Cd]5p ⁵
17	10.157	5	1.5	5d[5/2] ₂					

Table 4.10: Lowest 31 levels of Xe I by energy

n	m	$\chi_{nm}^* [\text{m}^2/\text{eV}]$	n	m	$\chi_{nm}^* [\text{m}^2/\text{eV}]$
1	3	1.16×10^{-22}	2	9	1.42×10^{-23}
1	5	5.41×10^{-23}	2	25	1.74×10^{-24}
1	12	2.56×10^{-24}	2	28	8.46×10^{-25}
1	19	9.06×10^{-23}	3	31	1.16×10^{-24}
1	21	2.12×10^{-23}	4	30	1.62×10^{-23}
1	27	4.82×10^{-25}			

Table 4.11: Atom impact excitation parameters for allowed transitions for Xenon.

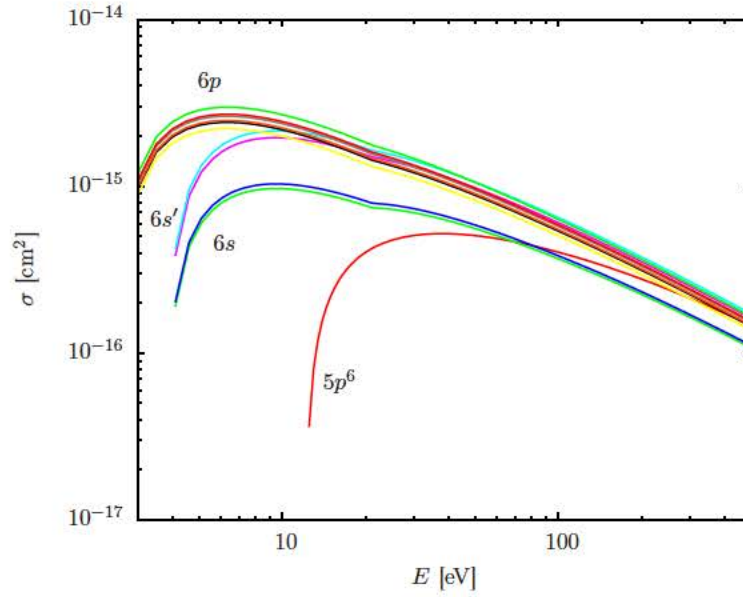


Figure 4.6: Ionization cross sections due to electron-impact for Xe I as computed from the work of Erwin and Kunc [108].

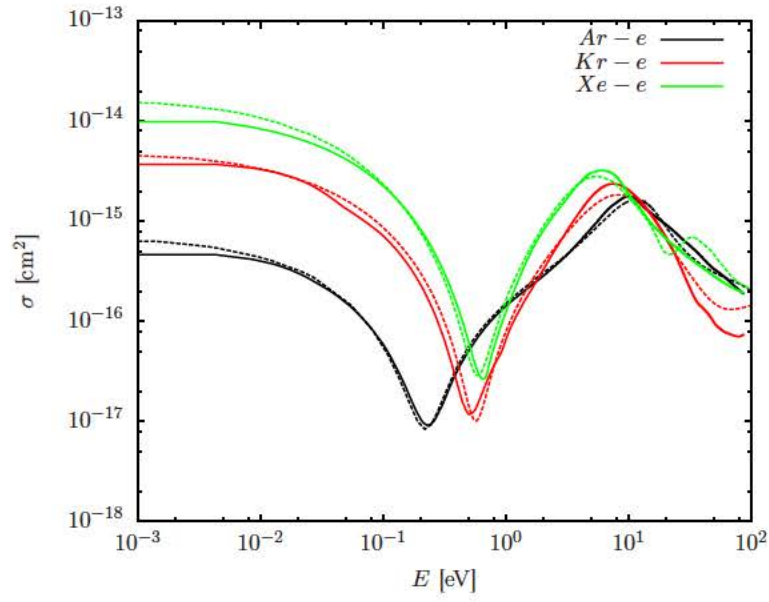


Figure 4.7: Momentum transfer cross sections for Argon, Krypton and Xenon. Solid lines are the results of McEachran *et al.* [104, 107]. Dashed lines are the results of Zatsarinny *et al.* [109].

Processes	Ref.
Atom-impact exc.	Drawin[99, 100]
Atom-impact ion.	Drawin[99, 100]
Electron-impact exc.	Zatsarinny[105] (from ground state) Drawin[99, 100] (others)
Electron-impact ion.	Erwin & Kunc[108] ($5p^6$, $6s$, $6p$) Deutsch-Märk[103] (others)
Line transition	NIST[98]
Photoionization	Modified Vlcěk[91]
Bremsstrahlung emission	Kramer's formula[83]
Elastic collisions	Mitroy[106] & McEachran[107]

Table 4.12: Summary of the elementary cross sections used in the CR model for Xenon

4.6 Benchmark studies

4.6.1 Steady-state flows

The CR models described in the previous section for Argon and Krypton are utilized to model the experiments performed at University of Toronto's Institute of Aerospace Studies (UTIAS) in 1977 [110, 111]. Neglecting unsteady effects, the flow properties of an ionizing shock layer can be computed by solving the steady 2T Euler equations with coupling source terms due to kinetics. The procedure for solving this equation is given in appendix B.

The UTIAS experiments provided detailed measurements of the electron number density and the total mass density of the flow behind the shock including the relaxation length as well as the radiative cooling region. The measurement of the induction length is particularly helpful for calibrating the atom-impact excitation

Cases	Ma	p_∞ (Torr)	T_∞ (K)	l^* (cm)
1	15.9	5.14	293.6	2.00
2	16.1	5.15	295.9	1.90
3	16.5	5.12	296.6	1.80
4	13.0	5.00	296.6	8.90

Table 4.13: Summary of test conditions of the UTIAS experiments for ionizing shock in Argon with the predicted thermal equilibrium flow properties. Data are taken from Glass and Liu [110].

rate. For the case of Argon, four different experimental conditions were used to assess the current CR model. The test conditions along with the experimentally measured relaxation lengths [110] are summarized in table 4.13.

Figure 4.8 shows a comparison of the computed electron number density and the total mass density along with the experimental data. It must be noted that acceptable agreement in the relaxation length was obtained by tuning the atom-impact cross sections. The calculation is performed utilizing 31 electronic states of neutral Argon. It has been shown that this level of details is required for an accurate prediction of the radiative cooling region [90]. This is because a major source of radiation is due to line radiation from the upper states. It must be pointed out that since radiation transport is not included, line radiation and radiative recombination are computed with the help of the escape factor. The value of the escape factors (either 1 or 0) is determined by an order of magnitude analysis of the radiation's mean-free-path compared with the shock tube dimension.

The temperature profile of the electrons and the heavy particles for the same test case is shown in figure 4.9, which help identifying severe regimes marking the transition from the atom-impact dominated kinetics to electron-impact dominated kinetics. In addition, figure 4.10 shows the ASDF at several locations behind

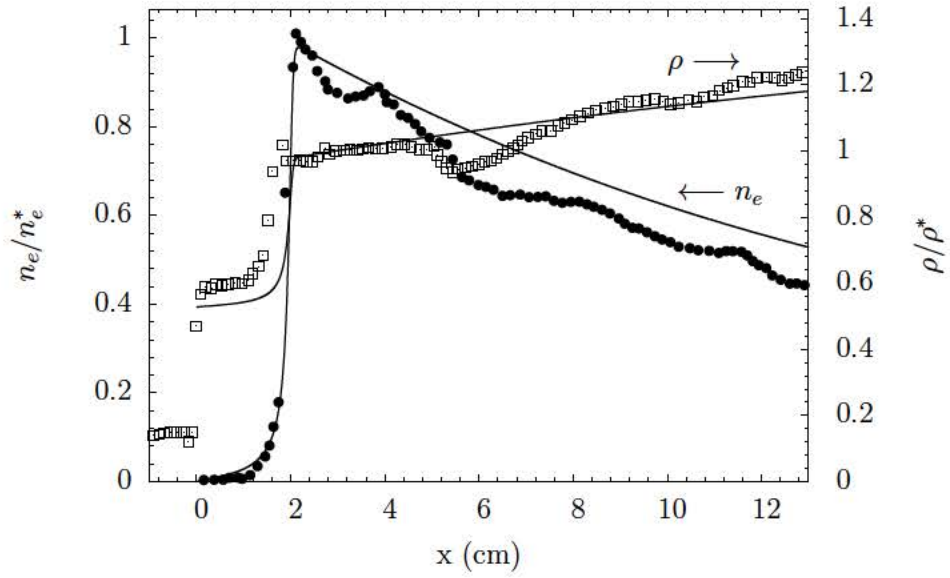


Figure 4.8: Computed and experimental results of ionizing shock in Argon for case 1: $p_\infty = 5.14$ Torr, $T_\infty = 293.6$ K, $Ma = 15.9$. The values of the electron number density and the total mass density are normalized by the equilibrium values: $n_e^* = 1.69 \times 10^{17} \text{ cm}^{-3}$, $\rho^* = 8.4 \times 10^{-3} \text{ g/cm}^3$. Symbols represent experimental data for n_e and ρ from Glass and Liu [110].

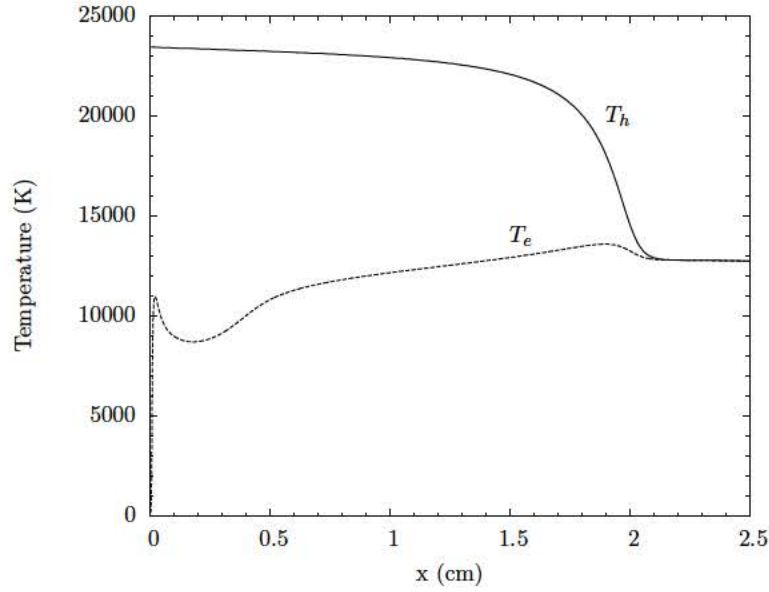


Figure 4.9: Temperature profile of the electrons and heavy particles for case 1 from table 4.13.

the shock. One can see in the region where the priming electrons are produced ($x = 0.01$ cm) and where electron kinetics starts to dominate ($x = 0.1$ cm), the ASDF exhibits a non-Boltzmann behavior, presumably due to a competition between the atom-impact and electron-impact processes. Further downstream from the shock, the ASDF relaxes toward a Boltzmann distribution.

It can be seen that all the upper levels beyond the $4s$ manifold in this test case can be well approximated by a Boltzmann distribution. This small deviation from a Boltzmann distribution (notably only from the $4s$ manifold) indicates that the flow might be approximated by a three-temperature model; however, one still needs to model the losses due to radiation in order to resolve the radiative cooling region behind the avalanche. The results of the steady state calculations for the other three cases are shown in figures 4.11, 4.12 and 4.13. Good agreement is obtained for cases 2 and 3. For case 4, the electron number density and the relaxation length are over-predicted compared to the experimental data. The discrepancies

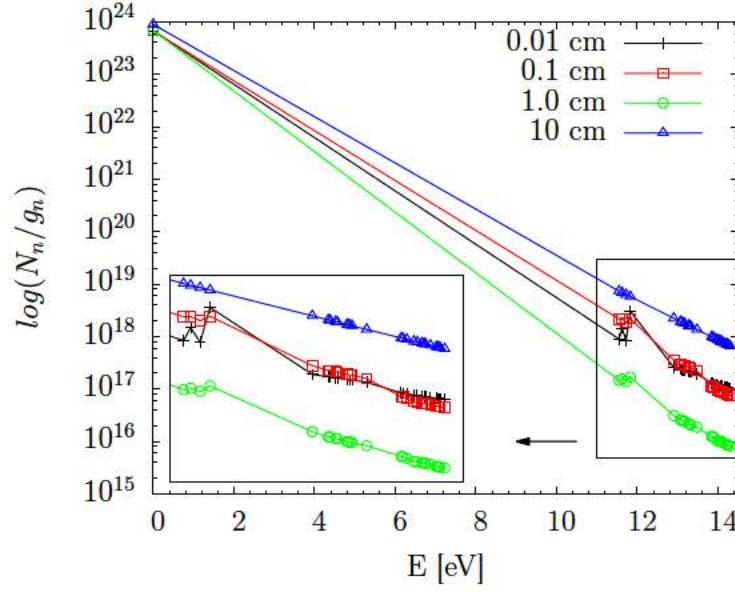


Figure 4.10: The ASDF plotted at different locations of starting from the shock front utilizing the experimental condition from case 1 of table 4.13.

can be attributed to unsteady effects and interaction with the boundary layer, both of which, can be verified by performing unsteady simulations incorporating viscous effects, i.e., solving Navier-Stokes equations.

Similarly, the steady state calculations are performed for the case of Krypton shocks. The flow conditions along with the experimental relaxation length are taken from Glass *et al.* [111] and summarized in table 4.14. The simulation results for case 1 are shown in figures 4.14 and 4.15 for the number densities and temperatures, respectively.

Similar to the Argon shock experiment, with the tuned value of the atom-impact cross section, we were able to obtain good agreement with the experimental relaxation length. For the radiative cooling reason behind the avalanche, the formula of Vlcěk with some modification yields satisfactory results. Non-Boltzmann population of the excited states can be seen most clearly in figure 4.16 at 0.01 and 0.1 cm. The results for case 2 are shown in figure 4.17 with excellent agreement

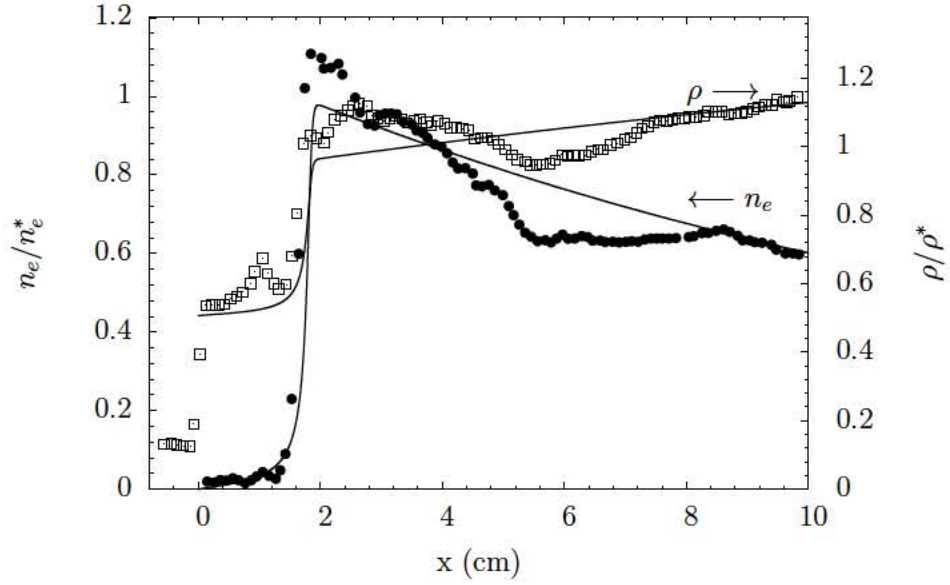


Figure 4.11: Electron number density and total density for $M_\infty = 16.1$ Ar shock corresponded to case 2 in table 4.13. The freestream conditions are: $p_\infty = 5.15$ Torr, $T_\infty = 295.9$ K. The values of the electron number density and the total mass density are normalized by the equilibrium values: $n_e^* = 1.83 \times 10^{17} \text{ cm}^{-3}$, $\rho^* = 0.87 \times 10^{-4} \text{ g/cm}^3$. Symbols represent experimental data for n_e and ρ from Glass and Liu [110].

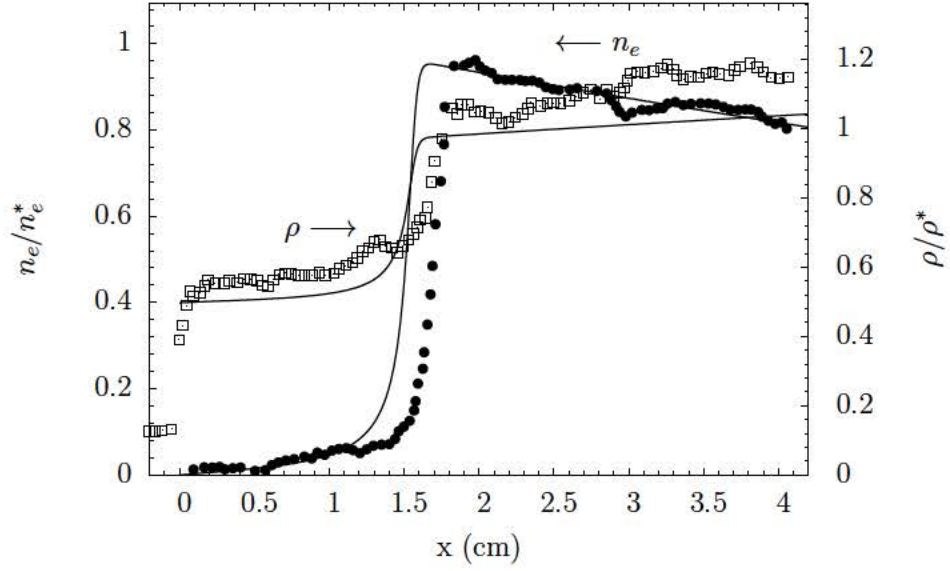


Figure 4.12: Electron number density and total density for $M_\infty = 16.5$ Ar shock corresponded to case 3 in table 4.13. The freestream conditions are: $p_\infty = 5.12$ Torr, $T_\infty = 296.6$ K. The values of the electron number density and the total mass density are normalized by the equilibrium values: $n_e^* = 2.1 \times 10^{17} \text{ cm}^{-3}$, $\rho^* = 0.88 \times 10^{-4} \text{ g/cm}^3$. Symbols represent experimental data for n_e and ρ from Glass and Liu [110].

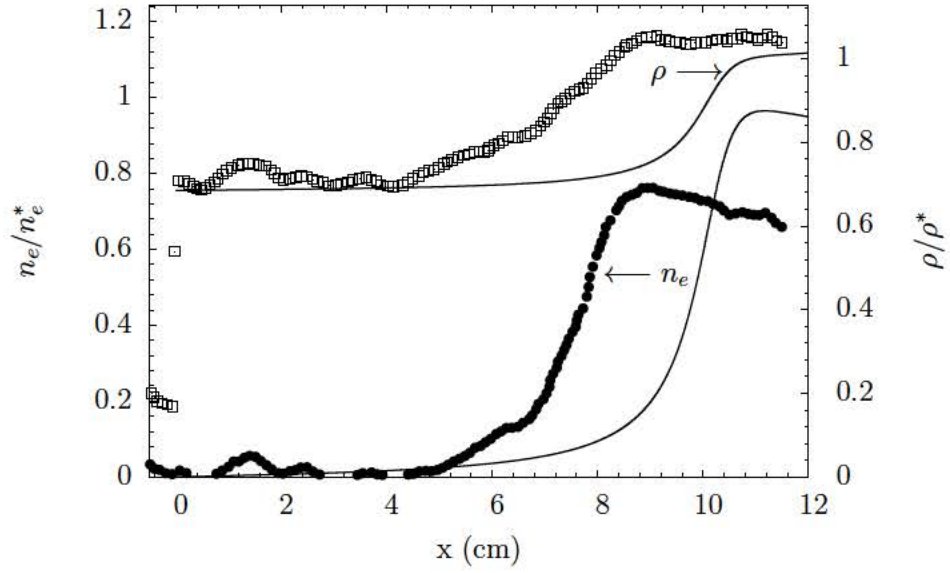


Figure 4.13: Electron number density and total density for $M_\infty = 13.0$ Ar shock corresponded to case 4 in table 4.13. The freestream conditions are: $p_\infty = 5.00$ Torr, $T_\infty = 296.6$ K. The values of the electron number density and the total mass density are normalized by the equilibrium values: $n_e^* = 5.62 \times 10^{16} \text{ cm}^{-3}$, $\rho^* = 0.62 \times 10^{-4} \text{ g/cm}^3$. Symbols represent experimental data for n_e and ρ from Glass and Liu [110].

Cases	Ma	p_∞ (Torr)	T_∞ (K)	l^* (cm)
1	15.05	5.15	296.2	1.75
2	15.17	5.07	295.4	1.90

Table 4.14: Summary of test conditions of the UTIAS experiments for ionizing shocks in Krypton with the predicted thermal equilibrium flow properties. Data are taken from Glass *et al.* [111].

to the experimental data.

Lastly, the CR model for Xenon is utilized to model the shock tube experiment by Ezumi *et al.* [112]. Similar to the UTIAS experiment, Ezumi *et al.* investigated the ionization relaxation and radiative cooling processes of an ionizing shock flow in Xenon. In their experiment, measurement of the electron number density and the heavy particle number density are carried out using interferometric techniques, and the results are taken at one particular location along the shock tube. The shock Mach number is 13.1 and the freestream pressure is 2.0 Torr. Figure 4.18 shows the steady-state calculation of the shock layer, with satisfactory agreement to experiment.

In this test case, due to the high uncertainty in the use of Drawin's formula for atom-impact rates, these rates are tuned to match the experimental relaxation time. Also, due to the lack of the cross sections data for the radiative cooling process, the values obtained from Vlček's expression [91] also need to be slightly modified. Therefore, the results for Xenon shock presented in this section should be considered as preliminary only. In order to improve the model, radiation transport should be included, and better atom-impact cross sections, those computed from ab initio calculation, should be implemented.

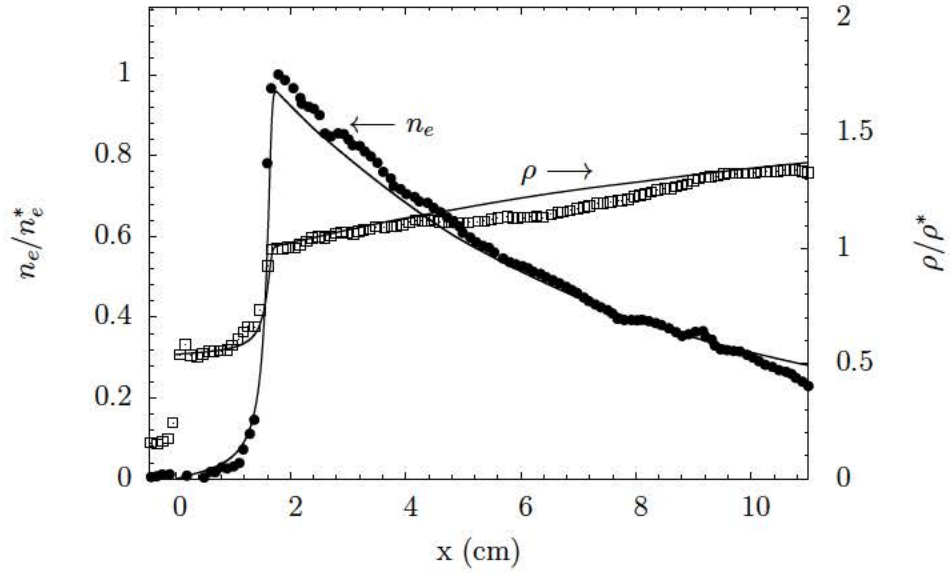


Figure 4.14: Electron number density and total density for $M_\infty = 15.05$ Kr shock corresponded to case 1 in table 4.14. The freestream conditions are: $p_\infty = 5.15$ Torr, $T_\infty = 296.2$ K. The values of the electron number density and the total mass density are normalized by the equilibrium values: $n_e^* = 1.677 \times 10^{17} \text{ cm}^{-3}$, $\rho^* = 1.712 \times 10^{-4} \text{ g/cm}^3$. Symbols represent experimental data for n_e and ρ from Glass *et al.* [111].

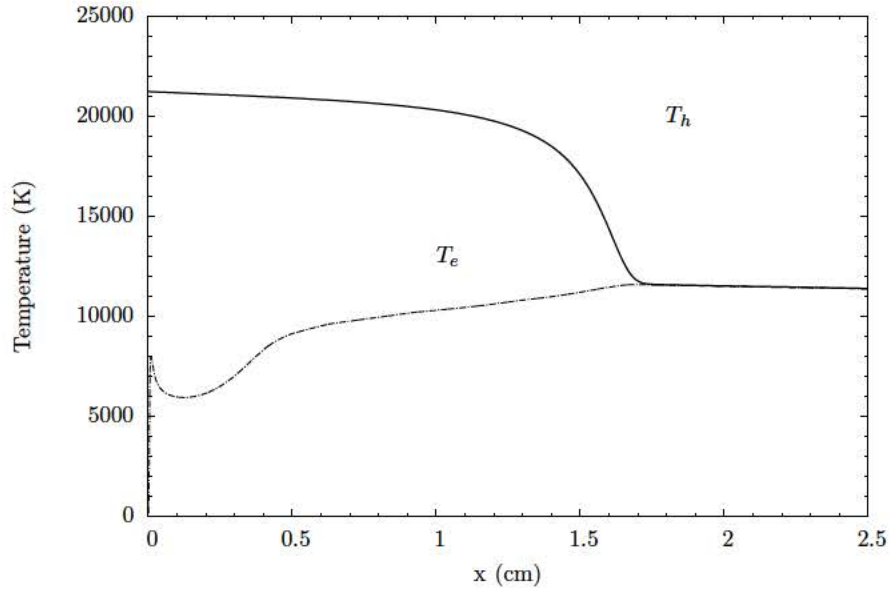


Figure 4.15: Temperature profile of the electrons and heavy particles for case 1 from table 4.14.

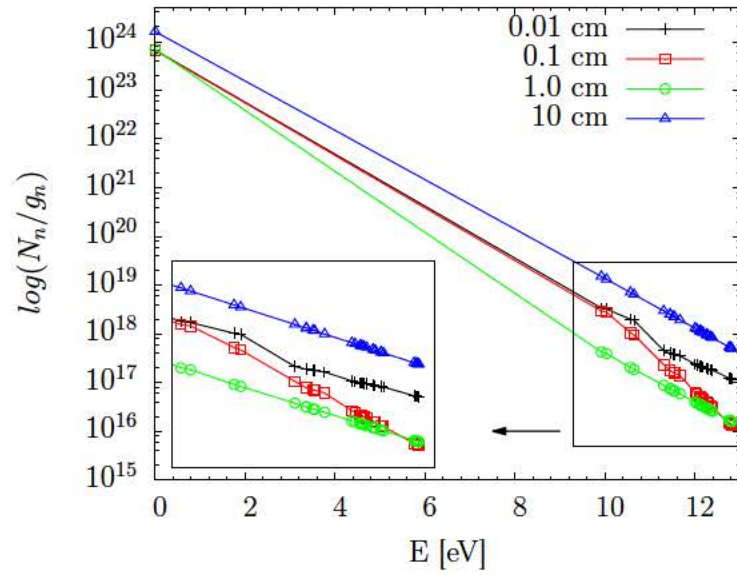


Figure 4.16: The ASDF plotted at different locations of starting from the shock front utilizing the experimental conditions from case 1 of table 4.14.

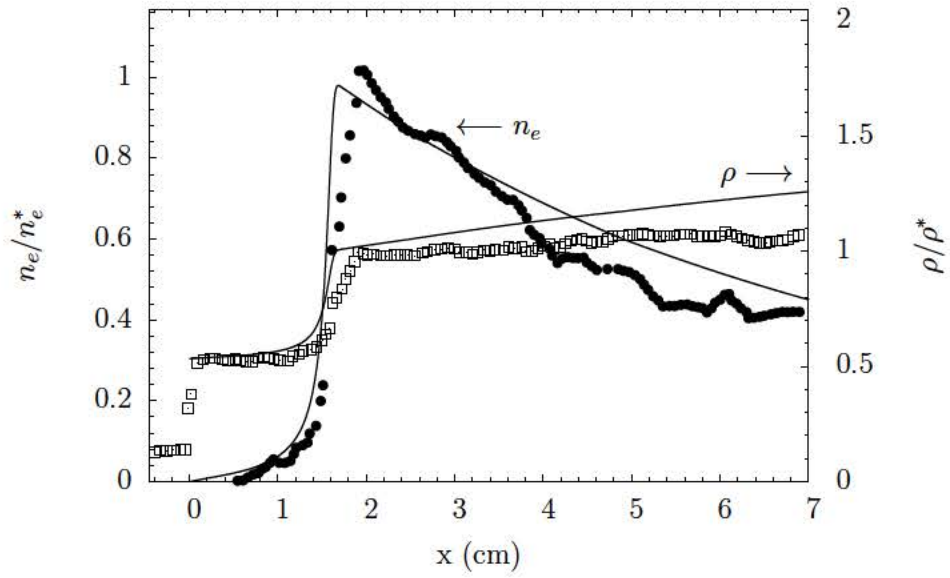


Figure 4.17: Computed and experimental results of ionizing shock in Krypton for case 2: $p_\infty = 5.07$ Torr, $T_\infty = 295.4$ K, $Ma = 15.17$. The values of the electron number density and the total mass density are normalized by the equilibrium values: $n_e^* = 1.712 \times 10^{17} \text{ cm}^{-3}$, $\rho^* = 1.708 \times 10^{-4} \text{ g/cm}^3$. Symbols represent experimental data for n_e and ρ from Glass *et al.* [111].

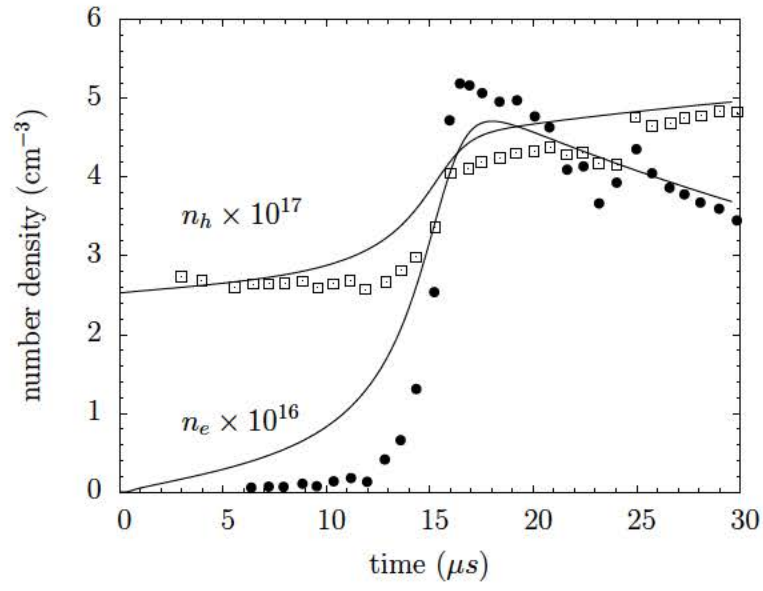


Figure 4.18: Electron number density and heavy particle number density for $M_\infty = 13.1$ Xe shock. Symbols represent experimental data for n_e and n_h from Ezumi *et al.* [112]. The freestream conditions are: $p_\infty = 2.00$ Torr, $T_\infty = 300$ K.

4.6.2 Unsteady flows

In this section, we performed time accurate calculation of the same test cases described in the previous section utilizing the calibrated CR model. The shock is initiated by imposing a uniform flow field on a 1D domain with the right boundary being a reflective wall. The freestream conditions are $T_\infty = 293.6$ K, $p_\infty = 5.14$ Torr, and $u_\infty = 4535$ m/s. The initial condition corresponds to case 1 of table 4.13 for Argon. This test case were studied previously by Kapper and Cambier [97], which reveals complex dynamics of the coupling between convection and chemical kinetics.

In this simulation, the 2T model described in section 2.4 is utilized with detailed kinetic source term as discussed in section 4.4. For the convection term, a third-order MP scheme is used in conjunction with a RK3 scheme for time integration. The reason for using a lower order scheme (as opposed to the 5th order scheme) is due to numerical difficulties encountered in resolving a high density gradient (up to 10 order of magnitude) at the shock.

The origin of such a high density gradient is due to the activation of the CR kinetics right after the shock. In this region, the atom-impact processes start taking place at the rates determined by the post-shock temperature of the heavy species, therefore populating the excited states at a much higher number density compared to the freestream values. In addition, the simplified treatment of the radiative processes also exacerbate the problem. In particular, since the escape factors are pre-determined from an order of magnitude analysis of the radiative mean free path, using the same set of escape factors for all the computational cells causes an artificial radiation in the free steam gas, which effectively lowers the population of the excited states and also raises the electron temperature². These high and low populations of the excited states cause a sharp density gradient

²This electron preheating artifact is specifically due to radiative recombination.

which makes high-order reconstruction schemes unstable. The use of an lower order scheme relieve the problem by introducing more numerical diffusion. This problem can be remedied by including the full solution of radiation transport, therefore avoiding the escape factors.

The results of the time accurate solutions are shown in figures 4.19 and 4.20 for the total mass density and electron number density, respectively. The highly unsteady evolution, especially in the induction zone, suggests a non-linear wave coupling mechanism between the shock and the avalanche layer. The coupling cycle, as indicated by Kapper and Cambier [97], starts with an initiation of a pressure wave travelling from the avalanche toward the shock. This pressure wave causes the shock to accelerate, which results in a reflection of a entropy wave. As the entropy wave travels toward the avalanche layer, the sensitivity of the chemical rates to the temperature rise causes an early new avalanche, and the cycle is repeated. The onset of the new avalanche can be seen most clearly from figure 4.20.

The time period of these cycles can be estimated from basic wave theory [113]:

$$\tau = \bar{l} \left(\frac{1}{a_2 - u_2} + \frac{1}{u_2} \right) \quad (4.72)$$

where \bar{l} is the average induction length, and u_2 and a_2 are the post shock velocity and speed of sound. Figure 4.21 shows the density contour on a $x - t$ diagram. One can clearly see the fluctuation in the induction length, and the periodicity of the shock structure. These features are strictly time-dependent, and cannot be revealed in steady-state simulations. The unsteady simulation shows that the sensitivity of the CR cross sections directly translates to the fluctuating mechanism via non-linear coupling with convection process. It must be pointed out that this mechanism possesses similar characteristics to instability in gaseous detonation, which can also be explained by non-linear wave-coupling [75].

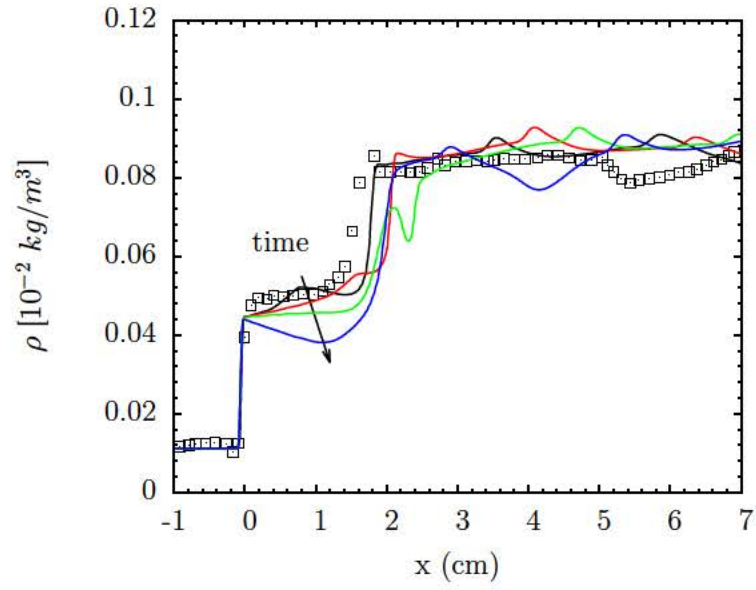


Figure 4.19: Total mass density of ionizing shock in Argon for case 1 of table 4.13. Different lines correspond to the solutions at the different times, and the arrow indicates flow solutions as time increases. The symbols are the experimental data from the UTIAS experiment [110].

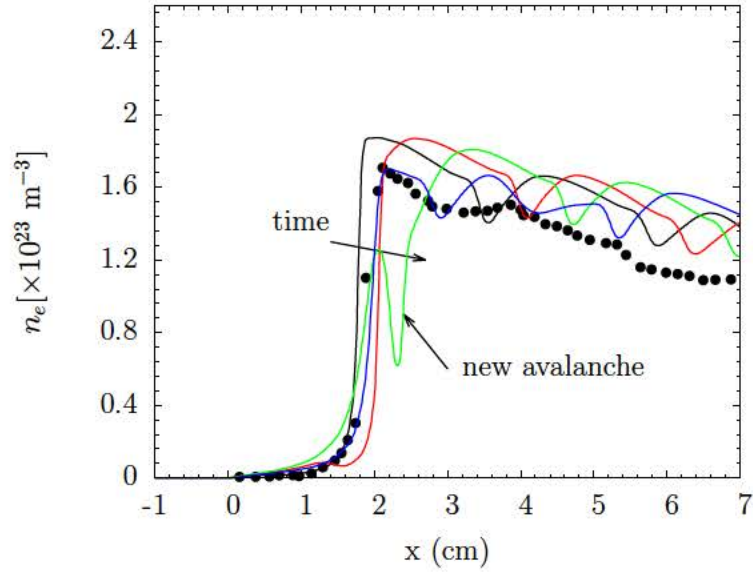


Figure 4.20: Electron number density of ionizing shock in Argon for case 1 of table 4.13. Different lines correspond to the solutions at different times. The symbols are the experimental data from the UTIAS experiment [110].

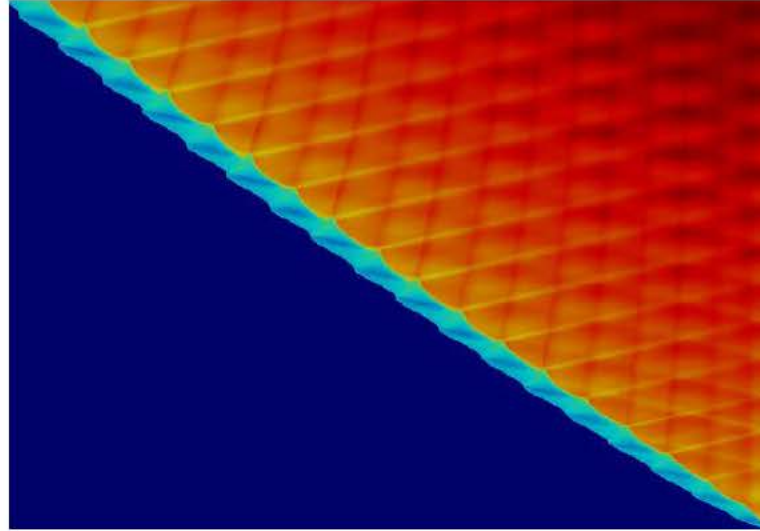


Figure 4.21: $x - t$ diagram of total mass density ρ for a Ma 15.9 ionizing shock in Argon showing complex dynamics of the coupling between convection and kinetics. Colormap: min ■ ■ max

CHAPTER 5

Complexity Reduction of Collisional-Radiative Kinetics

This chapter was taken with slight modification from the article “Complexity reduction of collisional-radiative kinetics for atomic plasma”, published in *Physics of Plasmas* [114].

5.1 Introduction

In the previous chapter, we demonstrate the use of the CR model in reproducing the correct structure of an ionizing shock in monatomic gases. This level of detail is needed for an accurate prediction of high-speed plasma flows. In addition, the unsteady coupling of the hydrodynamics and CR kinetics leads to physical phenomena which can, in turn, provide additional information useful for model validation and/or experimental measurement of various parameters. These CR models, although very accurate from a physics point of view, can be computationally very expensive due to the large number of internal states for which the number densities must be computed. For example, in the ionizing shock test case shown in section 4.6.1 for Argon, one needs to include excited states beyond the 4s manifold to accurately capture the line radiation responsible for the radiative cooling region behind the shock.

Due to the large computational workload involved in solving the CR master equations, simulations incorporating state-to-state kinetics have only been limited

to zero- or one-dimension with a few exceptions of two-dimensional calculations [115, 116, 90]. For example, the run-time for solving a set of rate equations for the CR kinetics of atomic hydrogen scales as the cubic power of the size of the ASDF when an implicit, backward-Euler method is employed. While better scaling laws could be obtained with iterative and more approximate schemes, their accuracy and stability for extremely stiff problems is still an issue.

The development of very efficient and accurate schemes for CR kinetics is still an ongoing research topic which will be presented elsewhere; here, we discuss a different approach, consisting of lowering the complexity of the calculations by developing a reduced-order kinetic model suitable for multi-dimensional flow calculations while maintaining a sufficient level of detail required to accurately model the plasma.

Several mechanism reduction schemes have been proposed in the literature with applications to various types of kinetics. Colonna *et al.* [117] utilize a two-level distribution model to study nitrogen dissociation rates in recombining flows, in which all the vibrational levels except for the last level are modeled by a single energy equation with an assumption of a Boltzmann distribution, and the last vibrational level is modeled using state-to-state kinetics to take in account the non-equilibrium effects of the upper states. Magin *et al.* [36] have developed a rovibrational collisional coarse-grain model to characterize the internal energy excitation and dissociation processes of nitrogen flow behind a strong shock wave. The coarse-grain model is derived by lumping the rovibrational energy levels into groups, in which the population is described by a uniform distribution. Guy *et al.* [37] proposed a multi-internal-temperatures models for a vibrationally non-equilibrium flow, in which the vibrational distribution is divided into two or three groups, each with its own vibrational temperature. Liu *et al.* [118], on the other hand, proposed a mechanism reduction to CR models based on the multi-group maximum entropy principle with the constraints being the macroscopic parame-

ters.

In this chapter, we examine several different level grouping schemes for the state-to-state kinetics of *atomic* electronic states. The first approach is similar to that of Magin *et al.* [36] for the rovibrational collisional coarse-grain model, and therefore is based on uniform (U) binning of the levels. The second approach here consists of grouping levels into groups with an assumed Boltzmann (B) distribution, allowing a higher-order description of the ASDF. In this case, the effective excitation temperatures are evolved in time by conserving a set of moments of the distribution function; the most obvious solution is to solve for number density and energy, similar to Guys *et al.*'s approach [37]. However, we will show that a different set of moment variables of the same order should be used, due to the specific nature of the ASDF.

The method developed here can be applied to a wide range of state-to-state kinetics models including the rovibrational [36, 58] (RVC) and vibrational [119] (VC) collisional models or the electronic collisional-radiative model [90, 91, 120, 121]. In the interest of simplicity, we consider here the collisional-radiative (CR) model of atomic Hydrogen, using classical models for the level energies and rates; the actual values of these parameters is unimportant here, as long as the structure of the ASDF is representative of the actual species, notably the geometric progression of the level energies of the ASDF and the stiffness ratio. The level grouping techniques are applied to reduce the cost of solving the full master equations and the results are compared with the reference solution computed from the full master equations.

5.2 Collisional-Radiative model

5.2.1 Definitions and rates

As mentioned above, we consider here the ASDF of atomic Hydrogen coupled to electron impact excitation and ionization, and the reverse processes (respectively deexcitation and recombination), as well as the radiative rates for line transitions in an optically-thin approximation. Radiative recombination is neglected and all radiation absorption is ignored, as is free-free (Bremsstrahlung) emission, since this does not directly affect the atomic level populations¹. The atomic states of the Hydrogen atom are listed as a function of their principal quantum number (n) only, following the Bohr atomic model; the splitting of states with respect to orbital and spin numbers is ignored, and all states have a degeneracy $g_n = 2n^2$. The states number from $n = 1$ to ∞ and we consider a finite number of states $n = 1, \dots, M < \infty$ before reaching the ionization limit². In this simplified model, the energy of each state is given as $E_n = I_H (1 - 1/n^2)$, as measured from the ground state ($E_1 \equiv 0$), and we will denote by $I_n = I_H (1/n^2 - 1/M^2) \simeq I_H/n^2$ the energy required for ionization of level n .

The classical form of the cross-section for energy exchange between a free electron and the atom [83], leading to an excitation from level n to level $m > n$ is:

$$\sigma_{nm}^e = (4\pi a_0^2) \frac{I_H^2 (E - \Delta E_{nm})}{E_{nm} E^2} \cdot (3f_{nm}) \quad (5.1)$$

where a_0 is the Bohr radius, E is the energy of the free electron, $\Delta E_{nm} = E_m - E_n$

¹Two of the test cases considered here are isothermal, i.e. $T_e = \text{constant}$. The third test case has a variable T_e but is designed only to test energy conservation, and hence radiative energy losses would not serve this purpose.

²Strictly speaking, the ionization limit I_H is attained for $n \rightarrow \infty$. In reality, the ionization potential is lowered as a result of interaction with the plasma (Debye shielding) and quantum uncertainty. In practice, the truncation is accomplished at a lower limit still; for the current purpose, details of this truncation procedure can be ignored. Suffice to say that the series extends to a number $n = M$, which can be considered large, e.g. $O(100)$.

is the energy gap between n and m and f_{nm} is the oscillator strength:

$$f_{nm} = \frac{32}{3\pi\sqrt{3}} \frac{1}{n^5} \frac{1}{m^3} \frac{1}{\left(\frac{1}{n^2} - \frac{1}{m^2}\right)^3} \quad (5.2)$$

The free electrons are assumed to follow an isotropic Maxwellian distribution, i.e., equation (4.11). The rate of excitation is obtained by averaging over the distribution function:

$$\alpha_{(m|n)}^e = \frac{\bar{v}_e}{(kT_e)^2} \int_{E_{nm}}^{\infty} \sigma_{nm}^e(E) E f_e(E) dE, \quad (5.3)$$

leading to

$$\alpha_{(m|n)}^e = (4\pi a_0^2) \bar{v}_e \left(\frac{I_H}{kT_e} \right)^2 (3f_{nm}) \psi_{nm} \quad (5.4)$$

where

$$\bar{v}_e = \left(\frac{8kT_e}{\pi m_e} \right)^{\frac{1}{2}}, \quad \psi_{nm} = \frac{e^{-x_{nm}}}{x_{nm}} - E_1(x_{nm}) \quad \text{and} \quad E_1(x) = \int_x^{\infty} \frac{e^{-y}}{y} dy \quad (5.5)$$

Here, \bar{v}_e is the mean thermal electron velocity, $x_{nm} = \Delta E_{nm}/kT_e$ and E_1 is the exponential integral. The reverse rate can be found from detailed balance:

$$\beta_{(n|m)}^e = \frac{n^2}{m^2} e^{+x_{nm}} \cdot \alpha_{(m|n)}^e \quad (5.6)$$

We use the low temperature approximation [83] ($x_{nm} \gg 1$)

$$E_1(x) \simeq \frac{e^{-x}}{x} \left(1 - \frac{1}{x} \right), \quad (5.7)$$

in which case:

$$\alpha_{(m|n)}^e \simeq \left[4\pi a_0^2 \cdot \frac{32}{\pi\sqrt{3}} \cdot \bar{v}_e \right] \frac{e^{-x_{nm}}}{n^5 m^3 (n^{-2} - m^{-2})^5} \quad (5.8a)$$

$$\beta_{(n|m)}^e \simeq \left[4\pi a_0^2 \cdot \frac{32}{\pi\sqrt{3}} \cdot \bar{v}_e \right] \frac{1}{n^3 m^5 (n^{-2} - m^{-2})^5} \quad (5.8b)$$

The factor in brackets is an upper bound, which is reached for the upper states when $x_{nm} \rightarrow 0$. Another scale is the factor I_H/kT_e in x_{nm} , which is effectively responsible for the stiffness. If that factor is very low (high temperatures), all

rates are of the same order; at low temperatures, the exponential term dominates and the range of time scales is increased.

The cross-section for ionization by electron impact has a form similar to (5.1), i.e.:

$$\sigma_n^e = (4\pi a_0^2) \frac{I_H^2 (E - I_n)}{I_n E^2} \quad (5.9)$$

This leads to an ionization rate coefficient [83]:

$$\alpha_{(+|n)}^e = (4\pi a_0^2) \bar{v}_e \left(\frac{I_H}{kT_e} \right)^2 \psi(x_n) \quad (5.10)$$

The final state $(+|$ is an ionized state, i.e. where one electron initially bound to the atom has reached the ionization limit ($n = \infty$) and is part of a free continuum of states. Using the principle of detailed balance, the reverse (recombination) rate is:

$$\beta_{(n|+)}^e \simeq \left[\frac{4}{\pi} \frac{a_0^2 h^3}{m_e^2 k T_e} \right] \left(\frac{I_H}{k T_e} \right)^2 n^2 \psi(x_n) e^{x_n} \quad (5.11)$$

Using the same low temperature approximation (5.7), we obtain [83]:

$$\alpha_{(+|n)}^e \simeq (4\pi a_0^2) \left(\frac{8kT_e}{\pi m_e} \right)^{1/2} n^4 e^{-x_n} \quad (5.12a)$$

$$\beta_{(n|+)}^e \simeq \left[\frac{4}{\pi} \frac{a_0^2 h^3}{m_e^2 k T_e} \right] n^6 \quad (5.12b)$$

The rates of radiative transitions between levels can also be obtained classically for the Hydrogen atom [86]. The spontaneous emission rates from an upper level m are:

$$A_{(n|m)} = \left(\frac{8\pi^2 e^2}{m_e c^3} \right) \frac{g_n}{g_m} f_{nm} = \frac{1.6 \times 10^{10}}{m^3 n (m^2 - n^2)} \text{sec}^{-1} \quad (5.13)$$

The expression on the right is for atomic Hydrogen only.

5.2.2 Master equations

Once all the macroscopic rates are obtained, we can construct the master equations describing the collisional-radiative kinetics of all levels. In this study we consider

atomic Hydrogen, which has only one ion state, and only electron collisions, which allows us to remove the super-script e in the rate definition hereafter. The rate of change of the population density of a level n is thus written as:

$$\begin{aligned} \frac{dN_n}{dt} = & - \sum_{m>n} \alpha_{(m|n)} N_e N_n + \sum_{m>n} \beta_{(n|m)} N_e N_m + \sum_{m>n} A_{(n|m)} N_m \\ & + \sum_{m<n} \alpha_{(n|m)} N_e N_m - \sum_{m<n} \beta_{(m|n)} N_e N_n - \sum_{m<n} A_{(m|n)} N_n \\ & - \alpha_{(+|n)} N_e N_n + \beta_{(n|+)} N_+ N_e^2 \end{aligned} \quad (5.14)$$

Similarly, we can write another equation for the rate of change of the population density of the ions according to the rate of ionization or recombination:

$$\frac{dN_+}{dt} = \sum_n \alpha_{(+|n)} N_e N_n - \sum_n \beta_{(n|+)} N_+ N_e^2 \quad (5.15)$$

Finally, the electron density is related to the ion density by the charge neutrality condition:

$$N_e = \sum_q Z_q N_q \quad (5.16)$$

We will compute the time evolution of a uniform plasma; if we assume a constant temperature bath, the conservation equations above constitute a complete set, but for constant-volume conditions – with time variation of the temperature – there is also conservation equation for the electron energy, which will be examined in more detail in section 5.5. The task of deriving a reduced model for the CR kinetics aims at modeling the shape of the atomic state distribution function (ASDF) at a lower computational cost compared to that required to solve the full master equations, while maintaining sufficient accuracy to capture the non-equilibrium effects. The most natural way to accomplish this is to partition the excited states into groups or “bins”, therefore reducing the number of variables in the system. Various assumptions can be made about the internal structure of each group, i.e. the distribution of states *within* the groups, and various approaches to solving the group-based variables can be devised.

5.3 Level grouping strategies

5.3.1 Uniform grouping

Consider a group of M individual levels $i = \{n_0, \dots, n_{M-1}\}$, abbreviated as $i \in n$ and denote the group, or “bin” number by n ; hereafter, n, m, \dots are the group indices and i, j, \dots are level indices. This first approach to model reduction is essentially a zeroth-order approximation of the internal³ distribution function, where only one moment variable, either the total number density of the group or the total excitation energy of the group, is required. The traditional choice is to conserve the total number density of the group, i.e., $\mathcal{N}_n = \sum_{i \in n} N_i$. Using (4.32), a Boltzmann approximation of the internal partition function \mathcal{Z}_n is obtained by⁴:

$$\mathcal{N}_n = N_{n_0} \sum_{i \in n} \frac{N_i}{N_{n_0}} \simeq \frac{N_{n_0}}{g_{n_0}} \underbrace{\sum_{i \in n} g_i e^{-\Delta E_i / T_n}}_{\mathcal{Z}_n} \quad (5.17)$$

where $\Delta E_i = E_i - E_{n_0}$ is the difference in energy between the level i and the first level of the group, n_0 . The approximation of a group with uniform internal distribution is equivalent to having a characteristic group temperature T_n approaching infinity, compared to the total energy width of the group, i.e.:

$$\mathcal{Z}_n \rightarrow g_n = \sum_{i \in n} g_i \quad (5.18)$$

where g_n is the overall group degeneracy. The simplest model therefore consists of assuming all levels within the group to be distributed uniformly, i.e., weighted by the level degeneracy

$$N_i = \frac{g_i}{g_n} \mathcal{N}_n \quad (5.19)$$

³That is, within the group.

⁴For further ease of notation, the Boltzmann constant k is not explicitly written.

The rate equation for a group n is obtained by summing the master rate equations (5.14-5.15) for all the levels i within the group, and utilizing relation (5.17):

$$\begin{aligned}
\frac{d\mathcal{N}_n}{dt} = & -N_e \mathcal{N}_n \left[\sum_{m>n} \sum_{i \in n} \frac{g_i}{g_n} \sum_{j \in m} \alpha_{(j|i)} + \sum_{m<n} \sum_{i \in n} \frac{g_i}{g_n} \sum_{j \in m} \beta_{(j|i)} \right] \\
& + N_e \mathcal{N}_m \left[\sum_{m<n} \sum_{i \in n} \sum_{j \in m} \frac{g_j}{g_m} \alpha_{(i|j)} + \sum_{m>n} \sum_{i \in n} \sum_{j \in m} \frac{g_j}{g_m} \beta_{(i|j)} \right] \\
& - \mathcal{N}_n \left[\sum_{m<n} \sum_{i \in n} \frac{g_i}{g_n} \sum_{j \in m} A_{(j|i)} \right] + \mathcal{N}_m \left[\sum_{m>n} \sum_{i \in n} \sum_{j \in m} \frac{g_j}{g_m} A_{(i|j)} \right] \\
& - N_e \mathcal{N}_n \left[\sum_{i \in n} \frac{g_i}{g_n} \alpha_{(+|i)} \right] + N_e^2 N_+ \left[\sum_{i \in n} \beta_{(i|+)} \right]
\end{aligned} \tag{5.20}$$

Similarly for the ion state, one obtains:

$$\frac{dN_+}{dt} = N_e \sum_n \mathcal{N}_n \left[\sum_{i \in n} \frac{g_i}{g_n} \alpha_{(+|i)} \right] - N_e^2 N_+ \sum_n \left[\sum_{i \in n} \beta_{(i|+)} \right] \tag{5.21}$$

The terms within brackets in equations (5.20-5.21) contain *effective* rates for the groups, which can be pre-computed. For example, in the first term on the right-hand-side of equation (5.20),

$$\tilde{\alpha}_{(m|n)} = \sum_{i \in n} \frac{g_i}{g_n} \sum_{j \in m} \alpha_{(j|i)}$$

is an effective excitation rate from group n to group m . Note that since this model does not require computing an excitation temperature T_n , all the effective transition rates between the groups can be expressed as a function of the kinetic temperature T_e only. It is important to emphasize that the grouping of levels is applied on the high energy states only; thus in any simulation we must choose a number of low-energy, “resolved” levels, as well as a variable number of groups combining the upper states. The number of discrete states, the number of groups and their widths are variable parameters of the model, whether we use uniform binning as above, or Boltzmann internal distributions, discussed below. In order to bound this parameter space (optimization is beyond the scope of the present work), we need to provide a reference solution, such that the population density

of each level can be compared to the one reconstructed from the assumed internal distribution within each group. Figure 5.1 shows the evolution of the electron density computed from the master equations. This test corresponds to a strong ionization regime and the time evolution of the ASDF shows an increasing population of the higher atomic levels while the electron density grows exponentially. It also demonstrates the effect of the number of levels included in the simulation, i.e. using a fewer number of atomic states has an impact on delaying the onset of the electron avalanche. This indicates that ionization from the high-energy states is an important process, and therefore the evolution of the upper states must be accurately captured. We could always increase the size of the ASDF to obtain higher accuracy, but with diminishing return; ultimately, the time-resolution of interest and the accuracy threshold dictate the number of levels required in a simulation. The mapping between the practical requirements and ASDF size is not a straightforward matter, but is an issue beyond the scope of this work. Convergence studies with respect to the size of the system showed that beyond 20 levels, there were no discernible differences in the results – see Figure 5.1. Thus, we chose our reference solution to be the one obtained for 20 levels, and all level-grouping models investigated here will be based on this extent of the ASDF.

5.3.2 Boltzmann grouping - number and energy

Several assumptions can be made regarding a Boltzmann-like structure within the group. Panesi *et al.* [121] and Munafo *et al.* [122] rely on the the assumption that the population within a group follows a Boltzmann distribution at the kinetic temperature, i.e. in this case, $T_n \equiv T_e$. This approach is only valid if the rates of exchange between the levels within the group are much faster than the exchange rates with levels outside the group; otherwise, one could then assume that the entire ASDF is governed by T_e and is always in Boltzmann equilibrium. The validity of this assumption is highly questionable for atomic state popula-

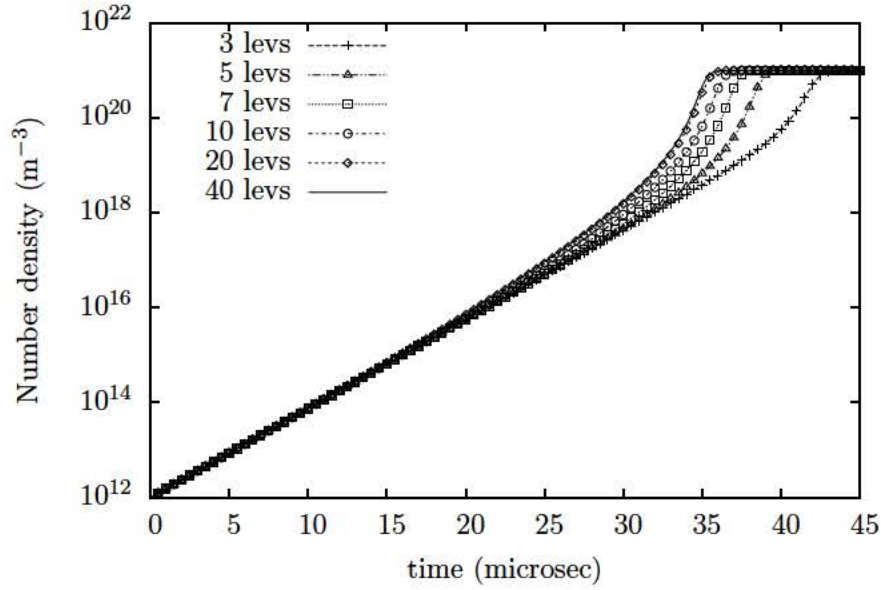


Figure 5.1: Time evolution of the electron number density using different total number of atomic levels. The electron temperature is set at 3.0 eV.

tions⁵. Furthermore, when different collision partners must be considered, the kinetic temperature can be either that of the heavy particles or the electrons (e.g. electron-impact excitation and heavy impact quenching); in this case, choosing either one of the kinetic temperature can impact on the results.

In order to accurately describe the population of a group with a Boltzmann distribution, two moment variables of the ASDF need to be conserved. The selection of these variables, however, can be arbitrary. Guy *et al.* [37] conserved the total number density of the group and the average excitation energy; these respectively correspond to zeroth- and first-order moment variables, and would appear to be a natural choice. Consider the total number of states \mathcal{N}_n - defined in equation (5.17) - and the total energy within the bin $\mathcal{E}_n = \sum_{i \in n} E_i N_i$, for which

⁵In a log-plot, this model assumes that the slope within each “bin” is always the same, and is not related to the average slope determined by the difference between adjacent bins.

we can write conservation equations, derived from (5.14):

$$\begin{aligned} \frac{d\mathcal{N}_n}{dt} = -N_e \mathcal{N}_n & \left[\sum_{m>n} \sum_{i \in n} \frac{g_i e^{-\Delta E_i/T_n}}{\mathcal{Z}_n} \sum_{j \in m} \alpha_{(j|i)} \right. \\ & \left. + \sum_{m<n} \sum_{i \in n} \frac{g_i e^{-\Delta E_i/T_n}}{\mathcal{Z}_n} \sum_{j \in m} \beta_{(j|i)} \right] + \dots \end{aligned} \quad (5.22a)$$

$$\begin{aligned} \frac{d\mathcal{E}_n}{dt} = -N_e \mathcal{N}_n & \left[\sum_{m>n} \sum_{i \in n} \frac{g_i e^{-\Delta E_i/T_n}}{\mathcal{Z}_n} \sum_{j \in m} E_i \alpha_{(j|i)} \right. \\ & \left. + \sum_{m<n} \sum_{i \in n} \frac{g_i e^{-\Delta E_i/T_n}}{\mathcal{Z}_n} \sum_{j \in m} E_i \beta_{(j|i)} \right] + \dots \end{aligned} \quad (5.22b)$$

For sake of brevity, we did not write the entire list of contributions in (5.22), which can be easily derived from (5.20) by generalizing the weighting factors g_i/g_n to $g_i e^{-\Delta E_i/T_n}/\mathcal{Z}_n$, and similarly for other groups. By solving for total number and total energy of each group, according to equations (5.22a-5.22b), we can guarantee direct conservation of both mass (total number of levels \mathcal{N}_n) and energy (\mathcal{E}_n). However this approach presents some problems in determining the internal Boltzmann temperature, as will now be shown. First, let us define a total group/bin energy measured from the lower bound, i.e. $\Delta \mathcal{E}_n = \sum_{i \in n} (E_i - E_{n_0}) N_i$; the rate of change of this shifted energy is still given by the right-hand-side of equation (5.22b). We can then write:

$$\Delta \mathcal{E}_n = \frac{N_{n_0}}{g_{n_0}} \sum_{i \in n} g_i \Delta E_i e^{-\Delta E_i/T_n} = \mathcal{N}_n \langle \Delta E \rangle_n \quad (5.23)$$

where

$$\langle \Delta E \rangle_n = \frac{1}{\mathcal{Z}_n} \sum_{i \in n} g_i \Delta E_i e^{-\Delta E_i/T_n} = T_n^2 \frac{d}{dT_n} \ln(\mathcal{Z}_n) \quad (5.24)$$

is the average group energy measured from the first internal level. Similarly, a specific heat at constant-volume can be determined, i.e.:

$$\begin{aligned} C_v(T_n) &= \frac{d}{dT_n} \langle \Delta E \rangle_n = T_n^{-2} \left[\frac{\sum_{i \in n} g_i (\Delta E_i)^2 e^{-\Delta E_i/T_n}}{\mathcal{Z}_n} - \langle \Delta E \rangle_n^2 \right] \\ &= T_n^{-2} [\langle \Delta E^2 \rangle_n - \langle \Delta E \rangle_n^2] \end{aligned} \quad (5.25)$$

Since \mathcal{N}_n and \mathcal{E}_n are conserved variables, we obtain new values at each time level (k) and in order to compute the Boltzmann temperature T_n , we need to iterate the equation

$$\langle \Delta E \rangle_n(T_n^*) + C_v(T_n^*) \delta T_n^* = \frac{\Delta \mathcal{E}_n^{(k)}}{\mathcal{N}_n^{(k)}} \quad (5.26)$$

where T_n^* is the running iterated value, until convergence ($\delta T_n^* \simeq 0$). However, the slope of the curve $\langle \Delta E \rangle_n(T_n)$ is extremely flat at low temperature, i.e. $C_v \rightarrow 0$. In fact, when $T_n \rightarrow 0$, to the leading order we have: $\mathcal{N}_n \simeq N_{n_0} o(1+\epsilon)$, $\langle \Delta E \rangle_n \simeq o(\epsilon)$ and $C_v(T_n) \simeq o(\epsilon)$, where $\epsilon = e^{-\Delta E_1/T_n}$ is a small parameter. Therefore during the iterations $\delta T_n^* = o(\epsilon)/o(\epsilon)$ and arbitrary temperature solutions can be obtained. Our studies showed that indeed, numerical instabilities prevent us from obtaining satisfactory solutions in many test cases. While it is possible to introduce limiters to prevent unphysical or improbable values and stop the iteration counters, this is not a satisfactory solution to the problem. We should also emphasize that the problem occurs when T_n is small, which does *not* imply that electronic levels are unpopulated, since we may very well have small *internal* group temperatures as a result of initial conditions or running iterations, but non-negligible overall electronic excitation ($\mathcal{N}_n \neq 0$)⁶.

5.3.3 Boltzmann grouping - partitioning

In the approach above, we are dealing with two reduced values \mathcal{N}_n and \mathcal{E}_n (or $\Delta \mathcal{E}_n$) which are both summations over the internal levels. An alternative may consist of keeping one of the level populations as a variable. Therefore we could instead choose for each group n to conserve the population of the lowest level in that group N_{n_0} and \mathcal{N}_n , whose evolution is given by a form similar to equation (5.22a). To evaluate the Boltzmann temperature of the group, we now have at

⁶Note that this problem is particularly relevant to ASDF kinetics because of the geometric progression of the energy levels. By performing tests on a pseudo-atom with equidistant energy levels, stability of the iterations was much improved, although not entirely eliminated for some conditions.

time step (k) , from (5.17):

$$\mathcal{N}_n^{(k)} = \frac{N_{n_0}^{(k)}}{g_{n_0}} \sum_{i \in n} g_i e^{-\Delta E_i / T_n} = \frac{N_{n_0}^{(k)}}{g_{n_0}} \mathcal{Z}_n(T_n^{(k)})$$

so that in order to evaluate the new bin temperature $T_n^{(k)}$ we need to solve

$$\mathcal{Z}_n(T_n^*) + \left(\frac{d\mathcal{Z}_n}{dT_n} \right) \delta T_n^* = \frac{\mathcal{N}_n^{(k)}}{N_{n_0}^{(k)}} g_{n_0} \quad (5.27)$$

until convergence. Using (5.24), this leads to:

$$\delta T_n^* \simeq \frac{T_n^{*2}}{\mathcal{Z}_n(T_n^*) \langle \Delta E \rangle_n(T_n^*)} \left[\frac{\mathcal{N}_n^{(k)}}{N_{n_0}^{(k)}} g_{n_0} - \mathcal{Z}_n(T_n^*) \right] \quad (5.28)$$

where, again, the dependencies on temperature have been explicitly written. At low T_n , the denominator is $o(\epsilon)(1+\epsilon)$ and the numerator is a difference between two terms of $o(1+\epsilon)$. Therefore, the iterative procedure is again numerically unstable.

To attempt to alleviate this problem, we have examined yet another approach: for each group n we conserve the population of the lowest level in that group N_{n_0} and \mathcal{N}'_n , the total population of the *remaining* upper states n' of that group, such that $n = n_0 \cup n'$. This is an effective partitioning *within* the group, which allows us to separate the variables, one of $o(1)$ and the other of $o(\epsilon)$. Clearly, we have now:

$$\mathcal{N}'_n = \frac{N_{n_0}}{g_{n_0}} \underbrace{\sum_{i \in n'} g_i e^{-\Delta E_i / T_n}}_{\mathcal{Z}'_n} \quad \text{using} \quad N_i = \frac{\mathcal{N}'_n}{\mathcal{Z}'_n} g_i e^{-\Delta E_i / T_n} \quad (5.29)$$

In order to evaluate the new temperature from the two conserved variables, we iterate on δT_n^* using a form similar to equation (5.27):

$$\mathcal{Z}'_n(T_n^*) + \left(\frac{d\mathcal{Z}'_n}{dT_n} \right) \delta T_n^* = \frac{\mathcal{N}'_n}{N_{n_0}} g_{n_0} \quad (5.30)$$

However, it is easy to see that since $\frac{d}{dT} \mathcal{Z}' \equiv \frac{d}{dT} \mathcal{Z}$, we obtain a similar equation to (5.28):

$$\delta T_n^* \simeq \frac{T_n^{*2}}{\mathcal{Z}'_n(T_n^*) \langle \Delta E \rangle_n(T_n^*)} \left[\frac{\mathcal{N}'_n}{N_{n_0}} g_{n_0} - \mathcal{Z}'_n(T_n^*) \right]$$

In the same limit $T_n \rightarrow 0$, both numerators and denominators are of $o(\epsilon)$ and the temperature iterations are again unstable; this was verified through extensive tests under a variety of conditions and configurations. To avoid this systematic numerical problem, we must consider another way to evaluate the Boltzmann temperature inside each group.

Consider instead the following expansion of the partition function near the mean relative energy value $\overline{\Delta E}_n = \frac{1}{g_n} \sum_{i \in n} g_i \Delta E_i$. Defining $\delta_i \equiv \Delta E_i - \overline{\Delta E}_n$ as the shifted energy gap, we have:

$$\begin{aligned} \mathcal{Z}_n(T_n) &= \sum_{i \in n} g_i e^{-\Delta E_i/T_n} = e^{-\overline{\Delta E}_n/T_n} \sum_{i \in n} g_i e^{-\delta_i/T_n} \\ &= e^{-\overline{\Delta E}_n/T_n} \sum_{i \in n} g_i \left[1 - \frac{\delta_i}{T_n} + \frac{1}{2} \frac{\delta_i^2}{T_n^2} + \dots \right] \\ &\simeq g_n e^{-\overline{\Delta E}_n/T_n} [1 + o(\langle \delta^2 \rangle / T_n^2)] \end{aligned} \quad (5.31)$$

where g_n is the total degeneracy - see equation (5.18). Therefore, up to second-order in the approximate ratio of the bin width to the temperature, the partition function can be approximated by a single exponential function and the relation (5.31) can be inverted. If we use the (N_{n_0}, \mathcal{N}) pair of conserved variables, we have:

$$\frac{\mathcal{N}_n^{(k)}}{N_{n_0}^{(k)}} g_0 = \mathcal{Z}_n(T_n^{(k)}) \simeq g_n e^{-\overline{\Delta E}_n/T_n^{(k)}} \quad (5.32)$$

However, the left-hand-side of (5.32) is $o(1+\epsilon)$, and the right-hand-side should be as well. To see that this is the case, consider the first terms in the expansion of (5.31)⁷:

$$\mathcal{Z}_n(T_n) \simeq e^{-\overline{\Delta E}_n/T_n} \left[g_0 e^{-(\Delta E_0 - \overline{\Delta E}_n)/T_n} + g_1 e^{-(\Delta E_1 - \overline{\Delta E}_n)/T_n} + \dots \right]$$

Since $\overline{\Delta E} \simeq \Delta E_1$ and $\Delta E_0 \equiv 0$, the right-hand-side is $o(\epsilon)[o(1/\epsilon) + 1 + \dots] \simeq o(1+\epsilon)$. Again, this is not a desirable situation, since the evaluation of the group

⁷We have here temporarily simplified the notation ($g_0 \equiv g_{n_0}, g_1 \equiv g_{n_0+1}, \dots$).

temperature T_n is of the form $1/\ln(1+\epsilon)$, and is subject to significant errors. Furthermore, by computing the average gap $\overline{\Delta E}$ from the lower-bound of the energy bin, the requirement $\langle \delta \rangle \ll T_n$ may be hard to justify at low group temperature.

Instead, we can take advantage of the self-similar structure of the atomic spectrum (exact for Hydrogen, approximate for other atoms) and the fact that the energy gaps become narrower as the level index increases. Thus, let us define the average energy counting from the first level *above* the lowest level, as obtained from \mathcal{Z}'_n , defined in equation (5.29):

$$\mathcal{Z}'_n = \sum_{i \in n'} g_i e^{-\Delta E_i/T_n} = e^{-\overline{\Delta E}'_n/T_n} \sum_{i > n_0} g_i e^{-\delta'_i/T_n} \quad (5.33)$$

By definition of the mean, the first-order term in the expansion of the exponential on the right-hand-side should be: $\sum_{i \in n'} g_i \delta'_i = 0$, where now $\delta'_i \equiv \Delta E_i - \overline{\Delta E}'$. This yields:

$$\overline{\Delta E}' = \frac{1}{g'_n} \sum_{i \in n'} g_i \Delta E_i \quad \text{with} \quad g'_n = \sum_{i > n_0} g_i \quad (5.34)$$

Therefore $\overline{\Delta E}'$ differs from $\overline{\Delta E}$ only by a normalization factor, since $\Delta E_0 \equiv 0$. Note that $\overline{\Delta E}' > \Delta E_1$ and to *lowest-order*, $\mathcal{Z}'(T_n) \simeq g'_n e^{-\overline{\Delta E}'_n/T_n} \simeq o(\epsilon)$. Using the conserved pair (N_{n_0}, \mathcal{N}') , the group temperature is now estimated by:

$$\frac{\mathcal{N}'^{(k)}_n}{N_{n_0}^{(k)}} g_{n_0} = \mathcal{Z}'_n(T_n) \quad \rightarrow \quad T_n^{(k)} \simeq -\frac{\overline{\Delta E}'_n}{\ln \left[\frac{\mathcal{N}'_n}{g'_n} \frac{g_{n_0}}{N_{n_0}} \right]} \simeq -\frac{1}{\ln(\epsilon)} \quad (5.35)$$

This is now a stable computation when $\epsilon \rightarrow 0$. Furthermore, the approximation $\langle \delta \rangle \ll T_n$ is more justifiable since the largest value ($\delta_0 = E_{n_0} - \overline{\Delta E}$) is removed from the average.

We see that we now have the means to compute the internal group temperature from conserved variables without risking fatal numerical errors; this is possible *only* by separating the lowest and upper levels within the group, i.e. by performing a sub-scale, internal partitioning of the group⁸. This is the approach used here

⁸This approach is a reflection of the self-similar structure of the atomic levels.

for the last Boltzmann (hereafter denoted as B5) group we investigated, for which the appropriate pair of conserved variables to use is therefore $(N_{n_0}, \mathcal{N}'_n)$. Note that it is also possible to improve on the temperature evaluation by incorporating all higher-order terms into the definition of the total degeneracy, i.e.:

$$\mathcal{Z}'_n(T_n) = \tilde{g}'_n(T_n) e^{-\overline{\Delta E}'_n/T_n} \quad \rightarrow \quad \frac{d\mathcal{Z}'_n}{dT_n} = \mathcal{Z}'_n(T_n) \cdot \left[\frac{\overline{\Delta E}'_n}{T_n^2} + \frac{d}{dT_n} \ln \tilde{g}'_n \right] \quad (5.36)$$

If T_n^* is the running iteration, first evaluated by (5.35), successive estimates of $T_n^{(k)}$ are obtained, using (5.36), from:

$$T_n^{(k)} - T_n^* = \frac{\ln \mathcal{Z}'_n(T_n^{(k)}) - \ln \mathcal{Z}'_n(T_n^*)}{\frac{d \ln \mathcal{Z}'_n}{dT_n}(T_n^*)} \quad \text{where} \quad \mathcal{Z}'_n(T_n^{(k)}) = g_{n_0} \frac{\mathcal{N}'_n{}^{(k)}}{N_{n_0}^{(k)}} \quad (5.37)$$

This iterative procedure can rapidly converge (as demonstrated in our tests) because we have an excellent approximation of the initial temperature from the lowest-order direct evaluation (5.35), and the $o(\epsilon)$ term has been factored as the leading term in the expansion. In other words, $\tilde{g}'_n(T_n)$ is a smooth function of temperature with a non-vanishing gradient, allowing gradient-descent iterations.

5.3.4 Boltzmann grouping - effective rates

As before, the master equations are used to derive the conservation equations for the two new variables $(N_{n_0}, \mathcal{N}'_n)$, by setting $i = n_0$ for the first one, and summing

over all levels $j \in n'$ in the second case. The latter yields the following:

$$\begin{aligned}
\frac{d\mathcal{N}'_n}{dt} = & -N_e \mathcal{N}'_n \left[\sum_{m>n} \sum_{i \in n'} \frac{g_i e^{-\Delta E_i/T_n}}{\mathcal{Z}'_n} \sum_{j \in m} \alpha_{(j|i)} + \sum_{m<n} \sum_{i \in n'} \frac{g_i e^{-\Delta E_i/T_n}}{\mathcal{Z}'_n} \sum_{j \in m} \beta_{(j|i)} \right] \\
& + N_e \mathcal{N}'_m \left[\sum_{m<n} \sum_{i \in n'} \sum_{j \in m} \frac{g_j e^{-\Delta E_j/T_m}}{\mathcal{Z}_m} \alpha_{(i|j)} + \sum_{m>n} \sum_{i \in n'} \sum_{j \in m} \frac{g_j e^{-\Delta E_j/T_m}}{\mathcal{Z}_m} \beta_{(i|j)} \right] \\
& - \mathcal{N}'_n \left[\sum_{m<n} \sum_{i \in n'} \frac{g_i e^{-\Delta E_i/T_n}}{\mathcal{Z}'_n} \sum_{j \in m} A_{(j|i)} \right] + \mathcal{N}'_m \left[\sum_{m>n} \sum_{i \in n'} \sum_{j \in m} \frac{g_j e^{-\Delta E_j/T_m}}{\mathcal{Z}_m} A_{(i|j)} \right] \\
& - N_e \mathcal{N}'_n \left[\sum_{i \in n'} \frac{g_i e^{-\Delta E_i/T_n}}{\mathcal{Z}'_n} \beta_{(n_0|i)} + \sum_{i \in n'} \frac{g_i e^{-\Delta E_i/T_n}}{\mathcal{Z}'_n} A_{(n_0|i)} \right] \\
& - N_e \mathcal{N}'_n \left[\sum_{i \in n'} \frac{g_i e^{-\Delta E_i/T_n}}{\mathcal{Z}'_n} \alpha_{(+|i)} \right] + N_e^2 N_+ \left[\sum_{i \in n'} \beta_{(i|+)} \right]
\end{aligned} \tag{5.38}$$

Note that we have used the total number $\mathcal{N}_m = N_{m_0} + \mathcal{N}'_m$ and the group total partition function $\mathcal{Z}_m = g_{m_0} + \mathcal{Z}'_m$ in the expressions on the right hand side, only as a way to group terms and lead to simpler expressions; the conserved variables remain N_{m_0} and \mathcal{N}'_m . Equation (5.38) takes in account all the interactions between the groups, assuming the Boltzmann distribution approximation within each group. The effective rates for group transitions can be expressed (and tabulated) as a function of two temperatures: the kinetic temperature T_e and the group excitation temperature T_n . Notice also that because of the bin-averaging, the effective radiative transition rates have also become temperature-dependent (T_n).

Similarly, the rate of change of the number density of the ground state of each

group is:

$$\begin{aligned}
\frac{dN_{n_0}}{dt} = & -N_e N_{n_0} \left[\sum_{m>n} \sum_{j \in m} \alpha_{(j|n_0)} + \sum_{m<n} \sum_{j \in m} \beta_{(j|n_0)} \right] \\
& + N_e \mathcal{N}_m \left[\sum_{m<n} \sum_{j \in m} \frac{g_j e^{-\Delta E_j/T_m}}{\mathcal{Z}_m} \alpha_{(n_0|j)} + \sum_{m>n} \sum_{j \in m} \frac{g_j e^{-\Delta E_j/T_m}}{\mathcal{Z}_m} \beta_{(n_0|j)} \right] \\
& - N_{n_0} \left[\sum_{m<n} \sum_{j \in m} A_{(j|n_0)} \right] + \mathcal{N}_m \left[\sum_{m>n} \sum_{j \in m} \frac{g_j e^{-\Delta E_j/T_m}}{\mathcal{Z}_m} A_{(n_0|j)} \right] \\
& + N_e \mathcal{N}'_n \left[\sum_{i \in n'} \frac{g_i e^{-\Delta E_i/T_n}}{\mathcal{Z}'_n} \beta_{(n_0|i)} + \sum_{i \in n'} \frac{g_i e^{-\Delta E_i/T_n}}{\mathcal{Z}'_n} A_{(n_0|i)} \right] \\
& - N_e N_{n_0} [\alpha_{(+|n_0)}] + N_e^2 N_+ [\beta_{(n_0|+)}]
\end{aligned} \tag{5.39}$$

Again, using the total number of levels $\mathcal{N}_m = N_{m_0} + \mathcal{N}'_m$ on the right-hand-side allows us to consider together transitions between lowest states at the boundaries of different groups ($N_{n_0} - N_{m_0}$), as well as the transitions with the excited subpartitions ($N_{n_0} - \mathcal{N}'_m$) and simply the expressions. Since the ion is conserved here as an individual state, the rate of change of its number density remains the same but can be rewritten in terms of the group number densities:

$$\frac{dN_+}{dt} = N_e \sum_n \mathcal{N}_n \left[\sum_{i \in n} \frac{g_i e^{-\Delta E_i/T_n}}{\mathcal{Z}_n} \alpha_{(+|i)} \right] - N_e^2 N_+ \left[\sum_n \sum_{i \in n} \beta_{(i|+)} \right] \tag{5.40}$$

Each term in brackets in equations (5.38-5.40) is an effective rate for transfer between the group variables $(N_{n_0}, \mathcal{N}'_n), \forall n$. As mentioned in 5.3.1, both individual levels and groups (Uniform or Boltzmann) are considered when solving the ASDF. The few individual states are the lowest in the energy scale, with the largest successive gaps, while the multitude of upper levels is distributed into a variable number of groups. This is justified on the basis of the kinetic rates, and as justification of the expansion (5.31).

Model	Variables	Equations	T_n evaluation
U	\mathcal{N}_n	(5.20-5.21)	none
B1	$(\mathcal{N}_n, \mathcal{E}_n)$	(5.22a-5.22b, 5.40)	C_v – unstable
B2	(N_{n_0}, \mathcal{N}_n)	(5.39, 5.22a)	C_v – unstable
B3	$(N_{n_0}, \mathcal{N}'_n)$	(5.39, 5.38)	C_v – unstable
B4	(N_{n_0}, \mathcal{N}_n)	(5.39, 5.22a)	equation (5.31) – unstable
B5	$(N_{n_0}, \mathcal{N}'_n)$	(5.39, 5.38)	equation (5.33) – stable

Table 5.1: Summary of level-grouping models investigated.

5.4 Accuracy of uniform and Boltzmann methods

5.4.1 Isothermal ionization test case

In the previous section, we have discussed several approaches to the level grouping strategy; these are summarized in Table 5.1. This sequence of models was developed as a result of preliminary tests and the failure to obtain converged solutions for the group Boltzmann temperature T_n in many instances. Thus, we found that the *only* model which was able to provide stable and satisfactory solutions for all test cases was model B5, using a sub-partition of the group into the ground level n_0 and the remainder, and the use of the form (5.33) for the partition function, which allowed us to factorize out the vanishingly small terms at low T_n . Therefore, considerations of the “equation of state” of the Boltzmann group dictated the correct approach to use here, and while all the models explored are listed in table 5.1, only the zeroth-order uniform binning described in 5.3.1 and the B5 models are shown here and compared to the reference solution obtained from solving the full master equations; these are indicated as (U) and (B) models respectively.

We conducted a large number of additional tests but for the sake of brevity, we are showing here the results of three representative cases: the initial conditions

Case	T_e	$x_e = N_+/N_H$	N_n
1	3 eV - isothermal	10^{-9}	$(1 - x_e)N_H$ for $n=1$ $10^{-20}N_H$ otherwise
2	1 eV - isothermal	Saha (3 eV)	Boltzmann (3 eV)
3	3 eV - isochoric	10^{-9}	$(1 - x_e)N_H$ for $n=1$ $10^{-20}N_H$ otherwise

Table 5.2: Initial conditions of test cases. For all cases, the total atomic density N_H is 10^{21} m^{-3} .

are summarized in Table 5.2. For all the results shown in this section, a constant time step of 10^{-7} second had been used for the test cases in the ionization regime (cases 1 and 3), and a time step of 10^{-5} second was used for the recombination regime (case 2); the same backward-Euler scheme of 3.2 was used throughout.

As indicated in 5.3, the reference solution is based on the detailed kinetics for 20 atomic levels, while the group-based solutions will be based on a few low energy levels individually monitored, and with partitioning of the remaining upper states into a variable number of groups. The first test case is the iso-thermal relaxation in the excitation and ionization regime, i.e. the initial population of excited states and electron density is well below equilibrium⁹. This test case is the same as the one shown in Figure 5.1 for a variable number of electronic levels, solving for the full master equations (5.14-5.15). As the plasma relaxes towards equilibrium, an increasing number of electronic levels become populated and the electron number density grows exponentially, until an ionization cascade occurs. The rates increase very rapidly just before equilibrium, and the system becomes very stiff.

Figure 5.2 shows a comparison of the number densities of all the atomic states

⁹Since we are considering electron collisions only, all test cases must start with an initial degree of ionization $x_e \neq 0$.

Method	Error
3 levels + 1 U-group	2618%
3 levels + 1 B-group	89.2%
4 levels + 1 U-group	165.8%
4 levels + 1 B-group	23.7%
6 levels + 1 U-group	20.9%
6 levels + 1 B-group	0.9%

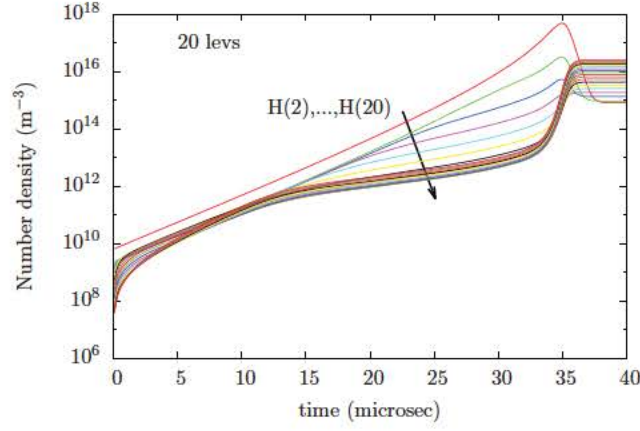
Table 5.3: Relative error on electron density at peak rate of growth (approx. 33 μsec).

for the iso-thermal test case (#1). In this simulation, the ground state and the first 4 excited states ($1, \dots, 5$) are conserved as discrete levels while the remaining upper states ($6, \dots, 20$) are partitioned into two groups, each of which has either a uniform or Boltzmann distribution. There are both significant and subtle differences in the traces of the upper states. First, comparison of the uniform (Figure 5.2-b) and Boltzmann (Figure 5.2-c) grouping shows the influence of the assumed internal distribution, as the reconstructed levels of the groups are clearly separated in the uniform case. Second, comparison with the reference solution of Figure 5.2-a shows that the Boltzmann groups are clearly more accurate. Slight differences remain in the very early stages of evolution¹⁰ below 1 μsec for example and around 10 μsec .

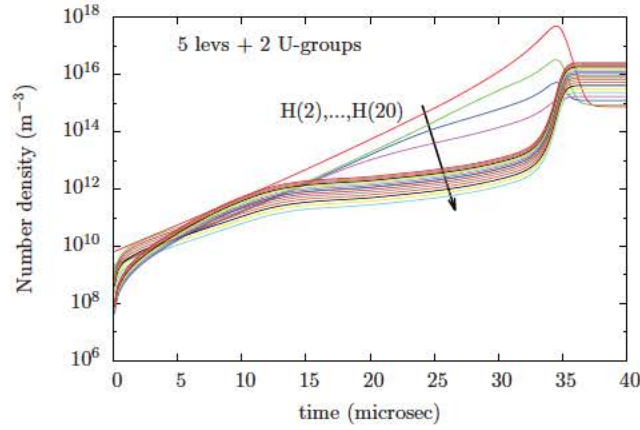
The combined effect of the number of resolved lower levels and grouping strategy is shown in Figure 5.3. Generally speaking, one can clearly observe a dramatic improvement, for the same number of resolved levels, by switching from a uniform to Boltzmann group¹¹. By selecting the time of maximum rate of growth of the

¹⁰This understandably so, since the ladder-climbing process of the early evolution would be difficult to describe with grouping methods, even by 1st-order approximation of the internal distribution within the groups.

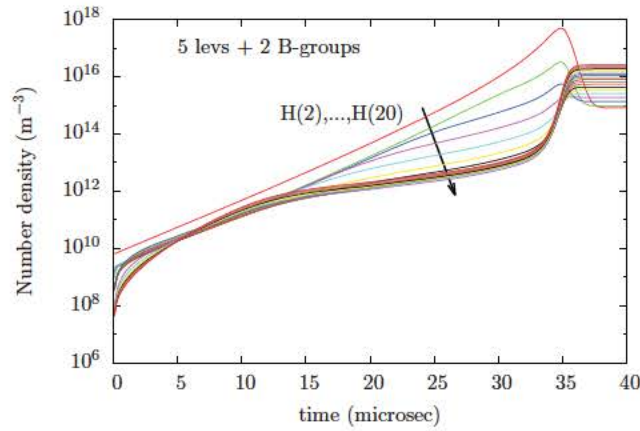
¹¹By coincidence, the results of uniform binning for 6 resolved levels is right on top of the



(a) Full solution with 20 levels.



(b) Solution with 5 levels and 2 Uniform groups



(c) Solution with 5 levels and 2 Boltzmann groups.

Figure 5.2: Comparison of the time evolution of the excited states during the isothermal heating test case ($T_e = 3$ eV). From top to bottom: (a) full solution with 20 levels; (b) solution with 5 levels and 2 Uniform groups; (c) solution with 5 levels and 2 Boltzmann groups. The first excited state - $H(2)$ - is the top curve, followed by the next higher level, etc.

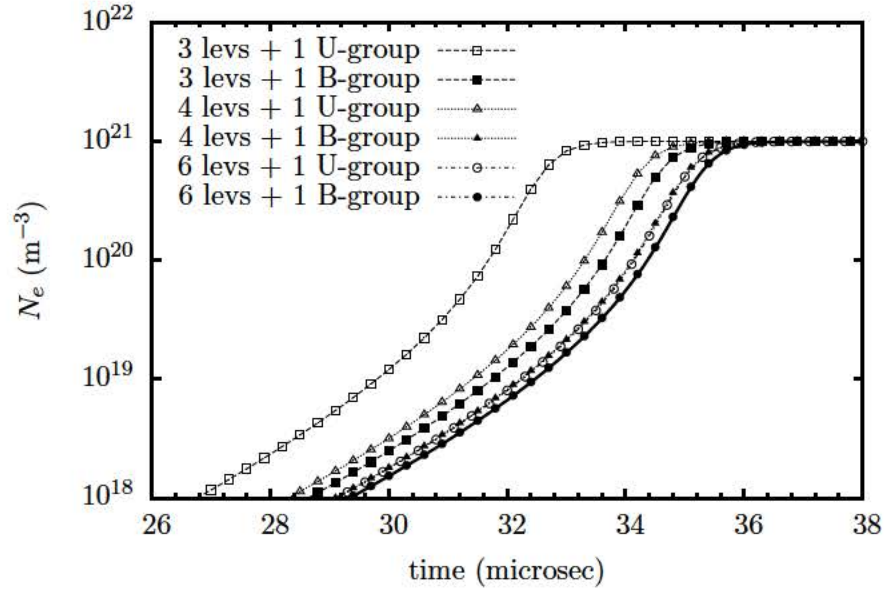


Figure 5.3: Comparison between the solution obtained using both level grouping approaches. The solid line represents the full solution.

electron density as the approximate location of the avalanche ionization, we can measure the relative error in density. As shown in Table 5.3, the error can be very substantial unless there is sufficient resolution of the ASDF kinetics, through the number of resolved lower levels and a higher-order (B) description of the groups. This is important when comparing, for example, with time-gated experimental results.

By conserving more discrete states and reducing the size of the upper state groups, the results are of course significantly improved. This is to be expected for ASDF kinetics, since the energy gaps are larger for the first levels, and grouping together these states would be less accurate, first by yielding excessive bin energy widths compared to mean energy and temperature scale – violating the validity condition for the expansion (5.31) – and also by disallowing potential deviations from Boltzmann equilibrium in the most populated range of excited states.

solution for a Boltzmann group with 4 lower levels.

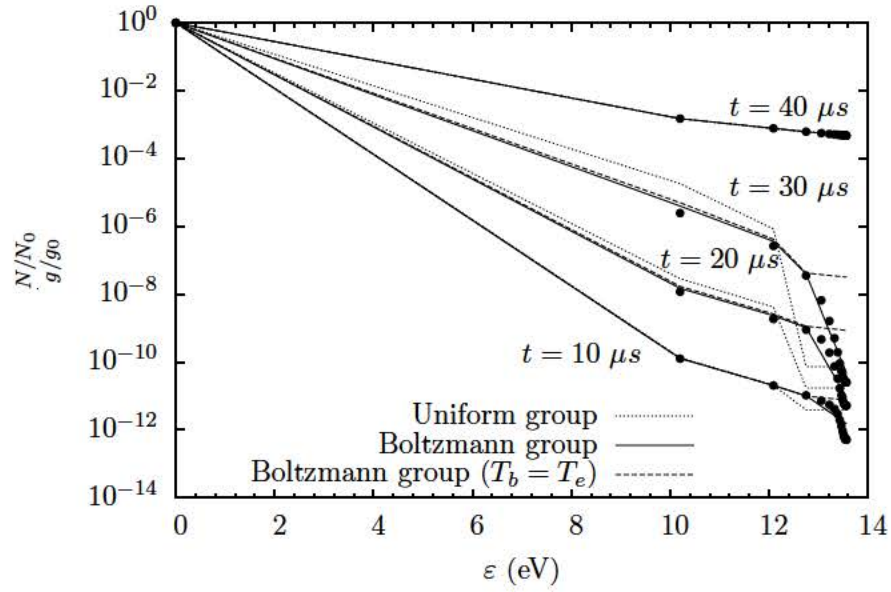


Figure 5.4: The internal states population during the heating process at various times. The solid symbols are the full solution; the solid lines are the level grouping with Boltzmann distribution; the dotted lines are for level grouping with uniform distribution; dashed lines are for a simplified model with $T_b \equiv T_e$.

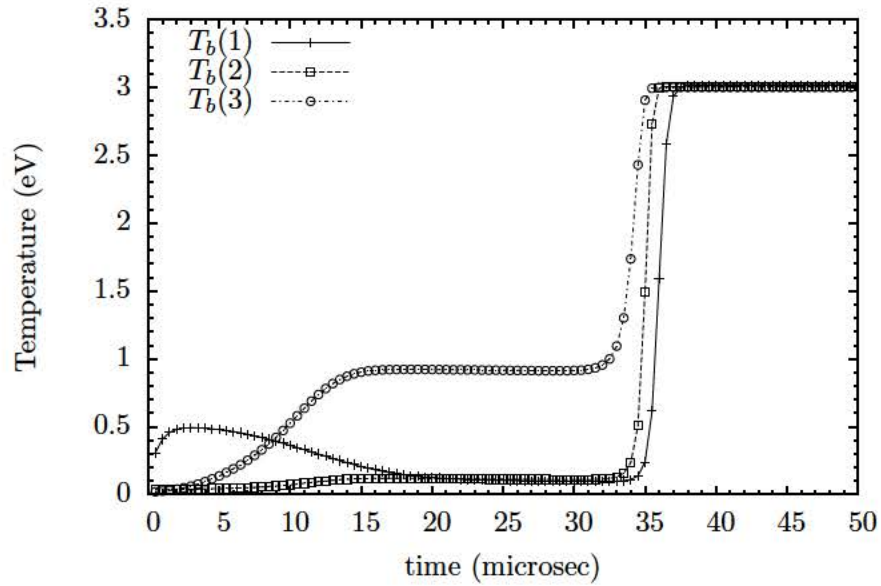


Figure 5.5: Boltzmann temperature of the upper states

There can of course be variations in the grouping strategy, but in all cases the general guidelines of keeping the *widths* of the groups small and the levels with the largest energy gaps as individual states are perfectly consistent with the objective of computational cost reduction, since the discrete lower energy states evolve more slowly and the upper states are numerous and have similar energy¹².

The relative accuracy of the grouping approaches can also be seen in Figure 5.4 where the ASDF is plotted at four different instances of time corresponding to $t = 10, 20, 30$ and $40 \mu\text{sec}$. Both solutions with level grouping are obtained from using 3 atomic levels and 1 group of upper states. It is clearly seen that the Boltzmann group gives a more accurate representation of the upper states distribution during the heating process. We also showed in Figure 5.4 the results of a simplified model where it is assumed (see section 5.3.2) that all groups have the same internal temperature, equal to the kinetic temperature, i.e. $T_b(i) \equiv T_e, \forall i$ (dashed line). This assumption is clearly violated, as shown in Figure 5.5, although the difference remains mostly confined to the upper states distribution. We should point out again that significant differences would be expected in a two-temperature kinetic system, i.e. including heavy-particle collisions.

We note also that the ASDF from the full solution indicates that the high lying states, starting from the third excited state, behave like a continuum state, although there appears to be two distinct sub-groups among the upper states, as can be seen most clearly at $t = 10 \mu\text{s}$. This suggests that the upper states are most effectively resolved by two groups or more, again confirming that relatively small widths of the groups are preferable, albeit at an increased computational expense. Figure 5.5 further illustrates this point by showing the evolution of the Boltzmann temperatures of the upper states, using here 4 discrete atomic states and partitioning the upper states into 3 groups. While the Boltzmann

¹²Although the grouping techniques are formulated here for a general set of kinetics, the effectiveness of the grouping approach is problem specific. For other situations, e.g. ro-vibrational states, a different strategy may be required than the one discussed here for atomic states.

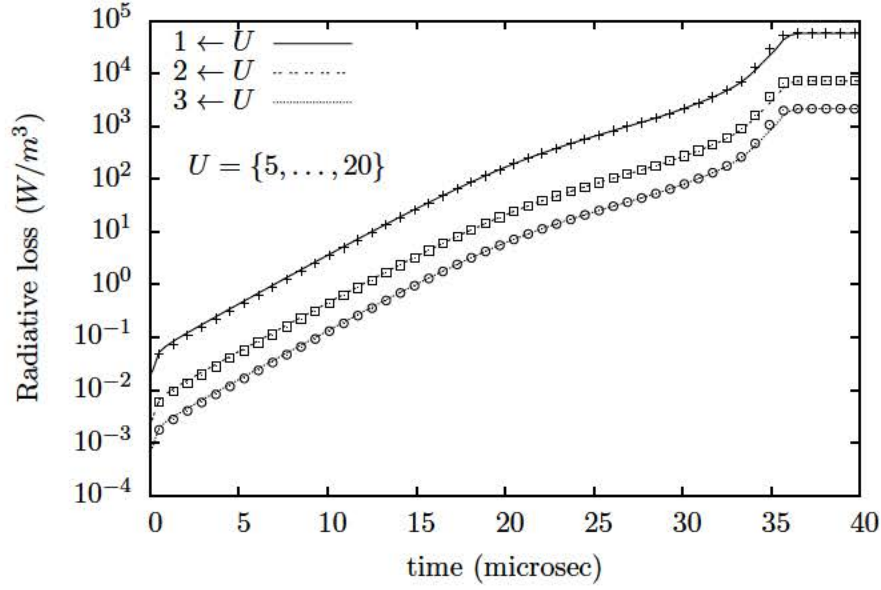


Figure 5.6: Radiative loss due to bound-bound radiation from the upper states to the first 3 atomic states. The lines indicate the solution obtained from the full CR kinetics. The dots represent solution obtained with level grouping (5 levels + 1 group).

temperatures of the first two groups are close to each other, the temperature of the third group is slightly higher. This again confirms that the upper states needs to be resolved by at least 2 groups. When the system is near equilibrium, both approaches give similar results.

In these simulations, we have assumed that the plasma is optically thin to all the radiation from the line transitions. Spectral signatures being a major diagnostic tool for determining plasma conditions, it is important to know the CR kinetics in detail in order to match experimental data. Usually, this is accomplished by post-processing the numerical solution with a highly resolved spectral code – including radiation transport (RT) if necessary – with detailed computation of line shapes. This approach is accurate if the key parameters of such a spectral model, in particular N_e and T_e , are also very accurate. As discussed above and shown in Table 5.3, our Boltzmann grouping procedure provides a significant improvement

over conventional approaches, leading to a potentially much more accurate spectral signature prediction in transient and non-equilibrium plasma conditions. In addition, the ASDF solution is much closer to the true physical state, which may also lead to faster integration of the detailed CR kinetics with RT. These will be investigated in the future.

Accurate evaluation of the radiative emission is also important during the computation of flow dynamics, from simple reasons of power coupling, e.g. radiative cooling. Figure 5.6 shows the radiative losses due to bound-bound radiation from the upper states $(5, \dots, 20)$ to the first three atomic states $(1, 2, 3)$ computed by grouping all the upper states together as a single group with a Boltzmann distribution. Although this is a somewhat coarse approximation to the ASDF, it is clear that the grouping scheme provides an excellent approximation to the radiative power. An accurate reproduction of the radiative spectrum depends inevitably on the reconstructed population of the atomic levels and, as can be seen by comparing the profiles in Figure 5.2, the agreement can be excellent.

5.4.2 Isothermal recombination test case

In this case, we performed a cooling test where the plasma is suddenly brought down from 3 eV to 1 eV. Thus, the simulation was run at a constant temperature ($T_e = 1$ eV), while the initial conditions are the Boltzmann and Saha equilibrium values at 3 eV; these are exactly the conditions which would be obtained at the end of the first test case in the absence of radiative losses. For all the simulations shown in this case, a constant time step of 10^{-5} sec has been used.

In this case, the cooling process occurs very rapidly and the plasma is in a deexcitation and recombination regime; the ground state and the electron number densities are quickly adjusted to their new equilibrium values, as can be seen in Figure 5.7. Strictly speaking, since bound-bound radiation is assumed to be

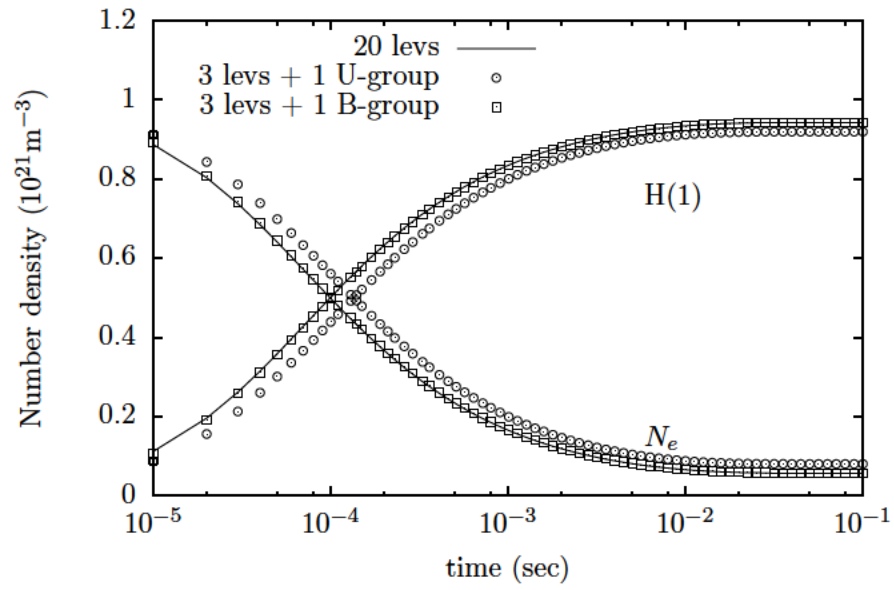
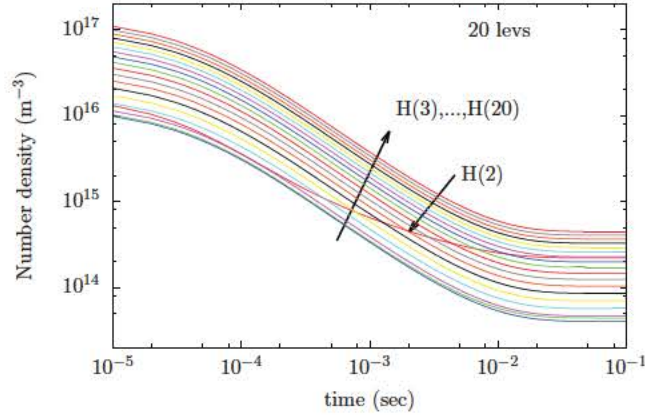
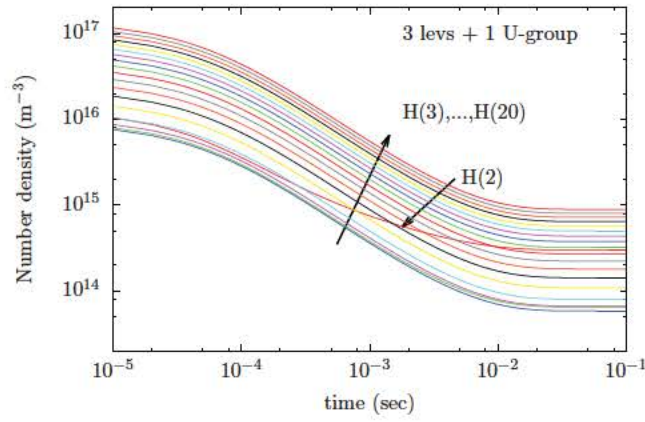


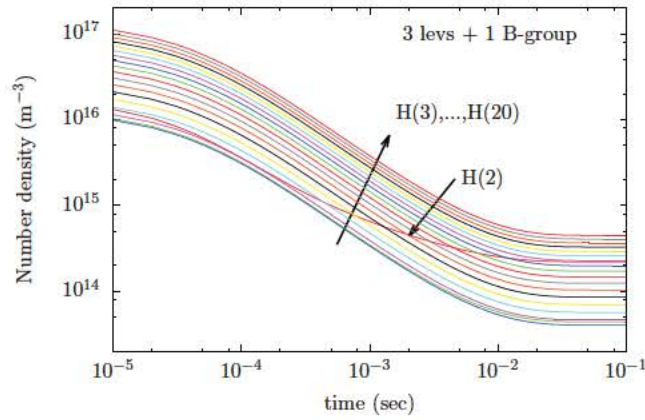
Figure 5.7: Comparison of the time evolution of the ground state and the free electrons during the isothermal cooling process ($3 \text{ eV} \rightarrow 1 \text{ eV}$) using level grouping with Uniform and Boltzmann distribution (3 levels + 1 group).



(a) Full solution with 20 levels.



(b) Solution with 3 levels and 1 Uniform group



(c) Solution with 3 levels and 1 Boltzmann group.

Figure 5.8: Comparison of the time evolution of the excited states during the isothermal cooling test case ($T_e = 1$ eV). From top to bottom: (a) full solution with 20 levels; (b) solution with 3 levels and 1 Uniform group; (c) solution with 3 levels and 1 Boltzmann group. $H(3)$ - is the bottom curve, followed by the next higher level, etc.; the non-conforming red curve is $H(2)$.

optically thin, the system cannot reach equilibrium. However, a quasi-equilibrium state is achieved at approximately 1 msec, after which the bound-bound radiation is the dominant *net* rate of change and the system continues to cool down at the radiative time scales. Note also that the uniform grouping is significantly less time-accurate than the Boltzmann method, as was already the case in the ionization regime – see Figure 5.3.

Figure 5.8 shows the evolution of the excited states as function of time for reference, uniform groups and Boltzmann groups. Once again, there is a noticeable discrepancy between the reference solution and the uniform bin model, especially concerning the red curve which crosses other levels during the relaxation process. This curve is the density of $H(2)$, the first excited state, and is an effect of the strong radiative decay of this state. Notice that the plot starts at $t = 10^{-5}$ sec, i.e. the first implicit time step, but already the solution is far from the Boltzmann equilibrium which is the initial condition at $t = 0$, such that there is a population inversion with respect to $H(2)$ for many upper states. Notice also that the time scale is logarithmic, and the processes considerably slow down as the electron density drops significantly. Because we are considering only electron impact collisions, the ASDF essentially becomes “frozen” in a quasi-static but non-equilibrium state. If collisions by heavy particles were also considered, these would rapidly become the dominant process, leading to faster relaxation towards equilibrium. However, in some case of rapid plasma expansion, similar “frozen-in” non-equilibrium distribution functions of the ASDF could be obtained.

To better appreciate the accuracy of the Boltzmann grouping procedure, Figure 5.9 shows the evolution of several excited states compared to the exact solution and similarly to the “heating” (ionization) case, excellent agreement was obtained. In this simulation, the first 3 atomic states (0, 1, 2) are conserved as discrete levels and the upper states (3, ..., 19) are lumped into 1 Boltzmann group.

Finally, we show in Figure 5.10 the snapshots of the ASDF during the recom-

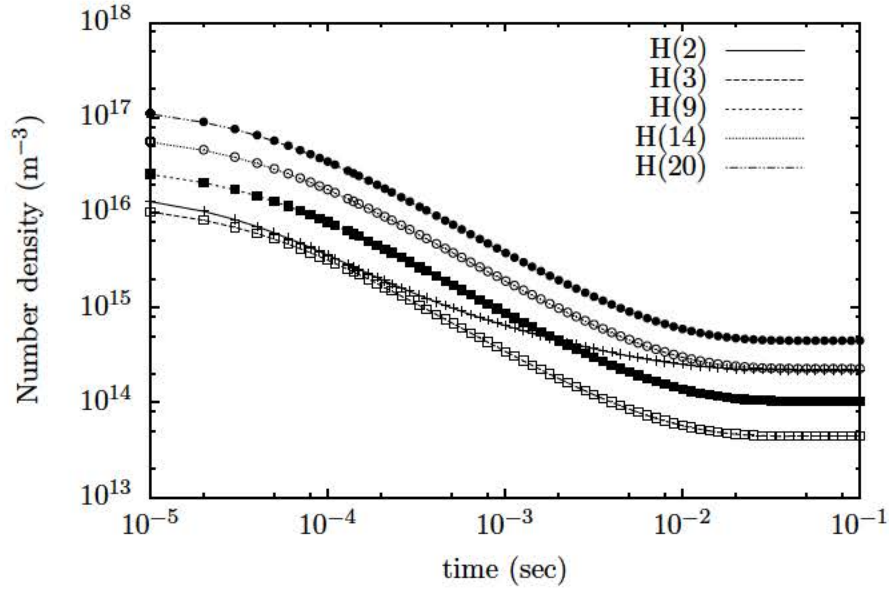


Figure 5.9: Comparison of the time evolution of the excited states number densities during the isothermal cooling process (3 levels + 1 B group).

bination. Contrary to the case of ionization, the upper states are not depleted but enhanced instead – as expected, since the recombination proceeds preferentially onto the upper states. As a reflection of the observation made for Figure 5.9, the agreement is excellent for all atomic states.

5.5 Energy conservation

The systems of equations (5.18-5.21) and (5.38-5.40) describe the complete evolution of the ASDF but for an iso-thermal plasma. In the more general case, the ASDF kinetics are coupled to the energy of the system; here, this includes only the total energy of the free electrons E_e . Thus for constant-volume or constant-pressure conditions, there must be an evolution equation for the energy or enthalpy (only constant-volume kinetics are considered here). We must then exert care that the formulation exactly conserves energy, i.e. that $E_e^{(k)} + \sum_n \mathcal{E}_n^{(k)}$ at any time level

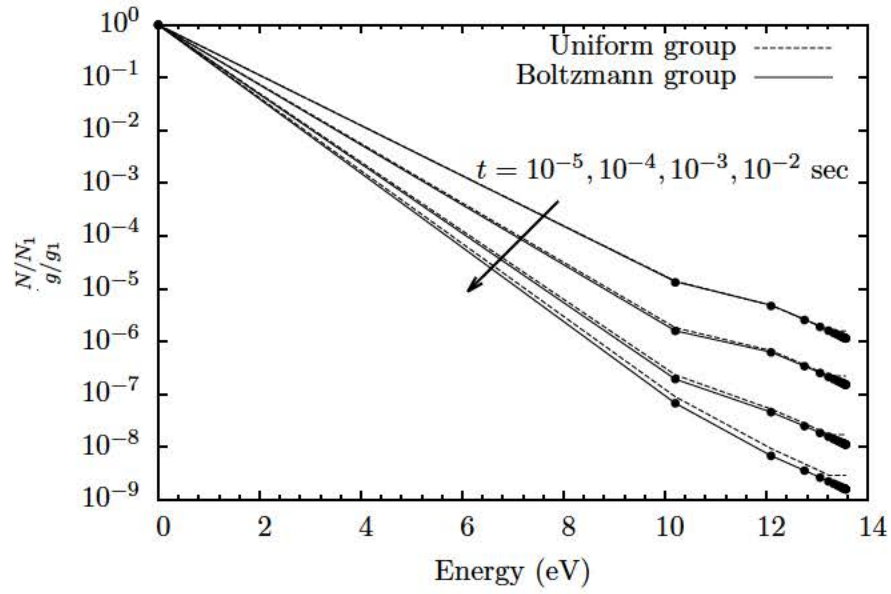


Figure 5.10: Snapshots of the ASDF at several times during the cooling process. The dots represent the full solution. The solid lines are the solution obtained using the level grouping with Boltzmann distribution. The broken lines are the solution obtained using the level grouping with uniform distribution.

(k) remains the same within numerical round-off errors. If we were dealing with only electron-impact collisions, it would be sufficient to sum the energies of all levels using the new population densities at the end of the time step, compute the difference and assign the change to E_e . However, there are two obvious problems with this scenario: a) when other collision partners must be accounted for, or when the electrons themselves are partitioned (e.g. for non-Maxwellian kinetics), one must be able to correctly apportion the changes in energy, e.g. to E_e and E_h (for heavy particles); and b) for large time steps, there is no guarantee that the subsequent change in E_e is physically acceptable, i.e. $E_e^{(k)} = E_e^{(k-1)} + \delta E_e > 0$. We must therefore include an evolution equation for E_e (and another for E_h if heavy particle collisions are included), which must then be fully coupled, so that the Jacobian of the system includes derivatives of the rates with respect to E_e , through the variation of T_e .

Energy conservation can be satisfied if the the construction of the source term on the right-hand-side of the master equations also satisfies it. Thus we must explicitly construct the energy source term from the master equations, as was already described briefly in equation (5.22). The same procedure is used, with the understanding that

$$\frac{dE_e}{dt} = - \sum_n \frac{d\mathcal{E}_n}{dt}$$

Thus we can combine contributions as follows:

$$\frac{dE_e}{dt} = -N_e \mathcal{N}_n \left[\sum_{\substack{m>n \\ i \in n}} \frac{g_i e^{-\Delta E_i/T_n}}{\mathcal{Z}_n} \sum_{j \in m} \Delta E_{ji} \alpha_{(j|i)} + \sum_{\substack{m<n \\ i \in n}} \frac{g_i e^{-\Delta E_i/T_n}}{\mathcal{Z}_n} \sum_{j \in m} \Delta E_{ji} \beta_{(j|i)} \right] \dots \quad (5.41)$$

where $\Delta E_{ji} = E_j - E_i$. Note that in the case of excitation from level $|i\rangle$, i.e. the first summation in equation (5.41), $\Delta E_{ji} > 0$, while $\Delta E_{ji} < 0$ in the second term for de-excitations from that level. We can then construct another set of effective rates, this time for the energy equation. Using the sub-partitioning of model B5,

the rates derived from the first term on the right of (5.38) are:

$$\tilde{\alpha}_{(m'|n')}^E = \left[\sum_{i \in n'} \frac{g_i e^{-\Delta E_i/T_n}}{\mathcal{Z}'_n} \sum_{j \in m'} \Delta E_{ji} \alpha_{(j|i)} \right] \quad (5.42a)$$

$$\tilde{\beta}_{(m'|n')}^E = \left[\sum_{i \in n'} \frac{g_i e^{-\Delta E_i/T_n}}{\mathcal{Z}'_n} \sum_{j \in m'} \Delta E_{ji} \beta_{(j|i)} \right] \quad (5.42b)$$

These rates enter the evolution equation for E_e as:

$$\frac{dE_e}{dt} = -N_e \mathcal{N}'_n \sum_{m>n} \tilde{\alpha}_{(m'|n')}^E - N_e \mathcal{N}'_n \sum_{m<n} \tilde{\beta}_{(m'|n')}^E + \dots \quad (5.43)$$

Note that the same formulation applies for uniform groups by taking the limit $T_n \rightarrow \infty$, and summing over the complete set $n = \{n_0, n'\}$. The rate of energy change can also be expressed as:

$$\tilde{\alpha}_{(m'|n')}^E = \tilde{\alpha}_{(m'|n')} \cdot \bar{\varepsilon}_{(m'|n')} \quad (5.44)$$

where $\alpha_{(m'|n')}$ is of course given by the effective rate for the conserved number densities:

$$\tilde{\alpha}_{(m'|n')} = \sum_{j \in m'} \sum_{i \in n'} \frac{g_i e^{-\Delta E_i/T_n}}{\mathcal{Z}'_n} \alpha_{(j|i)}$$

Equation (5.44) defines an average energy $\bar{\varepsilon}_{(m'|n')}$, transferred during excitation of levels of group n' to levels of group m' , which can be tabulated as function of the initial T_n and collisional (T_e) temperatures. This approach was successfully used, for example, for vibrational non-equilibrium [123].

5.5.1 Isochoric ionization test case

The third test case of Table 5.2 was designed to test for energy conservation. In this case, the energy loss and gain due to collisional processes are taken into account in the conservation equation for the electron energy. The evolution now proceeds at constant volume, and the electron temperature changes rapidly, as seen in Figure 5.11. The initial conditions are the same as those of the first

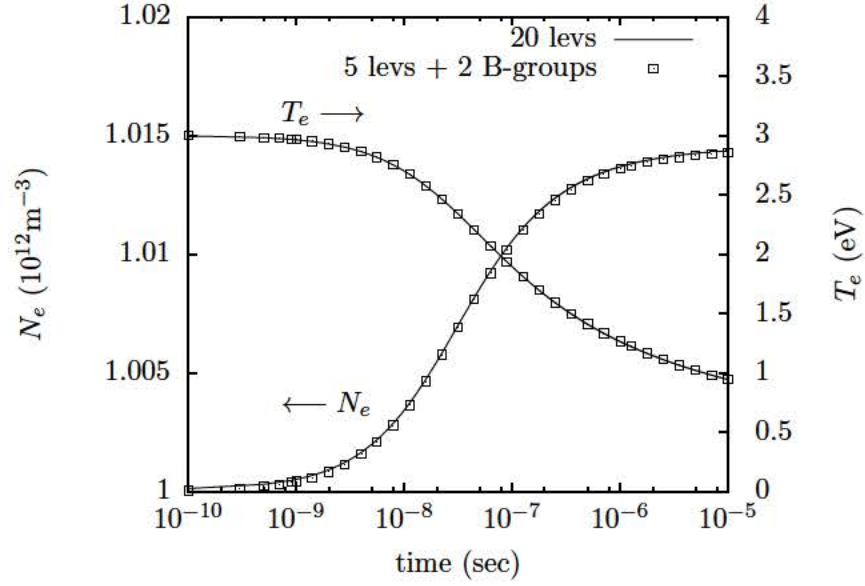


Figure 5.11: N_e, T_e evolution in constant-volume case.

test case, and the system is initially far below Boltzmann and Saha equilibrium. However, contrary to the isothermal case, the initial excitation and ionization processes deplete the electron energy and the system “freezes” rapidly, and the excited states remain at a low population density. If an external heating source was applied (e.g. Ohmic heating), the system would more closely resemble the isothermal test case, and the system would become stiff again. Here, we are mostly concerned with testing energy conservation and to simplify the analysis, the radiative rates were removed from the kinetics, so that no radiative energy losses were present.

We can monitor the error by comparing the values of E_e at the end of each time step with the total potential energy contained in the electronic states, by reconstruction of the level populations. Figure 5.12 shows both the accumulated error (symbols) and the one at each time step (blue line); this test was conducted with 5 resolved levels and 2 Boltzmann bins, and all computations were performed with a constant time step of 10^{-10} sec, using the same backward-Euler

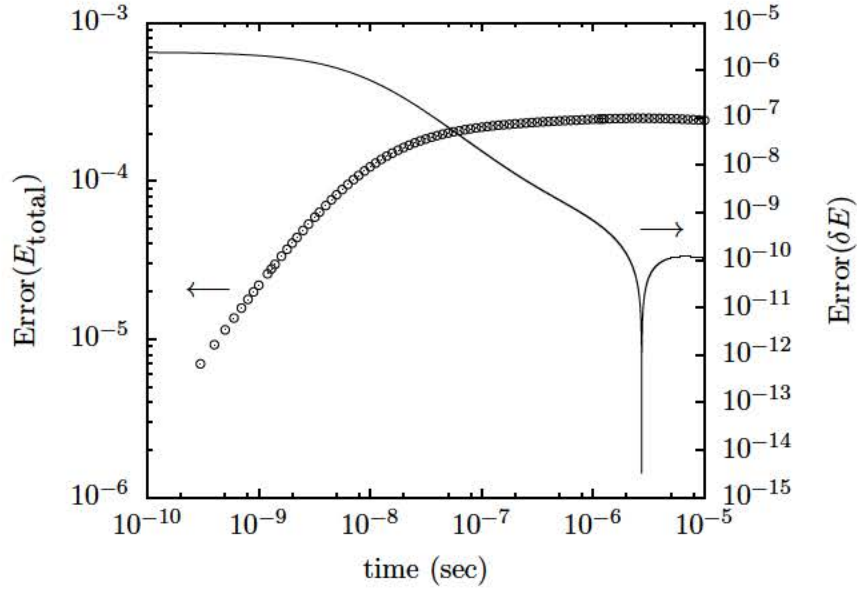


Figure 5.12: Cumulative and instantaneous relative errors in energy conservation - test case 3.

integration scheme ¹³.

The error is certainly acceptable, but it is not commensurate with numerical round-off, which we would have expected if the scheme was exactly energy-conserving. By comparison, the cumulative error in energy was below 10^{-13} when solving the full master equations without level grouping.

While the exact solution consists of summing-up the contributions from each individual level, leading to the rate of change expressed by equation (5.22). However, we are not using here the internal energy \mathcal{E}_n as a conserved variable, and we must be careful that the procedure be consistent with our definition, or *reconstruction* of the internal energy. The corrected procedure is described next.

¹³Note that the scheme includes numerical errors resulting from the forward and backward sweeps of the Gaussian elimination procedure. However, this is negligible here, since we have used double-precision.

5.5.2 Corrected energy rates

Consider for example the change in electron energy due to excitations and de-excitations, and let us examine first the case of uniform grouping.

$$\frac{dE_e}{dt} = - \sum_{m>n} \sum_n \tilde{\alpha}_{(m|n)}^E \mathcal{N}_n N_e + \sum_{m>n} \sum_n \tilde{\beta}_{(n|m)}^E \mathcal{N}_m N_e \quad (5.45)$$

There are two formulations of the effective rates of energy transfer:

Formulation 1

$$\tilde{\alpha}_{(m|n)}^E = \sum_{j \in m} \sum_{i \in n} \frac{g_i}{g_n} (E_j - E_i) \alpha_{(j|i)} \quad (5.46a)$$

$$\tilde{\beta}_{(m|n)}^E = \sum_{j \in m} \sum_{i \in n} \frac{g_j}{g_m} (E_j - E_i) \beta_{(i|j)} \quad (5.46b)$$

Formulation 2

$$\tilde{\alpha}_{(m|n)}^E = (\tilde{E}_m - \tilde{E}_n) \sum_{j \in m} \sum_{i \in n} \frac{g_i}{g_n} \alpha_{(j|i)} \quad (5.47a)$$

$$\tilde{\beta}_{(m|n)}^E = (\tilde{E}_m - \tilde{E}_n) \sum_{j \in m} \sum_{i \in n} \frac{g_j}{g_m} \beta_{(i|j)} \quad (5.47b)$$

where $\tilde{E}_n = \sum_{i \in n} \frac{g_i}{g_n} E_i$ and similarly for \tilde{E}_m .

Only the second formulation is exactly energy-conserving. This is quite clear because in that case, the term on the right side of (5.47) is the product of the change in number density of the groups ($d\mathcal{N}_n/dt$) and the difference in average group energy (\tilde{E}). Energy conservation follows from the definition of the total group energy $\mathcal{E}_n = \tilde{E}_n \mathcal{N}_n$. Thus, the model assumptions *constrain* us to choose the appropriate formulation of the effective rates for energy change that is consistent with the definition of group energy.

Let us now examine the case of the Boltzmann grouping (B5), using the pair of conserved variables (N_{n0}, \mathcal{N}'_n) ; the rates of energy exchange must therefore be

consistent with the electronic energy defined from these two variables, and with the equation of state used to describe the internal partition (i.e. T_n). We start with the conservation of the group energy:

$$\frac{d\mathcal{E}_n}{dt} = \frac{d}{dt} (N_{n_0} E_{n_0} + \mathcal{N}'_n \langle E \rangle_{n'}) = E_{n_0} \frac{dN_{n_0}}{dt} + \langle E \rangle_{n'} \frac{d\mathcal{N}'_n}{dt} + \mathcal{N}'_n \frac{d\langle E \rangle_{n'}}{dt} \quad (5.48)$$

Note that the averaging $\langle \rangle_{n'}$ is done for the remaining levels above the ground level n_0 of that group. We can write a similar equation for the total energy measured from the ground state of that group, i.e.:

$$\frac{d\Delta\mathcal{E}_n}{dt} \equiv \sum_{i \in n} \Delta E_i \frac{dN_i}{dt} = \frac{d}{dt} (\mathcal{N}'_n \langle \Delta E \rangle_{n'}) = \langle \Delta E \rangle_{n'} \frac{d\mathcal{N}'_n}{dt} + \mathcal{N}'_n \frac{d\langle \Delta E \rangle_{n'}}{dt} \quad (5.49)$$

The first term in equation (5.49) describes the change in group energy from the global change in population of the group, i.e. $\langle E \rangle_n d\mathcal{N}_n/dt$. The last term describes the change of the internal structure of the group as a result of the collisional transitions, since

$$\frac{d\langle \Delta E \rangle_{n'}}{dt} = \frac{1}{T_n^2} [\langle \Delta E^2 \rangle_{n'} - \langle \Delta E \rangle_{n'}^2] \frac{dT_n}{dt} = C_{v,n'} \frac{dT_n}{dt} \quad (5.50)$$

From (5.33),

$$\frac{d\mathcal{Z}'_n}{dt} = \frac{g_{n_0}}{N_{n_0}} \left[\frac{d\mathcal{N}'_n}{dt} - \frac{\mathcal{N}'_n}{N_{n_0}} \frac{dN_{n_0}}{dt} \right] = \mathcal{Z}'_n \left[\frac{\overline{\Delta E}'_n}{T_n^2} + \frac{d \ln \tilde{g}'_n}{dT_n} \right] \frac{dT_n}{dt} \quad (5.51)$$

Inserting into (5.49),

$$\mathcal{N}'_n \frac{d\langle \Delta E \rangle_{n'}}{dt} = \frac{C_{v,n'} T_n^2}{\left(\overline{\Delta E}'_n + T_n^2 \frac{d \ln \tilde{g}'_n}{dT_n} \right)} \left[\frac{d\mathcal{N}'_n}{dt} - \frac{\mathcal{N}'_n}{N_{n_0}} \frac{dN_{n_0}}{dt} \right] \quad (5.52)$$

We can now combine with the other terms of (5.49) to obtain an expression which only depends on the rates of change of the conserved variables $(N_{n_0}, \mathcal{N}'_n)$. Defining

$$\xi_{n'} = \frac{C_{v,n'} T_n^2}{\left(\overline{\Delta E}'_n + T_n^2 \frac{d \ln \tilde{g}'_n}{dT_n} \right)} \quad \text{and} \quad \omega_{n'} = \xi_{n'} \frac{\mathcal{N}'_n}{N_{n_0}} \quad (5.53)$$

and adding the contribution from the ground state of the group, we obtain:

$$\frac{d\mathcal{E}_n}{dt} = [E_{n_0} - \omega_{n'}] \frac{dN_{n_0}}{dt} + [E_{n_0} + \langle \Delta E \rangle_{n'} + \xi_{n'}] \frac{d\mathcal{N}'_n}{dt} \quad (5.54)$$

One can then identify the rates of change of the population density with the effective rates. Considering transitions between groups n and $m > n$, and using a similar expression for $d\mathcal{E}_m/dt$, we have:

$$\tilde{\alpha}_{(m_0|n_0)}^E = [E_{m_0} - \omega_{m'} - E_{n_0} + \omega_{n'}] \cdot \tilde{\alpha}_{(m_0|n_0)} \equiv \bar{\varepsilon}_{(m_0|n_0)} \cdot \tilde{\alpha}_{(m_0|n_0)} \quad (5.55a)$$

$$\tilde{\alpha}_{(m'|n_0)}^E = [E_{m_0} + \langle \Delta E \rangle_{m'} + \xi_{m'} - E_{n_0} + \omega_{n'}] \cdot \tilde{\alpha}_{(m'|n_0)} \equiv \bar{\varepsilon}_{(m'|n_0)} \cdot \tilde{\alpha}_{(m'|n_0)} \quad (5.55b)$$

$$\tilde{\alpha}_{(m_0|n')}^E = [E_{m_0} - \omega_{m'} - E_{n_0} - \langle \Delta E \rangle_{n'} - \xi_{n'}] \cdot \tilde{\alpha}_{(m_0|n')} \equiv \bar{\varepsilon}_{(m_0|n')} \cdot \tilde{\alpha}_{(m_0|n')} \quad (5.55c)$$

$$\tilde{\alpha}_{(m'|n')}^E = [E_{m_0} + \langle \Delta E \rangle_{m'} + \xi_{m'} - E_{n_0} - \langle \Delta E \rangle_{n'} - \xi_{n'}] \cdot \tilde{\alpha}_{(m'|n')} \equiv \bar{\varepsilon}_{(m'|n')} \cdot \tilde{\alpha}_{(m'|n')} \quad (5.55d)$$

It is instructive to examine the limit of infinite Boltzmann temperatures; in this case,

$$\mathcal{Z}_{n'} \rightarrow g'_n, \quad C_{v,n'}, \xi_{n'}, \omega_{n'} \rightarrow 0 \quad \text{and} \quad \langle \Delta E \rangle_{n'} \rightarrow \overline{\Delta E'}_n$$

and similarly for m' . Equation (5.54) becomes:

$$\begin{aligned} \frac{d\mathcal{E}_n}{dt} &= E_{n_0} \frac{dN_{n_0}}{dt} + \frac{\sum_{i \in n'} g_i E_i \mathcal{N}_{n'}}{g'_n} \frac{d\mathcal{N}_{n'}}{dt} = E_{n_0} \frac{dN_{n_0}}{dt} + \frac{\sum_{i \in n'} g_i E_i}{g_{n_0}} \frac{dN_{n_0}}{dt} \\ &= \frac{\sum_{i \in n} g_i E_i}{g_{n_0}} \frac{dN_{n_0}}{dt} = \tilde{E}_n \frac{d\mathcal{N}_n}{dt} \end{aligned} \quad (5.56)$$

where we have also used the fact that in that limit, $N_{n_0}/g_{n_0} = \mathcal{N}_n/g_n$, and used the definition of the average group energy – see equation (5.47). Since a similar equation is found for $d\mathcal{E}_m/dt$, the combination exactly yields (5.47). Thus, we have verified that by taking the limit $T_n, T_m \rightarrow 0$, we recover the uniform group model.

For ionizations and recombinations, a similar procedure can be found. Considering the change in electron energy due to ionization and recombination from

and to the group n , we have:

$$\left. \frac{dE_e}{dt} \right)_n = - \sum_{i \in n} \frac{dN_i}{dt} I_i = - \frac{d}{dt} [\langle I \rangle_n \mathcal{N}_n] = -I_{n_0} \frac{dN_{n_0}}{dt} - \langle I \rangle_{n'} \frac{d\mathcal{N}_{n'}}{dt} - \mathcal{N}_{n'} \frac{d\langle I \rangle_{n'}}{dt} \quad (5.57)$$

where I_i is the ionization potential for level i and $\langle I \rangle_{n'}$ is the group ionization potential averaged over the sub-partition n' . Using $I_i = I_H - E_i = I_{n_0} - \Delta E_i$, it is easy to see that:

$$\langle I \rangle_{n'} = I_{n_0} - \langle \Delta E \rangle_{n'} \quad \text{and} \quad \frac{d\langle I \rangle_{n'}}{dt} = -C_{v,n'} \quad (5.58)$$

Equations (5.51,5.52) are still valid, and using again the definitions (5.53), we obtain the final form:

$$\left. \frac{dE_e}{dt} \right)_n = - [I_{n_0} + \omega_{n'}] \frac{dN_{n_0}}{dt} - [I_{n_0} - \langle \Delta E \rangle_{n'} - \xi_{n'}] \frac{d\mathcal{N}_{n'}}{dt} \quad (5.59)$$

Note the similarity with (5.54). The effective rates are therefore:

$$\tilde{\alpha}_{(+|n_0)}^E = [I_{n_0} + \omega_{n'}] \cdot \tilde{\alpha}_{(+|n_0)} \equiv \bar{\varepsilon}_{(+|n_0)} \cdot \tilde{\alpha}_{(+|n_0)} \quad (5.60a)$$

$$\tilde{\alpha}_{(+|n')}^E = [I_{n_0} - \langle \Delta E \rangle_{n'} - \xi_{n'}] \cdot \tilde{\alpha}_{(+|n')} \equiv \bar{\varepsilon}_{(+|n')} \cdot \tilde{\alpha}_{(+|n')} \quad (5.60b)$$

Examination of equations (5.55) and (5.60) reveals that the overall procedure consists of replacing the energy of the group's ground state n_0 and sub-partition n' by *effective energies* for the energy exchange:

$$\tilde{E}_{n_0} = E_{n_0} - \omega_{n'} \quad \text{and} \quad \tilde{E}_{n'} = E_{n_0} + \langle \Delta E \rangle_{n'} + \xi_{n'} \quad (5.61)$$

Thus, the effective rates of energy transfer become:

$$\tilde{\alpha}_{(m_0|n_0)}^E = \left(\tilde{E}_{m_0} - \tilde{E}_{n_0} \right) \cdot \tilde{\alpha}_{(m_0|n_0)} \quad (5.62a)$$

$$\tilde{\alpha}_{(m'|n_0)}^E = \left(\tilde{E}_{m'} - \tilde{E}_{n_0} \right) \cdot \tilde{\alpha}_{(m'|n_0)} \quad (5.62b)$$

$$\tilde{\alpha}_{(m_0|n')}^E = \left(\tilde{E}_{m_0} - \tilde{E}_{n'} \right) \cdot \tilde{\alpha}_{(m_0|n')} \quad (5.62c)$$

$$\tilde{\alpha}_{(m'|n')}^E = \left(\tilde{E}_{m'} - \tilde{E}_{n'} \right) \cdot \tilde{\alpha}_{(m'|n')} \quad (5.62d)$$

and for ionization:

$$\tilde{\alpha}_{(+|n_0)}^E = \left(I_H - \tilde{E}_{n_0} \right) \cdot \tilde{\alpha}_{(+|n_0)} \quad (5.63a)$$

$$\tilde{\alpha}_{(+|n')}^E = \left(I_H - \tilde{E}_{n'} \right) \cdot \tilde{\alpha}_{(+|n')} \quad (5.63b)$$

The use of effective group energies¹⁴ provides a straightforward approach, and the effective rates of energy transfer for *all* transitions (including de-excitations, recombination and radiative transitions) can now be expressed in a simple form. Note that (5.63) is similar to the case of uniform grouping (5.47) and since we have already demonstrated that we can recover the uniform grouping case in the limit of infinite temperatures, we have achieved here a fully consistent model.

We are now left with the task of verifying energy conservation with this revised approach. Using the same test case (#3), we now find a much smaller level of error, as can be seen from Figure 5.13 – compare with Figure 5.12 – that is characteristic of the level of numerical round-off. Note that the cumulative error sums the absolute values of the stepwise error (L_1 norm), and is therefore a maximum bound. Figure 5.14 shows the effect of bin size on the relative error; this observation is similar to the one made regarding the accuracy of the ASDF – see Figure 5.4, i.e. smaller group widths are preferred. However, it is clear that even for one or two bins, the error on energy conservation remains very small.

¹⁴Contrary to the uniform grouping case, we need to use two values, one for n_0 and one for n' , which reflects the additional degrees of freedom in the Boltzmann model.

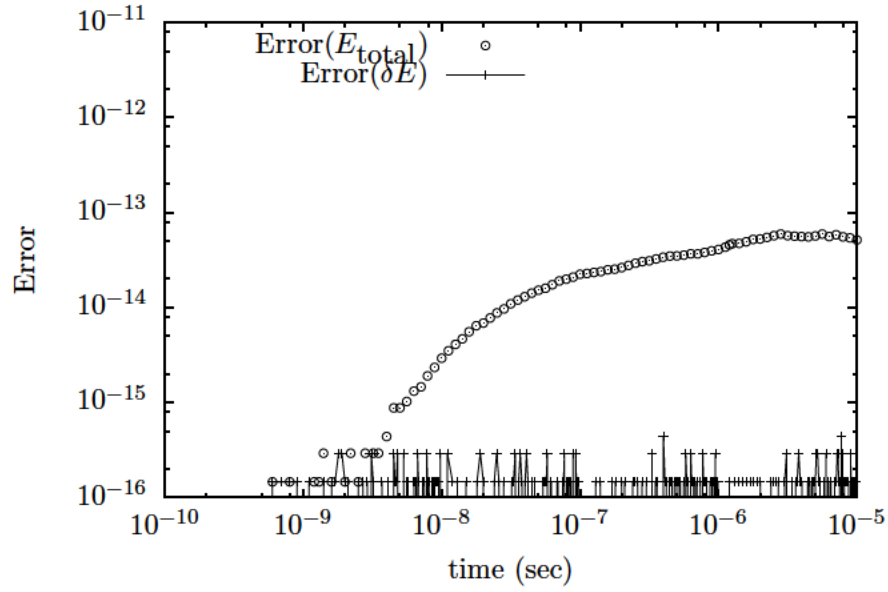


Figure 5.13: Cumulative and instantaneous relative errors in energy conservation
- test case 3 - with revised formulation

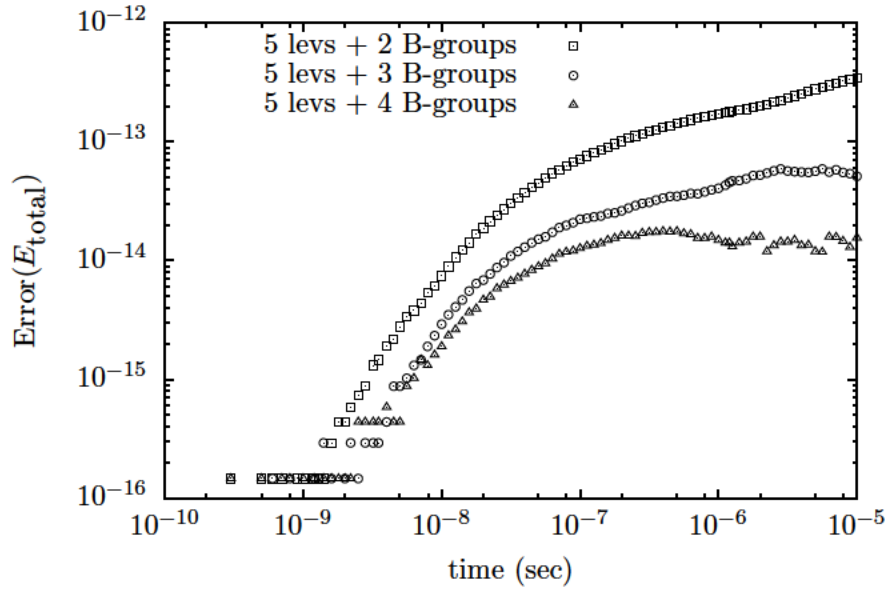


Figure 5.14: Cumulative relative errors in energy conservation as function of group
sizes; revised formulation.

CHAPTER 6

Modeling of Collisions in Multifluid Plasmas

6.1 Introduction

Modeling of elastic collisions in neutral gases and plasmas is a classical topic widely studied in the kinetic theory of transport phenomena [52, 44, 84, 53]. The derivation starts from the kinetic equation with a Boltzmann collision operator for neutral collision, and/or Landau-Fokker-Planck collision operator for charged particle collision. The transport terms appearing in the hydrodynamic equations, e.g., viscous shear stress and heat flux, are obtained by computing the collision integral with a perturbative expansion of the velocity distribution function (VDF) about a local Maxwellian one, i.e., $f = f^M + \epsilon \delta f + O(\epsilon^2)$, where ϵ is a small parameter. The Chapman-Enskog expansion [44] and Grad's method [47] are the two well-known moment closure schemes, from which the Euler/Navier-Stokes and the Grad-moment equations are derived, respectively.

The treatment of elastic collisions, within a *multi-fluid* framework, can be found from the works of Braginskii [46] and Burgers [43]. In 1965, Braginskii derived a two-fluid system of equations for a fully ionized plasma with a Chapman-Enskog closure for the transport fluxes taking into account the effect of the magnetic field; these equations are now commonly referred to as the Braginskii's equations. Burgers, on the other hand, presented a rather general framework for the modeling of elastic collisions, which is applicable for a general system of moment equations beyond the standard five-moment model.

In this chapter, we present a derivation of the exchange terms for number, momentum, and total energy densities due to *inelastic* collisions. These terms are relevant for the construction of a collisional-radiative (CR) model within the framework of the multi-fluid equations. We restrict ourselves to the case where the VDF of each fluid is a Maxwellian distribution function. Current work focuses on excitation and deexcitation collisions, but the method can be generalized to other collision types, e.g., ionization/recombination, charge exchange collision, etc.

6.2 Transfer integral

Let us consider an inelastic collision between two particles s and t , such that the particle t changes its internal state. The particles s and t are respectively the scattered and target in the laboratory frame of reference (LAB), the former being identified here as the electron and the target being the atom, but we will keep the s, t notation until explicit assumptions and approximations are made, such as neglecting terms of order m_s/m_t for final expressions.

$$s(\mathbf{v}_s) + t(\mathbf{v}_t) \Leftrightarrow s'(\mathbf{v}'_s) + t'(\mathbf{v}'_t) \quad (6.1)$$

The initial velocities are $\mathbf{v}_s, \mathbf{v}_t$, where $\mathbf{v} = \mathbf{u} + \mathbf{c}$ and \mathbf{u} is the fluid mean velocity in the LAB frame, and post-collision values are indicated by a prime. Thus, \mathbf{c} is the thermal velocity and if $\langle \dots \rangle$ denotes a statistical average over the corresponding distribution function, we have $\langle \mathbf{v} \rangle \equiv \mathbf{u}$ and $\langle \mathbf{c} \rangle \equiv 0$. It is more convenient to treat the collision in the center of mass (COM) reference frame, moving with velocity \mathbf{V} with respect to the LAB frame. Similarly, we can also define a mean velocity of this COM frame as \mathbf{U} . The subsequent Galilean transformations yield the following definitions:

$$\mathbf{V} = \frac{m_s \mathbf{v}_s + m_t \mathbf{v}_t}{M} \quad \mathbf{g} = \mathbf{v}_s - \mathbf{v}_t \quad (6.2a)$$

$$\mathbf{U} = \frac{m_s \mathbf{u}_s + m_t \mathbf{u}_t}{M} \quad \mathbf{w} = \mathbf{u}_s - \mathbf{u}_t \quad (6.2b)$$

where $M = m_s + m_t$. The inverse transformation yields:

$$\mathbf{v}_s = \mathbf{V} + \frac{m_t}{M} \mathbf{g} \quad \mathbf{u}_s = \mathbf{U} + \frac{m_t}{M} \mathbf{w} \quad (6.3a)$$

$$\mathbf{v}_t = \mathbf{V} - \frac{m_s}{M} \mathbf{g} \quad \mathbf{u}_t = \mathbf{U} - \frac{m_s}{M} \mathbf{w} \quad (6.3b)$$

One can also define a similar transformation for the post-collision variables. Expressed in the COM frame and for any inelastic collision with an energy transfer $\Delta\varepsilon$, momentum and energy conservation yield:

$$M\mathbf{V} \equiv M\mathbf{V}' \quad (6.4a)$$

$$\frac{1}{2}M\mathbf{V}^2 + \frac{1}{2}\mu\mathbf{g}^2 \equiv \frac{1}{2}M\mathbf{V}'^2 + \frac{1}{2}\mu\mathbf{g}'^2 + \Delta\varepsilon \quad (6.4b)$$

where \mathbf{V}' and \mathbf{g}' are defined similarly to (6.2), and $\mu = m_s m_t / M$ is the reduced mass. Note that we have also implicitly assumed that the collision produces only two particles, as evidenced by the expression for the kinetic energy – this assumption must be revisited when dealing with ionization and recombination, along with the assumption of equal masses of individual particles before and after the collision, e.g. $m'_s \equiv m_s$, such that mass conservation is automatically obtained. Therefore, we have the following constraints:

$$\mathbf{V} \equiv \mathbf{V}' \quad \text{and} \quad \mathbf{g}^2 = \mathbf{g}'^2 + \frac{2\Delta\varepsilon}{\mu} \quad (6.5)$$

For an excitation between two atomic levels, the transferred energy is a fixed value $\Delta\varepsilon \equiv \varepsilon^*$, the energy gap between levels, while for ionization the energy is a continuum of values: $\Delta\varepsilon \in [\varepsilon^*, \varepsilon]$, where $\varepsilon = \frac{1}{2}\mu\mathbf{g}^2$ is the available kinetic energy (in the COM frame). In the limit $\Delta\varepsilon \rightarrow 0$, the collision is elastic.

We can then define a transfer integral of the collision operator between the two species s and t [43].

$$\Psi_{st} = n_s n_t \int d^3\mathbf{v}_s d^3\mathbf{v}_t f_s f_t g \int \psi d\omega(\mathbf{v}_s, \mathbf{v}_t; \mathbf{v}'_s, \mathbf{v}'_t) \quad (6.6)$$

where g is the magnitude of the relative velocity ($g = |\mathbf{g}|$), $d\omega$ is the differential cross section, and ψ is any moment variable exchanged during the collision. Let

us now utilize the transformation defined in appendix C:

$$\mathbf{V}^* = \mathbf{V} - \mathbf{U} + \gamma \tilde{\mathbf{g}} \quad T^* = \frac{MT_s T_t}{m_s T_t + m_t T_s} \quad a^2 = \frac{2kT^*}{M} \quad (6.7a)$$

$$\tilde{\mathbf{g}} = \mathbf{g} - \mathbf{w} \quad \tilde{T} = \frac{m_s T_t + m_t T_s}{M} \quad \alpha^2 = \frac{2k\tilde{T}}{\mu} \quad (6.7b)$$

$$\gamma = \frac{\mu(T_t - T_s)}{m_s T_t + m_t T_s} \quad (6.7c)$$

One can easily show that the Jacobian of the transformations is unity, i.e.

$$d^3 \mathbf{v}_s d^3 \mathbf{v}_t \equiv d^3 \mathbf{V} d^3 \mathbf{g} \equiv d^3 \mathbf{V}^* d^3 \mathbf{g} \equiv d^3 \mathbf{V}^* d^3 \tilde{\mathbf{g}} \quad (6.8)$$

Using the transformed variables, the product of two Maxwellian VDFs in equation (6.6) becomes:

$$f_s \cdot f_t = \left(\frac{M}{2\pi k T^*} \right)^{\frac{3}{2}} \exp \left[-\frac{M \mathbf{V}^{*2}}{2k T^*} \right] \cdot \left(\frac{\mu}{2\pi k \tilde{T}} \right)^{\frac{3}{2}} \exp \left[-\frac{\mu \tilde{\mathbf{g}}^2}{2k \tilde{T}} \right] \equiv f_{V^*} \cdot f_g \quad (6.9)$$

Substituting the result of equation (6.9) into (6.6), the transfer integral can be written as follows:

$$\begin{aligned} \Psi_{st} = & n_s n_t \left(\frac{M}{2\pi k T^*} \right)^{\frac{3}{2}} \int d^3 \mathbf{V}^* \exp \left[-\frac{M \mathbf{V}^{*2}}{2k T^*} \right] \cdot \\ & \left(\frac{\mu}{2\pi k \tilde{T}} \right)^{\frac{3}{2}} \int d^3 \mathbf{g} \exp \left[-\frac{\mu (\mathbf{g} - \mathbf{w})^2}{2k \tilde{T}} \right] g \int \psi d\omega(\mathbf{g}; \mathbf{g}') \end{aligned} \quad (6.10)$$

In the COM reference frame, the differential cross section only depends on the relative velocities, i.e., $d\omega(\mathbf{v}_s, \mathbf{v}_t; \mathbf{v}'_s, \mathbf{v}'_t) \equiv d\omega(\mathbf{g}; \mathbf{g}')$, and can be expressed as:

$$d\omega(\mathbf{g}; \mathbf{g}') = \sigma_{st}(g, \Omega') d\Omega' \quad (6.11)$$

where Ω' is the solid angle between the initial and final relative velocities, i.e., $d\Omega' = d\rho d\cos\chi$ with $\mathbf{g} \cdot \mathbf{g}' = gg' \cos\chi$. Without loss of generality, we can now choose a reference frame (LAB) such that the relative *mean* velocity \mathbf{w} is aligned with the z axis, as shown in figure 6.1. Thus, the unit vectors $\hat{\mathbf{g}}, \hat{\mathbf{g}}'$ are obtained by subsequent rotations of the (x, y, z) frame. Using the abbreviated notation

$c_\varphi \equiv \cos \varphi$, $s_\varphi \equiv \sin \varphi$, etc, we define this rotation operator by the matrix:

$$R(\varphi, \theta) = \begin{pmatrix} c_\varphi s_\theta & -s_\varphi & c_\varphi s_\theta \\ s_\varphi c_\theta & c_\varphi & s_\varphi s_\theta \\ -s_\theta & 0 & c_\theta \end{pmatrix} \quad \text{and} \quad \hat{\mathbf{g}} = \frac{\mathbf{g}}{g} = R(\varphi, \theta) \cdot \hat{\mathbf{z}} = \begin{pmatrix} c_\varphi s_\theta \\ s_\varphi s_\theta \\ c_\theta \end{pmatrix} \quad (6.12)$$

Similarly, the post-collision relative velocity is rotated by the angles (ρ, χ) , such that $\hat{\mathbf{g}}' = R(\rho, \chi) \cdot \hat{\mathbf{g}}$.

Using $d^3\mathbf{g} = g^2 dg d\varphi dc_\theta = 2\pi g^2 dg dc_\theta$ and equation (6.11), the transfer integral can be written as:

$$\Psi_{st} = \frac{4n_s n_t}{\pi^{\frac{1}{2}} \alpha^3} e^{-w^2/\alpha^2} \cdot \int d^3\mathbf{V}^* f_{V^*} \cdot \int dg g^3 e^{-g^2/\alpha^2} \cdot \frac{1}{2} \int dc_\theta e^{2gwc_\theta/\alpha^2} \int d\rho dc_\chi \psi \sigma_{st}(g, \Omega') \quad (6.13)$$

Note that if ψ is independent of \mathbf{V}^* , the first integral on the RHS is simply the normalization of a Maxwellian VDF ($= 1$). For clarity, let us now consider the case where ψ is not a function of \mathbf{V}^* , so the integral $\int d^3\mathbf{V}^* f_{V^*}$ can be omitted. By symmetry, the differential cross-section σ_{st} does not depend on ρ , and we can write:

$$\sigma_{st}(g, \Omega') \equiv \bar{\sigma}_{st}(g) \cdot \mathcal{G}(g, \chi) \quad \text{s.t.} \quad \int d\rho d\cos\chi \mathcal{G}(g, \chi) \equiv 1 \quad (6.14)$$

More generally, we will define the averaging of any function ψ over the scattering angles as:

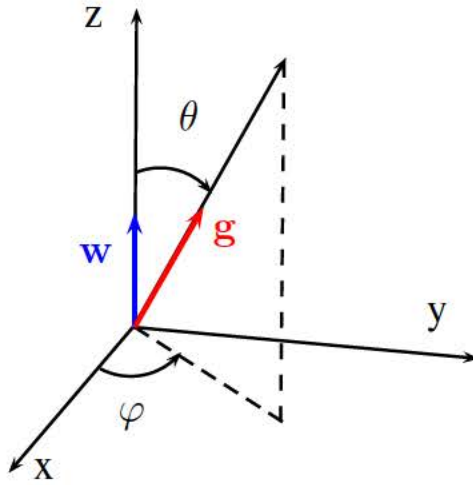
$$\langle \psi \rangle_{\Omega'} = 2\pi \int_{-1}^{+1} dc_\chi \psi \mathcal{G}(g, \chi) \quad (6.15)$$

We now define the following, normalized energy variables:

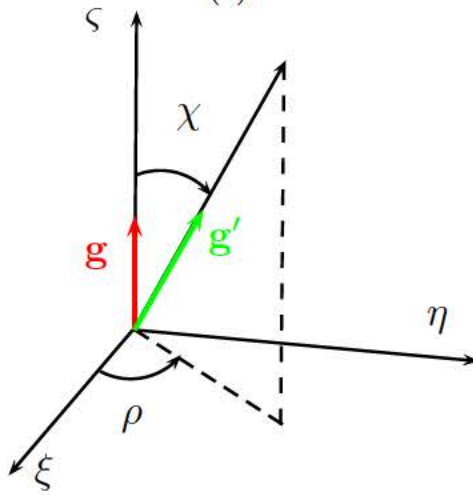
$$\varepsilon = \frac{1}{2} \mu g^2 \quad \bar{\varepsilon} = \frac{1}{2} \mu w^2 \quad (6.16a)$$

$$x = \frac{\varepsilon}{k\tilde{T}} \quad \lambda = \frac{\bar{\varepsilon}}{k\tilde{T}} \quad (6.16b)$$

$$x^* = \frac{\Delta\varepsilon}{k\tilde{T}} \quad x' = \frac{\varepsilon'}{k\tilde{T}} = x - x^* \quad (6.16c)$$



(a)



(b)

Figure 6.1: Frame rotation and relative orientation of (a) \mathbf{w} and \mathbf{g} and (b) \mathbf{g} and \mathbf{g}' . The rotation operator matrix $R(\varphi, \theta)$ (or $R(\rho, \chi)$) is defined such that $\hat{\mathbf{g}} = R(\varphi, \theta) \cdot \hat{\mathbf{w}}$ and $\hat{\mathbf{g}}' = R(\rho, \chi) \cdot \hat{\mathbf{g}}$.

Using $g^3 dg \equiv 2\varepsilon d\varepsilon/\mu^2$ and a trivial integration¹ over φ , we obtain:

$$\Psi_{st} = n_s n_t \underbrace{\left(\frac{8k\tilde{T}}{\pi\mu} \right)^{\frac{1}{2}}}_{\bar{g}_{\tilde{T}}} \frac{e^{-\bar{\varepsilon}/k\tilde{T}}}{(k\tilde{T})^2} \int_{\varepsilon^*}^{\infty} d\varepsilon \varepsilon e^{-\varepsilon/k\tilde{T}} \bar{\sigma}_{st}(\varepsilon) \cdot \frac{1}{2} \int_{-1}^{+1} dc_{\theta} e^{2\sqrt{\bar{\varepsilon}\varepsilon}c_{\theta}/k\tilde{T}} \cdot \langle \psi \rangle_{\Omega'} \quad (6.17)$$

where $\bar{g}_{\tilde{T}}$ is a thermal velocity based on the average temperature \tilde{T} . Equation (6.17) can be written in terms of the normalized variables as follows:

$$\Psi_{st} = n_s n_t \bar{g}_{\tilde{T}} e^{-\lambda} \int_{x^*}^{\infty} dx x e^{-x} \bar{\sigma}_{st}(x) \cdot \frac{1}{2} \int_{-1}^{+1} dc_{\theta} e^{2\sqrt{\lambda x}c_{\theta}} \cdot \langle \psi \rangle_{\Omega'} \quad (6.18)$$

Note that we have left the variable ψ undetermined, and since it could potentially depend on all integration variables (x, χ, θ) , it must be kept inside all integrals. We will see next what simplifications can be made, depending on which moment variables we are integrating. Note also that the lower limit of integration, x^* , is zero for elastic collisions.

6.3 Excitation/Deexcitation collisions

In this section, we consider an excitation collision and its reverse process:

$$s(\mathbf{v}_s) + t(E_{\ell}, \mathbf{v}_t) \Leftrightarrow s(\mathbf{v}'_s) + t(E_u, \mathbf{v}'_t) \quad (6.19)$$

where the particle indices (s, t) are kept the same to indicate that both internal states (ℓ, u) belong to the same fluid t . For the case of an excitation collision, particle t changes its internal states from ℓ to u ($\ell \rightarrow u$), where ℓ and u denote the lower and upper energy states, respectively. For a deexcitation collision, we have the reverse ($u \rightarrow \ell$). Conservation of momentum and energy are the same as those expressed in equation (6.4) with $\Delta\varepsilon = E_u - E_{\ell}$ and $\Delta\varepsilon > 0$.

In the CR model, each internal state is treated as a pseudo-species, so the rate of change in number density for each state (n_{ℓ}, n_u) is taken into account separately.

¹Using symmetry principles.

However, since both states (ℓ, u) belong to the same fluid, we only need to keep track of the net change of momentum and energy of each fluid due to the collision.

6.3.1 Zeroth-order moment: number density

The rate of change of the number density due to an excitation collision of type (6.19) can be obtained by setting $\psi \equiv 1$ in (6.18), so the average over all the scattering angle is trivially removed. We can express the rate of change of number density as:

$$\Gamma_{s\ell}^\uparrow = n_s n_\ell \bar{g}_{\bar{T}} e^{-\lambda} \int_{x^*}^{\infty} dx x e^{-x} \bar{\sigma}_{s\ell}^\uparrow(x) \cdot \frac{1}{2} \int_{-1}^{+1} dc_\theta e^{2\sqrt{\lambda x} c_\theta} \quad (6.20)$$

where superscript \uparrow denotes the forward process ($\ell \rightarrow u$), and (n_ℓ, n_u) are the number densities of the lower and upper states.

To perform the integral over dc_θ , we define:

$$\zeta^{(0)}(\xi) = \frac{1}{2} \int_{-1}^{+1} dy e^{2\xi y} = \frac{\sinh(2\xi)}{2\xi} \quad \text{s.t.:} \quad \lim_{\xi \rightarrow 0} \zeta^{(0)} = 1 \quad (6.21)$$

Combining all, we arrive at the following expression for the rate of change of the number density:

$$\Gamma_{s\ell}^\uparrow = n_s n_\ell \bar{g}_{\bar{T}} e^{-\lambda} \int_{x^*}^{\infty} dx x e^{-x} \zeta^{(0)}(\sqrt{\lambda x}) \bar{\sigma}_{s\ell}^\uparrow(x) \quad (6.22)$$

Note that

$$\frac{dn_\ell}{dt} = -\Gamma_{s\ell}^\uparrow = -\frac{dn_u}{dt}$$

In the case of electron-impact excitation ($s \equiv e$), we can neglect terms of order m_e/M , and for an atomic transition between levels $\ell \rightarrow u$, we obtain:

$$\Gamma_{e\ell}^\uparrow = n_e n_\ell \bar{v}_e e^{-\lambda} \int_{x^*}^{\infty} dx x e^{-x} \zeta^{(0)}(\sqrt{\lambda x}) \bar{\sigma}_{e\ell}^\uparrow(x) \quad (6.23)$$

where $\bar{v}_e = \sqrt{\frac{8kT_e}{\pi m_e}}$. In the limit of thermal plasma when multi-fluid effects are weak, i.e. $\lambda \rightarrow 0$, we obtain:

$$\Gamma_{e\ell}^\uparrow = n_e n_\ell \bar{v}_e \int_{x^*}^{\infty} dx x e^{-x} \bar{\sigma}_{e\ell}^\uparrow(x) \quad (6.24)$$

which is *exactly* the expected result for a single-fluid plasma.

The reverse process of deexcitation ($u \rightarrow \ell$) can be computed in a similar fashion by considering \mathbf{g}' , \mathbf{g} as the initial and final relative velocities respectively. The transfer integral becomes:

$$\Psi_{su}^\downarrow = n_s n_u \bar{g}_{\tilde{T}} e^{-\lambda} \int d^3 \mathbf{V}'^* f_{V'^*} \cdot \int_0^\infty dx' x' e^{-x'} \bar{\sigma}_{su}^\downarrow(x') \cdot \frac{1}{2} \int_{-1}^{+1} dc_\theta e^{2\sqrt{\lambda x'} c_\theta} \cdot \langle \psi \rangle_{\Omega'} \quad (6.25)$$

where superscript \downarrow indicates the reverse process ($u \rightarrow \ell$), and now $\cos \theta = \hat{\mathbf{g}}' \cdot \hat{\mathbf{w}}$. Setting $\psi = 1$, it is straightforward to obtain:

$$\Gamma_{su}^\downarrow = n_s n_u \bar{g}_{\tilde{T}} e^{-\lambda} \int_0^\infty dx' x' e^{-x'} \zeta^{(0)}(\sqrt{\lambda x'}) \bar{\sigma}_{su}^\downarrow(x') \quad (6.26)$$

Note that the lower limit of integration has changed, since deexcitation does not have an energy threshold (recall that $x' = x - x^*$). Using the Klein-Rosseland relation for detailed balance [87],

$$\bar{\sigma}_{s\ell}^\uparrow(x) g_\ell = \bar{\sigma}_{su}^\downarrow(x') g_u \quad (6.27)$$

where g_ℓ, g_u are the degeneracies of the lower and upper atomic levels respectively. The principle of detailed balance for various processes are discussed in detail in appendix D. We can write the excitation rate as follows:

$$\Gamma_{s\ell}^\uparrow = n_s n_\ell \bar{g}_{\tilde{T}} e^{-\lambda} \frac{g_u}{g_\ell} e^{-x^*} \int_0^\infty dx' x' e^{-x'} \zeta^{(0)}(\sqrt{\lambda(x^* + x')}) \bar{\sigma}_{su}^\downarrow(x') \quad (6.28)$$

One can then easily extract reaction rates, for example:

$$\Gamma_{s\ell}^\uparrow = \varpi_{s\ell}^\uparrow \cdot n_s n_\ell$$

It is instructive to consider the ratio of these rates:

$$\frac{\varpi_{s\ell}^\uparrow}{\varpi_{su}^\downarrow} = \left[\frac{g_u}{g_\ell} e^{-x^*} \right] \cdot \frac{\int_0^\infty dx' x' e^{-x'} \zeta^{(0)}(\sqrt{\lambda(x' + x^*)}) \bar{\sigma}_{su}^\downarrow(x')}{\int_0^\infty dx' x' e^{-x'} \zeta^{(0)}(\sqrt{\lambda x'}) \bar{\sigma}_{su}^\downarrow(x')} \quad (6.29)$$

The first term in brackets is the traditional Boltzmann equilibrium relation; the second term contains the correction due to the multi-fluid effects, and is apparent

only through the presence of the $\zeta^{(0)}$ function. A Taylor expansion near $\lambda = 0$ yields (with an obvious definition of the Boltzmann function \mathcal{B}):

$$\begin{aligned} \frac{\varpi_{s\ell}^\uparrow}{\varpi_{su}^\downarrow} &= \left[\frac{g_u}{g_\ell} e^{-x^*} \right] \cdot \frac{\int_0^\infty dx' x' e^{-x'} \left[1 + \frac{2\lambda(x^*+x')}{3} \right] \bar{\sigma}_{su}^\downarrow(x')}{\int_0^\infty dx' x' e^{-x'} \left[1 + \frac{2\lambda x'}{3} \right] \bar{\sigma}_{su}^\downarrow(x')} \\ &\simeq \left[\mathcal{B}_{\ell u}(\tilde{T}) \right] \cdot \left(1 + \frac{2\lambda x^*}{3} \right) \end{aligned} \quad (6.30)$$

Thus, we recover the expression for Boltzmann equilibrium in the single-fluid limit ($\lambda \rightarrow 0$). Note that the correction term is larger for large energy thresholds, i.e. transitions between high levels ($x^* \rightarrow 0$) will not be affected very much by the multi-fluid effects, while the impact will be stronger for excitation from low energy levels, with high energy gaps.

6.3.2 First-order moment: momentum density

Consider the forward reaction and the corresponding loss of momentum to the particles with velocity \mathbf{v}_s . The transfer variable in this case is $\psi = m_s \mathbf{v}_s$, and starting from equation (6.13), this leads to the following contribution to the momentum equation:

$$\mathbf{R}_s^- = -\frac{4n_s n_\ell}{\pi^{\frac{1}{2}} \alpha^3} \cdot \int d^3 \mathbf{V}^* f_{V^*} \cdot \int dg g^3 e^{-g^2/\alpha^2} \bar{\sigma}_{s\ell}^\uparrow(g) \cdot \frac{1}{2} \int dc_\theta e^{2gwc_\theta/\alpha^2} \langle m_s \mathbf{v}_s \rangle_{\Omega'} \quad (6.31)$$

Similarly, the gain in momentum is given by the production of new particles with velocity \mathbf{v}'_s :

$$\mathbf{R}_s^+ = +\frac{4n_s n_\ell}{\pi^{\frac{1}{2}} \alpha^3} \cdot \int d^3 \mathbf{V}^* f_{V^*} \cdot \int dg g^3 e^{-g^2/\alpha^2} \bar{\sigma}_{s\ell}^\uparrow(g) \cdot \frac{1}{2} \int dc_\theta e^{2gwc_\theta/\alpha^2} \langle m_s \mathbf{v}'_s \rangle_{\Omega'} \quad (6.32)$$

The *net* rate of change to the momentum density of species s is:

$$\mathbf{R}_s^\uparrow = -\frac{4\mu n_s n_\ell}{\pi^{\frac{1}{2}} \alpha^3} \cdot \int dg g^3 e^{-g^2/\alpha^2} \bar{\sigma}_{s\ell}^\uparrow(g) \cdot \frac{1}{2} \int dc_\theta e^{2gwc_\theta/\alpha^2} \langle \mathbf{g} - \mathbf{g}' \rangle_{\Omega'} \quad (6.33)$$

where we have used the relation:

$$m_s(\mathbf{v}_s - \mathbf{v}'_s) = \mu(\mathbf{g} - \mathbf{g}') \quad (6.34)$$

Note that in equation (6.33), the integral over \mathbf{V}^* -space is omitted since ψ does not depend on \mathbf{V}^* . Let us consider the last integral over the scattering angle. From figure 6.1, the vectors \mathbf{g}, \mathbf{g}' in the rotated frame (ξ, η, ς) are:

$$\mathbf{g} = g \hat{\mathbf{g}} = g \cdot \begin{pmatrix} 0 \\ 0 \\ 1 \end{pmatrix} \quad \mathbf{g}' = g' \hat{\mathbf{g}}' = g' \begin{pmatrix} c_\rho s_\chi \\ s_\rho s_\chi \\ c_\chi \end{pmatrix} \quad (6.35)$$

Therefore the integral yields, using (6.15):

$$\begin{aligned} \int d\Omega' (\mathbf{g}' - \mathbf{g}) \mathcal{G}(g, \Omega') &= 2\pi g' \int dc_\chi c_\chi \mathcal{G}(g, \chi) \hat{\mathbf{g}} - 2\pi g \int dc_\chi \mathcal{G}(g, \chi) \hat{\mathbf{g}} \\ &= [g' \langle \cos \chi \rangle_{\Omega'} - g] \hat{\mathbf{g}} \end{aligned} \quad (6.36)$$

We must now express the vector $\hat{\mathbf{g}}$ in the initial (x, y, z) frame, which is given by (6.12). Let us also utilize the normalized variables as defined in (6.16). This leads to the following expression:

$$\begin{aligned} \mathbf{R}_s^\uparrow &= -\hat{\mathbf{w}} \mu \alpha n_s n_\ell \bar{g}_{\bar{T}} e^{-\lambda} \int_{x^*}^{\infty} dx x e^{-x} \bar{\sigma}_{s\ell}^\uparrow(x) \left[\sqrt{x} - \sqrt{x'} \langle \cos \chi \rangle_{\Omega'} \right] \\ &\quad \cdot \frac{1}{2} \int_{-1}^{+1} dc_\theta c_\theta e^{2\sqrt{\lambda} x c_\theta} \end{aligned} \quad (6.37)$$

As before, we can define another function as follows:

$$\zeta^{(1)}(\xi) = \frac{3}{4\xi} \int_{-1}^{+1} dy y e^{2\xi y} = \frac{3}{4\xi^2} \left[\cosh(2\xi) - \frac{\sinh(2\xi)}{2\xi} \right] \quad \text{s.t.:} \quad \lim_{\xi \rightarrow 0} \zeta^{(1)} = 1 \quad (6.38)$$

The last integration in (6.37) then yields:

$$\mathbf{R}_s^\uparrow = -\frac{2}{3} \mu \mathbf{w} n_s n_\ell \bar{g}_{\bar{T}} e^{-\lambda} \int_{x^*}^{\infty} dx x^{\frac{3}{2}} e^{-x} \bar{\sigma}_{s\ell}^\uparrow(x) \zeta^{(1)}(\sqrt{\lambda} x) \left[\sqrt{x} - \sqrt{x'} \langle \cos \chi \rangle_{\Omega'} \right] \quad (6.39)$$

We can also define average cross-sections as follows:

$$\begin{aligned} \sigma_{s\ell}^{\uparrow(\ell)}(x) &= 2\pi \left(\frac{x'}{x} \right)^{\ell/2} \int_{-1}^1 (c_\chi)^\ell \sigma_{s\ell}^\uparrow(x, c_\chi) dc_\chi \\ &= \left(\frac{x'}{x} \right)^{\ell/2} \bar{\sigma}_{s\ell}^\uparrow(x) \langle (\cos \chi)^\ell \rangle_{\Omega'} \end{aligned} \quad (6.40)$$

Note that $\sigma_{s\ell}^{\uparrow(0)} = \bar{\sigma}_{s\ell}^{\uparrow}$ and $x = x' + x^*$. Using the average cross-sections in equation (6.40), equation (6.39) becomes:

$$\mathbf{R}_s^{\uparrow} = -\frac{2}{3}\mu\mathbf{w}n_sn_\ell\bar{g}_{\bar{T}}e^{-\lambda}\int_{x^*}^{\infty}dx\,x^2\,e^{-x}\,\zeta^{(1)}(\sqrt{\lambda x})\left[\sigma_{s\ell}^{\uparrow(0)}(x) - \sigma_{s\ell}^{\uparrow(1)}(x)\right] \quad (6.41)$$

A similar (but of opposite sign) expression can be obtained for the species of type t . Note that the expression (6.41) is obtained in a frame where \mathbf{w} is aligned with the z direction, and corresponds to the change in momentum density along that direction. Thus, it is the component of a force *parallel* to \mathbf{w} , while all components in the transverse directions are zero, by reason of symmetry². The components in an arbitrary rest-frame must be obtained by projecting \mathbf{w} . Since the force density is approximately proportional to \mathbf{w} , we can group all the other terms into the definition of a coefficient, such that

$$\mathbf{R}_s^{\uparrow} = -K_{s\ell}^{\uparrow}(\mathbf{u}_s - \mathbf{u}_t) \quad (6.42)$$

where $K_{s\ell}^{\uparrow}$ is known as the resistance coefficient:

$$K_{s\ell}^{\uparrow} = \frac{2}{3}\mu n_sn_\ell\bar{g}_{\bar{T}}e^{-\lambda}\int_{x^*}^{\infty}dx\,x^2\,e^{-x}\,\zeta^{(1)}(\sqrt{\lambda x})\left[\sigma_{s\ell}^{\uparrow(0)}(x) - \sigma_{s\ell}^{\uparrow(1)}(x)\right] \quad (6.43)$$

In the limit of weak divergence of mean fluid velocities ($\lambda \rightarrow 0$) and isotropic scattering ($\mathcal{G}(\chi) = 1/4\pi$), we have:

$$K_{s\ell}^{\uparrow} \simeq \frac{2}{3}\mu n_sn_\ell\bar{g}_{\bar{T}}\int_{x^*}^{\infty}dx\,x^2\bar{\sigma}_{s\ell}^{\uparrow}(x)e^{-x} \quad (6.44)$$

Consider now the reverse process ($u \rightarrow \ell$) and the transfer integral (6.25), the rate of change of momentum density of species s can be written as:

$$\mathbf{R}_s^{\downarrow} = -\mu n_sn_u\bar{g}_{\bar{T}}e^{-\lambda}\int_0^{\infty}dx'\,x'\,e^{-x'}\,\bar{\sigma}_{su}^{\downarrow}(x')\cdot\frac{1}{2}\int_{-1}^{+1}dc_{\theta}e^{2\sqrt{\lambda x'}c_{\theta}}\cdot\langle\mathbf{g}' - \mathbf{g}\rangle_{\Omega'} \quad (6.45)$$

Following the same procedure described above for the excitation process, we obtain:

$$\mathbf{R}_s^{\downarrow} = -\frac{2}{3}\mu n_sn_u\mathbf{w}\bar{g}_{\bar{T}}e^{-\lambda}\int_0^{\infty}dx'\,x'^2\,e^{-x'}\,\zeta^{(1)}(\sqrt{\lambda x'})\left[\sigma_{su}^{\downarrow(0)}(x') - \sigma_{su}^{\downarrow(1)}(x')\right] \quad (6.46)$$

²This is obtain by integrating over the φ angular variable.

where

$$\sigma_{su}^{\downarrow(\ell)}(x') = \left(\frac{x}{x'}\right)^{\ell/2} \bar{\sigma}_{su}^{\downarrow}(x') \langle (\cos\chi)^\ell \rangle_{\Omega'} \quad (6.47)$$

Since $\bar{\sigma}_{s\ell}^{\uparrow}(x)$ and $\bar{\sigma}_{su}^{\downarrow}(x')$ are related by the Klein-Rosseland relation (6.27), $\sigma_{su}^{\downarrow(\ell)}(x')$ can be computed as a function of x . We can also define a resistance coefficient similar to the case of excitation:

$$K_{su}^{\downarrow} = \frac{2}{3} \mu n_s n_u \bar{g}_T e^{-\lambda} \int_0^\infty dx' x'^2 e^{-x'} \zeta^{(1)}(\sqrt{\lambda x'}) [\sigma_{su}^{\downarrow(0)}(x') - \sigma_{su}^{\downarrow(1)}(x')] \quad (6.48)$$

such that

$$\mathbf{R}_s^{\downarrow} = -K_{su}^{\downarrow}(\mathbf{u}_s - \mathbf{u}_t) \quad (6.49)$$

Let us examine the ratio of the resistance coefficients for the forward and backward processes in the case of weak divergence of mean fluid velocities and isotropic scattering:

$$\frac{K_{s\ell}^{\uparrow}}{K_{su}^{\downarrow}} \simeq \left[\mathcal{B}_{\ell u}(\tilde{T}) \right] \cdot \frac{\int_0^\infty dx' e^{-x'} x' (x' + x^*) \left[1 + \frac{2}{5} \lambda (x' + x^*) \right] \bar{\sigma}_{su}^{\downarrow}(x')}{\int_0^\infty dx' e^{-x'} x'^2 \left[1 + \frac{2}{5} \lambda x' \right] \bar{\sigma}_{su}^{\downarrow}(x')} \quad (6.50)$$

Note that there is an additional contribution from high-order moment from the expansion. Therefore, there is no equivalence between the resistance coefficients of the forward and backward processes in the limit $\lambda \rightarrow 0$. Detailed balance is enforced through relation (6.27) at the microscopic level.

6.3.3 Second-order moment: total energy density

The rate of change of total energy of species s can be obtained by setting $\psi = \frac{1}{2} m_s (\mathbf{v}'^2 - \mathbf{v}_s^2)$ into equation (6.13):

$$Q_s^{\uparrow} = \frac{4n_s n_\ell}{\pi^{\frac{1}{2}} \alpha^3} \cdot \int d^3 \mathbf{V}^* f_{V^*} \cdot \int dg g^3 e^{-g^2/\alpha^2} \bar{\sigma}_{s\ell}^{\uparrow}(g) \cdot \frac{1}{2} \int dc_\theta e^{2gwc_\theta/\alpha^2} \left\langle \frac{1}{2} m_s (\mathbf{v}'^2 - \mathbf{v}_s^2) \right\rangle_{\Omega'} \quad (6.51)$$

Using the transformation defined in (6.7), we can obtain:

$$\frac{1}{2} m_s (\mathbf{v}'^2 - \mathbf{v}_s^2) = \mu (\mathbf{g}' - \mathbf{g}) \cdot [\mathbf{V}^* + \mathbf{U} + \gamma \mathbf{w} - \gamma \mathbf{g}] - \frac{m_t}{m_s + m_t} \Delta \varepsilon \quad (6.52)$$

Note that equation (6.51) must include f_{V^*} since the change in total energy depends on \mathbf{V}^* . The integration of the first term in the bracket is zero since $\int d^3\mathbf{V}^* \mathbf{V}^* f_{V^*} = 0$. The results for the second and the third terms are simply $\mathbf{R}_s^\dagger \cdot \mathbf{U}$ and $\gamma \mathbf{R}_s^\dagger \cdot \mathbf{w}$, respectively. The fourth integral can be expressed in terms of normalized variables as:

$$\begin{aligned} & \gamma \mu \alpha^2 n_s n_\ell \bar{g}_{\bar{T}} e^{-\lambda} \int_{x^*}^{\infty} dx x^{\frac{3}{2}} e^{-x} \bar{\sigma}_{s\ell}^\dagger(x) \zeta^{(0)}(\sqrt{\lambda}x) \left[\sqrt{x} - \sqrt{x'} \langle \cos \chi \rangle_{\Omega'} \right] \\ &= \gamma \mu \alpha^2 n_s n_\ell \bar{g}_{\bar{T}} e^{-\lambda} \int_{x^*}^{\infty} dx x^2 e^{-x} \zeta^{(0)}(\sqrt{\lambda}x) \left[\sigma_{s\ell}^{\dagger(0)} - \sigma_{s\ell}^{\dagger(1)} \right] \end{aligned} \quad (6.53)$$

The integral with the last term on the RHS of equation (6.52) is simply $-\frac{m_t}{m_s+m_t} \Gamma_{s\ell}^\dagger \Delta\varepsilon$.

By summing all the contributions, the expression for Q_s^\dagger becomes:

$$\begin{aligned} Q_s^\dagger &= \mathbf{R}_s^\dagger \cdot \mathbf{U} + \gamma \mathbf{R}_s^\dagger \cdot \mathbf{w} - \frac{m_t}{m_s+m_t} \Gamma_{s\ell}^\dagger \Delta\varepsilon + \\ & \gamma \mu \alpha^2 n_s n_\ell \bar{g}_{\bar{T}} e^{-\lambda} \int_{x^*}^{\infty} dx x^2 e^{-x} \zeta^{(0)}(\sqrt{\lambda}x) \left[\sigma_{s\ell}^{\dagger(0)} - \sigma_{s\ell}^{\dagger(1)} \right] \end{aligned} \quad (6.54)$$

Let us now define a thermal relaxation coefficient $K_{s\ell}^{\varepsilon^\dagger}$ as follows:

$$K_{s\ell}^{\varepsilon^\dagger} = \frac{2}{3} \mu n_s n_\ell \bar{g}_{\bar{T}} e^{-\lambda} \int_{x^*}^{\infty} dx x^2 e^{-x} \left[\zeta^{(0)}(\sqrt{\lambda}x) - \frac{2}{3} \lambda \zeta^{(1)}(\sqrt{\lambda}x) \right] \left(\sigma_{s\ell}^{\dagger(0)} - \sigma_{s\ell}^{\dagger(1)} \right) \quad (6.55)$$

The expression for Q_s^\dagger reduces to:

$$Q_s^\dagger = \frac{3k(T_t - T_s)}{m_s + m_t} K_{s\ell}^{\varepsilon^\dagger} + \mathbf{R}_s^\dagger \cdot \mathbf{U} - \frac{m_t}{m_s + m_t} \Gamma_{s\ell}^\dagger \Delta\varepsilon \quad (6.56)$$

where we have used the relation $\gamma \alpha^2 = \frac{2k(T_t - T_s)}{m_s + m_t}$. Note that due to the definition of the thermal relaxation coefficient, the contributions from the second and last terms of equation (6.54) to Q_s^\dagger are grouped together. It must be pointed out that the rate of change of thermal energy of species s , $H_s \equiv \frac{d\varepsilon_s}{dt}$, can always be related to Q_s^\dagger by the following expression:

$$H_s^\dagger = Q_s^\dagger - \mathbf{R}_s^\dagger \cdot \mathbf{u}_s \quad (6.57)$$

The rate of change of total energy of species t can be found similarly by setting $\psi = \frac{1}{2}m_t(\mathbf{v}'_t{}^2 - \mathbf{v}_t^2)$. Following the same procedure, we arrive at the following result:

$$Q_t^\uparrow = -\frac{3k(T_t - T_s)}{m_s + m_t} K_{s\ell}^{\varepsilon\uparrow} - \mathbf{R}_s^\uparrow \cdot \mathbf{U} - \frac{m_s}{m_s + m_t} \Gamma_{s\ell}^\uparrow \Delta\varepsilon \quad (6.58)$$

In the limit of $\lambda \rightarrow 0$ and isotropic scattering, the resistant and thermal relaxation coefficients reduce to:

$$K_{s\ell}^{\varepsilon\uparrow} \simeq K_{s\ell}^\uparrow \simeq \frac{2}{3} \mu n_s n_\ell \bar{g}_{\bar{T}} \int_{x^*}^{\infty} dx x^2 e^{-x} \bar{\sigma}_{s\ell}^\uparrow(x) \quad (6.59)$$

Let us now consider the reverse process ($u \rightarrow \ell$). Similarly, we set \mathbf{v}' , \mathbf{v} to be the initial and final velocities, respectively. The energy transfer rate for species s becomes:

$$Q_s^\downarrow = \frac{4n_s n_u}{\pi^{\frac{1}{2}} \alpha^3} \cdot \int d^3 \mathbf{V}'^* f_{V'^*} \cdot \int dg' g'^3 e^{-g'^2/\alpha^2} \bar{\sigma}_{su}^\downarrow(g') \cdot \frac{1}{2} \int dc_\theta e^{2g'wc_\theta/\alpha^2} \langle \frac{1}{2} m_s (\mathbf{v}_s^2 - \mathbf{v}'_s{}^2) \rangle_{\Omega'} \quad (6.60)$$

One can easily show that:

$$Q_s^\downarrow = \frac{3k(T_t - T_s)}{m_s + m_t} K_{su}^{\varepsilon\downarrow} + \mathbf{R}_s^\downarrow \cdot \mathbf{U} + \frac{m_t}{m_s + m_t} \Gamma_{su}^\downarrow \Delta\varepsilon \quad (6.61)$$

$$Q_t^\downarrow = -\frac{3k(T_t - T_s)}{m_s + m_t} K_{su}^{\varepsilon\downarrow} - \mathbf{R}_s^\downarrow \cdot \mathbf{U} + \frac{m_s}{m_s + m_t} \Gamma_{su}^\downarrow \Delta\varepsilon \quad (6.62)$$

where

$$K_{s\ell}^{\varepsilon\downarrow} = \frac{2}{3} \mu n_s n_u \bar{g}_{\bar{T}} e^{-\lambda} \int_0^\infty dx' x'^2 e^{-x'} \left[\zeta^{(0)}(\sqrt{\lambda x'}) - \frac{2}{3} \lambda \zeta^{(1)}(\sqrt{\lambda x'}) \right] (\sigma_{su}^{\downarrow(0)} - \sigma_{su}^{\downarrow(1)}) \quad (6.63)$$

6.4 Summary of results

All exchange terms the number density, momentum and total energy due to an excitation and deexcitation collisions of type (6.19) can be summarized as follows:

$$\frac{dn_s}{dt} = 0 \quad (6.64)$$

$$\frac{dn_\ell}{dt} = -\Gamma_{s\ell}^\uparrow + \Gamma_{su}^\downarrow \quad (6.65)$$

$$\frac{dn_u}{dt} = +\Gamma_{s\ell}^\uparrow - \Gamma_{su}^\downarrow \quad (6.66)$$

$$\frac{d(\rho_s \mathbf{u}_s)}{dt} = K_{s\ell}^\uparrow(\mathbf{u}_t - \mathbf{u}_s) + K_{su}^\downarrow(\mathbf{u}_t - \mathbf{u}_s) \quad (6.67)$$

$$\frac{d(\rho_t \mathbf{u}_t)}{dt} = -K_{s\ell}^\uparrow(\mathbf{u}_t - \mathbf{u}_s) - K_{su}^\downarrow(\mathbf{u}_t - \mathbf{u}_s) \quad (6.68)$$

$$\begin{aligned} \frac{dE_s}{dt} = & K_{s\ell}^\uparrow(\mathbf{u}_t - \mathbf{u}_s) \cdot \mathbf{U} + \frac{3k(T_t - T_s)}{m_s + m_t} K_{s\ell}^{\varepsilon\uparrow} - \frac{m_t}{m_s + m_t} \Gamma_{s\ell}^\uparrow \Delta\varepsilon \\ & + K_{su}^\downarrow(\mathbf{u}_t - \mathbf{u}_s) \cdot \mathbf{U} + \frac{3k(T_t - T_s)}{m_s + m_t} K_{su}^{\varepsilon\downarrow} + \frac{m_t}{m_s + m_t} \Gamma_{su}^\downarrow \Delta\varepsilon \end{aligned} \quad (6.69)$$

$$\begin{aligned} \frac{dE_t}{dt} = & -K_{s\ell}^\uparrow(\mathbf{u}_t - \mathbf{u}_s) \cdot \mathbf{U} - \frac{3k(T_t - T_s)}{m_s + m_t} K_{s\ell}^{\varepsilon\uparrow} - \frac{m_s}{m_s + m_t} \Gamma_{s\ell}^\uparrow \Delta\varepsilon \\ & - K_{su}^\downarrow(\mathbf{u}_t - \mathbf{u}_s) \cdot \mathbf{U} - \frac{3k(T_t - T_s)}{m_s + m_t} K_{su}^{\varepsilon\downarrow} + \frac{m_s}{m_s + m_t} \Gamma_{su}^\downarrow \Delta\varepsilon \end{aligned} \quad (6.70)$$

For the purpose of numerical calculation, one can precompute and tabulate all the reaction rate and resistance coefficients³ as a function of two parameters \tilde{T} and λ . It must be pointed out that the coefficients for the forward and the backward processes must be tabulated separately, since there is no correspondence between the two. The principle of detailed balance is enforced at the microscopic level.

³Note that all the product of number densities, e.g., $n_s n_t$, can be factored out.

CHAPTER 7

Simulations of Laser-Plasma Interactions

7.1 Introduction

Laser-plasma interactions (LPI) present a physically rich research topic with a wide range of applications. The dynamics of the interactions can span several physical regimes, and encompasses a great deal of physical phenomena, e.g., plasma instabilities, resonant absorption, X-ray generation, multi-phase ablation, particle acceleration [41, 38, 124, 125]. Due to the highly transient nature of the interaction, computational models for LPI are often designed to work only on a specific physical domain. For example, in ultra-short and ultra-high intensity LPI, the laser absorption occurs at very fast time scales requiring a kinetic treatment, i.e., PIC or Vlasov solver. On the contrary, once the plasma is formed and thermalized, the expansion of the plasma bulk¹ mostly occur at the hydrodynamic time scales and is often modeled by fluid codes.

In this chapter, a computational model for LPI is introduced based on the multi-fluid description of a plasma described in section 2.2. The multi-fluid model has several advantages over the traditional single-fluid model, often used in inertial fusion calculation [40]. The first advantage is that it permits a self-consistent coupling of the plasma with the electromagnetic field, which is relevant in the study of laser-induced electric and magnetic fields and their effects on hydrodynamic instabilities and charged particle acceleration [38]. The second advantage

¹with the exception of superthermal or relativistic electrons.

of the multi-fluid model is that it can be used to hybridize with a kinetic method. For instance, in the fast ignition concept proposed by Tabak *et al.* [126], the fuel is first compressed by a low intensity laser, and then quickly ignited with a petawatt laser. The incidence of the petawatt laser creates a channel into the compressed core from which the superthermal electron beam generated from the interaction of the laser can penetrate deep into the capsule and heat the compressed fuel. In this scenario, the electrons can be decomposed into two populations: cold and hot (superthermal) electrons. The interaction of the cold electrons with the ions can be described by a multi-fluid model, and the hot electrons can be treated by a kinetic method.

7.2 Electromagnetic wave propagation in plasmas

7.2.1 Electrodynamic equations

The physics of electromagnetic wave propagating in a plasma is first reviewed, leading to the physical model for the laser and corresponding exchange terms with the plasma. Let us now consider Maxwell's equations, which governs the evolution of the electric and magnetic field in a plasma [127, 128]:

$$\nabla \times \mathbf{E} = -\partial_t \mathbf{B} \quad (7.1)$$

$$\epsilon_0 c^2 \nabla \times \mathbf{B} = \mathbf{j} + \epsilon_0 \partial_t \mathbf{E} \quad (7.2)$$

The plasma current, \mathbf{j} , appearing on the RHS of equation (7.2) describes the plasma response and its modification to the electromagnetic wave. By taking the curl of (7.1) and utilizing the relation $\nabla \times \nabla \times \mathbf{A} = \nabla(\nabla \cdot \mathbf{A}) - \nabla^2 \mathbf{A}$, we get:

$$\partial_{tt} \mathbf{E} - c^2 \nabla^2 \mathbf{E} + c^2 \nabla(\nabla \cdot \mathbf{E}) + \frac{1}{\epsilon_0} \partial_t \mathbf{j} = 0 \quad (7.3)$$

Equation (7.3) is the wave equation governing the evolution of the electric field in the plasma. Similarly, by taking the curl of (7.2), we obtain the wave equation

governing the evolution of the magnetic field:

$$\partial_{tt}\mathbf{B} - c^2\nabla^2\mathbf{B} - \frac{1}{\epsilon_0}\nabla \times \mathbf{j} = 0 \quad (7.4)$$

For a high frequency oscillation of the electromagnetic field, the plasma current can be modeled by Ohm's law, i.e., equation (2.25). Here we only include the resistive term, so Ohm's law can be written as:

$$\partial_t\mathbf{j} + \nu\mathbf{j} = \epsilon_0\omega_p^2\mathbf{E} \quad (7.5)$$

where ν is the plasma collision frequency. Let us now consider a monochromatic oscillation with radian frequency ω for the quantities \mathbf{E} , \mathbf{B} and \mathbf{j} :

$$\mathbf{E}(\mathbf{x}, t) = \hat{\mathbf{E}}(\mathbf{x})e^{-i\omega t} + c.c. \quad (7.6)$$

$$\mathbf{B}(\mathbf{x}, t) = \hat{\mathbf{B}}(\mathbf{x})e^{-i\omega t} + c.c. \quad (7.7)$$

$$\mathbf{j}(\mathbf{x}, t) = \hat{\mathbf{j}}(\mathbf{x})e^{-i\omega t} + c.c. \quad (7.8)$$

Ohm's law immediately yields:

$$\hat{\mathbf{j}} = \sigma\hat{\mathbf{E}} \quad (7.9)$$

$$\sigma = \frac{i\epsilon_0\omega_p^2}{\omega(1 + i\nu/\omega)} \quad (7.10)$$

where σ is the complex conductivity of the plasma. Substituting (7.9) into the wave equation for the electric field (7.3), we obtain:

$$\nabla^2\hat{\mathbf{E}} + k_0^2\varepsilon\hat{\mathbf{E}} - \nabla(\nabla \cdot \hat{\mathbf{E}}) = 0 \quad (7.11)$$

where $k_0 = \omega/c$ and ε is the dielectric function of the plasma:

$$\varepsilon = \eta^2 = 1 - \frac{\omega_p^2}{\omega^2(1 + i\nu/\omega)} \quad (7.12)$$

and η is the refractive index. Similarly for the magnetic field \mathbf{B} , equation (7.4) becomes:

$$\nabla^2\hat{\mathbf{B}} + k_0^2\varepsilon\hat{\mathbf{B}} + \nabla(\ln \varepsilon) \times (\nabla \times \hat{\mathbf{B}}) = 0 \quad (7.13)$$

Equations (7.11) and (7.13) are the governing equations for a monochromatic wave propagating in a plasma. In practice, one only needs to solve for either $\hat{\mathbf{E}}$ or $\hat{\mathbf{B}}$; the remaining quantity can be determined from Faraday's or Ampere's law:

$$i\omega\hat{\mathbf{B}} = \nabla \times \hat{\mathbf{E}} \quad (7.14)$$

$$c\nabla \times \hat{\mathbf{B}} = -ik_0\varepsilon\hat{\mathbf{E}} \quad (7.15)$$

Note that here we assume that the refractive index is time independent. This is certainly a good approximation for long interaction times of laser-plasma system characterized by fluid equations ($\omega/k \gg v_T$)². For short interaction times, a kinetic description must be utilized, and the time dependent solution of the electromagnetic fields must be solved.

For a homogeneous medium with no charge separation, the wave equations for both $\hat{\mathbf{E}}$ and $\hat{\mathbf{B}}$ become identical, since $\nabla \cdot \hat{\mathbf{E}} = 0$ and $\nabla \ln \varepsilon = 0$. For simplicity, let us consider a simple case of a linearly polarized electromagnetic wave normally incident onto a homogeneous plasma medium. Let us define x to be the propagating direction and y and z are the directions of the oscillating electric and magnetic fields, respectively (see figure 7.1). The solution the wave equations can be written as:

$$\mathbf{E}(x, t) = \hat{\mathbf{e}}_y E_0 e^{i(kx - \omega t)} \quad (7.16)$$

$$\mathbf{B}(x, t) = \hat{\mathbf{e}}_z B_0 e^{i(kx - \omega t)} \quad (7.17)$$

where E_0 and B_0 are determined from boundary conditions, and the wave number k is given from the dispersion relation:

$$k^2 = k_0^2 \left(1 - \frac{\omega_p^2}{\omega^2(1 + i\nu/\omega)} \right) \quad (7.18)$$

It is interesting to note that in the absence of collision, i.e., $\nu = 0$, k is imaginary for $\omega < \omega_p$. In this case, the wave is evanescent with a skin depth of $\delta \approx \frac{c}{\omega_p}$. This indicates that the laser cannot propagate past the critical surface, i.e., $\omega = \omega_p$.

²We also assume that $\frac{\omega}{k} \gg \nu_{\text{ion}} \sim \frac{1}{n_e} \frac{dn_e}{dt}$ such that no ionization occurs during the interaction.

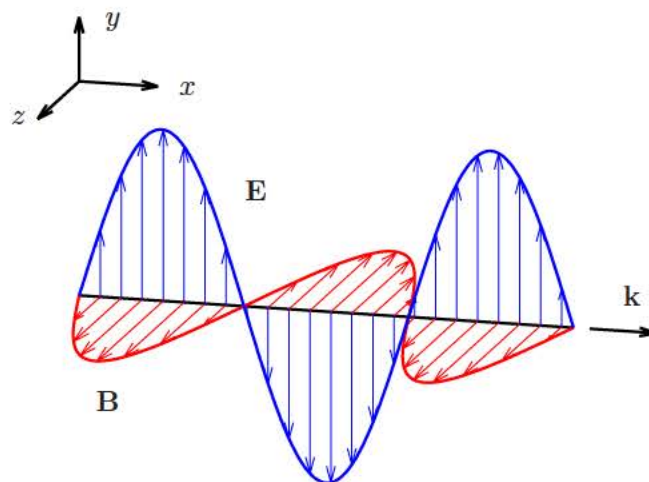


Figure 7.1: Coordinate system of a one dimensional electromagnetic wave propagation where x is the direction of propagation: $\mathbf{E} = E(x)\hat{\mathbf{e}}_y$, $\mathbf{B} = B(x)\hat{\mathbf{e}}_z$, and $\mathbf{k} = k\hat{\mathbf{e}}_x$.

7.2.2 WKB approximation

In this section, the Wentzel-Kramers-Brillouin (WKB) approximation for solving the wave equations is described. Let us now consider a one dimensional propagation of a monochromatic wave in an inhomogeneous medium. Using the same coordinate system as defined previously (see figure 7.1), the electric and magnetic fields can be written as:

$$\mathbf{E} = \hat{\mathbf{e}}_y \left[\hat{E}(x)e^{-i\omega t} + c.c. \right] \quad (7.19)$$

$$\mathbf{B} = \hat{\mathbf{e}}_z \left[\hat{B}(x)e^{-i\omega t} + c.c. \right] \quad (7.20)$$

The wave equations for the electric and magnetic fields, equation (7.11) and (7.13), reduce to second order ODEs:

$$\partial_{xx}\hat{E} + k_0^2\varepsilon(x)\hat{E} = 0 \quad (7.21)$$

$$\partial_{xx}\hat{B} + k_0^2\varepsilon(x)\hat{B} = 0 \quad (7.22)$$

where the dielectric function ε is defined in equation (7.12). The WKB approximation looks for a solution of the form:

$$\hat{E} = \hat{E}_0(x)e^{ik_0 \int_x \psi(\zeta) d\zeta} \quad (7.23)$$

For simplicity, we assume that there is no collision, hence ψ is real. If we substitute expression (7.23) to equation (7.21) and to the lowest and first order, we obtain the following:

$$\psi = \sqrt{\varepsilon} = \eta \quad (7.24)$$

$$\hat{E}_0(x) = \frac{E_V}{\eta^{1/2}} \quad (7.25)$$

where E_V is the electric field in free space.

$$E_V = \sqrt{\frac{2I}{\epsilon_0 c}} \quad (7.26)$$

The validation of the WKB approximation requires a smooth variation of the plasma density or the refractive index. This assumption breaks down in the region near the critical density where $\varepsilon \rightarrow 0$. Mathematically, the following relations needs to be satisfied for the WKB approximation to be valid [129]:

$$\frac{\sqrt{3}}{2} \frac{|\partial_x \eta|}{k_0 |\eta|^2} \ll 1 \quad (7.27)$$

$$\frac{1}{2} \frac{|\partial_{xx} \eta|}{k_0^2 |\eta|^3} \ll 1 \quad (7.28)$$

The WKB solution for the electric field reads:

$$\hat{E}(x) = \frac{E_V}{\eta^{1/2}} e^{ik_0 \int_x \eta d\zeta} \quad (7.29)$$

The solution for the magnetic field can be determined from Faraday's law:

$$\hat{B}(x) = \frac{1}{c} \eta^{1/2} E_V e^{ik_0 \int_x \eta d\zeta} + \frac{i}{2k_0 c} \frac{E_V}{\eta^{3/2}} \partial_x \eta e^{ik_0 \int_x \eta d\zeta} \quad (7.30)$$

One can see that the amplitude of the electric and magnetic fields can undergo increase or swelling when propagating in a medium with a spatially varying refractive index. The second term in (7.30) is referred to as a phase term [130]; this term is essential in the generation of non-linear forces, which will be described later in this chapter. In addition, we have not discussed collisional absorption yet, but one can see that since η can be complex, its imaginary component is related to the absorption of the electromagnetic energy.

7.2.3 Collisional absorption

When collision is included, the wave can be collisionally damped as it passes through the medium. Considering an electromagnetic wave propagating through a homogeneous medium and utilizing the WKB solution of the electric field, i.e., equations (7.29) and (7.30), one can compute the intensity of the wave as follows

[125]:

$$\begin{aligned}
I(x) &= \epsilon_0 c^2 |\langle \mathbf{E} \times \mathbf{B} \rangle| \\
&= \frac{1}{2} \epsilon_0 c E_V^2 e^{-2k_0 \int_x \eta_I d\zeta} \\
&= I(x_0) e^{-\int_{x_0}^x \kappa d\zeta}
\end{aligned} \tag{7.31}$$

where $I(x_0)$ is the intensity of the incident wave, $\langle \bullet \rangle$ denotes a time-average operator, and η_I is the imaginary part of the refractive index, i.e., $\eta = \eta_R + i\eta_I$. Equation (7.31) is a form of Beer's law [125]. The spatial damping rate κ , also known as the absorption coefficient, is related to the plasma refractive index as follows:

$$\kappa = 2k_0\eta_I \tag{7.32}$$

Using the dielectric function as defined in equation (7.12), the real and the imaginary parts of the refractive index for a plasma read:

$$\eta_R = \frac{1}{\sqrt{2}} \left[\sqrt{\left(1 - \frac{\omega_p^2}{\omega^2 + \nu^2}\right)^2 + \left(\frac{\nu}{\omega} \frac{\omega_p^2}{\omega^2 + \nu^2}\right)^2} + \left(1 - \frac{\omega_p^2}{\omega^2 + \nu^2}\right) \right]^{1/2} \tag{7.33}$$

$$\eta_I = \frac{1}{\sqrt{2}} \left[\sqrt{\left(1 - \frac{\omega_p^2}{\omega^2 + \nu^2}\right)^2 + \left(\frac{\nu}{\omega} \frac{\omega_p^2}{\omega^2 + \nu^2}\right)^2} - \left(1 - \frac{\omega_p^2}{\omega^2 + \nu^2}\right) \right]^{1/2} \tag{7.34}$$

For $\nu/\omega \ll 1$, one can do a series expansion and obtain an expression for the absorption constant:

$$\kappa = \frac{\nu}{c} \frac{\omega_p^2}{\omega^2} \left(1 - \frac{\omega_p^2}{\omega^2}\right)^{-1/2} \tag{7.35}$$

It must be noted that the absorption constant as described in equation (7.35) depends only on the plasma properties. In the so-called linear regime ($I \lesssim 10^{15}$ W/cm²), this is certainly a good approximation. However, if the laser intensity is high enough that the oscillation energy exceeds the electron thermal energy, i.e., the quivering motion of the electrons is comparable to or larger than their

thermal motion, the absorption becomes dependent on the laser and one has to add correction to the collision frequency and the absorption constant. This is typically referred to as non-linear collisional absorption [130]; the treatment of non-linear absorption in hydrodynamic codes will be described later in this chapter. If the laser intensity is much higher, relativistic particle beam can be generated; all the relativistic effects are neglected in the current framework.

In the general case, laser absorption can be computed directly from the conservation of electromagnetic energy, which is expressed by the Poynting theorem:

$$\frac{1}{2}\epsilon_0\partial_t(\mathbf{E}\cdot\mathbf{E}+c^2\mathbf{B}\cdot\mathbf{B})+\nabla\cdot\mathbf{S}=-\mathbf{j}\cdot\mathbf{E} \quad (7.36)$$

where $\mathbf{S} = \frac{1}{\mu_0}\mathbf{E}\times\mathbf{B}$ is the Poynting vector. Since transient effects of the electromagnetic fields are neglected, the first term in equation (7.36) is negligible. The heating rate due to laser absorption, denoted by W_L , is obtained by time averaging the Joule heating term, i.e., the work done on the plasma by the electromagnetic wave:

$$W_L = \langle \mathbf{j}\cdot\mathbf{E} \rangle = -\nabla\cdot\langle \mathbf{S} \rangle \quad (7.37)$$

where \mathbf{E} and \mathbf{B} are obtained from the wave equations.

7.2.4 Ponderomotive forces

When a high-frequency electromagnetic wave propagates through a plasma, it induces a slow time scale pressure force on the plasma as a result of conservation of momentum. This force is known as the ponderomotive force or light pressure, which plays an important roles in many physical phenomena occurring in laser produced plasma, such as momentum transfer, density modification, magnetic field generation, and parametric instabilities [38].

The derivation of the ponderomotive force, sometimes referred to as the non-linear force³ in the general case can get complicated. The most general expression

³The terms non-linear and pondermotive forces are often used interchangeably in the lit-

found in literature for the non-linear force caused by a transient monochromatic radiation in a plasma is as follows:

$$\mathbf{f}_{nl} = \mathbf{j} \times \mathbf{B} + \epsilon_0 \mathbf{E} \nabla \cdot \mathbf{E} + \epsilon_0 (1 + \omega^{-1} \partial_t) \nabla \cdot (\eta^2 - 1) \mathbf{E} \mathbf{E} \quad (7.38)$$

The complete derivation of equation (7.38) is given in appendix C of Hora [129], Zeidler *et al.* [131] and Hora [132]. The non-linear force in equation (7.38) can be rewritten in terms of the electromagnetic energy tensor. Conservation of momentum of the electromagnetic field gives:

$$\partial_t \mathbf{S} + \nabla \cdot \mathbb{T} = -\epsilon_0 \mathbf{E} \nabla \cdot \mathbf{E} - \mathbf{j} \times \mathbf{B} \quad (7.39)$$

where \mathbb{T} is the Maxwell tensor, written in index notation as follows:

$$\mathbb{T}_{ij} = -\epsilon_0 E_i E_j - \frac{1}{\mu_0} B_i B_j + \frac{1}{2} \delta_{ij} \left(\epsilon_0 E^2 + \frac{1}{\mu_0} B^2 \right) \quad (7.40)$$

Utilizing equations (7.38) and (7.39), we obtained the following expression for the non-linear force:

$$\mathbf{f}_{nl} = -\nabla \cdot [\mathbb{T} - \epsilon_0 (1 + \omega^{-1} \partial_t) (\eta^2 - 1) \mathbf{E} \mathbf{E}] - \frac{1}{c^2} \partial_t \mathbf{S} \quad (7.41)$$

The slow time-scale ponderomotive force is obtained by time averaging the non-linear force \mathbf{f}_{nl} over many oscillation cycles. In the current work, transient effects are neglected, so the expression for the ponderomotive force reduces to:

$$\mathbf{f}_p = \langle \mathbf{f}_{nl} \rangle = -\nabla \cdot [\langle \mathbb{T} \rangle - \epsilon_0 (\eta^2 - 1) \langle \mathbf{E} \mathbf{E} \rangle] \quad (7.42)$$

For a one-dimensional perpendicular incidence along x direction (see figure 7.1), the expression for the ponderomotive force is simplified to:

$$\begin{aligned} \mathbf{f}_p &= -\frac{\epsilon_0}{4} \partial_x \left(\hat{\mathbf{E}} \hat{\mathbf{E}}^* + \frac{1}{c^2} \hat{\mathbf{B}} \hat{\mathbf{B}}^* \right) \\ &= -\frac{\epsilon_0}{4} \partial_x \left(\hat{\mathbf{E}} \hat{\mathbf{E}}^* + \frac{1}{k_0^2} \partial_x \hat{\mathbf{E}} \partial_x \hat{\mathbf{E}}^* \right) \\ &= -\frac{\epsilon_0 \omega_p^2}{4\omega^2} \partial_x \left(\hat{\mathbf{E}} \hat{\mathbf{E}}^* \right) \end{aligned} \quad (7.43)$$

erature to indicate the radiation pressure force. Here we use the term ponderomotive force to indicate the slow time scale force, appearing on the hydrodynamic equations; the ponderomotive force is obtained simply by time averaging the non-linear force, i.e., $\mathbf{f}_p = \langle \mathbf{f}_{nl} \rangle$.

The last step is performed with the help of the wave equation (7.21). Although less general, equation (7.42) is commonly used to express the ponderomotive force [38]. An alternative derivation of the ponderomotive force, by considering a single particle motion, is given in appendix E, the result of which, leads to the same expression as (7.42). If the WKB approximation, i.e., equation (7.23) is used, the ponderomotive force can be simplified much further [129]:

$$\mathbf{f}_p = \hat{\mathbf{e}}_x \frac{\epsilon_0 E_V^2}{2\eta^2} \frac{\omega_p^2}{\omega^2} \partial_x \eta \quad (7.44)$$

where E_V is the electric field in vacuum, given by equation (7.26). As will be shown later, the solution of the ponderomotive force using WKB equations can develop a singularity near the critical layer, and do not take in account local reflection of the wave. The latter is responsible for the density modification due to ponderomotive bunching.

7.3 Multi-fluid model for laser plasma interactions

In this section, a self-consistent hydrodynamic model is introduced for simulations of laser plasma interactions. This model is based on the multi-fluid equations described in section 2.2 with additional coupling terms due to the interaction with the laser. In high intensity laser plasma interaction, the strong coupling with the laser can drive the electrons out of equilibrium with the ions, which gives rise to charge separation, sheath formation, magnetic field generation, etc. Furthermore, the electrons themselves can possibly be non-Maxwellian, in which the VDF must be resolved. A kinetic treatment of the electrons is beyond the scope of the current study. Here we assumed that the electron VDF is close to a Maxwellian distribution such that it can be characterized by fluid equations.

Considering a fully ionized plasma and assuming that inelastic collisions are

negligible, the continuity equations for the electrons (e) and ions (i) read:

$$\partial_t \rho_e + \nabla \cdot (\rho_e \mathbf{u}_e) = 0 \quad (7.45)$$

$$\partial_t \rho_i + \nabla \cdot (\rho_i \mathbf{u}_i) = 0 \quad (7.46)$$

In the multi-fluid model, the momentum of ions and electrons are conserved separately, leading to different averaged velocity for each species, and thus allowing charge separation. In the current work, we neglect the effect of the magnetic field and only consider electrostatic fields; the resultant equations are referred to as the Euler-Poisson system. When the magnetic field is included, the full Maxwell's equations need to be solved self-consistently.

The momentum equations for the ions and electrons are as follows:

$$\partial_t(\rho_e \mathbf{u}_e) + \nabla \cdot (\rho_e \mathbf{u}_e \mathbf{u}_e + p_e \mathbb{I}) = -en_e \mathbf{E} + \rho_e \nu_{ei} \mathbf{w}_{ei} + \mathbf{f}_p \quad (7.47)$$

$$\partial_t(\rho_i \mathbf{u}_i) + \nabla \cdot (\rho_i \mathbf{u}_i \mathbf{u}_i + p_i \mathbb{I}) = Z_i en_i \mathbf{E} - \rho_i \nu_{ei} \mathbf{w}_{ei} \quad (7.48)$$

where $\mathbf{w}_{ei} = \mathbf{u}_i - \mathbf{u}_e$ is the mean drift velocity, ν_{ei} is the Coulomb collision frequency between ions and electrons, and \mathbb{I} is an identity tensor. The first terms on the RHS of equations (7.47) and (7.48) correspond to the Coulomb force and the second terms correspond to the momentum relaxation term [46]. One can check that momentum conservation are satisfied. The third term, which only acts on the electron fluid, is due to the ponderomotive force, discussed in section 7.2.4. The ponderomotive force \mathbf{f}_p in the general case can be expressed by equation (7.42); for one dimensional problems studied here, we use the expression given by (7.43). For the ions, this force scales as m_e/m_i and can be neglected.

The collision frequency for Coulomb interaction is:

$$\nu_{ei} = \frac{4}{3}(2\pi)^{1/2} \left(\frac{Ze^2}{4\pi\epsilon_0 m_e} \right)^2 \left(\frac{m}{kT_e} \right)^{3/2} n_i \ln \Lambda \quad (7.49)$$

where $\Lambda = \lambda_D/b_{\min}$ and b_{\min} is the minimum impact parameter. In addition to collisional friction, the collision frequency ν_{ei} is also used to describe the dielectric

function of the medium. As pointed out earlier in this chapter, for high intensity lasers ($I > 10^{15}$ W/cm²), the electron quiver velocity is comparable to the thermal velocity, so the absorption process becomes dependent of the laser intensity (non-linear absorption). In hydrodynamic codes, this effect is taken into account by introducing an effective collision frequency ν_{ei}^* [129]:

$$\nu_{ei}^* \approx \nu_{ei} \frac{(kT_e)^{3/2}}{(kT_e + \mathcal{E})^{3/2}} \quad (7.50)$$

and $\mathcal{E} = I/cn_{cr}$ is the oscillation energy of the electrons due to the laser.

The conservation equations for the thermal energy of each species, denoted as ε_s , can be written as:

$$\begin{aligned} \partial_t \varepsilon_e + \nabla \cdot (\varepsilon_e \mathbf{u}_e) + p_e \nabla \cdot \mathbf{u}_e = & - \nabla \cdot \mathbf{q}_e + 3\tilde{m}_e n_e \nu_{ei} k(T_i - T_e) \\ & + \tilde{m}_i \rho_e \nu_{ei} \mathbf{w}_{ei} \cdot \mathbf{w}_{ei} + W_L \end{aligned} \quad (7.51)$$

$$\begin{aligned} \partial_t \varepsilon_i + \nabla \cdot (\varepsilon_i \mathbf{u}_i) + p_i \nabla \cdot \mathbf{u}_i = & - 3\tilde{m}_e n_e \nu_{ei} k(T_i - T_e) \\ & + \tilde{m}_e \rho_e \nu_{ei} \mathbf{w}_{ei} \cdot \mathbf{w}_{ei} \end{aligned} \quad (7.52)$$

where $\tilde{m}_s = \frac{m_s}{m_e + m_i}$. Here we include electron thermal conduction, which is the main heat transport mechanism in LPI. It must be pointed out that the thermal energy exchange process, i.e., RHS of equations (7.51) and (7.52), is due to both thermal relaxation effects (temperature difference) and frictional heating (velocity difference). The frictional heating term scales as $|\mathbf{w}_{ei}|/v_{Te}$, and can be neglected in the limit of small relative drift velocity. Laser absorption is taken into account by the heating term W_L , which represents the energy transfer from the laser to the plasma. W_L can be computed directly from the Poynting theorem via equation (7.37).

The thermal energy equations (7.51) and (7.52) can be combined with the momentum equations (7.47) and (7.48) to yield the conservation equations for the total energy of each species:

$$\begin{aligned} \partial_t E_e + \nabla \cdot [(E_e + p_e) \mathbf{u}_e] = & - \nabla \cdot \mathbf{q}_e + \mathbf{j}_e \cdot \mathbf{E} + \rho_e \nu_{ei} \mathbf{w}_{ei} \cdot \bar{\mathbf{u}}_{ei} \\ & + 3n_e \nu_{ei} k(T_i - T_e) + \mathbf{f}_p \cdot \mathbf{u}_e + W_L \end{aligned} \quad (7.53)$$

$$\partial_t E_i + \nabla \cdot [(E_i + p_i)\mathbf{u}_i] = \mathbf{j}_i \cdot \mathbf{E} - \rho_e \nu_{ei} \mathbf{w}_{ei} \cdot \bar{\mathbf{u}}_{ei} - 3n_e \nu_{ei} k(T_i - T_e) \quad (7.54)$$

where

$$\mathbf{j}_s = Z_s e n_s \mathbf{u}_s \quad (7.55)$$

$$E_s = \varepsilon_s + \frac{1}{2} \rho_s \mathbf{u}_s \cdot \mathbf{u}_s \quad (7.56)$$

$$\bar{\mathbf{u}}_{ei} = \frac{m_i \mathbf{u}_i + m_e \mathbf{u}_e}{m_i + m_e} \quad (7.57)$$

To close the system, an ideal gas equation of state is used, i.e., $p_s = n_s k T_s$ and $\varepsilon_s = p_s/(\gamma_s - 1)$. One can easily check that energy conservation is satisfied for the collision terms; this is only possible with the inclusion of the frictional heating terms in equations (7.51) and (7.52). The electrostatic field \mathbf{E} is determined from Gauss's law⁴:

$$\nabla \cdot \mathbf{E} = \frac{e}{\epsilon_0} (Z_i n_i - n_e) \quad (7.58)$$

It is often convenient to express the electric field in terms of the electrostatic potential, i.e., $\mathbf{E} = -\nabla \phi$, which leads to the Poisson equation:

$$\nabla^2 \phi = -\frac{e}{\epsilon_0} (Z_i n_i - n_e) \quad (7.59)$$

The electron heat flux takes the classical form of Spitzer-Harm (SH) [54]:

$$\mathbf{q}_{SH} = -\kappa_e \nabla T_e \quad (7.60)$$

where κ_e is the electron thermal conductivity:

$$\kappa_e = \frac{\gamma_Z n_e k^2 T_e}{m_e \nu_{ei}} \quad (7.61)$$

$$\gamma_Z \approx \frac{3.22554 (Z_i + 0.24)}{1 + 0.24 Z_i} \quad (7.62)$$

It must be noted that since $\nu_{ei} \sim T_e^{-3/2}$, $\kappa_e \sim T_e^{5/2}$. SH formula is valid for $\lambda_{ei} \ll T_e/|\nabla T_e|$ where λ_{ei} is the collisional mean free path between ions and

⁴This is the low frequency field induced by the plasma, which is different from the electric field of the laser.

electrons. Beyond this limit, non-local effects in heat transport becomes important, requiring a kinetic treatment. In most hydrodynamic codes, the heat flux from SH theory is limited such that it can never exceed the free-stream limit, $q_{FS} = \left(\frac{2}{\pi}\right)^{1/2} kT_e v_{Te}$, where v_{Te} is the thermal velocity of the electrons. The same approach was employed here, leading to the following modification for the heat flux:

$$\mathbf{q}_e = \min\left(f \frac{q_{FS}}{|\mathbf{q}_{SH}|} \mathbf{q}_{SH}, \mathbf{q}_{SH}\right) \quad (7.63)$$

where f is a flux limit value. Here we set $f = 0.15$.

7.4 Numerical solutions of the wave equations

7.4.1 Finite difference method

In this section, the numerical methods for solving the wave equations (7.21) and (7.22) for $\hat{\mathbf{E}}$ and $\hat{\mathbf{B}}$ are briefly described. Instead of solving both equations, it is more convenient to solve for $\hat{\mathbf{E}}$ from equation (7.21), and $\hat{\mathbf{B}}$ can be determined from Faraday's law. Equation (7.21) can be solved easily by a finite difference (FD) discretization; detail of such a discretization can be found in LeVeque[133] and will not be repeated here.

One can see that the general solution of equation (7.21) is of the form:

$$\hat{E}(x) = E_+ e^{ikx} + E_- e^{-ikx} \quad (7.64)$$

where the first term represents the wave coming from the left and the second term is due to the wave coming from the right. For a problem with laser incidence from the left, the boundary conditions are defined as follows:

$$E_+(x=0) = E_V \quad (7.65)$$

$$E_-(x=L) = 0 \quad (7.66)$$

where E_V given by equation (7.26). Note that here we assume that the phase of the incident wave is zero at $x = 0$, and there is no light coming in from $x = L$. The two conditions on E_+ and E_- lead to two mixed boundary conditions (Neumann and Dirichlet) on the two sides of the domain. The discretized version of the wave equation is a tridiagonal system of equations, which can be solved easily by the Thomas algorithm.

7.4.2 Transfer-matrix method

The second approach of solving the wave equations is the transfer-matrix method (TMM) [134, 135]. Instead of solving the second order wave equation, we look for the solution of a system of two first order ODEs:

$$\partial_x \hat{E} = i\omega \hat{B} \quad (7.67)$$

$$c\partial_x \hat{B} = ik_0\eta^2 \hat{E} \quad (7.68)$$

One can rewrite the system above into the form:

$$\frac{dU}{dx} = i\frac{\beta}{p}V \quad (7.69)$$

$$\frac{dV}{dx} = ip\beta U \quad (7.70)$$

where $p = \eta$, $\beta = \frac{\omega p}{c}$, $U \equiv \hat{E}$ and $V \equiv c\hat{B}$. The solution for the equation above in the region where η^2 is uniform reads:

$$U = E_+e^{i\beta x} + E_-e^{-i\beta x} \quad (7.71)$$

$$V = p(E_+e^{i\beta x} + E_-e^{-i\beta x}) \quad (7.72)$$

where $E_{\pm} = \frac{1}{2}(U \pm V/p)$. Assuming an uniform value of the complex refractive index within a computational cell, the field values at two faces next to each other can be related by the following analytical expression:

$$\begin{bmatrix} U_{j-1/2} \\ V_{j-1/2} \end{bmatrix} = \begin{bmatrix} \cos(\beta_j \Delta x) & -\frac{i}{p_j} \sin(\beta_j \Delta x) \\ -ip_j \sin(\beta_j \Delta x) & \cos(\beta_j \Delta x) \end{bmatrix} \begin{bmatrix} U_{j+1/2} \\ V_{j+1/2} \end{bmatrix} \quad (7.73)$$

Taking of the product of all the matrices for all the cells, one obtains a relation for the first and last faces:

$$\begin{bmatrix} U_{-1/2} \\ V_{-1/2} \end{bmatrix} = \begin{bmatrix} m_{11} & m_{12} \\ m_{21} & m_{22} \end{bmatrix} \begin{bmatrix} U_{N+1/2} \\ V_{N+1/2} \end{bmatrix} \quad (7.74)$$

Assuming the phase of the incident electric field is zero and there is no light incident from the right, the boundary conditions at the laser incident side (left) read:

$$E_{+,-1/2} = E_V = \frac{1}{2}(U_{-1/2} + V_{-1/2}) \quad (7.75)$$

$$E_{-,N+1/2} = 0 = \frac{1}{2}(U_{N+1/2} - V_{N+1/2}) \quad (7.76)$$

Utilizing equations (7.74), (7.75) and (7.76), we obtain the following relations:

$$U_{N+1/2} = \frac{2E_V}{m_{11} + m_{12} + m_{21} + m_{22}} \quad (7.77)$$

$$V_{N+1/2} = U_{N+1/2} \quad (7.78)$$

Once the solution at $N + 1/2$ is computed, one can recursively utilize relation (7.73) to find U and V at other faces.

7.4.3 Benchmark problems

In this section, the wave solver for the laser fields is validated with an analytical problem. For a linearly increasing plasma density profile $n \sim x$, the wave equation (7.21) can be solved exactly [124]. The dielectric function also follows the same linear relation:

$$\varepsilon(x) = \eta^2(x) = (x - x_c)/L \quad (7.79)$$

where x_c is the location of the critical surface, i.e., $n(x_c) = n_{cr}$. By using the transformation $\xi = (k_0^2/L)^{1/3}(x - x_c)$, equation (7.21) is reduced to the homogeneous Stokes equation:

$$\partial_{\xi\xi}\hat{E} + \xi\hat{E} = 0 \quad (7.80)$$

Assuming the wave is evanescent to the right halfspace ($\xi > 0$), the exact solution of the electric field is the Airy function, denoted as $\text{Ai}(\xi)$:

$$\hat{E}(\xi) = 2\sqrt{\pi}(k_0 L)^{1/6} E_V e^{i\varphi} \text{Ai}(\xi) \quad (7.81)$$

where φ is a phase factor which does not affect $|\hat{E}|$. The solution of the magnetic field is determined from Faraday's law, i.e., equation (7.14):

$$\hat{B}(\xi) = -\frac{i}{c} 2\sqrt{\pi}(k_0 L)^{-1/6} E_V e^{i\varphi} \text{Ai}'(\xi) \quad (7.82)$$

where $\text{Ai}'(\xi)$ is the derivative of the Airy function.

We tested the two numerical approaches finite difference and transfer matrix methods in solving the wave equations for the electromagnetic fields using the linear density profile defined in equation (7.79). In the first test case, collision is neglected, resulting in a real value of the refractive index, and hence there is no absorption of the electromagnetic energy. The numerical solutions of the electric field along with the exact solution are shown in figure 7.2. The results show excellent agreement between the numerical and the exact solutions. It can be seen that the solution obtained with the transfer-matrix method is slightly more accurate. However, the finite difference method can be easily generalized to multiple dimensions.

The ponderomotive force is computed for the same test case using equation (7.43) and plotted in figure 7.3. The same quantity was computed by Lindl and Kaw [136] using the analytical solution of the field. A discrepancy between the current numerical solution and Lindl and Kaw's result was found; the numerical result suggests that the term due to the magnetic field in the Maxwell tensor, i.e., second term on the RHS of equation (7.43), was missing from their calculation. It can be seen that at approximately $\xi = -1$, the ponderomotive force is pushing the cold plasma inward on the right side, and pushing the left side further away. On the left of $\xi = -2$, there exists a standing wave due to local reflection of the

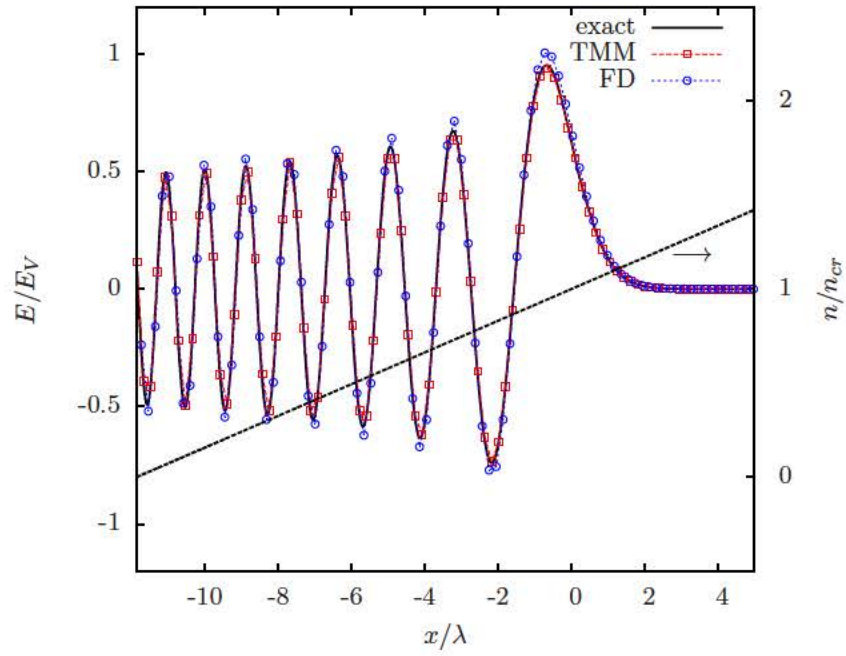


Figure 7.2: Solution of the electric field for a linear density profile (shown by the black dotted line) computed using both TMM and FD methods. The solid black line is the exact solution given by the Airy function. The length is normalized by the laser wavelength

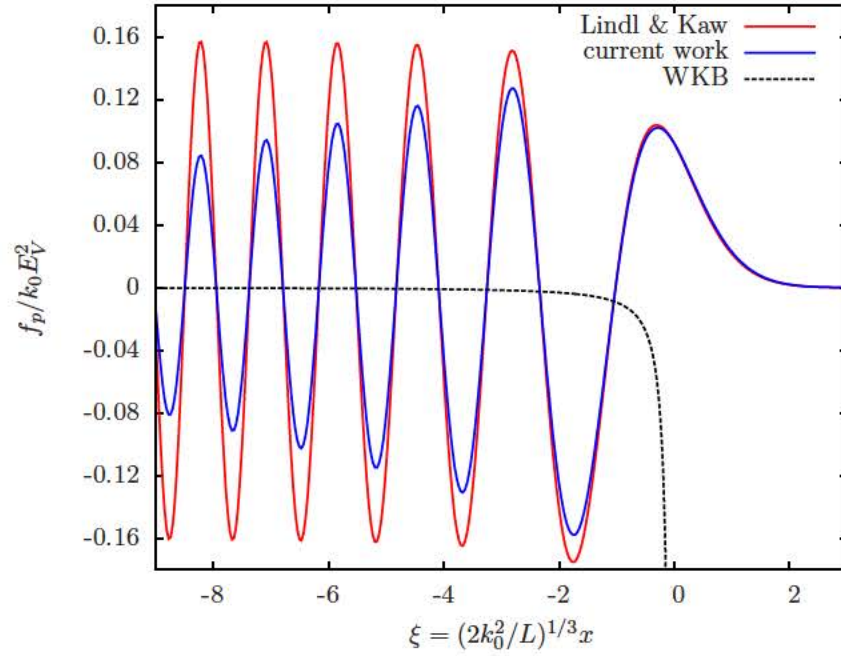


Figure 7.3: Ponderomotive force for a linear density profile. The numerical solution is obtained using the electric field computed in figure 7.2. The solution of Lindl and Kaw [136] is reproduced by omitting the term containing the magnetic field in the expression of the Maxwell stress tensor. The broken line is the solution obtained from the WKB approximation, i.e., equation (7.44).

electromagnetic wave, which gives rise to the ponderomotive bunching effects. The solution of the ponderomotive force computed using the equation (7.44) is also shown in the figure 7.3 with a singularity near $\xi = 0$ due to the breakdown of the WKB approximation.

In the second test case, collision is included in the expression of the refractive index, which allows the wave to be collisionally damped. The spatial profile of the intensity of the electromagnetic wave is shown in figure 7.4 using the field values obtained from solving the wave equations and the WKB approximation. The numerical solutions from both approaches (wave equations and WKB approximation) agree very well with unnoticeable difference near the critical layer. The

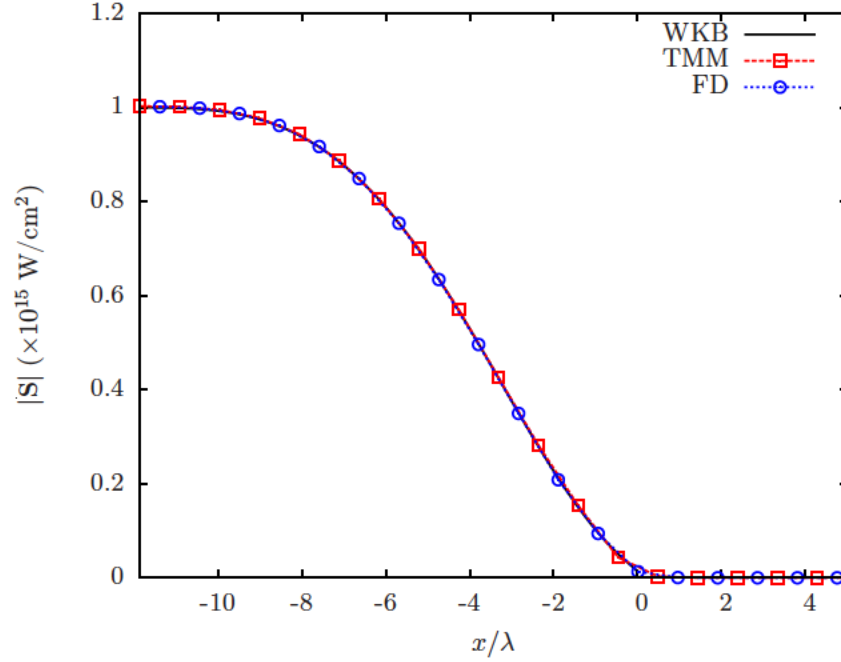


Figure 7.4: Spatial profile of the electromagnetic wave intensity as it propagates into the plasma. The wave energy is completely absorbed near the critical surface.

WKB solution is obtained by solving a radiation transport equation:

$$\partial_x I = -\kappa(x)I \quad (7.83)$$

where κ is given by equation (7.35).

7.5 Ion acceleration via Ponderomotive forces

In this section, we utilize the multi-fluid model described in the previous section to simulate ion acceleration by the ponderomotive force, commonly referred to as radiation pressure acceleration (RPA) mechanism [137]. Similar to another mechanism such as the target normal sheath acceleration (TNSA) [138, 139], ion acceleration is achieved as a direct consequence of an intense electric field, generated due to a large charge separation. The basics of the RPA process rely on the action of the laser ponderomotive force, accelerating electrons near the critical

surface and consequently creating a charge displacement. The TNSA process, on the other hand, refers to the direct conversion of the laser energy to kinetic energy of the electrons through various absorption mechanisms, leading to generation of relativistic electrons. These electrons are expanded to vacuum, thus creating an extremely large electric field, which accelerates the ions.

The RPA mechanism is reproduced by simulating the interaction of a high intensity laser pulse with a plasma density gradient using the multi-fluid equations. The effect of the laser ponderomotive force (appearing in the electron momentum equation) in modifying the plasma density and accelerating charged particles is examined. A similar problem was studied by Hora *et al.* in 1984 [140] albeit with a more compact domain size. Hora *et al.*'s work focuses on examining the generation of a double layer near the critical surface. In this work, we extended the domain to model the entire profile starting from the overdense plasma to near vacuum⁵.

The plasma is initialized using an Epstein transition layer profile [141] with a thickness $\delta = 4 \mu\text{m}$. The initial profile assumes a fully ionized hydrogen plasma at rest, and the computational domain is $x \in [0, L]$ where $L = 25 \mu\text{m}$. The initial density profile is as follows:

$$b = 1 - \frac{\exp[4(x - L/2)/\delta]}{1 + \exp[4(x - L/2)/\delta]} \quad (7.84)$$

$$n_i = n_e = a n_{cr} (1 - b) \quad (7.85)$$

where $a = 1.02$ and n_{cr} is the laser critical density. The initial temperatures of the ions and electrons are 1 keV. The laser wavelength is chosen to be $1.053 \mu\text{m}$. The laser pulse is simulated as a Gaussian pulse with a peak intensity of 10^{16} W/cm^2 , a pulse duration of 1 ps, and a FWHM of 0.2 ps (see figure 7.5). At $t = 0^+$, the laser

⁵Due to the use of an Eulerian code, one can not have zero number density, so a minimum value ($0.01n_{cr}$) for the number density is imposed in the “vacuum” region. This far field region does interact with the laser but does not affect the overall dynamics near the plasma density gradient.

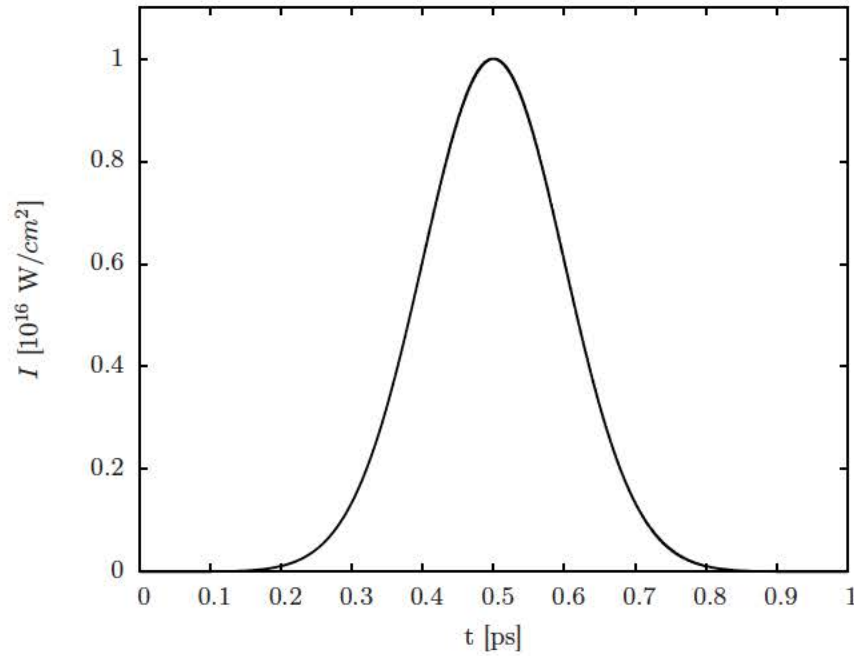


Figure 7.5: Gaussian laser pulse with a maximum intensity of 10^{16} W/cm^2

is incident from the left side of the domain. Although the calculation also includes absorption, its effect is negligible due to high temperature and laser intensity. Simulation results show little difference whether or not absorption is included. The reason for choosing a weak absorption condition is to enhance the effect of the ponderomotive force on the plasma acceleration and density modification. The initial conditions and the laser properties are chosen similarly to Hora's test case but with a longer computational domain and a slightly different density profile. This allows us to validate the code by comparing with Hora's result near the critical density layer, and also look at the evolution of the plasma density in the corona region.

Figure 7.6 shows the ion number density profile and the laser ponderomotive potential at various times during the laser pulse. At $t = 0.3 \text{ ps}$, the profile still looks very much similar to the initial one as the laser intensity begins to rise. One can see the formation of a large potential hill near the critical layer. The resultant

ponderomotive force due to this potential rapidly pushes the electrons down the hill, thus creating a charge displacement and an electrostatic field, which drags the ions along. At $t = 0.5$ ps, the laser is at its peak intensity, and we begin to see the formation of a caviton at $x \approx 16 \mu\text{m}$, as a direct consequence of the charge particle being rolled down the potential hill. This effects was also shown in the simulation of Hora *et al.* [140] with a more compact domain size. It must be pointed out that nonlinear force produced caviton was observed in the case of a plasma density gradient being imposed with an external rf field, and had been studied extensively by a number of researchers [142, 143]. In addition, the current simulation also shows an oscillatory structure of the density profile for $x < 16 \mu\text{m}$, which persists even after the laser is gone. The density ripples effectively make the plasma less transparent to the laser field; this can be seen from the density profile during the second half of the laser cycle where most of the laser is being reflected.

The appearance of the ripple in the density profile was not revealed in the previous simulation of Hora *et al.* [140] due to the limit on their computational domain size. This effect is due to local reflection of the laser electromagnetic wave as it propagates through the plasma medium, forming a standing wave pattern as can be seen in the ponderomotive potential profile. The standing wave nature of the potential results in an oscillatory (in space) acceleration of the electrons. The dynamics of the ions is mainly an electrostatic response to the charge separation as illustrated in figure 7.7. The magnitude of the electrostatic field induced in plasma can be significantly large during the laser period (up to 10^7 V/cm). Since plasma temperature is relatively high, collisional relaxation plays a minor role.

Figure 7.8 shows the ion velocity profile at different instances of time. Highly oscillatory velocity profile can be observed in the plasma corona region, and most importantly one can see that the ions are accelerated inward with an velocity of approximately 10^7 cm/sec. It must be clarified that the acceleration of the bulk

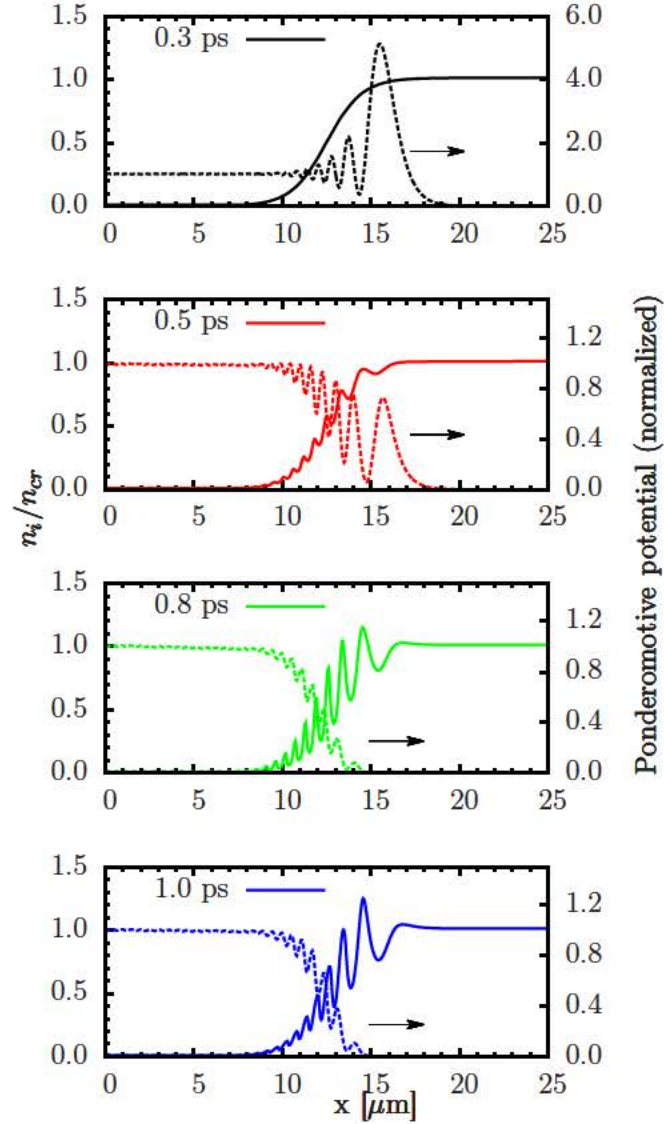


Figure 7.6: Ion number density (solid line) and the ponderomotive potential (dashed line) at four different times during the laser pulse. The ponderomotive potential is defined as $\epsilon_0(E^2 + c^2 B^2)$. The ion number density is normalized by the laser critical number density, and the potential is normalized by its value at the vacuum region.

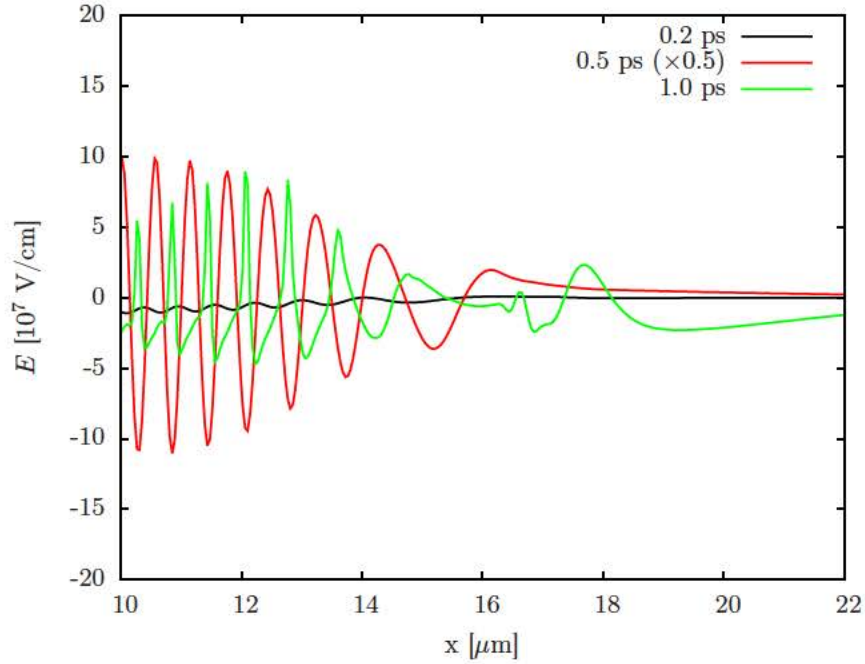


Figure 7.7: Electrostatic field generated in the plasmas due to charge separation.

of the plasma is merely due to the acoustic wave launched into the plasma. The ion acceleration, however, is a result of the intense electric field induced inside the plasma. This E-field consequently generates bursts of high energy ions in a transient fashion, which is the essence of RPA mechanism. The result in this simulation indicates that in the regime of weak collision and low absorption, non-linear force can dominate thermal action and plays an important role in charge acceleration. This is sometimes referred to as the laser piston regime. The same acceleration mechanism can be observed at kinetic time scale with ultra-high intensity laser-matter interaction, by which the ions can be accelerated to relativistic speed [144].

Let us now look at the evolution of the plasma after the laser pulse and the dependences on the laser parameters. In particular, we examine numerically the density modification effects due to a negatively chirped laser pulse. The effect of chirped lasers in LPI was examined in the context of charge acceleration both

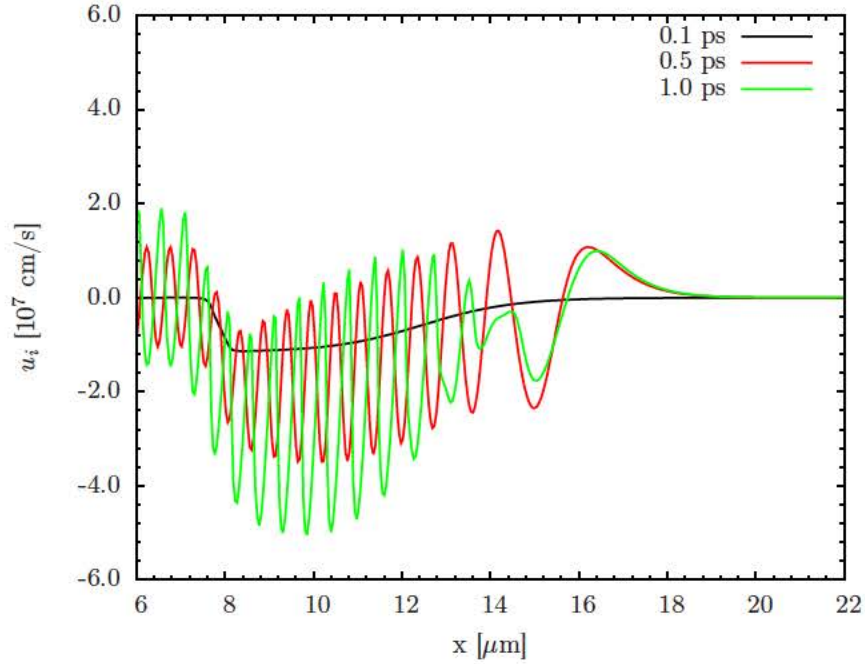


Figure 7.8: Ion velocity at various times after the laser pulse initiation.

from theoretical and application aspects [145, 146, 147, 148]. We focus here on characterizing the density steepening effect due to the action of ponderomotive force and variation of the laser frequency. Since the laser period is much shorter than the pulse duration ($2\pi\omega^{-1} \simeq 3.5$ fs), the effect of a chirped laser can be incorporated by imposing a time variation of the laser frequency ω in the wave equations. In this study, the laser frequency is modeled by a linear relation:

$$\omega(\tau) = \omega_0(1 - b\tau) \quad (7.86)$$

where b is the chirp parameter and τ is the time normalized by the laser pulse duration. In this study, we choose $b = 0.25$.

Figure 7.9 shows the ion densities for both cases of negatively chirped and unchirped lasers at several times. It can be seen that the formation of the density bump is delayed and the peak density value is higher when the laser is chirped. This can be explained by examining the dynamics of the laser ponderomotive forces during the laser pulse. Figure 7.10 shows the ponderomotive potential for

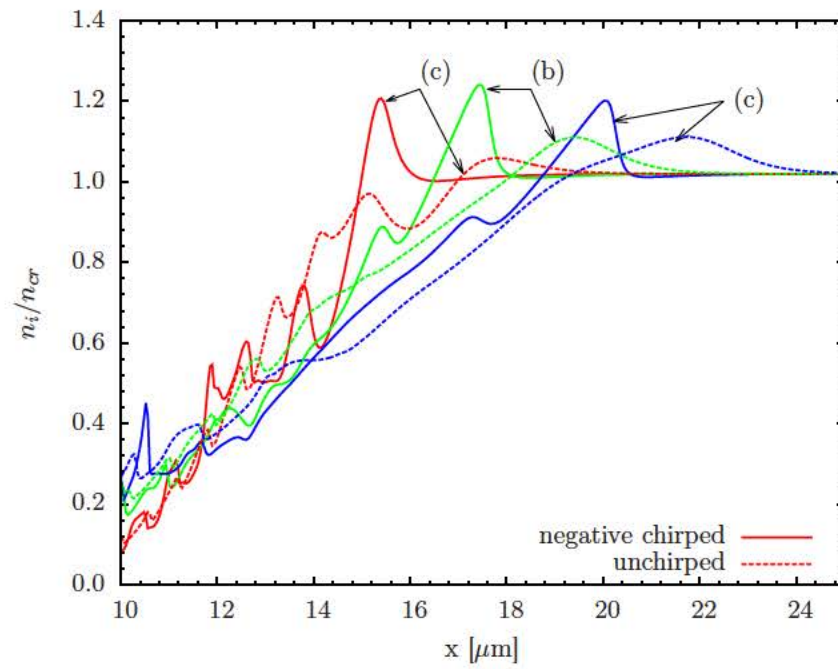
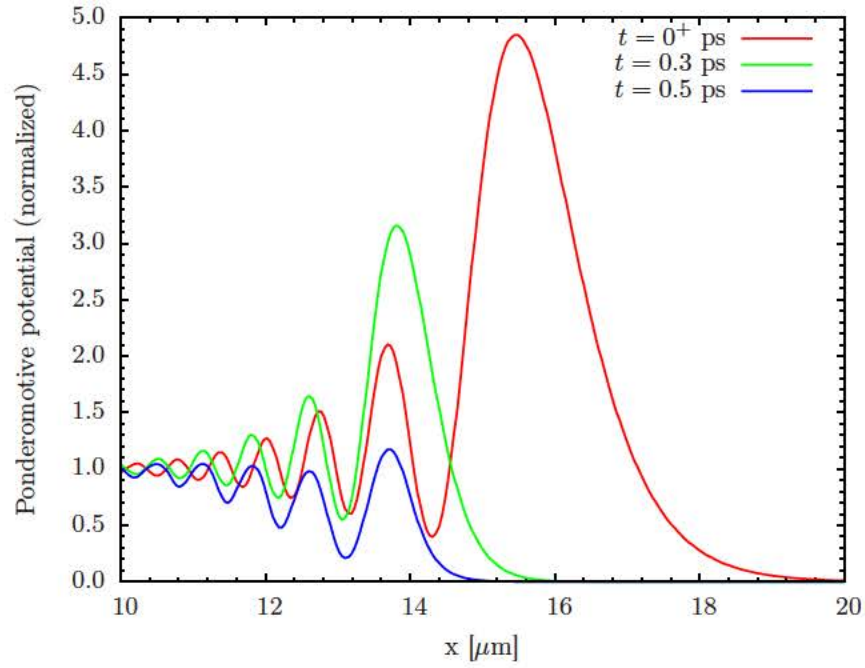
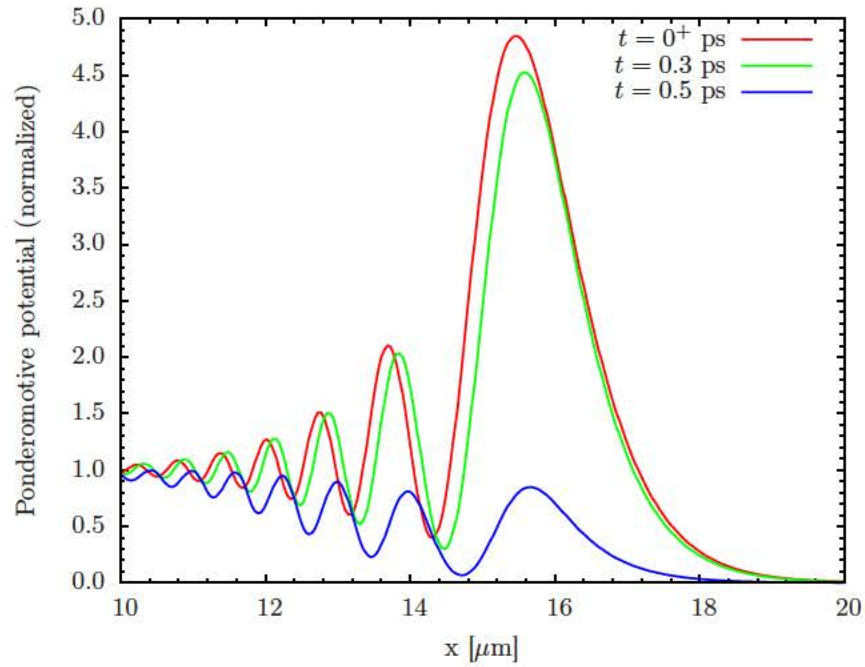


Figure 7.9: Ion number density at (a) 20 ps, (b) 50 ps, and (c) 90 ps for both cases of negatively chirped and unchirped laser pulse. For the negatively chirped laser, the frequency is linearly decreased 25 % over the entire pulse duration.

the first half the pulse. As expected, one can see a shift in the location of the potential hill when the laser is chirped as a indication of a change in the laser critical frequency. Consequently, as time progresses, the pressure force from the chirped laser starts pushing lower density plasma in the corona region inward, resulting a more compressed density bump. This suggests that the negatively chirped laser can enhance compression and steepen the plasma density near the critical layer. The existence of profile steepening is advantageous for energy transport process, i.e., excessive heating in the corona region can be minimized and resonance absorption is more efficient.



(a)



(b)

Figure 7.10: Comparison of the ponderomotive potential for (a) negatively chirped and (b) unchirped laser. The ponderomotive potential is defined as $\epsilon_0(E^2 + c^2B^2)$. The values of the potential are normalized by its value in the vacuum region.

CHAPTER 8

Conclusions and Future Directions

8.1 Achievements and contributions

In this dissertation, a hydrodynamic framework was developed to simulate multi-component plasmas including both elastic and inelastic interactions by means of a collisional-radiative (CR) model. The hydrodynamic equations can be derived by taking moments of the plasma kinetic equation with an appropriate closure of the transport fluxes. The CR model takes in account nonequilibrium distribution of the internal energy degrees of freedom. These energy states are convected as pseudo-species and their evolution due to CR kinetics are determined by solving a system of rate equations.

Two families of fluid models were considered in this work. The first one is the multi-fluid equations which characterize the plasma species in terms of their own set of conservation laws, which are coupled through collisional and electromagnetic interaction. The electromagnetic fields, governed by Maxwell's equations, are solved self-consistently with the plasmadynamics. In the limit of small electron inertia, the electron momentum reduces to the generalized Ohm's law, which relates the plasma current and the electromagnetic field. Various magnetohydrodynamic models can be derived from Ohm's law. Furthermore, in the limit of fast momentum exchange rate between the plasma components, the plasmadynamics can be characterized by the bulk fluid instead of individual components; this leads to the second family referred to as single-fluid models. Thermal nonequilib-

rium among different plasma components can be captured by multi-temperature equations, i.e., the thermal energy of each component is convected separately.

These hydrodynamic equations could be casted in system of conservation laws, which may be solved by a variety of numerical methods. In the current work, a finite volume discretization was utilized to solve for the fluid transport. The numerical fluxes were computed by solving an approximated Riemann solver at each interface. In order to achieve high-order accuracy, a high-order reconstruction procedure along with multi-stage Runge-Kutta method were employed for the flux integration and time marching, respectively. The coupling source terms were treated with an operator splitting approach. Stiff source terms were computed with a backward Euler method for stability reasons. An extensive set of benchmark problems for both single-fluid and multi-fluid equations were presented to validate the numerical methods and various physical modules implemented in the code.

Detailed CR models for Argon, Krypton and Xenon were constructed, taking into account excitation and ionization mechanisms both from collisional and radiative interaction, and thermal relaxation via elastic collision. The macroscopic rates were obtained directly from the cross section assuming a Maxwellian energy distribution function. A majority of the cross sections are based on ab initio calculations, and semi-empirical formula are used for missing data. Using both steady and unsteady 1D simulations, these CR models were calibrated against available experimental shock tube data with satisfactory agreement over a wide range of flow conditions. The source of remaining discrepancy discovered through these simulations calls for future multi-dimensional simulations with viscous phenomena.

In order to lower the complexity and computational requirement in solving the CR kinetics, a model reduction mechanism for atomic plasma was developed, by grouping electronic states into groups and deriving the corresponding macroscopic

rates to take in account all the transitions. In contrast to the common level-grouping approach, a higher-order description of the internal structure of the groups was developed here by assuming a Boltzmann distribution of the levels within the group, with different temperatures for each group. This approach provides substantial accuracy at minimal computational cost, making it suitable for multidimensional flow calculations.

The modeling of inelastic collisions is extended to the multi-fluid regime, with much emphasis on excitation collision and its reverse process. The exchange source terms due to collision are derived by taking moment of the collision transfer integral. It is shown that the macroscopic rates for multi-fluid equations can deviate significantly from the single-fluid limit due to the difference in the mean flow velocities. In addition, inelastic collisions impose momentum and energy exchange analogously to elastic collisions. The derivation also shows that common expressions of detailed balance for excitation and deexcitation collision does not hold at the macroscopic level when the relative mean drift velocity between the two components is apparent.

The multi-fluid equations were used to simulate laser-plasma interaction phenomena. In particular, the ion acceleration mechanism due to radiation pressure is modeled, showing a strong coupling between the laser, the plasma, and the induced electromagnetic field at high intensity ($I \geq 10^{15}$ W/cm²). These simulations highlighted the advantage of the multi-fluid model over the single-fluid model to capture charge separation and electromagnetic effects in plasma, which play an essential role in the dynamics of charged particle acceleration, magnetic field generation, and instabilities.

8.2 Future directions

The hydrodynamic models developed in this dissertation can be utilized to study a wide range of problems. In particular, the CR model is directly applicable for the study of plasma formation and radiation, which is relevant, for example, in field-reversed configuration (FRC) plasma formation [42] and aerothermodynamics [20]. The FRC modeling can be accomplished by solving the magnetohydrodynamic (MHD) equations or the multi-fluid equations with a detailed CR model. The validity of the MHD approximation in this plasma regime can be revealed via comparison with the multi-fluid solutions. The same set of equations can be used to study shock and instabilities, occurring in hypersonic reentry [20], inertial confinement devices [149], and astrophysical plasmas [150]. The aspect of excitation and ionization kinetics is of most interests in these simulations since it is often neglected (assuming a fully ionized plasma) or over-simplified (one-step kinetics, quasi steady-state model).

The CR model itself can be improved in several ways. The empiricism of the collision cross section (heavy-particle impact collision) can be removed by using *ab initio* cross sections. In addition, the simplified treatment of the radiative term can be improved with a radiation transport (RT) model, which takes into account the distribution of the radiation field [95]. Although the solution of the RT equation can be computationally very expensive, various approximations can be used to reduce the cost, e.g., tangent-slab method, multi-group diffusion approximation, etc. By combining the level-grouping method developed in this work with a simplified RT model, a time-dependent flow solution with detailed CR kinetics coupled with the radiation field can be made feasible, allowing us to extract the synthetic radiation spectra for comparison with experiments. In fact, this coupling approach was attempted by Cambier [113] albeit with the use of a simplified model for the CR kinetics. Cambier's work shows that precursor effects can be

of importance for very high shock Mach number; these phenomena are highly non-local and cannot be captured without a RT model.

Extension of the CR model to the multi-fluid regime requires a full description of all the macroscopic rates (density, momentum, and energy) for each transition. The rates must be consistent with kinetic theory, and obey the principle of detailed balance. The same derivation carried out for the excitation and deexcitation collisions can be extended to model ionization and recombination. The contribution of the radiative terms can be derived in a similar fashion with some simplification. Since the mean momentum of the photon is usually much smaller than the thermal momentum of the particle, momentum transfer can be neglected for the radiative transitions. The fully developed multi-fluid CR model can complement the existing work on multi-fluid transport to construct a self-consistent plasmadynamic model. This model is a generalization of the traditional MHD model, therefore having a wider range of applicability, and can potentially provide a robust coupling with hybrid fluid-kinetic methods.

APPENDIX A

Eigensystems

A.1 2T Model

The expressions for the pressure and energy derivatives, which enter the flux Jacobian matrix, are given here. From the equation of state (2.54), the total pressure derivatives can be determined as:

$$p_E \equiv \frac{\partial p}{\partial E} = \gamma_h - 1 \quad (\text{A.1})$$

$$p_{S_e} \equiv \frac{\partial p}{\partial S_e} = \rho^{\gamma_e-1} \left(1 - \frac{\gamma_h - 1}{\gamma_e - 1} \right) \quad (\text{A.2})$$

$$p_{\rho \mathbf{u}} \equiv \frac{\partial p}{\partial (\rho \mathbf{u})} = -(\gamma - 1) \mathbf{u} \quad (\text{A.3})$$

$$p_{\rho_e} \equiv \frac{\partial p}{\partial \rho_e} = (\gamma_e - \gamma_h) \frac{p_e}{\rho} + (\gamma_h - 1) \frac{\mathbf{u} \cdot \mathbf{u}}{2} \quad (\text{A.4})$$

$$p_{\rho_{s \neq e}} \equiv \frac{\partial p}{\partial \rho_{s \neq e}} = p_{\rho_e} - (\gamma_h - 1) \varepsilon_s + \frac{p_s}{\rho_s} \quad (\text{A.5})$$

$$p_\rho \equiv \frac{\partial p}{\partial \rho} = p_{\rho_e} - (\gamma_h - 1) \sum_{s \neq e} y_s \varepsilon_s + \frac{p - p_e}{\rho} \quad (\text{A.6})$$

The energy derivatives can also be obtained in a similar manner from equation (2.55):

$$E_{\rho_e} \equiv \frac{\partial E}{\partial \rho_e} = -\frac{1}{2} \mathbf{u} \cdot \mathbf{u} \quad (\text{A.7})$$

$$E_{\rho_{s \neq e}} \equiv \frac{\partial E}{\partial \rho_{s \neq e}} = \varepsilon_s + E_{\rho_e} - \frac{p_s}{(\gamma - 1) \rho_s} \quad (\text{A.8})$$

$$E_{\mathbf{u}} \equiv \frac{\partial E}{\partial \mathbf{u}} = \rho \mathbf{u} \quad (\text{A.9})$$

$$E_p \equiv \frac{\partial E}{\partial p} = \frac{1}{\gamma_h - 1} \quad (\text{A.10})$$

$$E_{p_e} \equiv \frac{\partial E}{\partial p_e} = \frac{1}{\gamma_e - 1} - \frac{1}{\gamma_h - 1} \quad (\text{A.11})$$

where y_s is the species mass fraction.

The vector of conservative variables and the inviscid flux vector in the two-temperature model within the context of a finite-volume approximation is as follows:

$$\mathbf{Q} = \begin{bmatrix} \rho_s \\ \rho u_x \\ \rho u_y \\ \rho u_z \\ E \\ S_e \end{bmatrix}, \quad \mathbf{F}_n = \begin{bmatrix} \rho_s u_n \\ \rho u_n u_x + p n_x \\ \rho u_n u_y + p n_y \\ \rho u_n u_z + p n_z \\ u_n H \\ u_n S_e \end{bmatrix} \quad (\text{A.12})$$

where \mathbf{F}_n is the numerical flux normal to the interface. The three components of the unit vector normal to the face are defined as n_x , n_y and n_z , and u_n is the normal component of the velocity:

$$u_n = u_x n_x + u_y n_y + u_z n_z \quad (\text{A.13})$$

We also define the two tangential velocities to the face

$$u_t = u_x t_x + u_y t_y + u_z t_z \quad (\text{A.14})$$

$$u_s = u_x s_x + u_y s_y + u_z s_z \quad (\text{A.15})$$

The flux Jacobian for the Euler equations for the 2T model is given as:

$$\mathbf{A} = \begin{bmatrix} u_n(\delta_{sr} - y_s) & y_s n_x & y_s n_y & y_s n_z & 0 & 0 \\ p_{\rho_r} n_x - u_n u_x & \mathcal{A}_{m_x, m_x} & \mathcal{A}_{m_y, m_x} & \mathcal{A}_{m_z, m_x} & p_E n_x & p_{S_e} n_x \\ p_{\rho_r} n_y - u_n u_y & \mathcal{A}_{m_x, m_y} & \mathcal{A}_{m_y, m_y} & \mathcal{A}_{m_z, m_y} & p_E n_y & p_{S_e} n_y \\ p_{\rho_r} n_z - u_n u_z & \mathcal{A}_{m_x, m_z} & \mathcal{A}_{m_y, m_z} & \mathcal{A}_{m_z, m_z} & p_E n_z & p_{S_e} n_z \\ u_n(p_{\rho_r} - h) & u_n p_{m_x} + h n_x & u_n p_{m_y} + h n_y & u_n p_{m_z} + h n_z & u_n(1 + p_E) & u_n p_{S_e} \\ -u_n \hat{s}_e & \hat{s}_e n_x & \hat{s}_e n_y & \hat{s}_e n_z & 0 & u_n \end{bmatrix} \quad (\text{A.16})$$

where $y_s = \rho_s/\rho$ is the species mass fraction, and $\mathcal{A}_{m_\alpha, m_\beta} = p_{m_\alpha} n_\beta + u_\beta n_\alpha + \delta_{\alpha\beta} u_n$.

The speed of sound can be extracted from the determinant of the flux Jacobian:

$$a^2 = \sum y_s \frac{\partial p}{\partial \rho_s} + \left(\varepsilon_h + \varepsilon_e + \frac{p}{\rho} - \frac{\mathbf{u} \cdot \mathbf{u}}{2} \right) \frac{\partial p}{\partial E} + \hat{s}_e \frac{\partial p}{\partial S_e} \quad (\text{A.17})$$

The similarity transformation matrices \mathbf{R} and \mathbf{L} are defined as:

$$\mathbf{R} = \begin{bmatrix} \delta_{sr} & y_s & 0 & 0 & y_s & 0 \\ u_x & u_x - n_x a & t_x \rho & s_x \rho & u_x + n_x a & 0 \\ u_y & u_y - n_y a & t_y \rho & s_y \rho & u_y + n_y a & 0 \\ u_z & u_z - n_z a & t_z \rho & s_z \rho & u_z + n_z a & 0 \\ E_{\rho_r} & h - a u_n & E_{u_t} & E_{u_s} & h + a u_n & E_{p_e} \\ (1 - \gamma_e) \hat{s}_e & \hat{s}_e & 0 & 0 & \hat{s}_e & \rho^{1-\gamma_e} \end{bmatrix} \quad (\text{A.18})$$

$$\mathbf{L} = \begin{bmatrix} \delta_{sr} - y_s \frac{p_{\rho_s}}{a^2} & -y_s \frac{p_{m_x}}{a^2} & -y_s \frac{p_{m_y}}{a^2} & -y_s \frac{p_{m_z}}{a^2} & -y_s \frac{p_E}{a^2} & -y_s \frac{p_{S_e}}{a^2} \\ \frac{p_{\rho_r} + c u_n}{2a^2} & \frac{p_{m_x} - c n_x}{2a^2} & \frac{p_{m_y} - c n_y}{2a^2} & \frac{p_{m_z} - c n_z}{2a^2} & \frac{p_E}{2a^2} & \frac{p_{S_e}}{2a^2} \\ -\frac{u_t}{\rho} & \frac{t_x}{\rho} & \frac{t_y}{\rho} & \frac{t_z}{\rho} & 0 & 0 \\ -\frac{u_s}{\rho} & \frac{s_x}{\rho} & \frac{s_y}{\rho} & \frac{s_z}{\rho} & 0 & 0 \\ \frac{p_{\rho_r} - c u_n}{2a^2} & \frac{p_{m_x} + c n_x}{2a^2} & \frac{p_{m_y} + c n_y}{2a^2} & \frac{p_{m_z} + c n_z}{2a^2} & \frac{p_E}{2a^2} & \frac{p_{S_e}}{2a^2} \\ \frac{(\gamma_e - 1)p_e}{\rho} - \frac{\gamma_e p_e p_{\rho_r}}{\rho a^2} & -\frac{\gamma_e p_e p_{m_x}}{\rho a^2} & -\frac{\gamma_e p_e p_{m_y}}{\rho a^2} & -\frac{\gamma_e p_e p_{m_z}}{\rho a^2} & -\frac{\gamma_e p_e p_E}{\rho a^2} & \frac{p_e}{S_e} - \frac{\gamma_e p_e p_{S_e}}{\rho a^2} \end{bmatrix} \quad (\text{A.19})$$

The diagonal matrix of eigenvalues of $\mathbf{\Lambda}$ is defined by

$$\mathbf{\Lambda} = \begin{bmatrix} u_n & \dots & 0 & 0 & 0 & 0 & 0 & 0 \\ \vdots & \ddots & \vdots & \vdots & \vdots & \vdots & \vdots & \vdots \\ 0 & \dots & u_n & 0 & 0 & 0 & 0 & 0 \\ 0 & \dots & 0 & u_n - a & 0 & 0 & 0 & 0 \\ 0 & \dots & 0 & 0 & u_n & 0 & 0 & 0 \\ 0 & \dots & 0 & 0 & 0 & u_n & 0 & 0 \\ 0 & \dots & 0 & 0 & 0 & 0 & u_n + a & 0 \\ 0 & \dots & 0 & 0 & 0 & 0 & 0 & u_n \end{bmatrix} \quad (\text{A.20})$$

A.2 Maxwell's equations

The vector of conservative variables and the inviscid flux vector in Maxwell's equations within the context of a finite-volume approximation is as follows:

$$\mathbf{Q} = \begin{bmatrix} B_x \\ B_y \\ B_z \\ E_x \\ E_y \\ E_z \end{bmatrix}, \quad \mathbf{F}_n = \begin{bmatrix} E_z n_y - E_y n_z \\ -E_z n_x + E_x n_z \\ E_y n_x - E_x n_y \\ c^2(-B_z n_y + B_y n_z) \\ c^2(B_z n_x - B_x n_z) \\ c^2(-B_y n_x + B_x n_y) \end{bmatrix} \quad (\text{A.21})$$

where n_x , n_y and n_z are the three component of a unit vector normal to a computational cell. The flux Jacobian for the Maxwell's equations is given as:

$$\mathbf{A} = \begin{bmatrix} 0 & 0 & 0 & 0 & -n_z & n_y \\ 0 & 0 & 0 & n_z & 0 & -n_x \\ 0 & 0 & 0 & -n_y & n_x & 0 \\ 0 & c^2 n_z & -c^2 n_y & 0 & 0 & 0 \\ -c^2 n_z & 0 & c^2 n_x & 0 & 0 & 0 \\ c^2 n_y & -c^2 n_x & 0 & 0 & 0 & 0 \end{bmatrix} \quad (\text{A.22})$$

The transformation matrices \mathbf{R} and \mathbf{L} are defined as:

$$\mathbf{R} = \begin{bmatrix} 0 & n_x & -\frac{n_x n_y}{c} & \frac{n_x n_z}{c} & \frac{n_x n_y}{c} & -\frac{n_x n_z}{c} \\ 0 & n_y & \frac{n_x^2 + n_z^2}{c} & \frac{n_y n_z}{c} & -\frac{n_x^2 + n_z^2}{c} & -\frac{n_y n_z}{c} \\ 0 & n_z & -\frac{n_y n_z}{c} & -\frac{n_x^2 + n_y^2}{c} & \frac{n_y n_z}{c} & \frac{n_x^2 + n_y^2}{c} \\ n_x & 0 & -n_z & -n_y & -n_z & -n_y \\ n_y & 0 & 0 & n_x & 0 & n_x \\ n_z & 0 & n_x & 0 & n_x & 0 \end{bmatrix} \quad (\text{A.23})$$

$$\mathbf{L} = \begin{bmatrix} 0 & 0 & 0 & n_x & n_y & n_z \\ n_x & n_y & n_z & 0 & 0 & 0 \\ -\frac{cn_y}{2n_x} & c/2 & 0 & -n_z/2 & -\frac{n_y n_z}{2n_x} & \frac{n_x^2 + n_y^2}{2n_x} \\ \frac{cn_z}{2n_x} & 0 & -c/2 & -n_y/2 & \frac{n_x^2 + n_z^2}{2n_x} & -\frac{n_y n_z}{2n_x} \\ \frac{cn_y}{2n_x} & -c/2 & 0 & -n_z/2 & -\frac{n_y n_z}{2n_x} & \frac{n_x^2 + n_y^2}{2n_x} \\ -\frac{cn_z}{2n_x} & 0 & c/2 & -n_y/2 & \frac{n_x^2 + n_z^2}{2n_x} & -\frac{n_y n_z}{2n_x} \end{bmatrix} \quad (\text{A.24})$$

The diagonal matrix of eigenvalues of \mathbf{L} is defined by

$$\mathbf{\Lambda} = \begin{bmatrix} 0 & 0 & 0 & 0 & 0 & 0 \\ 0 & 0 & 0 & 0 & 0 & 0 \\ 0 & 0 & -c & 0 & 0 & 0 \\ 0 & 0 & 0 & -c & 0 & 0 \\ 0 & 0 & 0 & 0 & c & 0 \\ 0 & 0 & 0 & 0 & 0 & c \end{bmatrix} \quad (\text{A.25})$$

where $c = 3 \times 10^8$ m/s is the speed of light.

APPENDIX B

Steady-state Flow Equations

This appendix describes the steady-state 1D flow approximation used to compute an ionizing shock profile. Utilizing the two temperature model described in section 2.4 and dropping the unsteady terms, the governing equations for steady-state flow are reduced to a system of ODEs:

$$\frac{d}{dx}(\rho_s u) = m_s \dot{\omega}_s \quad (\text{B.1})$$

$$\frac{d}{dx}(p + \rho u^2) = 0 \quad (\text{B.2})$$

$$\frac{d}{dx}(uH) = \dot{\omega}_{\varepsilon_h} + \dot{\omega}_{\varepsilon_e} \quad (\text{B.3})$$

$$\frac{d}{dx}(uS_e) = \frac{\gamma_e - 1}{\rho^{\gamma_e - 1}} \dot{\omega}_{\varepsilon_e} \quad (\text{B.4})$$

$$(\text{B.5})$$

where $H = E + p$. Using the Jacobian defined in appendix A, one can write the system as:

$$\mathbf{A} \frac{d\mathbf{Q}}{dx} = \dot{\mathbf{\Omega}} \quad (\text{B.6})$$

where \mathbf{Q} is the typical vector of hydrodynamic variables. Here we consider a semi-implicit approximation in which only the RHS is treated implicitly. The linearization follows from a Taylor series expansion:

$$\mathbf{A} \frac{d\mathbf{Q}^n}{dx} = \dot{\mathbf{\Omega}}^n + \frac{\partial \dot{\mathbf{\Omega}}}{\partial x} \Delta x \quad (\text{B.7})$$

$$\mathbf{A} \frac{d\mathbf{Q}^n}{dx} = \dot{\mathbf{\Omega}}^n + \mathbf{J} \frac{d\mathbf{Q}^n}{dx} \Delta x \quad (\text{B.8})$$

where $\mathbf{J} = \frac{\partial \dot{\Omega}}{\partial \mathbf{Q}}$. Note that the inviscid flux Jacobian \mathbf{A} is assumed constant in the expansion which makes the scheme not fully implicit. However, the main concern of the stiffness due to kinetics can be avoided. The final expression for the change in the conservative variables reads:

$$\Delta \mathbf{Q}^n = \Delta x (\mathbf{A} - \Delta x \mathbf{J})^{-1} \dot{\Omega}^n \quad (\text{B.9})$$

For the steady-state shock flow, we seek for a solution of an initial value problem with the initial conditions being the post-shock flow properties determined from the Rankine-Hugoniot conditions with frozen chemistry. The flow variables are then marched forward in space using the approximation given by equation (B.9). The size of Δx is selected such that sharp flow features such as the electron avalanche can be well resolved.

APPENDIX C

Collision kinematics

C.1 Two-body processes

Let us consider an inelastic collision¹ between two particles s and t , such that the post-collision particles can have modified internal states. The process is formally described as the relation

$$s(\mathbf{v}_s) + t(\mathbf{v}_t) \Leftrightarrow s'(\mathbf{v}'_s) + t'(\mathbf{v}'_t) \quad (\text{C.1})$$

Note that only two particles are produced by the collision, and that the reverse process is indicated by the left arrow in (C.1). The initial velocities are $\mathbf{v}_s, \mathbf{v}_t$. One can define a fluid velocity \mathbf{u} such that $\mathbf{u} \equiv \langle \mathbf{v} \rangle \equiv \int d^3\mathbf{v} \mathbf{v} f(\mathbf{v})$ and a thermal velocity $\mathbf{c} = \mathbf{v} - \mathbf{u}$. By definition, we also have $\langle \mathbf{c} \rangle \equiv 0$

The collision can be transformed to the center of mass (COM) reference frame, moving with velocity \mathbf{V} with respect to the LAB frame. Similarly, we can also define a mean velocity of this COM frame as \mathbf{U} . The subsequent Galilean transformations yield the following definitions:

$$\mathbf{V} = \frac{m_s \mathbf{v}_s + m_t \mathbf{v}_t}{M} \quad \mathbf{g} = \mathbf{v}_s - \mathbf{v}_t \quad (\text{C.2a})$$

$$\mathbf{U} = \frac{m_s \mathbf{u}_s + m_t \mathbf{u}_t}{M} \quad \mathbf{w} = \mathbf{u}_s - \mathbf{u}_t \quad (\text{C.2b})$$

¹The particles s and t are respectively the scattered and target in the laboratory frame of reference (LAB)

where $M = m_s + m_t$. The inverse transformation yields:

$$\mathbf{v}_s = \mathbf{V} + \frac{m_t}{M} \mathbf{g} \quad \mathbf{u}_s = \mathbf{U} + \frac{m_t}{M} \mathbf{w} \quad (\text{C.3a})$$

$$\mathbf{v}_t = \mathbf{V} - \frac{m_s}{M} \mathbf{g} \quad \mathbf{u}_t = \mathbf{U} - \frac{m_s}{M} \mathbf{w} \quad (\text{C.3b})$$

Mass conservation imposes the relation $m_s + m_t = M = m'_s + m'_t$. For the case of two-body processes such as excitation of internal states, the masses are individually conserved, i.e. $m'_s = m_s, m'_t = m_t$. Expressed in the COM frame, momentum and energy conservation yield, respectively:

$$M\mathbf{V} = M\mathbf{V}' \quad (\text{C.4a})$$

$$\frac{1}{2}M\mathbf{V}^2 + \frac{1}{2}\mu\mathbf{g}^2 = \frac{1}{2}M\mathbf{V}'^2 + \frac{1}{2}\mu\mathbf{g}'^2 + \Delta\varepsilon \quad (\text{C.4b})$$

where $\mu = m_s m_t / M$. Therefore, we have the following constraints:

$$\mathbf{V} = \mathbf{V}' \quad \text{and} \quad \mathbf{g}^2 = \mathbf{g}'^2 + \frac{2\Delta\varepsilon}{\mu} \quad (\text{C.5})$$

For an excitation between two atomic levels, the transferred energy is a fixed value $\Delta\varepsilon \equiv \varepsilon^*$, the energy gap between levels. In the limit $\Delta\varepsilon \rightarrow 0$, the collision is elastic.

Consider now the Maxwellian velocity distribution functions (VDF) of each particle type, normalized to unity, e.g. (recall that $\mathbf{c} = \mathbf{v} - \mathbf{u}$):

$$f_s(\mathbf{v}_s) = \left(\frac{m_s}{2\pi k T_s} \right)^{\frac{3}{2}} \exp \left[-\frac{m_s \mathbf{c}_s^2}{2k T_s} \right] \quad (\text{C.6})$$

and similarly for f_t . The averaging over initial states will yield a product of these two distributions:

$$f_s(\mathbf{v}_s) f_t(\mathbf{v}_t) = \left(\frac{m_s}{2\pi k T_s} \right)^{\frac{3}{2}} \left(\frac{m_t}{2\pi k T_t} \right)^{\frac{3}{2}} \exp[\mathcal{A}] \quad (\text{C.7})$$

where the argument of the exponential function is, from inverting (C.2):

$$\mathcal{A} = \frac{m_s}{2k T_s} \left[\mathbf{V} - \mathbf{U} + \frac{m_t}{M} (\mathbf{g} - \mathbf{w}) \right]^2 + \frac{m_t}{2k T_t} \left[\mathbf{V} - \mathbf{U} - \frac{m_s}{M} (\mathbf{g} - \mathbf{w}) \right]^2 \quad (\text{C.8})$$

Following Burgers [43], this expression can be simplified with an appropriate transformation of variables; since the basic procedure will be used elsewhere, we describe it below. First, we define the following variables

$$\beta_p = \frac{m_p}{2kT_p}, \quad \tilde{\mathbf{g}} = \mathbf{g} - \mathbf{w} \quad (\text{C.9})$$

such that

$$\begin{aligned} \mathcal{A} &= \beta_s \left[(\mathbf{V} - \mathbf{U}) + \frac{m_t}{M} \tilde{\mathbf{g}} \right]^2 + \beta_t \left[(\mathbf{V} - \mathbf{U}) - \frac{m_s}{M} \tilde{\mathbf{g}} \right]^2 \\ &= (\beta_s + \beta_t) (\mathbf{V} - \mathbf{U})^2 + \left[\beta_s \frac{m_t^2}{M^2} + \beta_t \frac{m_s^2}{M^2} \right] \tilde{\mathbf{g}}^2 + 2 \left[\beta_s \frac{m_t}{M} - \beta_t \frac{m_s}{M} \right] (\mathbf{V} - \mathbf{U}) \cdot \tilde{\mathbf{g}} \end{aligned} \quad (\text{C.10})$$

Define now

$$\mathbf{V}^* = \mathbf{V} - \mathbf{U} + \gamma \tilde{\mathbf{g}} \quad (\text{C.11})$$

and comparing the expression

$$(\beta_s + \beta_t) \mathbf{V}^{*2} = (\beta_s + \beta_t) (\mathbf{V} - \mathbf{U})^2 + (\beta_s + \beta_t) \gamma^2 \tilde{\mathbf{g}}^2 + 2\gamma(\beta_s + \beta_t) (\mathbf{V} - \mathbf{U}) \cdot \tilde{\mathbf{g}} \quad (\text{C.12})$$

with (C.10), we see that we can choose the appropriate value of the coefficient γ to eliminate the dot product from \mathcal{A} :

$$\gamma = \frac{1}{\beta_s + \beta_t} \left(\beta_s \frac{m_t}{M} - \beta_t \frac{m_s}{M} \right) \quad (\text{C.13})$$

We then obtain complete separation of variables:

$$\mathcal{A} = (\beta_s + \beta_t) \mathbf{V}^{*2} + \left[\beta_s \frac{m_t^2}{M^2} + \beta_t \frac{m_s^2}{M^2} - \frac{1}{\beta_s + \beta_t} \left(\beta_s \frac{m_t}{M} - \beta_t \frac{m_s}{M} \right)^2 \right] \tilde{\mathbf{g}}^2 \quad (\text{C.14})$$

The term in brackets is easily simplified:

$$[\dots] = \frac{\beta_s \beta_t}{\beta_s + \beta_t} \quad (\text{C.15})$$

We can now define effective, average temperatures:

$$\beta_s + \beta_t = \frac{m_s}{2kT_s} + \frac{m_t}{2kT_t} = \frac{M}{2k} \frac{m_s T_t + m_t T_s}{M T_s T_t} \equiv \frac{M}{2kT^*} \quad (\text{C.16a})$$

$$\frac{\beta_s \beta_t}{\beta_s + \beta_t} = \frac{\mu}{2k} \frac{M}{T_s T_t} \frac{T_s T_t}{m_s T_t + m_t T_s} \equiv \frac{\mu}{2k\tilde{T}} \quad (\text{C.16b})$$

and γ becomes:

$$\gamma = \frac{\mu}{M} \frac{T_t - T_s}{\tilde{T}} = \mu \frac{T_t - T_s}{m_s T_t + m_t T_s} \quad (\text{C.17})$$

To summarize, we have performed the following change of variables:

$$\mathbf{V}^* = \mathbf{V} - \mathbf{U} + \mu \frac{T_t - T_s}{m_s T_t + m_t T_s} \tilde{\mathbf{g}} \quad \tilde{\mathbf{g}} = \mathbf{g} - \mathbf{w} \quad (\text{C.18a})$$

$$T^* = M \frac{T_s T_t}{m_s T_t + m_t T_s} \quad \tilde{T} = \frac{m_s T_t + m_t T_s}{M} \quad (\text{C.18b})$$

These are the same expressions found in [43, pp. 45-46] (with an occasional change of naming convention) for which it is easy to verify that the Jacobian of the transformations is unity, i.e.

$$d^3 \mathbf{v}_s d^3 \mathbf{v}_t \equiv d^3 \mathbf{V} d^3 \mathbf{g} \equiv d^3 \mathbf{V}^* d^3 \tilde{\mathbf{g}} \quad (\text{C.19})$$

Furthermore, we note that:

$$\left(\frac{m_s}{2kT_s} \right)^{\frac{3}{2}} \left(\frac{m_t}{2kT_t} \right)^{\frac{3}{2}} \equiv (\beta_s \beta_t) = (\beta_s + \beta_t)^{\frac{3}{2}} \left(\frac{\beta_s \beta_t}{\beta_s + \beta_t} \right)^{\frac{3}{2}} \equiv \left(\frac{M}{2kT^*} \right)^{\frac{3}{2}} \left(\frac{\mu}{2k\tilde{T}} \right)^{\frac{3}{2}} \quad (\text{C.20})$$

The product of distributions can now be written as:

$$f_s \cdot f_t = \left(\frac{M}{2\pi k T^*} \right)^{\frac{3}{2}} \exp \left[-\frac{M \mathbf{V}^{*2}}{2k T^*} \right] \cdot \left(\frac{\mu}{2\pi k \tilde{T}} \right)^{\frac{3}{2}} \exp \left[-\frac{\mu \tilde{\mathbf{g}}^2}{2k \tilde{T}} \right] \equiv f^*(\mathbf{V}^*) \cdot \tilde{f}(\tilde{\mathbf{g}}) \quad (\text{C.21})$$

All subsequent expressions can now be simplified with this separation of variables, since for any operator \mathcal{O} that depends on variables expressed in the COM frame, we have:

$$\int d^3 \mathbf{v}_s d^3 \mathbf{v}_t f_s f_t \mathcal{O}(\mathbf{g}) = \underbrace{\int d^3 \mathbf{V}^* f^*(\mathbf{V}^*)}_{\equiv 1} \cdot \int d^3 \tilde{\mathbf{g}} \tilde{f}(\tilde{\mathbf{g}}) \mathcal{O}(\mathbf{g}) \quad (\text{C.22})$$

The elimination of the variable \mathbf{V}^* is simply a consequence of the Galilean invariance of the collision process.

The procedure above can be also used for the reverse process, where the initial

variables are now the prime quantities. Thus, similarly to (C.2,C.3), we have

$$\mathbf{V} = \frac{m_s \mathbf{v}'_s + m_t \mathbf{v}'_t}{M} \quad \mathbf{v}'_s = \mathbf{V} + \frac{m_t}{M} \mathbf{g}' \quad (\text{C.23a})$$

$$\mathbf{g}' = \mathbf{v}'_s - \mathbf{v}'_t \quad \mathbf{v}'_t = \mathbf{V} - \frac{m_s}{M} \mathbf{g}' \quad (\text{C.23b})$$

while the mean flow velocity relations are unchanged, since the s', t' particles belong to the same fluids as s, t . One can therefore use the exact same procedure described above to re-cast the product of the distribution functions of the initial variables into separated variables:

$$\begin{aligned} f_s(\mathbf{v}'_s) \cdot f_t(\mathbf{v}'_t) &\equiv \left(\frac{M}{2\pi k T^*} \right)^{\frac{3}{2}} \exp \left[-\frac{M \mathbf{V}'^{*2}}{2k T^*} \right] \cdot \left(\frac{\mu}{2\pi k \tilde{T}} \right)^{\frac{3}{2}} \exp \left[-\frac{\mu \tilde{\mathbf{g}}'^2}{2k \tilde{T}} \right] \\ &\equiv f^*(\mathbf{V}'^*) \cdot \tilde{f}(\tilde{\mathbf{g}}') \end{aligned} \quad (\text{C.24})$$

C.2 Three-body processes

Similarly to excitation, the ionization process has two particles in the initial state, but the final state includes a third particle, since an electron extracted from the target to yield an ion state ($t \rightarrow i + e$). The process is therefore:

$$s(\mathbf{v}_s) + t(\mathbf{v}_t) \Leftrightarrow s'(\mathbf{v}'_s) + i(\mathbf{v}''_i) + e(\mathbf{v}''_e) \quad (\text{C.25})$$

We have used double-prime variables for the ion and electron, for reasons which will soon become clear. In the case of ionization, one must integrate over the distribution functions of the initial variables, which remain s, t , and the procedure of section C.1 remains valid. However, for recombination, we have a triple product of VDFs:

$$\begin{aligned} f_s(\mathbf{v}'_s) f_i(\mathbf{v}''_i) f_e(\mathbf{v}''_e) &= \left(\frac{m_s}{2\pi k T_s} \right)^{\frac{3}{2}} e^{-\beta_s (\mathbf{v}'_s - \mathbf{u}_s)^2} \\ &\quad \left(\frac{m_i}{2\pi k T_i} \right)^{\frac{3}{2}} e^{-\beta_i (\mathbf{v}''_i - \mathbf{u}_i)^2} \left(\frac{m_e}{2\pi k T_e} \right)^{\frac{3}{2}} e^{-\beta_e (\mathbf{v}''_e - \mathbf{u}_e)^2} \end{aligned} \quad (\text{C.26})$$

In order to perform the separation of variables, it is necessary to proceed in two steps. Thus, we can consider the ionization process as follows:

- a) the formation of an excited state t' via scattering: $s(\mathbf{v}_s) + t(\mathbf{v}_t) \Rightarrow s'(\mathbf{v}'_s) + t'(\mathbf{v}'_t)$
- b) the spontaneous ionization of the t' state into ion and electron: $t'(\mathbf{v}'_t) \Rightarrow e(\mathbf{v}''_e) + i(\mathbf{v}''_i)$

The reverse process, recombination, would similarly follow two steps:

- a) the formation of an excited state t' via recombination: $e(\mathbf{v}''_e) + i(\mathbf{v}''_i) \Rightarrow t'(\mathbf{v}'_t)$
- b) the spontaneous deexcitation of the t' state via scattering: $s'(\mathbf{v}'_s) + t'(\mathbf{v}'_t) \Rightarrow s(\mathbf{v}_s) + t(\mathbf{v}_t)$

Consider now the following change of variables

$$\mathbf{g}' = \mathbf{v}'_s - \mathbf{v}'_t \quad (\text{C.27a})$$

$$\mathbf{g}'' = \mathbf{v}''_e - \mathbf{v}''_i \quad (\text{C.27b})$$

along with the COM velocity definition ($m_t = m_e + m_i$):

$$\mathbf{V} = \frac{m_s \mathbf{v}_s + m_t \mathbf{v}_t}{M} = \frac{m_s \mathbf{v}'_s + m_t \mathbf{v}'_t}{M} = \frac{m_s \mathbf{v}'_s + m_e \mathbf{v}''_e + m_i \mathbf{v}''_i}{M} \quad (\text{C.28})$$

Thus,

$$\begin{pmatrix} \mathbf{V} \\ \mathbf{g}' \\ \mathbf{g}'' \end{pmatrix} = \begin{pmatrix} m_s/M & m_e/M & m_i/M \\ 1 & -m_e/m_t & -m_i/m_t \\ 0 & 1 & -1 \end{pmatrix} \cdot \begin{pmatrix} \mathbf{v}'_s \\ \mathbf{v}''_e \\ \mathbf{v}''_i \end{pmatrix} \quad (\text{C.29})$$

One can easily verify that this transformation is unitary, i.e. $d\mathbf{V} d\mathbf{g}' d\mathbf{g}'' \equiv d\mathbf{v}'_s d\mathbf{v}''_e d\mathbf{v}''_i$.

Consider now the first part of this two-step recombination process, which involves the product of the two VDFs for electron and ion: $f_e(\mathbf{v}''_e) f_i(\mathbf{v}''_i)$. Therefore, the argument of the exponential function resulting from this product is:

$$\mathcal{A}_{ei} = \frac{m_e}{2kT_e} (\mathbf{v}''_e - \mathbf{u}_e)^2 + \frac{m_i}{2kT_i} (\mathbf{v}''_i - \mathbf{u}_i)^2 \quad (\text{C.30})$$

From (C.29) and $\mathbf{v}'_t = (m_e \mathbf{v}''_e + m_i \mathbf{v}''_i)/m_t$, we have:

$$\mathbf{v}''_e = \mathbf{v}'_t + \frac{m_i}{m_t} \mathbf{g}'' \quad (\text{C.31a})$$

$$\mathbf{v}''_i = \mathbf{v}'_t - \frac{m_e}{m_t} \mathbf{g}'' \quad (\text{C.31b})$$

Similarly, we can define mean fluid variables

$$\begin{aligned} \mathbf{u}'_t = \frac{m_e \mathbf{u}_e + m_i \mathbf{u}_i}{m_t} &\Rightarrow \mathbf{u}_e = \mathbf{u}'_t + \frac{m_i}{m_t} \mathbf{w}'' \\ \mathbf{w}'' = \mathbf{u}_e - \mathbf{u}_i &\Rightarrow \mathbf{u}_i = \mathbf{u}'_t - \frac{m_e}{m_t} \mathbf{w}'' \end{aligned} \quad (\text{C.32})$$

With the usual definition $\tilde{\mathbf{g}}'' = \mathbf{g}'' - \mathbf{w}''$, The argument (C.30) becomes

$$\begin{aligned} \mathcal{A}_{ei} &= \beta_e \left(\mathbf{v}'_t - \mathbf{u}'_t + \frac{m_i}{m_t} (\tilde{\mathbf{g}}'') \right)^2 + \beta_i \left(\mathbf{v}'_t - \mathbf{u}'_t - \frac{m_e}{m_t} (\tilde{\mathbf{g}}'') \right)^2 \\ &= (\beta_e + \beta_i) (\mathbf{v}'_t - \mathbf{u}'_t)^2 + \left(\beta_e \frac{m_i^2}{m_t^2} + \beta_i \frac{m_e^2}{m_t^2} \right) (\tilde{\mathbf{g}}'')^2 + 2 \left(\beta_e \frac{m_i}{m_t} - \beta_i \frac{m_e}{m_t} \right) (\mathbf{v}'_t - \mathbf{u}'_t) \cdot \tilde{\mathbf{g}}'' \end{aligned} \quad (\text{C.33})$$

We recognize the same form as (C.10); we can thus apply the same procedure, and define

$$\mathbf{C}_t = \mathbf{v}'_t - \mathbf{u}'_t + \gamma (\tilde{\mathbf{g}}'') \quad (\text{C.34})$$

where now

$$\gamma = \frac{1}{\beta_e + \beta_i} \left(\beta_e \frac{m_i}{m_t} - \beta_i \frac{m_e}{m_t} \right) \quad (\text{C.35})$$

such that the argument now becomes:

$$\mathcal{A}_{ei} = (\beta_e + \beta_i) \mathbf{C}_t^2 + \frac{\beta_e \beta_i}{\beta_e + \beta_i} (\tilde{\mathbf{g}}'')^2 \quad (\text{C.36})$$

We can now multiply by the VDF for the scattering particle for the second step of the recombination process. This leads to the total argument:

$$\mathcal{A} = (\beta_e + \beta_i) \mathbf{C}_t^2 + \frac{\beta_e \beta_i}{\beta_e + \beta_i} (\tilde{\mathbf{g}}'')^2 + \beta_s (\mathbf{v}'_s - \mathbf{u}_s)^2 \quad (\text{C.37})$$

Similarly to (C.32), we have

$$\begin{aligned} \mathbf{U} = \frac{m_s \mathbf{u}_s + m_t \mathbf{u}'_t}{M} &\Rightarrow \mathbf{u}_s = \mathbf{U} + \frac{m_t}{M} \mathbf{w}' \\ \mathbf{w}' = \mathbf{u}_s - \mathbf{u}'_t &\Rightarrow \mathbf{u}'_t = \mathbf{U} - \frac{m_s}{M} \mathbf{w}' \end{aligned} \quad (\text{C.38})$$

Let us also define

$$\mathbf{V}^* = \mathbf{V} - \mathbf{U} - \frac{m_s}{M} \tilde{\mathbf{g}}' \quad \text{with} \quad \tilde{\mathbf{g}}' = \mathbf{g}' - \mathbf{w}' \quad (\text{C.39})$$

This yields:

$$\mathbf{v}'_s - \mathbf{u}_s = \mathbf{V} - \mathbf{U} + \frac{m_t}{M} \tilde{\mathbf{g}}' = \mathbf{V}^* + \tilde{\mathbf{g}}' \quad (\text{C.40})$$

and, from (C.34)

$$\mathbf{C}_t = \mathbf{V}^* + \gamma \tilde{\mathbf{g}}'' \quad (\text{C.41})$$

Inserting into (C.37):

$$\begin{aligned} \mathcal{A} = & (\beta_s + \beta_e + \beta_i) \mathbf{V}^{*2} + \beta_s (\tilde{\mathbf{g}}')^2 \\ & + \left[(\beta_e + \beta_i) \gamma^2 + \frac{\beta_e \beta_i}{\beta_e + \beta_i} \right] (\tilde{\mathbf{g}}'')^2 \\ & + 2\gamma (\beta_e + \beta_i) \mathbf{V}^* \cdot \tilde{\mathbf{g}}'' + 2\beta_s \mathbf{V}^* \cdot \tilde{\mathbf{g}}' \end{aligned} \quad (\text{C.42})$$

Let us now try the following variable substitution

$$\mathbf{V}^{**} = \mathbf{V}^* + \tilde{\gamma} \tilde{\mathbf{g}}'' + \tilde{\delta} \tilde{\mathbf{g}}' \quad (\text{C.43})$$

Thus,

$$\begin{aligned} \mathbf{V}^{**2} = & \mathbf{V}^{*2} + \tilde{\gamma}^2 (\tilde{\mathbf{g}}'')^2 + \tilde{\delta}^2 (\tilde{\mathbf{g}}')^2 \\ & + 2\tilde{\gamma} \mathbf{V}^* \cdot \tilde{\mathbf{g}}'' + 2\tilde{\delta} \mathbf{V}^* \cdot \tilde{\mathbf{g}}' + 2\tilde{\gamma} \tilde{\delta} \tilde{\mathbf{g}}' \cdot \tilde{\mathbf{g}}'' \end{aligned}$$

Defining $\Sigma_\beta = \beta_s + \beta_e + \beta_i$ and choosing

$$\tilde{\delta} = \frac{\beta_s}{\Sigma_\beta}, \quad \tilde{\gamma} = \frac{\beta_e + \beta_i}{\Sigma_\beta} \gamma \quad (\text{C.44})$$

we obtain

$$\begin{aligned} \Sigma_\beta \mathbf{V}^{**2} = & \Sigma_\beta \mathbf{V}^{*2} + \frac{\beta_s^2}{\Sigma_\beta} (\tilde{\mathbf{g}}')^2 + \frac{(\beta_e + \beta_i)^2}{\Sigma_\beta} \gamma^2 (\tilde{\mathbf{g}}'')^2 \\ & + 2\gamma (\beta_e + \beta_i) \mathbf{V}^* \cdot \tilde{\mathbf{g}}'' + 2\beta_s \mathbf{V}^* \cdot \tilde{\mathbf{g}}' + 2\gamma \frac{\beta_s (\beta_e + \beta_i)}{\Sigma_\beta} \tilde{\mathbf{g}}' \cdot \tilde{\mathbf{g}}'' \end{aligned}$$

Comparing with (C.42), we can simplify the argument as:

$$\begin{aligned} \mathcal{A} = & \Sigma_\beta \mathbf{V}^{**2} + \left[\frac{\beta_s(\beta_e + \beta_i)}{\Sigma_\beta} \gamma^2 + \frac{\beta_e \beta_i}{\beta_e + \beta_i} \right] (\tilde{\mathbf{g}}'')^2 \\ & + \frac{\beta_s(\beta_e + \beta_i)}{\Sigma_\beta} [(\tilde{\mathbf{g}}')^2 - 2\gamma \tilde{\mathbf{g}}' \cdot \tilde{\mathbf{g}}''] \end{aligned} \quad (\text{C.45})$$

Define now

$$\mathbf{j} = (\mathbf{g}' - \mathbf{w}') - \gamma(\mathbf{g}'' - \mathbf{w}'') \quad (\text{C.46})$$

We can now eliminate the last dot product, since $(\tilde{\mathbf{g}}')^2 - 2\gamma \tilde{\mathbf{g}}' \cdot \tilde{\mathbf{g}}'' = \mathbf{j}^2 - \gamma^2 (\tilde{\mathbf{g}}'')^2$.

Inserting into (C.45), we finally obtain:

$$\mathcal{A} = (\beta_s + \beta_e + \beta_i) \mathbf{V}^{**2} + \frac{\beta_e \beta_i}{\beta_e + \beta_i} (\mathbf{g}'' - \mathbf{w}'')^2 + \frac{\beta_s(\beta_e + \beta_i)}{\beta_s + \beta_e + \beta_i} \mathbf{j}^2 \quad (\text{C.47})$$

We have achieved variable separation, i.e. all dot products have been removed with the proper change of variables. One can also show that:

$$\beta_s + \beta_e + \beta_i = \frac{M}{2k} \frac{m_s T_e T_i + m_e T_s T_i + m_i T_s T_e}{M T_s T_e T_i} \equiv \frac{M}{2k T^*} \quad (\text{C.48})$$

$$\frac{\beta_e \beta_i}{\beta_e + \beta_i} = \frac{m_e m_i}{2k(m_e + m_i)} \frac{m_e + m_i}{m_e T_i + m_i T_e} \equiv \frac{\mu_t}{2k \tilde{T}_t} \quad (\text{C.49})$$

$$\frac{\beta_s(\beta_e + \beta_i)}{\beta_s + \beta_e + \beta_i} = \frac{m_s(m_e + m_i)}{2kM} \frac{M \tilde{T}_t}{m_s T_e T_i + m_e T_s T_i + m_i T_s T_e} \equiv \frac{\mu}{2k \tilde{T}} \quad (\text{C.50})$$

where

$$T^* = \frac{M T_s T_e T_i}{m_s T_e T_i + m_e T_s T_i + m_i T_s T_e} \quad (\text{C.51})$$

$$\tilde{T}_t = \frac{m_e T_i + m_i T_e}{m_e + m_i} \quad (\text{C.52})$$

$$\tilde{T} = \frac{m_s T_e T_i + m_e T_s T_i + m_i T_s T_e}{M \tilde{T}_t} \quad (\text{C.53})$$

$$\mu_t = \frac{m_e m_i}{m_e + m_i} \quad (\text{C.54})$$

$$\mu = \frac{m_s(m_e + m_i)}{M} \quad (\text{C.55})$$

The product of the three Maxwellian VDF becomes:

$$\begin{aligned}
f_s(\mathbf{v}'_s) \cdot f_e(\mathbf{v}''_e) \cdot f_i(\mathbf{v}''_i) &= \left(\frac{M}{2\pi k T^*} \right)^{\frac{3}{2}} \exp \left[-\frac{M \mathbf{V}'^{*2}}{2k T^*} \right] \cdot \left(\frac{\mu_t}{2\pi k \tilde{T}_t} \right)^{\frac{3}{2}} \exp \left[-\frac{\mu_t \tilde{\mathbf{g}}''^2}{2k \tilde{T}_t} \right] \cdot \\
&\quad \left(\frac{\mu}{2\pi k \tilde{T}} \right)^{\frac{3}{2}} \exp \left[-\frac{\mu \mathbf{j}^{*2}}{2k \tilde{T}} \right] \equiv f^{**}(\mathbf{V}^{**}) \cdot \tilde{f}_t(\tilde{\mathbf{g}}'') \cdot \tilde{f}(\mathbf{j}^*)
\end{aligned}
\tag{C.56}$$

Since $m_e/m_i \ll 1$, $\tilde{T}_t \simeq T_e + o(m_e/m_i)$. For a heavy particle induced recombination, $m_e/m_s \ll 1$ and $\tilde{T} \simeq \frac{m_s T_i + m_i T_s}{m_s + m_i} + o(m_e/M)$. If $m_s \simeq m_i$, $\tilde{T} \rightarrow \frac{T_s + T_i}{2}$. For an electron induced recombination, $\tilde{T} \rightarrow T_e$.

APPENDIX D

Microscopic Detailed Balance

In this appendix, the principle of detailed balance (DB) are described for various inelastic processes occurring in an atomic plasma. These are essentially explicit forms of the reciprocal relations introduced in section 4.2. The notation of differential and total cross section for various processes are introduced and the reciprocal relation is derived by considering microscopy reaction balance.

D.1 Collisional excitation and deexcitation

Consider now a collisional excitation between particles s and t and its reverse process similar to section C.1:

$$s(\mathbf{v}_s) + t(\mathbf{v}_t, E_\ell) \Leftrightarrow s'(\mathbf{v}'_s) + t'(\mathbf{v}'_t, E_u) \quad (\text{D.1})$$

where E_ℓ and E_u are the energy of the lower and upper states of particle t , respectively. Conservation of momentum and energy lead to:

$$m_s \mathbf{v}_s + m_t \mathbf{v}_t = m_s \mathbf{v}'_s + m_t \mathbf{v}'_t \quad (\text{D.2})$$

$$\frac{1}{2} m_s \mathbf{v}_s^2 + \frac{1}{2} m_t \mathbf{v}_t^2 = \frac{1}{2} m_s \mathbf{v}'_s{}^2 + \frac{1}{2} m_t \mathbf{v}'_t{}^2 + \Delta\epsilon \quad (\text{D.3})$$

It can be shown that in the COM frame, momentum conservation indicates that the COM velocity is unchanged after collision.

$$\mathbf{V}' = \mathbf{V} = \frac{m_s \mathbf{v}_s + m_t \mathbf{v}_t}{m_s + m_t} = \frac{m_s \mathbf{v}'_s + m_t \mathbf{v}'_t}{m_s + m_t} \quad (\text{D.4})$$

Energy conservation gives the change in the magnitude of the relative velocity:

$$g' = \left(g^2 - \frac{2\Delta\varepsilon}{\mu} \right)^{1/2} \quad (\text{D.5})$$

where

$$\mathbf{g} = \mathbf{v}_s - \mathbf{v}_t \quad (\text{D.6})$$

$$\mathbf{g}' = \mathbf{v}'_s - \mathbf{v}'_t \quad (\text{D.7})$$

$$\mu = \frac{m_s m_t}{m_s + m_t} \quad (\text{D.8})$$

One can also show that:

$$\left| \frac{\partial(\mathbf{V}, \mathbf{g})}{\partial(\mathbf{v}_s, \mathbf{v}_t)} \right| = \left| \frac{\partial(\mathbf{V}', \mathbf{g}')}{\partial(\mathbf{v}'_s, \mathbf{v}'_t)} \right| = 1 \quad (\text{D.9})$$

such that

$$d^3\mathbf{v}_t d^3\mathbf{v}_s = d^3\mathbf{V} d^3\mathbf{g} \quad (\text{D.10})$$

$$d^3\mathbf{v}'_t d^3\mathbf{v}'_s = d^3\mathbf{V}' d^3\mathbf{g}' \quad (\text{D.11})$$

$$d^3\mathbf{V} = d^3\mathbf{V}' \quad (\text{D.12})$$

$$g dg = g' dg' \quad (\text{D.13})$$

$$\frac{d^3\mathbf{g}}{d^3\mathbf{g}'} = \frac{g'}{g} \quad (\text{D.14})$$

Equation (D.14) is a direct result of the collision dynamics where the relative orientation of \mathbf{g} and \mathbf{g}' is always fixed. We can then write a rate equation for this process as follows:

$$\begin{aligned} & n_s f_s(\mathbf{v}_s) d^3\mathbf{v}_s \cdot n_\ell f_t(\mathbf{v}_t) d^3\mathbf{v}_t \cdot g \cdot \sigma_{s\ell}(g, \Omega) d\Omega \\ &= n_s f_s(\mathbf{v}'_s) d^3\mathbf{v}'_s \cdot n_u f_t(\mathbf{v}'_t) d^3\mathbf{v}'_t \cdot g' \cdot \sigma_{su}(g', \Omega) d\Omega \end{aligned} \quad (\text{D.15})$$

where n_ℓ, n_u are the number densities of the lower and upper states, and $\sigma_{s\ell}, \sigma_{su}$ are the differential cross sections for excitation and deexcitation. By utilizing equation (4.14) for n_ℓ, n_u , equation (4.11) for f_s , conservation of momentum and energy, and change of variables, we arrive at the following expression:

$$g_\ell g^2 \sigma_{s\ell}(g, \Omega) = g_u g'^2 \sigma_{su}(g', \Omega) \quad (\text{D.16})$$

where g is the state degeneracy factor. A special case of zero net energy, $\Delta\varepsilon = 0$, corresponds to elastic collision. This relation can also be expressed in term of total energetic cross sections by integrating over all scattering solid angle, i.e., $\bar{\sigma}(\varepsilon) = \int \sigma d\Omega$:

$$g_\ell \varepsilon \bar{\sigma}_{s\ell}(\varepsilon) = g_u \varepsilon' \bar{\sigma}_{su}(\varepsilon') \quad (\text{D.17})$$

where $\varepsilon = \frac{1}{2}\mu g^2$. This expression is known as the *Klein-Rosseland* relation which describes DB of collisional excitation and deexcitation at the microscopic level¹.

D.2 Collisional ionization and recombination

We consider now a collisional ionization and a three body recombination process similar to (C.25):

$$s(\mathbf{v}_s) + t(\mathbf{v}_t) \Leftrightarrow s'(\mathbf{v}'_s) + i(\mathbf{v}''_i) + e(\mathbf{v}''_e) \quad (\text{D.18})$$

Again, momentum and energy are conserved which leads to:

$$m_s \mathbf{v}_s + m_t \mathbf{v}_t = m_s \mathbf{v}'_s + \underbrace{m_i \mathbf{v}''_i + m_e \mathbf{v}''_e}_{m_t \mathbf{v}'_t} \quad (\text{D.19})$$

$$\frac{1}{2}m_s \mathbf{v}_s^2 + \frac{1}{2}m_t \mathbf{v}_t^2 = \frac{1}{2}m_s \mathbf{v}'_s{}^2 + \frac{1}{2}m_i \mathbf{v}''_i{}^2 + \frac{1}{2}m_e \mathbf{v}''_e{}^2 + \Delta\varepsilon \quad (\text{D.20})$$

where $\Delta\varepsilon$ is now the ionization potential of t . The rate equations for the both processes are:

$$\begin{aligned} & n_s f_s(\mathbf{v}_s) d^3 \mathbf{v}_s \cdot n_t f_t(\mathbf{v}_t) d^3 \mathbf{v}_t \cdot g \cdot \sigma_{ion}(\mathbf{g}; \mathbf{g}', \mathbf{g}'') d^3 \mathbf{g}' d^3 \mathbf{g}'' \\ &= n_s f_s(\mathbf{v}'_s) d^3 \mathbf{v}'_s \cdot n_i f_i(\mathbf{v}''_i) d^3 \mathbf{v}''_i \cdot n_e f_e(\mathbf{v}''_e) d^3 \mathbf{v}''_e \cdot g' g'' \cdot \sigma_{rec}(\mathbf{g}', \mathbf{g}''; \mathbf{g}) d^3 \mathbf{g} \end{aligned} \quad (\text{D.21})$$

where we have previously defined $\mathbf{g} = \mathbf{v}_s - \mathbf{v}_t$, $\mathbf{g}' = \mathbf{v}'_s - \mathbf{v}'_t$ and $\mathbf{g}'' = \mathbf{v}''_e - \mathbf{v}''_i$ (see section C.2). Note that in the COM reference frame, σ_{ion} is a triply differential cross section.

¹which is, independent of the form of the distribution function.

By utilizing the transformation defined in section C.2, one can obtain the following relations:

$$d^3\mathbf{v}_s d^3\mathbf{v}_t = d^3\mathbf{V} d^3\mathbf{g} \quad (\text{D.22})$$

$$d^3\mathbf{v}'_s d^3\mathbf{v}''_i d^3\mathbf{v}''_e = d^3\mathbf{V} d^3\mathbf{g}' d^3\mathbf{g}'' \quad (\text{D.23})$$

We can proceed similarly by introducing the Maxwell distribution for f_s , f_t , f_i and f_e , and Saha distribution for $n_i n_e / n_t$ in equation (D.21). This leads to the following expression:

$$g_t g \sigma_{ion}(\mathbf{g}; \mathbf{g}', \mathbf{g}'') = 2g_i \frac{\mu_t^3}{h^3} g' g'' \sigma_{rec}(\mathbf{g}', \mathbf{g}''; \mathbf{g}) \quad (\text{D.24})$$

For an electron impact ionization process, this expression reduces to the Fowler's relation:

$$g_t v \sigma_{ion}(\mathbf{v}; \mathbf{v}', \mathbf{v}'') = 2g_i \frac{m_e^3}{h^3} v' v'' \sigma_{rec}(\mathbf{v}', \mathbf{v}''; \mathbf{v}) \quad (\text{D.25})$$

where \mathbf{v} , \mathbf{v}' , and \mathbf{v}'' are the velocities of the incident, reflected, and ejected electrons, respectively. The cross section can be averaged over all angular variables to yield the following:

$$g_t \varepsilon \bar{\sigma}_{ion}(\varepsilon; \varepsilon', \varepsilon'') = \frac{16\pi m_e}{h^3} g_i \varepsilon' \varepsilon'' \bar{\sigma}_{rec}(\varepsilon', \varepsilon''; \varepsilon) \quad (\text{D.26})$$

It must be noted that $\bar{\sigma}_{ion}$ is now a singly differential ionization cross section; one can define total ionization cross section by integrating over all the possible energy transfer values, i.e., $\Sigma_{ion} = \int_{\Delta\varepsilon}^{\infty} \bar{\sigma}_{ion} dW$ where $W = \varepsilon - \varepsilon'$. It is, however, not possible to obtain a total recombination cross section in a similar fashion; integrating over the final states of the recombination process is not possible without also partially summing over the initial states. Due to energy conservation, once the initial state is determined by the pair $(\varepsilon', \varepsilon'')$, the final state ε is also fully determined; there is only one final state possible, and $\bar{\sigma}_{rec}$ from equation (D.26) is the total cross section of recombination for the given initial state.

D.3 Line emission and absorption

Consider now a bound bound emission and absorption process, written as:

$$t(E_u) \Leftrightarrow t(E_\ell) + h\nu \quad (\text{D.27})$$

where $h\nu = \Delta\varepsilon = E_u - E_\ell$ for energy conservation. In this transition, we assume that the momentum transfer between particle t and the photon is negligible. One can construct a rate equation for this process by taking in account absorption, stimulated and spontaneous emission processes:

$$n_u(A_{ul} + B_{ul}I_\nu) = n_\ell B_{\ell u}I_\nu \quad (\text{D.28})$$

where A_{ul} , $B_{\ell u}$ and B_{ul} are Einstein coefficients. Comparing this with equation (4.22), it is easy to see that:

$$\frac{B_{ul}}{A_{ul}} = \frac{c^2}{2h\nu^3} \quad (\text{D.29})$$

Combining the result above with equation (D.28), we obtain the relation of B_{ul} and $B_{\ell u}$:

$$g_\ell B_{\ell u} = g_u B_{ul} \quad (\text{D.30})$$

which is known as the Einstein relations.

D.4 Photoionization and radiative recombination

Consider now a balance of the photoionization and radiative recombination processes:

$$t(\varepsilon) + h\nu \Leftrightarrow i(\varepsilon_i) + e^-(\mathbf{v}) \quad (\text{D.31})$$

For simplicity, we assume that the atom (t) and ion (i) are stationary and neglect their translational degree of freedom. The rate equation corresponding to this

reaction is:

$$\begin{aligned}
& n_t \cdot \frac{I_\nu}{h\nu} d\nu d\Omega \cdot \sigma_{ion}^\nu(\nu; \chi) d\Omega_e \\
& = n_i \cdot n_e f_e(\mathbf{v}) \underbrace{v^2 dv d\Omega_e}_{d^3\mathbf{v}} \cdot v \cdot \sigma_{rec}^\nu(v; \chi) d\Omega \left(1 + \frac{c^2}{2h\nu^3} I_\nu \right)
\end{aligned} \tag{D.32}$$

where χ is the angle between the photon beam and the electron. Inserting the Maxwell distribution for f_e , Saha distribution for $n_i n_e / n_t$ and Planck distribution for I_ν , one obtain:

$$g_t(h\nu)^2 \sigma_{ion}^\nu(\nu; \chi) = g_i m_e^2 c^2 v^2 \sigma_{rec}^\nu(v; \chi) \tag{D.33}$$

For isotropic distribution function, one can write the DB relation in terms of total cross sections $\bar{\sigma}_{ion}^\nu = \int \sigma_{ion}^\nu d\Omega_e$:

$$g_t(h\nu)^2 \bar{\sigma}_{ion}^\nu(\nu) = 2g_i m_e^2 c^2 \varepsilon \bar{\sigma}_{rec}^\nu(\varepsilon) \tag{D.34}$$

APPENDIX E

Derivation of the Ponderomotive Force for a Single Particle

In this appendix, we derive the expression of the ponderomotive force for a single particle [38]. We start with the equation of motion for an electron moving in the laser fields:

$$m_e \frac{d\mathbf{v}}{dt} = -e (\mathbf{E} + \mathbf{v} \times \mathbf{B}) \quad (\text{E.1})$$

Let us consider a monochromatic field of the form:

$$\mathbf{E} = \mathbf{E}_L(\mathbf{x}) \cos(\omega t) \quad (\text{E.2})$$

$$\mathbf{B} = -\frac{1}{\omega} \sin(\omega t) \nabla \times \mathbf{E}_L(\mathbf{x}) \quad (\text{E.3})$$

where the second relation came from Faraday's law. For nonrelativistic electrons, the second term in equation (E.1) due to the Lorentz force is small compared to the first. Let us perform an expansion of the position and velocity vectors:

$$\mathbf{x} = \mathbf{x}_0 + \mathbf{x}_1 + \mathbf{x}_2 + \dots \quad (\text{E.4})$$

$$\mathbf{v} = \mathbf{v}_0 + \mathbf{v}_1 + \mathbf{v}_2 + \dots \quad (\text{E.5})$$

where $\mathbf{v}_0 = 0$, $\mathbf{v}_1 = \frac{d\mathbf{x}_1}{dt}$, $\mathbf{v}_2 = \frac{d\mathbf{x}_2}{dt}$, \dots . The fields can also be expressed via a Taylor series expansion:

$$\mathbf{E} = \mathbf{E}(\mathbf{x}_0) + (\mathbf{x}_1 \cdot \nabla) \mathbf{E}(\mathbf{x}_0) + \dots \quad (\text{E.6})$$

$$\mathbf{B} = \mathbf{B}(\mathbf{x}_0) + (\mathbf{x}_1 \cdot \nabla) \mathbf{B}(\mathbf{x}_0) + \dots \quad (\text{E.7})$$

The lowest order reads:

$$m_e \frac{d\mathbf{v}_1}{dt} = -e \mathbf{E}_L(\mathbf{x}_0) \cos(\omega t) \quad (\text{E.8})$$

Integrating twice equation (E.8) yields the equations for \mathbf{v}_1 and \mathbf{x}_1 :

$$\mathbf{v}_1 = -\frac{e}{m_e \omega} \mathbf{E}_L(\mathbf{x}_0) \sin(\omega t) \quad (\text{E.9})$$

$$\mathbf{x}_1 = \frac{e}{m_e \omega^2} \mathbf{E}_L(\mathbf{x}_0) \cos(\omega t) \quad (\text{E.10})$$

The next order reads:

$$m_e \frac{d\mathbf{v}_2}{dt} = -e [(\mathbf{x}_1 \cdot \nabla) \mathbf{E}_L(\mathbf{x}_0) + \mathbf{v}_1 \times \mathbf{B}_L(\mathbf{x}_0)] \quad (\text{E.11})$$

Utilizing the relations above, we get:

$$m_e \frac{d\mathbf{v}_2}{dt} = -\frac{e^2}{m_e \omega^2} [\cos^2(\omega t) (\mathbf{E}_L \cdot \nabla) \mathbf{E}_L + \sin^2(\omega t) \mathbf{E}_L \times \nabla \times \mathbf{E}_L] \quad (\text{E.12})$$

By averaging the force over a laser period, we get:

$$\tilde{\mathbf{f}}_p = -\frac{e^2}{2m_e \omega^2} [(\mathbf{E}_L \cdot \nabla) \mathbf{E}_L + \mathbf{E}_L \times \nabla \times \mathbf{E}_L] \quad (\text{E.13})$$

where $\tilde{\mathbf{f}}_p$ is the ponderomotive force on a single electron. For the electron fluid, we simply multiply expression (E.13) by n_e :

$$\begin{aligned} \mathbf{f}_p &= -\frac{n_e e^2}{4m_e \omega^2} \nabla \mathbf{E}_L^2 \\ &= -\frac{\epsilon_0 \omega_p^2}{4\omega^2} \nabla \mathbf{E}_L^2 \end{aligned} \quad (\text{E.14})$$

Since $\mathbf{f}_p \sim 1/m$, one can see that the ponderomotive force acting on the ions is negligible compared to the electrons.

REFERENCES

- [1] F. F. Chen. *Introduction to plasma physics and controlled fusion*. Plenum Press, 2nd ed edition, 1984.
- [2] P. A. Sturrock. *Plasma physics: an introduction to the theory of astrophysical, geophysical, and laboratory plasmas*. Cambridge University Press, 1994.
- [3] T. E. Cravens. *Physics of Solar System Plasmas*. Cambridge University Press, 2004.
- [4] R. G. Jahn. *Physics of electric propulsion*. Dover books on physics. Dover Publications, Inc, Mineola, N.Y, 2006.
- [5] M. A. Lieberman. *Principles of plasma discharges and materials processing*. Wiley-Interscience, 2nd ed edition, 2005.
- [6] N. A. Krall. *Principles of plasma physics*. McGraw-Hill, 1973.
- [7] P. M. Bellan. *Fundamentals of plasma physics*. Cambridge University Press, 2008.
- [8] T. ONeil and F. Coroniti. The collisionless nature of high-temperature plasmas. *Reviews of Modern Physics*, 71(2):S404–S410, March 1999.
- [9] L. Landau. On the vibration of the electronic plasma. *J. Phys. USSR*, 10:25, 1946.
- [10] F. R. Chang Diaz. The vasmr rocket. *Scientific American*, 283(5), 2000.
- [11] M. Capitelli, C. M. Ferreira, B. F. Gordiets, and A. I. Osipov. *Plasma Kinetics in Atmospheric Gases*. Springer Berlin Heidelberg, 2000.
- [12] I. V. Adamovich, W. R. Lempert, J. W. Rich, Y. G. Utkin, and M. Nishihara. Repetitively pulsed nonequilibrium plasmas for magnetohydrodynamic flow control and plasma-assisted combustion. *Journal of Propulsion and Power*, 24(6):1198–1215, 2008.
- [13] I. V. Adamovich, I. Choi, N. Jiang, J.-H. Kim, S. Keshav, W. R. Lempert, E. Mintusov, M. Nishihara, M. Samimy, and M. Uddi. Plasma assisted ignition and high-speed flow control: non-thermal and thermal effects. *Plasma Sources Science and Technology*, 18(3):034018, August 2009.
- [14] S. M. Starikovskaia. Plasma assisted ignition and combustion. *Journal of Physics D: Applied Physics*, 39(16):R265–R299, August 2006.

- [15] G. Pilla, D. Galley, D. A. Lacoste, F. Lacas, D. Veynante, and C. O. Laux. Stabilization of a turbulent premixed flame using a nanosecond repetitively pulsed plasma. *IEEE Transactions on Plasma Science*, 34(6):2471–2477, 2006.
- [16] L. S. Jacobsen, C. D. Carter, R. A. Baurle, T. A. Jackson, S. Williams, D. Bivolaru, S. Kuo, J. Barnett, and C.-J. Tam. Plasma-assisted ignition in scramjets. *Journal of Propulsion and Power*, 24(4):641–654, July 2008.
- [17] S. Serbin, A. Mostipanencko, I. Matveev, and A. Topina. Improvement of the gas turbine plasma assisted combustor characteristics. Paper AIAA-2011-61, January 2011.
- [18] J.-L. Cambier, T. Roth, C. Zeineh, and A. R. Karagozian. The pulse detonation rocket induced MHD ejector (PDRIME) concept. Paper AIAA-2008-4688, 44th AIAA/ASME/SAE/ASEE Joint Propulsion Conference and Exhibit, July 2008.
- [19] C. F. Zeineh, L. K. Cole, T. Roth, A. R. Karagozian, and J.-L. Cambier. Magnetohydrodynamic augmentation of pulse detonation rocket engines. *Journal of Propulsion and Power*, 28(1):146–159, January 2012.
- [20] P. A. Gnoffo. Planetary-entry gas dynamics. *Annual Review of Fluid Mechanics*, 31(1):459–494, January 1999.
- [21] C. Park. *Nonequilibrium hypersonic aerothermodynamics*. Wiley, 1990.
- [22] B. A. Cruden. Recent progress in entry radiation measurements in the NASA ames electric ARC shock tube facility. Barcelona, Spain, 2012.
- [23] J. H. Grinstead, M. J. Wright, D. W. Bogdanoff, and G. A. Allen. Shock radiation measurements for mars aerocapture radiative heating analysis. *Journal of Thermophysics and Heat Transfer*, 23(2):249–255, April 2009.
- [24] B. A. Cruden, R. Martinez, J. Grinstead, and J. Olejniczak. Simultaneous vacuum-ultraviolet through near-IR absolute radiation measurement with spatiotemporal resolution in an electric arc shock tube. Paper AIAA-2009-4240, 2009.
- [25] A. M. Brandis, R. Morgan, T. McIntyre, and P. A. Jacobs. Nonequilibrium radiation intensity measurements in simulated titan atmospheres. *Journal of Thermophysics and Heat Transfer*, 24(2):291–300, April 2010.
- [26] B. Cruden, D. Prabhu, R. Martinez, H. P. Le, J. Grinstead, and D. Bose. Absolute radiation measurement in high mass venus and mars entry conditions. Paper AIAA-2010-4508, June 2010.

- [27] C. O. Johnston. *Nonequilibrium Shock-Layer Radiative Heating for Earth and Titan Entry*. Ph.d. thesis, Virginia Tech, 2006.
- [28] C. Johnston. A comparison of EAST shock-tube radiation measurements with a new air radiation model. Paper AIAA-2008-1245, January 2008.
- [29] M. Panesi, Y. Babou, and O. Chazot. Predictions of nonequilibrium radiation: analysis and comparison with EAST experiments. Paper AIAA-2008-3812, June 2008.
- [30] R. Jaffe, D. Schwenke, G. Chaban, and W. Huo. Vibrational and rotational excitation and relaxation of nitrogen from accurate theoretical calculations. Paper AIAA-2008-1208, January 2008.
- [31] F. Esposito and M. Capitelli. Quasiclassical molecular dynamic calculations of vibrationally and rotationally state selected dissociation cross-sections: $N+n_2(v,j)3n$. *Chemical Physics Letters*, 302(12):49–54, March 1999.
- [32] M. G. Kapper. *A High-Order Transport Scheme for Collisional-Radiative and Nonequilibrium Plasma*. Ph.d. thesis, Ohio State University, 2009.
- [33] W. Wang, H. C. Yee, B. Sjgreen, T. E. Magin, and C.-W. Shu. Construction of low dissipative high-order well-balanced filter schemes for non-equilibrium flows. *Journal of Computational Physics*, 230(11):4316–4335, May 2011.
- [34] W. Wang, C.-W. Shu, H. C. Yee, and B. Sjgreen. High order finite difference methods with subcell resolution for advection equations with stiff source terms. *Journal of Computational Physics*, 231(1):190–214, January 2012.
- [35] D. V. Kotov, H. C. Yee, M. Panesi, D. Prabhu, and A. A. Wray. Computational challenges for simulations related to the NASA electric arc shock tube (EAST) experiments. *Journal of Computational Physics*, 269:215–233, July 2014.
- [36] T. E. Magin, M. Panesi, A. Bourdon, R. L. Jaffe, and D. Schwenke. Coarse-grain model for internal energy excitation and dissociation of molecular nitrogen. *Chemical Physics*, 398:90–95, April 2012.
- [37] A. Guy, A. Bourdon, and M.-Y. Perrin. Consistent multi-internal-temperatures models for nonequilibrium nozzle flows. *Chemical Physics*, 420:15–24, July 2013.
- [38] S. Eliezer. *The Interaction of High-Power Lasers with Plasmas*. CRC Press, 2002.
- [39] S. Eliezer and K. Mima, editors. *Applications of laser-plasma interactions*. Series in plasma physics. CRC Press/Taylor & Francis, Boca Raton, 2009.

- [40] S. Atzeni and J. Meyer-ter Vehn. *The Physics of Inertial Fusion*. Number 125 in International Series of Monographs on Physics. Oxford University Press, 2009.
- [41] P. Gibbon and E. Forster. Short-pulse laser-plasma interactions. *Plasma Physics and Controlled Fusion*, 38(6):769–793, June 1996.
- [42] L. C. Steinhauer. Review of field-reversed configurations. *Physics of Plasmas*, 18(7):070501, 2011.
- [43] J. M. Burgers. *Flow equations for composite gases*. Academic Press, 1969.
- [44] S. Chapman and T. G. Cowling. *The mathematical theory of non-uniform gases*. Cambridge mathematical library. Cambridge University Press, 3rd edition, 1990.
- [45] D. Burnett. The distribution of velocities in a slightly non-uniform gas. *Proceedings of the London Mathematical Society*, s2-39(1):385–430, 1935.
- [46] S. I. Braginskii. Transport processes in a plasma. In *Review of plasma physics*, volume 1, pages 205–311. Consultants Bureau, New York, 1965.
- [47] H. Grad. On the kinetic theory of rarefied gases. *Communications on Pure and Applied Mathematics*, 2(4):331–407, December 1949.
- [48] B. Alexeev, A. Chikhaoui, and I. Grushin. Application of the generalized chapman-enskog method to the transport-coefficient calculation in a reacting gas mixture. *Physical Review E*, 49(4):2809–2825, 1994.
- [49] E. V. Kustova and D. Giordano. Cross-coupling effects in chemically non-equilibrium viscous compressible flows. *Chemical Physics*, 379(1-3):83–91, 2011.
- [50] C. K. Birdsall and A. B. Langdon. *Plasma physics via computer simulation*. Taylor & Francis, 2005.
- [51] G. Lapenta. Particle simulations of space weather. *Journal of Computational Physics*, 231(3):795–821, February 2012.
- [52] J. O. Hirschfelder, C. F. Curtiss, and R. B. Bird. *The Molecular Theory of Gases and Liquids*. Wiley-Interscience, 1964.
- [53] V. Giovangigli. *Multicomponent flow modeling*. Birkhauser, 1999.
- [54] L. Spitzer. *Physics of fully ionized gases*. Dover Publications, 2006.
- [55] A. Decoster. *Modeling of collisions*. Gauthier-Villars, 1998.

- [56] L. Landau, L. P. Pitaevskii, and E. M. Lifshitz. *Electrodynamics of Continuous Media*, volume 8 of *Course of Theoretical Physics*. 2nd edition, 1979.
- [57] R. J. Rosa. *Magnetohydrodynamic Energy Conversion*. McGraw-Hill, 1968.
- [58] M. Panesi, R. L. Jaffe, D. W. Schwenke, and T. E. Magin. Rovibrational internal energy transfer and dissociation of n₂-n system in hypersonic flows. *The Journal of Chemical Physics*, 138(4):044312, 2013.
- [59] H. S. Reksoprodjo and R. Agarwal. A kinetic scheme for numerical solution of ideal magnetohydrodynamics equations with a bi-temperature model. Paper AIAA-2000-0448, 2000.
- [60] J.-L. Cambier, M. Carroll, and M. G. Kapper. Development of a hybrid model for non-equilibrium high-energy plasmas. Paper AIAA 2004-2166, 2004.
- [61] J.-L. Cambier. *Unpublished*.
- [62] G. Strang. On the construction and comparison of difference schemes. *SIAM Journal on Numerical Analysis*, 5(3):506–517, 1968.
- [63] M. Duarte, M. Massot, S. Descombes, C. Tenaud, T. Dumont, V. Louvet, and F. Laurent. New resolution strategy for multiscale reaction waves using time operator splitting, space adaptive multiresolution, and dedicated high order implicit/explicit time integrators. *SIAM Journal on Scientific Computing*, 34(1):A76–A104, 2012.
- [64] H. Lomax. *Fundamentals of computational fluid dynamics*. Scientific computation. Springer, 2001.
- [65] B. Einfeldt, C.D Munz, P.L Roe, and B Sjogreen. On godunov-type methods near low densities. *Journal of Computational Physics*, 92(2):273–295, 1991.
- [66] A. Suresh and H.T. Huynh. Accurate monotonicity-preserving schemes with rungekutta time stepping. *Journal of Computational Physics*, 136(1):83–99, September 1997.
- [67] X.-D. Liu, S. Osher, and T. Chan. Weighted essentially non-oscillatory schemes. *Journal of Computational Physics*, 115(1):200–212, 1994.
- [68] G.-S. Jiang and C.-W. Shu. Efficient implementation of weighted ENO schemes. *Journal of Computational Physics*, 126(1):202–228, 1996.
- [69] A. Harten, B. Engquist, S. Osher, and S. R. Chakravarthy. Uniformly high order accurate essentially non-oscillatory schemes, III. *Journal of Computational Physics*, 71(2):231–303, 1987.

- [70] E. S. Oran and J. P. Boris. *Numerical Simulation of Reactive Flow*. Cambridge University Press, 2nd edition, 2005.
- [71] P. Colella and P. R. Woodward. The piecewise parabolic method (PPM) for gas-dynamical simulations. *Journal of Computational Physics*, 54(1):174–201, 1984.
- [72] P. Woodward and P. Colella. The numerical simulation of two-dimensional fluid flow with strong shocks. *Journal of Computational Physics*, 54(1):115–173, 1984.
- [73] M. Van Dyke. *An Album of Fluid Motion*. Parabolic Press, Inc., 1982.
- [74] C. L. Gardner, J. Glimm, O. McBryan, R. Menikoff, D. H. Sharp, and Q. Zhang. The dynamics of bubble growth for rayleigh-taylor unstable interfaces. *Physics of Fluids*, 31(3):447, 1988.
- [75] L. K. Cole, A. R. Karagozian, and J.-L. Cambier. Stability of flame-shock coupling in detonation waves: 1d dynamics. *Combustion Science and Technology*, 184(10-11):1502–1525, 2012.
- [76] C. J. Jachimowski. An analysis of combustion studies in shock expansion tunnels and reflected shock tunnels. Technical report, NASA-TP-3224, 1992.
- [77] G. J. Sharpe and M. I. Radulescu. Statistical analysis of cellular detonation dynamics from numerical simulations: one-step chemistry. *Combustion Theory and Modelling*, 15(5):691–723, 2011.
- [78] M. A. Lieberman. Model of plasma immersion ion implantation. *Journal of Applied Physics*, 66(7):2926, 1989.
- [79] J. Freidberg. Ideal magnetohydrodynamic theory of magnetic fusion systems. *Reviews of Modern Physics*, 54(3):801–902, 1982.
- [80] R. J. Thompson, A. Wilson, R. Moeller, and C. L. Merkle. A strong conservative riemann solver for the solution of the coupled maxwell and navier-stokes equations. *Journal of Computational Physics*, 258:431–450, February 2014.
- [81] U. Shumlak and J. Loverich. Approximate riemann solver for the two-fluid plasma model. *Journal of Computational Physics*, 187(2):620–638, 2003.
- [82] O. V. Batishchev, V. Yu. Bychenkov, F. Detering, W. Rozmus, R. Sydora, C. E. Capjack, and V. N. Novikov. Heat transport and electron distribution function in laser produced plasmas with hot spots. *Physics of Plasmas*, 9(5):2302, 2002.

- [83] Y. B. Zeldovich and Y. B. Raizer. *Physics of shock waves and high-temperature hydrodynamic phenomena*. Dover Publications, 2002.
- [84] V. M. Zhdanov. *Transport processes in multicomponent plasma*. Taylor & Francis, 2002.
- [85] A. R. Bell. Non-spitzer heat flow in a steadily ablating laser-produced plasma. *Physics of Fluids*, 28(6):2007, 1985.
- [86] M. Mitchner. *Partially ionized gases*. Wiley, 1973.
- [87] J. Oxenius. *Kinetic theory of particles and photons*, volume 20 of *Springer Series in Electronics and Photonics*. Springer, 1986.
- [88] J.A.M. van der Mullen. Excitation equilibria in plasmas; a classification. *Physics Reports*, 191(2-3):109–220, 1990.
- [89] L. M. Biberman, V. S. Vorobev, and I. T. Yakubov. *Kinetics of Nonequilibrium Low-temperature Plasmas*. Springer Verlag, 2012.
- [90] M. G. Kapper and J.-L. Cambier. Ionizing shocks in argon. part i: Collisional-radiative model and steady-state structure. *Journal of Applied Physics*, 109(11):113308, 2011.
- [91] J. Vlcek. A collisional-radiative model applicable to argon discharges over a wide range of conditions. i. formulation and basic data. *Journal of Physics D: Applied Physics*, 22(5):623–631, 1989.
- [92] A. Bultel, B. van Ootegem, A. Bourdon, and P. Vervisch. Influence of Ar^{2+} in an argon collisional-radiative model. *Physical Review E*, 65(4), March 2002.
- [93] T. E. Magin and M. G. Kapper. Advanced physical models and numerical methods for high enthalpy and plasma flows applied to hypersonics. Technical report AFRL-AFOSR-UK-TR-2011-0023, 2011.
- [94] J.-L. Cambier. Numerical methods for TVD transport and coupled relaxing processes in gases and plasmas. Paper AIAA-90-1574, 1990.
- [95] W. M. Huo, M. Panesi, and T. E. Magin. Ionization phenomena behind shock waves. In *High Temperature Phenomena in Shock Waves*. Springer, 2012.
- [96] M. A. Liberman and A. L. Velikovich. *Physics of shock waves in gases and plasmas*, volume 19 of *Springer series in electrophysics*. Springer-Verlag, 1986.

- [97] M. G. Kapper and J.-L. Cambier. Ionizing shocks in argon. part II: Transient and multi-dimensional effects. *Journal of Applied Physics*, 109(11):113309, 2011.
- [98] A. Kramida, Y. Ralchenko, J. Reader, and NIST ASD Team. *NIST Atomic Spectra Database*. 2013.
- [99] H. W. Drawin. *Z. Physik*, 225(470), 1969.
- [100] H. W. Drawin. Report EUR-CEA-FC-510, 1969.
- [101] P. O. Haugsjaa and R. C. Amme. Ionization and metastable excitation in low-energy collisions of ground-state argon atoms. *The Journal of Chemical Physics*, 52(9):4874, 1970.
- [102] O. Zatsarinny and K. Bartschat. B-spline breit-pauli r -matrix calculations for electron collisions with argon atoms. *Journal of Physics B: Atomic, Molecular and Optical Physics*, 37(23):4693–4706, 2004.
- [103] H. Deutsch, K. Becker, S. Matt, and T. D. Mark. Calculated cross sections for the electron-impact ionization of metastable atoms. *Journal of Physics B: Atomic, Molecular and Optical Physics*, 32(17):4249–4259, 1999.
- [104] R. P. McEachran and A. D. Stauffer. Relativistic effects in low-energy electron - argon scattering. *Australian Journal of Physics*, 50(3):511, 1997.
- [105] O. Zatsarinny and K. Bartschat. Benchmark calculations for near-threshold electron-impact excitation of krypton and xenon atoms. *Journal of Physics B: Atomic, Molecular and Optical Physics*, 43(7):074031, 2010.
- [106] J. Mitroy. The momentum transfer cross section for krypton. *Australian Journal of Physics*, 43(1):19–25, 1990.
- [107] R. P. McEachran and A. D. Stauffer. Elastic scattering of electrons from krypton. *Journal of Physics B: Atomic, Molecular and Optical Physics*, 36(19):3977–3984, October 2003.
- [108] D. Erwin and J. Kunc. Ionization of excited xenon atoms by electrons. *Physical Review A*, 70(2), 2004.
- [109] O. Zatsarinny, K. Bartschat, and M. Allan. High-resolution experiments and b-spline r-matrix calculations for elastic electron scattering from krypton. *Physical Review A*, 83(3), 2011.
- [110] I. I. Glass and W. S. Liu. Effects of hydrogen impurities on shock structure and stability in ionizing monatomic gases. part 1. argon. *Journal of Fluid Mechanics*, 84(01):55, 1978.

- [111] I. I. Glass, W. S. Liu, and F. C. Tang. Effects of hydrogen impurities on shock structure and stability in ionizing monatomic gases: 2. krypton. *Canadian Journal of Physics*, 55(14):1269–1279, 1977.
- [112] H. Ezumi, M. Kawamura, and N. Gohda. Shock-tube measurements of the excitational cross-section in xenon-hydrogen mixture. *Journal of the Physical Society of Japan*, 53(2):592–600, 1984.
- [113] J.-L. Cambier. Numerical simulations of a nonequilibrium argon plasma in a shock-tube experiment. Paper AIAA-91-1464, 1991.
- [114] H. P. Le, A. R. Karagozian, and J.-L. Cambier. Complexity reduction of collisional-radiative kinetics for atomic plasma. *Physics of Plasmas*, 20(12):123304, 2013.
- [115] E. Josyula and W. F. Bailey. Vibration-dissociation coupling using master equations in nonequilibrium hypersonic blunt-body flow. *Journal of Thermophysics and Heat Transfer*, 15(2):157–167, 2001.
- [116] D. Giordano, V. Bellucci, G. Colonna, M. Capitelli, I. Armenise, and C. Bruno. Vibrationally relaxing flow of n past an infinite cylinder. *Journal of Thermophysics and Heat Transfer*, 11(1):27–35, 1997.
- [117] G. Colonna, L. D. Pietanza, and M. Capitelli. Recombination-assisted nitrogen dissociation rates under nonequilibrium conditions. *Journal of Thermophysics and Heat Transfer*, 22(3):399–406, 2008.
- [118] Y. Liu, M. Vinokur, M. Panesi, and T. E. Magin. A multi-group maximum entropy model for thermo-chemical non-equilibrium. Paper AIAA-2010-4332, 2010.
- [119] C. O. Laux, L. Pierrot, and R. J. Gessman. State-to-state modeling of a recombining nitrogen plasma experiment. *Chemical Physics*, 398:46–55, 2012.
- [120] A. Bultel, B. G. Cheron, A. Bourdon, O. Motapon, and I. F. Schneider. Collisional-radiative model in air for earth re-entry problems. *Physics of Plasmas*, 13(4):043502, 2006.
- [121] M. Panesi, T. E. Magin, A. Bourdon, A. Bultel, and O. Chazot. Electronic excitation of atoms and molecules for the FIRE II flight experiment. *Journal of Thermophysics and Heat Transfer*, 25(3):361–374, 2011.
- [122] A. Munafo, M. Panesi, and T. E. Magin. Boltzmann rovibrational collisional coarse-grained model for internal energy excitation and dissociation in hypersonic flows. *Physical Review E*, 89(2), 2014.

- [123] J.-L. Cambier and S. Moreau. Simulations of a molecular plasma in collisional-radiative nonequilibrium. Paper AIAA-93-3196, 1993.
- [124] W. Kruer. *The Physics Of Laser Plasma Interactions*. Frontiers in Physics, 2003.
- [125] P. Mulser and D. Bauer. *High power laser-matter interaction*. Number 238 in Springer tracts in modern physics. Springer, Heidelberg ; New York, 2010.
- [126] M. Tabak, J. Hammer, M. E. Glinsky, W. L. Kruer, S. C. Wilks, J. Woodworth, E. M. Campbell, M. D. Perry, and R. J. Mason. Ignition and high gain with ultrapowerful lasers. *Physics of Plasmas*, 1(5):1626, 1994.
- [127] V. L. Ginzburg. *Propagation of Electromagnetic Waves in Plasma*. Gordon & Science, 1961.
- [128] J. D. Jackson. *Classical electrodynamics*. Wiley, New York, 2nd edition, 1975.
- [129] H. Hora. *Plasmas at high temperature and density: applications and implications of laser-plasma interaction*. Number m1 in Lecture notes in physics. Springer-Verlag, 1991.
- [130] H. Hora. *Laser plasma physics: forces and the nonlinearity principle*. SPIE Optical Engineering Press, 2000.
- [131] A. Zeidler, H. Schnabl, and P. Mulser. Light pressure of timedependent fields in plasmas. *Physics of Fluids*, 28(1):372–376, 1985.
- [132] H. Hora. The transient electrodynamic forces at laserplasma interaction. *Physics of Fluids*, 28(12):3705, 1985.
- [133] R. J. LeVeque. *Finite difference methods for ordinary and partial differential equations: steady-state and time-dependent problems*. Society for Industrial and Applied Mathematics, 2007.
- [134] R. Ramis, K. Eidmann, J. Meyer-ter Vehn, and S. Hller. MULTI-fs a computer code for laserplasma interaction in the femtosecond regime. *Computer Physics Communications*, 183(3):637–655, 2012.
- [135] M. Born and E. Wolf. *Principles of Optics*. Pergamon Press, 1980.
- [136] J. D. Lindl and P. Kaw. Ponderomotive force on laser-produced plasmas. *Physics of Fluids*, 14(2):371, 1971.
- [137] A. Macchi, F. Cattani, T. Liseykina, and F. Cornolti. Laser acceleration of ion bunches at the front surface of overdense plasmas. *Physical Review Letters*, 94(16), April 2005.

- [138] S. C. Wilks, A. B. Langdon, T. E. Cowan, M. Roth, M. Singh, S. Hatchett, M. H. Key, D. Pennington, A. MacKinnon, and R. A. Snavely. Energetic proton generation in ultra-intense laser-solid interactions. *Physics of Plasmas*, 8(2):542, 2001.
- [139] M. Passoni, L. Bertagna, and A. Zani. Target normal sheath acceleration: theory, comparison with experiments and future perspectives. *New Journal of Physics*, 12(4):045012, 2010.
- [140] H. Hora, P. Lalouis, and S. Eliezer. Analysis of the inverted double layers produced by nonlinear forces in a laser-produced plasma. *Physical Review Letters*, 53(17):1650–1652, October 1984.
- [141] K. Rawer. *Ann. Phys.*, 35(385), 1939.
- [142] H. Kim, R. Stenzel, and A. Wong. Development of “caviton” and trapping of rf field. *Physical Review Letters*, 33(15):886–889, October 1974.
- [143] G. Morales and Y. Lee. Ponderomotive-force effects in a nonuniform plasma. *Physical Review Letters*, 33(17):1016–1019, October 1974.
- [144] T. Esirkepov, M. Borghesi, S. Bulanov, G. Mourou, and T. Tajima. Highly efficient relativistic-ion generation in the laser-piston regime. *Physical Review Letters*, 92(17), 2004.
- [145] F. V. Hartemann, E. C. Landahl, A. L. Troha, J. R. Van Meter, H. A. Baldis, R. R. Freeman, N. C. Luhmann, L. Song, A. K. Kerman, and D. U. L. Yu. The chirped-pulse inverse free-electron laser: A high-gradient vacuum laser accelerator. *Physics of Plasmas*, 6(10):4104, 1999.
- [146] A. G. Khachatryan, F. A. van Goor, J. W. J. Verschuur, and K.-J. Boller. Effect of frequency variation on electromagnetic pulse interaction with charges and plasma. *Physics of Plasmas*, 12(6):062116, 2005.
- [147] D. N. Gupta and H. Suk. Frequency chirping for resonance-enhanced electron energy during laser acceleration. *Physics of Plasmas*, 13(4):044507, 2006.
- [148] F. Sohbatzadeh, S. Mirzanejad, and M. Ghasemi. Electron acceleration by a chirped gaussian laser pulse in vacuum. *Physics of Plasmas*, 13(12):123108, 2006.
- [149] B. Srinivasan, G. Dimonte, and X.-Z. Tang. Magnetic field generation in rayleigh-taylor unstable inertial confinement fusion plasmas. *Physical Review Letters*, 108(16), 2012.

- [150] J. F. Hansen, M. J. Edwards, D. H. Froula, G. Gregori, A. D. Edens, and T. Ditmire. Laboratory observation of secondary shock formation ahead of a strongly radiative blast wave. *Physics of Plasmas*, 13(2):022105, 2006.

This Page Intentionally Left Blank

Appendix E: Combustion and Magnetohydrodynamic Processes in Advanced Pulse Detonation Rocket Engines

Lord Kahil Cole

UNIVERSITY OF CALIFORNIA

Los Angeles

Combustion and Magnetohydrodynamic Processes in Advanced Pulse Detonation Rocket Engines

A dissertation submitted in partial satisfaction
of the requirements for the degree
Doctor of Philosophy in Aerospace Engineering

by

Lord Kahil Cole

2012

Approved for public release; distribution unlimited. PA Clearance 13019 - Jan 14 2013

© Copyright by
Lord Kahil Cole
2012

ABSTRACT OF THE DISSERTATION

**Combustion and Magnetohydrodynamic Processes
in Advanced Pulse Detonation Rocket Engines**

by

Lord Kahil Cole

Doctor of Philosophy in Aerospace Engineering

University of California, Los Angeles, 2012

Professor Ann Karagozian, Chair

A number of promising alternative rocket propulsion concepts have been developed over the past two decades that take advantage of unsteady combustion waves in order to produce thrust. These concepts include the Pulse Detonation Rocket Engine (PDRE), in which repetitive ignition, propagation, and reflection of detonations and shocks can create a high pressure chamber from which gases may be exhausted in a controlled manner. The Pulse Detonation Rocket Induced Magnetohydrodynamic Ejector (PDRIME) is a modification of the basic PDRE concept, developed by Cambier (1998), which has the potential for performance improvements based on magnetohydrodynamic (MHD) thrust augmentation. The PDRIME has the advantage of both low combustion chamber seeding pressure, per the PDRE concept, and efficient energy distribution in the system, per the rocket-induced MHD ejector (RIME) concept of Cole, et al. (1995).

In the initial part of this thesis, we explore flow and performance characteristics of different configurations of the PDRIME, assuming quasi-one-dimensional transient

flow and global representations of the effects of MHD phenomena on the gas dynamics. By utilizing high-order accurate solvers, we thus are able to investigate the fundamental physical processes associated with the PDRIME and PDRE concepts and identify potentially promising operating regimes.

In the second part of this investigation, the detailed coupling of detonations and electric and magnetic fields are explored. First, a one-dimensional spark-ignited detonation with complex reaction kinetics is fully evaluated and the mechanisms for the different instabilities are analyzed. It is found that complex kinetics in addition to sufficient spatial resolution are required to be able to quantify high frequency as well as low frequency detonation instability modes. Armed with this quantitative understanding, we then examine the interaction of a propagating detonation and the applied MHD, both in one-dimensional and two-dimensional transient simulations. The dynamics of the detonation are found to be affected by the application of magnetic and electric fields. We find that the regularity of one-dimensional cesium-seeded detonations can be significantly altered by reasonable applied magnetic fields ($B_z \leq 8T$), but that it takes a stronger applied field ($B_z > 16T$) to significantly alter the cellular structure and detonation velocity of a two-dimensional detonation in the time in which these phenomena were observed. This observation is likely attributed to the additional coupling of the two-dimensional detonation with the transverse waves, which are not captured in the one-dimensional simulations. Future studies involving full ionization kinetics including collisional-radiative processes, will be used to examine these processes in further detail.

The dissertation of Lord Kahil Cole is approved.

Owen Smith

Chris Anderson

Xiaolin Zhong

Jean-Luc Cambier

Ann Karagozian, Committee Chair

University of California, Los Angeles

2012

To my mother, Linda, the enduring memory of my father, Otha, and my fiancée,
Kendra.

TABLE OF CONTENTS

Nomenclature	1
1 Introduction	5
1.1 Background on Detonation Engine Concepts	5
1.1.1 Engine Impulse and Efficiency	7
1.1.2 Pulse Detonation Engines	8
1.1.3 AJAX and RIME concepts for thrust augmentation	9
1.2 Plasma Flows	10
1.2.1 The Lorentz Force	10
1.2.2 Plasmas and Cesium Ionization	11
1.3 Pulse Detonation Rocket Induced Magnetohydrodynamic Ejectors and other Alternative Configurations	13
1.3.1 PDRIME	14
1.3.2 Cambier's Quasi-1D Model and Verification	16
1.4 Detonation Waves and MHD Effects	18
1.5 Goals of the Present Studies	20
2 Governing Equations and Physical Phenomena	27
2.1 Conservative Formulation	27
2.1.1 Single-Temperature(1T) Hydrodynamic Formulation	28

2.1.2	Single-Temperature(1T) Ideal MHD Formulation ($Re_m \rightarrow \infty$)	29
2.1.3	Two-Temperature(2T) Formulation	30
2.2	Overview of Source Terms for Governing Equations	32
2.2.1	Combustion and Ionization Reaction Kinetics	32
2.2.2	MHD Transport	33
2.3	Kinetics	34
2.3.1	Combustion Kinetics	35
2.3.2	Ionization Kinetics	38
2.3.3	Two-Temperature(2T) Relaxation	39
2.4	MHD Transport	40
3	Numerical Methods	44
3.1	Operator Splitting	44
3.2	Time Step Restrictions	45
3.2.1	Convection	45
3.2.2	Kinetics Resolution	46
3.2.3	Diffusion	47
3.3	Explicit Runge Kutta Scheme	47
3.4	Hyperbolic Solvers – Approximate Riemann Solvers	48
3.4.1	Weighted Essentially Non-Oscillatory (WENO) Schemes . . .	50
3.4.2	Monotonicity Preserving (MP) Schemes	53
3.4.3	Advection-Diffusion-Reaction (ADER) Schemes	55

3.5	Point-Implicit Euler	57
3.6	Spatial-Implicit Euler	58
4	Verification of Numerical Schemes	65
4.1	Inviscid Hydrodynamics	65
4.1.1	Sod's Shock Tube	66
4.1.2	Hydrodynamical Interacting Blast Wave Problem	66
4.1.3	Shock-Entropy Wave Interaction	67
4.1.4	Shock Diffraction Down a Backward Facing Step	68
4.1.5	Rayleigh-Taylor Hydrodynamic Instability	68
4.2	Ideal Magnetohydrodynamics(MHD)	69
4.2.1	1D MHD Shock Tube Problems	69
4.2.2	Orszag-Tang Problem	70
4.2.3	Balsara's Rotor Problem	71
4.2.4	Rayleigh Taylor MHD Instability	71
4.3	Two-Temperature(2T) Model	73
5	Simplified Approach for PDRIME Simulations	100
5.1	PDRIME with Bypass Configurations	102
5.2	Temporal/Temperature Controllers of the Magnetic Field	103
5.3	PDRIME with 2D Bypass Configuration	106
6	Detonation Stability Phenomena	121

6.1	Ignition and Instabilities	121
6.2	Simplified Model	128
6.3	Discussion	131
7	Magnetic Field and Detonation Interactions	147
7.1	Detonation Instabilities with Applied Magnetic Fields	147
7.2	Detonation Instabilities with MHD	150
7.3	2D Cellular Detonation in an Applied Magnetic Field	152
7.3.1	Enhanced Kinetics	154
7.3.2	Strong Applied Fields	155
7.4	Conclusions	156
8	Conclusions and Future Work	198
A	Reaction Mechanism	201
A.1	H_2 -Air Reaction Mechanism	201
A.2	Cesium Reaction Mechanism	202
B	Eigenvector Matrices	203
B.1	Governing Equation	203
B.2	Roe Averaged Weighting	204
B.3	Eigensystem and Flux Jacobian Matrix	204
B.3.1	Right Eigenvectors	205

B.3.2	Left Eigenvectors	207
B.3.3	Riemann ‘Jump’ conditions	209
C	MHD Divergence Cleaning for General Coordinate Systems . . .	211
D	Jacobians and Transforms	212
D.1	Chemical Jacobian	212
D.2	Chemical Jacobian($\frac{\partial \dot{\Omega}}{\partial Q}$) Derivation	213
E	Steady State Detonation	214
F	Iterative & Direct Solvers	215
F.1	Thomas’ Algorithm	215
F.2	Black-Red Gauss-Seidel	216
G	Message Passing Interface (MPI) Implementation	219
G.1	Grid Connectivity	219
	References	221

LIST OF FIGURES

1.1	Generic PDE Cycle	22
1.2	PDRE flight configuration.	23
1.3	Pulse Detonation Rocket Engine with MHD nozzle generation flight configuration.	23
1.4	Pulse Detonation Rocket Induced MHD Ejector.	24
1.5	Pulse Detonation Rocket Engine with Chamber Magnetic Piston. . .	24
1.6	Pulse Detonation Rocket Induced MHD Ejector with Chamber Mag- netic Piston.	25
1.7	Orientation of Electromagnetic Fields and associated Forces.	26
2.1	Induction delay vs Initial Temperature	43
3.1	Basic Operator Splitting	62
3.2	Strang Splitting	63
3.3	ENO/WENO Stencil	63
3.4	Strang Time Splitting	64
4.1	Density distribution for 1D Sod's Shock Tube problem.	75
4.2	Density distribution for 1D Blastwave problem.	76
4.3	Density distribution of contact discontinuities for 1D Blastwave problem.	77
4.4	Density distribution for 1D Shock-Entropy Wave Interaction problem.	78
4.5	Mach 2.4 flow over backward facing step: MW5	79

4.6	Density distribution for hydrodynamic Rayleigh Taylor Instability: $t = 0.75s$	80
4.7	Density distribution for hydrodynamic Rayleigh Taylor Instability: $t = 1.50s$	81
4.8	Density distribution for hydrodynamic Rayleigh Taylor Instability: $t = 2.25s$	82
4.9	Density distribution for hydrodynamic Rayleigh Taylor Instability: $t = 3.00s$	83
4.10	Density distribution for 1D Brio-Wu problem.	84
4.11	Density distribution for 1D Brio-Wu problem – compound wave and contact discontinuity.	85
4.12	u_x distributions for 1D Brio-Wu problem.	86
4.13	u_y distribution for 1D Brio-Wu problem.	87
4.14	Pressure distribution for 1D Brio-Wu problem.	88
4.15	B_y distribution for 1D Brio-Wu problem.	89
4.16	Density distributions for Orszag-Tang problem.	90
4.17	Balsara’s Rotor Problem (MW5): $t = 0.295s$	91
4.18	Balsara’s Rotor Problem (MP5): $t = 0.295s$	92
4.19	Balsara’s Rotor Problem (AW5): $t = 0.295s$	93
4.20	Density distribution for MHD Rayleigh Taylor Instability: $t = 2s$	94
4.21	MHD Rayleigh Taylor Instability Growth (MW5): $t = 2s$	95
4.22	MHD Rayleigh Taylor Instability Growth (MP5): $t = 2s$	96

4.23	MHD Rayleigh Taylor Instability suppression via a normal magnetic field (MW5): $t = 2s$	97
4.24	MHD Rayleigh Taylor Instability suppression via a normal magnetic field (MP5): $t = 2s$	98
4.25	Mach 10 Argon Shock with/without T_e Relaxation	99
5.1	Variation In Impulse For A PDRE	108
5.2	Quasi 1D Computational Domain	109
5.3	Quasi 1D Performance: Impulse Loss in Nozzle Energy Generation . .	110
5.4	Quasi 1D Component Performance: Bypass vs. Nozzle Impulse . . .	111
5.5	Magnetic Field Strength vs. Time, $\Pi(t)$	112
5.6	PDRIME: Effects of Flight Mach number, $B(t) \sim t^2$	113
5.7	PDRIME: Effects of Flight Mach number, $B(T)$	114
5.8	PDRIME: Effects of Flight Mach number, $B(T)$	115
5.9	PDRIME: Effects of Flight Mach number, $B(T)$	116
5.10	PDRIME: Effects of Flight Mach number, $B(T)$	117
5.11	PDRIME 2D Results: altitude = 20 km	118
5.12	PDRIME 2D Results: altitude = 25 km	119
5.13	PDRIME 2D Results: altitude = 30 km	120
6.1	Detonation Pressure Contour - MP5	134
6.2	Peak Pressure trace ($\Delta x = 2.5\mu m$ & $12.5\mu m$)	135
6.3	Peak Pressure Trace: High Frequency(HF) Mode	136

6.4	Peak Pressure Trace: High Amplitude(HA) Mode	137
6.5	Peak Pressure Trace: Post-“re-explosion”	138
6.6	Induction Length Trace: Post-“re-explosion”	139
6.7	Time to re-explosion vs Grid Resolution	140
6.8	Fourier Transform of Typical Peak Pressure Traces	141
6.9	Induction Zone in Detonation Reference Frame	142
6.10	Simplified model of the peak Pressure Cycle	142
6.11	High Frequency(HF) Mode Peak Pressure Cycle (phase 1 of 2)	143
6.12	High Amplitude(HA) Mode Peak Pressure Cycle (phase 1 of 2)	144
6.13	High Frequency(HF) Mode Peak Pressure Cycle (phase 2 of 2)	145
6.14	High Amplitude(HA) Mode Peak Pressure Cycle (phase 2 of 2)	146
7.1	Peak Pressure Traces with Cesium Addition	159
7.2	Configuration of Magnetic Field	160
7.3	Peak Pressure Traces with various applied magnetic fields (%Cs = 1)	161
7.4	Peak Pressure Traces with various applied magnetic fields (%Cs = 5)	162
7.5	Peak Pressure Traces with various applied magnetic fields (%Cs = 10)	163
7.6	Peak Pressure Traces with various applied electric and magnetic fields (%Cs = 1)	164
7.7	Peak Pressure Traces with various applied electric and magnetic fields (%Cs = 5)	165

7.8	Peak Pressure Traces with various applied electric and magnetic fields (%Cs = 10)	166
7.9	Time trace comparisons of $B_z = 0, 3$, and 8 T 1D detonations in the accelerator and generator configuration	167
7.10	Numerical setup for 2D detonation simulations	168
7.11	Schlieren-type plot of cellular detonation	169
7.12	Stoichiometric $H_2 - Air$ detonation	170
7.13	Stoichiometric $H_2 - Air - 1\% Cs$ detonation	171
7.14	Stoichiometric $H_2 - Air - 5\% Cs$ detonation	172
7.15	Stoichiometric $H_2 - Air - 10\% Cs$ detonation	173
7.16	X-t plot: no MHD/generator/accelerator with 1% Cs	174
7.17	X-t plot: no MHD/generator/accelerator with 5% Cs	175
7.18	X-t plot: no MHD/generator/accelerator with 10% Cs	176
7.19	Peak pressure trace: no MHD/generator/accelerator with 1% Cs . . .	177
7.20	Peak pressure trace: no MHD/generator/accelerator with 5% Cs . . .	178
7.21	Peak pressure trace: no MHD/generator/accelerator with 10% Cs . .	179
7.22	Centerline pressure and conductivity profiles: accelerator & generator configurations $B_z = 8T$, $t = 75\mu s$	180
7.23	Conductivity distribution in a 2D detonation with a linear color map overlaid with Schlieren-type plot using density gradients of the deto- nation front with varying EK in the generator configuration	181

7.24	Conductivity distribution in a 2D detonation with a linear color map overlaid with Schlieren-type plot using density gradients of the detonation front with varying EK in the accelerator configuration	182
7.25	Centerline peak pressure trace: accelerator configuration with 10% Cs with various EK	183
7.26	Centerline peak pressure trace: generator configuration with 10% Cs with various EK	184
7.27	X-t plot: no MHD/generator/accelerator with 10% Cs with $EK = 100$	185
7.28	Centerline peak pressure trace: accelerator configuration with 10% Cs and various B_z	186
7.29	Centerline peak pressure trace: generator configuration with 10% Cs and various B_z	187
7.30	X-t plot: generator configuration with 10% Cs and various B_z	188
7.31	X-velocity profiles at different times: generator configuration with 10% Cs and various B_z	189
7.32	Conductivity profiles at different times: generator configuration with 10% Cs and various B_z	190
7.33	Pressure profiles at different times: generator configuration with 10% Cs and various B_z	191
7.34	Temperature profiles at different times: generator configuration with 10% Cs and various B_z	192
7.35	Detonation history: no MHD with 10% Cs	193

7.36 Detonation history: Accelerator configuration with $B_z = 8T$ and 10% Cs	194
7.37 Detonation history: Accelerator configuration with $B_z = 16T$ and 10% Cs	195
7.38 Detonation history: Accelerator configuration with $B_z = 32T$ and 10% Cs	196
7.39 X-t plot: accelerator configuration with 10% Cs and various B_z . . .	197
F.1 Grid Cell Checkerboard Pattern	218
G.1 Domain and subdomains	220
G.2 Domain-to-domain Connection Example	220

LIST OF TABLES

2.1	Simplified $H_2 - O_2$ Reaction Thermodynamic Properties	42
2.2	Ionization Temperatures	42
3.1	WENO Coefficients	62
4.1	RTI problem hydrodynamic initial conditions	74
4.2	Balsara's rotor problem initial conditions	74
7.1	Detonation Velocity with Cesium	158
G.1	Generic Memory Window List	220

ACKNOWLEDGMENTS

I would like to acknowledge the many people who helped make this dissertation possible. I would like to first thank Professor Ann Karagozian for her great insight, patience, and her infectious drive and energy. I would like to thank my mentor, Dr. Jean-Luc Cambier, for encouraging me to explore the physics deeply and tackle the hard questions. I gratefully acknowledge Professor Owen Smith for his numerous helpful ideas and insight throughout the course of this work. I would also like to thank the members of my committee, Professor Xiaolin Zhong and Professor Chris Anderson, for their guidance.

I would like to thank my current and past labmates, Chris, Hai, Cory, Dan, Sophonias, and Jeff, and classmates, Naveen, Patrick, Pilbum, Morad, Clifton, and Ladan, at UCLA for their support and enjoyable discussions. I also gratefully acknowledge the good folks at the In-Space Propulsion Branch of the Air Force Research Laboratory: Carrie, Kooj, Rob, Carl, and David, for their helpful ideas and technical assistance.

I would particularly like to thank my parents and siblings, Otha and Khalila, for their inspiration and support. Specifically, to my dad, for not giving into the pressures of my bored siblings and prematurely leaving the theater playing *Apollo 13*. Thank you, dad, for nurturing the spark which led to the pursuit of this current work. And finally, and most importantly, I would like to thank my fiancée, Kendra, for her unwavering support and encouragement.

Financial support for this project has come from the U.S. Air Force Office of

Scientific Research under the Space Power and Propulsion program managed by Dr. Mitat Birkan under grants FA9550-07-1-0156 and FA9550-07-1-0368, ERC Inc. under Subcontract RS100226, the AFRL Co-op Program, and the UCLA Cota-Robles Fellowship program. This support is gratefully acknowledged.

VITA

2005	B.S. (Physics), United States Naval Academy.
2005–2007	United States Naval Officer.
2008	M.S. (Aerospace Engineering), UCLA, Los Angeles, California.
2008–2009	Teaching Assistant, Mechanical and Aerospace Engineering Department, UCLA. Taught Aircraft Propulsion Section
2010–present	Research Co-Op, Air Force Research Laboratory, Propulsion Directorate, Edwards AFB, CA.

PUBLICATIONS AND PRESENTATIONS

Le, H., Cambier, J.-L., and Cole, L.K., “GPU-based flow simulation with detailed chemical kinetics,” to appear in *Computer Physics Communications*.

Cole, L.K., Karagozian, A.R., and Cambier, J.-L., “Stability of Flame-Shock Coupling in Detonation Waves: 1D Dynamics,” *Combustion Science & Technology*, Vol. 184, Issue 10-11, pp. 1502-1525, 2012.

Zeineh, C.F., Cole, L.K., Roth, T., Karagozian, A.R., and Cambier J.-L., “Magnetohydrodynamic

Thrust Augmentation of Pulse Detonation Rocket Engines,” *Journal of Propulsion and Power*, Vol. 28, No. 1, pp. 146-159, 2012.

Cole, L.K. and A. Karagozian, A.R., “Numerical Simulations of Detonation Wave - Magnetic Field Interactions” presented at the 65th APS/DFD Meeting, San Diego, CA, November 2012.

Cole, L.K., Le, H., J.-L. Cambier, and A. Karagozian, A.R., “Numerical Simulations of Detonation Instabilities and Magnetic Field Interaction” presented at the 64th APS/DFD Meeting, Baltimore, MD, November 2011.

Cole, L.K., Karagozian, A.R., and Cambier J.-L., “Stability of Flame-Shock coupling in Detonation Waves: 1D Dynamics,” presented at 23rd International Colloquium on Dynamics of Explosions and Reactive Systems, Irvine, CA, July 2011.

Cole, L.K., Cambier J.-L., and Karagozian, A.R., “Simulation of a Detonation in Transverse Magnetic Fields” presented at the 63rd APS/DFD Meeting, Long Beach, CA, November 2010.

Cole, L.K., Roth, T., Zeineh, C.F., and Karagozian, A.R., “Magnetohydrodynamic Augmentation of Pulse Detonation Engines: Simplified Modeling and Performance Estimates” presented at 3rd Southern California Symposium on Flow Physics, 2009.

Nomenclature

\tilde{A}	Jacobian Matrix
AR	Exit-to-throat nozzle area ratio
\mathbf{B}	Magnetic field, $\{B_x, B_y, B_z\}$
c_i	Mass fraction of species i
c_p	Specific heat capacity at constant pressure
c_v	Specific heat capacity at constant volume
D	Detonation speed
D_{CJ}	Chapman-Jouget detonation velocity
\mathbf{D}	Displacement Field
e	Internal energy per unit mass
e_0	Internal energy of formation per unit mass
\hat{E}	Total energy per unit volume
\mathbf{E}	Electric field, $\{E_x, E_y, E_z\}$
EK	Enhanced kinetics factor
f	Overdrive factor ($f \equiv (D/D_{CJ})^2$)
f_{loss}	Bypass pressure loss factor

\mathcal{F}	Thrust
\mathbf{g}	Gravitational acceleration
h	Enthalpy per unit mass
\mathbf{H}	Magnetizing Field
I	Impulse
I_{tot}	Total impulse
I_{sp}	Specific impulse ($I_{sp} \equiv I/\rho V g$)
\mathbf{j}	current density
k	Boltzmann's constant
k_b	Backward reaction coefficient
k_f	Forward reaction coefficient
K	Reaction-rate multiplier
\mathbf{K}	Loading factor, $\{K_x, K_y\}$
L	Cellular detonation cell length
M	Mach Number
M_i	Molar mass of species i

n_i	Number density of species i
N	Total number density
P	Static pressure
P^*	Static and Magnetic pressure
q	Heat release per unit mass
P_{ref}	Reference pressure
\mathcal{Q}_{rs}	Elastic collision cross-section of the r^{th} and s^{th} species
R_u	Universal gas constant
R_{prod}	Specific gas constant (products)
R_{reac}	Specific gas constant (reactants)
Re_m	Magnetic Reynolds Number
\hat{s}_e	Specific electron entropy
S_e	Electron entropy per unit volume
T	Temperature
T_A	Activation temperature
T_f	Peak flame temperature

\mathbf{u}	Fluid velocity
V	Specific volume ($V \equiv 1/\rho$)
σ	Electrical conductivity
γ	Specific heat ratio ($\gamma \equiv c_p/c_v$)
λ	Cellular detonation cell size (height)
$\nu_{i,j}$	Stoichiometric coefficient for species i at reaction j
ρ	Mass density
$\dot{\omega}$	Reaction source term (see equation (2.22))
Θ	Characteristic Temperature
ϵ_0	Permittivity of free space
μ_0	Permeability of free space
$()_i$	i^{th} numerical grid cell
\vec{q}	$(\dots, q_{i-1}, q_i, q_{i+1}, \dots)^T$
\mathbf{q}	$\{q_x, q_y, q_z\}$

CHAPTER 1

Introduction

1.1 Background on Detonation Engine Concepts

The chemical rocket can be considered the oldest technical development in jet propulsion. In a solid propellant rocket, for example, the exit plane momentum is due to the flow of a hot gas created by the rapid burning of solid fuel composed of a mixture of a fuel and oxidizer. Gun powder emerged in China around AD 850 as the result of accidental discovery by Chinese alchemist. For centuries after this discovery, little was done in the advancement of rocket propulsion, until in 1903, a Russian school teacher by the name of Konstantin Tsiolkovsky[1] published the paper ‘The Investigation of Outer Space by Means of Reaction Apparatus’. In this paper, Tsiolkovsky postulated that man could escape the clutches of earth’s gravity with rockets. His calculations led him to the idea of multi-staging. Subsequently, he went on to discuss the use of liquid oxygen and liquid hydrogen for those purposes. Piggy-backing off of these ideas, the American physicist, Robert Goddard, designed constant pressure rocket combustion chamber nozzles and propellant feed systems. Goddard[2] went on to lead the advancement of liquid fueled rockets and in 1919 published, ‘A Method of Reaching Extreme Altitudes’, which not only provided the mathematical analysis for achieving high altitudes, but also to reach the moon. He devoted much

of his effort to thrust chamber development and to the turbo-machinery needed for pumping the liquid propellants [3].

Still today, almost a century later, the modern aerospace community finds itself facing the same challenges as the founding fathers of modern rocketry. These challenges include, but are not limited to, developing lighter and more efficient propulsion systems and more efficient multi-staging techniques. The present studies focus on exploring potential rocket propulsion systems that take advantage of magnetohydrodynamics(MHD) phenomena.

In 1998, Dr. Jean-Luc Cambier proposed a novel combined cycle propulsive concept, the Pulse Detonation Rocket-Induced Magnetohydrodynamic Ejector (PDRIME)[4]. The PDRIME is one of many MHD thrust augmentation ideas that shows promise for application in advanced propulsion systems. Taking advantage of the unsteady wave engine concept of the constant volume Pulse Detonation Engine (PDE), the PDRIME utilizes temporal periodic energy divergence into a seeded air stream, then MHD acceleration for thrust augmentation. Because of the nature of the unsteady waves in the PDE, the PDRIME does not need heavy turbo-machinery to pump liquid propellants. With the elimination of heavy turbo-machinery, paired with the energy augmentation of the MHD accelerator in the bypass air stream, the PDRIME could potentially be able to achieve the velocities necessary for Single-Stage-to-Orbit (SSTO) flight, thus breaking with the expensive tradition of complicated, expensive multistage propulsive systems.

Another concept developed by Cambier in [5] is the ‘Magnetic Piston’. This concept involves energy extraction from the expansion portion of the nozzle, energy reintroduction into the combustion chamber, followed by acceleration of the com-

bustion products from the combustion chamber. The ‘Magnetic Piston’ builds upon the PDE and the PDRIME, but also gains some advantages of traditional constant pressure rocket propulsion systems. These and other alternative rocket propulsion concepts will be explored in this dissertation. The present chapter provides the technical background for these concepts.

1.1.1 Engine Impulse and Efficiency

Before we can compare the properties and advantages of various propulsion systems, we must first have a quantitative means of expressing various properties. Impulse and efficiency are the properties we are most interested in. Impulse is defined as the integral of thrust, \mathcal{F} , over a given time period:

$$I \equiv \int_0^t \mathcal{F}(\tau) d\tau \quad (1.1)$$

Efficiency in a propulsion system is quantified by the specific impulse, I_{sp} , which is defined as $I_{sp} \equiv \frac{I}{M_p g}$, where $M_p g$ is the weight of the propellant used. A typical rocket engine uses a converging-diverging (Laval) nozzle to convert high pressure and temperature propellant into thrust. The larger the area ratio (AR), ratio of nozzle exit area to nozzle throat area, of the nozzle the faster the exit velocity of the propellant, u_e , and lower the exit pressure, P_e . The thrust generated by rockets is typically expressed as:

$$\mathcal{F} = \dot{m} u_e + (P_e - P_{atm}) A_e \quad (1.2)$$

where \dot{m} is the mass flux of gas exiting the nozzle and A_e is the area of the nozzle exit plane. For optimal thrust, P_e is equal to the ambient pressure, P_{atm} , when this is achieved, a nozzle is said to be ‘perfectly’ expanded. When traveling in altitudes which range from sea level to the edge of space (the Von Karman line, or 100 km),

there is a large variation in the ambient pressures, so that most often $P_e \neq P_{atm}$. These variations in ambient pressure lead to significant losses in nozzle efficiency.

1.1.2 Pulse Detonation Engines

The Pulse Detonation Engines (PDE) in simple terms is an engine that utilizes detonation waves to derive its thrust. The PDE operates in a cycle, shown schematically in Figure 1.1. In this simple configuration, a stoichiometric mixture of reactants is placed in a long tube with an open and closed end (i.e., thrust wall). The mixture is then ignited from the thrust wall (a). This results in a shock and deflagration wave (subsonic flame) quickly coalescing into a detonation wave (supersonic flame – see section 1.4) propagating into the reactant mixture (b). The high pressure region behind the wave imparts force on the thrust wall. When the detonation wave reaches the open end of the tube (c), it will be reflected back into the tube as an expansion wave (d). The expansion wave propagates into the tube, while at the same time purging the combustion products from the tube (e). The expansion wave will then reflect off of the thrust wall, and at that time the lowered pressure will draw fresh reactants into the tube (f). The expansion wave will propagate into the tube, then reflect back from the open end as a compression wave (h). This compression wave will propagate through the re-introduced reactants (i), after which it will reflect off of the thrust wall as a shock (j) and a new cycle will begin. There are many advantages to the PDE over conventional rockets propulsion systems. The conventional rocket engines have to pump reactants at very high pressures into a combustion chamber, requiring heavy turbo machinery, while the PDE does not need heavy turbo machinery, but rather naturally introduces the reactants into the combustion chamber

at much lower pressures. The simplicity of the concept is quite attractive, and the PDE's have been tested extensively over the years [22]. PDE's have even been tested as the sole source of propulsion on an experimental aircraft, the Scaled Composites Long E-Z[24], which used an abundance of off-the-shelf parts.

1.1.3 AJAX and RIME concepts for thrust augmentation

Ejectors have been considered for years as a viable method of thrust augmentation for various aerospace propulsion systems. Ejectors rely on the transfer of energy from one stream (primary) to another stream (secondary). Higher thrust can be achieved if the primary stream has a high specific energy and the secondary has a high mass flow rate. A generic Rocket Induced Magnetohydrodynamic Ejector (RIME) [25] consist of 3 parts, each consisting of variable area stream-tubes; (1) the generator, (2) the accelerator, and (3) the mixer. The streams can be described by different power plants, for example a rocket stream, a bypass tube, and the mixer. In the RIME described by [25], the “rocket stream” serves as the MHD generator while the “mixer” is the MHD accelerator. The MHD generator transforms the internal energy of a fluid into electrical power. The fluid itself is a conductor of electricity, the motion of this fluid through a magnetic field gives rise to electromotive force (drag) and flow current in accordance with Faraday's law of inductance. An MHD accelerator uses the same principles, but in this particular case electrical energy is applied to the system resulting in an electromotive force (thrust). In the AJAX system, energy is diverted from the inlet flow via MHD generation, it is then re-applied after the fluid passes through the combustor via MHD generation[26].

1.2 Plasma Flows

1.2.1 The Lorentz Force

The various advanced rocket engine configurations explored and reviewed in this dissertation utilize electromotive forces (Lorentz forces) generated by a moving charge to augment thrust. The Lorentz Force is defined as the Coulombic attractive/repulsive force between single or collection of charged particle(s) moving through an electromagnetic field:

$$\mathbf{F} = \mathbf{j} \times \mathbf{B} \quad (1.3)$$

where \mathbf{F} is the Lorentz force, \mathbf{j} is the current density, and \mathbf{B} is the applied magnetic field. The current density is defined by Ohm's law:

$$\mathbf{j} = \sigma(\mathbf{E} + \mathbf{u} \times \mathbf{B}) \quad (1.4)$$

where σ is the conductivity, \mathbf{E} is the electric field, and \mathbf{u} is the fluid velocity. Expressing the electric field using Ohm's law and using vector identities, the total rate of energy deposition into the fluid can be expressed as :

$$\mathbf{j} \cdot \mathbf{E} = \mathbf{j} \cdot \left(\frac{\mathbf{j}}{\sigma} - \mathbf{u} \times \mathbf{B} \right) = \frac{\mathbf{j}^2}{\sigma} + \mathbf{u} \cdot (\mathbf{j} \times \mathbf{B}) \quad (1.5)$$

where the first term on the right side is the heating of the fluid (dissipation) and the second term on the right side is the mechanical power obtained from the Lorentz force (non-dissipative). The separation of the different forms of power expended in the fluid becomes important as we evaluate efficiency later in this document [4].

1.2.2 Plasmas and Cesium Ionization

A plasma is defined as a collection of charged particles where the long-range Coulombic force is a factor in determining the statistical properties, but where the collection of particles is low enough in density so that the forces exerted by a particles nearest-neighbor is less than the long-range Coulombic force exerted by the particle's many neighbors. Thus, the study of plasma often coincides with the study of low-density ionized gases. An ion is a molecule or atom which acquires enough energy to liberate a valence, outer shell, electron from the respective molecule/atom. A collection of ions, liberated electrons, and neutral particle's form a plasma. In a weakly ionized plasma, which we shall investigate throughout the remainder of this study, the ion remains in close proximity with a liberated electron, thus the plasma as a whole can be thought of as charge neutral, but locally charged [27].

One of the necessary properties of the configurations discussed earlier in this document, the AJAX, the RIME, and other advanced configurations, is the ability for the working fluid to conduct electricity. In order for a fluid to conduct electricity it must be at least partially ionized. These advanced configurations achieved ionization through thermal ionization. Thermal ionization follows mass action laws like any chemical reaction. The heat of ionization, when expressed in Kelvin is referred to as the characteristic temperature of ionization, $\Theta_i \equiv H_{ionization}/k$, where k is Boltzmann's constant. Most common gases and combustion products, i.e., air, CO, CO_2 , and noble gases, have high characteristic temperatures, so they do not thermally ionize until temperatures in excess of 4000K are reached. However, if an alkali metal, which has a low characteristic temperature of ionization, is added in small amounts (on the order of 1 part in 100 or less) thermal ionization can be achieved

at temperatures as low as 2000K. This process, referred to as *seeding*, changes the working fluid into a plasma and allows the previously mentioned configurations to conduct electricity under realistic operating temperatures [28].

A plasma will often take on different characteristics, depending on the temperature, conductivity, and mean velocity, to name a few. Before we delve into the various regimes in which the plasma being studied will exist, we must first look to Maxwell's equations for free charge[29]:

$$\begin{aligned}
\nabla \times \mathbf{H} &= \frac{\partial \mathbf{D}}{\partial t} + \mathbf{j} \\
\nabla \times \mathbf{E} &= -\frac{\partial \mathbf{B}}{\partial t} \\
\nabla \cdot \mathbf{B} &= 0 \\
\nabla \cdot \mathbf{E} &= \frac{e(n_i - n_e)}{\epsilon_0}
\end{aligned} \tag{1.6}$$

where n_e is the number density of electrons, ϵ_0 is the permittivity of free space, \mathbf{H} is the magnetic field, \mathbf{D} is the electric displacement field, and e is the charge of an electron. As an example, if a one-dimensional gas were to flow perpendicularly to a magnetic field, the induced electric field could be expressed as $E_y \approx \frac{1}{2}u_x B_z$, which can be shown as follows for the idealize case, $\mathbf{j}/\sigma \rightarrow 0$:

$$\begin{aligned}
\mathbf{j} &= \sigma (\mathbf{E} + \mathbf{u} \times \mathbf{B}) \\
\mathbf{E} &\approx -\mathbf{u} \times \mathbf{B} \\
E_y &\approx u_x B_z
\end{aligned} \tag{1.7}$$

The work done by a unit volume of this gas moving a length, L , oriented perpendicularly to the magnetic field, \mathbf{B} , using Equations 1.3 and 1.6, would produce the following[28]:

$$FL = \frac{1}{2}\sigma_g u B^2 L \tag{1.8}$$

The energy stored in a magnetic field per unit volume is $\frac{B^2}{2\mu_0}$, which is often referred to as the magnetic pressure. The ratio of these is

$$\frac{\text{Work done by the gas}}{\text{Energy stored in the field}} = \mu_0 \sigma_g u L = Re_m \quad (1.9)$$

The Magnetic Reynolds number, Re_m , is a good measure of the degree in which a field induced by gas motion compares to the original magnetic field. This parameter plays a very important role in determining the performance of the MHD accelerator and generator.

1.3 Pulse Detonation Rocket Induced Magnetohydrodynamic Ejectors and other Alternative Configurations

Spawned from the concept of AJAX [26] and RIME [25], Pulse Detonation Rocket Induced Magnetohydrodynamic Ejectors (PDRIME) and other alternative configurations are meant to push the bounds of MHD thrust augmentation. The Pulse Detonation Rocket Engine (PDRE) is the core of the various alternative engine configuration currently under review. The PDRE is composed of two major components: a combustion chamber and a converging-diverging nozzle shown in Figure 1.2. The combustion chamber introduces reactants on the front end, while the downstream end connects to the converging-diverging nozzle. The converging end of the nozzle has an extremely short length and a high exit-to-throat area ratio, $AR \sim 16$, the significance of which will be explained momentarily. A typical PDRE cycle is at the core a PDE cycle, where reactants are introduced to the combustion chamber and the reactants are ignited at the front end. A detonation wave is formed and propagates downstream, but unlike the PDE cycle previously mentioned, the detonation

wave will reflect off of the high area ratio converging section nozzle and reflect back as a shock wave. The reflected detonation will raise the chamber temperature and pressure so rapidly that the expelled gases can be thought of as started from this high pressure or ‘blow down’ state [30]. The fluid is then accelerated out of the nozzle where more thrust is derived. Over a cycle, the pressure of the chamber will decrease as more products are being expelled. The chamber will then reach a critical pressure in which reactants will be introduced at relatively low pressure, and a new cycle will commence.

1.3.1 PDRIME

The PDRIME is actual a composite of some of the systems previously discussed, that is, the AJAX, the RIME, and PDRE. The PDRIME is physically composed of PDRE (the combustion chamber and nozzle), a bypass tube that sits directly on top of the PDRE and magnets which are placed around the nozzle as well as around the bypass tube which is illustrated in Figure 1.3 and 1.4. The effect of the strengths of these magnetics will be explored later in this dissertation. In a PDRIME cycle, reactants as well as a gas of low ionization energy, e.g., cesium, are introduced into the combustion chamber and a PDRE cycle will commence. The fluid in the combustion chamber will be heated sufficiently to ionize the seeded cesium. During this process, hot products and ions will be expelled out of the nozzle. As the fluid expands through the nozzle, the MHD generator in the nozzle will be engaged. The generator will extract energy from the fluid moving at high velocities and reduce the Mach number, $M = u/a$, to approximately unity at the nozzle exit. With $M \approx 1$ at the nozzle exit, an unsteady shock will migrate from the nozzle exit into the

bypass tube. The front entrance of the bypass tube is seeded with cesium, and as the unsteady shock migrates upstream, the cesium will also pass through the shock and be ionized. From there, the MHD accelerators in the bypass will be employed and will utilize the Lorentz force to accelerate the fluid out of the bypass tube. The aim of this configuration is to take energy out of the nozzle and more effectively utilize it in the bypass tube in order to increase thrust and thus gain more impulse and efficiency.

The PDRE has many good performance characteristics, e.g., low seeding pressure, but one characteristic that we wish to improve is the nature of the unsteady pressure throughout the PDRE cycle. As previously described, the pressure in the chamber is quickly increased with the chemical reactions and subsequent reflection of detonation waves, then gas is expelled from the combustion chamber and expanded through the nozzle. As more combustion products are purged from the combustion chamber, the pressure in the combustion chamber drops drastically with time. In a PDRIME configuration, this drastic drop in pressure severely handicaps the effectiveness of the MHD accelerator in the bypass tube. This impairment works as follows: as the pressure drops in the chamber and nozzle, the back pressure driving the nozzle flow drops. This dropping of pressure driving the nozzle correlates to a drop in pressure entering the bypass tube exit. The pressure at the end of the bypass tube supports the unsteady shock wave in the tube, so as this pressure drops, so does the strength of the unsteady shock heating the fluid in the bypass. As the strength of the unsteady shock dies down is strength, the temperature jump across shock is reduced, therefore less ionization takes place. Less ionization leads to lower conductivity, and with lower conductivity the MHD accelerator is less effective.

In order to prevent the negative effects of the unsteady pressure drop through-

out the cycle, MHD forces can be utilized in the combustion chamber to drive the heated fluid out of the combustion chamber at a more constant pressure. This configuration, with applications of energy extracted from the nozzle into the chamber, for a “magnetic chamber piston” configuration, would then possess the advantages of low seeding pressure demonstrated in the aforementioned PDRE [31] as well as the property of constant pressure possessed by a conventional rocket engine [5]. For the basic PDRIME configuration, this combustion chamber has chemical reactions, ionization of seeding ionizable gas, and reflection of detonation waves. But unlike the PDRIME cycle, with a “chamber piston”, after the chamber is sufficiently heated, a MHD accelerator is placed around the combustion chamber to create the piston forces fluid out of the chamber using the Lorentz force. The ‘magnetic piston’ concept is illustrated in Figure 1.5, and the PDRIME with the ‘magnetic piston’ is illustrated in Figure 1.6. The concept of a ‘magnetic piston’ was first introduced by Kolb in 1957[32]. In his experimentation of magnetic shock tubes, Kolb found by applying a magnetic field to a plasma, that the shock waves produced were stronger than that produced in the absence of the magnetic field. The fundamental interaction of a magnetic field with shocks and detonations will be explored in the present studies.

1.3.2 Cambier’s Quasi-1D Model and Verification

Cambier has performed analysis and numerical simulations of various PDRE configurations; i.e., the PDRIME and the PDRE with a ‘magnetic piston’. The assumptions that are part of the analysis are as follows. In his preliminary studies, Cambier selected a simple configuration where the fluid velocity, electric field, and magnetic field form a right hand coordinate system shown in Figure 1.7, indicating generator

(decelerator) and accelerator configurations. The current density from Equation 1.4 can now be expressed as:

$$j_y = \sigma(E_y - u_x B_z) \approx \sigma u_x B_z (K_y - 1) \quad (1.10)$$

where \mathbf{K} is the loading parameter, i.e., the ratio of the applied electric field to the induced field: $K_y = \frac{E_y}{u_x B_z}$. This is an important parameter in Cambier's simplified modeling of MHD interaction [4]. When $u_x > 0$ and $0 < K_y < 1$, energy is extracted from the fluid, the Lorentz force is negative, as is j_y , and the device acts as a “generator”, shown in Figure 1.7(a). When $K_y > 1$, a positive application of energy takes place, the Lorentz force is positive, as is j_y , and the device acts as an “accelerator”, shown in Figure 1.7(b). It is the generator configuration that allows energy extraction as shown in Figure 1.3, with energy input to accelerate the flow, as shown in Figures 1.4–1.6. In the present studies we use $K_y = 0.5$ for the generator and $K_y = 1.5$ for the accelerator. The ideal case of no ohmic heating, $\mathbf{j}^2/\sigma \approx 0$, is of particular interest, because it forms a very simple analytical expression, but it is not always valid. In order to neglect the ohmic heating as compared to the mechanical work, the following condition must be satisfied:

$$\left| \frac{\mathbf{j}^2/\sigma}{\mathbf{u} \cdot (\mathbf{j} \times \mathbf{B})} \right| = \left| \frac{j_y}{\sigma u_x B_z} \right| = \left| \frac{E_y - u_x B_z}{u_x B_z} \right| = |K_y - 1| \ll 1 \quad (1.11)$$

Cambier also assumes a constant magnetic field as well as a sufficiently low Re_m . In the case of a highly conducting plasma ($\sigma \approx 1000$ mhos/m), which can be seen in the combustion chamber, the constant magnetic field assumption is only valid if the loading factor is small, which also leads to the low dissipation approximation[4].

1.4 Detonation Waves and MHD Effects

The foregoing discussion pertains to the proposed ability of magnetohydrodynamics (MHD) to affect reactive processes via seeding the flow with potentially ionizing species such as cesium. While this notion will be explored in a global sense for the PDRIME and alternative detonation-based engine configurations in Chapter 5, the ability of magnetic and electric fields to influence combustion processes requires a more detailed examination, in particular, including the effect of complex reaction kinetics. Hence a fundamental understanding of transient detonation processes, and the ultimate impact of MHD on these processes, is required and will also be examined in this thesis.

The study of detonation waves dates back to the late 19th century, where Chapman[6] and Jouguet[7] modeled detonations as a shock wave supported by the heat release of the combustible material in an infinitely thin zone, where all chemistry and diffusive transport takes place. Later Zel'dovich[8], Von Neumann[9], and Doering[10] independently represented the detonation as a confluence of a one-dimensional shock wave moving at a detonation velocity, followed by a chemical reaction zone of finite length; this came to be known as the ZND model for a detonation wave.

While the true structure of detonation waves inevitably calls for representation of multi-dimensional effects with complex reaction kinetics, the simple one-dimensional detonation structure provides a rich spectrum of dynamical features which are worthy of detailed exploration and which have relevance to multi-dimensional phenomena, e.g., cellular detonations [11]. Even with single step Arrhenius kinetics [12, 13, 14, 15], pulsations or instabilities associated with a 1D overdriven ZND detonation may be explored in detail, with important physical features and computational requirements

established. For a rapidly initiated, spark-induced detonation, where the detonation decays from an over-driven state toward the self-sustaining Chapman-Jouguet limit cycle, one obtains a sequence of different modes of physical oscillation between the flame and shock front. The numerical analysis of this effect has been explored previously by Cambier[16] using complex H_2 -air detonation kinetics and highly-resolved numerical simulations, but with only a spatially and temporally second-order convergence rate shock capturing scheme. The initiation of evolving 1D detonation instability modes is also observed in calculations by Leung et al.[17] using a two-step chain-branching reaction model [18] and a Roe scheme, with an overdriven ZND detonation as the initial condition. Similar calculations with a second-order accurate slope-limited centered scheme and a 7-step reduced chemical mechanism for acetylene-oxygen detonations [19] have allowed exploration of the stabilizing effect of dilution of the mixture with argon.

In the present study (Chapters 6 and 7), we combine higher-order numerical methods and complex reaction kinetics for the detailed analysis of the non-linear dynamics associated with a spark-induced detonation. While simplified one-step and two-step chemistry models have provided useful guidance in elucidating the dynamics of detonation instability, it is important to understand the influence of the complexity of a realistic reaction mechanism, since energy release and unsteadiness in the coupling of the wave front and induction zone can affect detonation initiation or failure [20]. Moreover, important physical processes associated with deflagration to detonation transition (DDT) require an understanding of the formation and amplification of localized explosion centers and positive-feedback flame acceleration mechanisms [21, 22, 23]. These phenomena are often easier to understand through dimensionality reduction, while preserving some of the complexity of the physics (i.e.

reaction kinetics). The use of high-order numerical methods can also be a powerful tool in the analysis of such complex flows, but we need to understand the interaction of numerical (spatial accuracy) and physical (chemical) length scales. This must be done before adding other effects such as species diffusion and viscosity; hence our study is limited to reactive Euler flow. Since the use of high-order numerical methods can become a powerful tool in studying the non-linear detonation dynamics, it is also important to gain a good understanding of the effect of the non-linear algorithms on the flow dynamics. In a similar fashion to many previous studies of detonation dynamics, the objective of the present work is not to provide realistic detonation simulations, but to systematically investigate these dynamics through the addition of increasing complexity in the models. We expect of course that adding physical diffusion will eliminate some characteristic length scales of instability, an effect which can be investigated in the future.

1.5 Goals of the Present Studies

Among the goals of the present research is first to explore alternative configurations of the PDRIME to achieve optimal performance from the MHD augmentation. The various engine configurations used in our research took on a multitude of forms, these forms are shown in figures 1.2 through 1.6. While the present studies described in Chapter 5 focused on quasi-one dimensional simulations, these results, together with those in Zeineh [33], were published in a complete study[34].

Inherent to the ability of the PDRIME and its modified configurations to operate is the ability of an applied magnetic field to affect a chemical reaction. Hence in the present study we have separately studied the propagation of a detonation wave

with complex kinetics, including its inherent instabilities (Chapter 6), and then to examine the effects of the cesium seeding and an applied magnetic field on the dynamics of the detonation (Chapter 7). Thus both aspects of this dissertation, the simplified modeling and the detailed detonation simulations, may be used to validate the PDRIME and related MHD propulsion concepts.

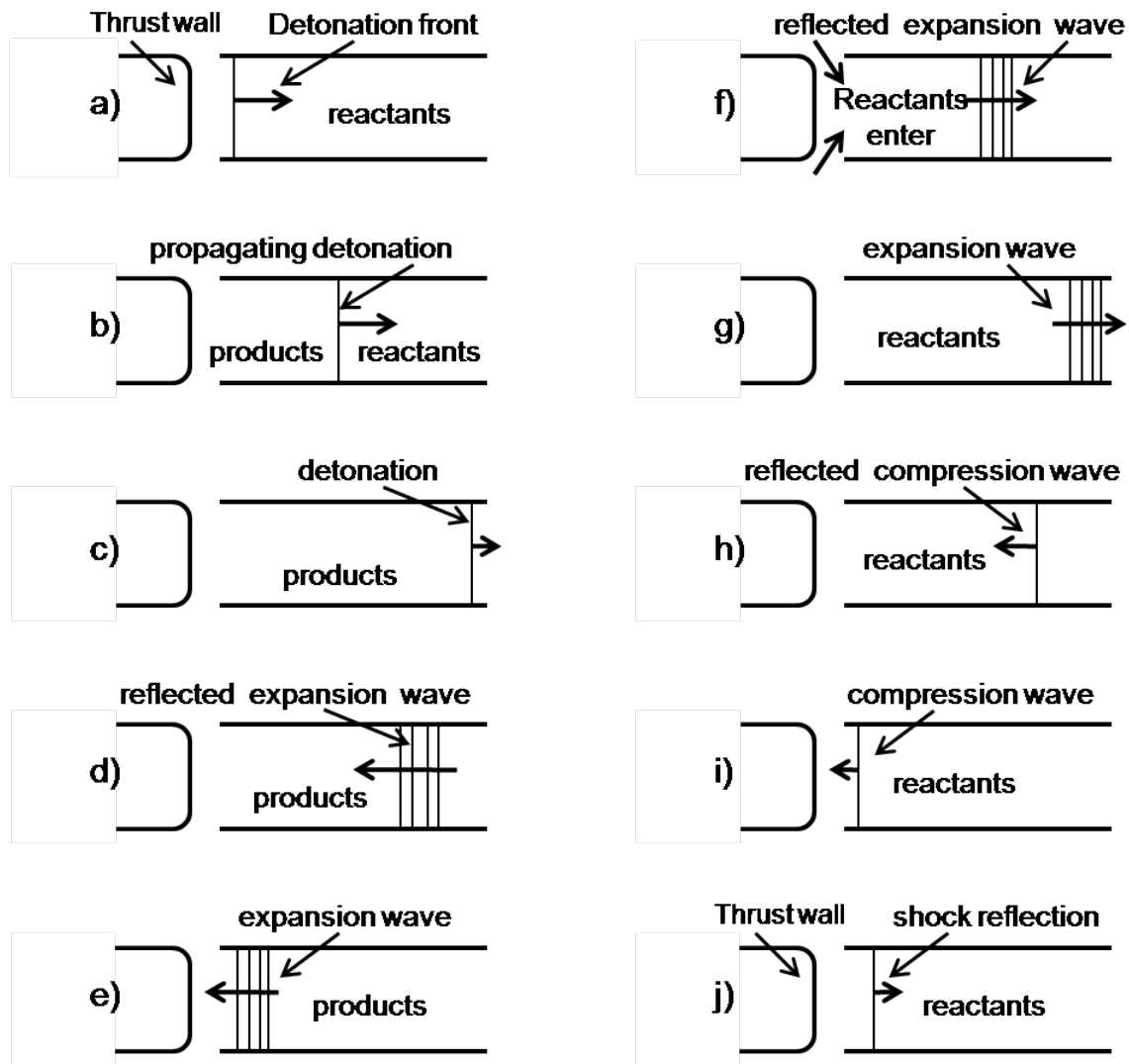


Figure 1.1: The generic pulse detonation cycle. (a)-(c) represent ignition and detonation wave propagation. (d)-(g) represents reflection of an expansion wave from the tube opening to the thrust wall and back to the tube opening. (h)-(j) represents the reflection of compression waves which eventually leads to the re-ignition of the reactants which are drawn into the tube at stage (f).

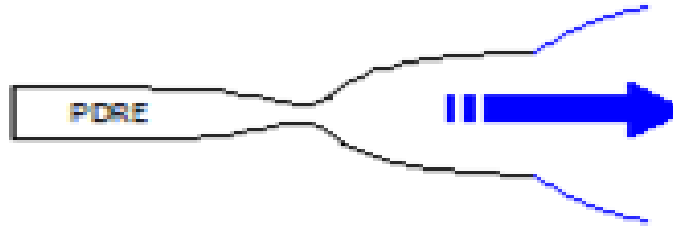


Figure 1.2: PDRE Pulse Detonation Rocket Engine

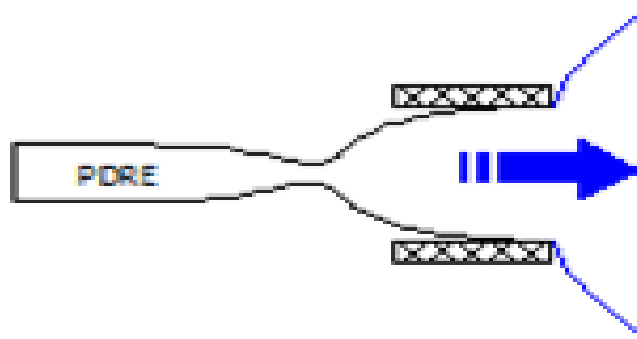


Figure 1.3: Pulse Detonation Rocket Engine with with Nozzle Generator (NG) with MHD nozzle generation flight configuration

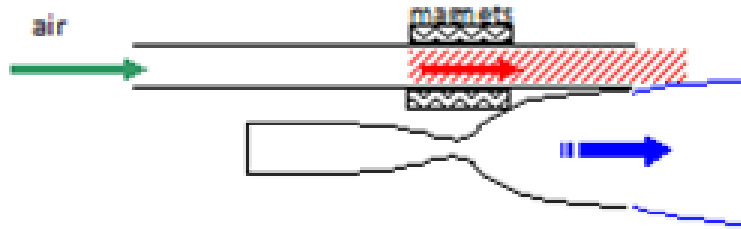


Figure 1.4: Pulse Detonation Rocket Induced MHD Ejector (PDRIME), the MHD accelerator is located in the Bypass Section

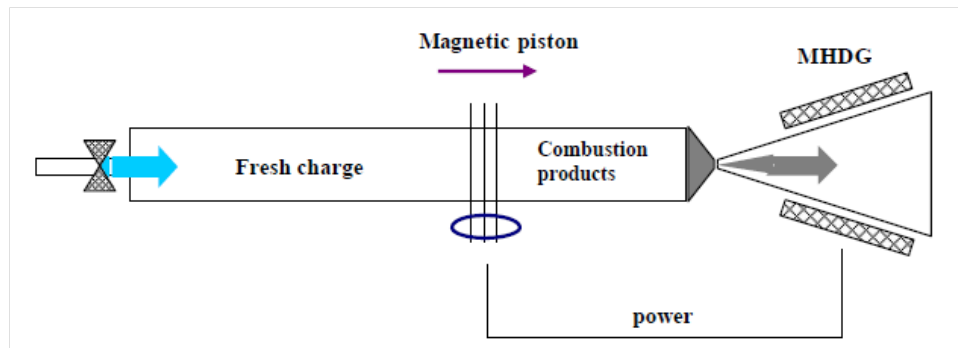


Figure 1.5: Pulse Detonation Rocket Engine with Chamber Magnetic Piston (CP) (from Cambier[5])

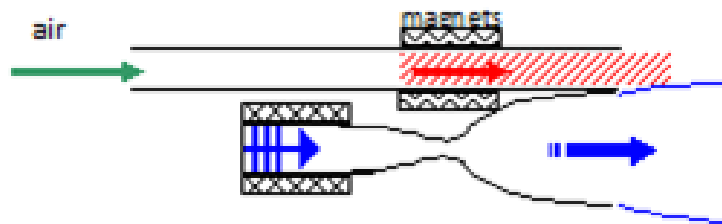


Figure 1.6: Pulse Detonation Rocket Induced MHD Ejector with Chamber Magnetic Piston

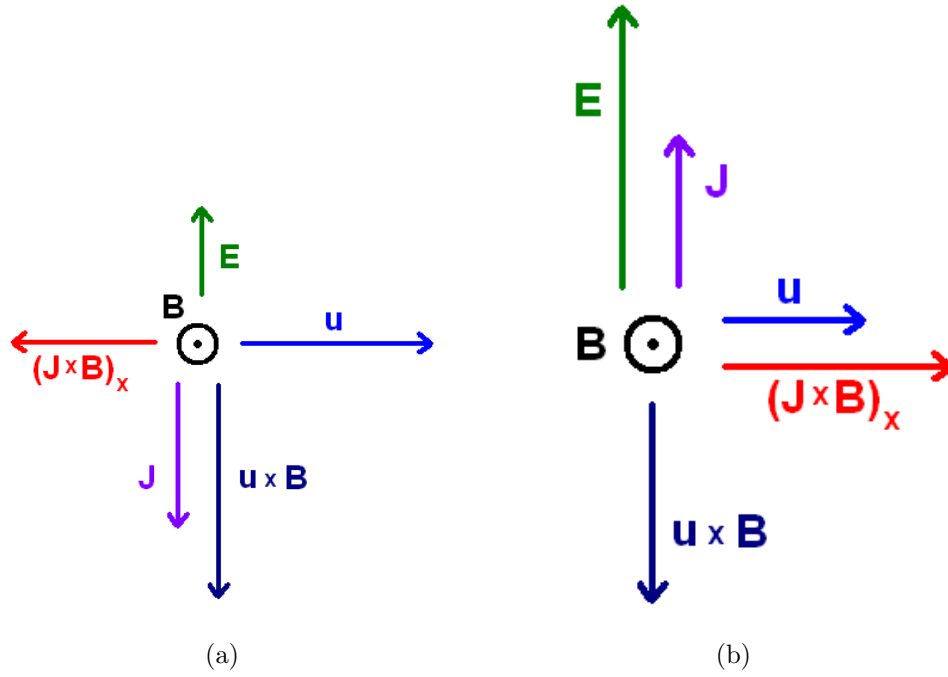


Figure 1.7: Lorentz Force $(\mathbf{J} \times \mathbf{B})_x$ when (a) the MHD generator is on, with fluid moving in the positive x-direction, applied magnetic field in the positive z-direction, and current flowing in the negative y-direction, and (b) the MHD accelerator is on, with fluid moving in the positive x-direction, applied magnetic field in the positive z-direction, and current flowing in the positive y-direction.

CHAPTER 2

Governing Equations and Physical Phenomena

An accurate description of the governing equations is presented here, describing the flow and evolution of properties associated with detonation and MHD processes.

2.1 Conservative Formulation

The governing equations are presented here in the differential form, but later will be expressed in the integral form, which is necessary for the finite-volume formulation used in some simulations of the PDRIME. The flow equations are expressed as a hyperbolic equation with a source term:

$$\frac{\partial \mathbf{Q}}{\partial t} + \nabla_n \cdot \mathbf{F} = \dot{\mathbf{\Omega}} \quad (2.1)$$

where the \mathbf{Q} , \mathbf{F} , and $\dot{\mathbf{\Omega}}$ are arrays of conserved variables, normal component of the flux density of \mathbf{Q} , and source terms, respectively. In the current study all terms on the left hand side (LHS) of Eqn 2.1 are strictly in the hyperbolic form, while the right hand side (RHS) will express all other terms which will be referred to as source terms. Source terms can describe the diffusion, chemical kinetics, or enforcement of geometric coordinate constraint. Operator splitting, which will be discussed in greater detail in Section 3.1, can be employed to compute the convective contribution,

$$\left. \frac{\partial \mathbf{Q}}{\partial t} \right|_{conv} = -\nabla_n \cdot \mathbf{F} \quad (2.2)$$

as well as various source terms,

$$\left. \frac{\partial \mathbf{Q}}{\partial t} \right|_{mhd} = \dot{\mathbf{Q}}_{mhd}, \quad \left. \frac{\partial \mathbf{Q}}{\partial t} \right|_{kinetics} = \dot{\mathbf{Q}}_{kinetics} \quad (2.3)$$

These terms then can be combined to describe the total change of the conserved variables,

$$\frac{\partial \mathbf{Q}}{\partial t} = \left. \frac{\partial \mathbf{Q}}{\partial t} \right|_{conv} + \left. \frac{\partial \mathbf{Q}}{\partial t} \right|_{mhd} + \left. \frac{\partial \mathbf{Q}}{\partial t} \right|_{kinetics} + \dots \quad (2.4)$$

2.1.1.1 Single-Temperature(1T) Hydrodynamic Formulation

The hydrodynamic formulation of Eqn. 2.1 is well established and can be used to describe the evolution of the density, velocity, and pressure fields of the fluid where the conserved variables and normal fluxes can be described as such:

$$\mathbf{Q} = \begin{pmatrix} \rho_s \\ \rho \mathbf{u} \\ E \end{pmatrix} \quad \mathbf{F} = \begin{pmatrix} \rho_s u_n \\ \rho \mathbf{u} \cdot u_n + P \mathbf{n} \\ (E + P) u_n \end{pmatrix} \quad (2.5)$$

where the total mixture density $\rho \equiv \sum_s \rho_s$, \mathbf{n} is an arbitrary direction, $u_n = \mathbf{u} \cdot \mathbf{n}$, and the total energy and pressure can be expressed as:

$$E = \sum_s \rho_s e_{int,s} + \frac{1}{2} \rho \mathbf{u}^2 \quad (2.6)$$

$$P = (\gamma - 1) \left(E - \frac{1}{2} \rho \mathbf{u}^2 \right) \quad (2.7)$$

where $e_{int,s}$ is the specific internal energy of the s^{th} species and γ is the adiabatic index. For a calorically perfect gas (constant c_v) the specific internal energy can be expressed as:

$$e_{int,s} = \frac{P}{\gamma - 1} \quad (2.8)$$

For thermally perfect gases, which is of particular interest in the present study, the specific internal energy of a species can be expressed as:

$$e_{int,s} = \int c_{v,s}(T) dT + e_{0,s} \quad (2.9)$$

where $c_{v,s}$ is the specific heat capacity at constant pressure for the s^{th} species and the $e_{0,s}$ is the specific internal energy of formation for the s^{th} species.

2.1.2 Single-Temperature(1T) Ideal MHD Formulation ($Re_m \rightarrow \infty$)

By combining Maxwell's equations and the induction equation, Equations 1.6 and 1.4 respectively, as well as adding a zero charge separation approximation, $n_e - n_i \approx 0$, one can describe the time evolution of the magnetic field as:

$$\frac{\partial \mathbf{B}}{\partial t} = - \underbrace{\frac{1}{\mu_0 \sigma} \nabla \times \nabla \times \mathbf{B}}_{\text{diffusive}} - \underbrace{\nabla \times \mathbf{u} \times \mathbf{B}}_{\text{convective}} \quad (2.10)$$

The time varying \mathbf{B} contains a convective term which behaves as a hyperbolic equation and a diffusive term, which behaves as a parabolic equation. Using the criteria set in previous sections, the convective term will be treated as the LHS, of the form of Eqn. 2.1, and the diffusive term as the source term. If the conductivity were to be extremely large such that $\sigma \rightarrow \infty$, then the diffusive term of Equation 2.10 would become zero, leaving only the convective portion of the equation. When this particular case is cast into the divergence form of Eqn. 2.1 as well as incorporating the

magnetic pressure contribution to the momentum and energy equations, i.e. Lorentz force and Joule heating terms, with hydrodynamic formulation of Equation 2.5, it is referred to as the ideal MHD formulation,

$$\mathbf{Q} = \begin{pmatrix} \rho \\ \rho \mathbf{u} \\ \mathbf{B} \\ E^* \end{pmatrix} \quad \mathbf{F} = \begin{pmatrix} \rho u_n \\ \rho \mathbf{u} u_n + P^* \mathbf{n} - \frac{1}{\mu_0} \mathbf{B} B_n \\ u_n \mathbf{B} - \mathbf{u} B_n \\ (E^* + P^*) u_n - \frac{1}{\mu_0} \mathbf{u} \cdot \mathbf{B} B_n \end{pmatrix} \quad (2.11)$$

where $B_n = \mathbf{B} \cdot \mathbf{n}$, and the total energy and pressure can be expressed as:

$$E^* = \sum_s \rho_s e_{int,s} + \frac{1}{2} \rho \mathbf{u}^2 + \frac{\mathbf{B} \cdot \mathbf{B}}{2\mu_0}$$

$$P^* = P + \frac{\mathbf{B} \cdot \mathbf{B}}{2\mu_0}$$

Where E^* is the total energy, P is the mechanical pressure, and the total pressure is defined as $P^* \equiv P + P_m$. Often, $\frac{\mathbf{B} \cdot \mathbf{B}}{2\mu_0}$ is referred to as the magnetic pressure, P_m . Without the presence of a magnetic field, $\mathbf{B} \cdot \mathbf{B} = 0$, the formulation of Equation 2.11 will reduce to the hydrodynamical formulation of Equation 2.5.

2.1.3 Two-Temperature(2T) Formulation

It has been shown by Cambier[35] that under certain conditions the electrons can be heated adiabatically while the bulk fluid can be heated non-isentropically. Conversely, the electrons can be heated non-adiabatically while the bulk fluid is heated adiabatically. One example of the latter is when a microwave is used to excite the electrons in the fluid. In the case of the former, a fluid may pass through a stationary shock at Mach $M = 10$, but while the electron entropy speed is the same as that of the bulk fluid, the speed of sound of the electron is considerably faster, $c_e = \sqrt{\frac{\gamma P_e}{\rho_e}}$,

where the ratio of molar masses of Nitrogen and the electron is $\frac{MW_{N_2}}{MW_e} \sim 10^5$. In the electron reference frame there is therefore no shock, $M_e \ll 1$. When this occurs, the bulk fluid and the electrons have different temperatures, and these temperatures will relax on time scales proportional to the electron-heavy particle elastic collision frequency. The two-temperature MHD formulation (MHD2T), Equation 2.1, builds from the MHD1T formulation but contains additional terms which describe the evolution of the electron energy. The electron thermal energy is transported as:

$$\frac{dE_e}{dt} + \nabla \cdot (\mathbf{u}E_e) = -P_e \nabla \cdot \mathbf{u} \quad (2.12)$$

Because the electron is convected at \mathbf{u} and $|\mathbf{u}|/c_e \ll 0$, the convection of the electron is subsonic and can be treated isentropically. This allows for the recasting of the electron energy into the electron entropy, S_e , which is a conserved quantity and does not require a special source term for convective transport, where the conserved variables and normal fluxes can be described for the two-temperature formulation:

$$\mathbf{Q} = \begin{pmatrix} \rho \\ \rho \mathbf{u} \\ \mathbf{B} \\ E^* \\ S_e \end{pmatrix} \quad \mathbf{F} = \begin{pmatrix} \rho u_n \\ \rho \mathbf{u} u_n + P^* \mathbf{n} - \frac{1}{\mu_0} \mathbf{B} B_n \\ u_n \mathbf{B} - \mathbf{u} B_n \\ (E^* + P^*) u_n - \frac{1}{\mu_0} \mathbf{u} \cdot \mathbf{B} B_n \\ S_e u_n \end{pmatrix} \quad (2.13)$$

where the electron entropy is defined $S_e \equiv \frac{P_e}{\rho \gamma_e}$ and $\gamma_e \equiv \frac{5}{3}$. The electron energy, total energy and total pressure are defined:

$$E_e = \frac{S_e \rho^{\gamma_e - 1}}{\gamma_e - 1} = \frac{n_e k T_e}{\gamma_e - 1} \quad (2.14)$$

$$E^* = \sum_{s \neq e} \rho_s e_{int,s} + \frac{1}{2} \rho \mathbf{u}^2 + \frac{\mathbf{B} \cdot \mathbf{B}}{2\mu_0} + E_e \quad (2.15)$$

Without the presences of a magnetic field, $\mathbf{B} \cdot \mathbf{B} = 0$, and this formulation will reduce to the two-temperature hydrodynamical formulation (EULER2T).

2.2 Overview of Source Terms for Governing Equations

2.2.1 Combustion and Ionization Reaction Kinetics

In the present study, the kinetic processes which include the chemical reactions of combustion processes, the ionization of the fluid, and the temperature relaxation of the electron must be properly captured. In the case of chemical reactions and ionization, chemical species are not strictly conserved, but particles (chemical elements) and mass are, while in the case of temperature relaxation, energy can be transferred from the heavy particles to the electrons and vice-versa. This source term can be represented in the following way,

$$\mathbf{Q} = \begin{pmatrix} \rho_s \\ \rho \mathbf{u} \\ E \\ S_e \end{pmatrix} \quad \dot{\mathbf{Q}}_{kinetics} = \begin{pmatrix} \dot{\omega}_s \\ 0 \\ \dot{\omega}_E \\ \dot{S}_e \end{pmatrix} \quad (2.16)$$

where $\dot{\omega}_s$ is the production of the s^{th} species, $\dot{\omega}_E$ is the energy production due to change in formation energy, and \dot{S}_e is the electron entropy production. A more detailed description of these terms will be discussed in the following sections as well as Section 2.3.

2.2.2 MHD Transport

2.2.2.1 Fixed Magnetic Field ($R_m \rightarrow 0$)

In the MHD source formulation that is used to study the PDRIME configurations, and some of the MHD-detonation interactions, there is no conservation law for the magnetic field, but rather the Lorentz force and Joule heating are incorporated into a hydrodynamic formulation of the governing equations. By incorporating the Lorentz force exerted by an applied magnetic field, Eqn. 1.3, as well as the mechanical power obtained from the Lorentz force and the associated Joule heating, Eqn. 1.5, one can recover the following MHD source terms for a fixed magnetic field:

$$\mathbf{Q} = \begin{pmatrix} \rho_s \\ \rho \mathbf{u} \\ E \end{pmatrix} \quad \dot{\mathbf{Q}}_{mhd, fixed} = \begin{pmatrix} 0 \\ \mathbf{j} \times \mathbf{B} \\ \mathbf{j} \cdot \mathbf{E} \end{pmatrix} \quad (2.17)$$

In the present study, when this approximation of MHD is used, Cambier's [4] simplified MHD model will be implemented, which was previously discussed in Section 1.3.2. In that model, the system includes the electric and magnetic fields as orientated in Figure 1.7. In addition, one can simplify the expression for current density with Equation 1.10, such that the x-component of the Lorentz force becomes:

$$(\mathbf{j} \times \mathbf{B})_x \approx \sigma u_x B_z^2 (K_y - 1) \quad (2.18)$$

and the Joule heating term becomes:

$$\mathbf{j} \cdot \mathbf{E} \approx \sigma u_x^2 B_z^2 (K_y - 1) K_y \quad (2.19)$$

This formulation will be employed in the simplified PDRIME simulations and in some of the detonation-MHD studies.

2.2.2.2 Resistive MHD ($Re_m \sim O(1)$)

Seldom do real problems act ideally, as described in the perfectly conducting ideal MHD approximation of Eqn. 2.11 or the perfectly resistive fixed field line approximation of Equation 2.17. Typically, there is a finite conductivity such that the diffusive and convective terms of Eqn. 2.10 are of the same order of magnitude, thus neither can be neglected. The diffusion of magnetic field and magnetic energy can be expressed as the following source term:

$$\dot{\Omega}_{mhd, diffuse} = \begin{pmatrix} 0 \\ 0 \\ \nabla \cdot \left(\frac{1}{\mu_0 \sigma} \nabla \mathbf{B} \right) \\ \mathbf{j} \cdot \mathbf{E} \end{pmatrix} \quad (2.20)$$

where the evolution of the magnetic energy is prescribed by

$$\mathbf{j} \cdot \mathbf{E} = \nabla \cdot \left(\frac{1}{\mu_0 \sigma} \nabla \mathbb{T} \right) \quad (2.21)$$

where the Maxwell stress tensor is defined as $\mathbb{T}^{\alpha\beta} = \frac{|B|^2}{2\mu_0} \delta^{\alpha\beta} - \frac{B^\alpha B^\beta}{\mu_0}$. A more detailed discussion of magnetic field diffusion will be presented in Section 2.4.

2.3 Kinetics

In order to properly resolve the chemical reaction and ionization processes, one must first characterize the plasma and chemical kinetics. Using detailed balancing one can express the rate of species production and destruction in the following manner.

$$\dot{\omega}_s = \sum_r \nu_{rs} k_{fr} \prod_j \rho_j^{\nu'_{rj}} - \sum_r \nu_{rs} k_{br} \prod_j \rho_j^{\nu''_{rj}} \quad (2.22)$$

$$\nu_{rs} = \nu''_{rs} - \nu'_{rs}$$

where ν''_{rk} and ν'_{rk} are the coefficients of s^{th} species in the r^{th} forward and backward reactions, respectively, and k_{fr} and k_{br} and the forward and backward chemical rates of the r^{th} reaction. When the temperature of the fluid is near thermal equilibrium, detailed balancing can be used to determine backward rates:

$$k_b = k_f \exp \left(\sum_s \nu_s \Delta G_s / T \right) \quad (2.23)$$

where ΔG_s is the change in Gibbs free energy of the s^{th} species. In cases where the temperature is far from equilibrium, for example when there is a heavy and electron temperature, detailed balance would not be appropriate to determine the backward rates. The forward reaction rates are given by the modified Arrhenius equation of the form:

$$k = AT^\eta \exp(-\Theta/T) \quad (2.24)$$

Where A is the Arrhenius pre-factor, η is the Arrhenius coefficient, and Θ is the activation temperature. Using the form of Equation 2.16 with Equation 2.22, the energy production due to the internal energy change can be expressed as $\dot{\omega}_E = \sum_s \omega_s e_{0,s}$.

2.3.1 Combustion Kinetics

2.3.1.1 Single Step Kinetics

During preliminary testing, we simulated a single-step $H_2 - O_2$ reaction, reactants H_2 and O_2 form product H_2O



The H_2O production rate takes the Arrhenius form of Equation 2.24 in which $\dot{\omega}_p = K\rho_f e^{-\theta/T}$. In this particular case, ρ_f is the density of a stoichiometric mixture of the fuel, H_2 , and oxidizer, O_2 , and ρ_p is the density of the product, H_2O . The thermodynamic properties of the reactants and product are given in Table 2.1. The differences in the thermodynamic properties between reactants and products found in this table are due to the differences in the molar mass, M , and the degrees of freedom associated with the molecular configuration of each species.

2.3.1.2 Detailed Reaction Kinetics

In the present study, we have primarily focused on detailed kinetics of a simple combustion system ($H_2 - O_2$). Another approach to the single step reaction in Equation 2.25, commonly chosen in fundamental studies of detonation dynamics, is a constant-volume one-step reaction model, in which the entire chemistry is described by the evolution of a single progress variable that follows an exponential relaxation with a characteristic time-scale given by the induction delay. This progress variable is also associated with the fractional amount of heat released into the flow. In that model, the induction delay time, τ_{ind} , follows a simple exponential fit, $t_{ind} \simeq e^{\theta_a/T}$. The delay being essentially caused by the need for a sufficient amount of radicals from chain-branching reactions, and the production of those being an endothermic process, the parameter θ_a in this formulation is an averaged activation energy of the key radical-producing reactions.

This is a reasonable approximation to the chemistry in that region, albeit within limits. To study detonation dynamics more completely, we have used the detailed chemistry to compute and parametrize the induction delay as a function of initial

temperature and pressure, with the mixture held fixed to stoichiometric hydrogen-air. As in a previous study [16], the chemical kinetics of a dilute hydrogen-air mixture were solved here. The chemistry includes eight reacting species, H_2 , O_2 , H , O , OH , HO_2 , H_2O_2 , H_2O , and the non-reacting diluent, N_2 , where a compilation of NASA and JANNAF thermo-chemical data is obtained from [36]. As prescribed by [37], 38 elementary reactions, found in Appendix A, are used in this mechanism and the backward rates are computed from equilibrium constants. As shown in Figure 2.1, the delay does follow an exponential form, $t_i \propto \alpha(P)e^{\beta(P)/T}$, as expected. The parameter β in this formulation is an averaged activation energy of the key radical-producing reactions. However, this approach yields unrealistic profiles of the post-shock region, since the heat release is gradual.

A better description is obtained with a two-step reaction model [38, 39], where the heat release is associated with a second progress variable whose evolution can start only at the end of the induction delay, which now follows a linear time variation. While this two-step model allows a separation between the induction and heat release zones, the model is unsatisfactory in several ways. First, the rate of heat release is assumed independent of temperature, which is unrealistic, as the flow heating accelerates the combustion. Generally speaking, a stiff differential equation for the progress variable can be used to reproduce this non-linear effect, but the dynamics can be different from the real conditions. Second, when the flame is accelerated towards the shock, the two reaction zones (induction and flame) start to merge, even if species diffusion is neglected; the enforcing of two separate zones with a two-step model could thus modify the dynamics of the strongly coupled shock-flame system. It is for these reasons we will utilize detailed reaction kinetics to perform the simulations in the present study, per Equations 2.22 – 2.24 and the full $H_2 - O_2$

combustion mechanism described in Appendix A.

2.3.2 Ionization Kinetics

The existence of plasma in a working fluid is studied via the field of magnetohydrodynamics. If a working fluid's characteristic temperature of first ionization, Θ_i , is high relative to the fluid temperature, it is imperative to seed the fluid with a species with a sufficiently low characteristic temperature to create the flow of ionized gas. The principle components of the working fluids in this study, air, H_2 , O_2 , and H_2O , have high characteristic temperatures relative to the fluid temperature in the scope of the present study. A sampling of ionization temperatures are shown in Table 2.2. As prescribed by Cambier in [40], cesium is chosen as the seeded species due to its low characteristic temperature of ionization. In the modeling of the ionization and recombination of cesium in the working fluid, we start with a simple three-body reaction mechanism:



where M in this particular case represents a third-body species. In the present study, it is extremely important to be able to calculate the conductivity of the plasma in order to correctly simulate MHD. The scalar conductivity, σ , is defined as:

$$\sigma = \frac{n_e e^2}{m_e \nu_m} \quad (2.27)$$

where n_e is the electron number density, m_e is the electron mass, and e is the Coulombic charge where the electron collisional frequency, ν_m is defined as:

$$\nu_m = \underbrace{n_e \mathcal{Q}_{ei} \bar{v}_e}_{\nu_{ei}} + \underbrace{N \sum_{s \neq e} \int_0^\infty d\epsilon \mathcal{Q}_{es}(\epsilon) v \cdot f(\epsilon)}_{\nu_{en}} \quad (2.28)$$

where \mathcal{Q}_{ei} and ν_{ei} is the electron-ion elastic collisional cross-section and collisional frequency, \mathcal{Q}_{es} and ν_{es} is the electron-neutral elastic collisional cross-section and collisional frequency of the s^{th} species, v_e is the electron thermal velocity, and f is the electron distribution function. Electron-neutral cross-section data are found in [41] while the electron-ion cross-section, commonly referred to as the Coulombic cross-section is given by [42]:

$$\mathcal{Q}_{ei} = \frac{2.87 \times 10^{-14}}{T_{[eV]}^2} \ln \Lambda \quad (2.29)$$

where the Coulombic logarithm is $\ln \Lambda = 13.57 + 1.5 \log T_{[eV]} - 0.5 \log n_e$. In the regime where the fluid is strongly ionized, $\alpha \gtrsim 10^{-4}$, the electron-ion collision term of Equation 2.28 dominates, and the conductivity scales as follows:

$$\sigma \sim T_e^{5/2} \quad (2.30)$$

2.3.3 Two-Temperature(2T) Relaxation

When a plasma is rapidly heated by a shock, radiation, or other process, the heavy particle and the electron temperatures can be altered from equilibrium and must undergo a series of elastic collisions to return them to equilibrium, or thermalize. If the collisional time scale is significantly faster than the fluid time scale, the heavy particles and electrons can be assumed to be in equilibrium. But, when the collisional time scales are much slower than that of the fluid, the temperatures can be treated completely separately. In the event the time scale associated with thermalization is on the order of the fluid time scale, the finite rate of elastic energy relaxation must be taken into account. The relaxation of the electron energy is as follows [42]:

$$\frac{dE_e}{dt} = \nu_m \left(\frac{2m_e}{M} \right) \frac{3}{2} n_e k_b (T_h - T_e) \quad (2.31)$$

where T_h is the translational temperature of the heavy particles. Equation 2.31 can be recast in terms of electron entropy as follows:

$$\dot{S}_e = \frac{dS_e}{dt} = \nu_m \left(\frac{2m_e}{M} \right) \frac{3}{2} n_e k_b (T_h - T_e) (\gamma_e - 1) \rho^{1-\gamma_e} \quad (2.32)$$

2.4 MHD Transport

In order to properly characterize a non-ideal system in the presence of an imposed magnetic field, one must account for both the convective and diffusive transport of the magnetic field. Let us re-examine the formulation of the temporal evolution of the magnetic field expressed in Equation 2.10:

$$\frac{\partial \mathbf{B}}{\partial t} = - \underbrace{\frac{1}{\mu_0 \sigma} \nabla \times \nabla \times \mathbf{B}}_{\text{diffusive}} - \underbrace{\nabla \times \mathbf{u} \times \mathbf{B}}_{\text{convective}}$$

Starting from 2.1 and the description of the source term from Eqn. 2.20, one can define a system which describes the evolution of the magnetic field and magnetic pressure due to diffusive transport in the divergence form as follows:

$$\begin{aligned} \frac{\partial \mathbf{B}}{\partial t} &= \nabla \cdot \frac{1}{\mu_0 \sigma} \nabla \mathbf{B} \\ \frac{\partial P_B}{\partial t} &= \nabla \cdot \frac{1}{\mu_0 \sigma} \nabla \mathbb{T} \end{aligned} \quad (2.33)$$

where P_B is the magnetic pressure which was previously defined as $P_B = \frac{\mathbf{B}^2}{2\mu_0}$. Now let us rewrite Eqn. 2.33 in a flux formulation of the form,

$$\mathbf{Q}_t = \nabla \cdot \mathbf{F}^\nu \quad (2.34)$$

where \mathbf{F}^ν represents the magnetic diffusive flux,

$$\mathbf{Q} = \begin{pmatrix} B_x \\ B_y \\ B_z \\ P_B \end{pmatrix} \quad \mathbf{F}^\nu = \frac{1}{\mu_0 \sigma} \begin{pmatrix} \nabla B_x \\ \nabla B_y \\ \nabla B_z \\ \nabla \mathbb{T} \end{pmatrix} \quad (2.35)$$

This description of MHD diffusive transport is particularly useful when the conductivity of a fluid is finite, as in the problems represented in this thesis. The limits of ideal MHD and perfectly resistive MHD, where $\sigma \rightarrow \infty$ and $\sigma \approx 0$, respectively will also be investigated.

Species	R [$\frac{J}{kg-K}$]	c_v [$\frac{J}{kg-K}$]	e_0 [$\frac{J}{kg}$]
$H_2 - O_2$	692.8	2.425×10^3	0
H_2O	461.9	2.079×10^3	1.344×10^7

Table 2.1: List of thermodynamic properties of a stoichiometric mixture of $H_2 - O_2$, reactant, and H_2O , product, for a simple, single-step reaction.

Species	Θ_i , [K]
Cs	45,141
K	50,364
Na	59,647
Li	62,548
O_2	139,834
H_2O	146,217
O	157,937
CO_2	167,105
H_2	181,030
N_2	181,030
Ar	182,887
He	285,239

Table 2.2: Listing of characteristic temperatures of first ionization of selected species[43].

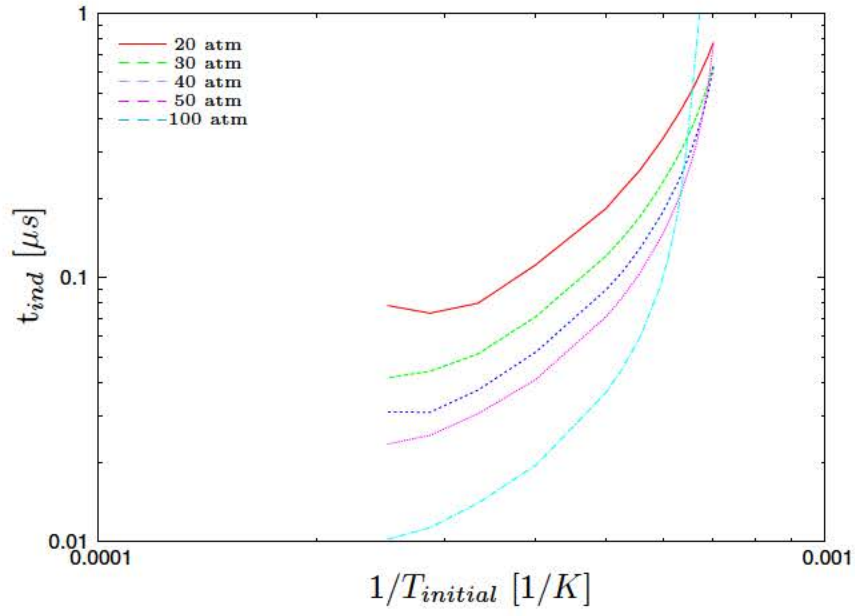


Figure 2.1: Computed induction delay as a function of initial temperature at various pressures P for the stoichiometric H_2 -air reaction with complex kinetics. Curves can be fitted as $t \sim \alpha(P)e^{\frac{\beta(P)}{T}}$.

CHAPTER 3

Numerical Methods

The following chapter will list and describe the numerical methods utilized to solve the governing equations described in the previous section.

3.1 Operator Splitting

As shown in Equation 2.4, it is often necessary to solve the LHS with one solver while solving the various RHS source terms with other solvers. For example, one might wish to solve a problem which involves convection, LHS, as well as chemical kinetics, RHS, and utilize different solvers, or *operators*, \mathcal{L}^{conv} and \mathcal{L}^{chem} , respectively. By utilizing these operators, the solution of \mathbf{Q} at $t = t^{n+1}$, where $t^{n+1} = t_0 + \Delta t$, can be determined as follows:

$$\begin{aligned}\Delta \mathbf{Q}^{chem} &= \mathcal{L}^{chem} \mathbf{Q}^n - \mathbf{Q}^n \\ \Delta \mathbf{Q}^{conv} &= \mathcal{L}^{conv} \mathbf{Q}^n - \mathbf{Q}^n \\ \mathbf{Q}^{n+1} &= \mathbf{Q}^n + \Delta \mathbf{Q}^{chem} + \Delta \mathbf{Q}^{conv}\end{aligned}\tag{3.1}$$

Figure 3.1 illustrates the contribution of the two operators in attaining the solution at $t = t^{n+1}$.

When stronger coupling is needed amongst multiple operators, either for stability or accuracy, Strang splitting[44] can be employed. Strang splitting the convective

and chemical kinetic operator of the previous example would go as follows:

$$\begin{aligned}\tilde{\mathbf{Q}} &= \mathcal{L}^{chem} \mathbf{Q}^n \\ \mathbf{Q}^{n+1} &= \mathcal{L}^{conv} \tilde{\mathbf{Q}}\end{aligned}$$

which can be simply expressed in the compact notation:

$$\mathbf{Q}^{n+1} = \mathcal{L}^{conv} \mathcal{L}^{chem} \mathbf{Q}^n \quad (3.2)$$

Figure 3.2(a) illustrates how the chemical kinetic solver operates on the solution at $t = t^n$, and the convective solver operates on the updated solution in order to obtain the solution at $t = t^{n+1}$. Since Strang splitting is not a commutative operation, the ordering of the operators can indeed yield unique solutions,

$$\mathcal{L}^{chem} \mathcal{L}^{conv} \mathbf{Q}^n \neq \mathcal{L}^{conv} \mathcal{L}^{chem} \mathbf{Q}^n \quad (3.3)$$

Figures 3.2(a) and 3.2(b) illustrate how commuting the operators could yield a different solution.

3.2 Time Step Restrictions

3.2.1 Convection

For linear or linearized hyperbolic equations, the Courant-Friedrich-Levy(CFL) condition ensures that information does not propagate further than one grid cell in a given time step:

$$\Delta t_{conv} \leq \frac{\nu \Delta x}{\lambda} \quad (3.4)$$

where Δt_{conv} represents the convection-limited time step, ν is the Courant number, for linear stability $0 < \nu \leq 1$, Δx is the grid cell size, λ is the wave speed of the

convected information. For a purely convective simulation, where there is no kinetic or diffusive processes, the CFL would be sufficient for stability of the time integration.

3.2.2 Kinetics Resolution

Solving kinetics presents a different challenge in that the reaction time scale must be taken into consideration in order to determine the proper time step restriction. For the simple case of an explicit single step reaction with the form, $\dot{\omega}_p = \rho_f K e^{-\theta/T}$, the time step restriction would be determined as,

$$\Delta t_{chem} \leq |K^{-1} e^{\theta/T}| \quad (3.5)$$

In the case of an explicit complex reaction of the form of Equation 3.41,

$$\Delta t_{chem} \leq \min \left(\frac{\rho_k}{\dot{\omega}_k}, \frac{E_{int}}{\dot{\omega}_E} \right) \quad (3.6)$$

Since the kinetic source term of Equation 2.3 is often extremely stiff and $\Delta t_{chem} \sim 0$ when $\rho_k \sim 0$, an implicit approach will be taken. When a strictly implicit numerical scheme is employed, the time step restrictions for stability of Equation 3.6 are no longer required. But even though restrictions for stability are no longer required, there still exist accuracy considerations. The following *accuracy* time step restriction was introduced in the present study:

$$\Delta t_{chem} = \min \left(\epsilon_c \frac{\rho_k^*}{|\dot{\omega}_k|}, \epsilon_T \frac{E_{int}}{|\dot{\omega}_E|} \right) \quad (3.7)$$

Where ρ_k^* is the greater value of ρ_k and a floor density, ϵ_c is the maximum species creation/destruction fraction, and ϵ_T is the maximum temperature cooling/heating fraction.

3.2.3 Diffusion

When solving diffusive transport problems, which are expressed as parabolic partial differential equations of the form, $u_t = -\mu u_{xx}$, the explicit time step restriction is quite similar to that of the convective transport. The explicit time step restriction is given by,

$$\Delta t_{diff} \leq \frac{0.5\Delta x^2}{\mu} \quad (3.8)$$

where μ represents the “kinematic viscosity”. This time step can become quite constraining with the increase in the diffusivity, μ , or with moderate grid spacing reduction ($\Delta t \sim \Delta x^2$). For these reasons, spatially implicit numerical schemes will be utilized to solve problems of this type.

3.3 Explicit Runge Kutta Scheme

In order to obtain stable high order convergent solutions in time, a TVD Runge-Kutta (RK) time integrator is used. This particular version of the Runge Kutta family was implemented by Shu and Osher in [45]. For 3rd order Runge-Kutta (RK3), $\forall j$

$$\begin{aligned} \mathbf{Q}_j^{(0)} &= \mathbf{Q}_j^n \\ \mathbf{Q}_j^{(1)} &= \mathbf{Q}_j^{(0)} + L_j(\mathbf{Q}_j^{(0)}) \\ \mathbf{Q}_j^{(2)} &= \frac{3}{4}\mathbf{Q}_j^{(0)} + \frac{1}{4}\mathbf{Q}_j^{(1)} + \frac{1}{4}L_j(\mathbf{Q}_j^{(1)}) \\ \mathbf{Q}_j^{n+1} &= \frac{1}{3}\mathbf{Q}_j^{(0)} + \frac{2}{3}\mathbf{Q}_j^{(2)} + \frac{2}{3}L_j(\mathbf{Q}_j^{(2)}) \end{aligned} \quad (3.9)$$

where L_j represents the flux into the j^{th} grid cell and $\mathbf{Q}^{(k)}$ represents the conserved variables of the k^{th} step of the Runge-Kutta integration. Equation 3.9 will serve as the fluid convection operator, \mathcal{L}^{conv} , for the remainder of this study, unless otherwise stated, while the temporally and spatially integrated flux, L_j , will be determined by

Riemann solvers which will be discussed in the next sections.

3.4 Hyperbolic Solvers – Approximate Riemann Solvers

In the present study, it is imperative that the fluid convection solver be able to capture shocks without introducing dispersion or excess dissipation into the solution. Let us now recast the LHS of our governing equation, Equation 2.1, into its integral or conservative form:

$$\frac{\partial}{\partial t} \int \mathbf{Q} dV + \int \mathbf{F} dS = 0 \quad (3.10)$$

We will next assume a given grid cell is uniform in its properties, and can be approximated with its cell-averaged value. Then Equation 3.10 can take the following form:

$$\frac{\partial \mathbf{Q}}{\partial t} + \frac{1}{V} \sum_s \mathbf{F}_s dA_s = 0 \quad (3.11)$$

where \mathbf{F}_s and dA_s are the areas and normal fluxes of the s^{th} face of a given grid cell. As a building block, we will utilize Roe's scheme[46] to solve for the flux at the face, $\mathbf{F}_{i+1/2}$ as follows:

$$\mathbf{F}_{i+1/2} = \frac{1}{2} (\mathbf{F}_R + \mathbf{F}_L) - \frac{1}{2} \mathbf{R} \tilde{\Lambda} \mathbf{L} (\mathbf{Q}_R - \mathbf{Q}_L) \quad (3.12)$$

where $\mathbf{F}_{R,L}$ and $\mathbf{Q}_{R,L}$ represent the normal fluxes and conserved variables of the right and left side of the face, respectively, \mathbf{L} is the matrix of eigenvector, \mathbf{R} is the inverse of the matrix of eigenvector, and $\tilde{\Lambda}$ are the HLLE[47] conditioned eigenvalues. The eigen-system is discussed in more detail in Appendix B. For the 1st order spatial accuracy convergent Roe scheme, the right fluxes and conserved variables are, \mathbf{F}_{i+1} and \mathbf{Q}_{i+1} , respectively and the left fluxes and conserved variables are, \mathbf{F}_i and \mathbf{Q}_i ,

respectively. In the proceeding sections, the numerical schemes used to calculate high order spatially convergent conserved variable solutions will be discussed.

In order to achieve a spatially high order convergent interpolation of the conserved variables at the cell interface, $\mathbf{Q}_{R,L}$, the governing system of equations, Equation 2.1, must be linearized in the following manner:

$$\begin{aligned}\mathbf{Q}_t + \mathbf{F}_n &= 0 \\ \mathbf{Q}_t + \mathbf{A}\mathbf{Q}_n &= 0 \\ \mathbf{L}\mathbf{Q}_t + \mathbf{L}\mathbf{R}\mathbf{A}\mathbf{L}\mathbf{Q}_n &= 0 \\ \mathbf{W}_t + \mathbf{\Lambda}\mathbf{W}_n &= 0\end{aligned}\tag{3.13}$$

where $()_n$ represents the spatial derivative in an arbitrary direction, the convective flux jacobian is $\mathbf{A} = \frac{\partial \mathbf{F}}{\partial \mathbf{Q}}$ and the characteristic variable array, $\mathbf{W} = (w_1, w_2, \dots)^T$ is defined as the projection of the conserved variables, $\mathbf{W} = \mathbf{L}\mathbf{Q}$, and by definition $\mathbf{L}\mathbf{R} = \mathbf{R}\mathbf{L} = \mathbf{I}$. Now that the governing equations have been linearized with the process shown in Equation 3.13, it can now be expressed as a system of scalar hyperbolic differential equations:

$$w_t + \lambda w_n = 0\tag{3.14}$$

where the eigenvalues are the diagonal components of the matrix of eigenvalues, $\lambda_i = \Lambda_{i,i}$. After using one of the high order spatially convergent methods, which will be discussed in greater detail in the preceding sections, to approximate the characteristic variable solution at the cell interface, $\mathbf{W}_{R,L}$, the characteristic variables can be projected back to its component form using the following operation:

$$\mathbf{Q}_{R,L} = \mathbf{R}\mathbf{W}_{R,L}\tag{3.15}$$

The updated conserved variables determined from Equation 3.15 are then used to calculate the interface flux, $\mathbf{F}_{R,L}$, as well as construct a new eigensystem.

3.4.1 Weighted Essentially Non-Oscillatory (WENO) Schemes

In Weighted Essentially Non-Oscillatory (WENO) schemes, first introduced by Liu, Osher, & Chan [48], high spatial order of convergence is achieved where the solution is smooth and a spatial convergence of no greater than $O(1)$ near a discontinuity in the solution. In the present study, we utilized a 5th order spatially convergence variant of WENO which weights the contribution of three stencils, illustrated in Figure 3.3. Here we will describe how $w_{L,i+1/2}$ is computed in [48] on the basis of the ENO stencil[49]. For simplicity, the “L” subscript will be dropped. The formula for the right characteristics are symmetric and will only be shown when they vary from the left characteristics.

The r^{th} order ENO scheme chooses the “smoothest” stencil from r candidate stencils to approximate $w_{i+1/2}$. In the case of $r = 3$, the stencil S_k , where $k \in [0, 2]$, shown in Figure 3.3, happens to be chosen as the ENO interpolation stencil, the r^{th} -order ENO approximation of $w_{i+1/2}$ to produce

$$w_k = q_k^r(w_{i+k-r+1}, \dots, w_{i+k}) \quad (3.16)$$

where

$$q_k^r(g_0, \dots, g_{r-1}) = \sum_{l=0}^{r-1} a_{k,l}^r g_l \quad (3.17)$$

Here $a_{k,l}^r$, $0 \leq k, l \leq r-1$, are constant coefficients, which are provided in Table 3.1. Using the smoothest of the r^{th} stencil would be desirable near a discontinuity, but in smooth regions, information from all stencils can be used in the final solution. Thus, in smooth regions, it would be desirable to combine the ENO stencils in a manner that will generate a higher than r order solution. As shown in [48], one can use all of the r candidate stencils, which all together would contain $(2r-1)$ grid values of

$w_{i+1/2}$ to give a $(2r - 1)$ th-order approximation of w

$$w_k = q_{r-1}^{2r-1}(w_{i-r+1}, \dots, w_{i+r-1}) \quad (3.18)$$

which is the solution of a $(2r - 1)$ th-order *upstream central scheme*. Since high order upstream central schemes (in space), combined with high order Runge-Kutta methods (in time) are stable and dissipative under appropriate CFL numbers, they are convergent. Using this fact, one can now use the $(2r - 1)$ th-order upstream central scheme in smooth regions and the r^{th} order ENO scheme near discontinuities. As shown in Equation 3.16, each of the stencils can approximate $w_{i+1/2}$. If the stencil is smooth, an r^{th} order approximation of the stencil can be recovered, but if the stencil is discontinuous, a less accurate or inaccurate approximation would be recovered. So WENO assigns a weight, $\hat{\omega}_k$, to each of the candidate stencil S_k , where $k \in [0, r - 1]$, and uses these weights to combine the r different approximations to obtain the final approximation of the solution as:

$$w_{i+1/2} = \sum_{k=0}^{r-1} \hat{\omega}_k q_k^r(w_{i+k-r+1}, \dots, w_{i+k}) \quad (3.19)$$

where q_k^r is defined in Equation 3.17. To achieve essentially non-oscillatory properties, WENO requires that the weights adapt to the relative smoothness of w . Discontinuous stencils contributions should be assigned weights of zero. In the smooth regions the weights should be adjusted so the upstream central scheme, Equation 3.18, is recovered.

In the present study, the 5^{th} order WENO(WENO5) scheme ($r = 3$) is utilized

as prescribed by Jiang and Shu in [45]. The stencils, S_k , are calculated as:

$$\begin{aligned} S_0(w_{i-2}, w_{i-1}, w_i) &= \frac{1}{6} (2w_{i-2} - 7w_{i-1} + 11w_i) \\ S_1(w_{i-1}, w_i, w_{i+1}) &= \frac{1}{6} (-1w_{i-1} + 5w_i + 2w_{i+1}) \\ S_2(w_i, w_{i+1}, w_{i+2}) &= \frac{1}{6} (2w_i + 5w_{i+1} - 1w_{i+2}) \end{aligned} \quad (3.20)$$

And the right solution is stencils, S_k^R are calculated as:

$$\begin{aligned} S_0^R(w_{i+3}, w_{i+2}, w_{i+1}) &= \frac{1}{6} (2w_{i+3} - 7w_{i+2} + 11w_{i+1}) \\ S_1^R(w_{i+2}, w_{i+1}, w_i) &= \frac{1}{6} (-1w_{i+2} + 5w_{i+1} + 2w_i) \\ S_2^R(w_{i+1}, w_i, w_{i-1}) &= \frac{1}{6} (2w_{i+1} + 5w_i - 1w_{i-1}) \end{aligned} \quad (3.21)$$

The smoothness of each stencil is then calculated as:

$$\begin{aligned} IS_0 &= \frac{13}{12} (w_{i-2} - 2w_{i-1} + w_i)^2 + \frac{1}{4} (w_{i-2} - 4w_{i-1} + 3w_i)^2 \\ IS_1 &= \frac{13}{12} (w_{i-1} - 2w_i + w_{i+1})^2 + \frac{1}{4} (w_{i-1} - w_{i+1})^2 \\ IS_2 &= \frac{13}{12} (w_i - 2w_{i+1} + w_{i+2})^2 + \frac{1}{4} (3w_i - 4w_{i+1} + w_{i+2})^2 \end{aligned} \quad (3.22)$$

The smoothness of each stencil for the right solution is then calculated as:

$$\begin{aligned} IS_0^R &= \frac{13}{12} (w_{i+3} - 2w_{i+2} + w_{i+1})^2 + \frac{1}{4} (w_{i+3} - 4w_{i+2} + 3w_{i+1})^2 \\ IS_1^R &= \frac{13}{12} (w_{i+2} - 2w_{i+1} + w_i)^2 + \frac{1}{4} (w_{i+2} - w_i)^2 \\ IS_2^R &= \frac{13}{12} (w_{i+1} - 2w_i + w_{i-1})^2 + \frac{1}{4} (3w_{i+1} - 4w_i + w_{i-1})^2 \end{aligned} \quad (3.23)$$

We can now calculate the new weights, $\hat{\omega}'_k$, based on the smoothness, IS_k , and the optimal weights, $\hat{\omega}_k^{opt}$, which are defined as $\hat{\omega}^{opt} = (\frac{3}{10}, \frac{6}{10}, \frac{1}{10})$ for approximation of w by using the procedure from [45],

$$\hat{\omega}'_k = \frac{\hat{\omega}_k^{opt}}{(\epsilon + IS_k)^2} \quad (3.24)$$

where $\epsilon = 10^{-6}$ is there to guarantee non-singular behavior. These new weights, $\hat{\omega}'_k$, are then normalized to become the final WENO weights:

$$\hat{\omega}_k = \frac{\hat{\omega}'_k}{\sum_{z=0}^2 \hat{\omega}'_z} \quad (3.25)$$

where $\sum_k \hat{\omega}_k = 1$. The weighted solutions from each stencil are then summed, in the same manner as Equation 3.18, to form our WENO5 approximated solution:

$$w_{i+1/2} = \sum_{k=0}^2 \hat{\omega}_k q_k^5 \quad (3.26)$$

After all characteristics at all of the cell interfaces are calculated, the characteristics are then projected back to real space using Equation 3.15 then the final flux at the cell interface, $\mathbf{F}_{i+1/2}$, is determined by Equation 3.12 using the updated approximations to the conserved variables.

3.4.2 Monotonicity Preserving (MP) Schemes

The Monotonicity Preserving (MP) scheme, first introduced by Suresh & Huynh[50], uses a high order spatially convergent reconstruction of the interface, the original value, then limits this solution in order to obtain the final interface value. We will adopt the notation of the previous section and drop the “L” subscript for solutions at the face. For the 5th order MP scheme (MP5), which will be used throughout the present study, the original value, $w_{i+1/2}^{OR}$, is given as:

$$w_{i+1/2}^{OR} = (2w_{i-2} - 13w_{i-1} + 47w_j + 27w_{i+1} - 3w_{i+2}) / 60 \quad (3.27)$$

To find the MP5 solution, a few constraints must be satisfied. The first constraint is *monotonicity*-preservation, which Suresh & Huynh [50] define as the upper limit,

$$w^{UL} = w_i + \alpha(w_i - w_{i-1}) \quad (3.28)$$

where $\alpha = 2$, represents a parabolic reconstruction. The second constraint, *accuracy*-preserving, is accomplished by bounding the solution with the median and large curvature solutions. The median (denoted by superscript “MD”) value at the interface, $x_{i+1/2}$, is given by

$$w^{MD} = w^{AV} - \frac{1}{2}d_{i+1/2}^{MD} \quad (3.29)$$

While the large curvature (denoted by superscript “LC”) value at the interface is given by

$$w^{LC} = w_i + \frac{1}{2}(w_i - w_{i-1}) + \frac{\beta}{3}d_{i-1/2}^{LC} \quad (3.30)$$

where $\beta = 4$, w^{AV} is the average solution, d_i is the curvature, and $d_{i+1/2}^{LC}$ is the minmod approximation of the curvature at the zone boundary, all of which are defined as follows:

$$\begin{aligned} w^{AV} &= \frac{1}{2}(w_i + w_{i+1}) \\ d_i &= w_{i-1} + w_{i+1} - 2w_i \\ d_{i+1/2}^{MM} &= \text{minmod}(d_i, d_{i+1}) \end{aligned} \quad (3.31)$$

The superscript “MM” indicates the use of a minmod function. Suresh & Huynh[50] recommended the use of a slightly more restrictive curvature measure than $d_{i+1/2}^{MM}$, which is given by:

$$d_{i+1/2}^{M4} = \text{minmod}(4d_i - d_{i+1}, 4d_{i+1} - d_i, d_i, d_{i+1}) \quad (3.32)$$

For the MP5 scheme $d_{i+1/2}^{MD} = d_{i+1/2}^{LC} = d_{i+1/2}^{M4}$. Now that the mechanisms for the two constraints, *monotonicity*-preserving and *accuracy*-preserving, have been stated, the minimum and maximum value of the solution, w^{MIN} and w^{MAX} , respectively, are given by:

$$\begin{aligned} w^{MIN} &= \max [\min(w_i, \min(w_{i+1}, w^{MD})), \min(w_i, \min(w^{UL}, w^{LC}))] \\ w^{MAX} &= \min [\max(w_i, \max(w_{i+1}, w^{MD})), \max(w_i, \max(w^{UL}, w^{LC}))] \end{aligned} \quad (3.33)$$

The solution at the face, $w_{i+1/2}$, can now simply be expressed as:

$$w_{i+1/2} = \text{median} (w_{i+1/2}^{OR}, w^{MIN}, w^{MAX}) \quad (3.34)$$

The 5th order convergent Monotonicity Preserving WENO (MW5) scheme by Balsara & Shu [51], which is based on the MP5 scheme, has the smooth solution of WENO5, but is strictly monotonicity-preserving near discontinuities. Balsara & Shu were able to demonstrate that the solutions to ideal MHD simulations were far superior to that of MP5 and WENO5. The form of the MW5 solution is the same MP5, Equation 3.34, but the key difference is in how MW5 is used to determine the original value, w^{OR} , and the curvature at the median and large curvature values, d^{MD} and d^{LC} , respectively. By using the WENO stencils for $r = 3$, Equation 3.20 with WENO coefficients from Table 3.1, and the optimal weights, the MW5 original value, w^{OR} , is recovered:

$$w^{OR} = (6w_{i-2} - 27w_{i-1} + 65w_i + 17w_{i+1} - w_{i+2}) / 60 \quad (3.35)$$

In an attempt to filter out extremal features with small domains of support, while keeping extremal features with large domains of support intact, $d_{i+1/2}^{MD} = d_{i+1/2}^{LC} = d_{i+1/2}^{M4X}$, where

$$d_{i+1/2}^{M4X} = \text{minmod} (4d_i - d_{i+1}, 4d_{i+1} - d_i, d_i, d_{i+1}, d_{i-1}, d_{i+2}) \quad (3.36)$$

3.4.3 Advection-Diffusion-Reaction (ADER) Schemes

The Advection-Diffusion-Reaction (ADER) schemes of Titarev & Toro [52] utilize high order spatial derivatives calculated by the underlying scheme to generate the

temporal derivatives using the Cauchy-Kovalevskaya procedure:

$$\begin{aligned}
\partial_t w &= -\lambda \partial_x w \\
\partial_{tt} w &= \lambda^2 \partial_{xx} w \\
\partial_{ttt} w &= -\lambda^3 \partial_{xxx} w \\
&\vdots \\
\partial_t^{(k)} w &= (-\lambda)^k \partial_x^{(k)} w
\end{aligned} \tag{3.37}$$

Where λ is the characteristic wave speed. With the high order temporal derivatives generated from Equation 3.37, a simple Taylor series expansion is performed to acquire a higher order temporally and spatially convergent scheme. But first, we must take the temporal series expansion at the interface,

$$w_{i+1/2} = \tilde{w} + \sum_{k=1}^{m-1} \partial_t^{(k)} \tilde{w} \frac{\tau^k}{k!} \tag{3.38}$$

Where τ is the time step size and $\tilde{w} = w(x_{i+1/2}, 0^+)$ is the approximation of the solution at the interface from the underlying scheme. In the present study, we wish to achieve 3^{rd} order convergence in time, so we will start from Equation 3.38 with $m = 3$ to give,

$$w_{i+1/2} = \tilde{w} + \partial_t \tilde{w} \tau + \partial_{tt} \tilde{w} \frac{\tau^2}{2} \tag{3.39}$$

By performing the Cauchy-Kovalevskaya procedure on Equation 3.39, the solution, $w_{i+1/2}$, will become a function of the time step size and spatial derivatives of the approximate solution as follows:

$$w_{i+1/2} = \tilde{w} - \lambda \partial_x \tilde{w} \tau + \lambda^2 \partial_{xx} \tilde{w} \frac{\tau^2}{2} \tag{3.40}$$

Equation 3.40 will serve as the general form of the temporally 3^{rd} order convergent ADER (ADER3) scheme. Since the expensive Runge-Kutta time integration steps

are no longer required, ADER schemes are extremely efficient and well suited for parallel computation.

By combining the 5th order spatially convergent WENO5's reconstruction to calculate the approximate solution and its spatial derivatives, \tilde{w} and $\partial_x^{(k)}\tilde{w}$, respectively, with the 3rd order temporally convergent ADER3, we form the 3rd order temporal and 5th order spatial convergent ADER-WENO (AW5) scheme [53]. At discontinuities, $\partial_x^{(k)}\tilde{w} = 0 \quad \forall \quad k > 1$ is satisfied in order to prevent spurious oscillations.

3.5 Point-Implicit Euler

The finite rate kinetic systems in the present study are extremely stiff. When solving a stiff ODE, it is often beneficial to solve the problem implicitly. The stiff chemical kinetics ODEs will be expressed in the form of Equation 2.3:

$$\frac{d\mathbf{Q}}{dt} = \dot{\mathbf{\Omega}}_{kinetic} \quad (3.41)$$

where \mathbf{Q} and $\dot{\mathbf{\Omega}}_{kinetic}$ are defined by Equation 2.16. The 1st order point-implicit Euler will be utilized to solve problems of this particular form. First, let us discretize the time into uniform intervals of size Δt and denote $t^n = t_0$ and $t^{n+1} = t_0 + \Delta t$. Upon discretization, a Taylor series expansion can be performed on Equation 3.41 and is expressed as follows:

$$\begin{aligned} \frac{\Delta \mathbf{Q}}{\Delta t} &= \dot{\mathbf{\Omega}}^{n+1} \\ \frac{\Delta \mathbf{Q}}{\Delta t} &= \dot{\mathbf{\Omega}}^n + \frac{\partial}{\partial t} \dot{\mathbf{\Omega}}^n \Delta t \\ \frac{\Delta \mathbf{Q}}{\Delta t} &= \dot{\mathbf{\Omega}}^n + \frac{\partial}{\partial \mathbf{Q}} \dot{\mathbf{\Omega}}^n \frac{\partial}{\partial t} \mathbf{Q} \Delta t \\ \frac{\Delta \mathbf{Q}}{\Delta t} &= \dot{\mathbf{\Omega}}^n + \frac{\partial \dot{\mathbf{\Omega}}^n}{\partial \mathbf{Q}} \Delta \mathbf{Q} \end{aligned} \quad (3.42)$$

Then we shall proceed and solve for the change in the conserved variables, $\Delta \mathbf{Q}$, and arrive with the following form:

$$\Delta \mathbf{Q} = \left(\mathbf{I} - \frac{\partial \dot{\mathbf{Q}}^n}{\partial \mathbf{Q}} \Delta t \right)^{-1} \dot{\mathbf{Q}}^n \Delta t \quad (3.43)$$

From here we arrive at the solution to our implicit formulation as:

$$\mathbf{Q}^{n+1} = \mathbf{Q}^n + \left(\mathbf{I} - \frac{\partial \dot{\mathbf{Q}}^n}{\partial \mathbf{Q}} \Delta t \right)^{-1} \dot{\mathbf{Q}}^n \Delta t \quad (3.44)$$

This can also be expressed in the operator form: $\mathbf{Q}^{n+1} = \mathcal{L}^{chem} \mathbf{Q}^n$, where the operator is defined as:

$$\mathcal{L}^{chem} = 1 + \left(\mathbf{I} - \frac{\partial \dot{\mathbf{Q}}^n}{\partial \mathbf{Q}} \Delta t \right)^{-1} \frac{\partial \dot{\mathbf{Q}}^n}{\partial \mathbf{Q}} \Delta t \quad (3.45)$$

3.6 Spatial-Implicit Euler

Diffusive MHD transport will often have much stricter explicit time step restrictions, Equation 3.8, than that of convective transport, Equation 3.4. Since the maximum allowable explicit diffusive time step is determined by $\Delta t \leq 0.5 \Delta x^2 \sigma_{min} \mu_0$, it becomes apparent that as $\sigma \rightarrow 0$ then $\Delta t \rightarrow 0$. This can become quite cost prohibitive, so in order to ensure stability with a non prohibitive time step, an implicit time marching scheme is utilized.

Before we can cast the diffusive MHD transport into an implicit formulation, we must start from the magnetic diffusion flux formulation of the RHS, Equation 2.34, and define the magnetic field diffusion Jacobian, A'' , for the dimensionally split

magnetic diffusion as

$$\frac{\partial \mathbf{Q}}{\partial t} = \frac{\partial}{\partial x} \left(A_x^\nu \frac{\partial \mathbf{Q}}{\partial x} \right) \quad (3.46)$$

where the magnetic field diffusion Jacobian, $A_x^\nu = \frac{\partial \mathbf{F}_x^\nu}{\partial \mathbf{Q}}$,

$$A_x^\nu = \frac{1}{\mu_0 \sigma} \begin{pmatrix} 1 & 0 & 0 & 0 \\ 0 & 1 & 0 & 0 \\ 0 & 0 & 1 & 0 \\ -\frac{B_x}{\mu_0} & 0 & 0 & 1 \end{pmatrix}$$

Assuming a one-dimensional discretization on a uniformly-spaced grid, the spatial derivatives can be approximated by finite-differences and the subscript in A_x^ν will be ignored, thereby reducing the PDE to a system of ODE's,

$$\frac{d\mathbf{Q}_i}{dt} = \frac{1}{\Delta x^2} \left(A_{i+\frac{1}{2}}^\nu \mathbf{Q}_{i+1} - (A_{i+\frac{1}{2}}^\nu + A_{i-\frac{1}{2}}^\nu) \mathbf{Q}_i - A_{i-\frac{1}{2}}^\nu \mathbf{Q}_{i-1} \right) \quad (3.47)$$

the system of equations can be written in matrix notation as

$$\frac{\partial \vec{\mathbf{Q}}}{\partial t} = \tilde{\Phi} \vec{\mathbf{Q}} \quad (3.48)$$

where $\tilde{\Phi}$ is a tridiagonal matrix and $\vec{\mathbf{Q}}$ is the spatial vector of the conserved element array,

$$\tilde{\Phi} = \frac{1}{\Delta x^2} \begin{pmatrix} \ddots & & & & \\ & \ddots & & & \\ & & -A_{i-\frac{1}{2}}^\nu & (1 + A_{i-\frac{1}{2}}^\nu + A_{i+\frac{1}{2}}^\nu) & -A_{i+\frac{1}{2}}^\nu \\ & & \ddots & \ddots & \ddots \end{pmatrix}, \quad \vec{\mathbf{Q}} = \begin{pmatrix} \vdots \\ \mathbf{Q}_{i-1} \\ \mathbf{Q}_i \\ \mathbf{Q}_{i+1} \\ \vdots \end{pmatrix} \quad (3.49)$$

Now, we can determine the implicit formulation by evaluating the RHS of Eqn. 3.48 at time $t + \Delta t$,

$$\vec{Q}^{n+1} = \vec{Q}^n + \Delta t \tilde{\Phi} \vec{Q}^{n+1} \quad (3.50)$$

By applying backwards Euler to Equation 3.50, one can recover the operator form, $\vec{Q}^{n+1} = \mathcal{L}_\alpha^{diff} \vec{Q}^n$, where the MHD diffusion matrix operator for the α -direction is

$$\mathcal{L}_\alpha^{diff} = \left(1 - \Delta t \tilde{\Phi}_\alpha\right)^{-1} \quad (3.51)$$

In order to apply the diffusive MHD transport in all directions, one might perform the following operation:

$$\mathbf{Q}^{n+1} = \mathcal{L}_x^{diff} \mathcal{L}_y^{diff} \mathcal{L}_z^{diff} \mathbf{Q}^n \quad (3.52)$$

Upon inspection of Equation 3.49, \mathcal{L}^{diff} is merely the inverse of a tridiagonal system of equations. Rather than applying a scheme with a relatively high computation cost, i.e. GMRes or Gaussian Elimination, one can exploit the fact the system is tridiagonal and implement Thomas' Algorithm, which is discussed in more detail in Appendix F.1.

The diffusive MHD operators, $\mathcal{L}_\alpha^{diff}$, use line relaxation to proceed in time. If the grid and fluid properties, i.e. conductivity, grid resolution, etc., are not spatially uniform the diffusive MHD transport will have different time scales for each directional sweep. When this occurs, it becomes necessary to split a given operator, \mathcal{L}_x , in time using the Strang operator splitting technique demonstrated in Section 3.1. The superscript 'diff' has been discarded for the remainder of this section. One permutation of applying multiple spatial operators to a generic 2D diffusive MHD problem would go as follows:

$$\mathbf{Q}^{n+1} = \mathcal{L}_x^{\Delta t/2} \mathcal{L}_y^{\Delta t} \mathcal{L}_x^{\Delta t/2} \mathbf{Q}^n \quad (3.53)$$

which is illustrated in Figure 3.4(a). In order to avoid developing a bias toward a particular direction, after applying Equation 3.53 one should use the following:

$$\mathbf{Q}^{n+2} = \mathcal{L}_y^{\Delta t/2} \mathcal{L}_x^{\Delta t} \mathcal{L}_y^{\Delta t/2} \mathbf{Q}^{n+1} \quad (3.54)$$

which is illustrated in Figure 3.4(b). A similar permutation can be performed when solving a 3-D diffusive MHD problem.

r	k	$l = 0$	$l = 1$	$l = 2$
2	0	-1/2	3/2	
	1	1/2	1/2	
3	0	1/3	-7/6	11/6
	1	-1/6	5/6	1/3
	2	1/3	5/6	-1/3

Table 3.1: WENO Coefficients, $a_{k,l}^r$

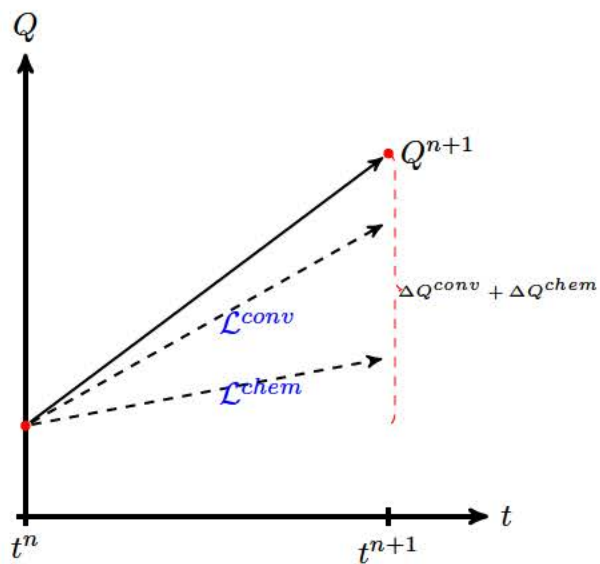


Figure 3.1: Operator splitting of two generic operators, \mathcal{L}^{chem} & \mathcal{L}^{conv} .

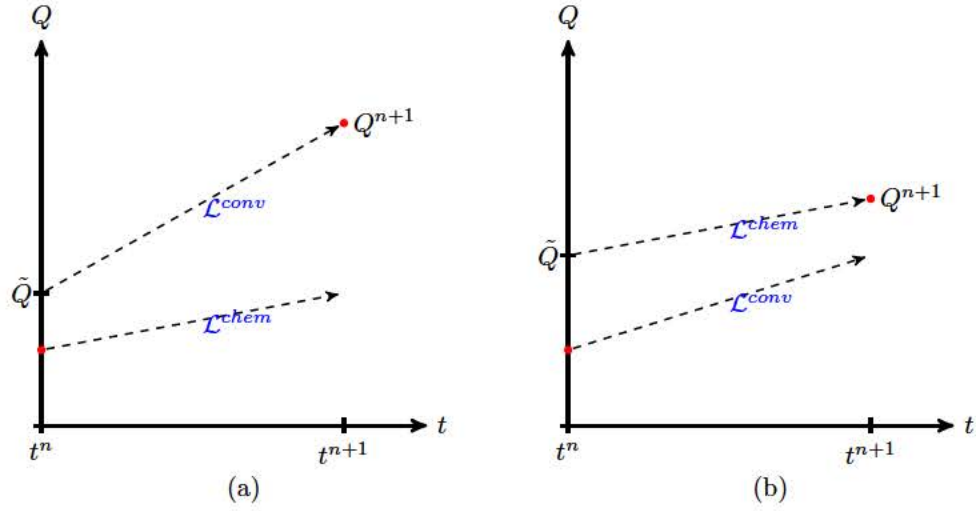


Figure 3.2: Demonstration that with Strang splitting coupled operators, the ordering of the operators can significantly change the solution.

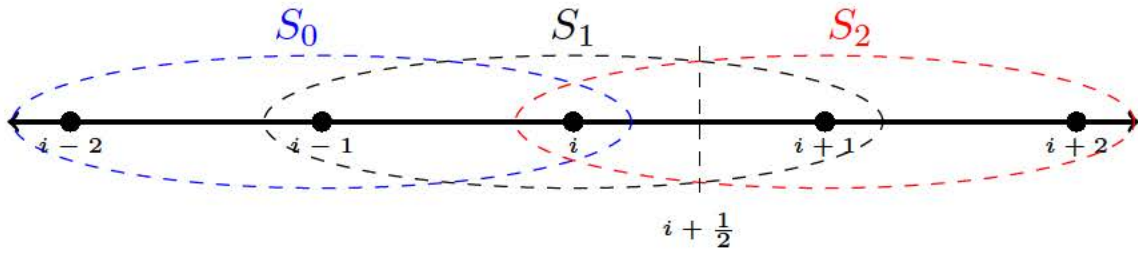


Figure 3.3: WENO stencil for $r = 3$.

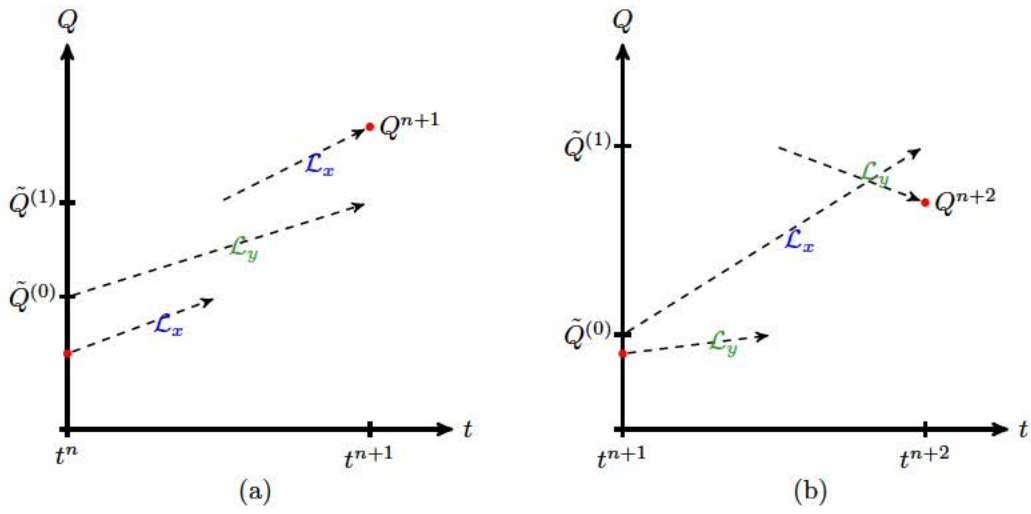


Figure 3.4: Strang operator splitting in time for three operations illustrated with different ordering of the operators, \mathcal{L}_x and \mathcal{L}_y .

CHAPTER 4

Verification of Numerical Schemes

The numerical schemes used in the present study must be validated and verified to ensure their accuracy and proper usage. The 1-dimensional, 2-dimensional, and 3-dimensional forms of the hydrodynamic and magnetohydrodynamic governing equations assume the form of Equation 2.1:

$$\frac{\partial \mathbf{Q}}{\partial t} + \nabla_n \cdot \mathbf{F} = \dot{\mathbf{\Omega}}$$

For the 1-D subset of the governing equations, the variation in the y- and z-dimensions are set to zero, $\frac{\partial}{\partial y} \equiv 0$ and $\frac{\partial}{\partial z} \equiv 0$, respectively. While in the 2-D subset of the governing equations, there is no variation in the z-direction, $\frac{\partial}{\partial z} \equiv 0$.

4.1 Inviscid Hydrodynamics

The hydrodynamic test cases will show that the physical wave (acoustic and entropy) speeds present in the simulation are properly captured and that the approximate Riemann solution matches the proper jump conditions in the event of a shock. In the hydrodynamic limit the conserved variables, \mathbf{Q} , and flux, \mathbf{F} , are expressed as

Equation 2.5:

$$\mathbf{Q} = \begin{pmatrix} \rho \\ \rho \mathbf{u} \\ E \end{pmatrix} \quad \mathbf{F} = \begin{pmatrix} \rho u_n \\ \rho \mathbf{u} \cdot u_n + P \mathbf{n} \\ (E + P) u_n \end{pmatrix}$$

4.1.1 Sod's Shock Tube

There are a few classic test cases performed utilizing our Riemann solvers, in order to test their ability to resolve shocks, contact discontinuities, and rarefactions as well as the interactions of these structures. The first test case was introduced by Sod [54], known presently as Sod's shock tube. We will adopt the same initial and boundary conditions. The left and right states are

$$\begin{aligned} (\rho_L, u_{x,L}, P_L) &= (1 \text{ kg/m}^3, 0 \text{ m/s}, 1 \text{ Pa}) & x < 0 \\ (\rho_R, u_{x,R}, P_R) &= (0.125 \text{ kg/m}^3, 0 \text{ m/s}, 0.1 \text{ Pa}) & x > 0 \end{aligned} \quad (4.1)$$

where the adiabatic index, $\gamma \equiv 1.4$, unless otherwise stated, and over a domain $x \in (-5, 5] \text{ mm}$. Figure 4.1(a) shows the solution for the schemes at $t = 200 \text{ } \mu\text{s}$ which contains a single shock, contact discontinuity and rarefaction. The figure clearly shows that all of the schemes used resolved the problem reasonably well compared to the exact solution. Figure 4.1(b) illustrates MW5 solution converging to the exact solution at the contact discontinuity as Δx is decreased.

4.1.2 Hydrodynamical Interacting Blast Wave Problem

Blast waves are generally described as strong and rapid release of energy which are often characterized by regions containing drastic temperatures and pressure rises. For the second test of our 1D hydrodynamic test problems, we ran the interacting

blast wave problem which was first proposed by Woodward and Collela [55]. The problem consist of the left, middle, and right initial states, L, M, and R respectively, which are as follows:

$$\begin{aligned}
(\rho_L, u_{x,L}, P_L) &= (1, 0, 10^3) & x < 0.1 \\
(\rho_M, u_{x,M}, P_M) &= (1, 0, 10^{-2}) & 0.1 < x < 0.8 \\
(\rho_R, u_{x,R}, P_R) &= (1, 0, 10^2) & x > 0.8
\end{aligned} \tag{4.2}$$

where $x \in (0, 1]$. Figure 4.2 shows the density profiles at $t = 38$ seconds using the MP5, AW5, and MW5 schemes with greater detail in Figure 4.3. While all of the schemes resolve the shocks at $x \approx 0.65$ & 0.87 reasonably well, the contact discontinuities at $x \approx 0.75$ & 0.8 are slightly better resolved by MP5. None of the schemes used artificial compression methods.

4.1.3 Shock-Entropy Wave Interaction

In the last of our 1-D hydrodynamic test cases, we wish to test our numerical schemes ability to resolve smooth flow disturbances which is of particular interest because of the nature of the problems in the present study. The Shu-Osher problem [56] has been extensively used to simulate a Mach 3 shock wave interacting with an oscillatory density disturbance which generates a flow field with a combination of smooth structures and discontinuities. The initial conditions are given for the left and right state as follows:

$$\begin{aligned}
(\rho_L, u_{x,L}, P_L) &= (3.857143, 2.629369, 10.33333) & x < 0.8 \\
(\rho_R, u_{x,R}, P_R) &= (1 + 0.2\sin(5\pi x), 0, 1) & x > 0.8
\end{aligned} \tag{4.3}$$

where $x \in (-1, 1]m$. From the density profile in Figure 4.4(a) at $t = 360ms$, one can see that three schemes resolved the entropy disturbances quite well. Upon closer

inspection, Figure 4.4(b) clearly shows that while AW5 was slightly diffused and MW5 slightly amplified, MP5 was clearly able to resolve the transient entropy waves the best.

4.1.4 Shock Diffraction Down a Backward Facing Step

The next test problem describes the diffraction of a Mach 2.4 shock down a backward facing step[57]. The strong rarefaction generated by the diffraction at the 90° corner often results in numerical errors described by over-expansion and negative pressure for many Riemann solvers[58]. The problem is simulated using a resolution of $\Delta x = \Delta y = \frac{1}{1024}$ with the MW5 solver. The numerical simulation is shown side-by-side with the experimental images in Figure 4.5. The numerical solution is presented using a Schlieren-type plot as prescribed by [58] which uses density gradients in an analogous way to index of refraction gradients, which makes it ideal for comparison with experimental images. The figure shows that the MW5 scheme was able correctly reproduce the flow features in the region of the rarefaction.

4.1.5 Rayleigh-Taylor Hydrodynamic Instability

In the next test, a heavy fluid is supported by a lighter fluid in a gravitational field, or equivalent, which accelerates the heavier fluid into a lighter fluid. This condition is unstable once the interface between the two fluids is perturbed. The instability is known as the Rayleigh-Taylor(RT) instability. Earlier analytical investigations date back to the detailed analysis given by Chandrasekhar[59].

In the initial configuration, two fluids with a prescribed density ratio ($\rho_L/\rho_U = 2$) are left to evolve between two planes ($y = -1$ m and $y = +1$ m), with gravity oriented

in the upward direction ($\mathbf{g} = \{0, +1\}^T$). The boundaries are adiabatic solid walls. The remainder of the fluid initial conditions above and below the diaphragm, U & L respectively, are found in Table 4.1. The solutions produced by the MP5, AW5, and MW5 scheme were compared for this problem against the test solution at various times in Figures 4.6-4.9. From these figures, it becomes quite clear that sharp features and rolled up vortices in the MW5 solution are far superior to that of the solutions produced by MP5 and AW5.

4.2 Ideal Magnetohydrodynamics(MHD)

The ideal MHD test cases will demonstrate that the physical waves (entropy, fast & slow magneto-acoustic, and Alfvén) are properly captured under various configurations by the present schemes.

4.2.1 1D MHD Shock Tube Problems

The Brio-Wu problem [60] was used to ensure the numerical scheme sufficiently captured all of the important features, ie, a contact discontinuity, fast shock, fast rarefaction, compound wave, and slow shock. The initial conditions are analogous to Sod's shock tube problem where the initial left and the right states are as follows:

$$\begin{aligned} (\rho_l, u_{x,l}, u_{y,l}, u_{z,l}, B_{x,l}, B_{y,l}, B_{z,l}, P_l) &= (0.1, 0, 0, 0, 0.75, -1, 0, 1) \quad x < 0 \\ (\rho_r, u_{x,r}, u_{y,r}, u_{z,r}, B_{x,r}, B_{y,r}, B_{z,r}, P_r) &= (1, 0, 0, 0, 0.75, +1, 0, 10) \quad x > 0 \end{aligned} \quad (4.4)$$

where $\gamma \equiv 2$ and $x \in (-1, 1]$. Figure 4.10 - 4.15 show the distributions of various fluid properties at the solution time, $t = 0.1$. Figure 4.11(a) shows a zoom in of the compound wave at $x \approx -0.03m$. From this figure, it is clear that the MW5

scheme is able to resolve the major features (compound wave, fast & slow rarefaction) better than MP5 & AW5. All of the schemes (MP5, AW5, & MW5) resolve the contact discontinuity fairly well, shown in Figure 4.11(b). The undershoot observed in the velocity profile, Figure 4.12(a), at $x \approx 0.35$ m is a well documented feature in literature for higher order MHD schemes at magneto-sonic points; Jiang and Shu [61] suggest performing the test problem in a moving reference frame in order to suppress the oscillations.

4.2.2 Orszag-Tang Problem

Various 2D MHD test cases were performed to ensure that the solver correctly captured all physical waves and to ensure the solution remains divergence free, $\nabla \cdot \mathbf{B} \equiv 0$. The divergence cleaning procedure used when performing MHD simulations is given in Appendix C. The first numerical test case is that of the Orszag-Tang vortex problem, first introduced by Orszag & Tang[62]. This is a well-known model problem for testing the transition to supersonic 2D MHD turbulence. The initial conditions of the problem are given by:

$$(\rho, u_x, u_y, B_x, B_y, P) = (2.778, -\sin(y), \sin(x), -\sin(y)\sqrt{\mu_0}, \sin(2x)\sqrt{\mu_0}, 1.667) \quad (4.5)$$

where $\gamma \equiv \frac{5}{3}$. The problem is set on a periodic domain with the dimensions $x : y \in [0, 2\pi)m : [0, 2\pi)m$. Figure 4.16 shows the temperature distribution of the solutions at $t = 3s$. Although the images illustrated appear similar, upon further inspection the flow features in Figures 4.16(a) & (c) are sharper than those in Figure 4.16(b).

4.2.3 Balsara’s Rotor Problem

The following test, which was originally introduced by Balsara & Spicer[63], consists of the propagation of strong torsional Alfvén waves into an ambient fluid. The problem consists of a dense, rapidly spinning cylinder of fluid (the rotor) surrounded by a light, stationary fluid (ambient fluid). Because there is no diffusive transport in this problem, the two fluids are connected by an initially uniform magnetic field. The rapidly spinning rotor causes torsional Alfvén waves to propagate into the ambient fluid, which will lead to a decrease of angular momentum in the rotor. The magnetic field is strong enough that as it wraps itself around the rotor, the increased magnetic pressure will compress the rotor into an oblong shape. Balsara & Spicer applied a slight taper to the initial density and velocity of the rotor as to avoid generating strong start-up transient from the computational scheme. The computation domain is described by $x : y \in [0, 1] : [0, 1]$ and the initial conditions are described in Table 4.2.

At the solution time, $t = 0.295$ s, MW5 and MP5 shown in Figures 4.17 & 4.18, respectively, agree quite well with the results of Balsara & Spicer[63] using $CFL = 0.3$, while AW5 is unstable at this CFL number. Figure 4.19 illustrates that AW5 can remain stable and resolve Balsara’s rotor problem quite well by reducing the CFL to 0.15.

4.2.4 Rayleigh Taylor MHD Instability

Equally as important as the stability of the chemical processes is that of the stability of the MHD. As previously demonstrated in Section 4.1.5, Rayleigh-Taylor Instabilities (RTI) can arise from infinitesimal disturbances in amplitude and grow because

of the gradient in the applied force, e.g., a buoyant force. In [59], Chandrasekhar analytically demonstrated RTI with a uniform tangential magnetic field in both fluids, where the stability growth rate is:

$$n^2 = gk \frac{\rho_2 - \rho_1}{\rho_2 + \rho_1} - \frac{\mathbf{B}^2 k^2 \cos^2 \theta}{2\pi(\rho_2 + \rho_1)} \quad (4.6)$$

where k is the wave number, n is the growth rate, and θ is the angle between \mathbf{B} and \mathbf{k} . The critical strength of a magnetic field to suppress instability of a mode of wavelength λ is:

$$\mathbf{B}_c = \frac{\sqrt{g\lambda(\rho_2 - \rho_1)}}{\cos \theta} \quad (4.7)$$

Similarly, the critical wavelength for a given strength of a magnetic field can be expressed as:

$$\lambda_c = \frac{\mathbf{B}^2 \cos^2 \theta}{g(\rho_2 - \rho_1)} \quad (4.8)$$

where $\lambda < \lambda_c$ are suppressed.

As specified by Remacle et al.[64], a domain with dimensions $x : y \in [0, 0.25]m : [-0.5, 0.5]m$ is enclosed by reflective, adiabatic walls. The heavy, upper fluid is separated from the light, lower fluid at $y = 0.01\cos(8\pi x)$. The acceleration due to gravity is $\mathbf{g} = \{0, -1\}^T$. The initial conditions of the fluid are listed in Table 4.1. Figures 4.20(a) - (c) show the solution of the density distribution of MW5, MP5, and AW5, respectively, at $t = 2$ s with grid resolution $\Delta x = \Delta y = \frac{1}{400}m$. Due to the lack of rolled up vortices in Figure 4.20(c), AW5 cannot properly resolve the instability of the current problem. Thus, only MW5 and MP5 will be used in the next portion of the test.

The suppression of the instability growth with tangential magnetic field strengths of $B_x = 0, 0.2B_c, 0.5B_c$, and $0.8B_c$ at $t = 2$ s using MW5 & MP5, respectively, is

illustrated in Figures 4.21 & 4.22 . The illustrations support the well established theory of Chandrasekhar[59] that there is a critical tangential magnetic field that will suppress a perturbations growth in this particular test case. A normal magnetic field with the strengths $B_y = 0.5B_c$, $1.5B_c$, and $2B_c$ are illustrated at $t = 2$ s in Figures 4.23 & 4.24. The normal magnetic field did not have a significant affect on the growth of the instabilities until a larger field was applied relative to the tangential field strength, which is confirmed by Jun et al.[65]. Additionally, Jun et al. show that the growth of the instability in the nonlinear regime is enhanced by the normal field up to a certain field strength.

4.3 Two-Temperature(2T) Model

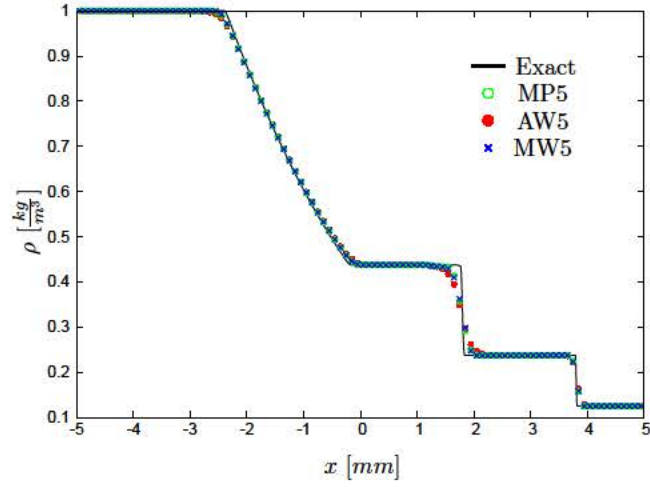
When there is significant ionization due to shocks or non-isentropic processes, the electron temperature, T_e , is adiabatic and must relax to the translational temperature of the heavy particles, T_h . Next, we present a 1D test case of a Mach 10 fully ionized plasma of argon passing through a normal shock. Figure 4.25(a) illustrates the electron and heavy particle temperatures when they are conserved separately and are not allowed to relax toward equilibrium, while Figure 4.25(b) illustrates the electron and heavy particle temperatures relaxing via electron-ion collisions toward equilibrium. In these figures we see that MP5 is able properly conserve electron entropy as well relax to the correct equilibrium temperature, $T_e = T_h = 7800K$.

	upper part	lower part
ρ	2	1
P	$2 - 2y$	$2 - y$
u_x	$\epsilon_x \sin(8\pi x) \cos(\pi y) \sin^{\tau-1}(\pi y)$	same as upper part
u_y	$-\epsilon_y \cos(8\pi x) \sin^\tau(\pi y)$	same as upper part

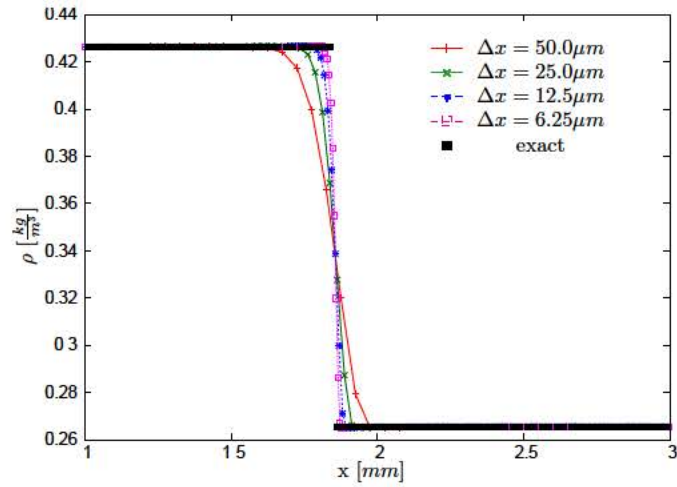
Table 4.1: RTI problem hydrodynamic initial conditions as specified by Remacle et al.[64] where $\tau = 6$, $M_0 = 0.1$, $\epsilon_y = M_0 \sqrt{\gamma/2}$, and $\epsilon_x = -\epsilon_y \tau/16$.

	$r < r_0$	$r_0 < r < r_1$	$r > r_1$
ρ	10	1	$1 + 9f$
P	0.5	0.5	0.5
u_x	$-\frac{v_0(y-y_0)}{r_0}$	$-f \frac{v_0(y-y_0)}{r_0}$	0
u_y	$\frac{v_0(x-x_0)}{r_0}$	$f \frac{v_0(x-x_0)}{r_0}$	0

Table 4.2: Balsara's rotor problem initial conditions as specified by Tóth[66] with a magnetic field $B_x = 2.5/\mu_0$, where $r_0 = 0.1$, $r_1 = 0.115$, $f = \frac{r_1-r}{r_1-r_0}$, $v_0 = 1$, $v_0 = 1$, $(x_0, y_0) = (0.5, 0.5)$, and $\gamma = 5/3$.



(a)



(b)

Figure 4.1: Density distribution of Sod's[54] 1D Shock Tube problem at runtime = 2 s and CFL=0.4, where (a) compares the MP5, AW5, and MW5 solutions with $\Delta x = 100\mu m$ and (b) is an expanded view near the contact discontinuity showing the convergence of MP5 with successively reduced grid size Δx .

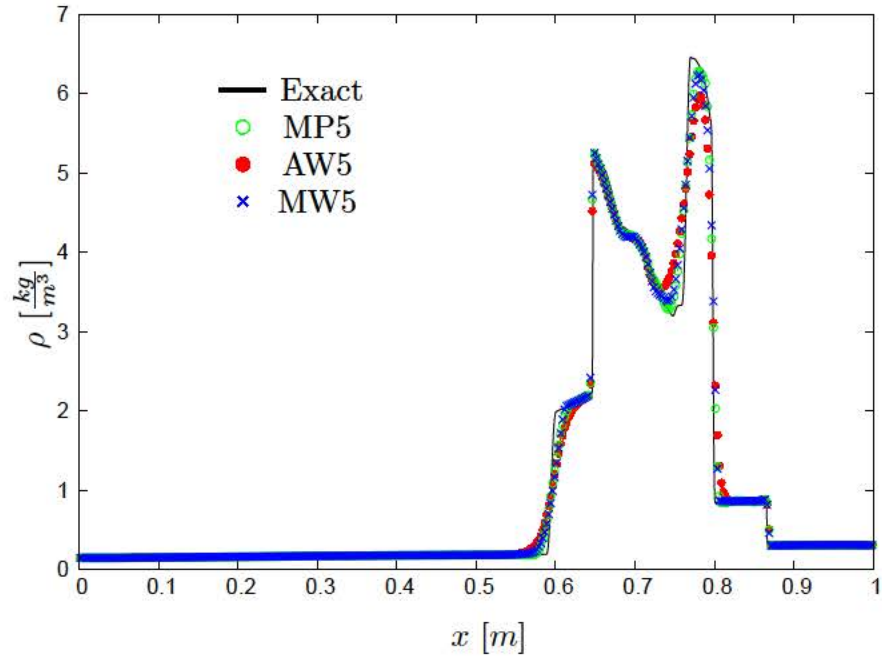
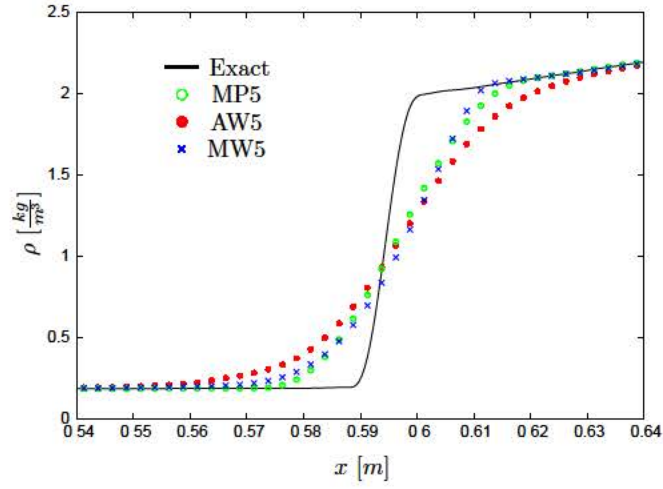
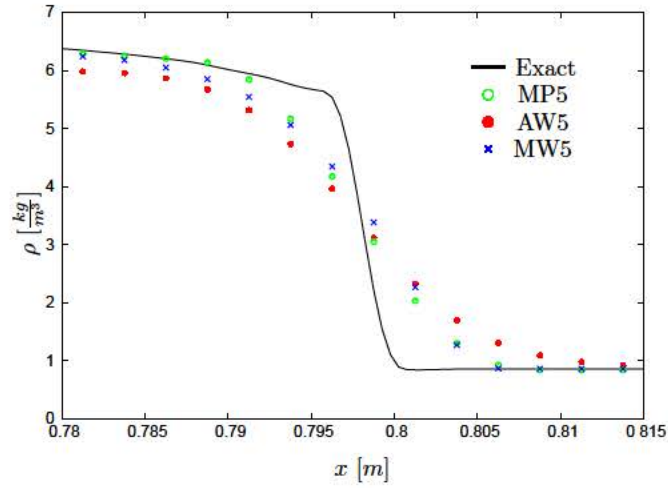


Figure 4.2: Density distribution of Woodward and Collela's[55] 1D Blastwave problem using MP5, AW5, and MW5, $\Delta x = 2.5 \times 10^{-3}m$, CFL = 0.4, runtime = 38ms.

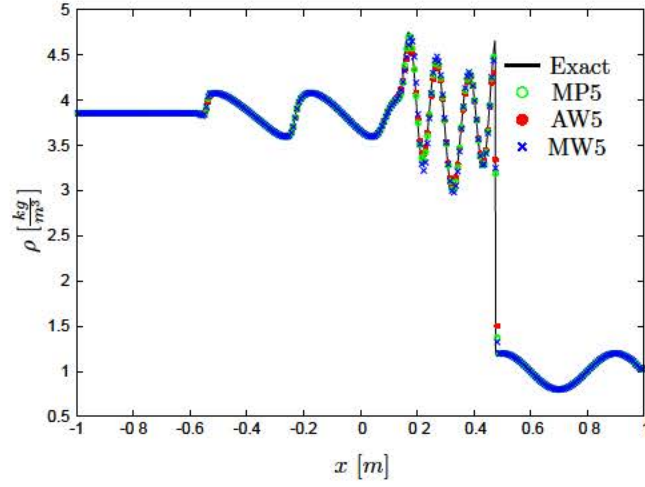


(a)

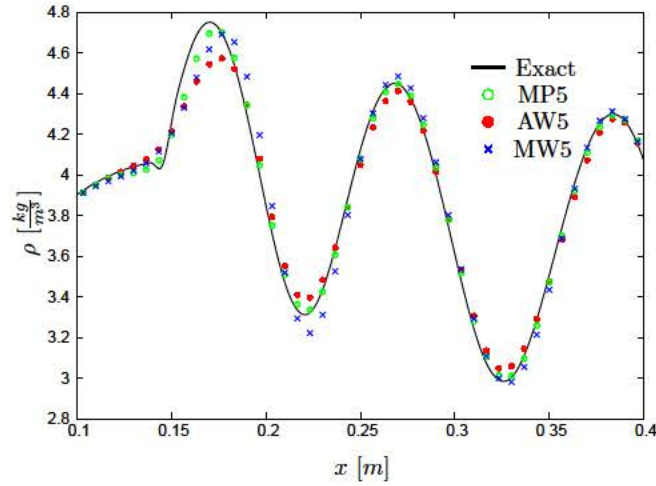


(b)

Figure 4.3: Density distribution of the contact discontinuities for the 1D Blastwave problem [55] using MP5, AW5, and MW5, $\Delta x = 2.5 \times 10^{-3}m$, CFL = 0.4, runtime = 38ms, where (a) and (b) are expanded views near contact discontinuities of Figure 4.2.



(a)



(b)

Figure 4.4: Density distribution of the 1D Shock-Entropy Interaction problem [56] using MP5, AW5, and MW5, $\Delta x = 6.67 \times 10^{-3}m$, CFL = 0.4, runtime = 360ms, where (a) is the wide view and (b) is an expanded view near an entropy disturbance.

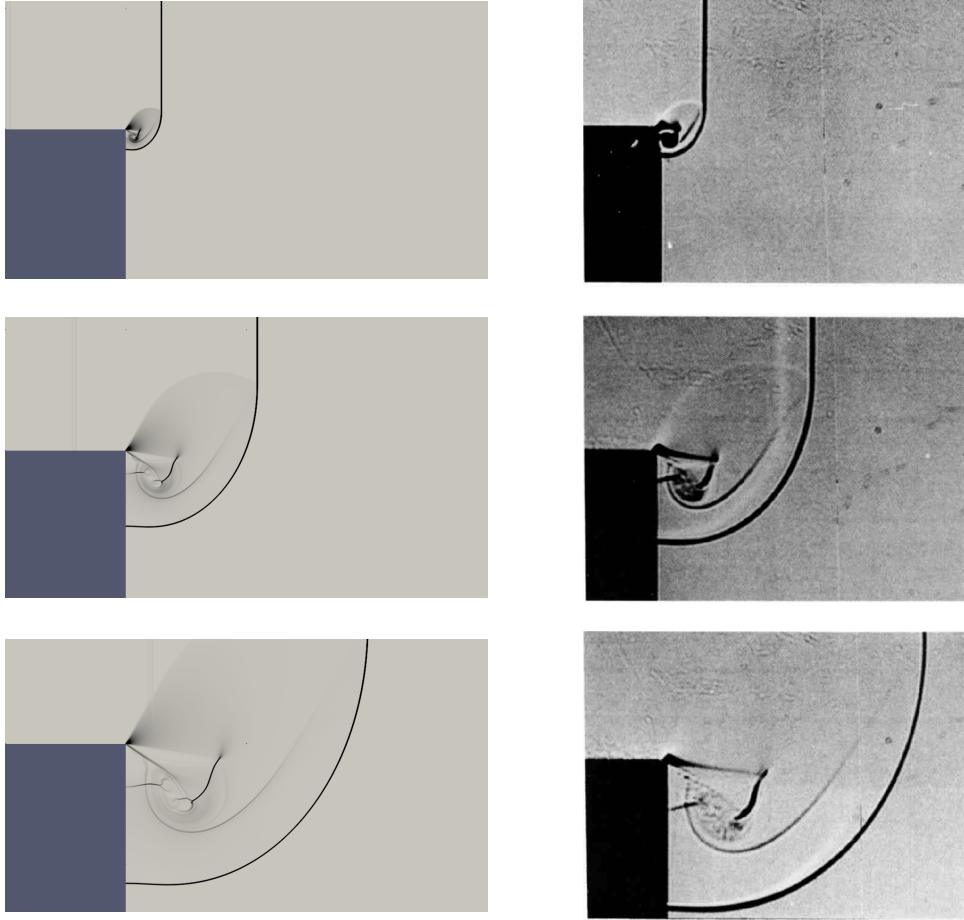


Figure 4.5: Mach 2.4 flow over a backward facing step solution (left) using MW5 with $\Delta x = \Delta y = \frac{1}{1024}m$ compared to the experimental results (right) [57].

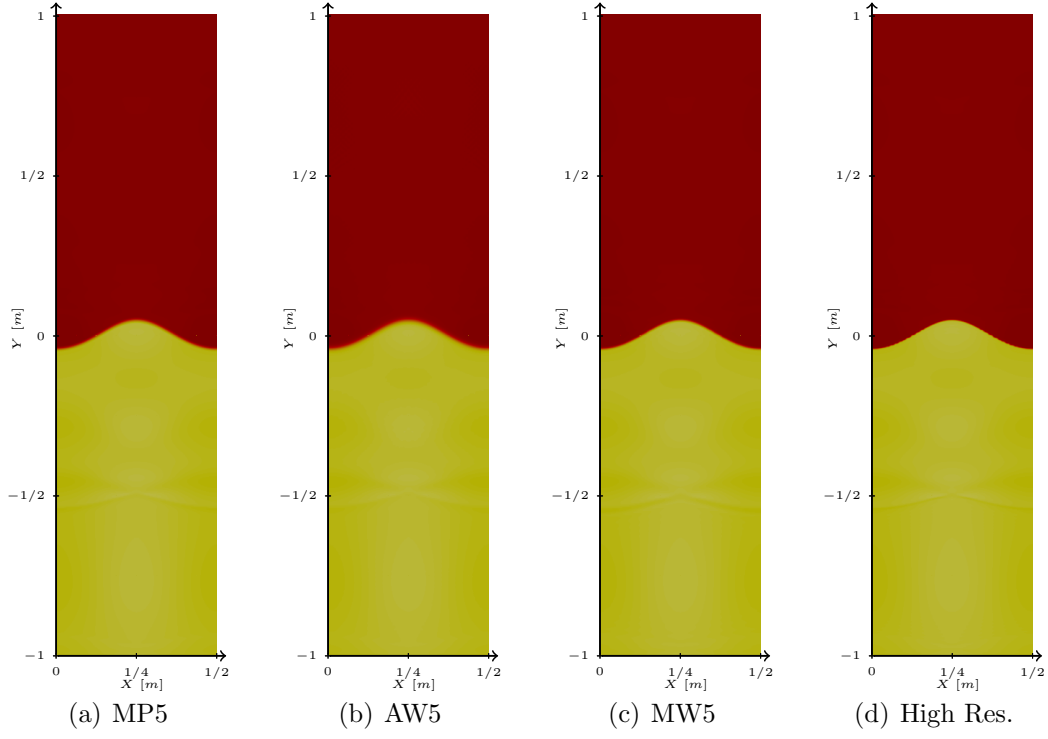



Figure 4.6: Density distribution for hydrodynamic Rayleigh Taylor Instability problem at $t = 0.75s$, where $\Delta x = \Delta y = \frac{1}{800}m$ (For High Resolution, MW5 was used with $\Delta x = \Delta y = 6.25 \times 10^{-4}m$), min  max .

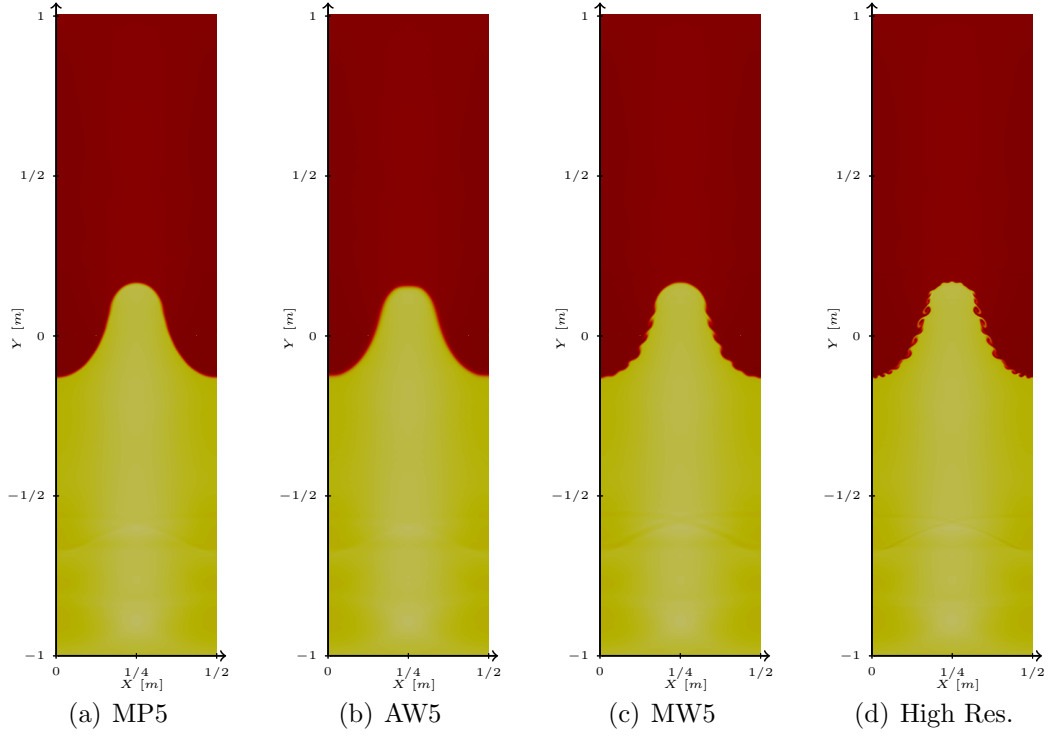



Figure 4.7: Density distribution for hydrodynamic Rayleigh Taylor Instability problem at $t = 1.50s$, where $\Delta x = \Delta y = \frac{1}{800}m$ (For High Resolution, MW5 was used with $\Delta x = \Delta y = 6.25 \times 10^{-4}m$), min  max .

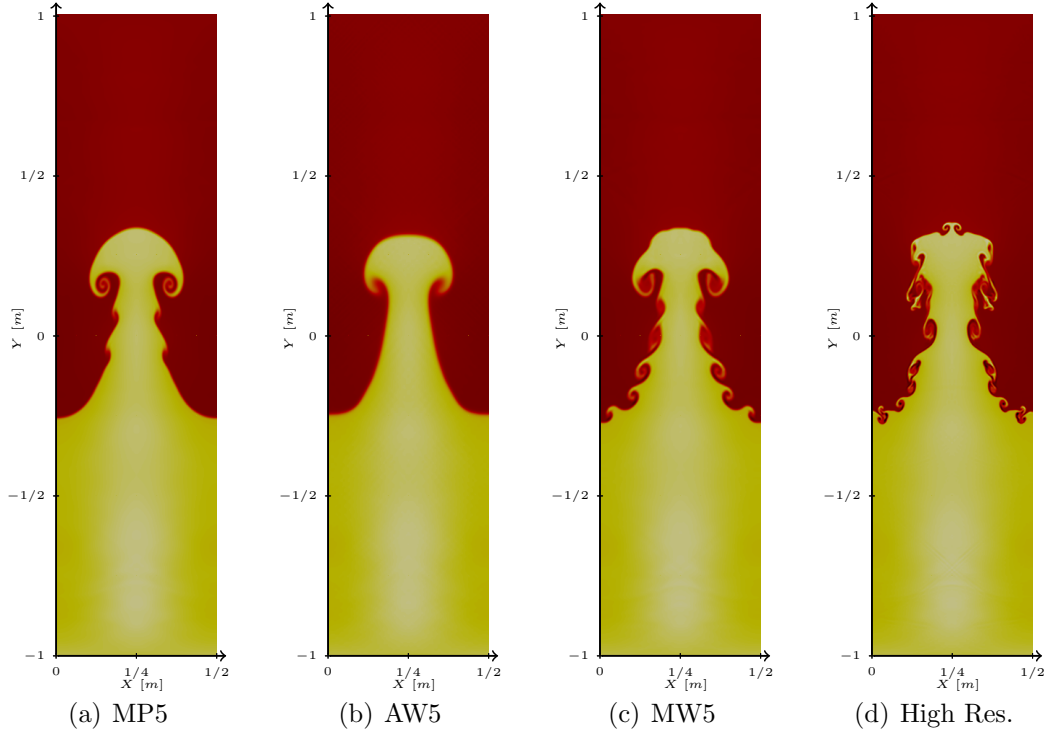



Figure 4.8: Density distribution for hydrodynamic Rayleigh Taylor Instability problem at $t = 2.25s$, where $\Delta x = \Delta y = \frac{1}{800}m$ (For High Resolution, MW5 was used with $\Delta x = \Delta y = 6.25 \times 10^{-4}m$), min  max .

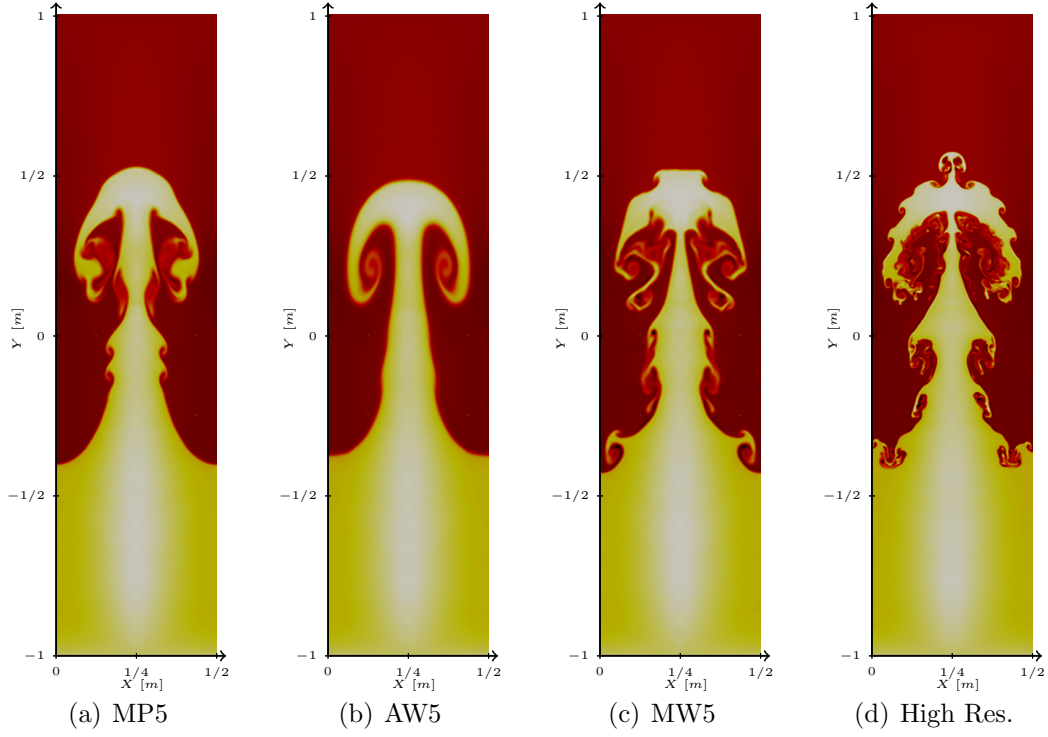



Figure 4.9: Density distribution for hydrodynamic Rayleigh Taylor Instability problem at $t = 3.00s$, where $\Delta x = \Delta y = \frac{1}{800}m$ (For High Resolution, MW5 was used with $\Delta x = \Delta y = 6.25 \times 10^{-4}m$), min  max .

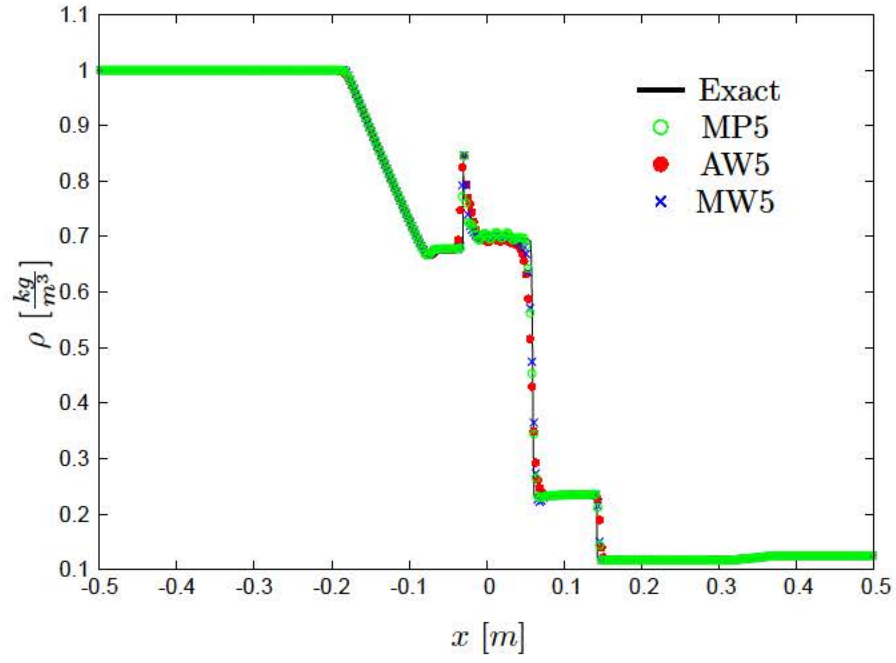


Figure 4.10: Density distribution of the Brio-Wu[60] problem using MP5, AW5 and MW5, $\Delta x = 2.5 \times 10^{-3}m$, CFL = 0.4, runtime = 100ms

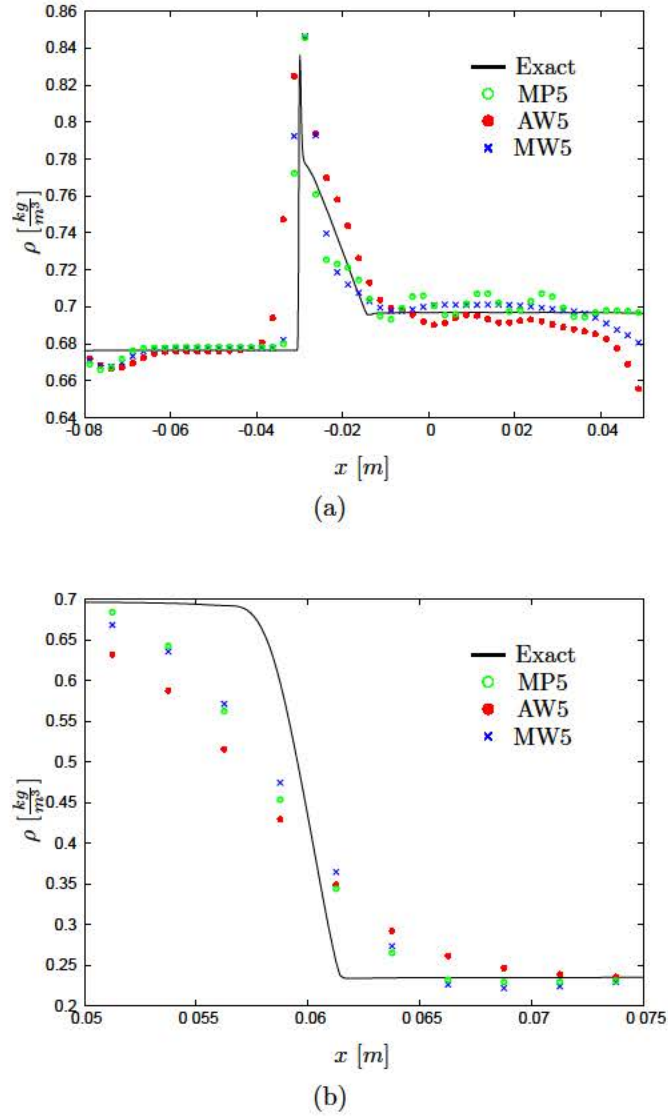
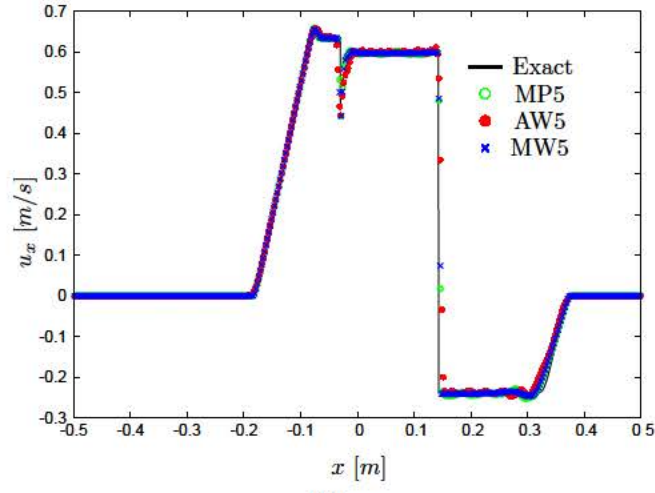
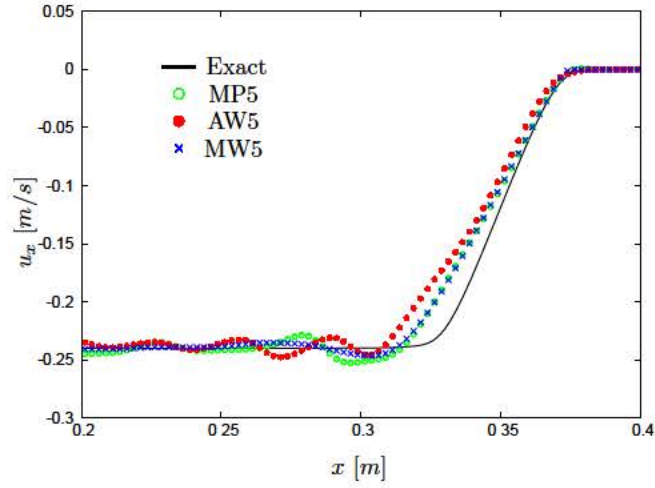


Figure 4.11: Density distribution for the 1D Brion-Wu[60] problem using MP5, AW5, and MW5, $\Delta x = 2.5 \times 10^{-3}m$, CFL = 0.4, runtime = 100ms, which illustrate the expanded views near the compound wave (a) and contact discontinuity (b) of Figure 4.10.



(a)



(b)

Figure 4.12: Velocity distribution of the x-component for the 1D Brio-Wu[60] problem using MP5, AW5, and MW5, $\Delta x = 2.5 \times 10^{-3} \text{m}$, CFL = 0.4, runtime = 100ms, which (b) illustrates the expanded views near the trailing edge of the fast rarefaction of (a).

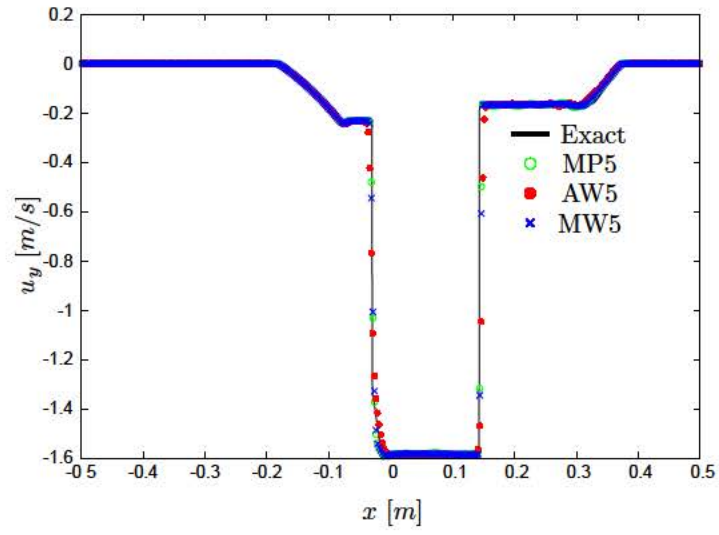


Figure 4.13: Velocity distribution of the y-component for the Brio-Wu[60] problem using MP5, AW5 and MW5, $\Delta x = 2.5 \times 10^{-3}m$, CFL = 0.4, runtime = 100ms

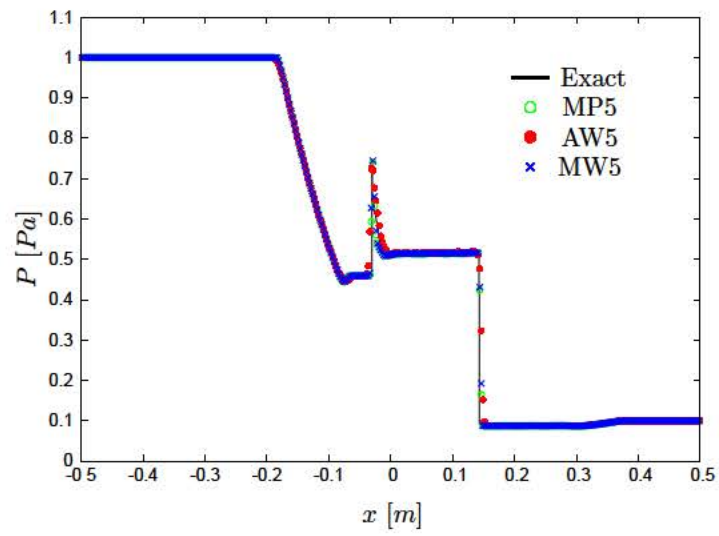


Figure 4.14: Pressure distribution of the Briou-Wu[60] problem using MP5, AW5 and MW5, $\Delta x = 2.5 \times 10^{-3}m$, CFL = 0.4, runtime = 100ms

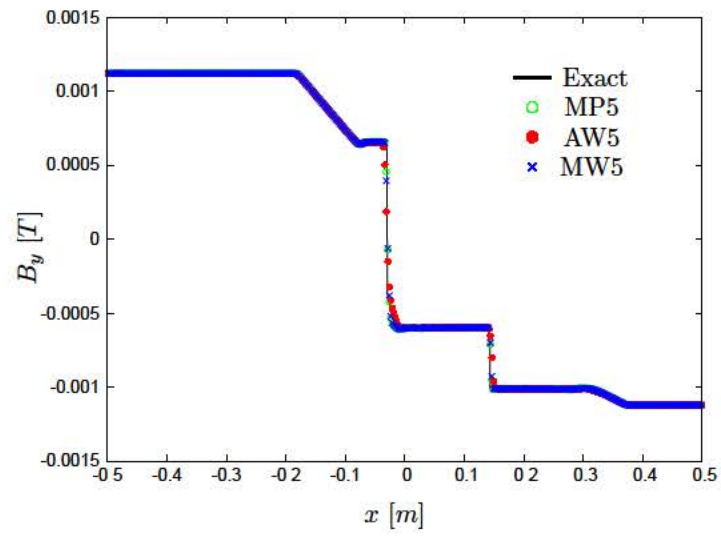


Figure 4.15: B_y distribution of the Brio-Wu[60] problem using MP5, AW5 and MW5, $\Delta x = 2.5 \times 10^{-3}m$, CFL = 0.4, runtime = 100ms

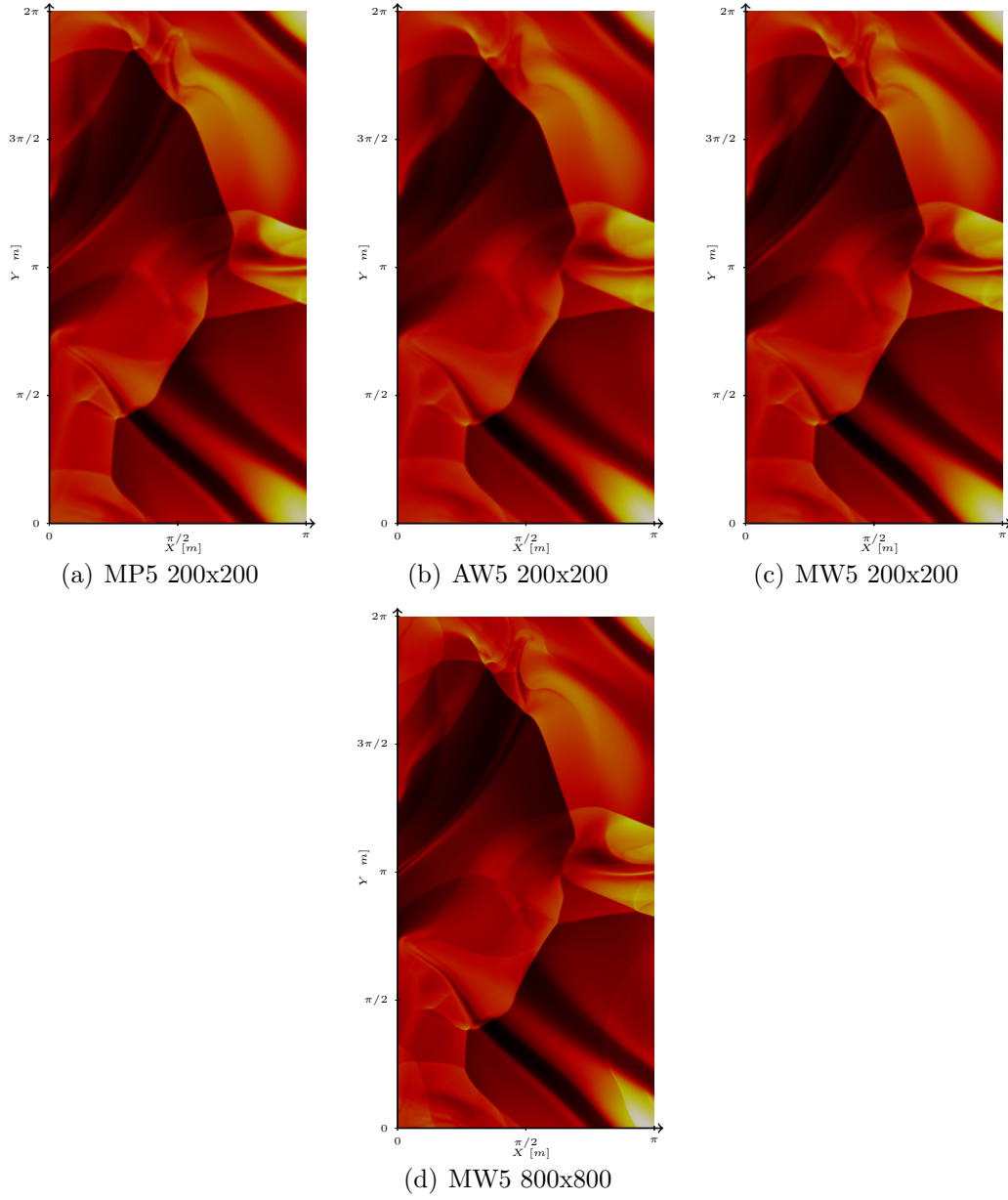


Figure 4.16: Density distribution for Orszag-Tang problem for $x \times y \in [0, \pi]m \times [0, 2\pi]m$ CFL = 0.4, runtime = 3 s, \min \max .

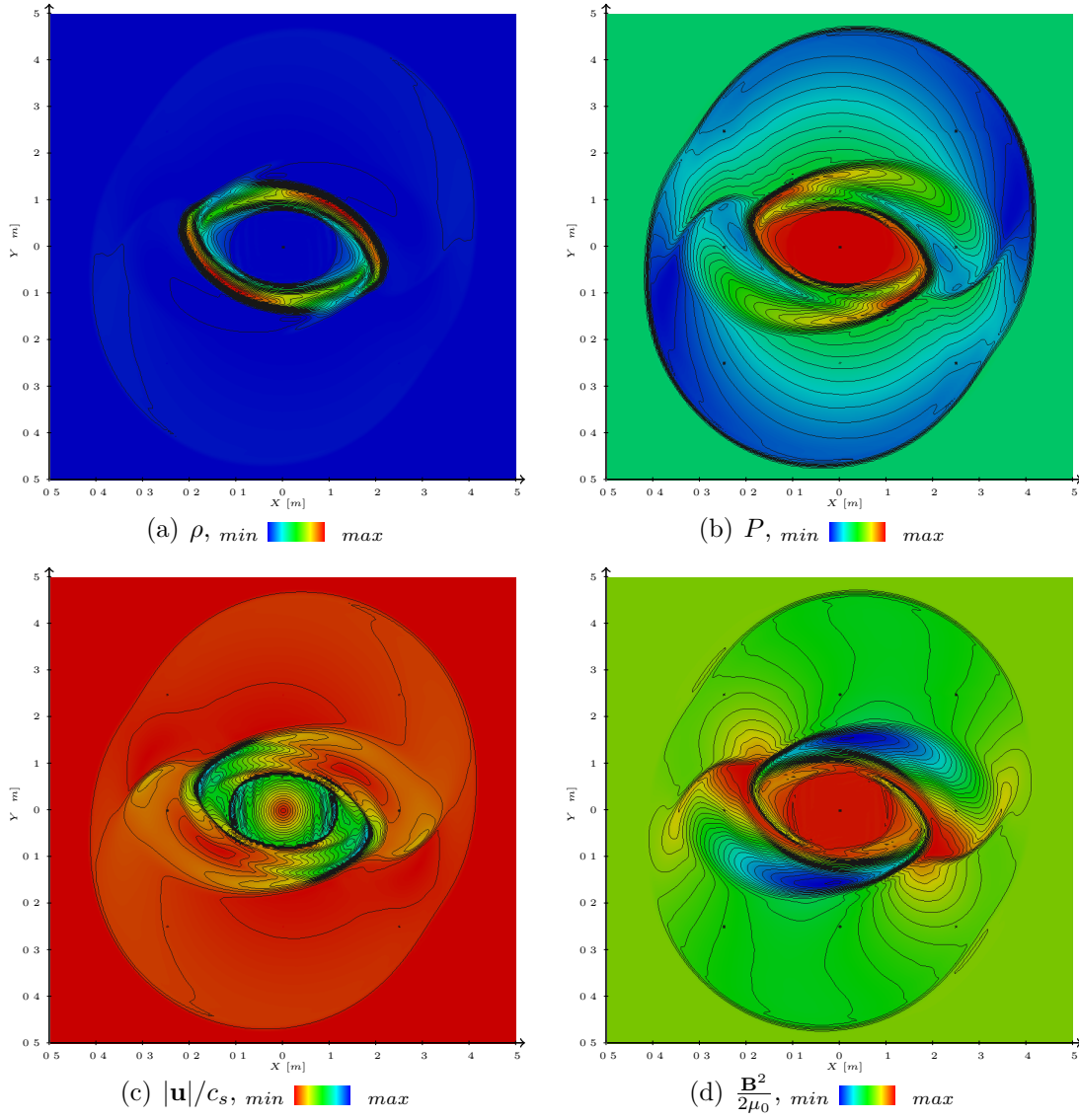


Figure 4.17: The density, thermal pressure, Mach number, and the magnetic pressure distributions at $t = 0.295s$ for Balsara's rotor problem. The solution was obtained using MW5 with a grid resolution of $\Delta x = \Delta y = \frac{1}{400}m$ and $CFL = 0.3$. The 30 contour lines are shown for the ranges $0.532 < \rho < 10.83 \frac{kg}{m^3}$, $.007 < P < 0.702 Pa$, $0 < \frac{|\mathbf{u}|}{c_s} < 3.64$, and $0.007 < \frac{\mathbf{B}^2}{2\mu_0} < 0.702 Pa$, as prescribed by Tóth [66].

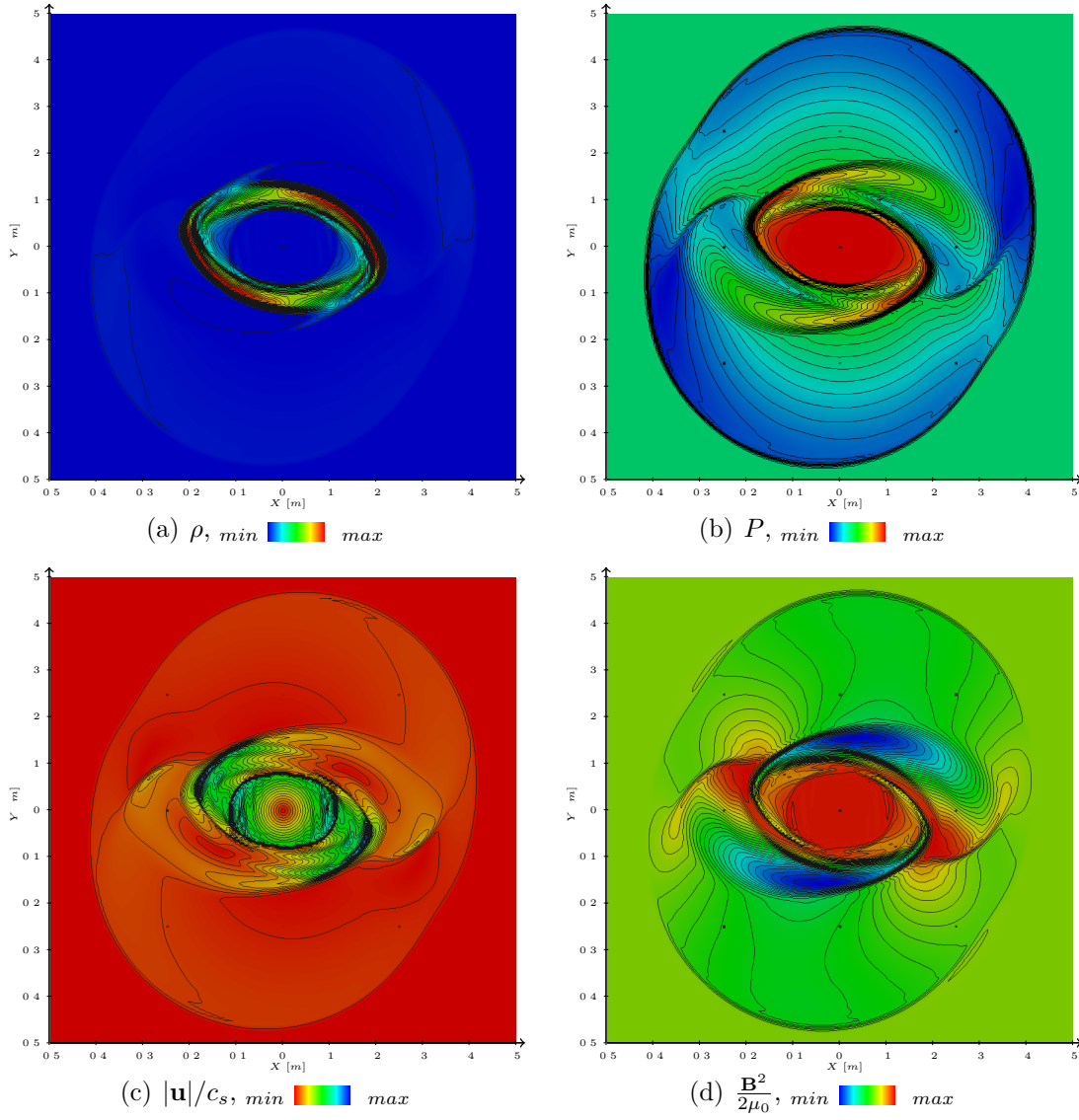


Figure 4.18: The density, thermal pressure, Mach number, and the magnetic pressure distributions at $t = 0.295s$ for Balsara's rotor problem. The solution was obtained using MP5 with a grid resolution of $\Delta x = \Delta y = \frac{1}{400}m$ and $CFL = 0.3$. The 30 contour lines are shown for the ranges $0.532 < \rho < 10.83 \frac{kg}{m^3}$, $.007 < P < 0.702 Pa$, $0 < \frac{|\mathbf{u}|}{c_s} < 3.64$, and $0.007 < \frac{\mathbf{B}^2}{2\mu_0} < 0.702 Pa$, as prescribed by Tóth [66].

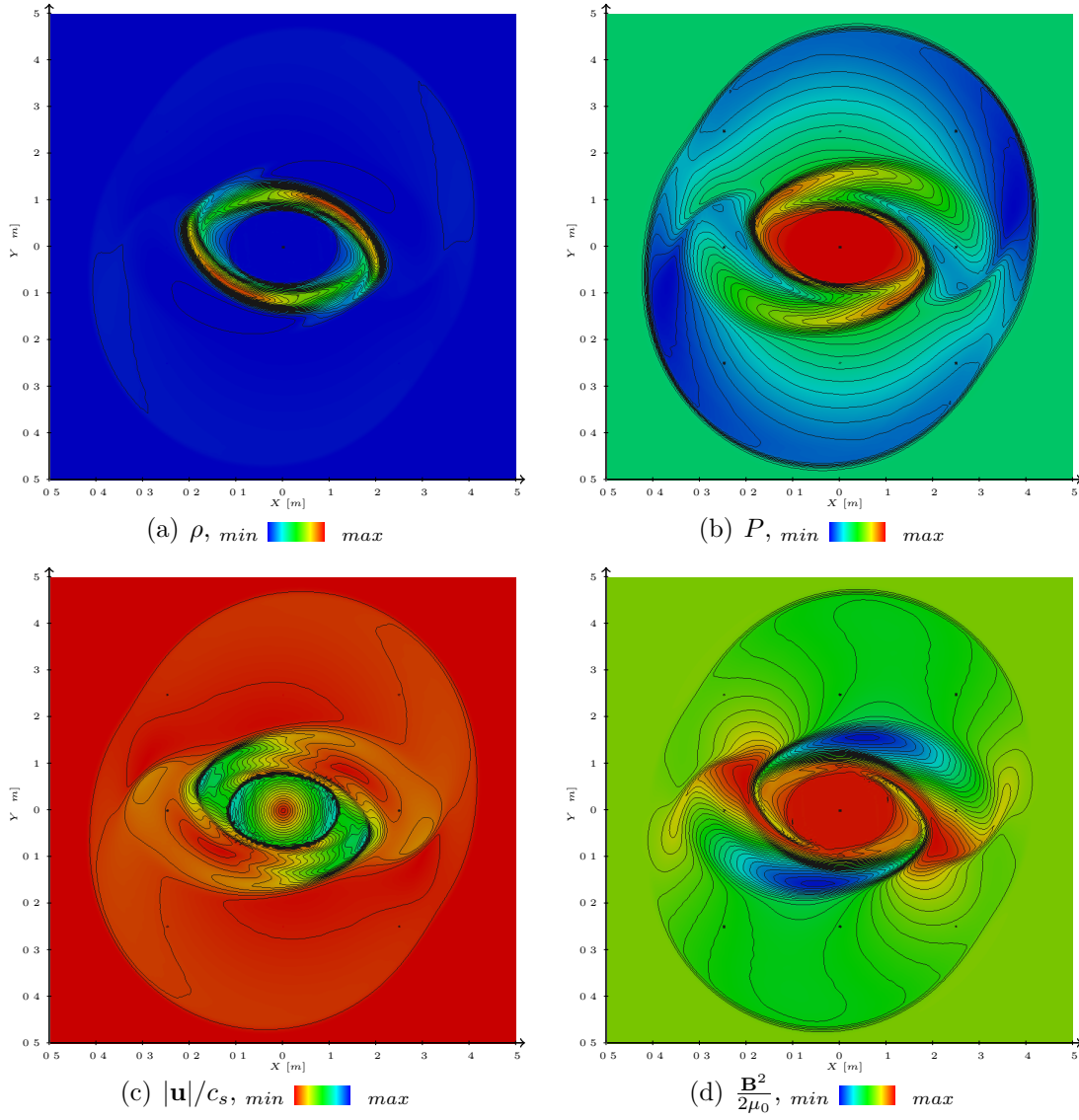


Figure 4.19: The density, thermal pressure, Mach number, and the magnetic pressure distributions at $t = 0.295s$ for Balsara's rotor problem. The solution was obtained using AW5 with a grid resolution of $\Delta x = \Delta y = \frac{1}{400}m$ and $CFL = 0.15$. The 30 contour lines are shown for the ranges $0.532 < \rho < 10.83 \frac{kg}{m^3}$, $.007 < P < 0.702 Pa$, $0 < \frac{|\mathbf{u}|}{c_s} < 3.64$, and $0.007 < \frac{\mathbf{B}^2}{2\mu_0} < 0.702 Pa$, as prescribed by Tóth [66].

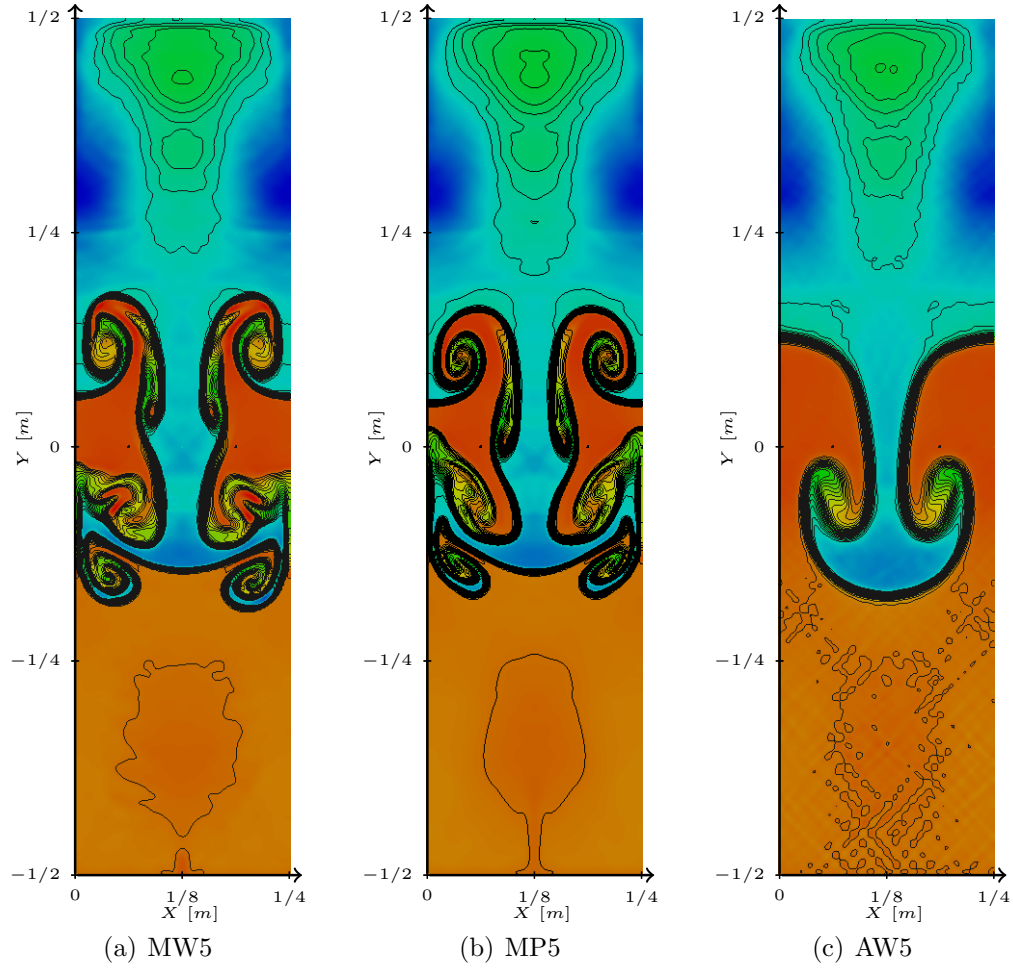



Figure 4.20: Growth of instability without the presence of a magnetic field at $t = 2s$ for MW5, MP5, and AW5 where $\Delta x = \Delta y = \frac{1}{400}m$. Density distribution with 20 density contours between 1  2.

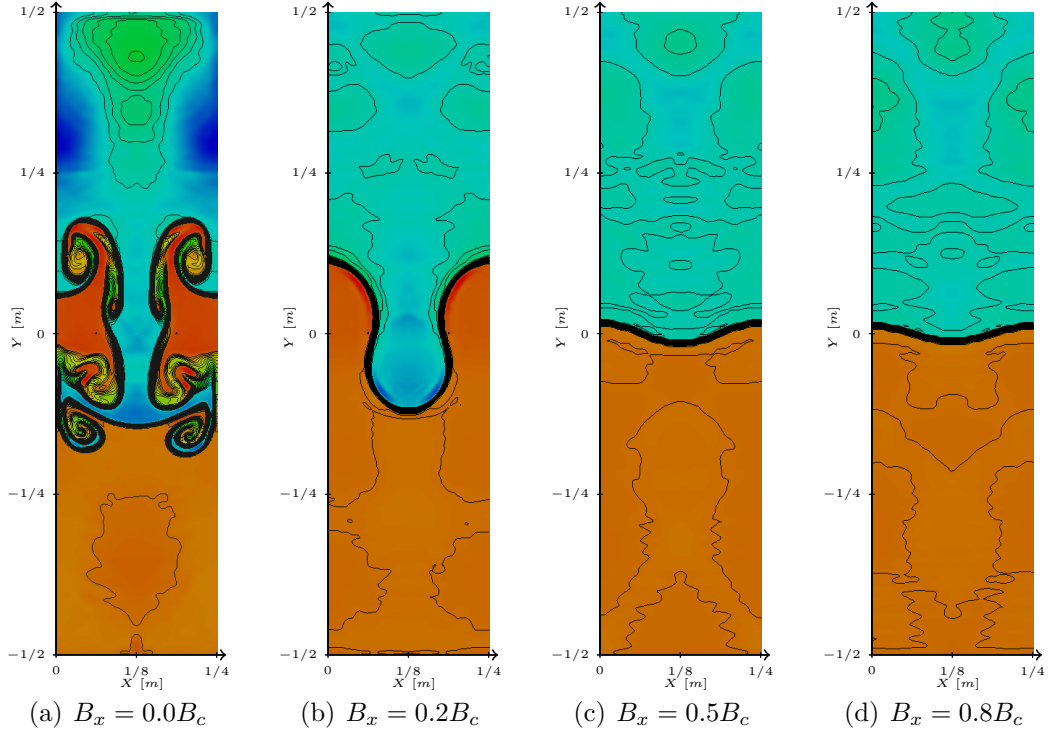



Figure 4.21: The impact of the tangential magnetic field, B_x , on the growth of instabilities at $t = 2s$ where $\Delta x = \Delta y = \frac{1}{400}m$ and $B_c = 0.5T$ using MW5. Density distribution with 20 density contours between 1  2.

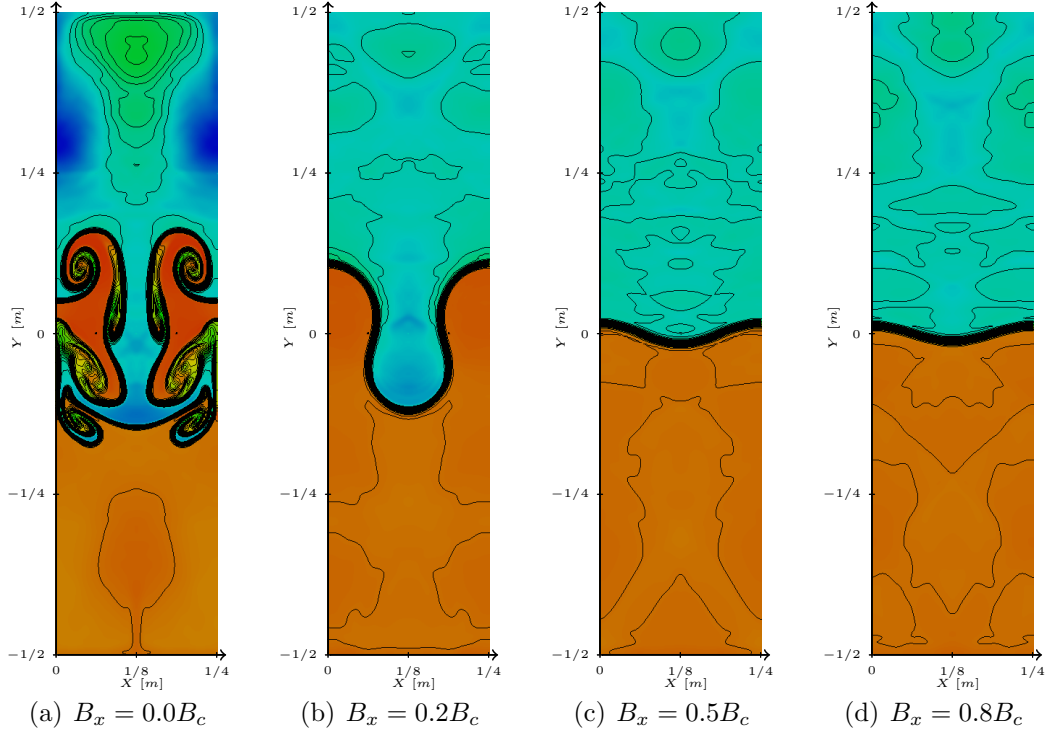



Figure 4.22: The impact of the tangential magnetic field, B_x , on the growth of instabilities at $t = 2s$ where $\Delta x = \Delta y = \frac{1}{400}m$ and $B_c = 0.5T$ using MP5. Density distribution with 20 density contours between 1  2.

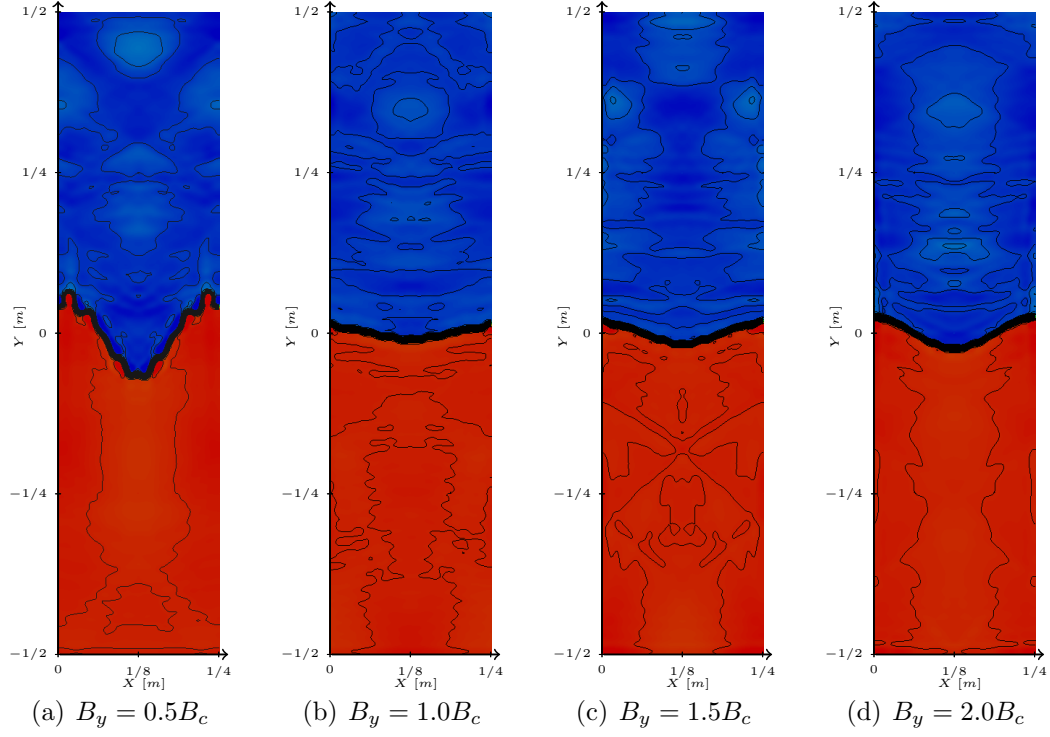



Figure 4.23: The impact of the normal magnetic field, B_x , on the growth of instabilities at $t = 2s$ where $\Delta x = \Delta y = \frac{1}{400}m$ and $B_c = 0.5T$ using MW5. Density distribution with 30 density contours between 1  2.

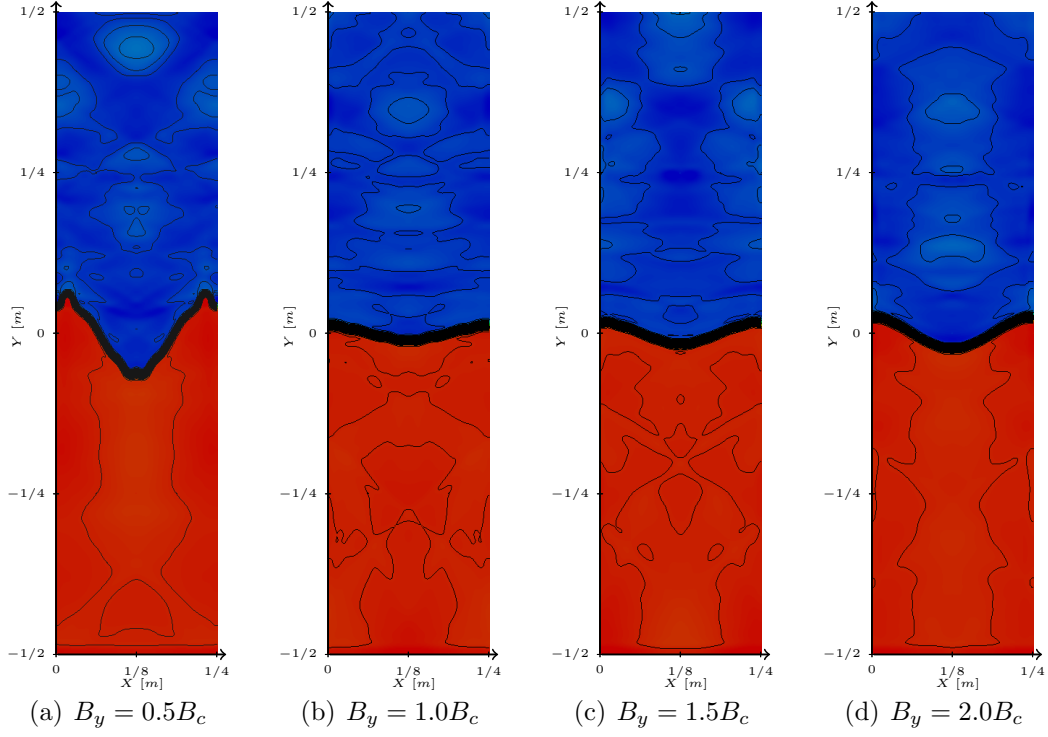

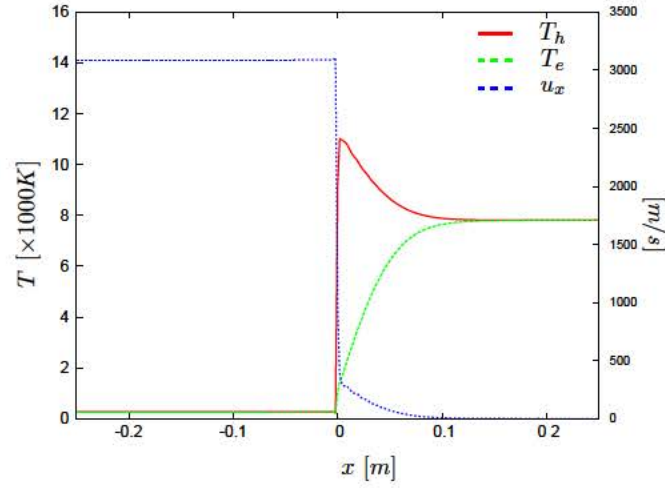
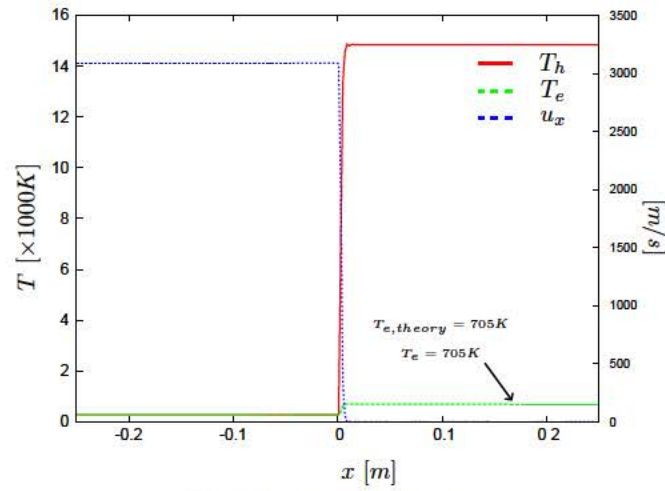


Figure 4.24: The impact of the normal magnetic field, B_x , on the growth of instabilities at $t = 2s$ where $\Delta x = \Delta y = \frac{1}{400}m$ and $B_c = 0.5T$ using MP5. Density distribution with 30 density contours between 1  2.



(a) With T_e relaxation



(b) Without T_e relaxation

Figure 4.25: Mach 10 fully ionized Argon shock in shock reference frame with(a) and without(b) T_e relaxation where $\Delta x = \frac{1}{500}m$ using MP5.

CHAPTER 5

Simplified Approach for PDRIME Simulations

Now that the various numerical schemes have been validated, we first investigate the performance of a PDRE flight configuration, and later the PDRIME, using a simplified non-reactive model, Equation 2.5. In the simplification, we assumed that all reactants (H_2 and O_2) in the combustion chamber have been consumed, leaving just products (H_2O) and the seeded Cesium. We also assumed that the detonation has left the chamber. This model has been shown to replicate blowdown conditions in a rocket nozzle reasonably accurately, as shown in Figure 5.1 from the work by Cambier. Following Cambier’s blowdown model[67], we initialize the combustion chamber with the post-combustion and post-detonation conditions:

$$\left\{ \begin{array}{l} \hat{P}_0 = 100 \text{ atm} \\ \hat{T}_0 = 3000 \text{ K} \\ \hat{\rho}_0 = \frac{\hat{P}_0}{R\hat{T}_0} \end{array} \right.$$

Rather than simulating the combustion chamber, the combustion chamber is modeled as a “reservoir” whose conditions (P_0 , T_0) temporally evolve as prescribed by Cambier’s blowdown equations[67]:

$$P_0 = \hat{P}_0[f(t)]^{\gamma/(\gamma-1)} \tag{5.1a}$$

$$\rho_0 = \hat{\rho}_0[f(t)]^{1/(\gamma-1)} \quad (5.1b)$$

$$T_0 = \hat{T}_0[f(t)] \quad (5.1c)$$

where $f(t) = \frac{1}{1+\nu t}$ and ν is the blowdown frequency and is equal to 87.5 Hz for this particular case. Now, by using the isentropic relations, we can determine the conditions at the PDRE throat as a function of time. With this simplification, our computational domain no longer needs to include the combustion chamber, this is illustrated in Figure 5.2. Next, we assume that the back pressure, the atmospheric pressure P_{atm} , is sufficiently low, so that there is no back flow into the nozzle. Pressures at the altitudes we are simulating are high enough that even with the expansion in the nozzle, the nozzle exit pressure is greater than the atmospheric pressure, $P_{exit} > P_{atm}$. Because of the extremely high flight altitudes (altitude $\approx 15 - 20$ km), the PDRE performance does not have any significant variance with regard to altitude.

Next, we extend this simplified model of the PDRE to the PDRIME with a ‘Magnetic Piston’. In this extension, we assume that if the temperature is greater than 3000K; the conductivity is a constant non-zero value, in this particular case $\sigma = 1000mho/m$ in the nozzle and $\sigma = 500mho/m$ in the bypass tube. The nozzle impulse contribution is calculated the same way as the PDRE, while bypass tube impulse contribution is calculated by integrating the Lorentz force over the cycle duration, as follows:

$$I_{bypass} = \int_0^t (\mathbf{j} \times \mathbf{B})_x d\tau \approx \int_0^t \sigma u B_z (K_x - 1) d\tau \quad (5.2)$$

where all variables have been previously defined. We also assumed a constant magnetic field for both the nozzle and bypass section of the PDRIME, as illustrated in Figure 1.7. The configuration called ‘NG’ refers to the PDRE with energy extraction in the nozzle (for use of the ‘nozzle generator’), so, as expected there is a drop in impulse as shown in Figure 5.3. A promising concept postulated by Cambier[40] involving the PDRE with ‘Magnetic Piston’ was also simulated, but due to the lack of energy supplied to the ‘Magnetic Piston’ by the generator, this flight configuration could not be effectively utilized. In Chapter 7, the true energy ‘cost’ of the chamber piston will be investigated by exploring the nature of the ionized gas and chemical kinetics subjected to the Lorentz force. We will now explore other PDRE flight configurations which will build off of the PDRE with ‘NG’ concept in order to further optimize the PDRE.

5.1 PDRIME with Bypass Configurations

There were multiple flight configurations as well as different flight condition tested. Using the standard combustion chamber condition, nozzle, and nozzle generation configuration we were able to test various configurations of the Bypass Tube. Figure 5.3 shows the performance of the standard PDRIME configuration under various flight condition as they compare the performance of a PDRE, which we will refer to as the baseline. With this configuration, there are some marginal performance gains above the baseline case. The standard PDRIME utilizes a constant magnetic field, which is active only if the fluid temperature is greater than 3000K and the fluid is moving in the stream-wise direction. When activated, a constant magnetic field of 3T is applied to the applicable fluid.

5.2 Temporal/Temperature Controllers of the Magnetic Field

We performed component evaluations for the various flight configurations with different assumptions. This involved examining the net energy consumed compared to impulse gained or lost by a particular component of the flight configuration. During the course of component performance evaluation, it was determined that an MHD bypass accelerator, where a “piston” like acceleration was applied in the bypass section as done for the magnetic chamber piston, was under-performing relative to the nozzle which is shown in Figure 5.4. Zeineh[33] also saw the same under-performance in his 2-D simulations. The bypass available energy, ΔE_{gen} , is being applied to the bypass over approx 0.1 ms within a relatively small volume, dV , wherein most of the available energy is directed towards Joule heating rather than accelerating the fluid. This leads to large temperature spikes and little impulse increase.

From $E = \int c_v dT + \frac{1}{2}\rho v^2$ with introduction of Energy at constant volume

$$\Delta E_{\text{gen}} = c_v \Delta T + \frac{1}{2}\rho \Delta v^2 \quad (5.3)$$

We can see where and how the energy is being used in the bypass. ΔE_{gen} is a fixed amount of energy produced by the MHD generator in the nozzle. $c_v \Delta T$ represents the amount of energy that is converted to internal energy, which for our simplified model of constant heat capacity is represented by a rise in temperature. Lastly, $\frac{1}{2}\rho \Delta v^2 \propto \Delta KE$ represents the amount of kinetic energy which is imparted upon the fluid, and since energy is introduced at constant volume, ρ remains constant, so this change in kinetic energy is directly related to our change in impulse, $I \propto \Delta KE^{\frac{1}{2}}$. In order to reduce the temperature spikes and thus increase the impulse, when applying MHD to the bypass, one must regulate the ΔE_{gen} available for use by the bypass accelerator. To control this energy reintroduction, one must either control the conductivity of the

fluid, σ , or the strength of the magnetic field, B , acting on the bypass. Since it is impractical if not impossible to dynamically control the conductivity in the bypass, we chose the latter.

Our first approach is to scale the maximum magnetic field in the bypass with time, for which we prescribe a simple algorithm. First, the magnetic field is initially zero until the initiation time, t_0 , when at least one grid cell in the bypass meets the normal criteria for MHD accelerator: $T_i > 3000K$ and $u_i > 0$. The magnetic field is then scaled with the maximum field applied, B_0 . The magnetic field in the bypass is prescribed as follows:

$$B(t) = \begin{pmatrix} 0 & t < t_0 \\ \Pi(t) \cdot B_0 & t_0 < t < t_0 + \Delta t \\ B_0 & t > t_0 + \Delta t \end{pmatrix} \quad (5.4)$$

B_0 : Maximum Magnetic Field Strength

t_0 : time at which $T > 3000K$ and $u > 0$

Δt : ramp up time

$\Pi(t)$: Magnetic Field Scaling Factor

We ran a series of simulations incorporating this prescribed magnetic field, adjusting both $\Pi(t)$ and Δt as a means of “open loop” control. Our tests utilized three different magnetic field scaling factors:

$\Pi(t) = (\frac{t-t_0}{\Delta t})$ linear scaling where $B \propto t$

$\Pi(t) = (\frac{t-t_0}{\Delta t})^{\frac{1}{2}}$ energy scaling ($Energy \propto B^2$), where $B \propto t^{\frac{1}{2}}$

$\Pi(t) = (\frac{t-t_0}{\Delta t})^n$ power law scaling ($n = 3$) where $B \propto t^n$

Figure 5.5 compares the evolution of these magnetic field scaling factors with time. Figure 5.6 shows that the temporally varied bypass magnetic field with the “open loop” control shown in Equation 5.4 has the same marginal performance improvements performance as the standard bypass configuration. The optimal configuration of the bypass magnetic field is dictated by the flight conditions which include flight Mach number and altitude.

In our next approach, we return to the same problem of controlling the rate at which energy is consumed by the bypass. It was previously stated, that it was impractical to dynamically control the conductivity in the bypass, σ . When evaluating the nature of the conductivity of a fluid in the current regime, Equation 2.30 shows the conductivity’s strong dependency on the temperature, T . Rather than dynamically controlling the conductivity of the fluid, we modeled the behavior of an ‘ideally’ conductive fluid by prescribing its dependency to temperature, $\sigma = \sigma(T)$. We wish to implement this “closed loop” controller in the bypass in order to scale the magnetic field, B_i , with the sensible local temperature in the bypass, T_i . The normal criteria for MHD acceleration are still utilized. The bypass magnetic field “feedback” function is prescribed as follows:

$$B(T) = \begin{pmatrix} 0 & T < T_{min} \\ \Theta(T) \cdot B_0 & T_{min} < T < (T_{max} - T_{ref}) \\ B_0 & T > (T_{max} - T_{ref}) \end{pmatrix} \quad (5.5)$$

B_0 : Maximum Magnetic Field

T_{min} : Minimum Temperature (3000K)

$\Theta(T)$: Magnetic Field Scaling Factor

$$\Theta(T) = \left(\frac{T - T_{\text{ref}}}{T_{\text{max}} - T_{\text{ref}}} \right) \text{ linear scaling } B \propto T$$

T_{ref} and T_{max} are adjusted to optimize performance

The term “feedback” here is used in the sense that temperature is measured, and the magnetic field is adjusted according to Equation 5.5. Figures 5.7 through 5.10 show that the “closed-loop” controller in the bypass tube is able to match the performance of the standard configuration at a flight altitude of 25km and $T_{\text{max}} < 8 \times 10^3 K$. But at other flight altitudes, this “closed loop” controller falls short. The $B(T)$ model is much more feasible for implementing into a physical system because of the temperature dependency of many of the parameters that contribute to impulse from the bypass accelerator, e.g., $\sigma(T)$ and $B(T)$.

5.3 PDRIME with 2D Bypass Configuration

There was further examination of the PDRIME with various configurations performed in Zeineh[33] and Zeineh et al.[34]. In their study, Zeineh et al. found the flight configuration of the PDRIME at altitudes 20, 25, and 30 km at relatively low Mach numbers ($M \leq 5$) had significant performance increases over the baseline PDRE. Figures 5.11 through 5.13 show some of the performance gains of the PDRIME at different altitudes with the optimal bypass section lengths ($L_{\text{bypass}} = 3, 4, \text{ and } 6 \text{ m}$) demonstrated in [34]. While the results of Zeineh’s multidimensional simulations were quite promising, the effects of complex kinetics (i.e. hydrogen-air chemistry and ionization process) were not rigorously investigated. The constant conductivity assumption does not allow for the “closed loop” evolution of the conductivity (i.e. Joule heating further ionizing fluid), therefore in Chapter 7 we will

discuss and examine the effects of MHD when the conductivity is described more accurately via Equation 2.27.

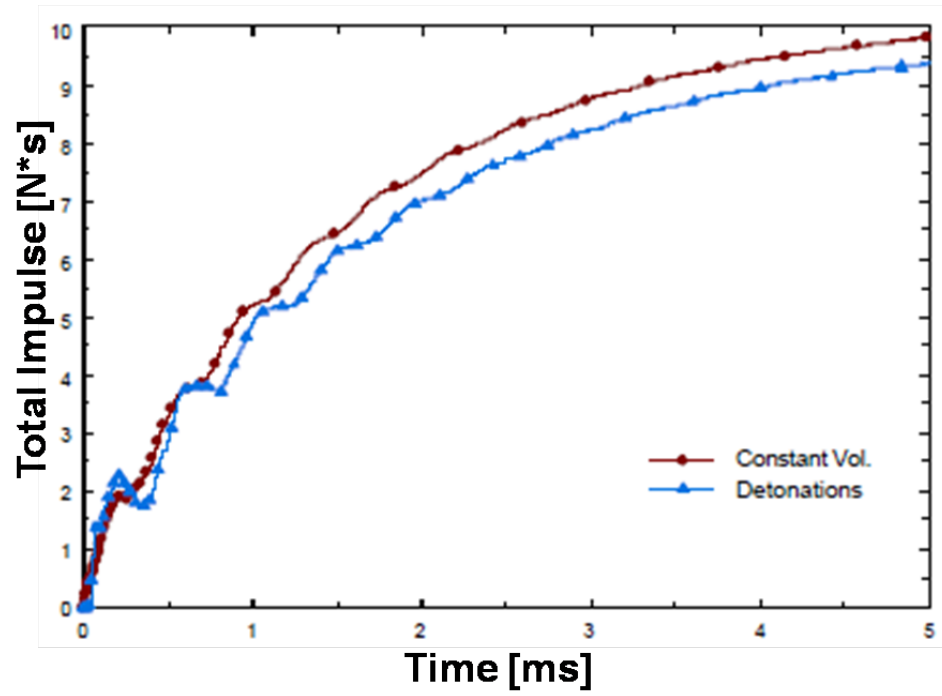


Figure 5.1: Variation in impulse for a PDRE. Results are shown from a full quasi-1D transient PDRE simulation and a cycle approximated by a constant volume reaction and a blow-down period(from Cambier[67])

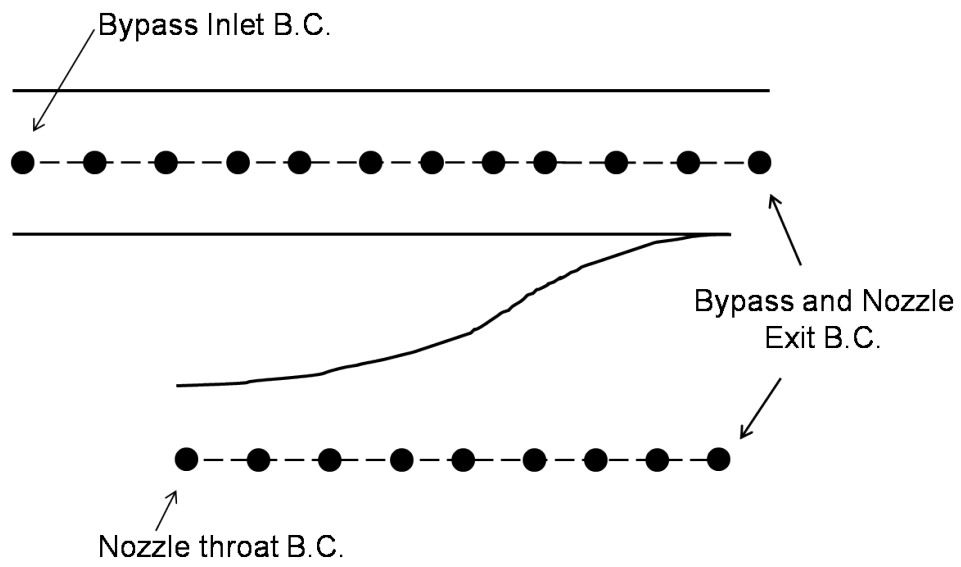


Figure 5.2: Quasi 1D Computational Domain, where the Bypass and Nozzle inlet and exit boundary conditions are shown

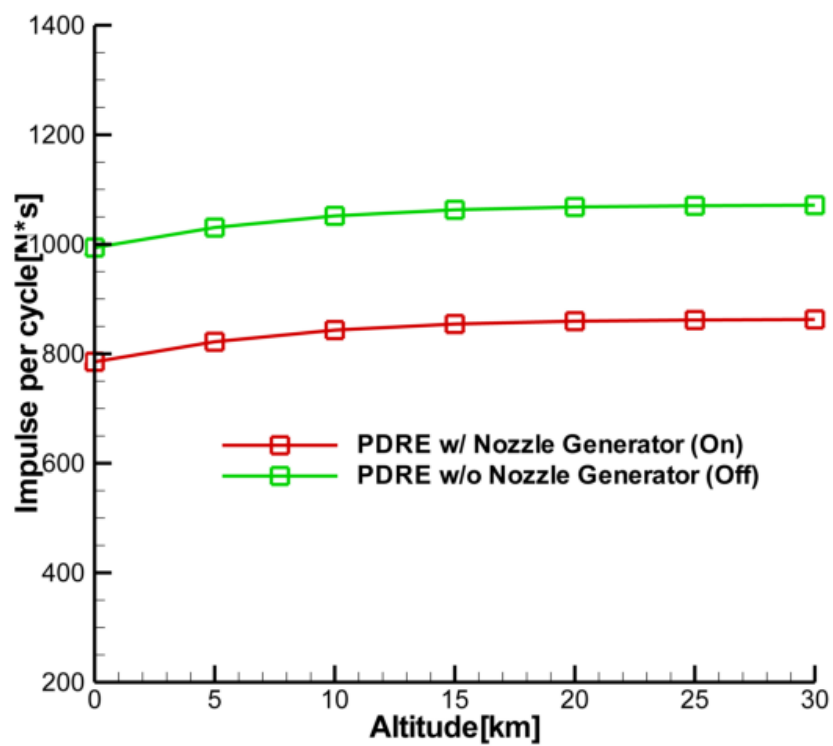


Figure 5.3: Quasi 1D Performance: Impulse Loss in Nozzle Energy Generation with H_2O product

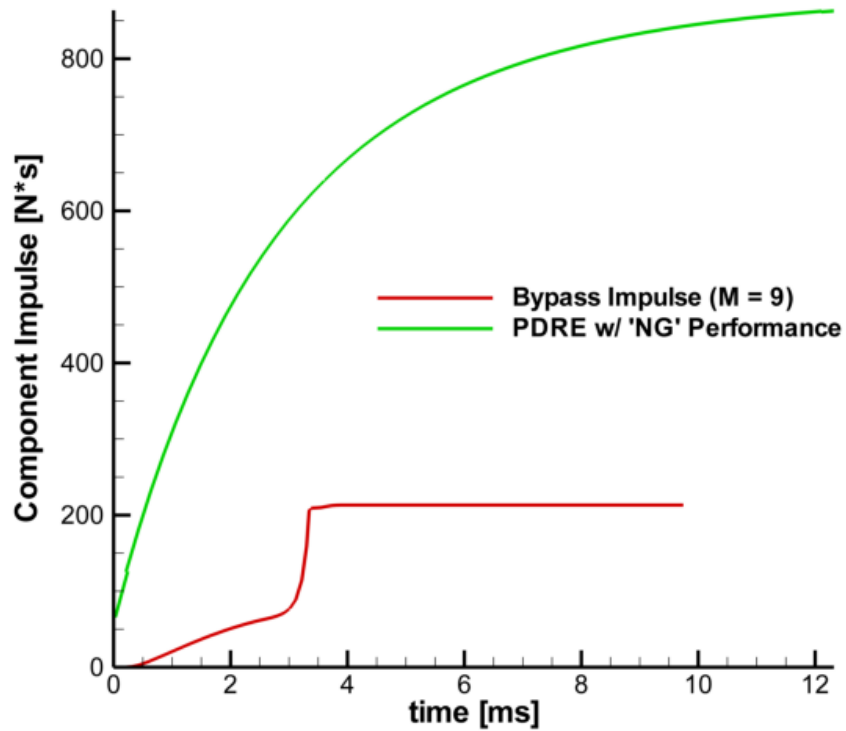


Figure 5.4: Quasi 1D Component Performance: Bypass vs. Nozzle Impulse at $M = 9$ and Alt: 25km with H_2O product

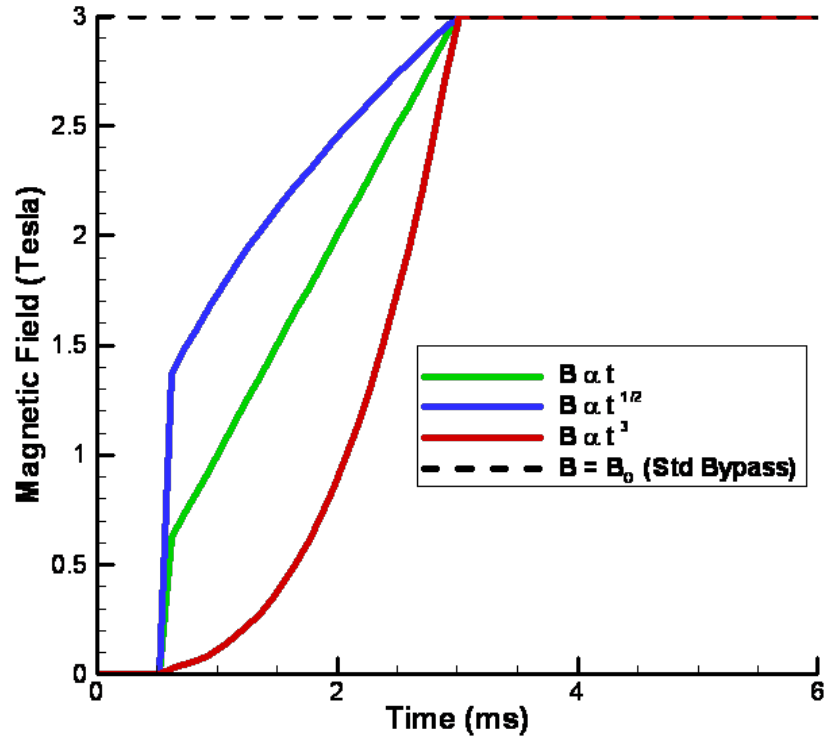


Figure 5.5: Magnetic Field Strength, B , as a function of time, using various Magnetic Field Strength functions, $\Pi(t)$

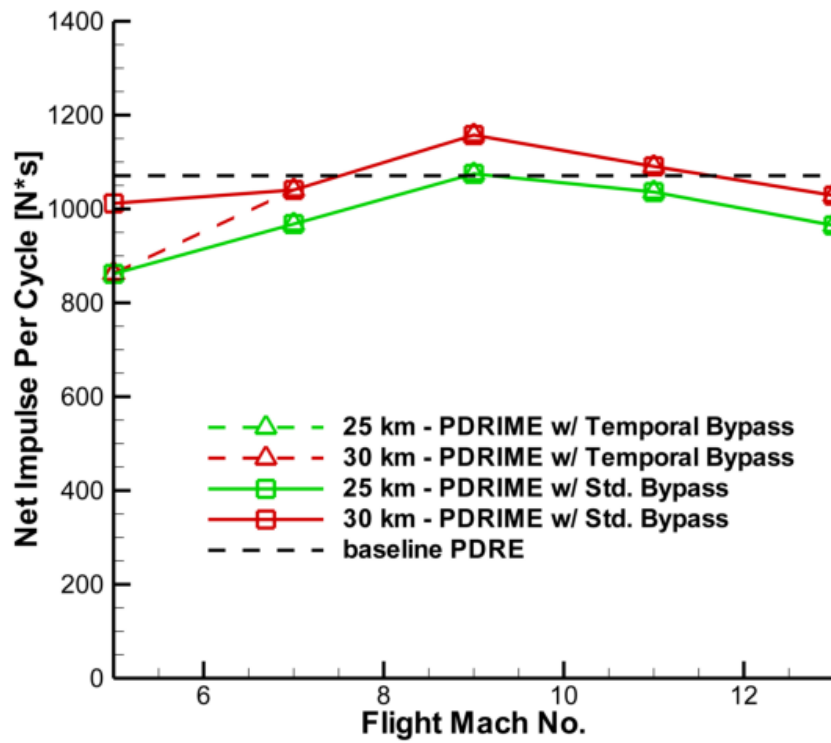


Figure 5.6: PDRIME: effects of flight Mach number. Magnetic Field, $B(t) \sim t^2$

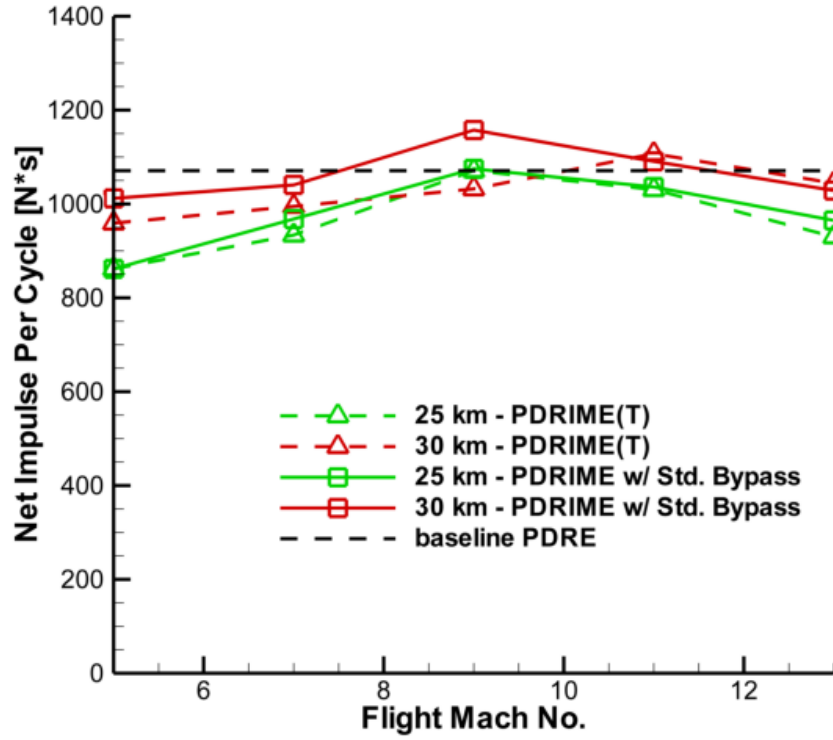


Figure 5.7: PDRIME with Chamber Piston: effects of flight mach number. Magnetic Field $B(T)$, $T_{\text{ref}} = 0K$ and $T_{\text{max}} = 6 \times 10^3 K$

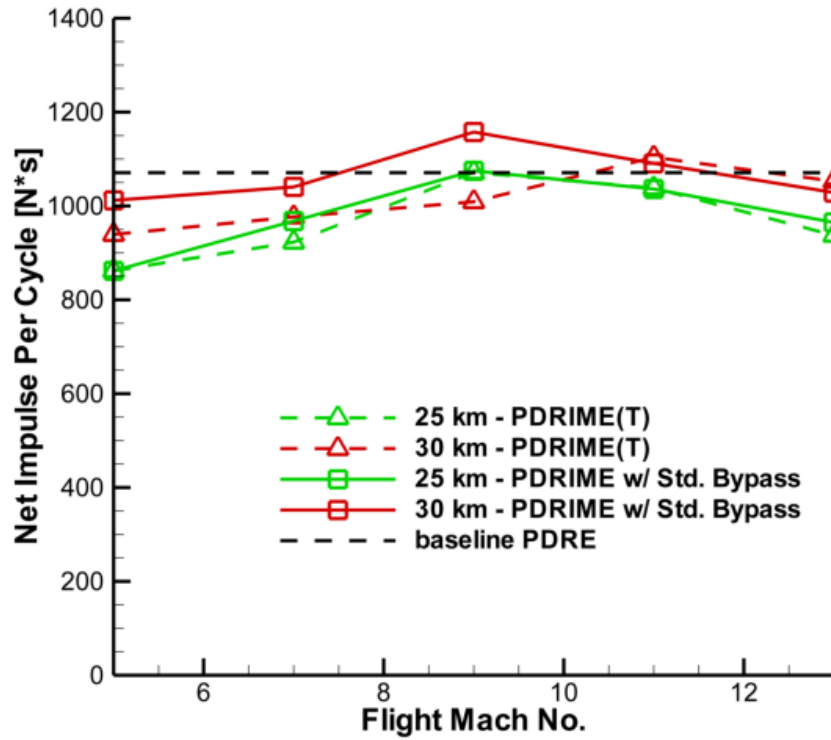


Figure 5.8: PDRIME: effects of flight mach number. Magnetic Field $B(T)$, $T_{\text{ref}} = 0K$ and $T_{\text{max}} = 7 \times 10^3 K$

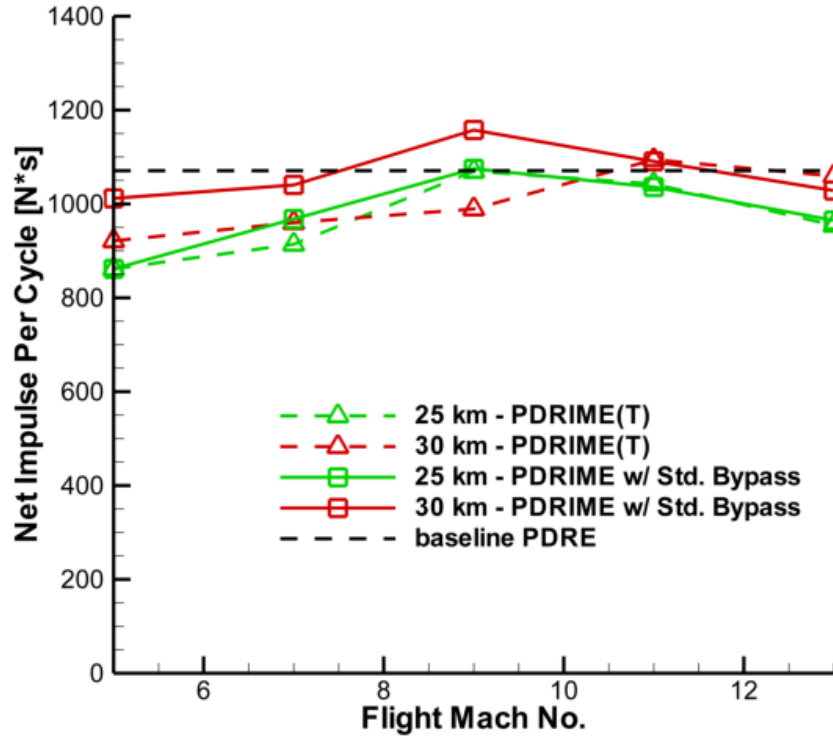


Figure 5.9: PDRIME: effects of flight mach number. Magnetic Field $B(T)$, $T_{\text{ref}} = 0K$ and $T_{\text{max}} = 8 \times 10^3 K$

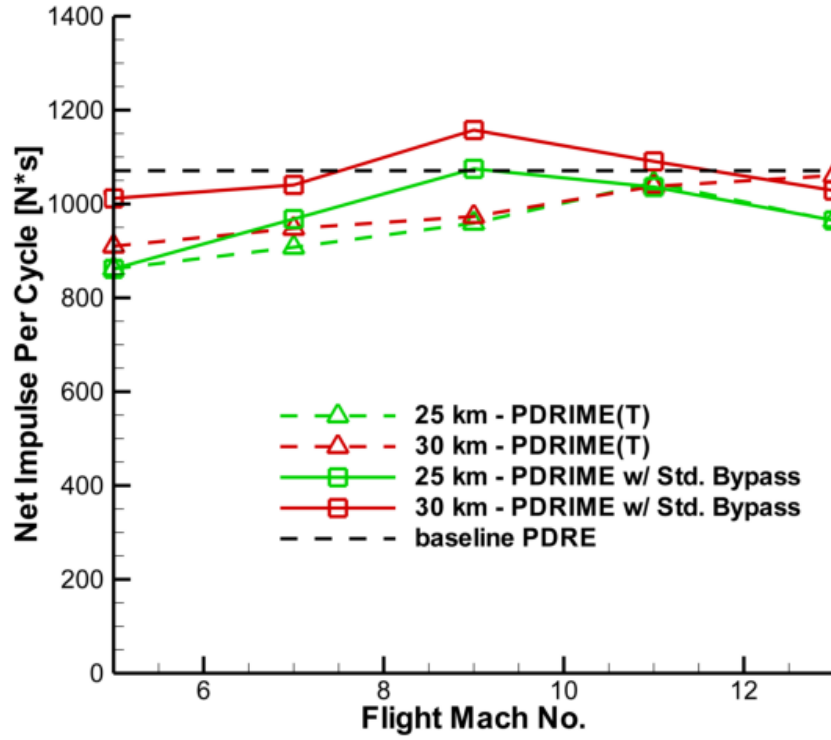


Figure 5.10: PDRIME: effects of flight mach number. Magnetic Field $B(T)$, $T_{\text{ref}} = 0K$ and $T_{\text{max}} = 9 \times 10^3 K$

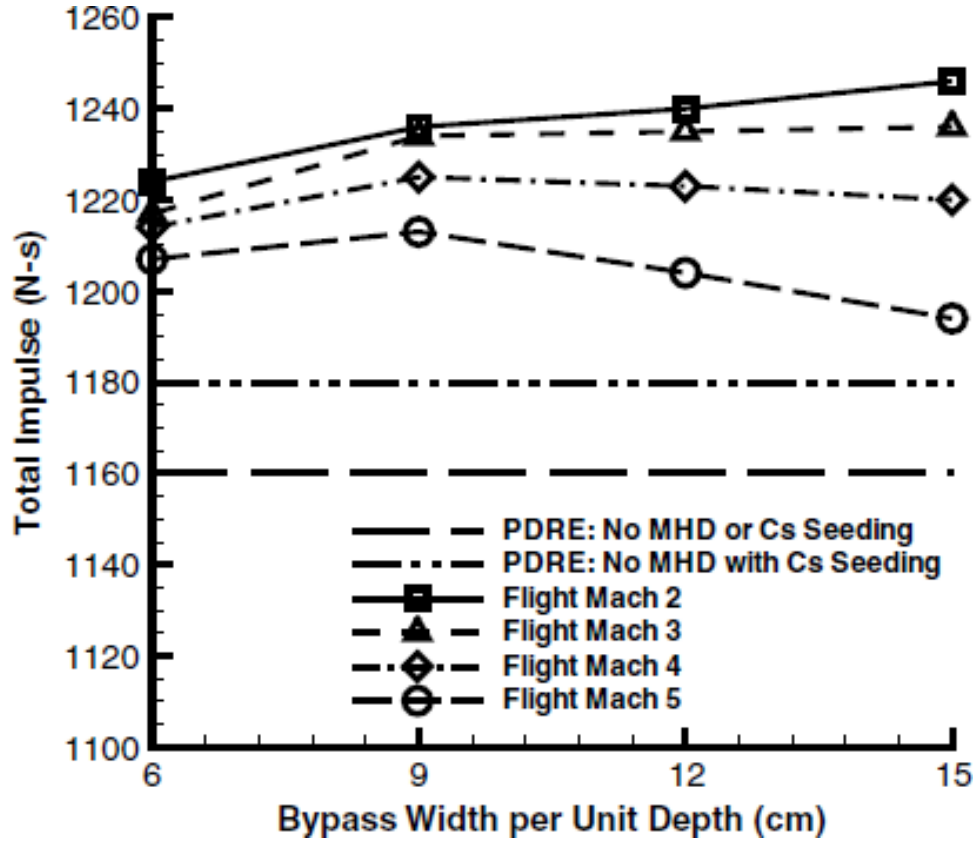


Figure 5.11: PDRIME impulse per cycle at 20 km plot against various Mach numbers and bypass area per unit depth. The chamber is initially seeded with 0.5% cesium by number at an initial temperature of 3000 K. The bypass length is $L_{bypass} = 3$ m and is seeded with 0.1% cesium by number. (from Zeineh et al.[34])

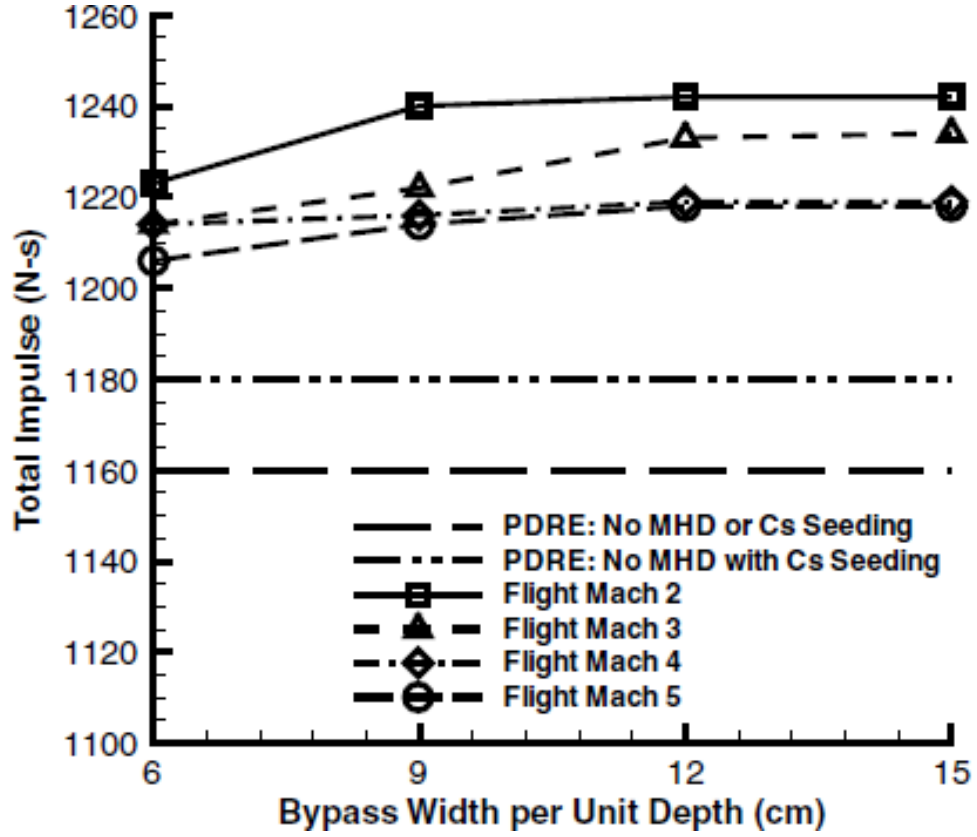


Figure 5.12: PDRIME impulse per cycle at 25 km plot against various Mach numbers and bypass area per unit depth. The chamber is initially seeded with 0.5% cesium by number at an initial temperature of 3000 K. The bypass length is $L_{bypass} = 4$ m and is seeded with 0.1% cesium by number. (from Zeineh et al.[34])

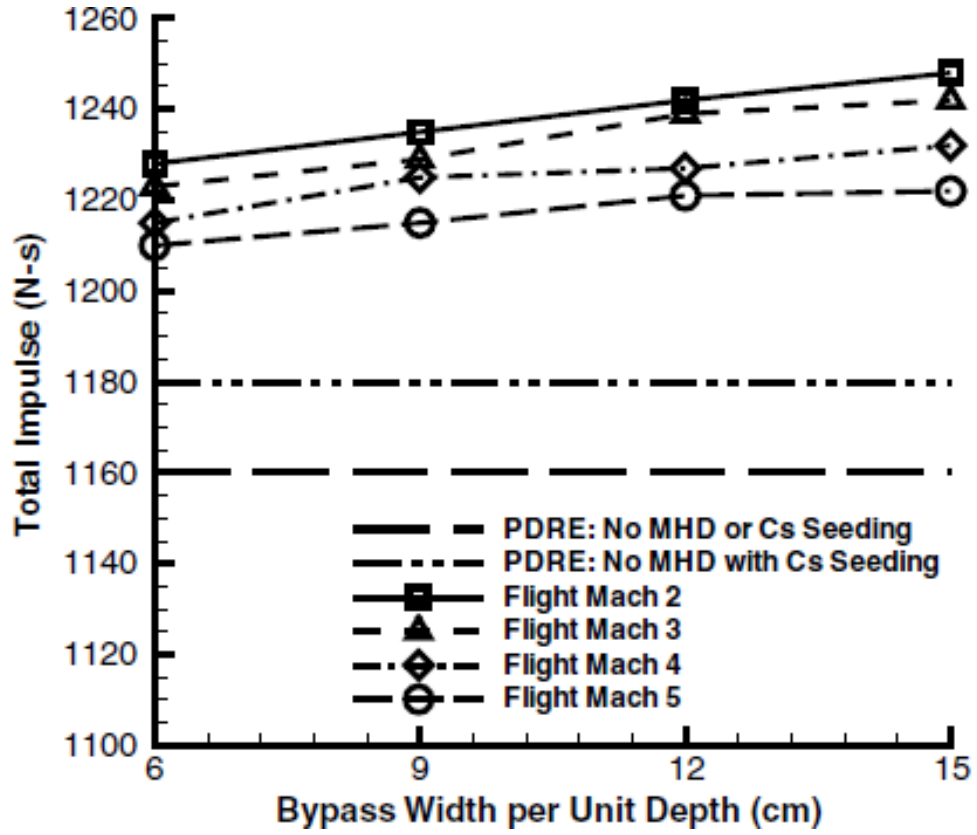


Figure 5.13: PDRIME impulse per cycle at 30 km plot against various Mach numbers and bypass area per unit depth. The chamber is initially seeded with 0.5% cesium by number at an initial temperature of 3000 K. The bypass length is $L_{bypass} = 6$ m and is seeded with 0.1% cesium by number. (from Zeineh et al.[34])

CHAPTER 6

Detonation Stability Phenomena

This chapter was taken with slight modification from the article “Stability of flame-shock coupling in detonation waves: 1D dynamics”, published in the journal Combustion Science and Technology [68].

6.1 Ignition and Instabilities

Direct initiation of the 1D detonation and the ensuing instabilities are now examined, in part for fundamental understanding but also to establish a baseline against which the effects of MHD may be compared in Chapter 7. In this study, a chamber is filled with a stoichiometric mixture of H_2 and air (temperature 300 K and pressure 1 atm), and ignition is achieved by setting a region adjacent to an end-wall of the simulated shock tube at high pressure (40 atm for most computations) and temperature (1500 K), as a simulated spark. This direct initiation is preferable to a deflagration-to detonation transition (DDT), since the latter is much more sensitive to initial conditions and grid resolution, it requires inclusion of species diffusion, and it requires a very long computational domain to reproduce both the DDT and the subsequent evolution of the detonation. Nevertheless, even direct initiation is sensitive to initial conditions and resolution. The requirements to achieve detonation

ignition with the MP5 scheme include a grid cell size Δx of less than $50 \mu\text{m}$ and a distributed simulated spark region (of length ℓ_{spark} ranging from 0.25 to 0.5 cm) with sufficiently high pressure. For example, Figure 6.1(a) is an x-t diagram illustrating the pressure contours of a spark-ignited mixture with initial pressure 20 atm, $\ell_{spark} = 0.25 \text{ cm}$, and grid size $\Delta x = 50 \mu\text{m}$, which does not achieve detonation. In contrast, Figure 6.1(b) illustrates contours of the same mixture and grid resolution but with a higher spark pressure, 50 atm, and larger region ($\ell_{spark} = 0.5 \text{ cm}$), which does achieve detonation. The constraints on initial spark conditions can be related to the concepts of minimum energy and kernel size for direct initiation [69]; similar studies by Eckett et al.[20] and He & Karagozian[70] indicate there are both pressure and temperature requirements for the spark. With an understanding of the range of satisfactory kernel/spark sizes and pressures, we fix the spark conditions to consistently achieve a rapid initiation, in order to remove the dependence of the long-term dynamics on the initial conditions. For the remainder of the studies in this chapter, the spark conditions are $\ell_{spark} = 0.25 \text{ cm}$, $P_{spark} = 40 \text{ atm}$, and $T_{spark} = 1500 \text{ K}$.

The succesful detonation initiation event proceeds in two phases. First, the gas in the spark region rapidly burns and increases the pressure, in a nearly constant-volume combustion process. This high pressure generates a strong shock which propagates into the unburnt mixture, which itself is ignited after a time delay and rapidly burns, starting from the region closest to the spark. In a scenario described as the SWACER mechanism [71], the combustion wave is amplified as it overtakes the leading shock, and the coalescence of the two fronts leads to extremely high peak pressures for a very short time. This event is easily identified in the trace of the peak pressure versus time as shown, for example, in Figure 6.2, and is referred to hereafter as the “re-explosion” event, the first explosion having taken place within the initial spark

region. Two different grid sizes are used in Figures 6.2(a) and 6.2(b), $\Delta x = 12.5 \mu\text{m}$ and $2.5 \mu\text{m}$, respectively, using the MP5 scheme. A more detailed examination of the dynamics for these two different grid sizes is shown in Figures 6.3 and 6.4, as will be discussed below.

The high pressure of this re-explosion event initiates another strong shock, which is followed, after an induction length (ℓ , measured in the reference frame of the shock) by the combustion zone. This flame is initially strongly coupled to the shock ($\ell \rightarrow 0$) and the wave is strongly over-driven, i.e., its speed exceeds that of the Chapman-Jouget (CJ) detonation. As the degree of overdrive decays and the detonation approaches the CJ limit, instabilities begin to appear, as shown in Figure 6.2(a) after about $35 \mu\text{s}$ and in Figure 6.2(b) after about $25 \mu\text{s}$.

These spark-ignited detonation simulations demonstrate the appearance of different instability modes. For both sets of results in Figure 6.2, instabilities appear when the detonation becomes close to the CJ condition, starting with a small-amplitude, but high-frequency mode – hereafter referred to as the ‘HF’ mode. For the low-resolution case in Figure 6.2(a), the transition to the high-frequency (HF) mode occurs at a time of the order of $30 - 35 \mu\text{s}$; this instability regime is shown in detail in Figure 6.3(a). For the high-resolution case, Figure 6.2(b), the transition occurs earlier, close to $25 \mu\text{s}$; this regime is shown in detail in Figure 6.3(b) for roughly the same time period as in Figure 6.3(a). For both grid sizes, we observe that at around $45 \mu\text{s}$, there is a transition towards a lower frequency but high-amplitude mode – referred to here as the ‘HA’ mode. This transition is more gradual in the high-resolution case, with both modes coexisting during a period of time (between approximately 44 and $48 \mu\text{s}$), as shown in more detail in Figure 6.4(b). In the low-resolution case of Figure 6.4(a), however, the behavior is less gradual and more

chaotic. The contrast between these two profiles is striking; while a periodic signal can still be detected in Figure 6.4(a), the characteristics and frequencies are both very different. Besides the smoothness of the temporal waveforms of the high amplitude instabilities, we also note that a period-doubling in the high resolution case, i.e., the HA signal has a dual oscillation (high-low pressures) which is not apparent at lower resolution¹. We note also that there are other manifest differences in the specific dynamical features of these instabilities, e.g., in the appearance of noise in the waveform after the re-explosion event (Figure 6.2(a)), which is eliminated for the higher resolution case in Figure 6.2(b). Thus, it is clear that there can be significant effects of the grid resolution on the dynamics of the instabilities. Furthermore, the appearance of sharp features in the traces also suggests that special care must be exercised in avoiding numerical procedures which can arbitrarily sharpen gradients, as mentioned earlier.

There is no obvious “very high frequency” mode that arises after the re-explosion event and before the initiation of the high frequency mode, as seen by Leung et al.[17], in the well-resolved result in Figure 6.2(b). But if one explores in detail the time regime after the re-explosion event, for grid sizes Δx of $2.5 \mu\text{m}$ and even smaller, as shown in Figure 6.5, one does observe relatively low amplitude and very high frequency oscillations, with frequencies and amplitudes dependent on the grid resolution. To examine the origin of these low amplitude oscillations, the variation in induction length as a function of time, determined from peaks in the concentration of H atoms, may be explored for these different resolutions. A plot of induction length as a function of time is shown in Figure 6.6(a), with an expanded view in Figure 6.6(b) corresponding to the same time period as shown in Figure 6.5. The

¹This was verified for longer time periods than shown; for clarity purposes, the extent of the simulation results shown in the figures has been truncated.

results in Figure 6.6 indicate that the amplitude of oscillations in induction length corresponds to the grid size Δx , and moreover, the frequency of oscillation corresponds to the ratio of the CFL number here (0.4) to the sampling period (1 nanosecond). Thus it appears that the very high frequency (and very low amplitude) oscillations seen using complex kinetics merely correspond to numerical uncertainties associated with the location of the peak pressure or peak in atomic hydrogen (mole fraction).

Because the re-explosion event is clearly identifiable, we can use this feature to conduct a more detailed study of the effect of grid resolution. For example, one can examine the variation of the measured time delay to this second explosion event, t_{exp} , for the specific initial spark conditions noted previously. Here the uniform grid spacing Δx is varied from $0.5 \mu m$ to $20 \mu m$. Figure 6.7 illustrates how the time to re-explosion for the MP5, AW5, and MW5 schemes varies with the grid resolution. Since the AW5 & MW5 schemes are more diffusive than MP5, it is not surprising that the AW5 & MW5 curves exhibit a shallower profile. The most striking feature here is the non-monotonic behavior, i.e. the presence of a maximum in the time to explosion, which delineates two regimes. The peak in t_{exp} for MP5 in Figure 6.7 occurs at approximately $\Delta x = 7 \mu m$, whereas the critical Δx value is slightly lower, at approximately $5.5 \mu m$, for AW5, and even lower for MW5 at $\Delta x \approx 4 \mu m$. For grid resolutions Δx below the critical value, the numerical simulation is in a “convectively” dominant regime, where the combination of the numerical scheme and fine grid resolution is sufficient to effectively mitigate the effects of numerical diffusion in the detonation formation. AW5 & MW5 produce similar values of t_{exp} for $\Delta x < 3 \mu m$, but for this complex kinetics scheme, time convergence for t_{exp} may not be reached except for $\Delta x < 0.5 \mu m$, consistent with findings by Powers & Paolucci[72]. In the case of AW5, grid convergence is observed at $\Delta x \approx 0.5 \mu m$.

For grid resolutions greater than the critical value of Δx in Figure 6.7, we enter the numerically dissipative regime, where coupling of the fluid mechanics and kinetics is enhanced due to numerical diffusion of temperature and chemical concentrations. The value of t_{exp} thus decreases with increasing Δx in this numerically dissipative regime.

To obtain results that are truly insensitive to the numerical effects, one requires $\Delta x \rightarrow 0$, since the two methods converge in that limit to a single value for t_{exp} , but of course this is a practical impossibility. The results in Figure 6.7 suggest that, to be able to reasonably resolve detonation propagation and shock-flame coupling dynamics, a grid spacing of $\Delta x = 2.5 \mu\text{m}$ or smaller may produce acceptable accuracy, given less than a 5% difference between the two different schemes. Yet the time to re-explosion is but one parameter that is affected by grid resolution, and calculations of the shock-flame instabilities at smaller grid spacings are needed to be able to explore other quantitative features.

A simple fast Fourier transform (FFT) can be used to find the spectral content of the two instability modes, HF and HA, which are observed in Figures 6.2 - 6.4. Figure 6.8 shows FFT results for the MP5 scheme and grid sizes $\Delta x = 2.5, 1.5$, and $1.0 \mu\text{m}$. There is remarkable consistency in the dominant frequencies here; for both HA instabilities near a frequency of approximately 0.35 MHz and HF instabilities near 2.3 MHz, there is relatively little difference in results for $\Delta x \leq 2.5 \mu\text{m}$. This observation suggests that the spectral content of the resulting instability is relatively insensitive to the grid spacing, as long as Δx lies below the critical value for the start of numerical diffusion. At high frequencies, above 4 MHz, there is some grid dependency; in fact, frequencies above 4 MHz are not seen for $\Delta x = 1.5 \mu\text{m}$. The spectral content around 4.5 MHz is likely to be a harmonic of the strong 2.3 MHz

signal. Note that since the instabilities develop for a finite time only, the sampling statistics of the FFT are limited. The use of a wavelet decomposition did not provide improvements in the signal-to-noise ratio.

These results confirm earlier complex kinetics findings [16] which indicate that a detonation near the CJ limit has two physically distinct instability modes. The high frequency mode always appears first and marks the transition from a ‘stable’ CJ detonation, where a low frequency mode appears later in time. The overdriven detonation simulations by Leung et al.[17] with a two-step reaction mechanism also demonstrate multiple instability modes, but with distinct differences from those seen here, as noted above.

Our observed fluctuations in key properties (e.g., in species concentration, temperature, and pressure) of the fluid within the induction zone are described by Oran & Boris[73] as ‘hot spots’. The present study with complex reaction kinetics shows that these ‘hot spots’ contribute to an initial stage of the flame dynamics. In this regime, the induction length is very small ($\ell \ll \ell_{CJ}$), and acoustic waves generated by the perturbed chemistry are rapidly transmitted to the shock, i.e. leading to high-frequency modes. Because there is a very limited amount of fluid that can participate in the fluctuation of the heat release, only low-amplitude perturbations of the CJ peak pressure appear. As these acoustic waves reach the leading shock and strengthen it, their frequency can be measured as that of the fluctuations of the peak pressure. Eventually the average induction length continues to increase and the second mode appears, which directly couples the flame speed with the shock, resulting in fluctuations with lower frequency but much higher amplitude. This interpretation of our observations will be elaborated upon and verified in the next section.

6.2 Simplified Model

To better understand and interpret the coupling between reactive and fluid mechanical/acoustic phenomena that generates our observed results, a model for the induction zone may be constructed and explored. This model is composed of a leading shock, a heated, post-shock medium(fluid), and a flame front, all of which are illustrated in Figure 6.9. A single period of the detonation oscillation can be described, in the reference frame of the shock, in a manner similar to that of McVey & Toong[74], as follows. Fluctuations at the flame front create an acoustic (pressure) disturbance, which travels at the acoustic wave speed, λ_{ac} , through the induction zone until it reaches the leading shock; this process occurs between reference times t_a and t_b . Upon contact, the pressure fluctuation carried by the acoustic wave will accelerate the shock and alter the post-shock conditions, thus creating an entropy disturbance (temperature fluctuation). This entropy disturbance will propagate back into the induction zone at the entropy wave speed, λ_{en} , toward the flame front, this process occurring between times t_b and t_c . A resonant condition is achieved when, upon contact with the flame, the entropy wave creates a new acoustic disturbance in the flame, and the cycle repeats. Figure 6.9 illustrates this phenomenon, with relations for the entropy and acoustic wave speeds as follows, respectively:

$$\lambda_{en}(x, t) = \left. \frac{dx}{dt} \right|_{en} = u_2(x, t) \quad (6.1)$$

$$\lambda_{ac}(x, t) = \left. \frac{dx}{dt} \right|_{ac} = c(x, t) - u_2(x, t) \quad (6.2)$$

Here $u(x, t)$ is the fluid velocity, $c(x, t)$ is local speed of sound, $D(t)$ is the detonation velocity, and $u_2(x, t) = |u(x, t) - D(t)|$ is the post-shock fluid velocity in the

detonation reference frame. From these wave speeds the period of the cycle, τ , may be expressed by

$$\tau = \left| \int_{x_f}^{x_s} \frac{1}{\lambda_{ac}(x, t)} dx \right| + \left| \int_{x_s}^{x_f} \frac{1}{\lambda_{en}(x, t)} dx \right| \quad (6.3)$$

where $x_s = (t - t_0) \cdot D(t)$ is the position of the shock and x_f is the position of the flame.

At a zeroth-order approximation, the fluid properties in the induction region, $Q_2(x, t)$, are assumed to weakly vary with time for a given half cycle, $\frac{\partial Q_2(x, t)}{\partial t} \simeq 0$ & $\frac{\partial Q_2(x, t)}{\partial x} \simeq 0$. This also implies that the relative positions of the flame and shock front are approximately constant. From this approximation, the period can be determined

$$\tau = \frac{\bar{\ell}}{c_{ab} + u_{ab} - \bar{D}_{ab}} + \frac{\bar{\ell}}{u_{bc} - \bar{D}_{bc}} \quad (6.4)$$

where $\bar{\ell}$ is the period-averaged induction length, ab is the fluid state at the acoustic wave half-cycle, bc is the fluid state during the entropy wave half cycle, and u_α , c_α , and \bar{D}_α are the the fluid speed in the detonation reference frame, speed of sound, and average detonation speed, respectively, for half-cycle α . The model for acoustic and entropy half cycles are illustrated in Figure 6.10, corresponding to observed oscillations as indicated in the inset. From the period of the combined cycles, the frequency in oscillations of the peak pressure trace is $f = \tau^{-1}$.

Data may be extracted from the full kinetics results at different peak pressure cycles from the high frequency as well as high amplitude regime, and compared with the simplified model expressed in Equation 6.4. Figure 6.12 illustrates the evolution of the induction zone temperature profile in the detonation reference frame for a given period of the high amplitude mode, with data for the acoustic wave

propagation in (a) and for the entropy wave in (b). The density distributions for the corresponding HA mode are shown in Figure 6.14. Using the induction zone data and the period from Eq. (6.4), the frequency $f \approx 310 \text{ kHz}$ may be estimated for the HA mode, which is in excellent agreement with that obtained from the spectral analysis using the full simulation, $310 \pm 40 \text{ kHz}$, shown in Figure 6.8. Performing the same analysis on the high frequency (HF) mode, illustrated in the temperature profiles in Figure 6.11 and the density profiles in Figure 6.13, the frequency $f \approx 2.08 \text{ MHz}$ may be estimated, which is also in good agreement with that extracted from the spectral analysis ($2.29 \pm 0.4 \text{ MHz}$) in Figure 6.8. Hence this simple model appears to capture reasonably well the global processes that lead to the high- and low-frequency detonation instability modes.

We should point out that this simple model has been successfully applied to another case of shock-induced instability. For strong, ionizing shocks in a noble gas (specifically, argon), a similar structure of shock, induction zone and reaction front can be observed [75, 76, 77]. The instability in this case has lower amplitudes, due to the absence of exo-thermic reactions, but is also well explained by a resonant coupling between the shock front and reaction zone through the transmission and reflection of entropy and acoustic waves [75]. In fact, the 2D structure of that flow could be found to have features remarkably similar to detonations including, for example, artificial soot patterns [77]. This indicates that the model, despite its simplicity, provides a good insight into the true physical mechanisms involved and may have relevance to a universal class of instabilities in reactive shock systems.

6.3 Discussion

The ‘hot spot’ which appears in the high frequency mode temperature profiles (Figure 6.11) is of particular interest in interpreting the differences between modes. This hot spot burns only a fraction of the overall mixture and the heat release is not sufficient to significantly alter the characteristic speeds of the flow (especially since the speed of sound only varies with the square-root of the temperature). Examination of the temperature profiles in Figure 6.11, in particular panel (a), shows that the reaction zone fluctuates from a ‘hot-spot’ position without significant change in location; if at all, the perturbed region of accelerated burning is actually convected *downstream*. This pre-ignition effect does not allow the flame to accelerate, and in the case of the high frequency mode, the detonation is still slightly overdriven. The resonance between the perturbation of the chemical rates at the hot spot and the shock front still remains, though, and is the basis for the observed oscillation pattern, as indicated by the agreement between computed and measured frequencies.

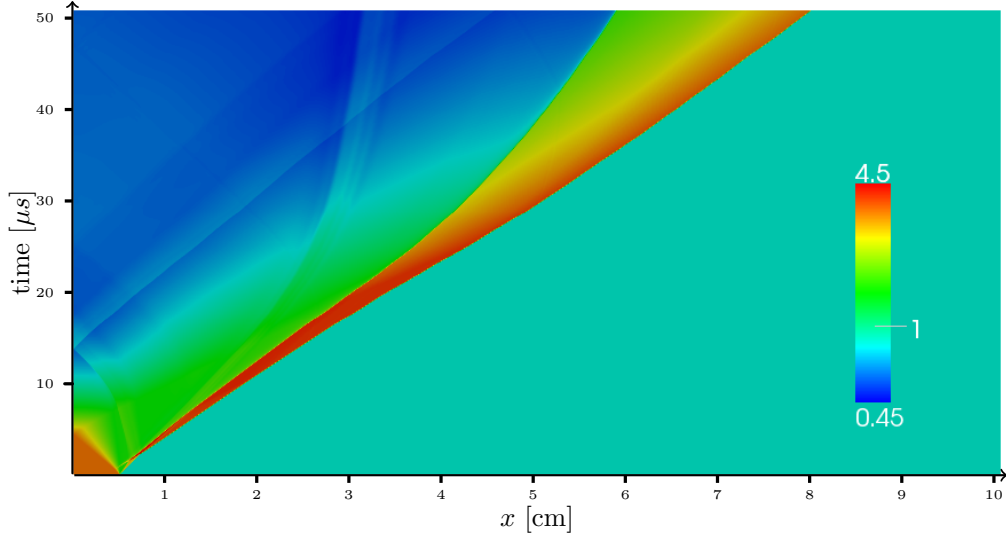
By contrast in the high amplitude mode’s temperature profiles, seen in Figure 6.12, there is no observed ‘hot spot’. More likely, the perturbation has moved to the flame region and any acceleration of the chemical rates in that region can enhance the rate of heat release much more significantly. This allows what is presumably a SWACER-like [71] mechanism to govern this high amplitude regime, starting from a flame at the furthest distance from the shock, $\bar{\ell}_{max}$, and accelerating towards the shock as it burns the fluid in the induction zone, releasing large amounts of energy up to the point of contact with the shock. This can be seen in Figure 6.12(a), where the temperature profiles for the HA mode clearly exhibit a dramatic reduction of the distance between the shock and flame fronts in time. Thus, the HA mode is very

much a SWACER-like mechanism, while the HF mode is not. This large change in shock-flame distance is not seen in the two-step model results of Leung et al.[17], thus highlighting another important feature of the true kinetics.

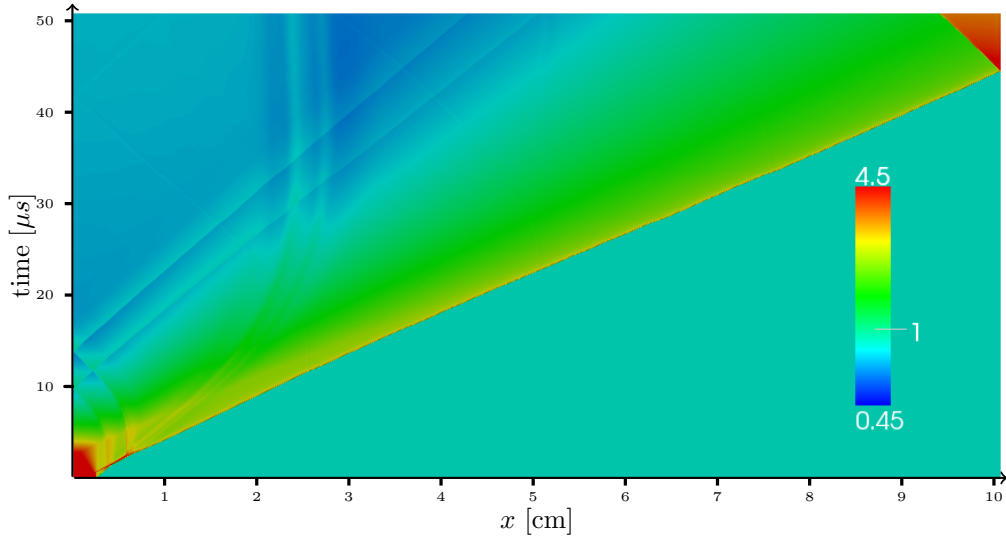
From the density profiles illustrated in Figures 6.13 and 6.14, it becomes quite apparent, even in the high-frequency regime, that there is a large variation of density within the induction zone throughout a given cycle. Neither single-step Arrhenius kinetics [12, 13, 14, 15] nor a two-step reaction model [17] account for these large density variations; their ZND approximation is only valid for a brief portion of the cycle in the HA regime. Therefore, more complex reaction kinetics than have been incorporated in the past should be utilized to capture the full quantitative features of the evolving detonation instabilities. The simple two-wave resonant model explored in Section 6.2 also depends on approximately constant flow properties within the induction zone, and thus the same limitations apply to this model, except that we have separated the cycle into two sections, each with different average flow properties and induction lengths. Hence a reasonable representation of global dynamical character is achieved with the simple model.

As the detonation relaxes toward the CJ condition prior to the onset of the instabilities, the post shock conditions can be used to determine the chemical time scale corresponding to the induction zone. For the present simulations this time scale is approximately $\tau_{hydr} = 300 \pm 10 ns$. Using the same post shock conditions in a zero-dimensional reactive simulation produces time scale $\tau_{chem} = 215 \pm 5 ns$. This level of disparity is to be expected, because the zero-dimensional calculations are performed at constant volume, and as the system approaches the peak of the H concentration (the criterion used to define the flame center), the energy liberated remains confined and leads to a more rapid rate of reaction. Using the τ_{hydr} value as a normalization

factor, the two modes observed in the present simulations, HF and HA, correspond to normalized periods of 1.6 and 10.75, respectively. This is within the range of instabilities observed by Leung et al.[17]; a more exact correspondence is difficult to obtain, since several parameters are being varied in their two-step model, with no direct relation to the actual chemical system. As noted in Section 6.1, in the present studies we do not observe the so-called “very-high frequency” mode seen by Leung et al.[17], except for very low amplitude oscillations that are shown to be a numerical artifact. In fact, a physical instability at very high frequency would correspond to an oscillation period that is *less* than the induction delay, implying that the “hot spot” be located very close to the shock. In that case, the extent of this perturbation (i.e., the reaction time) would need to be much smaller than the induction period. With realistic chemistry, this may not be possible. Thus, it is conjectured here that the very high frequency mode may be an artifice of the two-step model.

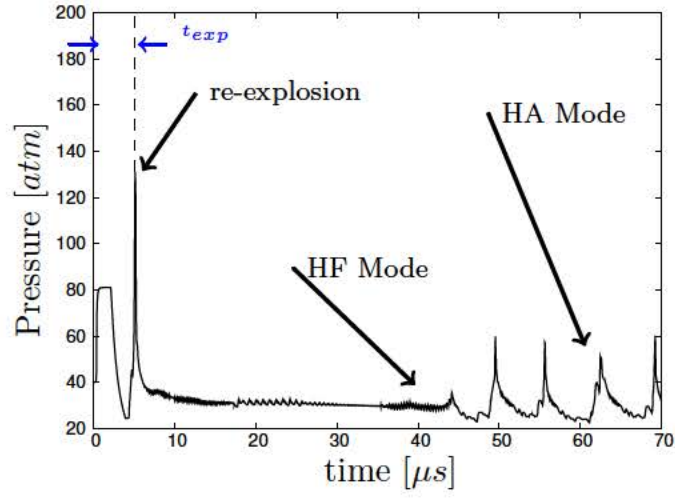


(a) $P_{spark} = 20 \text{ atm}$ with 0.25 cm spark length where detonation is not achieved

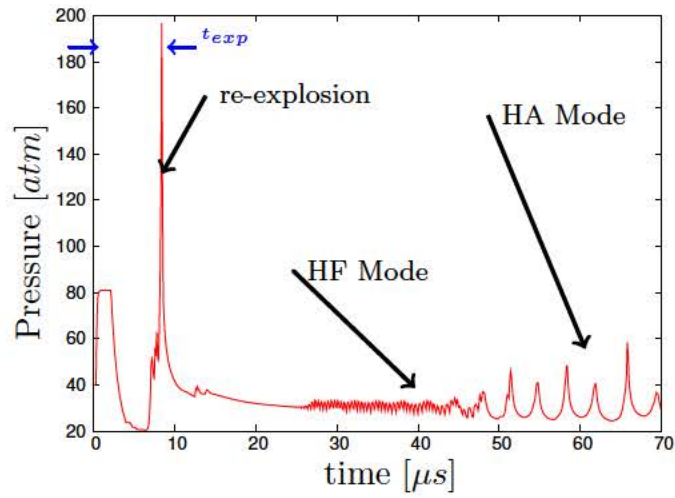


(b) $P_{spark} = 40 \text{ atm}$ with 0.25 cm spark length where detonation is achieved

Figure 6.1: Pressure contours on an x-t diagram for a spark ignited H_2 -Air mixture with $\Delta x = 50 \mu m$, computed using the MP5 scheme.

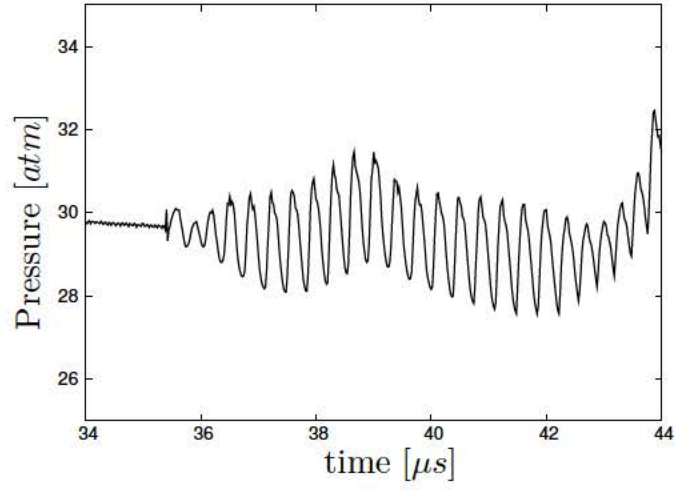


(a) $\Delta x = 12.5 \mu m$

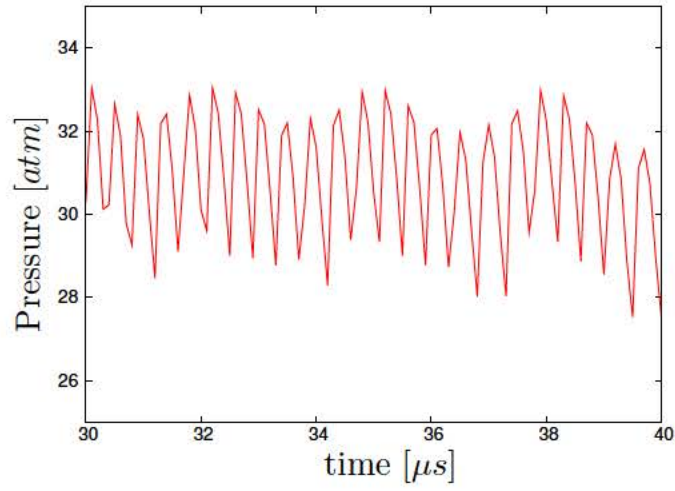


(b) $\Delta x = 2.5 \mu m$

Figure 6.2: Peak pressure-time history of a spark-ignited H_2 -air mixture simulated with two different grid cell sizes Δx using the MP5 scheme. The time to re-explosion, t_{exp} , high amplitude mode, HA, and high frequency mode, HF, are illustrated.

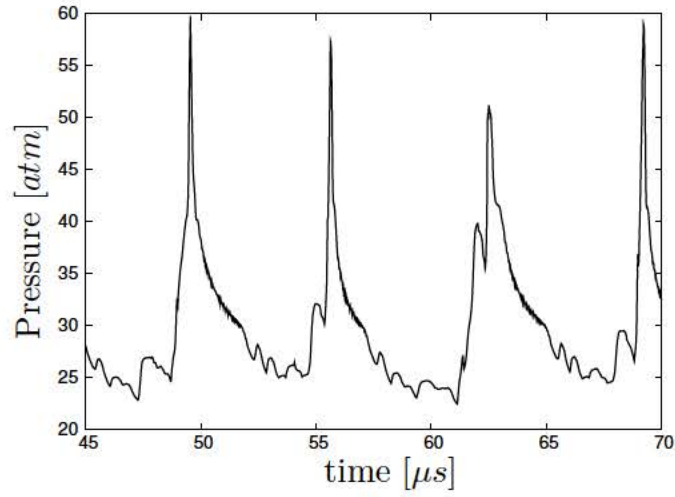


(a) $\Delta x = 12.5 \mu m$

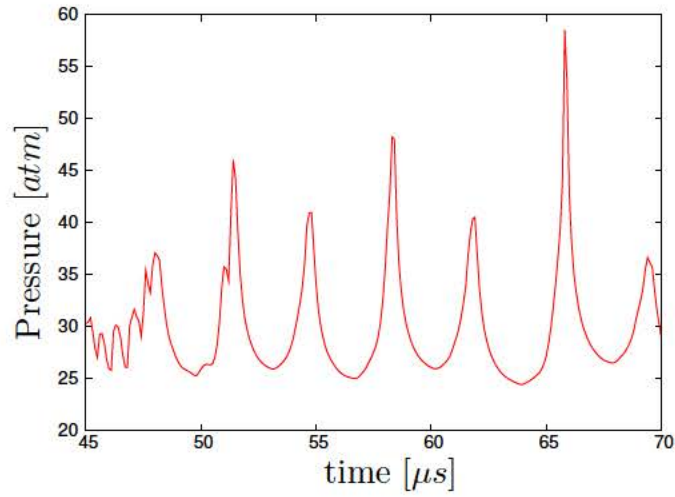


(b) $\Delta x = 2.5 \mu m$

Figure 6.3: High frequency portion of peak pressure time history as in Fig. 6.2, simulated with two different grid cell sizes Δx .



(a) $\Delta x = 12.5 \mu m$



(b) $\Delta x = 2.5 \mu m$

Figure 6.4: High amplitude portion of peak pressure time history as in Fig. 6.2, simulated with two different grid cell sizes Δx .

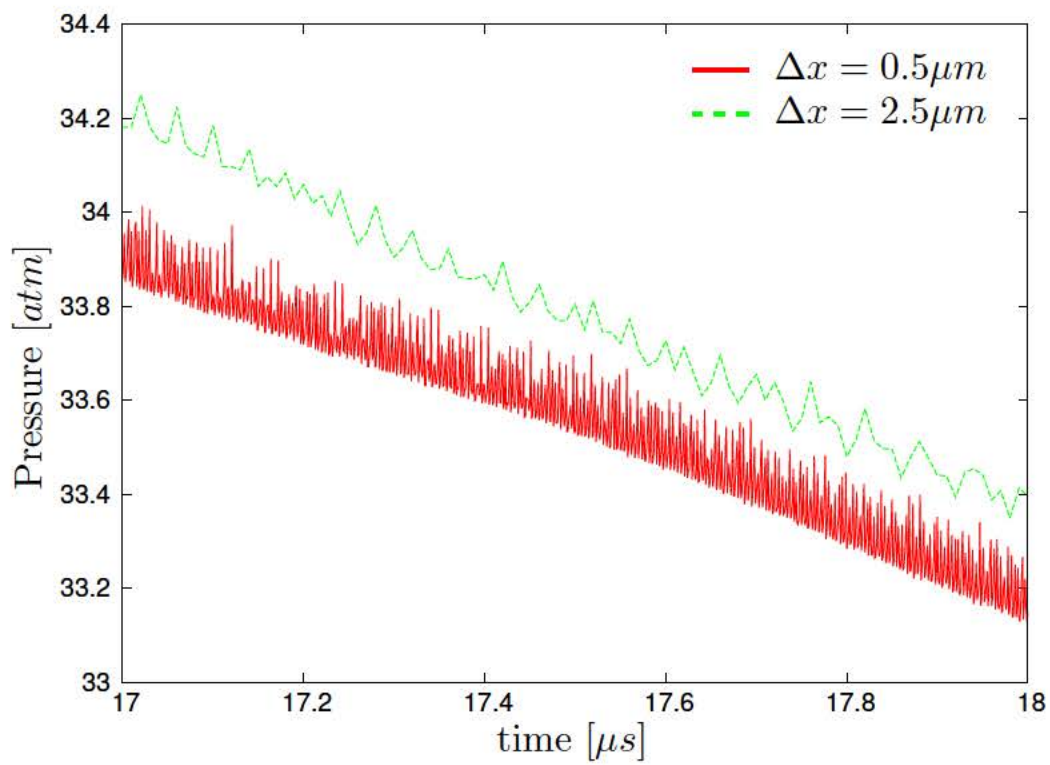
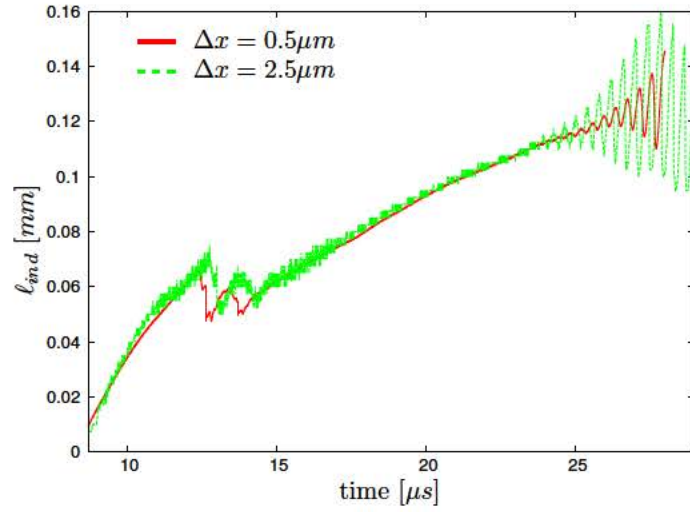
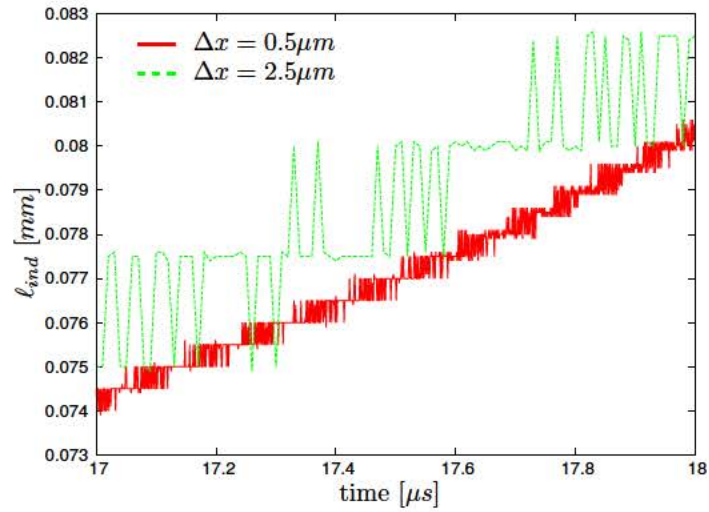


Figure 6.5: Early portion of peak pressure time history after re-explosion, simulated with two different grid cell sizes Δx .



(a) Induction length vs. time



(b) Induction length vs. time (zoom)

Figure 6.6: Early portion of induction length time history after re-explosion, simulated with two different grid cell sizes Δx .

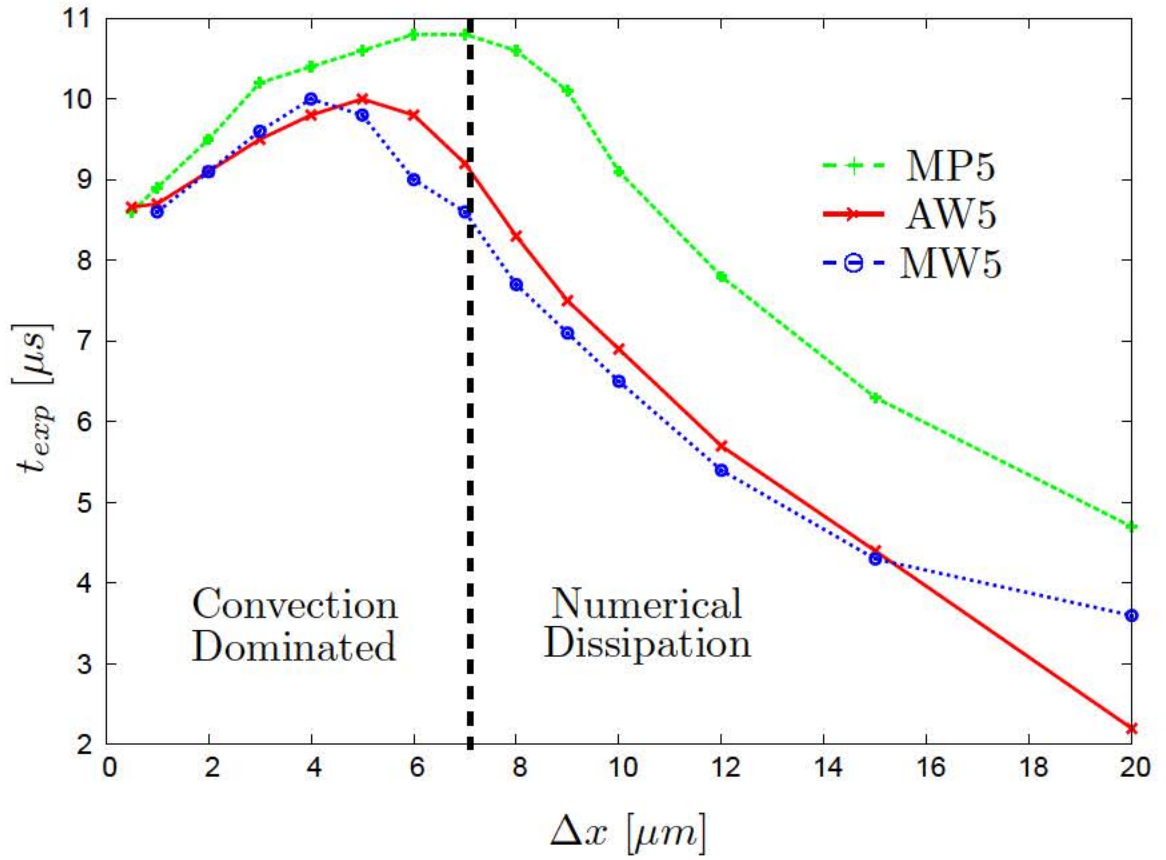


Figure 6.7: Time to re-explosion as a function of grid resolution size Δx for the MP5, AW5, and MW5 schemes.

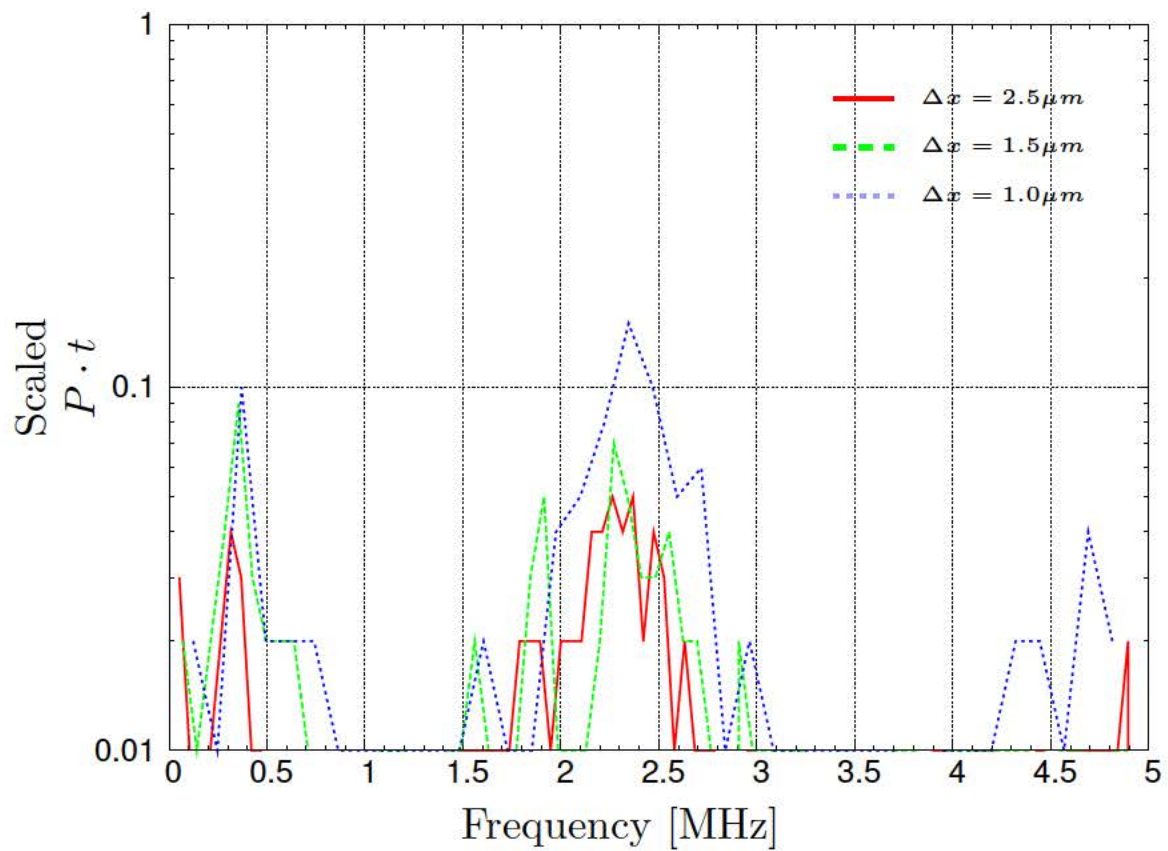


Figure 6.8: Fast Fourier transform of peak pressure traces for the unstable detonation with 3 different grid sizes Δx , simulated using the MP5 scheme.

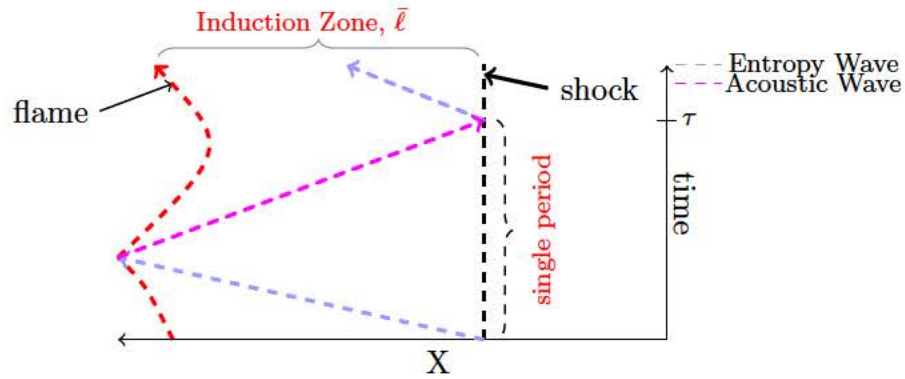


Figure 6.9: A simple model involving the shock, flame, induction zone, and transmission of entropy and acoustic waves to represent shock-flame coupling.

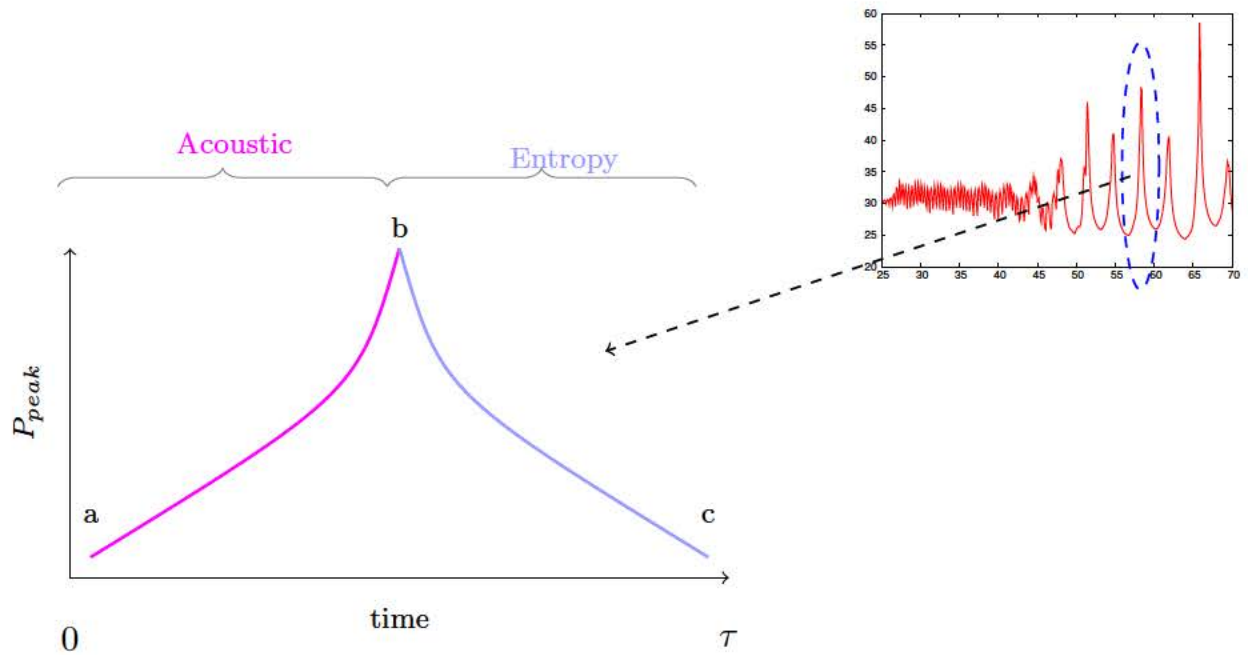
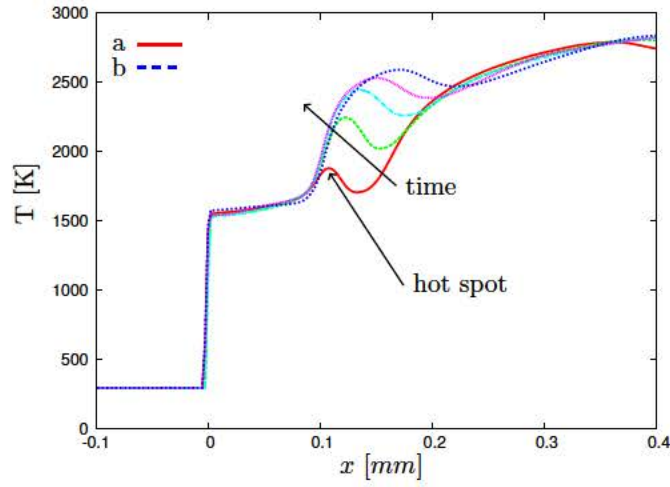
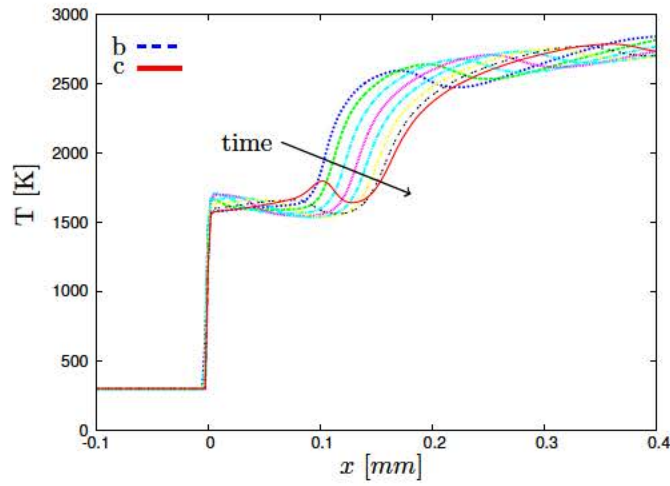


Figure 6.10: Simplified model of the peak pressure cycle (left) used to represent the numerically observed pulsations in peak pressure (right inset).

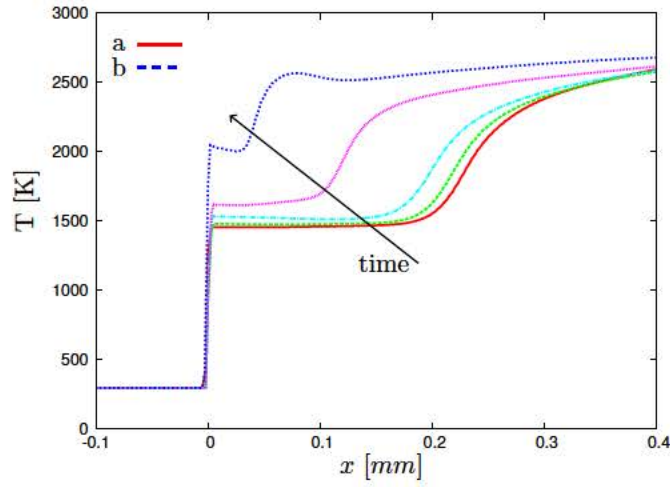


(a) acoustic wave cycle

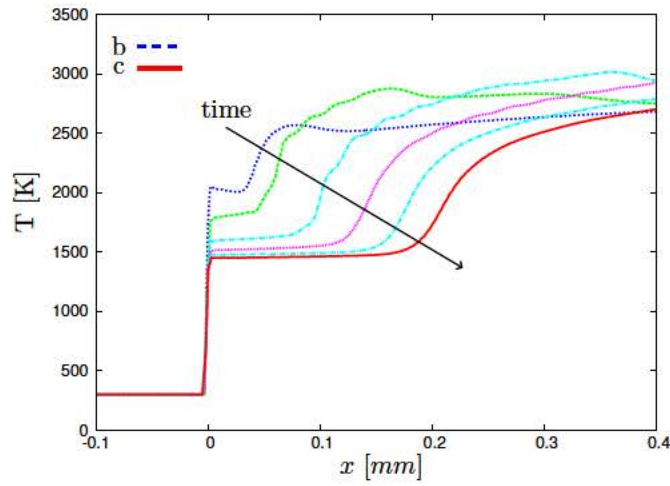


(b) entropy wave cycle

Figure 6.11: Temperature distribution in shock reference frame at different times within: (a) the acoustic wave cycle (times $a = 29.1 \mu s$ to $b = 29.3 \mu s$) and (b) the entropy wave cycle (times $b = 29.3 \mu s$ to $c = 29.5 \mu s$). Data are extracted from high frequency (HF) mode results.

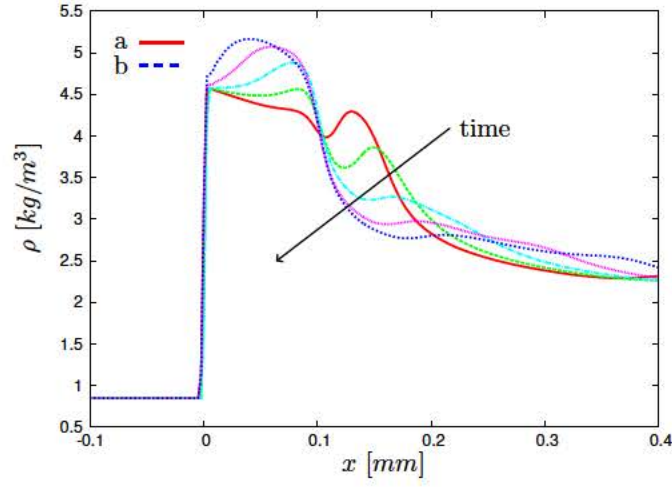


(a) acoustic wave cycle

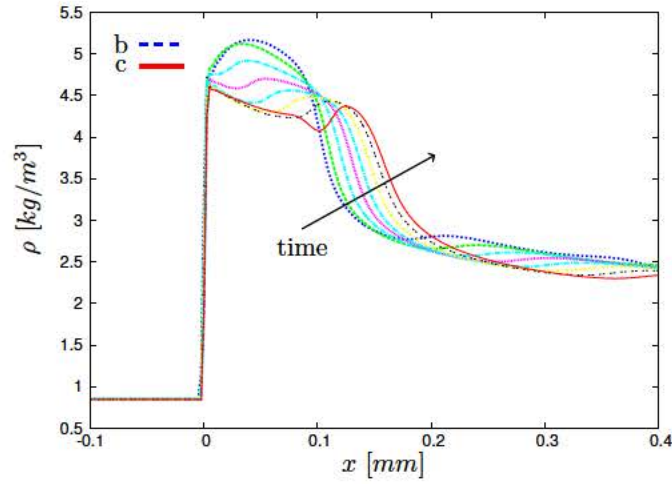


(b) entropy wave cycle

Figure 6.12: Temperature distribution in shock reference frame at different times within: (a) the acoustic wave cycle (times $a = 57.1 \mu s$ to $b = 58.3 \mu s$) and (b) the entropy wave cycle (times $b = 58.3 \mu s$ to $c = 60.7 \mu s$) Data are extracted from high amplitude (HA) mode results.

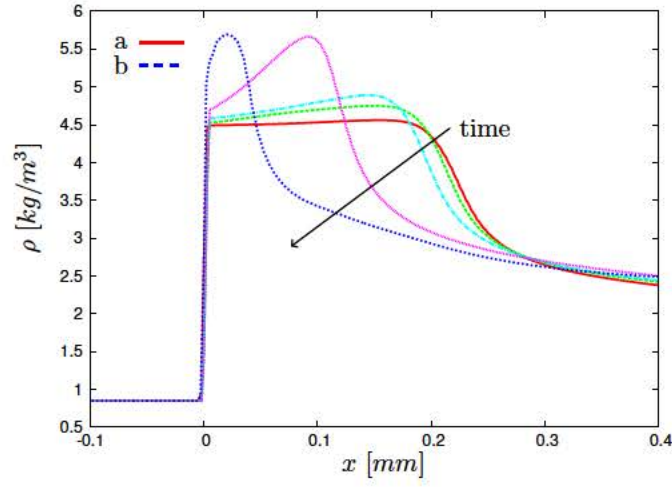


(a) acoustic wave cycle

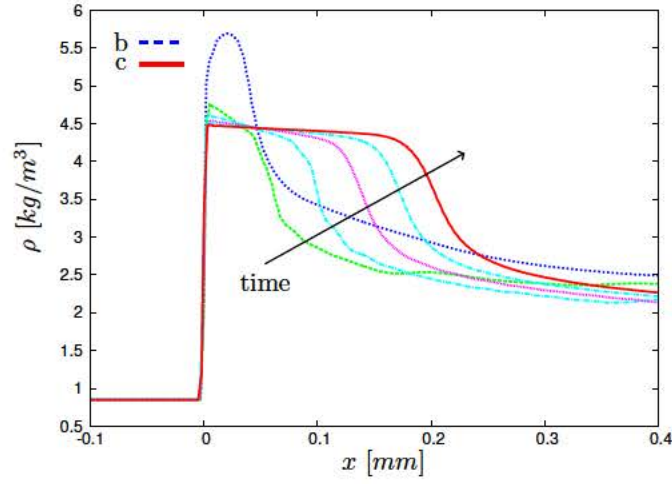


(b) entropy wave cycle

Figure 6.13: Density distribution in shock reference frame at different times within: (a) the acoustic wave cycle (times $a = 29.1 \mu s$ to $b = 29.3 \mu s$) and (b) the entropy wave cycle (times $b = 29.3 \mu s$ to $c = 29.5 \mu s$). Data are extracted from high frequency (HF) mode results.



(a) acoustic wave cycle



(b) entropy wave cycle

Figure 6.14: Density distribution in shock reference frame at different times within: (a) the acoustic wave cycle (times $a = 57.1 \mu s$ to $b = 58.3 \mu s$) and (b) the entropy wave cycle (times $b = 58.3 \mu s$ to $c = 60.7 \mu s$). Data are extracted from high amplitude (HA) mode results.

CHAPTER 7

Magnetic Field and Detonation Interactions

In evaluating the feasibility of the PDRIME configurations we must examine how a magnetic field will interact with a conducting, reacting flow such as the detonation as well as the amount of conductivity required in the fluid for sufficient interaction of the magnetic field and detonation. In Chapter 5, various PDRIME configurations have been evaluated using simplified combustion kinetics and the exploration of the effect of MHD to accelerate the reactive flow in the bypass section or magnetic chamber piston concept(CP) or decelerate the flow in the nozzle via nozzle generator concept(NG). In these prior calculations, the ability of MHD to affect combustion was modeled globally, but not in detail. The goal of the studies in this chapter is to determine if such MHD-based acceleration/deceleration is possible for detonation phenomena.

7.1 Detonation Instabilities with Applied Magnetic Fields

In Section 6.1, the stability of an unsupported detonation was evaluated. For the next simulations, we began with the same initial conditions used in the previous chapter and seeded the fluid with different amounts of cesium (1%, 5%, and 10% by mole). Because of the large molecular weight of cesium ($\frac{M_{Cs}}{M_{H_2}} \approx 70$, $\frac{M_{Cs}}{M_{Air}} \approx 5$), adding

upwards of 10% Cs can significantly affect the dynamics of the detonation (e.g., CJ detonation speed D_{CJ} , flame temperature T_f , post-leading shock pressure and temperature P^{vN}, T^{vN} , etc.) even without the presence of an applied magnetic field. Figure 7.1 illustrates the peak pressure traces of unmagnetized spark-ignited H_2 –air detonations with the addition of 0, 1, 5, & 10 % Cs. A grid resolution of $5\mu m$ and the MP5 scheme were used to perform the 1D detonation simulations in the remainder of this section. Figure 7.1(a), in the absence of Cs addition, shows the initiation of HF and HA instability modes, as observed in Figures 6.2(a) & (b) for different grid cell sizes. With a grid resolution of $5\mu m$ it is possible to capture the essential dynamics of the detonation, within the “convection” dominated regime (see Figure 6.7), although parameters such as time to re-explosion may not be as accurately determined. Nevertheless, $5\mu m$ resolution is sufficient to enable computation of additional ionization processes of Cs and their effect on instabilities.

From Figure 7.1 (a)-(d), one will notice the oscillations become less erratic and, at 5% and 10% molar addition, approaching consistent HA behavior, as more cesium is added. Extinction, where the peak pressure decays, is significantly delayed for higher Cs concentrations. This trend is consistent with the observations of Radulescu et al.[19] where argon was incrementally added to acetylene-oxygen mixture to stabilize the detonation. Heavy argon dilution in the mixture led to large-frequency, small amplitude regular oscillations of the shock front pressure. Radulescu et al. attributed the stabilizing effect of the diluent to the lower temperature in the reaction zone which leads to slower exothermic reaction rates. For the present calculations, regularization of both the HF and HA modes with Cs addition could result from the lowering of the reaction front temperature. The addition of Cs is also observed to reduce the effective 1D detonation speed, as also determined by the theoretical reduction in the

CJ speed (see Table 7.1). The results shown in Figure 7.1 will serve as the “baseline” case for the 1D dynamics as affected by an applied magnetic field.

Now that the “baseline” behavior has been established for cesium-seeded detonations, let us now examine how the behavior of these instabilities change when one gradually increases the strength of an applied magnetic field. A fixed magnetic field is used, per Equation 2.17, with a loading factor, $\mathbf{K} = 0$ (no applied electric field). The magnetic field configuration is illustrated in Figure 7.2 where a transverse magnetic field will be applied with strengths ranging from 0 to 8 Tesla. A spark-ignited detonation will propagate into the region of this magnetic field, as shown. Figures 7.3, 7.4, and 7.5 show the peak pressure traces of detonations seeded with 1%, 5%, and 10% Cs, respectively, under the influence of various applied magnetic field strengths. Without an applied magnetic field, the peak pressure trace of a detonation with a 1% Cs has an irregular periodicity (Figures 7.1(b) & 7.3(a)). As the magnetic field is strengthened (see Figures 7.3(b)-(f)) the detonation peak pressure trace shows more prolonged erratic behavior, with no clear trend in the time at which extinction (pressure decay) takes place. But Figure 7.4 shows that as the magnetic field strength is increased, the oscillations of the peak pressure trace are driven to become less regular at earlier times and extinguish sooner. Similarly findings are observed in Figure 7.5. There are a few qualitative assessments that can be made from these results. Figures 7.3(a), 7.4(d), & 7.5(e) illustrate peak pressure traces of detonations seeded with 1%, 5%, and 10% cesium under applied field strengths of $B_z = 0, 6$, and 7 Tesla, respectively. These peak pressure traces demonstrate a general trend. It would appear as though the stabilizing effect of the presence of diluent, cesium, becomes less effective when the fluid at the flame has a greater conductivity and thus introduces an additional scale to the flame-shock dynamics. One

could attempt to find the modes that exist within the peak pressure trace to give some quantitative insight into the effects of these fields, but the data would prove unreliable due to the small time frame during which these large oscillations exist. The fact that the application of the magnetic field can degrade the cyclic stability of the 1D detonation at earlier times does indicate the ability of the \mathbf{B} field to alter the flame-detonation coupling as well as the combustion process itself.

7.2 Detonation Instabilities with MHD

The behavior of a detonation with an applied field using the MHD accelerator configuration will now be investigated. The study will begin with a fixed magnetic field, Equation 2.17, and the loading factors recommended by Cambier[4], $K_y = 1.5$ and 0.5 (i.e., the electric field scaled with $u_x \times B_z$), for the accelerator and generator, respectively. The remainder of the current detonation configuration is as specified in Section 7.1.

The previous section demonstrated that the H_2 -air, 1D spark-induced detonation under investigation is unstable under normal operating conditions with or without an applied magnetic field. Figures 7.6-7.8 show the peak pressure traces of detonation seeded with 1%, 5%, and 10% Cs, respectively, with an electric field in the accelerator configuration ($K_y = 1.5$) under the influence of various applied magnetic field strengths. In the 1% Cs test case, it becomes quite clear, when comparing Figures 7.6(b)-(f) with the unmagnetized case of Figure 7.6(a) that the MHD acceleration has the ability to regularize and sustain the oscillating detonation; the detonation does not extinguish, for the time period shown, as it does in Figure 7.6(a). When the amount of cesium is increased to 5%, as the magnetic field is increased as shown

in Figures 7.7(a)-(f) the detonation is cyclically stabilized and the peak pressure amplitude greatly reduced, by around 30%. When the amount of cesium is increased to 10%, as the magnetic field is increased from $B_z = 0T$, Figure 7.8(a), to $B_z = 8T$, Figure 7.8(f), the detonation goes from a cyclically stable galloping detonation to a nearly stable CJ detonation, with a slightly delayed onset of the initial instabilities.

Because of the strong effect the magnetic field had on the detonation stability and sustainment, in both the accelerator and generator configurations, we now examine these features side-by-side. Figures 7.9(a)(c)(e) illustrate the time dependent peak pressure, induction length, and detonation velocity, respectively, for a 10 % Cs in the accelerator configuration with applied magnetic field strengths of 0, 3, and 8 T. Figures 7.9(b)(d)(f) show the same thing for the generator configuration. Figure 7.9(a) & (c) show a significant decrease in amplitude of the peak pressure and induction length, respectively, as the magnetic field strength is increased for an accelerator, while figure 7.9(e) shows the detonation speed stabilizes near but above the Chapman-Jouguet velocity, with little propensity for extinction. In contrast, Figures 7.9(b) & (f) for the generator configuration show that peak pressure and detonation speed become erratic, with increasing magnetic field strength, and Figure 7.9(d) shows that the induction length oscillations becomes unbounded, leading to extinction for the 8 Tesla case. This contrast is quite striking, especially in the generator's influence on extinguishing the detonation. There appears to be some acceleration of the detonation, to a speed greater than CJ for the accelerator configuration (Figure 7.9(e), 8T), but overall there is no significant difference in the detonation velocities between accelerator and generator configurations.

7.3 2D Cellular Detonation in an Applied Magnetic Field

While the effects of MHD on the stability of the 1D detonation are interesting, the more realistic flow is that of a two-dimensional detonation structure. Before the effects of an applied magnetic field on a two-dimensional detonation are examined, however, one must first examine the effects of seeding cesium on the evolving cellular detonation. The detonation front as well as the underlying detonation structure may be found in the contours of the maximum pressure, P_{max} , at each point in space. These maximum pressure traces have been observed in experiments over decades in smoke-foil records[78]. The unmagnetized 2D detonation with various amounts of cesium will be examined first.

The 2D detonation initiated with a computational spark is illustrated in Figure 7.10. A grid resolution of $\Delta x = \Delta y = 50\mu m$ and the MW5 scheme are used to perform the 2D detonation simulations in the remainder of this chapter; much finer grid resolution becomes prohibitively expensive, yet this is found to be sufficient for the study of the overall detonation structure. Figure 7.11 shows that evolution of an H_2 -air detonation front (Schlieren-like plot and smoke-foil record) without the presence of an applied magnetic field and without Cs injection. From the series of figures, the Mach stem, transverse shocks, and incident shocks are well resolved. Figure 7.12 shows the detonation front and smoke-foil record after $75\mu s$ of the same detonation. At this resolution, it can be clearly seen in the smoke-foil record, Figure 7.12(b), that cellular detonation is achieved, and is consistent with the established literature for cellular detonations[78, 79, 80, 81]. The simulated detonation cellular length and width for this configuration are $\lambda_L = 2.7 \pm 0.1 mm$ and $\lambda_W = 1.67 \pm 0.1 mm$, respectively. It can also be demonstrated that an unmagnetized H_2 -air-Cs mixture

seeded with cesium ranging from 1-10% can achieve the same cellular detonation and detonation front resolution, shown in Figures 7.13 -7.15. The decreased detonation velocity as cesium is increased from 1% to 10% is consistent with the 1D simulations as well as the theoretical CJ velocity, which are tabulated in Table 7.1.

In the previous sections, 7.1 and 7.2, we demonstrated that an applied field can alter the cyclic stability of a 1D detonation. Now we will investigate if an applied field can affect the regularity or velocity of a 2D cellular detonation. Due to the large spatial variation of the longitudinal velocity, u_x , the static electric field should no longer be optimally tailored to u_x and B_z . In order to more accurately account for the static electric fields contribution to the MHD forces, while still keeping the loading factor concept for the accelerator and generator configurations, the static electric field is prescribed as $E_y = K_y U B_z$, where U is the mean velocity, and will not evolve with the flow. The optimal condition $U \approx 1000 \text{ m/s}$ is assumed. As performed with the one-dimensional test cases, 2D detonations in the both the accelerator and generator configurations were computed with varying amounts of cesium(1, 5, and 10%) using the highest magnetic field strength used previously in the 1D detonation simulations, $B_z = 8T$. From the X-t plots of the centerline of the 2D shock front, illustrated in Figures 7.16-7.18, there is no noticeable/significant altering of the detonation velocity in either generator or accelerator modes, as compared with the detonation in the absence of MHD. The peak pressure evolution in Figures 7.19-7.21 similarly do not show any noticeable change in the cyclic stability of these detonations. The differences in the two configurations can be seen in the centerline pressure and conductivity profiles, where the 10 % Cs and $B_z = 8T$ case at $t = 75\mu s$ case is illustrated in Figure 7.22. These differences in the profiles are seen further downstream, however, and do not play a role in the detonation dynamics. Hence even

at a very high magnetic field strength, 8T, and for 10% Cs, there does not appear to be a significant influence of the MHD on detonation dynamics. In an attempt to see if the two-dimensional detonation can be altered by MHD in some meaningful way, but under different conditions, two alternative approaches were taken. The first was to artificially enhance the kinetics of the cesium, (the original formulation of which is described in Appendix A). The second approach drastically increased the strengths of the applied magnetic and electric fields. For both cases, 10 % Cs was seeded because it allowed for more optimal levels of ionization as compared to 1 and 5% Cs addition.

7.3.1 Enhanced Kinetics

In the enhanced kinetics approach, the Arrhenius pre-factor of the cesium forward reaction mechanisms, A , was increased by factors of 10 and 100, respectively. Conductivity and Schlieren-type plots are shown in Figures 7.23 and 7.24 for the generator and accelerator configurations, respectively. One can see a significant increase in conductivity of the detonation close to the leading shock for both the accelerator and generator configurations, with an increase in the “enhanced kinetic factor”, EK , where the modified Arrhenius pre-factor in Equation 2.24 is $A' = EK \times A$. Slight deceleration and acceleration of the detonation front is observed, respectively, in Figures 7.23 & 7.24. The centerline peak pressure traces for the accelerator configuration, illustrated in Figure 7.25, show that as the EK is increased, the amplitude of the peak pressure decreases. In contrast, the centerline peak pressure traces for the generator configuration, illustrated in Figure 7.26, show that as EK is increased the amplitude of the peak pressure increases. These results are consistent with the

1D results from Section 7.2 for the accelerator and generator configurations, in that when there is sufficient conductivity, with a larger concentration of Cs for the 1D detonation, the applied magnetic and electric fields affect the amplitude of the peak pressure. But even with the large increase in conductivity shown in Figures 7.23 and 7.24 for $EK = 100$, the X-t diagram of the unmagnetized, accelerator, and generator configurations, illustrated in Figure 7.27, shows only a small alteration of the detonation velocity: $+30m/s$ (increase) and $-20m/s$ (decrease) for the accelerator and generator configurations, respectively.

7.3.2 Strong Applied Fields

Next, we subjected the 2D detonation to significantly stronger magnetic fields (16T and 32 T) without enhancing the cesium kinetics.¹ Figures 7.28 and 7.29 show the centerline peak pressure traces for $B_z = 8, 16$, and 32 T in the accelerator and generator configurations, respectively. Even when the 2D detonation in the generator configuration is subjected to a strong field, the peak pressure amplitude, shown in Figure 7.29, is slightly increased. The X-t plot for the generator configuration, illustrated in Figure 7.30, shows only a marginal decrease in the detonation velocity. By comparing the profiles of the x-velocity, conductivity, pressure, and temperature for the generator, illustrated in Figures 7.31 - 7.34, respectively, one will see that the MHD effects are manifested significantly far downstream of ($\gg \lambda_W$) the leading shock.

The accelerator configuration with a strong field, on the other hand, has a more significant effect on the 2D detonation dynamics. From Figure 7.28 one can see a transition, from $B_z = 8T$ where the amplitude and frequency of oscillations are

¹Unrealistic but only interested in scaling and dynamics

regular, to $B_z = 16T$ where the amplitude begins to noticeably decrease at $t \approx 50\mu s$, and finally to $B_z = 32T$ where at $t = 40\mu s$ there is a significant decrease in amplitude and an increase in the mean peak pressure. Because of the significant change in the oscillation frequency, amplitude and mean of the centerline peak pressure, the associated smoke-foil record, illustrated in Figures 7.35 - 7.38, for field strengths $B_z = 0, 8T, 16T$ and $32T$, respectively, can be used to see the alteration of the underlying structure of the cellular detonation. In Figure 7.36, we see that for the $B_z = 8T$ case, cellular structure pattern remains regular, and from Figure 7.37 for the $B_z = 16T$ case, the cellular patterns become irregular at $x \approx 9.5cm$. The detonation case where $B_z = 32T$ (Figure 7.38) shows that there is a transition from a cellular structure to quasi-1D detonation at $x \approx 7.2cm$. The X-t plot for the accelerator configuration, illustrated in Figure 7.39, shows marginal increases in the detonation velocity of $+5m/s$ for the $B_z = 16$, but there is an increase of $338m/s$ for $B_z = 32T$, a 21% increase above the non-MHD case.

7.4 Conclusions

In this chapter, we examined the effects of a diluent (cesium) on the dynamics of a 1D spark-ignited detonation and confirmed the observation of Radulescu et al.[19] that the diluent had a regularizing effect on the oscillations of the 1D detonation. We also studied a cesium-seeded 1D spark-ignited detonation subjected to an applied magnetic field in both a accelerator and generator configurations and found that the accelerator mode had a regularizing effect on the detonation oscillations, while the generator mode had the opposite effect (see Figure 7.9). While it was demonstrated that the dynamics of a cesium-seeded 1D spark-ignited detonation can

be significantly altered when subjected to an applied magnetic field of reasonable strength ($B_z \leq 8T$), the same statement does not hold true for the two-dimensional case. When the enhanced kinetics factor EK for a cesium-seeded 2D spark-ignited detonation was increased ($EK = 1, 10, 100$), the conductivity behind the leading shock was significantly increased (see Figures 7.23 and 7.24), but there was no alteration to the detonation velocity (see Figures 7.30 and 7.31). The 2D spark-ignited detonation required a significantly stronger magnetic field ($32T$) than the 1D detonation to accelerate the detonation in the time ($75\mu s$) and length ($15cm$) scales of the problem (see Figure 7.39). These findings suggest that multidimensional effects play an important role in MHD acceleration. Perhaps a set of reactants/diluent with an increased flame temperature, for increased conductivity, and a lower density, for less inertia, would be more amenable for MHD acceleration.

%Cs	Theoretical CJ [m/s]	1-D [m/s]	2-D [m/s]
0	1967	1998	1938
1	1917	1950	1883
5	1754	1763	1714
10	1584	1600	1551

Table 7.1: The effects of the addition of Cesium on the detonation velocity of a 1D and 2D $H_2 - Air$ detonation. The theoretical Chapman-Jouguet(CJ) velocity is calculated with the initial conditions: $P_0 = 1$ atm and $T_0 = 300K$.

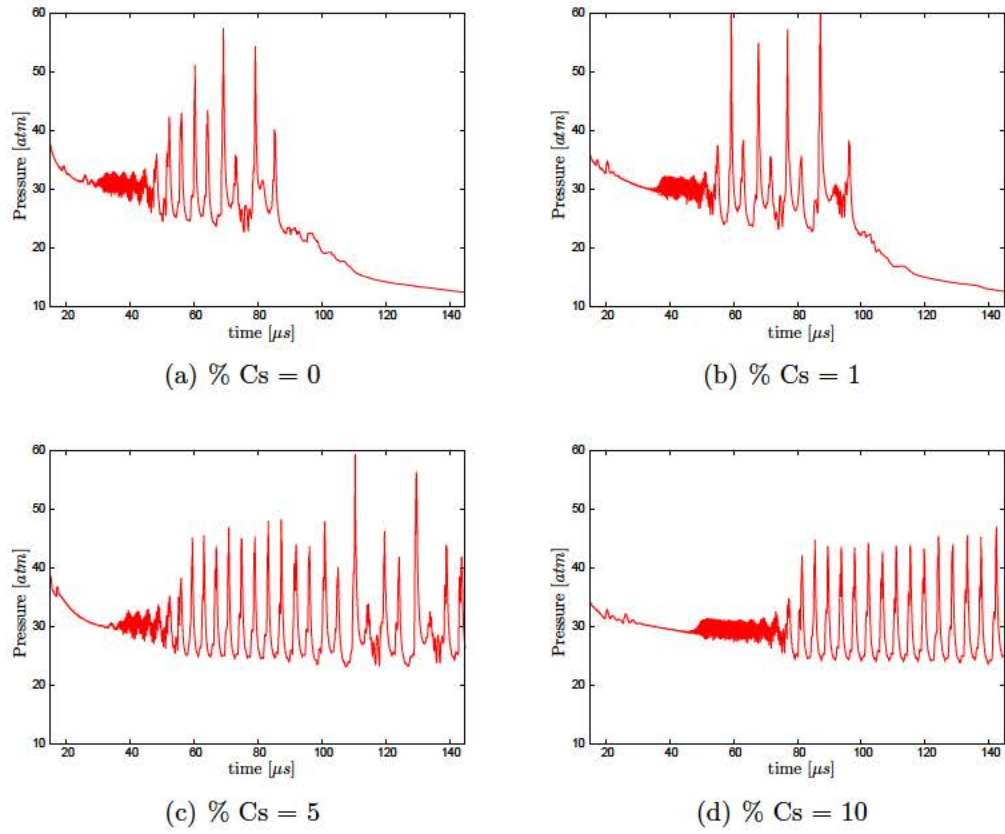


Figure 7.1: Peak pressure traces of spark-ignited H_2 -air detonations with different amounts of seeded cesium without an applied magnetic field ($B = 0$). The MP5 scheme with $\Delta x = 5\mu m$ was used here.

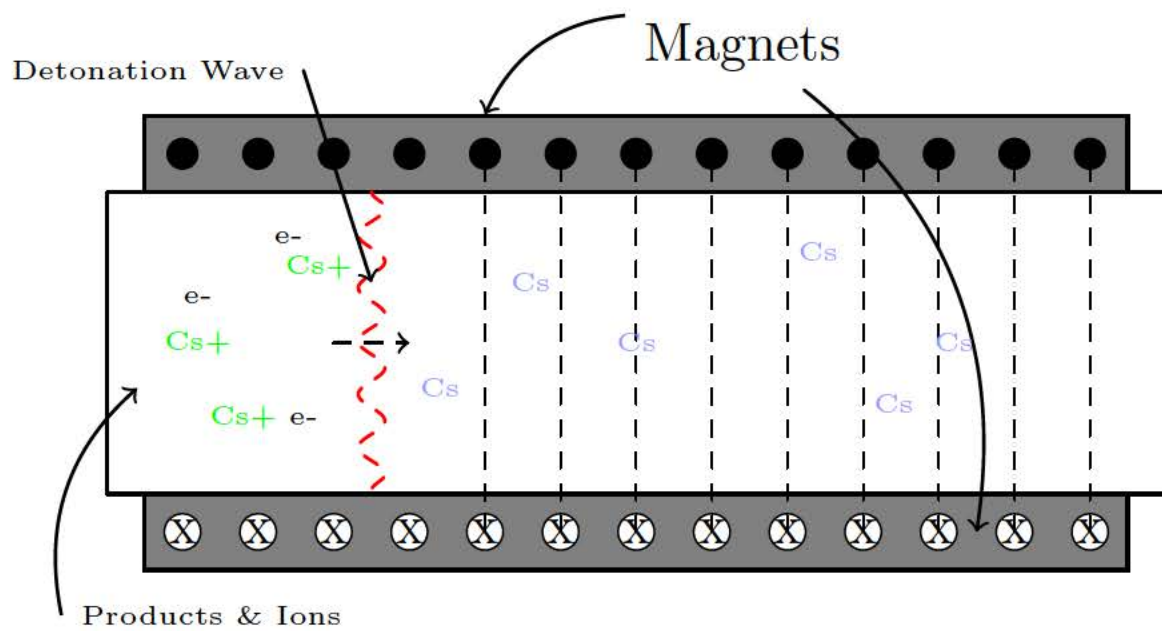


Figure 7.2: Configuration of spark-ignited detonation with an applied magnetic field.

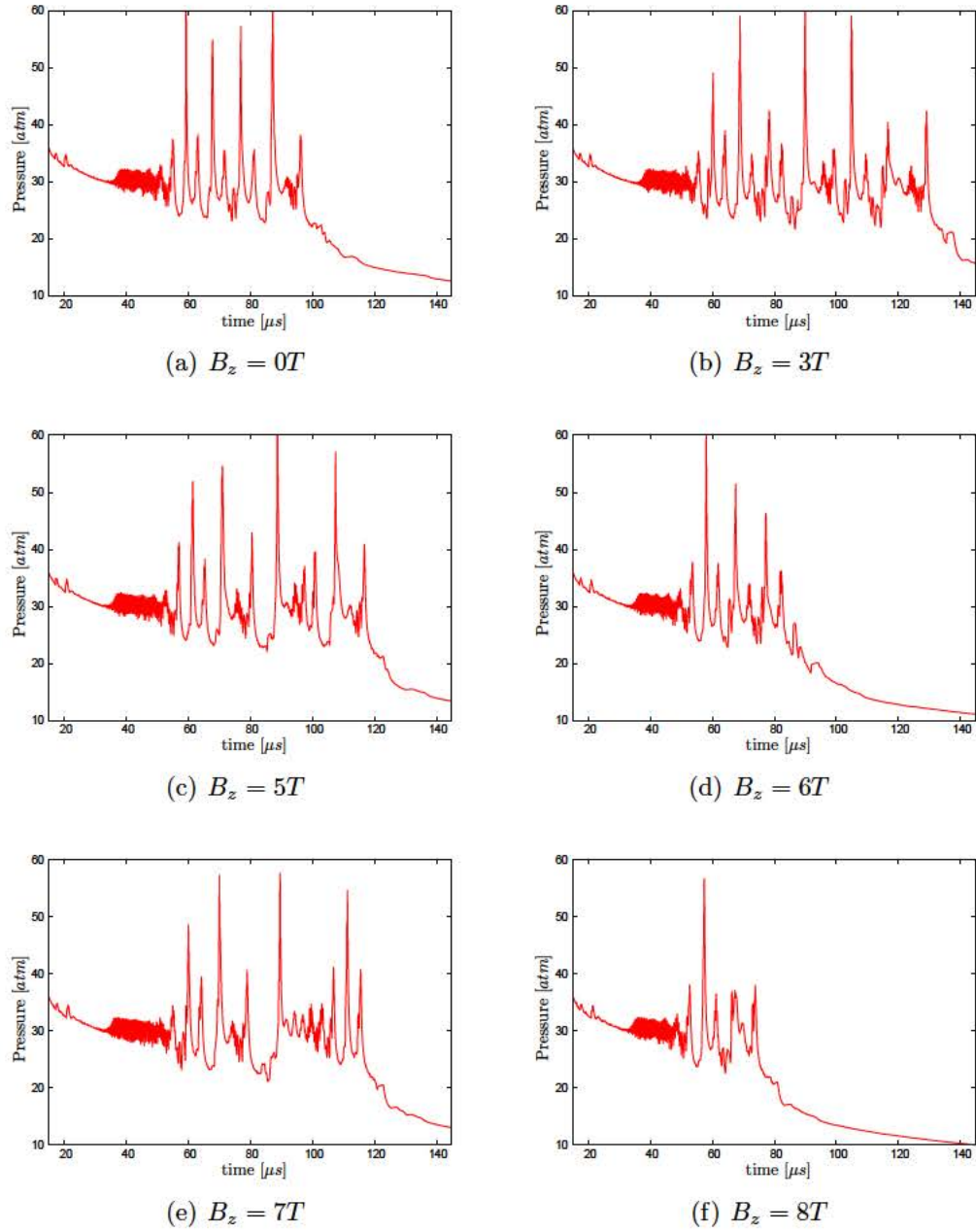


Figure 7.3: Peak pressure traces of detonations seeded with 1% cesium subjected to various magnetic field strengths B_z without an applied electric field ($\mathbf{K} = 0$). The MP5 scheme with $\Delta x = 5\mu m$ was used here.

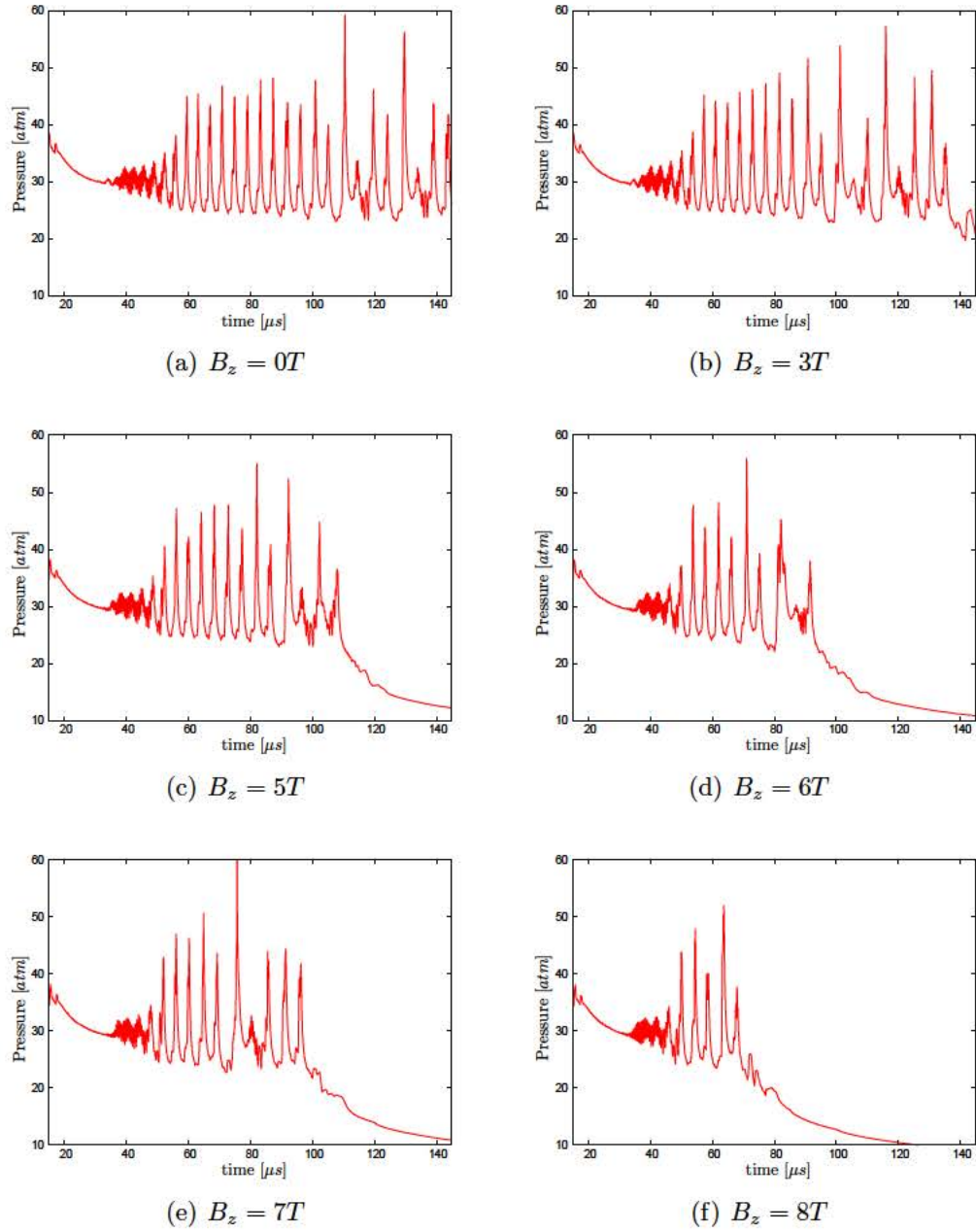


Figure 7.4: Peak pressure traces of detonations seeded with 5% cesium subjected to various magnetic field strengths, B_z without an applied electric field ($K = 0$). The MP5 scheme with $\Delta x = 5\mu m$ was used here.

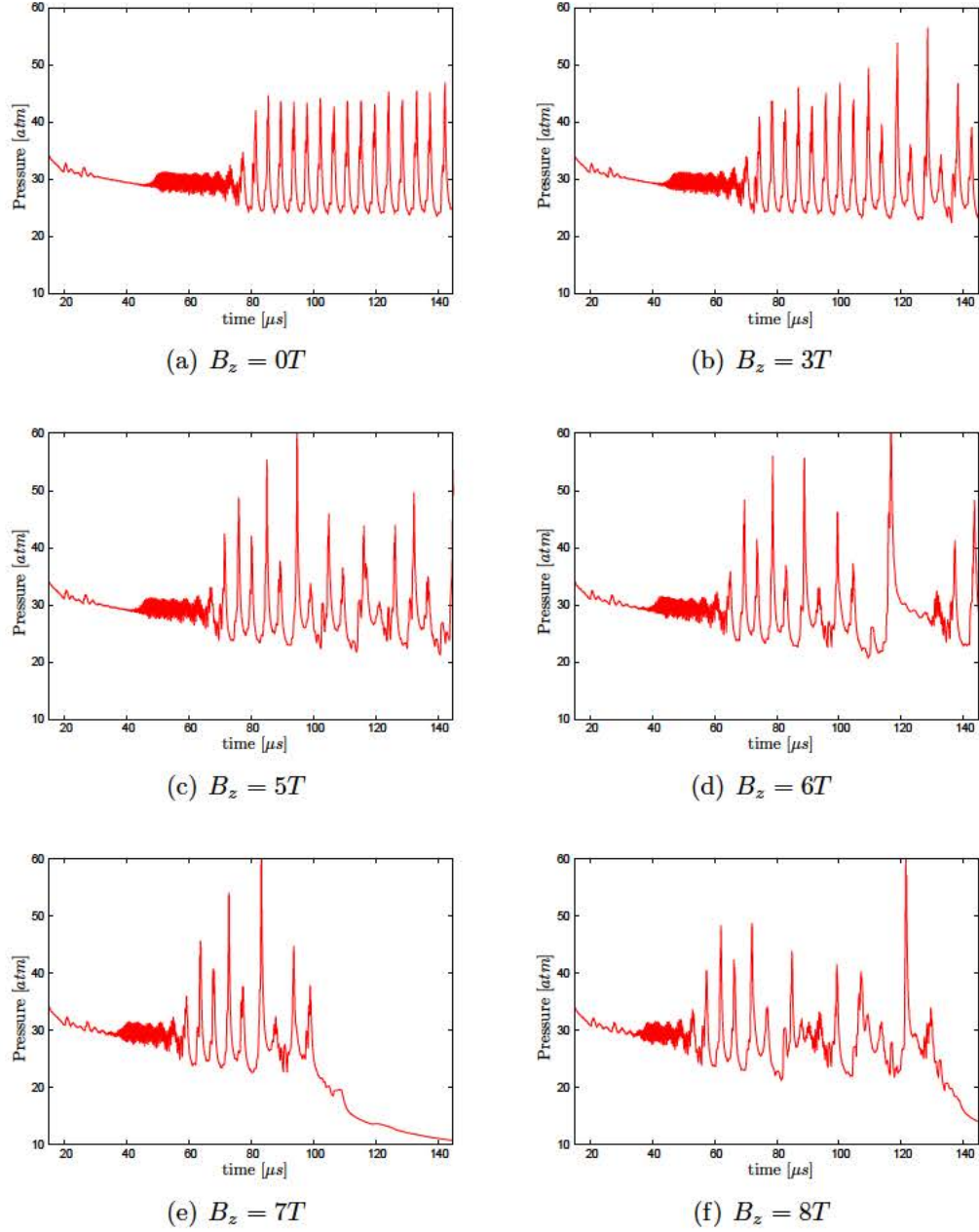


Figure 7.5: Peak pressure traces of detonations seeded with 10% cesium subjected to various magnetic field strengths B_z without an applied electric field ($\mathbf{K} = 0$). The MP5 scheme with $\Delta x = 5\mu m$ was used here.

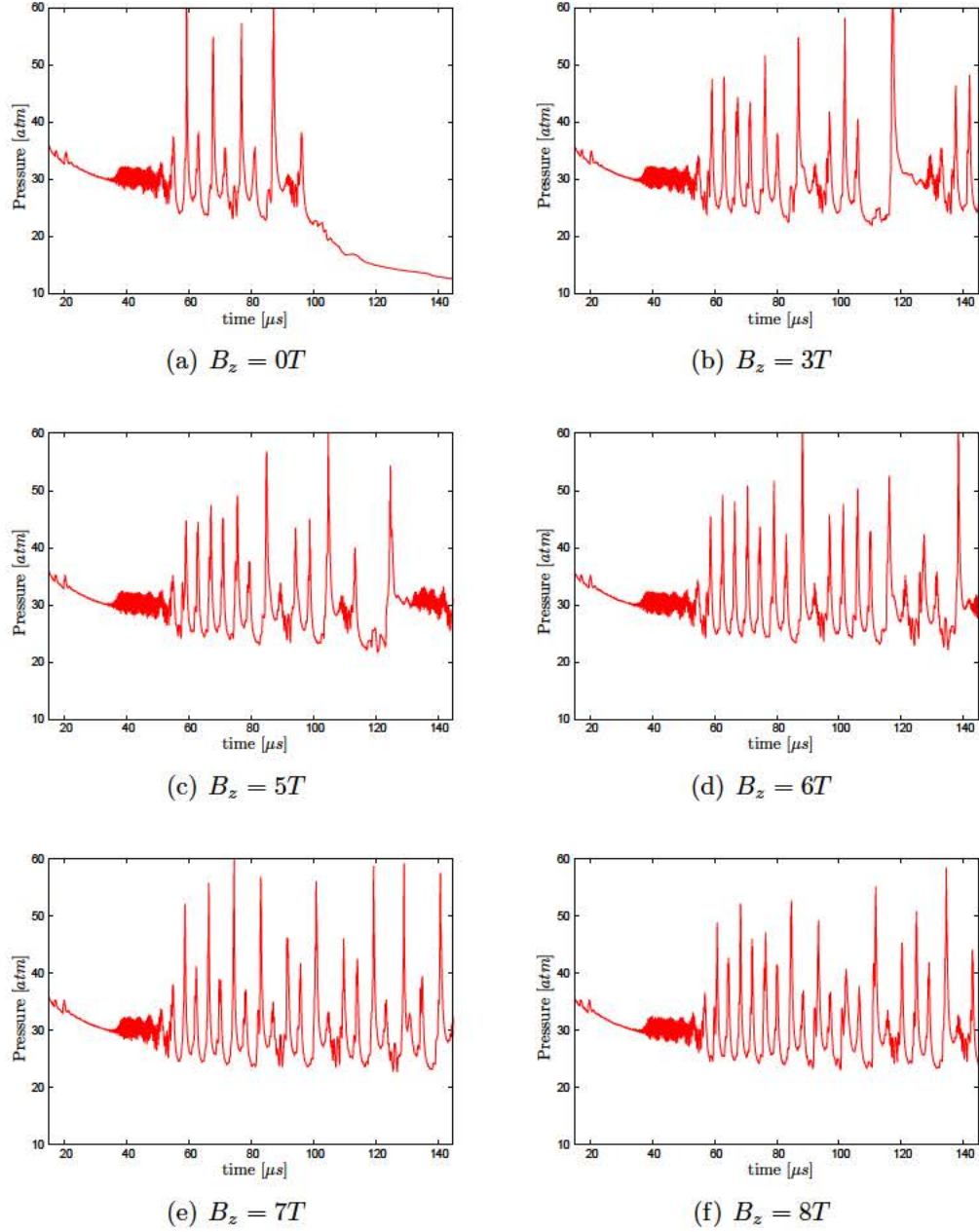


Figure 7.6: Peak pressure traces of detonations seeded with 1% cesium subjected to various magnetic field strengths B_z with an applied electric field ($K_y = 1.5$), for an “accelerator” configuration. The MP5 scheme with $\Delta x = 5\mu m$ was used here.

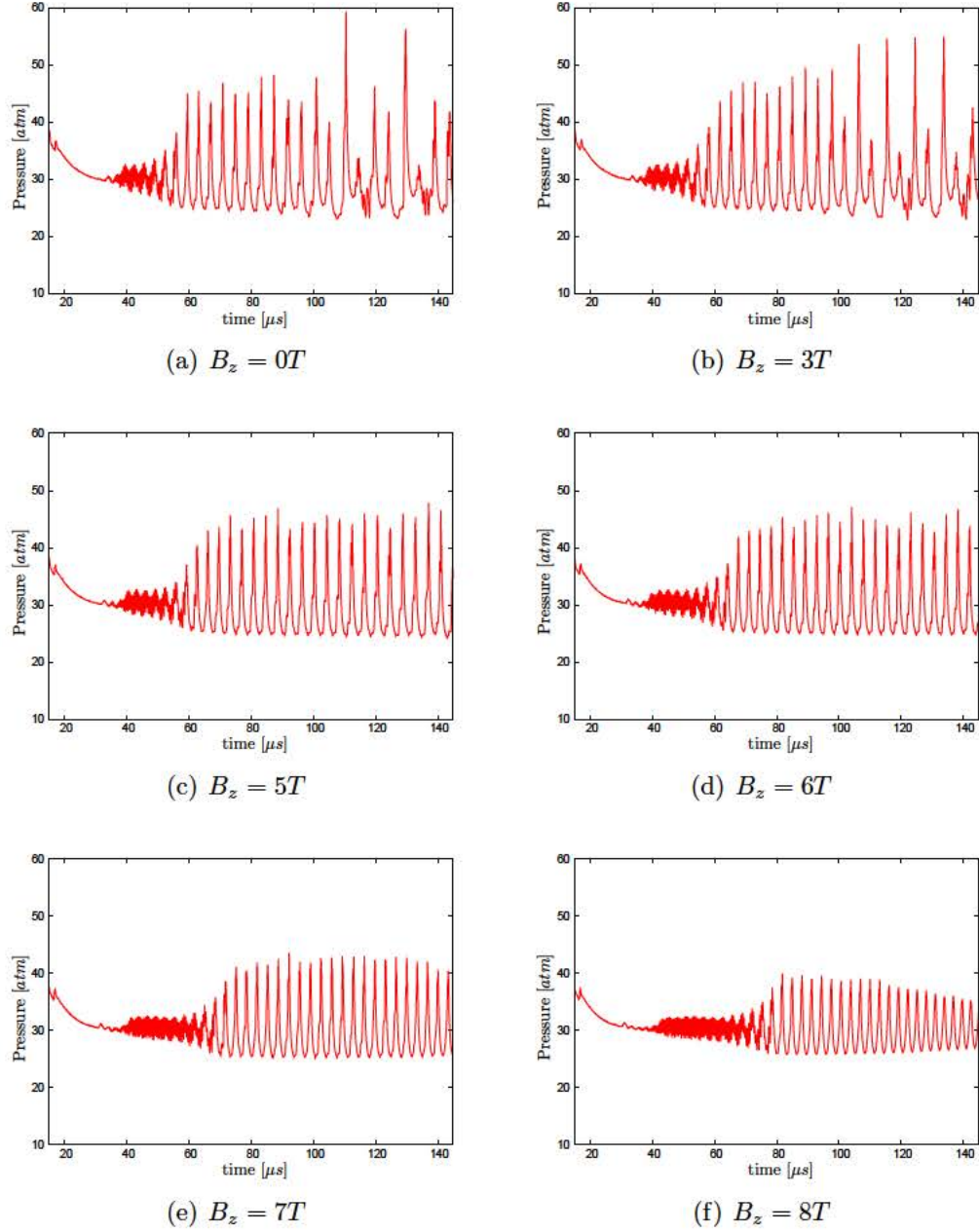


Figure 7.7: Peak pressure traces of detonations seeded with 5% cesium subjected to various magnetic field strengths B_z with an applied electric field ($K_y = 1.5$), for an “accelerator” configuration. The MP5 scheme with $\Delta x = 5\mu m$ was used here.

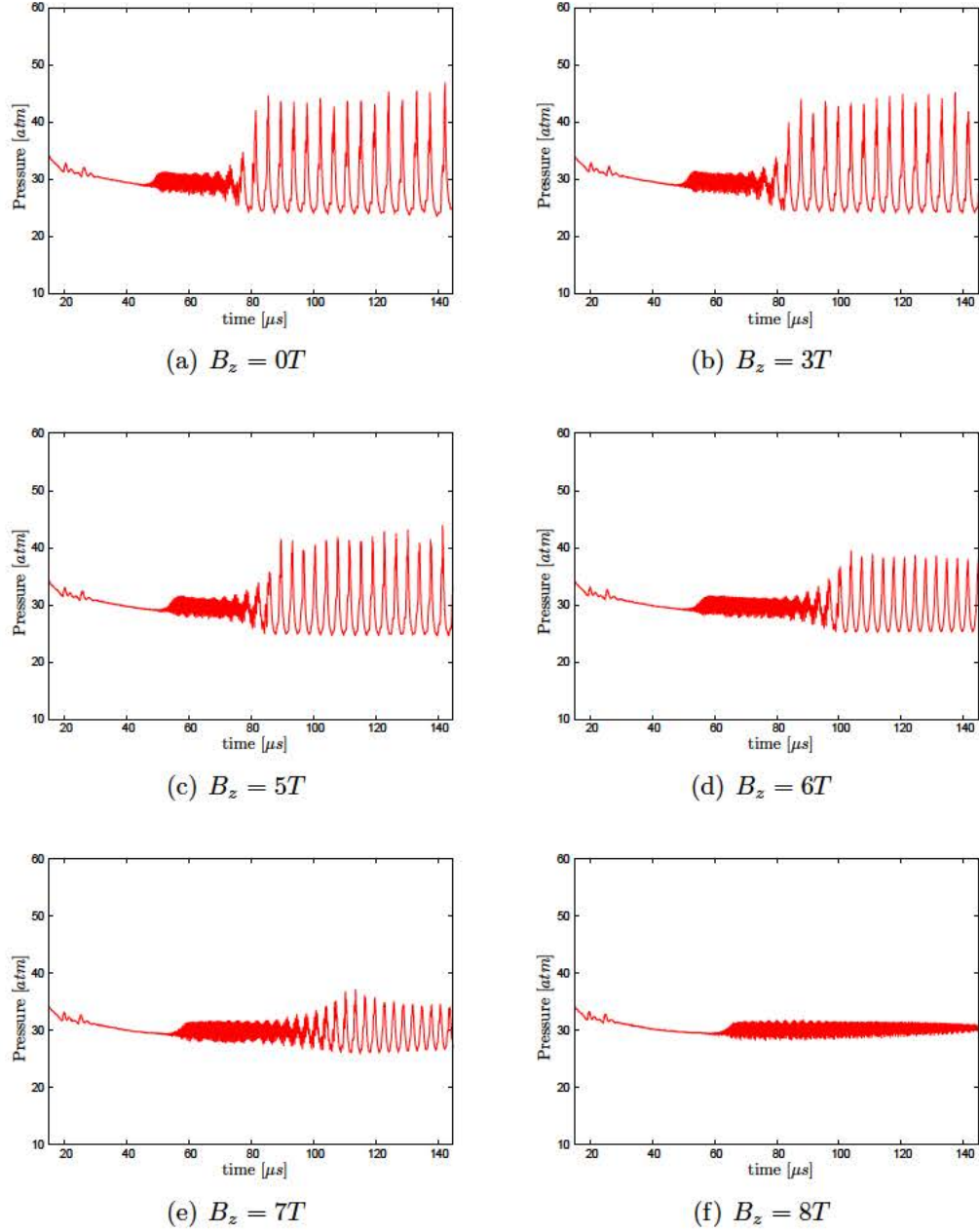
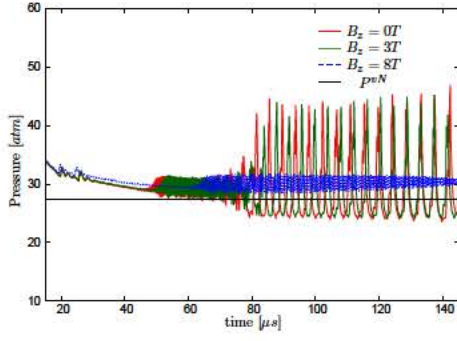
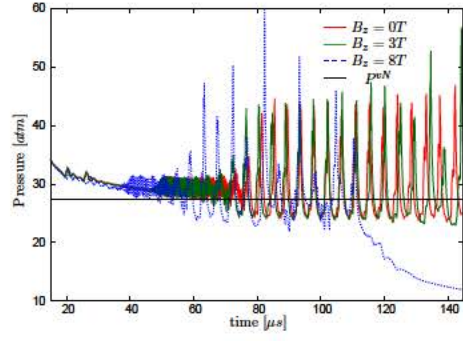


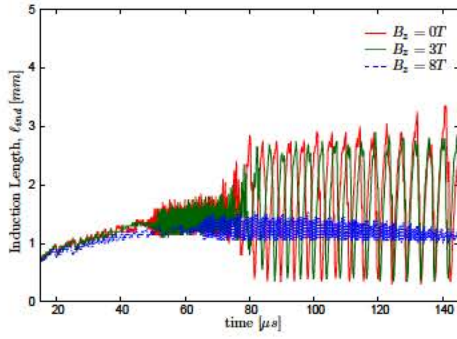
Figure 7.8: Peak pressure traces of detonations seeded with 10% cesium subjected to various magnetic field strengths B_z with an applied electric field ($K_y = 1.5$), for an “accelerator” configuration. The MP5 scheme with $\Delta x = 5\mu m$ was used here.



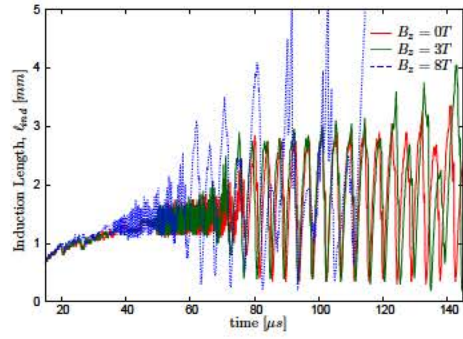
(a) Accelerator Peak pressure trace



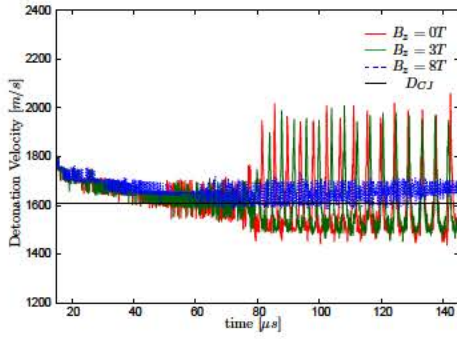
(b) Generator Peak pressure trace



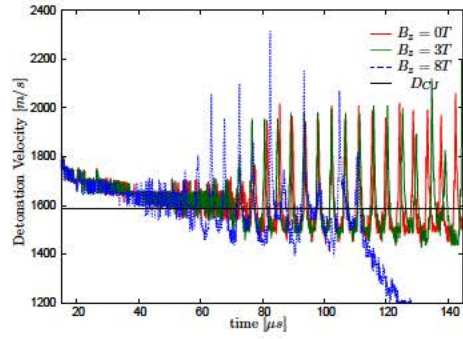
(c) Accelerator Induction Length



(d) Generator Induction Length



(e) Accelerator Detonation Velocity



(f) Generator Detonation Velocity

Figure 7.9: Time trace comparisons of $B_z = 0, 3,$ and $8T$ 1D detonations with 10% Cs in the accelerator configuration($K_y = 1.5$) and generator configuration($K_y = 0.5$) with $\Delta x = 5\mu m$.

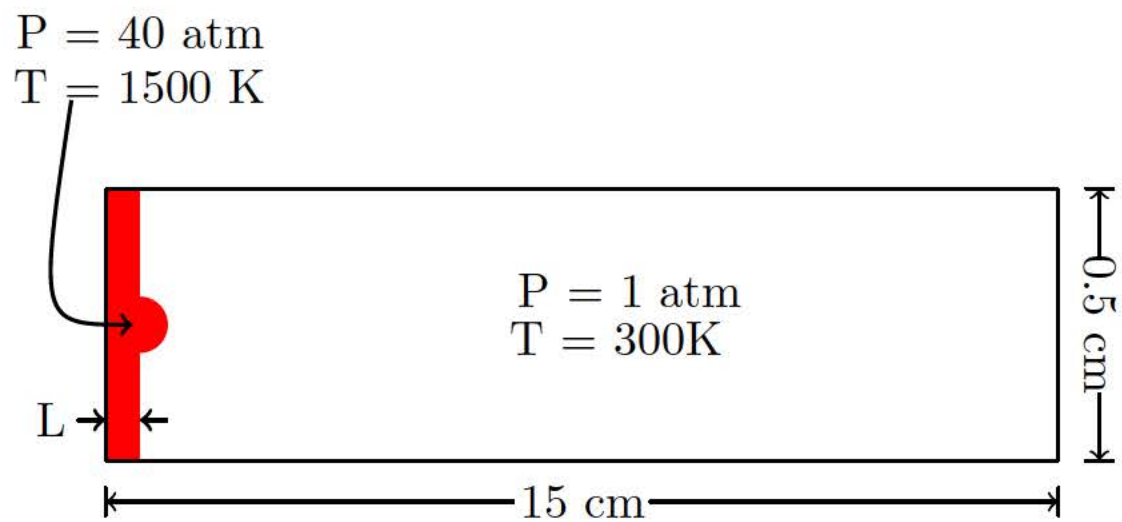


Figure 7.10: Computational setup for 2D detonation simulations, where the red region represents the computational spark.

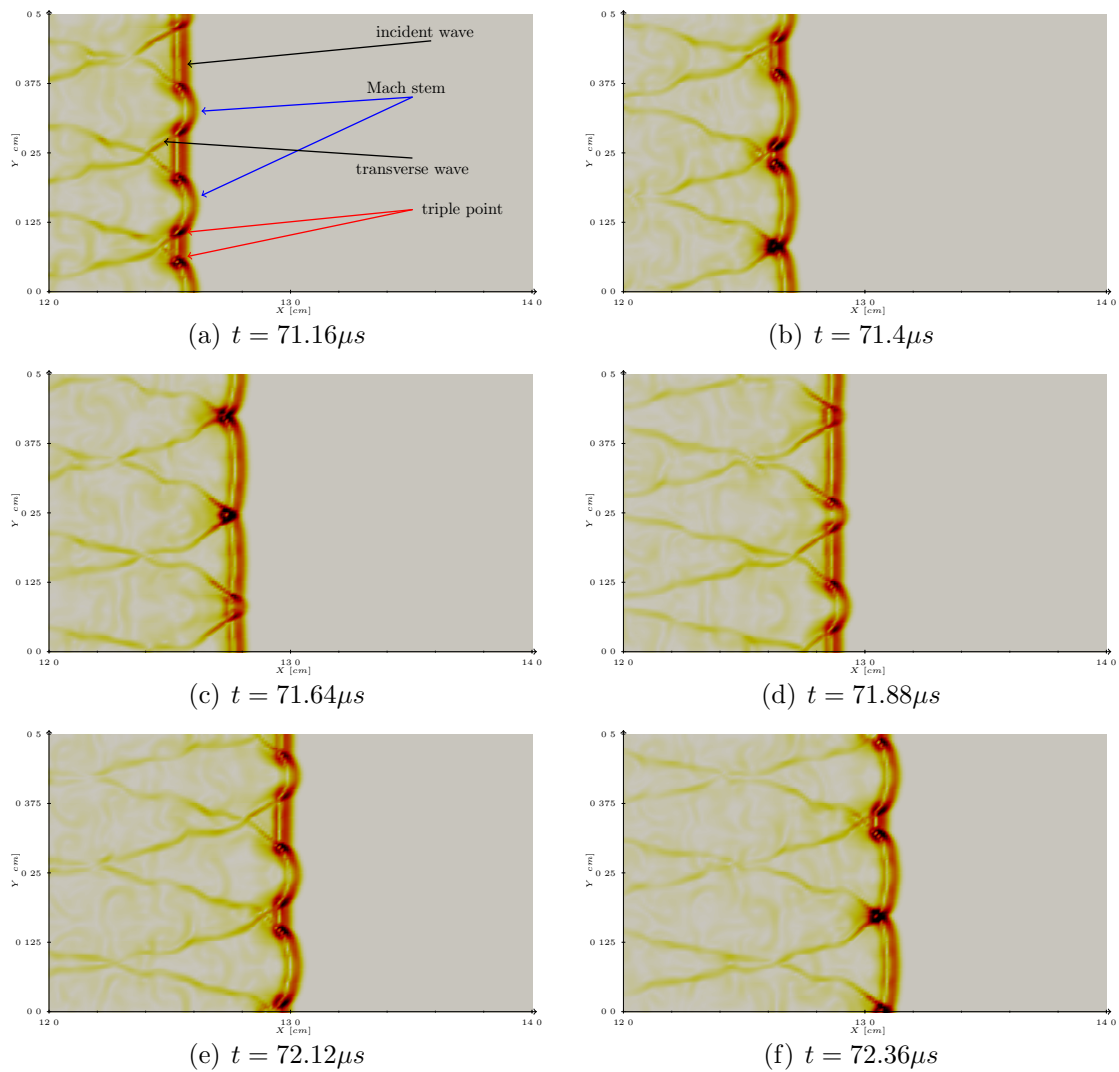
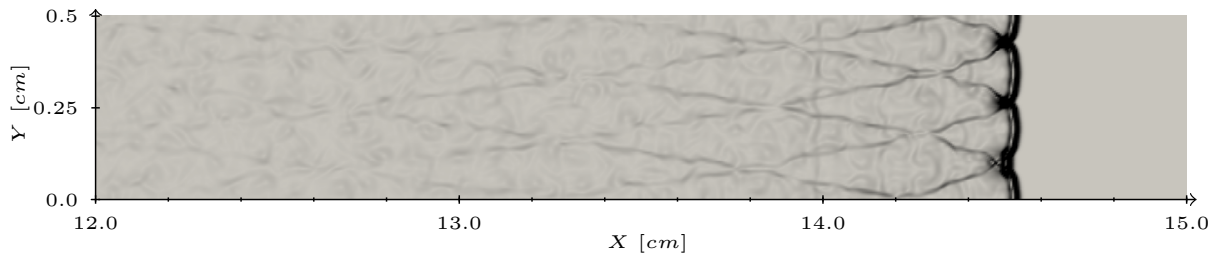
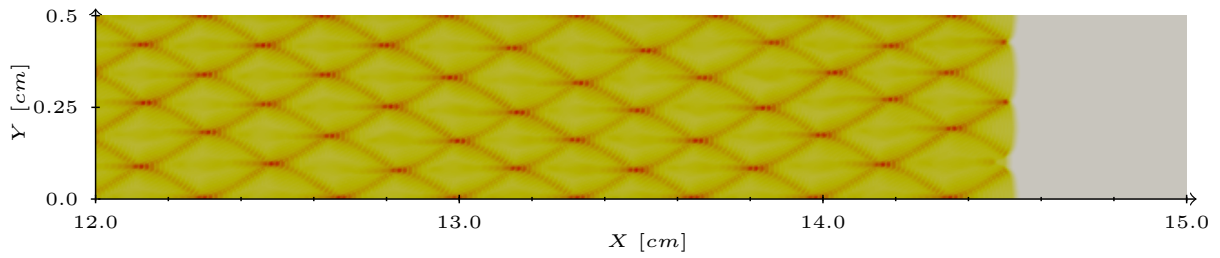


Figure 7.11: Schlieren-type plot using density gradients of the detonation front from time $71.16\mu s$ to $72.36\mu s$.



(a) Schlieren-type plot using density gradients of the detonation front




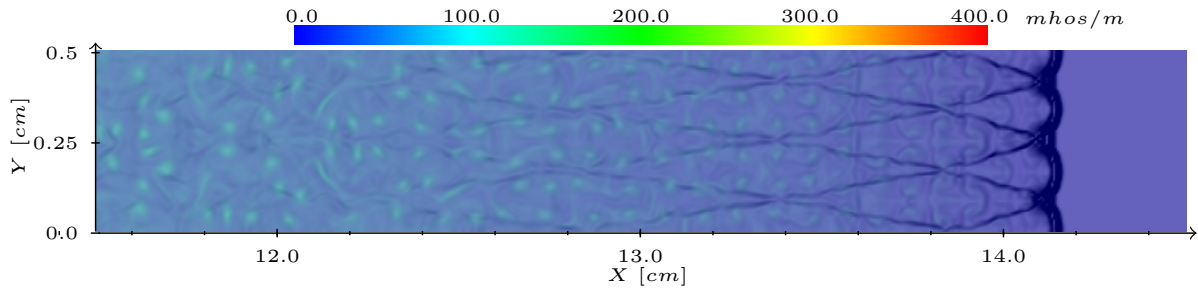
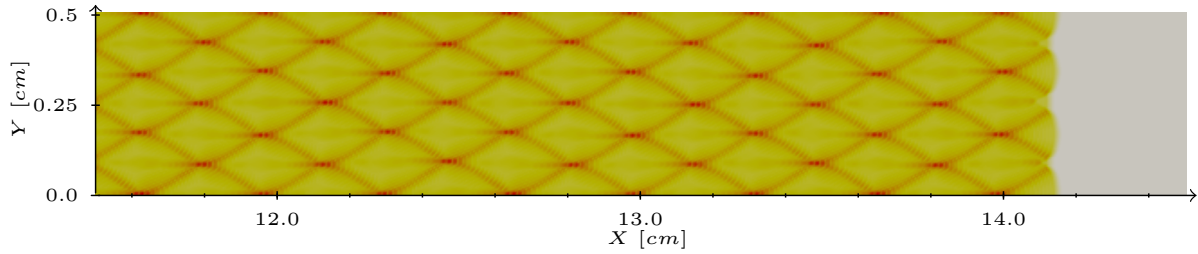
(b) Maximum pressure contour with linear color map (min  max)

Figure 7.12: Stoichiometric H_2 – Air detonation at $t = 75\mu s$ where $\Delta x = \Delta y = 50\mu m$ and $x : y \in [12, 15]cm : [0, 0.5]cm$.

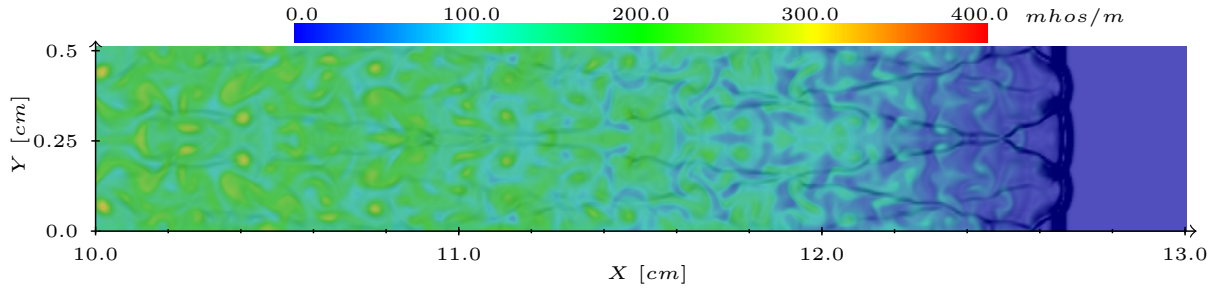


(a) Conductivity distribution with a linear color map overlaid on Schlieren-type plot using density gradients of the detonation front

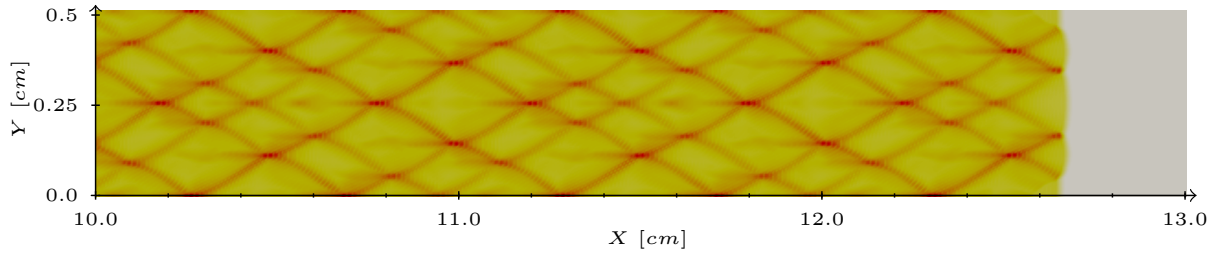


(b) Maximum pressure contour with linear color map (*min* to *max*)

Figure 7.13: Stoichiometric $H_2 - Air - 1\%Cs$ detonation at $t = 75\mu s$ where $\Delta x = \Delta y = 50\mu m$ and $x : y \in [11.5, 14.5]cm : [0, 0.5]cm$.



(a) Conductivity distribution with a linear color map overlaid on Schlieren-type plot using density gradients of the detonation front




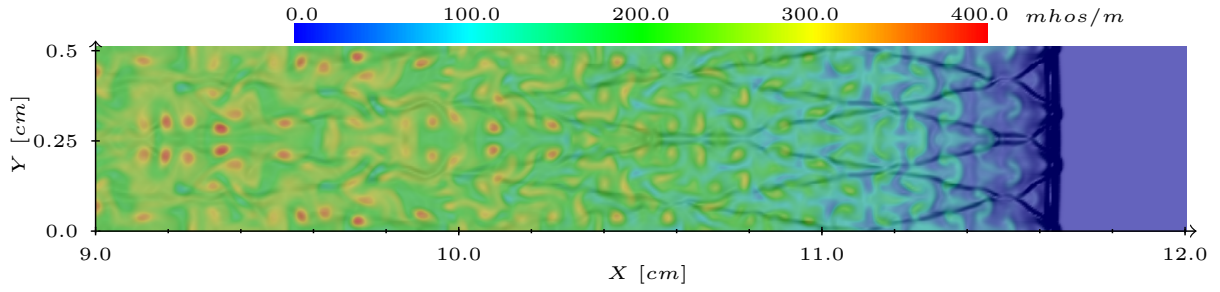
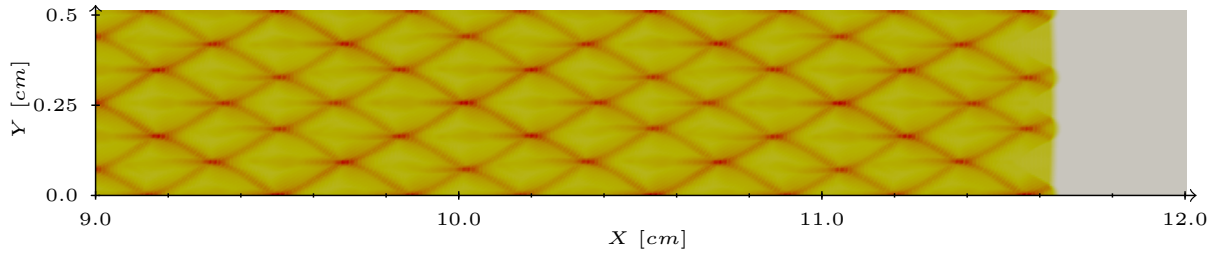
(b) Maximum pressure contour with linear color map (min  max)

Figure 7.14: Stoichiometric $H_2 - Air - 5\%Cs$ detonation at $t = 75\mu s$ where $\Delta x = \Delta y = 50\mu m$ and $x : y \in [10, 13]cm : [0, 0.5]cm$.



(a) Conductivity distribution with a linear color map overlaid on Schlieren-type plot using density gradients of the detonation front




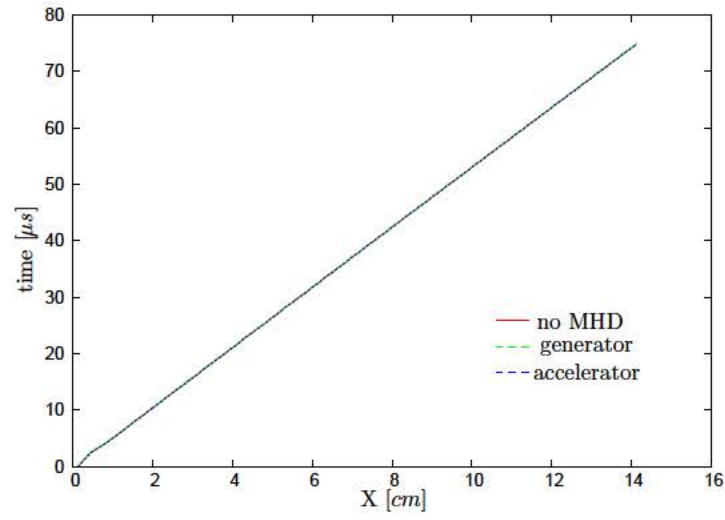
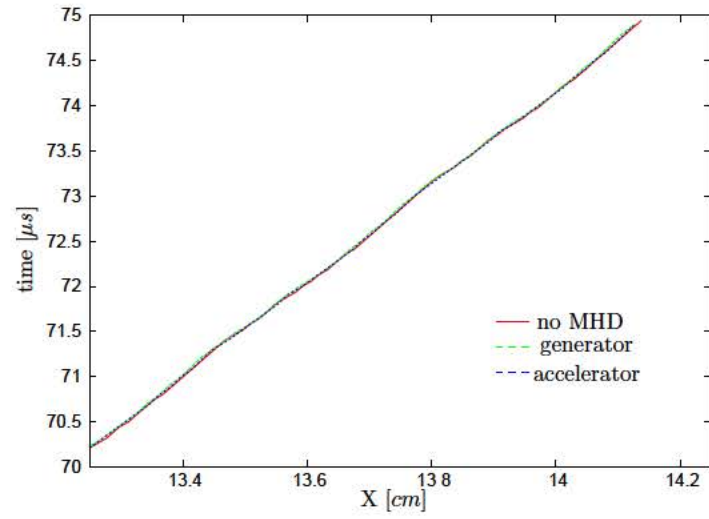
(b) Maximum pressure contour with linear color map (min  max)

Figure 7.15: Stoichiometric $H_2 - Air - 10\%Cs$ detonation at $t = 75\mu s$ where $\Delta x = \Delta y = 50\mu m$ and $x : y \in [9, 12]cm : [0, 0.5]cm$.

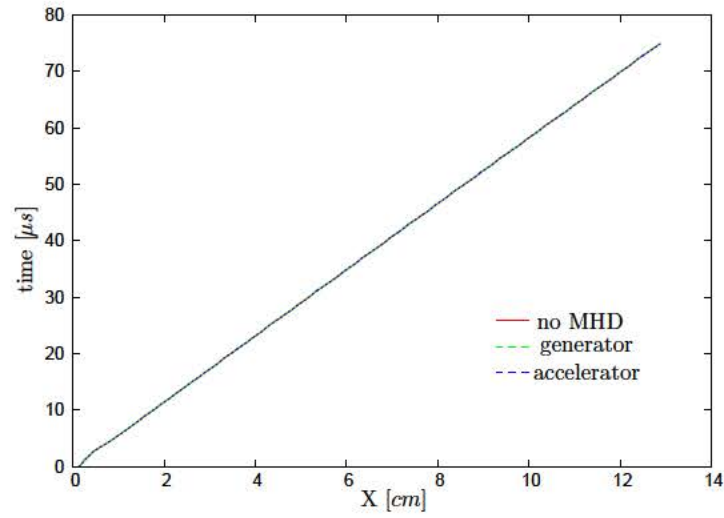


(a) Wide view

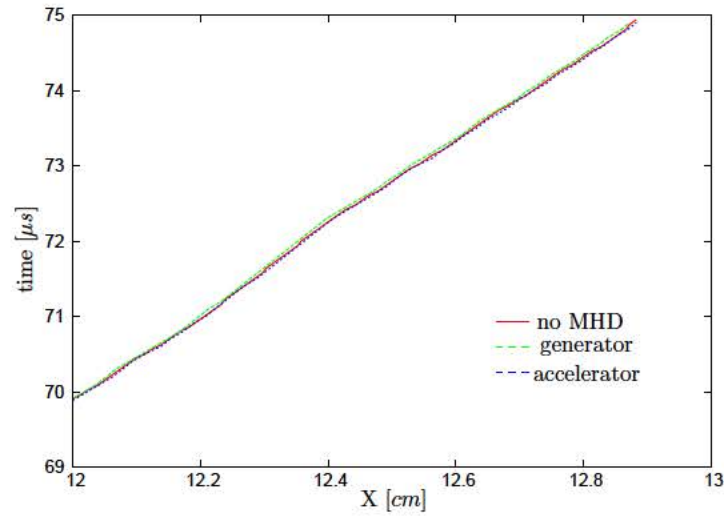


(b) Enlarged view

Figure 7.16: X-t plot comparing the progression of the leading shocks at the centerline of the 2D detonation with no MHD, generator, and accelerator configurations. Here the mixture has 1% Cs and $B_z = 8T$.

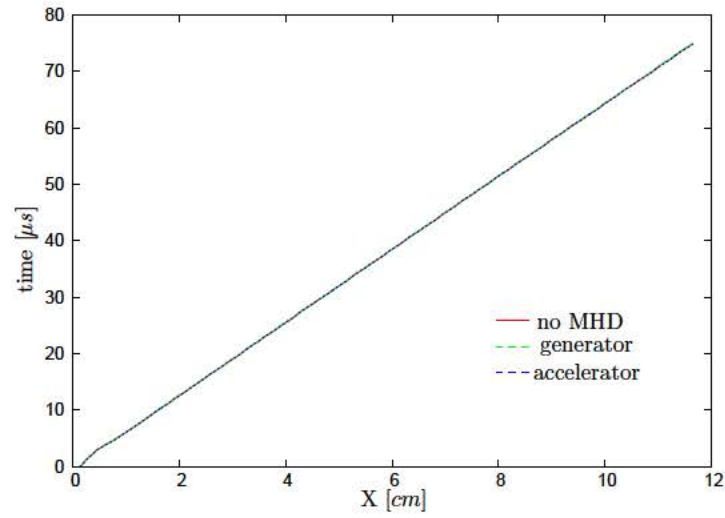


(a) Wide view

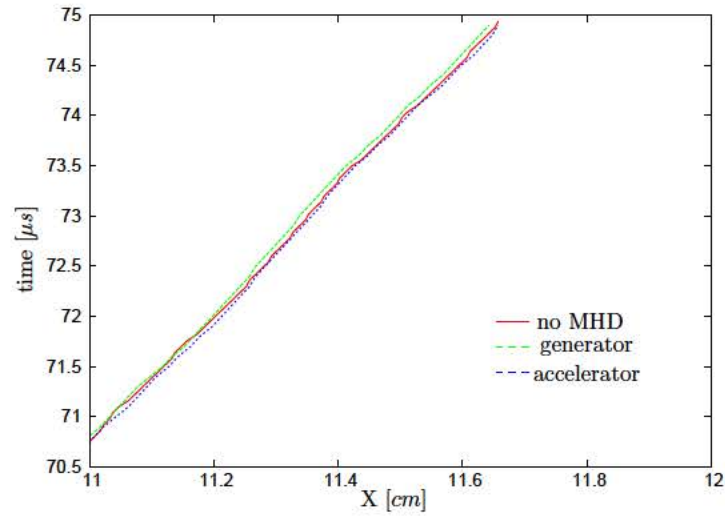


(b) Enlarged view

Figure 7.17: X-t plot comparing the progression of the leading shocks at the centerline of the 2D detonation with no MHD, generator, and accelerator configurations. Here the mixture has 5% Cs and $B_z = 8T$.

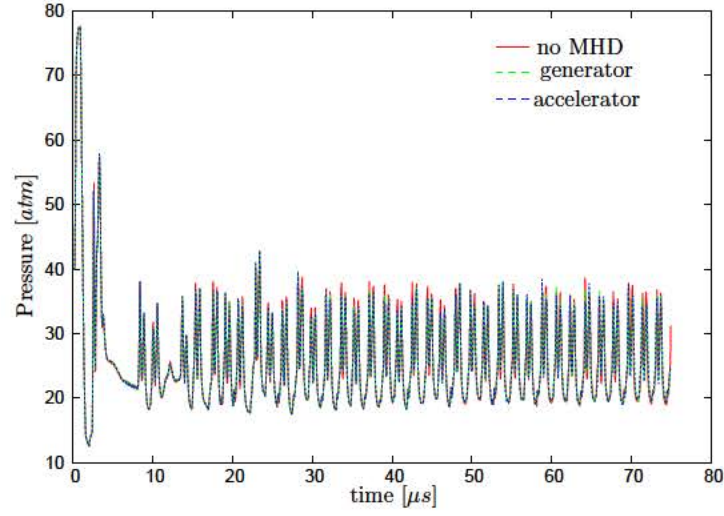


(a) Wide view

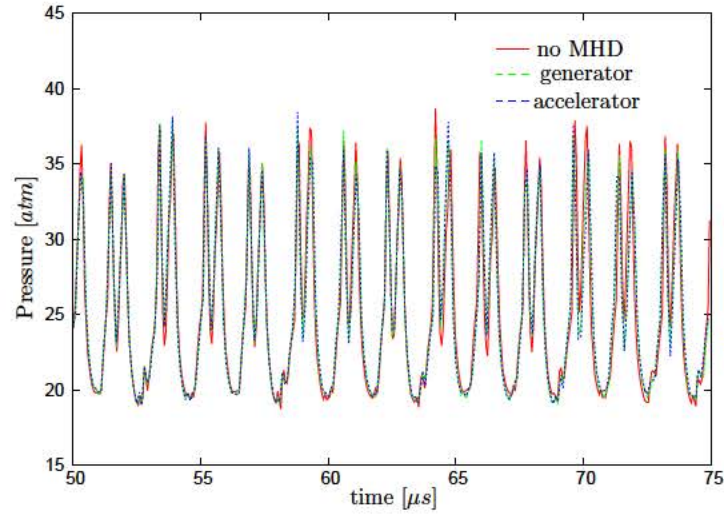


(b) Enlarged view

Figure 7.18: X-t plot comparing the progression of the leading shocks at the centerline of the 2D detonation with no MHD, generator, and accelerator configurations. Here the mixture has 10% Cs and $B_z = 8T$.

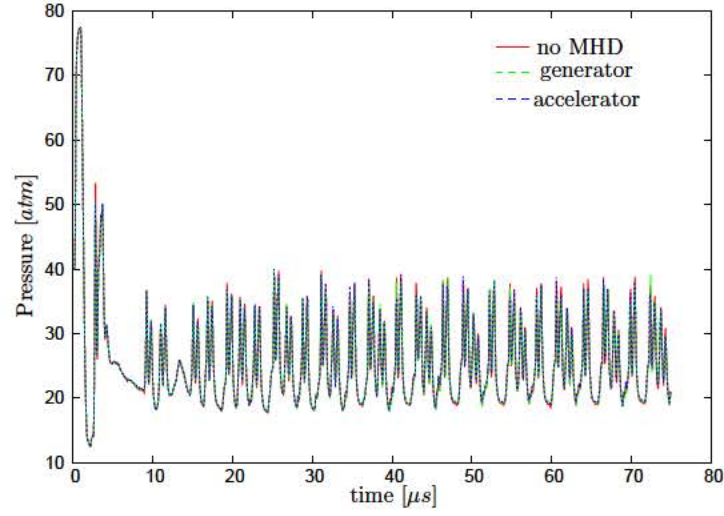


(a) Wide view

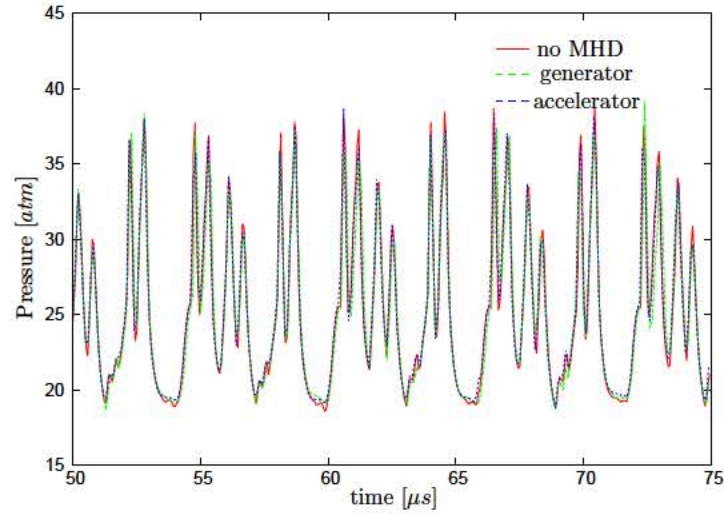


(b) Enlarged view

Figure 7.19: Peak pressure trace of the centerline of the leading shock of the 2D detonation with no MHD, generator, and accelerator configurations. Here the mixture has 1% Cs and $B_z = 8T$.

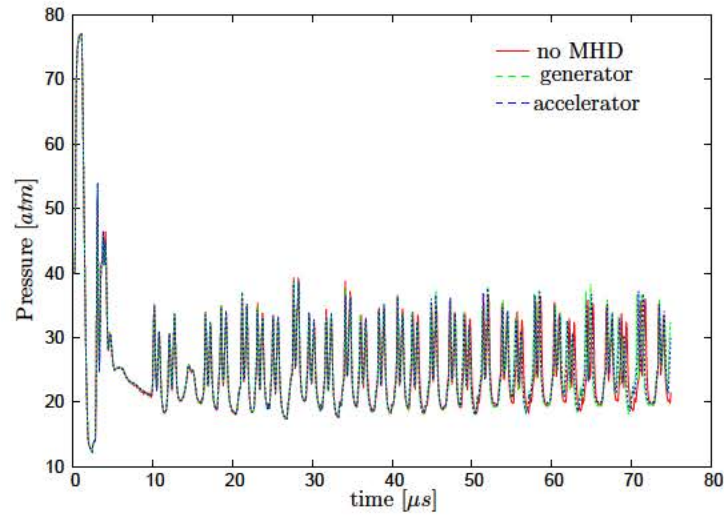


(a) Wide view

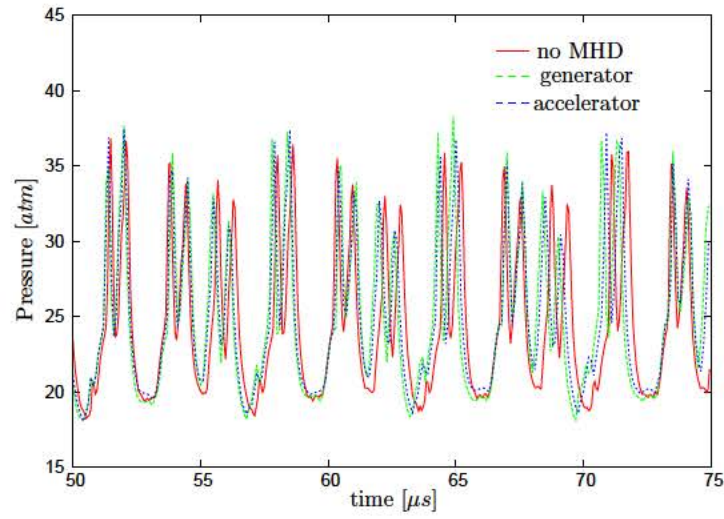


(b) Enlarged view

Figure 7.20: Peak pressure trace of the centerline of the leading shock of the 2D detonation with no MHD, generator, and accelerator configurations. Here the mixture has 5% Cs and $B_z = 8T$.



(a) Wide view



(b) Enlarged view

Figure 7.21: Peak pressure trace of the centerline of the leading shock of the 2D detonation with no MHD, generator, and accelerator configurations. Here the mixture has 10% Cs and $B_z = 8T$.

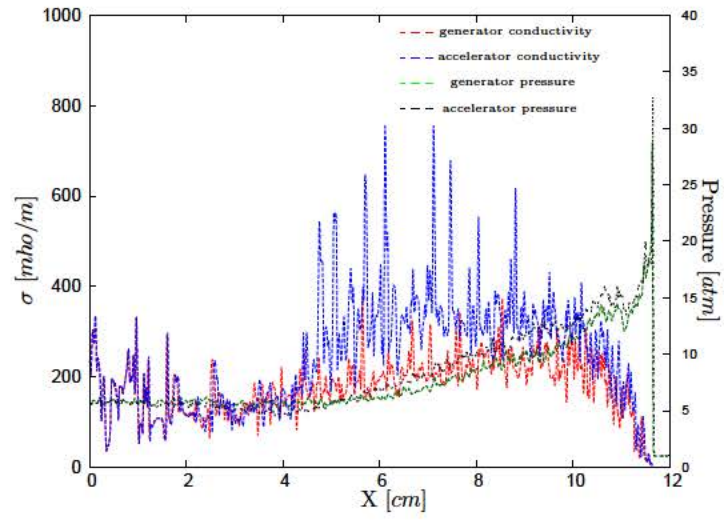


Figure 7.22: Centerline pressure and conductivity profiles for the accelerator and generator configurations with $B_z = 8T$ at $t = 75\mu s$.

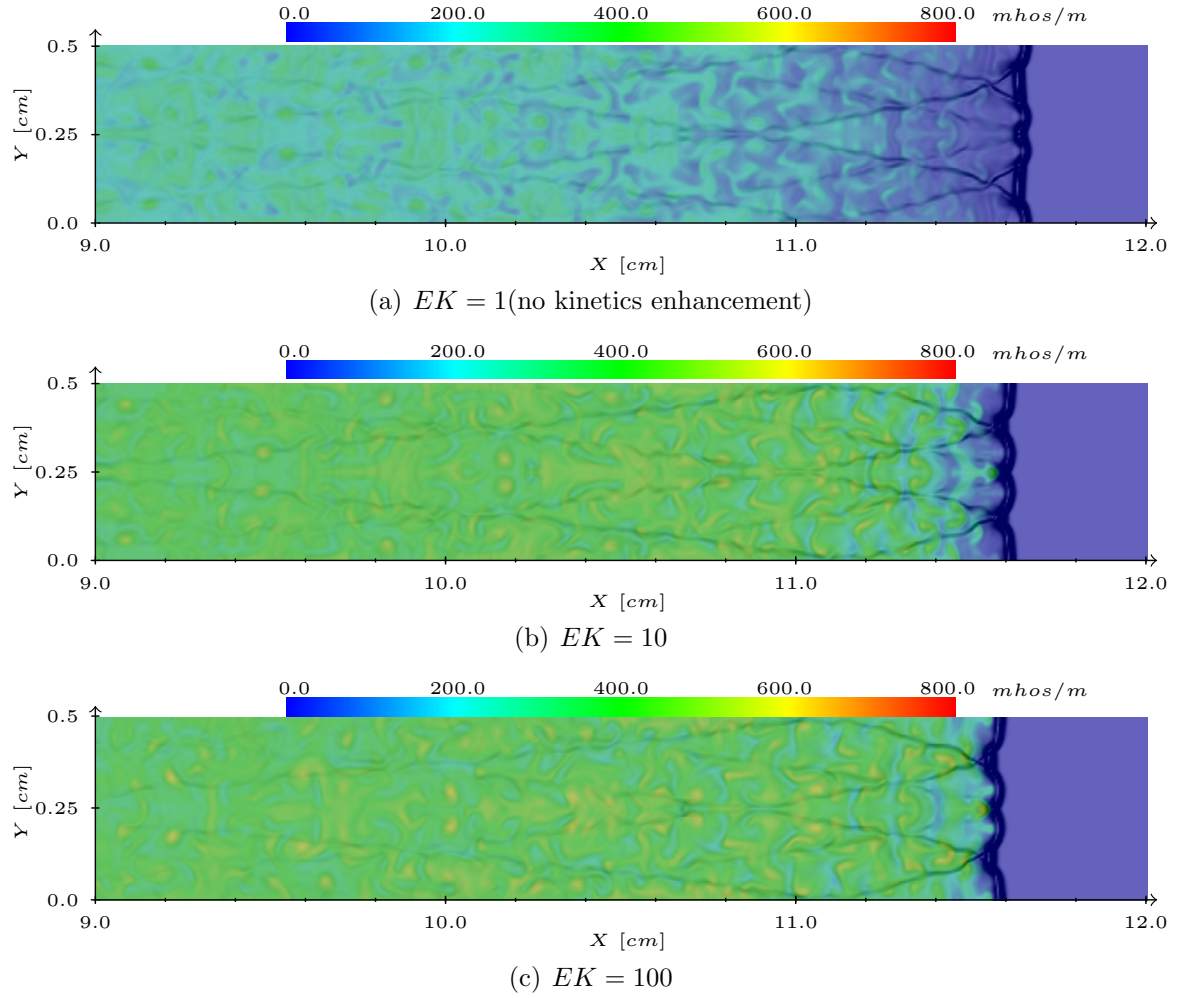


Figure 7.23: Conductivity distribution with a linear color map overlaid with Schlieren-type plot using density gradients of the detonation front in the generator configuration with 10% Cs and $B_z = 8T$, for different enhanced kinetic(EK) factors.

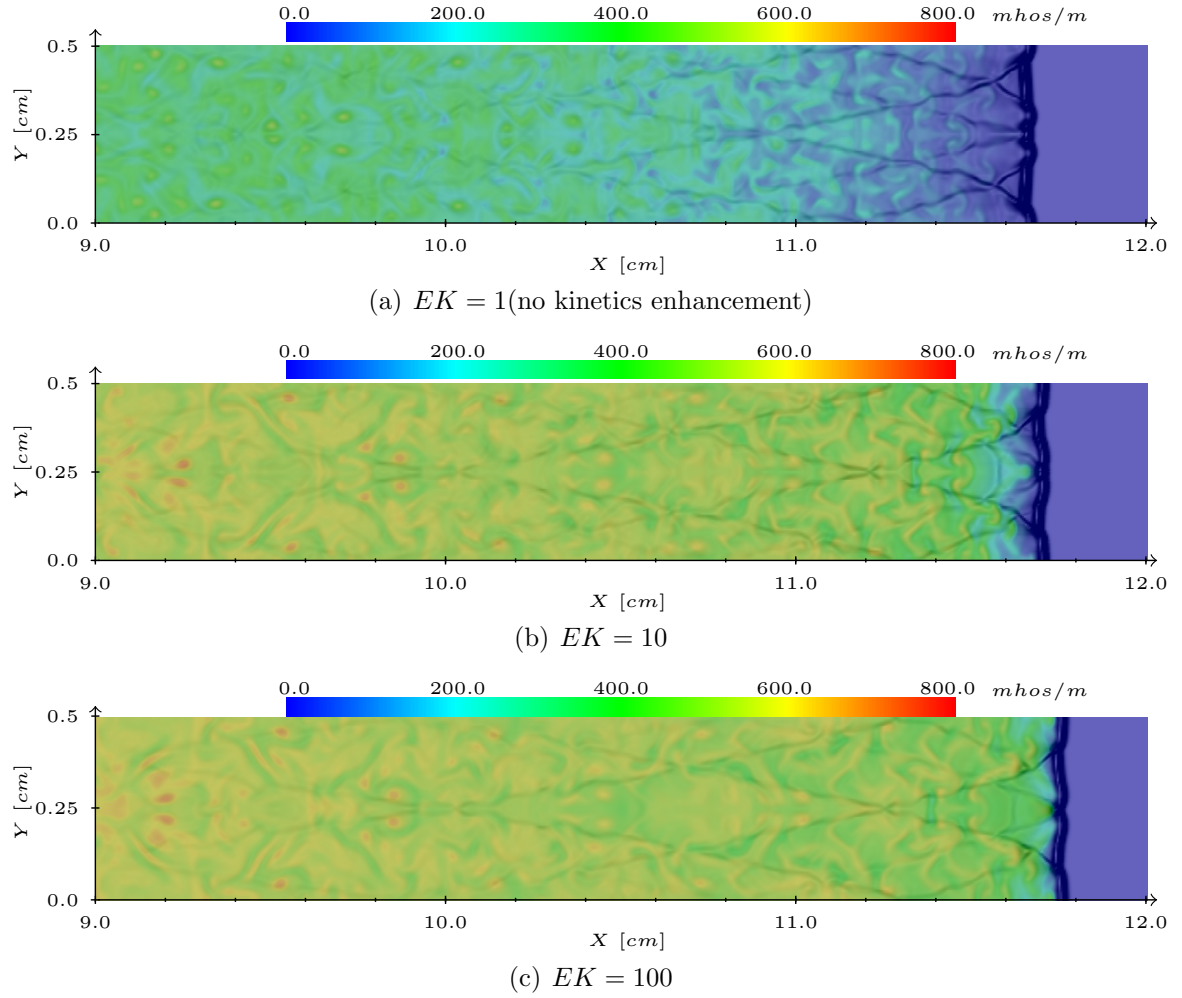
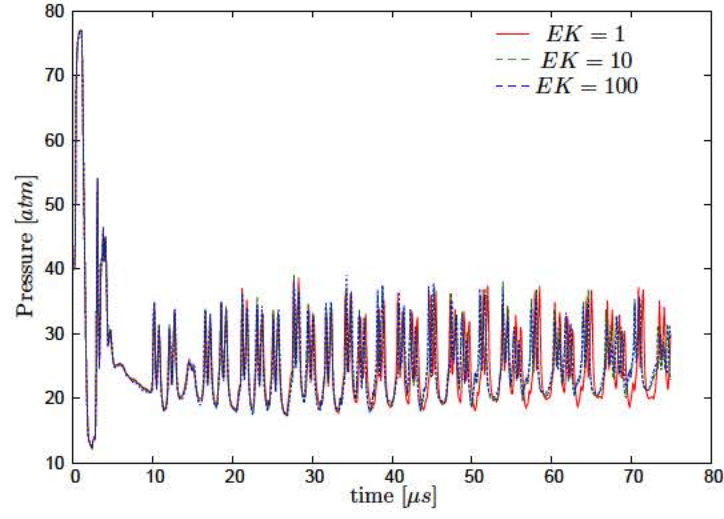
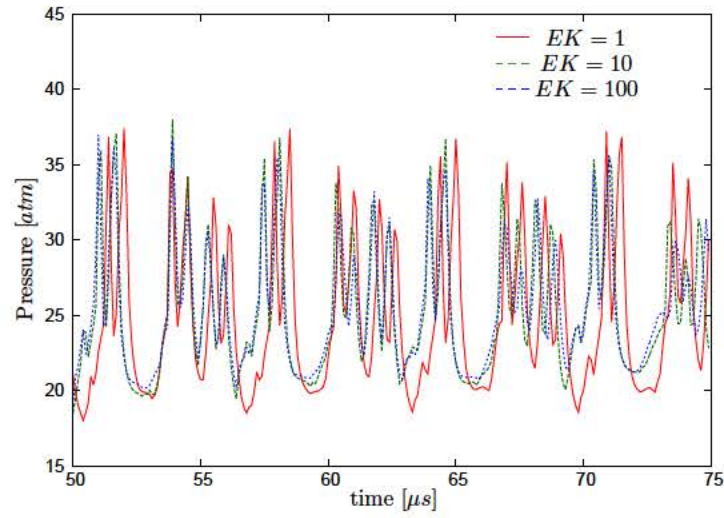


Figure 7.24: Conductivity distribution with a linear color map overlaid with Schlieren-type plot using density gradients of the detonation front in the accelerator configuration with 10% Cs and $B_z = 8T$, for different enhanced kinetic(EK) factors.

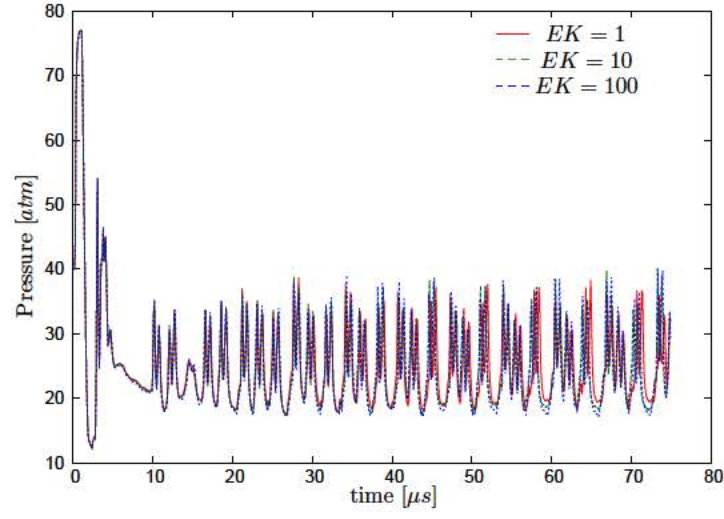


(a) Wide view

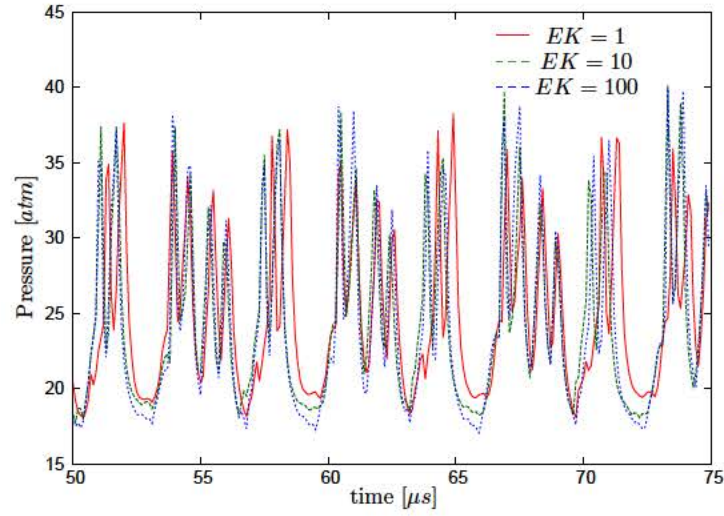


(b) Enlarged view

Figure 7.25: Centerline peak pressure trace of 2D detonation for the accelerator configurations with 10% Cs and $B_z = 8T$ with various enhanced kinetics values EK .

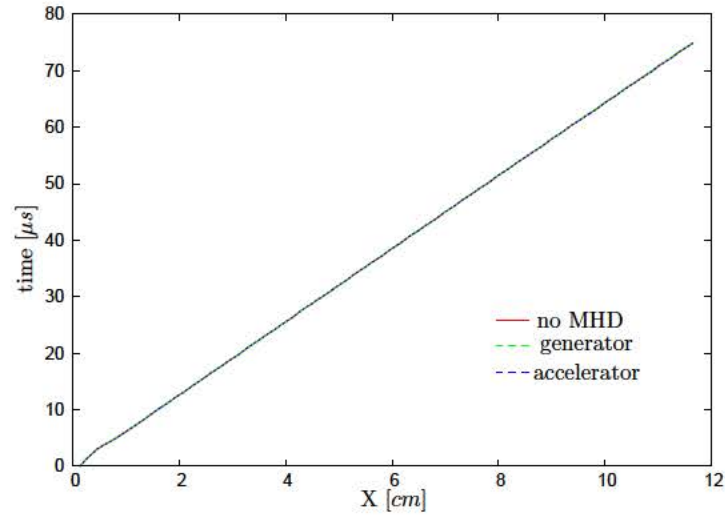


(a) Wide view

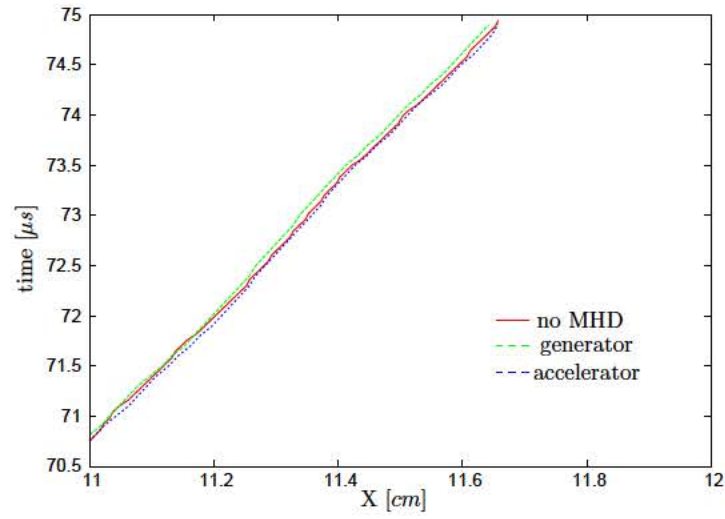


(b) Enlarged view

Figure 7.26: Centerline peak pressure trace of 2D detonation for the generator configurations with 10% Cs and $B_z = 8T$ with various enhanced kinetics values EK .

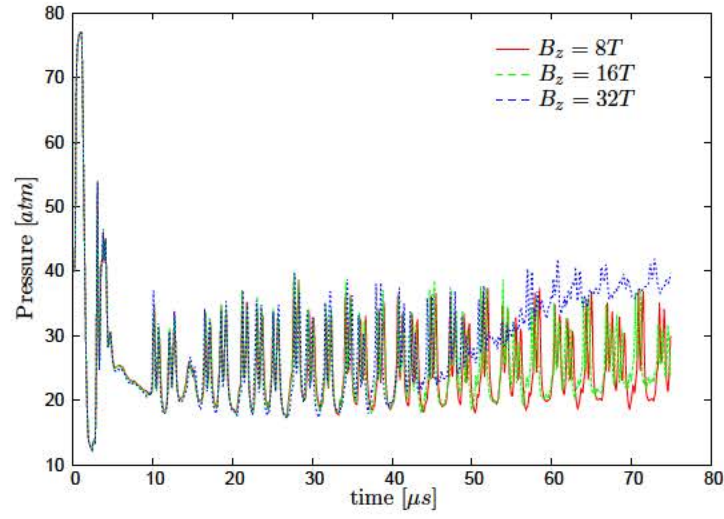


(a) Wide view

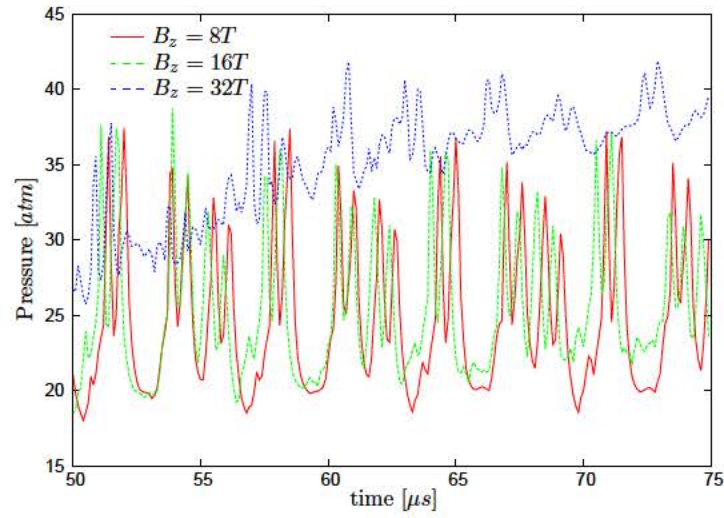


(b) Enlarged view

Figure 7.27: X-t plot of 2D detonation comparing the progression of the leading shocks at the centerline of the no MHD, generator, and accelerator configurations with $EK = 100$, 10% Cs and $B_z = 8T$.

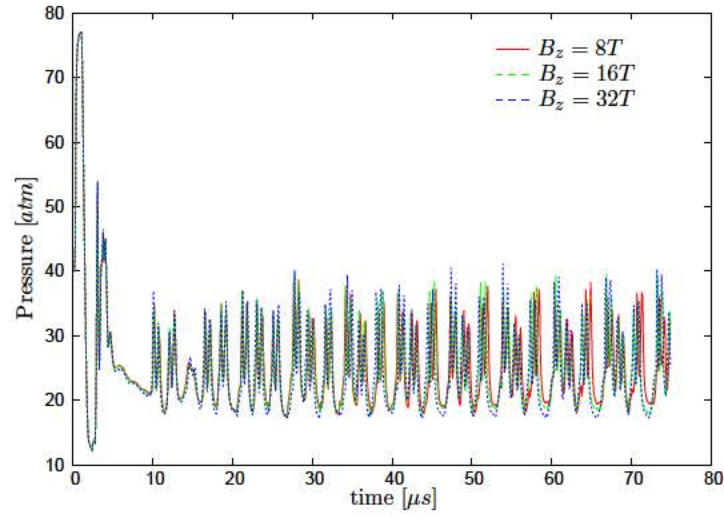


(a) Wide view

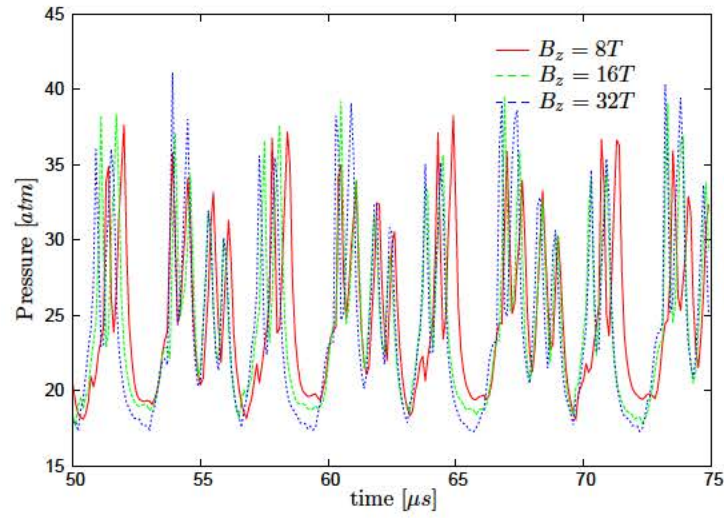


(b) Enlarged view

Figure 7.28: Centerline peak pressure trace of 2D detonation for the accelerator configuration with 10% Cs and various B_z values without enhanced kinetics.

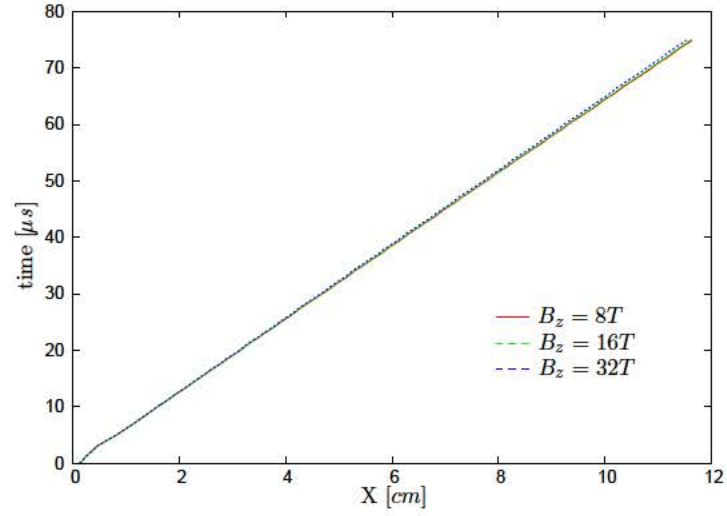


(a) Wide view

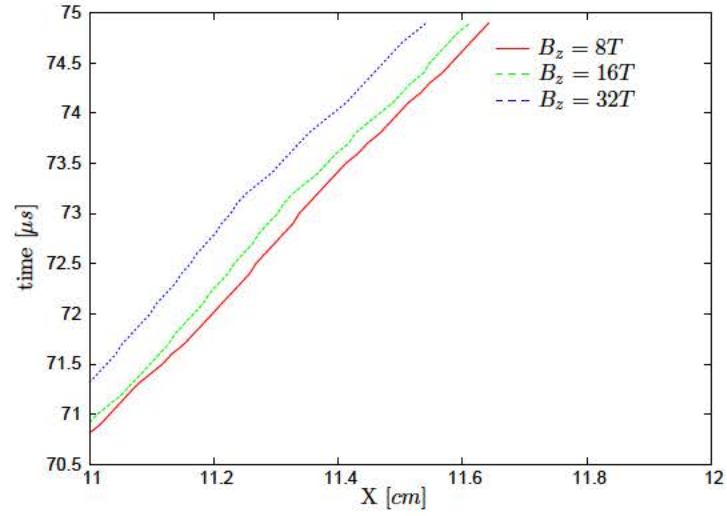


(b) Enlarged view

Figure 7.29: Centerline peak pressure trace of 2D detonation for the generator configuration with 10% Cs and various B_z values without enhanced kinetics.



(a) Wide view



(b) Enlarged view

Figure 7.30: X-t plot of 2D detonation comparing the progression of the leading shocks at the centerline of the generator configuration with 10% Cs and various B_z values without enhanced kinetics.

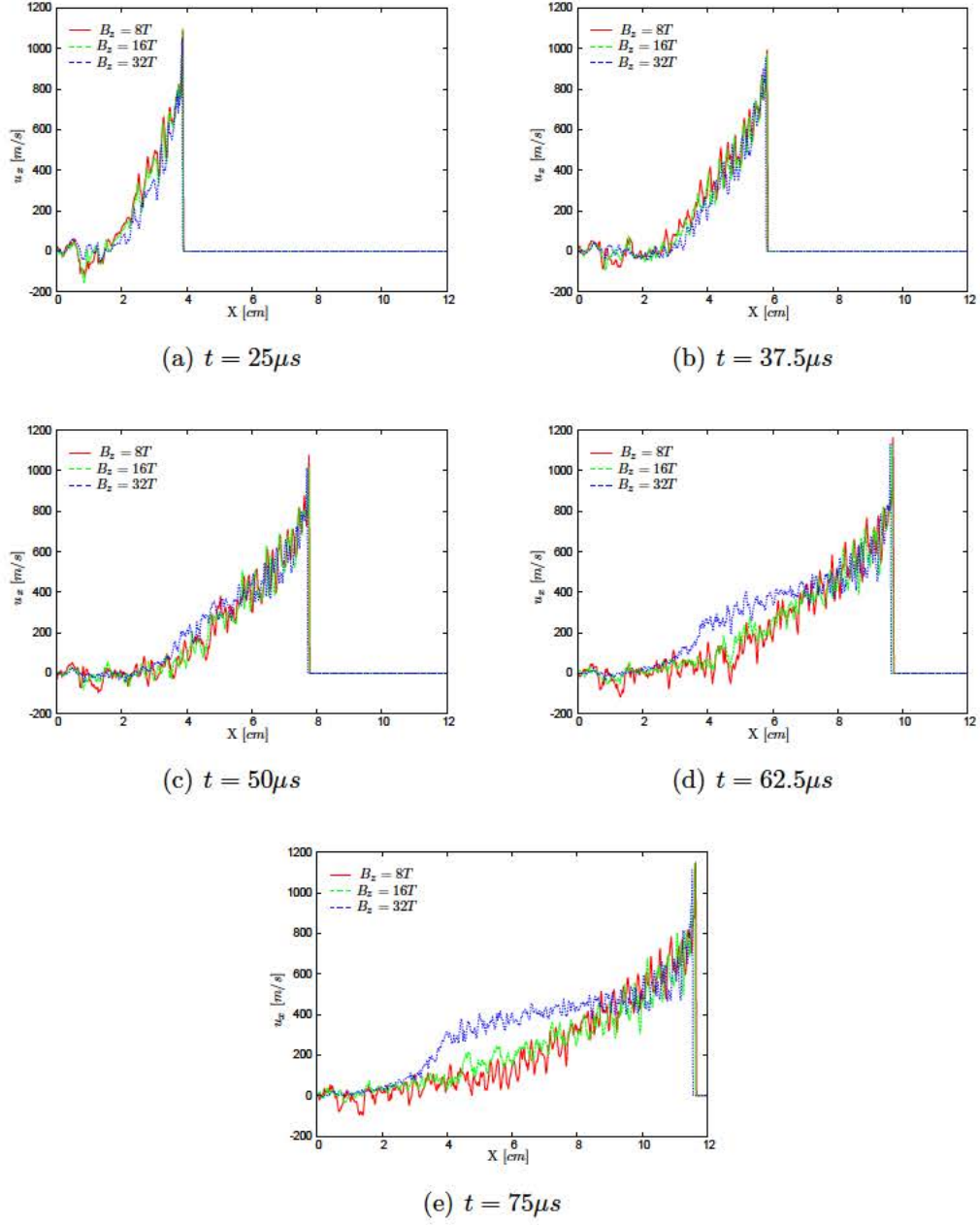


Figure 7.31: X-velocity profiles of 2D detonation at different times for the generator configuration with 10% Cs and various B_z values without enhanced kinetics.

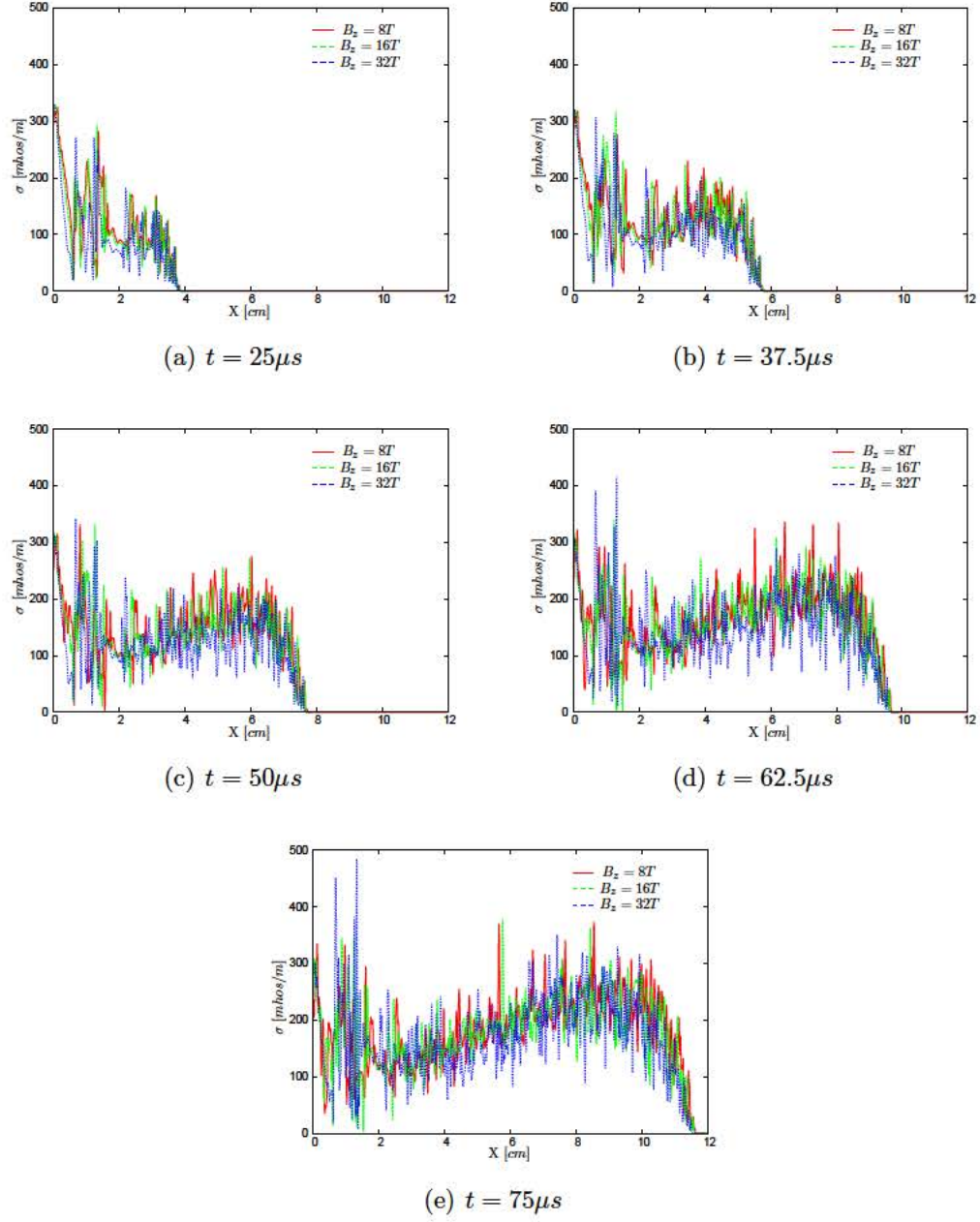


Figure 7.32: Conductivity profiles of 2D detonation at different times for the generator configuration with 10% Cs and various B_z values without enhanced kinetics.

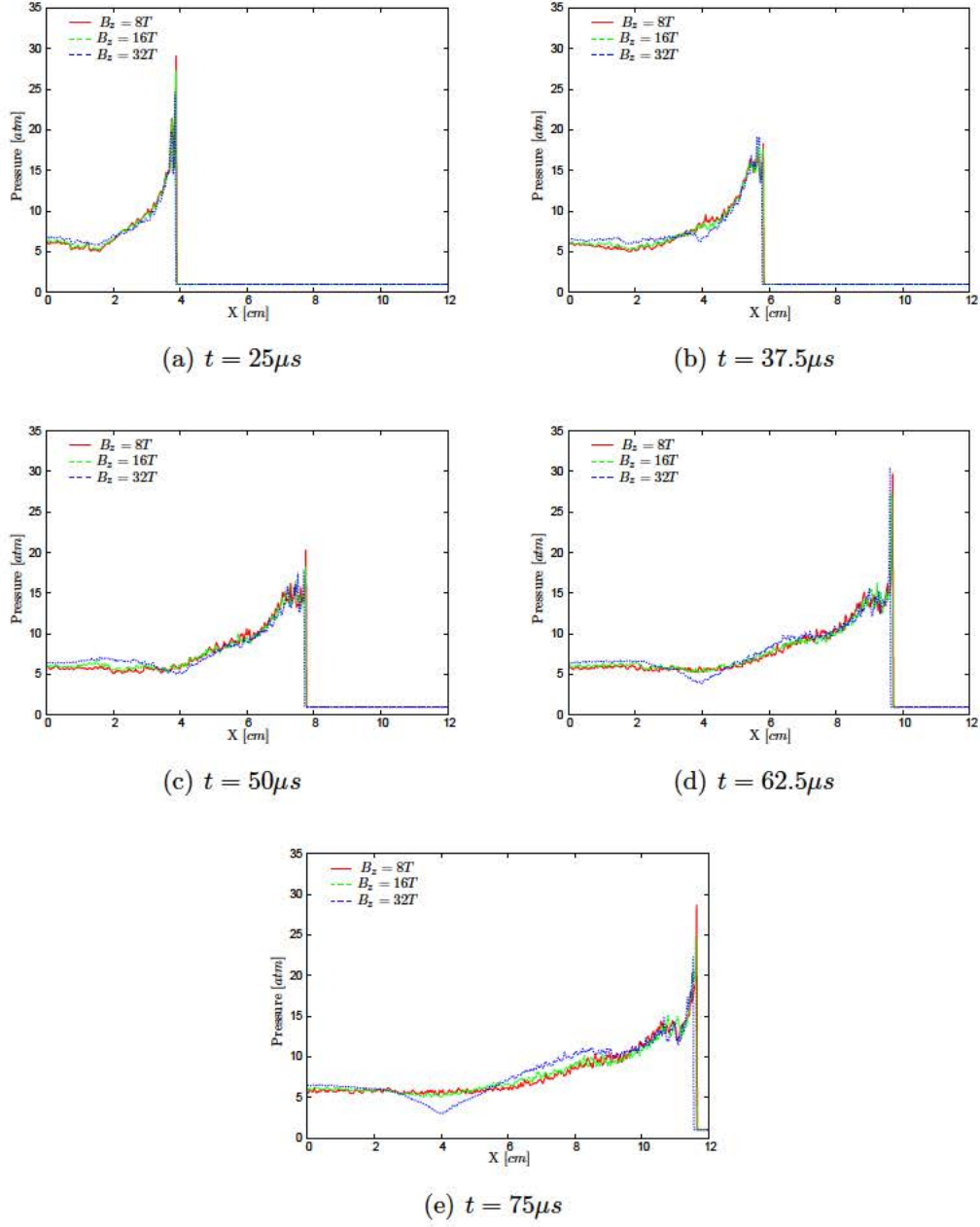


Figure 7.33: Pressure profiles of 2D detonation at different times for the generator configuration with 10% Cs and various B_z values without enhanced kinetics.

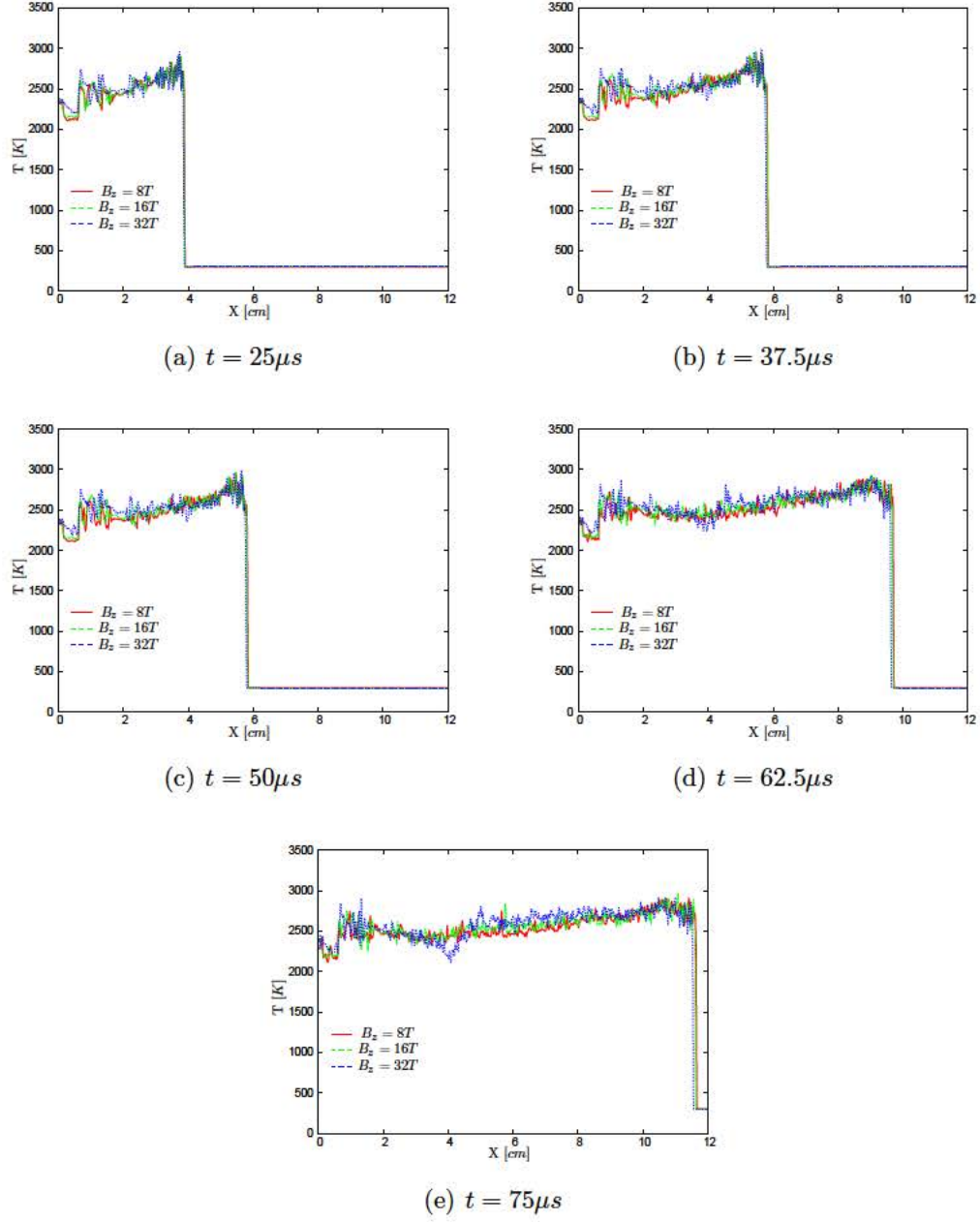


Figure 7.34: Temperature profiles of 2D detonation at different times for the generator configuration with 10% Cs and various B_z values without enhanced kinetics.

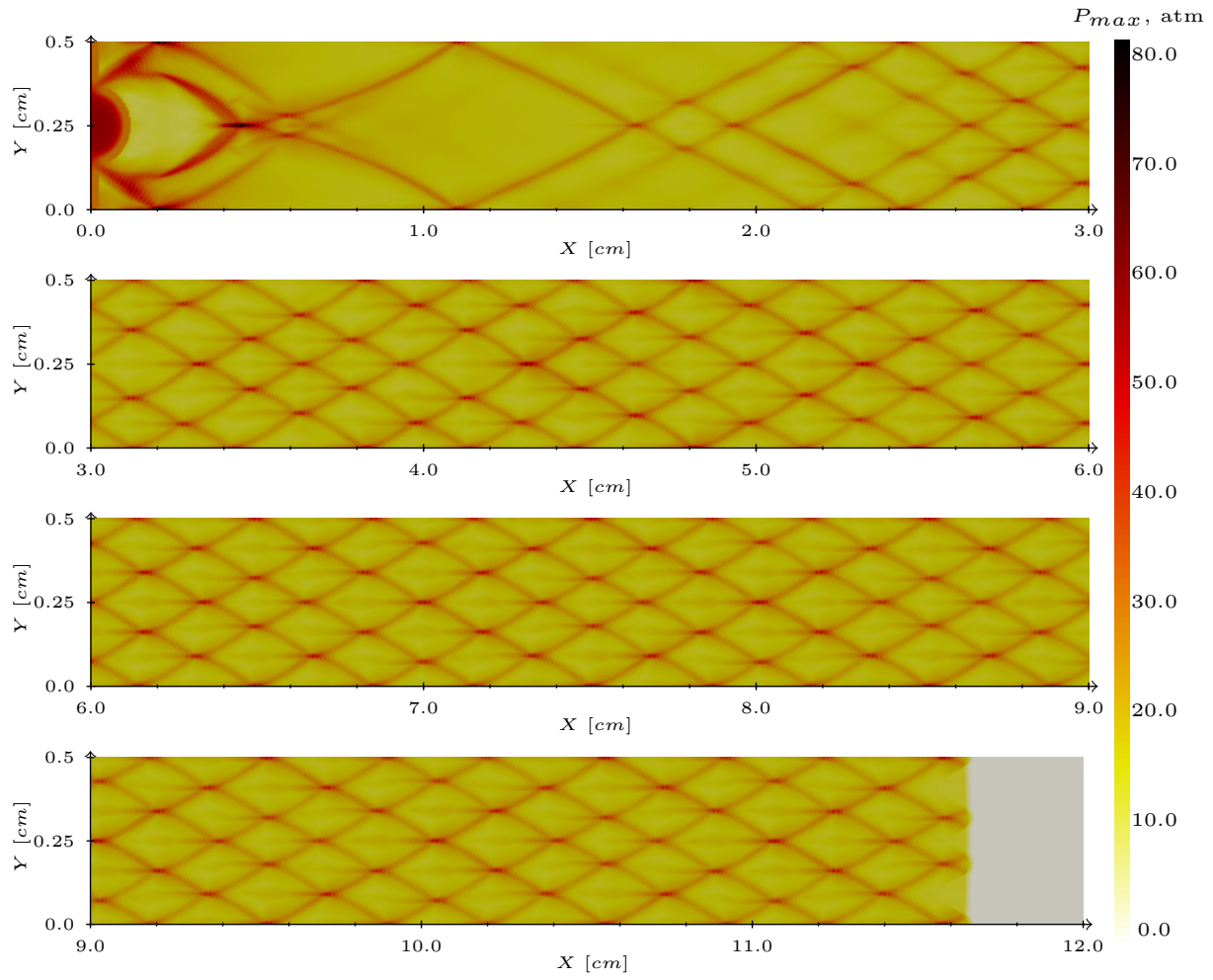


Figure 7.35: Detonation history presented by maximum pressure contours without MHD($B_z = 0T$) for 10% Cs.

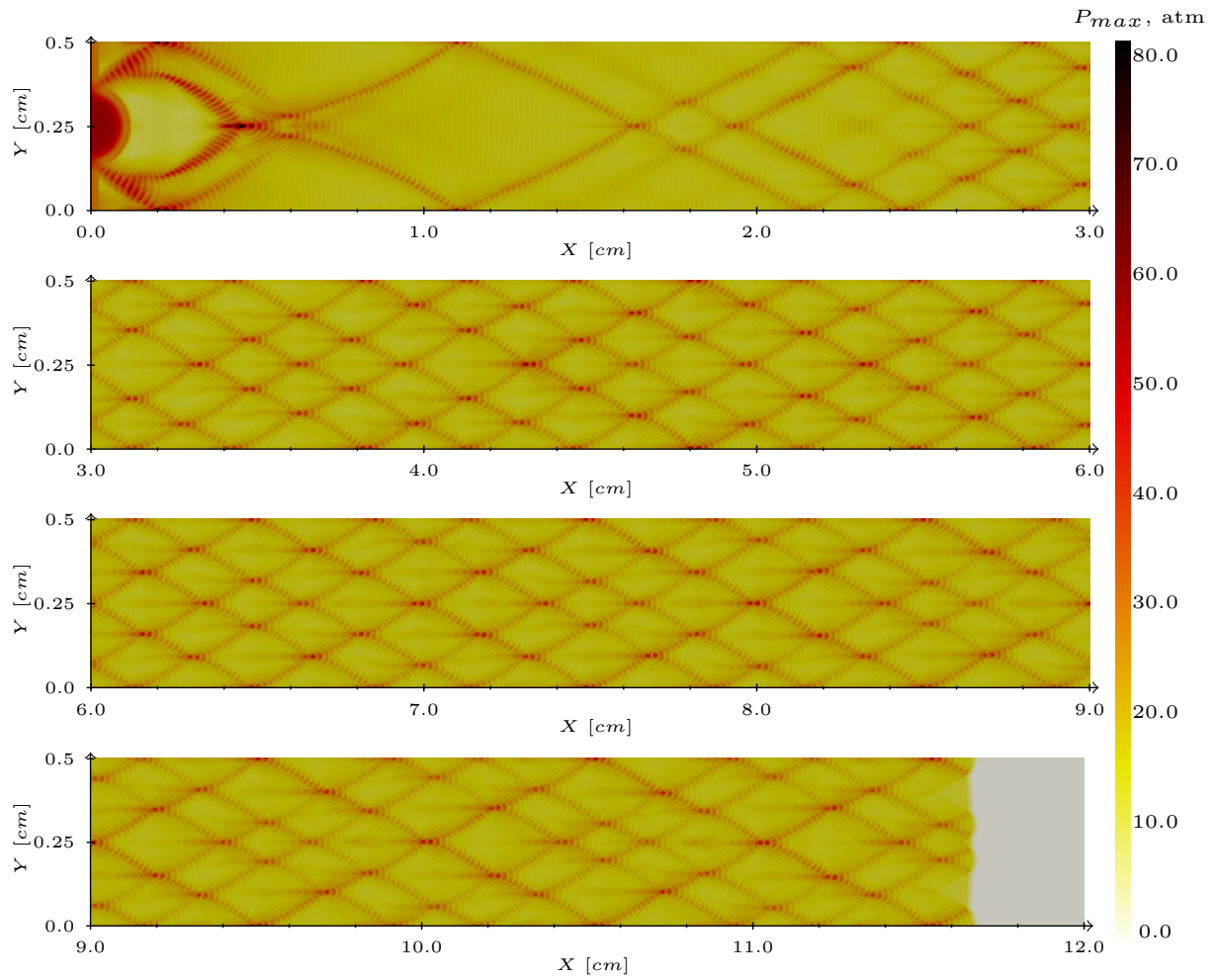


Figure 7.36: Detonation history presented by maximum pressure contours. Accelerator configuration with $B_z = 8T$ and 10% Cs.

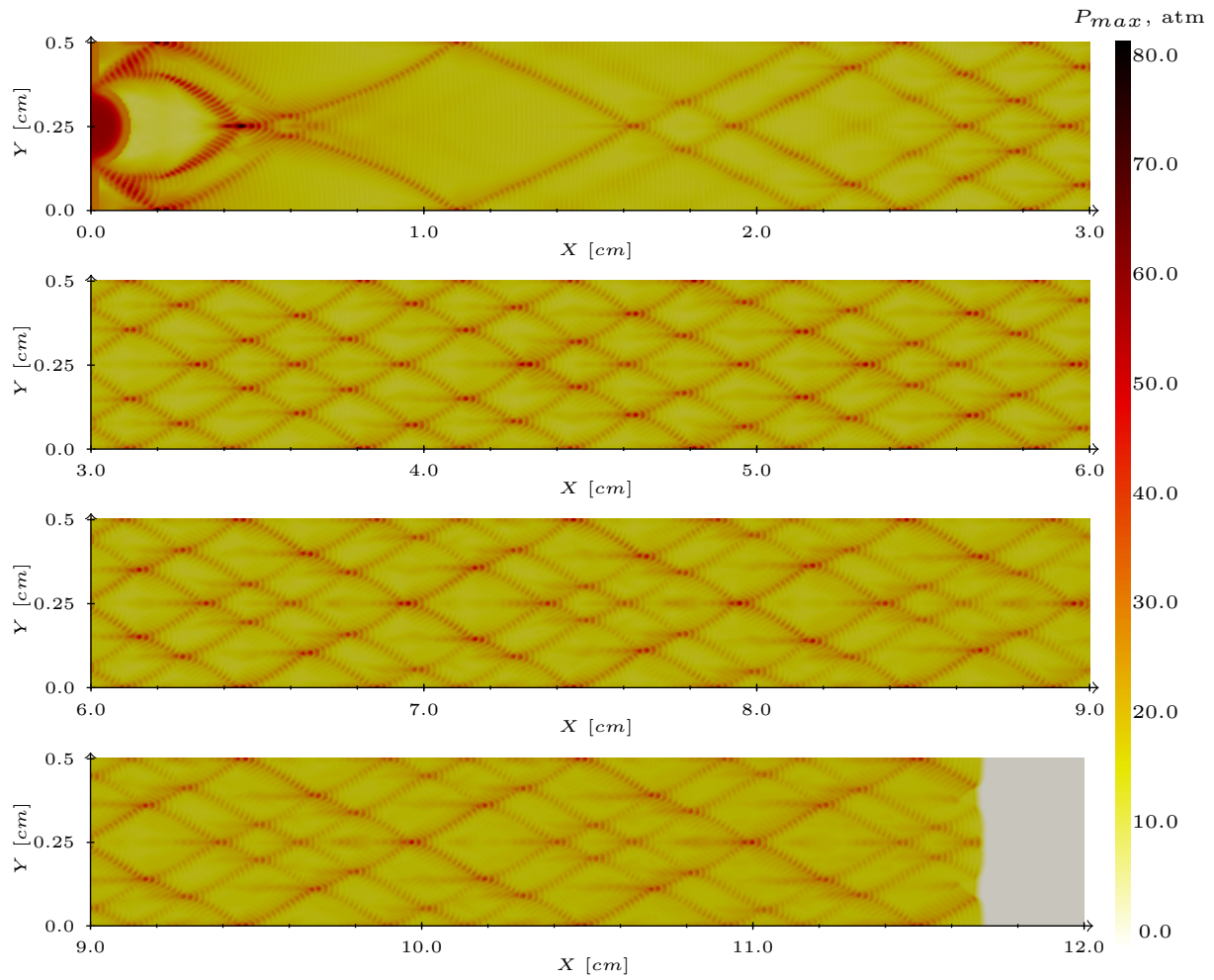


Figure 7.37: Detonation history presented by maximum pressure contours. Accelerator configuration with $B_z = 16T$ and 10% Cs.

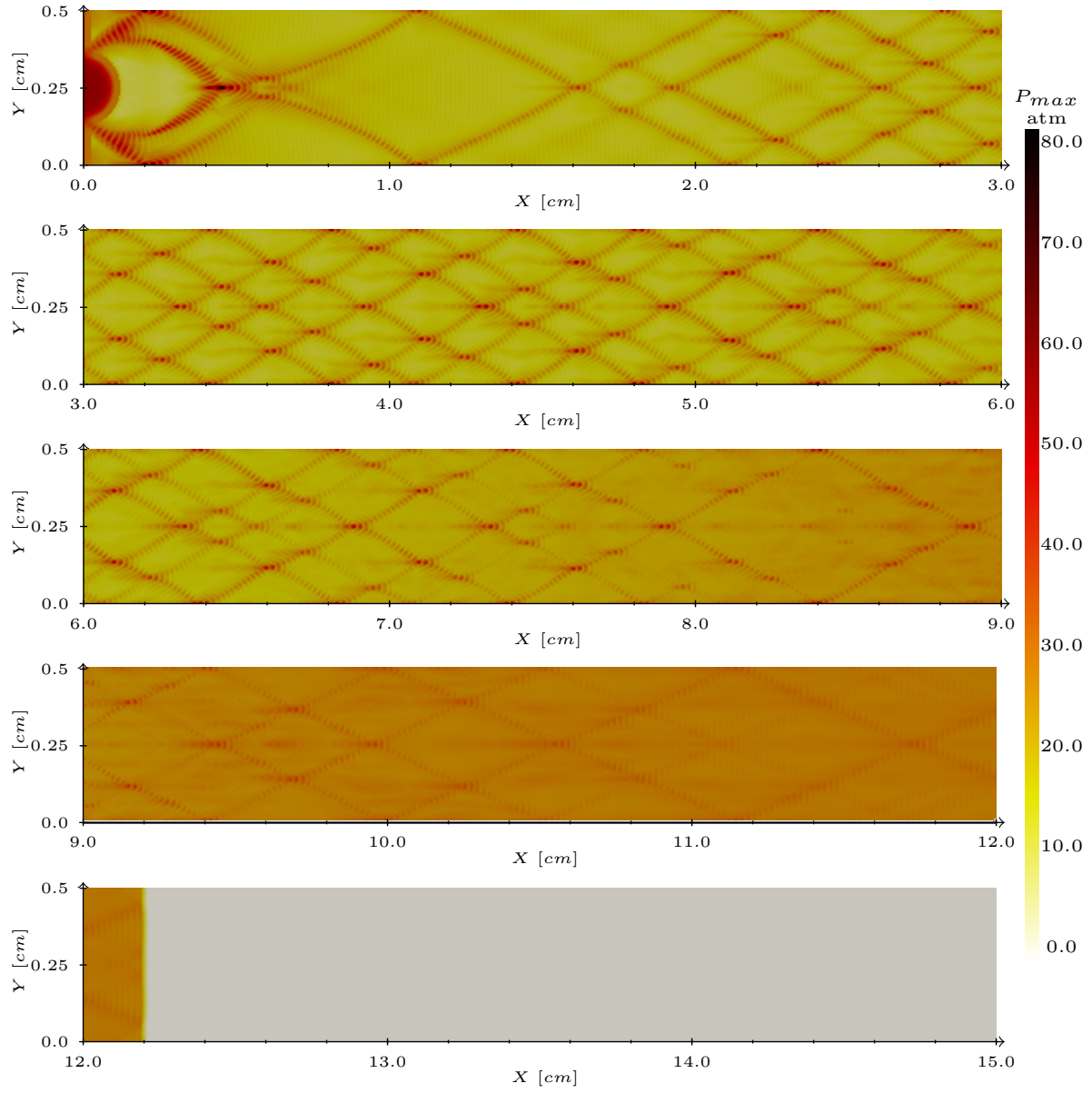
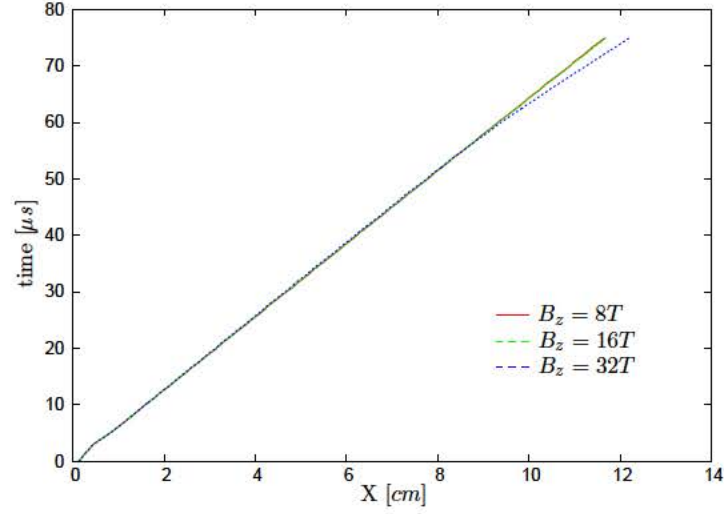
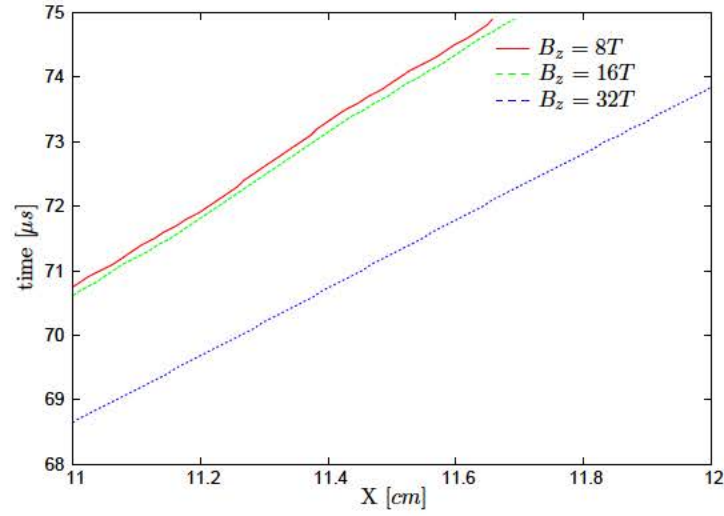


Figure 7.38: Detonation history presented by maximum pressure contours. Accelerator configuration with $B_z = 32T$ and 10% Cs.



(a) Wide view



(b) Enlarged view

Figure 7.39: X-t plot of 2D detonation comparing the progression of the leading shocks at the centerline of the accelerator configuration with 10% Cs and various B_z values without enhanced kinetics.

CHAPTER 8

Conclusions and Future Work

The present computational studies have enabled both a global exploration of PDRIME concepts for propulsive devices, as well as a detailed exploration of the underlying physics of detonation-MHD interactions.

For the standard PDRIME utilizing a constant magnetic field, there was marginal gains in performance over the baseline PDRE configuration using simplified modelling approaches. We investigated closed and open loop control of the magnetic field utilizing, temporal and temperature controllers, respectively. We found that these methods of control had marginal performance gains, at best. When the flight Mach number was significantly lowered ($M \leq 5$), we found significant performance increases without the use of controllers.

The stability and dynamics of a 1D spark-ignited detonation with complex kinetics were also investigated. We developed a model to understand and interpret the coupling between the reactive and fluid mechanical/acoustic phenomena. We found that the frequency in oscillations of the peak pressure trace is inversely related to the time it takes for an acoustic wave to propagate from the flame to the leading shock and the entropy wave generated from the perturbed shock to travel back to the flame. We verified the model by finding out it was in agreement with the peak pressure cycles extracted from the 1D complex kinetics detonation simulation.

After gaining insight into the stability of the 1D detonation, we investigated the stability of a cesium-seeded detonation. We confirmed previous findings by Radulescu et al.[19] that the diluent had a regularizing effect on the 1D detonation. We then applied MHD using a loading factor, K_y , to the 1D cesium-seeded detonation with both the generator and accelerator configurations at various magnetic field strengths, B_z , and concentrations of cesium. We found that for a given concentration of cesium and applied field strength the accelerator had a regularizing effect, while the generator had the opposite effect. We then investigated the effect the applied fields had on the 2D cesium-seeded spark-ignited detonation with the same parameters used for the 1D simulations (i.e., B_z and cesium concentration) and found that the MHD had little to no effect on the detonation dynamics, i.e., cellular structure and detonation velocity. Next, we increased the Arrhenius pre-factor of the cesium forward reaction mechanism by factors of 10 and 100. We observed a significant increase of conductivity near the leading shock of the 2D detonation, but little change in the detonation velocity in either the accelerator or generator configurations. Lastly, we significantly increased the strength of the magnetic field ($16T$ and $32T$) without enhancing the cesium kinetics. The generator mode had little effect on the detonation dynamics, while the accelerator mode significantly altered the detonation velocity.

In Chapter 7, the conductivity of the fluid played an important role in the MHD acceleration of the detonation. But in order to properly calculate the conductivity, the number density of electrons as well as the electron temperature, T_e , must be determined (per Equation 2.27). Section 2.3.3 describes how the electron energy is coupled to the bulk fluid via a two-temperature model. One future direction of this research is to investigate the dynamics of the detonation in 1D and 2D simulations using the two-temperature model to more accurately characterize the thermal non-

equilibrium effects of the bulk fluid. Additionally, the kinetics of excitation and ionization of the gas can be further investigated by means of a collisional radiative model[75, 76], commonly used in the study of gas discharges[82, 83], which allow for a more accurate representation of the atomic state distribution function.

The simulations performed in this dissertation utilized high-order accurate methods which significantly reduced numerical dissipation. The high-order accuracy allowed for the capturing of sharp flow features (i.e., shocks and contact discontinuities). Oran et al.[84] demonstrated that the viscous effects did not change the dynamics of the leading shock, thus did not have a significant effect on the detonation cellular structure. But unlike, previous works[68, 84, 85] with detonations, the downstream effects play an important role in the overall dynamics of the detonation with MHD acceleration. Future studies involving full ionization kinetics, including collisional-radiative processes, will be used to examine these processes in further detail. In addition, a more physically accurate model based on the Navier-Stokes equations and including species diffusion is needed to correctly model the transport of the fluid. In addition, precursor effects[86] might play a role in heating the upstream fluid, which then alters the flame temperature. It might also be interesting to investigate the thermal losses to the wall as well as the interactions of the boundary layer with the shock[87].

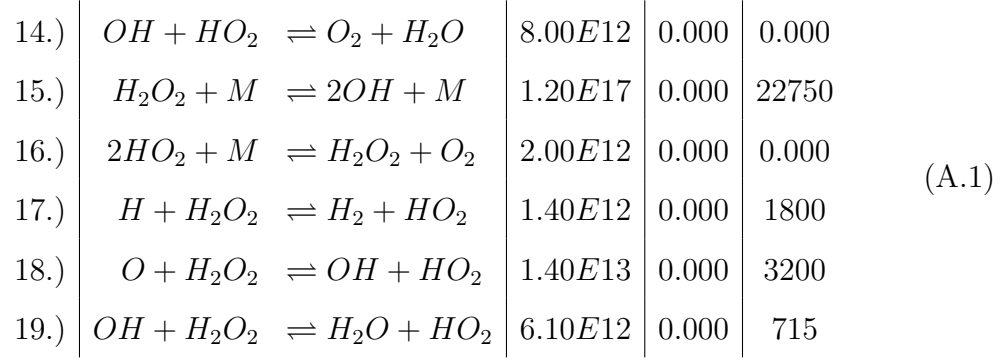
APPENDIX A

Reaction Mechanism

A.1 H_2 -Air Reaction Mechanism

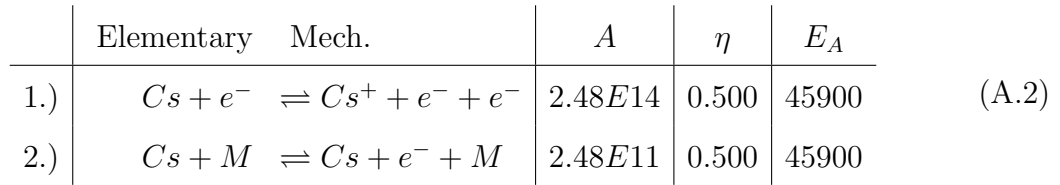
The H_2 -air reaction mechanism and Arrhenius coefficients used in the present study contains 19 reversible elementary mechanisms composed of 9 species[37].

	Elementary Mech.	A	η	E_A
1.)	$H + O_2 \rightleftharpoons O + OH$	$2.60E14$	0.000	8400
2.)	$O + H_2 \rightleftharpoons H + OH$	$1.80E10$	1.000	4450
3.)	$H_2 + OH \rightleftharpoons H + H_2O$	$2.20E13$	0.000	2575
4.)	$2OH \rightleftharpoons H_2O + O$	$6.30E12$	0.000	545
5.)	$H + OH + M \rightleftharpoons H_2O + M$	$2.20E22$	-2.00	0.000
6.)	$2H + M \rightleftharpoons H_2 + M$	$6.40E17$	-1.000	0.000
7.)	$H + O + M \rightleftharpoons OH + M$	$6.00E16$	-0.600	0.000
8.)	$2O + M \rightleftharpoons O_2 + M$	$6.00E13$	0.000	-900
9.)	$H_2 + O_2 \rightleftharpoons HO_2 + H$	$1.00E14$	0.000	28000
10.)	$H + O_2 + M \rightleftharpoons HO_2 + M$	$2.10E15$	0.000	-500
11.)	$H + HO_2 \rightleftharpoons 2OH$	$1.40E14$	0.000	540
12.)	$H + HO_2 \rightleftharpoons O + H_2O$	$1.00E13$	0.000	540
13.)	$O + HO_2 \rightleftharpoons O_2 + OH$	$1.50E13$	0.000	475



A.2 Cesium Reaction Mechanism

The cesium reaction mechanism and Arrhenius coefficients used in the present study contains 2 reversible elementary mechanisms composed of Cs , Cs^+ , and e^- .



APPENDIX B

Eigenvector Matrices

The following was derived for a multi-species, two-temperature eigen-system[35, 88].

B.1 Governing Equation

The governing equation for a non-reactive multi-species, multi-temperature three-dimensional flow without LHS is:

$$\mathbf{Q}_t + \nabla_n \mathbf{F} = 0 \quad (\text{B.1})$$

Here the vector containing the conserved variables, \mathbf{Q} , and the flux normal to control volume surface , \mathbf{F} , are:

$$\mathbf{Q} = \begin{pmatrix} \rho_s \\ \rho \mathbf{u} \\ \mathbf{B} \\ E^* \\ S_e \end{pmatrix} \quad \mathbf{F} = \begin{pmatrix} \rho_s u_n \\ \rho \mathbf{u} u_n + P^* \mathbf{n} - \frac{1}{\mu_0} B_n \mathbf{B} \\ u_n \mathbf{B} - \mathbf{u} B_n \\ (E^* + P^*) u_n - \frac{1}{\mu_0} B_n \mathbf{u} \cdot \mathbf{B} \\ S_e u_n \end{pmatrix} \quad (\text{B.2})$$

B.2 Roe Averaged Weighting

Before the eigensystem can be determined, the Roe Averaged variables[46], i.e., mass fraction, spatial components of velocity and enthalpy, must first be determined on a flux interface, $i + \frac{1}{2}$. First the primitive variables are calculated for i and $i + 1$ as:

$$\mathbf{V} = \begin{pmatrix} c_s \\ \mathbf{u} \\ \mathbf{b} \\ h \\ \hat{s}_e \end{pmatrix} \quad (\text{B.3})$$

$$h = \frac{1}{\rho} \left(E + P - \frac{\mathbf{B}^2}{2\mu_0} - E_e \right), \quad c_s = \frac{\rho_s}{\rho}, \quad \mathbf{b} = [b_n, b_t]^T / \sqrt{\rho\mu_0}, \quad \text{and} \quad \hat{s}_e = \frac{S_e}{\rho}$$

where c_s represents the mass fraction of the s^{th} species, h represents the specific enthalpy, and \hat{s}_e represents the specific electron entropy. Next, by using the densities at i and $i + 1$, the Roe-averaged variables at the face, $i + \frac{1}{2}$, are determined by:

$$\mathbf{V}_{i+\frac{1}{2}} = \frac{\mathbf{V}_i\sqrt{\rho_i} + \mathbf{V}_{i+1}\sqrt{\rho_{i+1}}}{\sqrt{\rho_i} + \sqrt{\rho_{i+1}}} \quad (\text{B.4})$$

B.3 Eigensystem and Flux Jacobian Matrix

The flux Jacobian represents the relation $\tilde{A} = \frac{\partial \mathbf{F}}{\partial \mathbf{Q}}$. From here we diagonalize the flux Jacobian to get a formulation involving the Jacobian, left and right eigenvector matrices, and the eigen-matrix.

$$\tilde{A} = \frac{\partial \mathbf{F}}{\partial \mathbf{Q}} = \mathbf{R}\mathbf{A}\mathbf{L} \quad (\text{B.5})$$

The eigen-matrix is defined as the following,

$$\mathbf{\Lambda} = \begin{pmatrix} u_n & 0 & 0 & 0 & 0 & 0 & 0 & 0 & 0 & 0 \\ 0 & \ddots & 0 & 0 & 0 & 0 & 0 & 0 & 0 & 0 \\ 0 & 0 & u_n + c_f & 0 & 0 & 0 & 0 & 0 & 0 & 0 \\ 0 & 0 & 0 & u_n - c_f & 0 & 0 & 0 & 0 & 0 & 0 \\ 0 & 0 & 0 & 0 & u_n + c_s & 0 & 0 & 0 & 0 & 0 \\ 0 & 0 & 0 & 0 & 0 & u_n & 0 & 0 & 0 & 0 \\ 0 & 0 & 0 & 0 & 0 & 0 & u_n - c_s & 0 & 0 & 0 \\ 0 & 0 & 0 & 0 & 0 & 0 & 0 & u_n + c_A & 0 & 0 \\ 0 & 0 & 0 & 0 & 0 & 0 & 0 & 0 & u_n - c_A & 0 \\ 0 & 0 & 0 & 0 & 0 & 0 & 0 & 0 & 0 & u_n \end{pmatrix} \quad (\text{B.6})$$

Where the diagonal entries are the eigen-values of the system. The definitions of the fast(slow) magneto-acoustic, $c_{f(s)}$, and the Alfvén, c_A , wave speeds can be found in [88]. The similarity transformation matrices \mathbf{R} and \mathbf{L} are defined in the next sections.

B.3.1 Right Eigenvectors

The system satisfies $\Delta Q = \mathbf{R} \cdot \tilde{\alpha}$ where

$$\mathbf{R} = \begin{pmatrix} 1 & r_f & r_f & r_s & 0 & r_s & 0 & 0 & 0 \\ u_x & \Theta_{f,x}^+ & \Theta_{f,x}^- & \Theta_{s,x}^+ & 0 & \Theta_{s,x}^- & \sqrt{\rho}s_x & \sqrt{\rho}s_x & 0 \\ u_y & \Theta_{f,y}^+ & \Theta_{f,y}^- & \Theta_{s,y}^+ & 0 & \Theta_{s,y}^- & \sqrt{\rho}s_y & \sqrt{\rho}s_y & 0 \\ u_z & \Theta_{f,z}^+ & \Theta_{f,z}^- & \Theta_{s,z}^+ & 0 & \Theta_{s,z}^- & \sqrt{\rho}s_z & \sqrt{\rho}s_z & 0 \\ 0 & \tilde{\Delta}_f t_x & \tilde{\Delta}_f t_x & \tilde{\Delta}_s t_x & n_x & \tilde{\Delta}_s t_x & -s_B s_x \sqrt{\mu_0} & s_B s_x \sqrt{\mu_0} & 0 \\ 0 & \tilde{\Delta}_f t_y & \tilde{\Delta}_f t_y & \tilde{\Delta}_s t_y & n_y & \tilde{\Delta}_s t_y & -s_B s_y \sqrt{\mu_0} & s_B s_y \sqrt{\mu_0} & 0 \\ 0 & \tilde{\Delta}_f t_z & \tilde{\Delta}_f t_z & \tilde{\Delta}_s t_z & n_z & \tilde{\Delta}_s t_z & -s_B s_z \sqrt{\mu_0} & s_B s_z \sqrt{\mu_0} & 0 \\ \frac{\tilde{u}^2}{2} & \mathcal{H}_f^+ & \mathcal{H}_f^- & \mathcal{H}_s^+ & 0 & \mathcal{H}_s^- & u_s \sqrt{\rho} & u_s \sqrt{\rho} & \mathcal{H}_e \\ 0 & r_f \hat{s}_e & r_f \hat{s}_e & r_s \hat{s}_e & 0 & r_s \hat{s}_e & 0 & 0 & 1 \end{pmatrix} \quad (\text{B.7})$$

where s_B is the sign of the normal component of the magnetic field and for the purpose of a compact expression of \mathbf{R} , the following variables are defined,

$$\tilde{\Delta}_f = r_s \frac{c_f}{\sqrt{\rho}} \quad (\text{B.8a})$$

$$\tilde{\Delta}_s = -r_f \frac{a^2}{c_f^2} \frac{c_f}{\sqrt{\rho}} \quad (\text{B.8b})$$

$$\tilde{\Gamma}_f = -s_B b_n r_s \quad (\text{B.8c})$$

$$\tilde{\Gamma}_s = +s_B a r_f \quad (\text{B.8d})$$

$$\mathcal{H}_e = \frac{\zeta_e}{\gamma_e - 1} \rho^{\gamma_e - 1} \quad (\text{B.8e})$$

$$\mathcal{H}_{f(s)}^\pm = r_{f(s)} h \pm r_{f(s)} u_n c_{f(s)} \pm u_t \tilde{\Gamma}_{f(s)} + \frac{B_t}{\mu_0} \tilde{\Delta}_{f(s)} \quad (\text{B.8f})$$

$$\Theta_{f(s),x}^\pm = r_{f(s)} u_x \pm r_{f(s)} c_{f(s)} n_x \pm \tilde{\Gamma}_{f(s)} t_x \quad (\text{B.8g})$$

similarly for the y, z components and $\zeta_e = 1 - \frac{\gamma_e - 1}{\gamma_h - 1}$. As noted by Brio & Wu[60], renormalization factors, r_f and r_s , are needed to avoid singular solutions when the magnetic field vanishes. Their definitions and identities are as follows¹,

¹Identities computed with $\epsilon_t = \frac{b_t^2}{a^2 + b_n^2} > \epsilon_t^* \sim 10^{-6}$

$$r_f = \sqrt{\frac{c_f^2 - b_n^2}{c_f^2 - c_s^2}} \quad (\text{B.9a})$$

$$r_s = \sqrt{\frac{c_f^2 - a^2}{c_f^2 - c_s^2}} = \frac{c_f}{b_n} \sqrt{\frac{b_n^2 - c_s^2}{c_f^2 - c_s^2}} \quad (\text{B.9b})$$

$$r_f r_s = \frac{c_f b_t}{c_f^2 - c_s^2} \quad (\text{B.9c})$$

$$r_s^2 + r_f^2 \frac{a^2}{c_f^2} = 1 \quad (\text{B.9d})$$

$$r_f^2 + r_s^2 \frac{c_s^2}{a^2} = 1 \quad (\text{B.9e})$$

B.3.2 Left Eigenvectors

The systems satisfies $\mathbf{L} = \mathbf{R}^{-1}$, where

$$\mathbf{L} = \begin{pmatrix} L_c \\ L_f^+ \\ L_f^- \\ L_s^+ \\ L_{pseudo} \\ L_s^- \\ L_A^+ \\ L_A^- \\ L_e \end{pmatrix} \quad (\text{B.10})$$

$$\begin{aligned}
L_c = \frac{1}{a^2} \begin{pmatrix} a^2 - \beta \frac{\vec{u}^2}{2} \\ \beta u_x \\ \beta u_y \\ \beta u_z \\ \beta \frac{B_t}{\mu_0} t_x \\ \beta \frac{B_t}{\mu_0} t_y \\ \beta \frac{B_t}{\mu_0} t_z \\ -\beta \\ \beta \mathcal{H}_e \end{pmatrix}^T, \quad L_f^\pm = \frac{1}{2c_f^2} \begin{pmatrix} r_f \beta \frac{\vec{u}^2}{2} \mp r_f u_n c_f \pm r_s s_B b_n u_t \\ -r_f \beta u_x \pm r_f c_f n_x \mp r_s s_B t_x \\ -r_f \beta u_y \pm r_f c_f n_y \mp r_s s_B t_y \\ -r_f \beta u_z \pm r_f c_f n_z \mp r_s s_B t_z \\ -r_f \beta \frac{B_t}{\mu_0} t_x + r_s \sqrt{\frac{\rho}{\mu_0}} c_f t_x \\ -r_f \beta \frac{B_t}{\mu_0} t_y + r_s \sqrt{\frac{\rho}{\mu_0}} c_f t_y \\ -r_f \beta \frac{B_t}{\mu_0} t_z + r_s \sqrt{\frac{\rho}{\mu_0}} c_f t_z \\ \beta r_f \\ -\beta r_f \mathcal{H}_e \end{pmatrix}^T \\
L_A^\pm = \frac{1}{2\sqrt{\rho}} \begin{pmatrix} -u_s \\ s_x \\ s_y \\ s_z \\ \mp s_B \sqrt{\frac{\rho}{\mu_0}} s_x \\ \mp s_B \sqrt{\frac{\rho}{\mu_0}} s_y \\ \mp s_B \sqrt{\frac{\rho}{\mu_0}} s_z \\ 0 \\ 0 \end{pmatrix}^T, \quad L_s^\pm = \frac{1}{2a^2} \begin{pmatrix} r_s \beta \frac{\vec{u}^2}{2} \mp r_s u_n c_s \mp r_f s_B u_t a \\ -r_s \beta u_x \pm r_s c_s n_x \pm r_f s_B a t_x \\ -r_s \beta u_y \pm r_s c_s n_y \pm r_f s_B a t_y \\ -r_s \beta u_z \pm r_s c_s n_z \pm r_f s_B a t_z \\ -r_s \beta \frac{B_t}{\mu_0} t_x - r_f \sqrt{\frac{\rho}{\mu_0}} \frac{a^2}{c_f} t_x \\ -r_s \beta \frac{B_t}{\mu_0} t_y - r_f \sqrt{\frac{\rho}{\mu_0}} \frac{a^2}{c_f} t_y \\ -r_s \beta \frac{B_t}{\mu_0} t_z - r_f \sqrt{\frac{\rho}{\mu_0}} \frac{a^2}{c_f} t_z \\ \beta r_s \\ -\beta r_s \mathcal{H}_e \end{pmatrix}^T,
\end{aligned}$$

$$L_e = \frac{1}{a^2} \begin{pmatrix} -\hat{s}_e \beta \frac{\vec{u}^2}{2} \\ \beta u_x \hat{s}_e \\ \beta u_y \hat{s}_e \\ \beta u_z \hat{s}_e \\ \beta \frac{B_t}{\mu_0} \hat{s}_e t_x \\ \beta \frac{B_t}{\mu_0} \hat{s}_e t_y \\ \beta \frac{B_t}{\mu_0} \hat{s}_e t_z \\ -\beta \hat{s}_e \\ 1 + \beta \mathcal{H}_e \hat{s}_e \end{pmatrix}^T, \quad L_{pseudo} = \begin{pmatrix} 0 \\ 0 \\ 0 \\ 0 \\ n_x \\ n_y \\ n_z \\ 0 \\ 0 \end{pmatrix}^T$$

B.3.3 Riemann ‘Jump’ conditions

The ‘jump’ conditions satisfy $\tilde{\alpha} = \mathbf{L} \cdot \Delta \mathbf{Q}$ and is defined,

$$\tilde{\alpha} = \begin{pmatrix} \tilde{\alpha}_c \\ \tilde{\alpha}_f^+ \\ \tilde{\alpha}_f^- \\ \tilde{\alpha}_s^+ \\ \tilde{\alpha}_s^- \\ \tilde{\alpha}_A^+ \\ \tilde{\alpha}_A^- \\ \tilde{\alpha}_e \end{pmatrix} \quad (\text{B.11})$$

where,

$$\tilde{\alpha}_c = \left(1 - \beta \frac{\vec{u}^2}{2a^2}\right) \Delta \rho + \frac{\beta \vec{u}}{a^2} \Delta(\rho \vec{u}) + \beta \frac{B_t}{a^2} \Delta B_t - \frac{\beta}{a^2} \Delta E^* \quad (\text{B.12a})$$

$$\text{or... } \tilde{\alpha}_c = \Delta\rho - \frac{\Delta P}{a^2}$$

$$\tilde{\alpha}_f^\pm = \frac{r_f}{2c_f^2} [\Delta P \pm \rho c_f \Delta u_n] + r_s \frac{\sqrt{\rho}}{2c_f} \left[\Delta B_t \mp s_B \sqrt{\rho} \frac{b_n}{c_f} \Delta u_t \right] \quad (\text{B.12b})$$

$$\tilde{\alpha}_s^\pm = \frac{r_s}{2a^2} [\Delta P \pm \rho c_s \Delta u_n] - r_f \frac{\sqrt{\rho}}{2c_f} \left[\Delta B_t \mp s_B \sqrt{\rho} \frac{c_f}{a} \Delta u_t \right] \quad (\text{B.12c})$$

$$\tilde{\alpha}_A^\pm = \frac{1}{2} [\sqrt{\rho} \Delta u_s \mp s_B \Delta B_s] \quad (\text{B.12d})$$

$$\tilde{\alpha}_e = \Delta \hat{s}_e - \frac{E_e}{\rho} \frac{\Delta P}{a^2} \quad (\text{B.12e})$$

APPENDIX C

MHD Divergence Cleaning for General Coordinate Systems

The pseudo electric field is defines as $\Omega = \mathbf{u} \times \mathbf{B}$. From Maxwell's Equations the temporal evolution can be described by

$$\frac{\partial \mathbf{B}}{\partial t} = -\nabla \times \Omega \quad (\text{C.1})$$

For a cartesian coordinate system with x , y , and z dependants $\frac{\partial \mathbf{B}}{\partial t}$ is described as:

$$\begin{aligned} \frac{\partial B_x}{\partial t} &= \frac{\partial}{\partial y} \Omega_z - \frac{\partial}{\partial z} \Omega_y \\ \frac{\partial B_y}{\partial t} &= \frac{\partial}{\partial z} \Omega_x - \frac{\partial}{\partial x} \Omega_z \\ \frac{\partial B_z}{\partial t} &= \frac{\partial}{\partial x} \Omega_y - \frac{\partial}{\partial y} \Omega_x \end{aligned} \quad (\text{C.2})$$

For a coordinate system with a $r - z$ dependants $\frac{\partial \mathbf{B}}{\partial t}$ is described as:

$$\begin{aligned} \frac{\partial B_r}{\partial t} &= -\frac{1}{r} \frac{\partial}{\partial z} (r \Omega_\theta) \\ \frac{\partial B_z}{\partial t} &= \frac{1}{r} \frac{\partial}{\partial r} (r \Omega_\theta) \\ \frac{\partial B_\theta}{\partial t} &= -\frac{\partial}{\partial r} \Omega_z + \frac{\partial}{\partial z} \Omega_r \end{aligned} \quad (\text{C.3})$$

For a coordinate system with a $r - \theta$ dependants $\frac{\partial \mathbf{B}}{\partial t}$ is described as:

$$\begin{aligned} \frac{\partial B_r}{\partial t} &= \frac{1}{r} \frac{\partial}{\partial \theta} \Omega_z \\ \frac{\partial B_z}{\partial t} &= -\frac{1}{r} \frac{\partial}{\partial \theta} \Omega_r + \frac{1}{r} \frac{\partial}{\partial r} (r \Omega_\theta) \\ \frac{\partial B_\theta}{\partial t} &= -\frac{\partial}{\partial r} \Omega_z \end{aligned} \quad (\text{C.4})$$

APPENDIX D

Jacobians and Transforms

D.1 Chemical Jacobian

We first start out with the model ordinary differential equation for the kinetics:

$$\frac{dQ}{dt} = \dot{\Omega} \quad (\text{D.1})$$

where

$$\mathbf{Q} = \begin{pmatrix} n_s \\ E \end{pmatrix} \quad \dot{\Omega} = \begin{pmatrix} \dot{\omega}_s \\ \dot{\omega}_E \end{pmatrix} \quad (\text{D.2})$$

n_s is the number density of the s^{th} species, and $\dot{\omega}_s$ and $\dot{\omega}_E$ are the species and energy production terms, respectively. The number density, n_s , was used in lieu of mass density, ρ_s , out of convenience and can be easily transformed, $\frac{\partial \rho_l}{\partial n_k} = M_k \delta_{kl}$. The implicit 1st order numerical formulation of Equation D.1 is carried out with the following steps:

$$\begin{aligned} \frac{\Delta \mathbf{Q}}{\Delta t} &= \dot{\Omega}^{n+1} \\ \frac{\Delta \mathbf{Q}}{\Delta t} &= \dot{\Omega}^n + \frac{\partial \dot{\Omega}}{\partial t} \Delta t \\ \frac{\Delta \mathbf{Q}}{\Delta t} &= \dot{\Omega}^n + \frac{\partial \dot{\Omega}}{\partial \mathbf{Q}} \frac{\Delta \mathbf{Q}}{\Delta t} \Delta t \\ \frac{\Delta \mathbf{Q}}{\Delta t} &= \dot{\Omega}^n + \frac{\partial \dot{\Omega}}{\partial \mathbf{Q}} \Delta \mathbf{Q} \\ \left(\mathbf{I} - \frac{\partial \dot{\Omega}}{\partial \mathbf{Q}} \Delta t \right) \Delta \mathbf{Q} &= \dot{\Omega}^n \Delta t \\ \Delta \mathbf{Q} &= \left(\mathbf{I} - \frac{\partial \dot{\Omega}}{\partial \mathbf{Q}} \Delta t \right)^{-1} \dot{\Omega}^n \Delta t \end{aligned} \quad (\text{D.3})$$

D.2 Chemical Jacobian($\frac{\partial \dot{\Omega}}{\partial Q}$) Derivation

$$\frac{\partial \dot{\omega}_s}{\partial n_k} = \sum_r \nu_{rs} \frac{\nu'_{rk}}{n_k} \prod_j n_j^{\nu'_{rj}} \quad (\text{D.4})$$

$$\frac{\partial \dot{\omega}_s}{\partial E} = \frac{\partial \dot{\omega}_s}{\partial T} \frac{\partial T}{\partial E} = \frac{\partial \dot{\omega}_s}{\partial T} \frac{1}{C_v}$$

$$\frac{\partial \dot{\omega}_s}{\partial T} = \sum_r \nu_{rs} \frac{dk_r}{dT} \prod_k n_k^{\nu'_{rk}}$$

$$\frac{\partial k_r}{\partial T} = \frac{\eta_r}{T} A_r T^{\eta_r} \exp\left(\frac{-\theta_r}{T}\right) + \frac{\theta_r}{T^2} A_r T^{\eta_r} \exp\left(\frac{-\theta_r}{T}\right)$$

$$\frac{\partial k_r}{\partial T} = \left(\frac{\eta_r}{T} + \frac{\theta_r}{T^2}\right) k_r$$

$$\frac{\partial \dot{\omega}_s}{\partial E} = \frac{1}{C_v} \sum_r \nu_{rs} \left(\frac{\eta_r}{T} + \frac{\theta_r}{T^2}\right) k_r \prod_k n_k^{\nu'_{rk}} \quad (\text{D.5})$$

$$\dot{\omega}_E = \sum_s \omega_s e_{0s} = \sum_s e_{0s} \sum_r \nu_{rs} k_r \prod_k n_k^{\nu'_{rk}}$$

$$\frac{\partial \dot{\omega}_E}{\partial n_k} = \sum_s \frac{\partial \dot{\omega}_s}{\partial n_k} e_{0s} \quad (\text{D.6})$$

$$\frac{\partial \dot{\omega}_E}{\partial E} = \sum_s \frac{\partial \dot{\omega}_s}{\partial E} e_{0s} \quad (\text{D.7})$$

APPENDIX E

Steady State Detonation

We will first begin with our model equation with the steady state approximation:

$$\cancel{\frac{\partial \mathbf{Q}}{\partial t}}^0 + \frac{\partial \mathbf{F}}{\partial x} = \dot{\mathbf{\Omega}} \quad (\text{E.1a})$$

$$\mathbf{A} \frac{\partial \mathbf{Q}}{\partial x} = \dot{\mathbf{\Omega}} \quad (\text{E.1b})$$

$$\frac{\partial \mathbf{Q}}{\partial x} = \mathbf{A}^{-1} \dot{\mathbf{\Omega}} \quad (\text{E.1c})$$

From Equation E.1c, the explicit space-marching formulation is defined as:

$$\frac{\Delta \mathbf{Q}}{\Delta x} = \mathbf{A}^{-1} \dot{\mathbf{\Omega}}_i \quad (\text{E.2})$$

The implicit space-marching formulation is also defined,

$$\frac{\Delta \mathbf{Q}}{\Delta x} = \mathbf{A}^{-1} \dot{\mathbf{\Omega}}_{i+1} \quad (\text{E.3a})$$

$$\frac{\Delta \mathbf{Q}}{\Delta x} = \mathbf{A}^{-1} \left(\dot{\mathbf{\Omega}}_i + \frac{\partial \dot{\mathbf{\Omega}}}{\partial \mathbf{Q}} \Delta \mathbf{Q} \right) \quad (\text{E.3b})$$

$$\frac{\Delta \mathbf{Q}}{\Delta x} - \mathbf{A}^{-1} \frac{\partial \dot{\mathbf{\Omega}}}{\partial \mathbf{Q}} \Delta \mathbf{Q} = \mathbf{A}^{-1} \dot{\mathbf{\Omega}}_i \quad (\text{E.3c})$$

Now by solving for $\Delta \mathbf{Q}$ the final form is expressed as:

$$\Delta \mathbf{Q} = \left(\mathbf{A} - \Delta x \frac{\partial \dot{\mathbf{\Omega}}}{\partial \mathbf{Q}} \right)^{-1} \dot{\mathbf{\Omega}}_i \Delta x \quad (\text{E.4})$$

APPENDIX F

Iterative & Direct Solvers

F.1 Thomas' Algorithm

The triadiagonal matrix algorithm, commonly referred to as Thomas' algorithm, is a simplified form of Gaussian elimination used to solve triadiagonal system of equation.

These systems of equations take on the following form:

$$a_i x_{i-1} + b_i x_i + c_i x_{i+1} = d_i \quad (\text{F.1})$$

where $a_0 = 0$ and $c_N = 0$. And represented in the matrix form as:

$$\begin{bmatrix} b_1 & c_1 & & & 0 \\ a_2 & b_2 & c_2 & & \\ & a_3 & b_3 & . & \\ & & . & . & c_{N-1} \\ 0 & & & a_N & b_N \end{bmatrix} \begin{bmatrix} x_1 \\ x_2 \\ . \\ . \\ x_N \end{bmatrix} = \begin{bmatrix} d_1 \\ d_2 \\ . \\ . \\ d_N \end{bmatrix} \quad (\text{F.2})$$

Just as in Gaussian elimination, Thomas' algorithm consist of a forward elimination and backward substitution to solve the system as follows:

Forward Elimination

for $k = 2$ loop through N

$$\begin{aligned} m &= \frac{a_k}{b_{k-1}} \\ b_k &= b_k - mc_{k-1} \\ d_k &= d_k - md_{k-1} \end{aligned}$$

Backward Substitution

$$x_N = \frac{d_N}{b_N}$$

for $k = N - 1$ loop through 1

$$x_k = \frac{d_k - c_k x_{k+1}}{b_k}$$

This algorithm is applicable for diagonally dominant matrices, where

$$|b_i| > |a_i| + |c_i| \quad i \in 1, \dots, N \quad (\text{F.3})$$

F.2 Black-Red Gauss-Seidel

Gauss-Seidel is an iterative method used to solve problems of the general form:

$$\mathbf{U} = f(\vec{\mathbf{U}}) \quad (\text{F.4})$$

If one were to solve this equation explicitly, it would simply take the form,

$$\mathbf{U}^{n+1} = f(\vec{\mathbf{U}}^n) \quad (\text{F.5})$$

If $\vec{\mathbf{U}}$ is the spatially distribution of \mathbf{U} , Equation F.4 can be solved implicitly using Gauss-Seidel. In this procedure, one would begin with an initial solution at $t = t^{n+1}$, $\mathbf{U}^{(s)}$, where $s=0$ initially. The solution at $\mathbf{U}^{(s)}$ is used to determine $\mathbf{U}^{(s+1)}$ until convergence which is as follows:

$$\begin{aligned}
\mathbf{U}_{i,j}^{(s+1)} &= f(\vec{\mathbf{U}}^{(s)}) \\
\text{error} &= \max ||\mathbf{U}_{i,j}^{(s+1)} - \mathbf{U}_{i,j}^{(s)}|| \\
&\text{continue until ...} \\
\text{error} < \epsilon &\rightarrow \mathbf{U}^{n+1} = \mathbf{U}^{(s+1)} \text{ (convergence!)}
\end{aligned} \tag{F.6}$$

Using this procedure, the update solution, $\mathbf{U}^{(s+1)}$, is solved for using the latest solution. In order to speed up this process, instead of sweeping through all of the cells (i & j for 2D), one can first sweep through and solve for the computational grid cells colored red in Figure F.1, then using the updated solutions, $\mathbf{U}_{red}^{(s+1)}$, sweep through and solve for the black grid cells, $\mathbf{U}_{black}^{(s+1)}$. The procedure would be as follows:

$$\begin{aligned}
\mathbf{U}_{red}^{(s+1)} &= f(\vec{\mathbf{U}}_{black}^{(s)}) \\
\mathbf{U}_{black}^{(s+1)} &= f(\vec{\mathbf{U}}_{red}^{(s+1)}) \\
\text{error} &= \max ||\mathbf{U}_{i,j}^{(s+1)} - \mathbf{U}_{i,j}^{(s)}|| \\
&\text{continue until ...} \\
\text{error} < \epsilon &\rightarrow \mathbf{U}^{n+1} = \mathbf{U}^{(s+1)} \text{ (convergence!)}
\end{aligned} \tag{F.7}$$

The procedure shown above is referred to as *Red-Black Gauss-Seidel*.

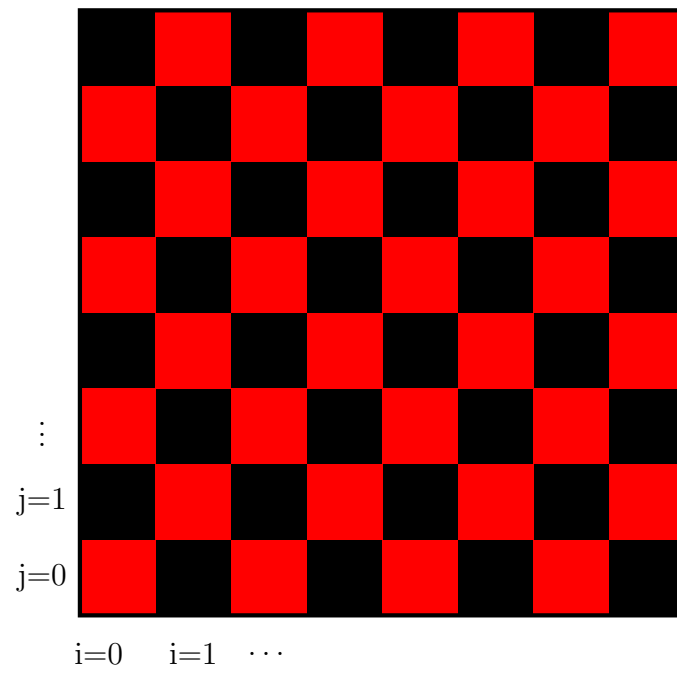


Figure F.1: Computational domain split into red and black computational cells.

APPENDIX G

Message Passing Interface (MPI) Implementation

G.1 Grid Connectivity

A three dimensional computational domain can be broken up into rectangular cuboid subdomains; each containing 6 rectangular faces. A face can connect with one or more faces from adjacent domain(s), which is illustrated in Figure G.1. This illustration also shows that domain p0 is connected with 2 domains(p1 & p2), domain p1 is connected with 3 domains(p1,p2,p3), and domain p3 is connected with 2 domains (p1 & p2). The red numbers in the figure represent unique domain-to-domain connection of which there are 5. Domains p0 & p2 of Figure G.1 are illustrated with there associated ghost layers iin Figure G.2. For this connection, labeled 1 in Figure G.1, p0 would pass information of its interior cells to the ghost layer of p1 and p1 would in turn information of its interior to p2. This example shows that for each connection, there are two receive buffers required, which will be refered to as memory windows without explanation for the moment. From the 5 connections in Figure G.1, a list of 10 memory windows and its associated domains are created in Table G.1.

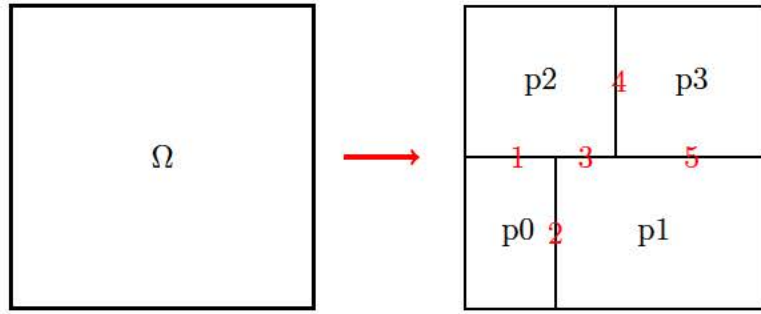


Figure G.1: The computational domain, Ω is decomposes into 4 subdomains.

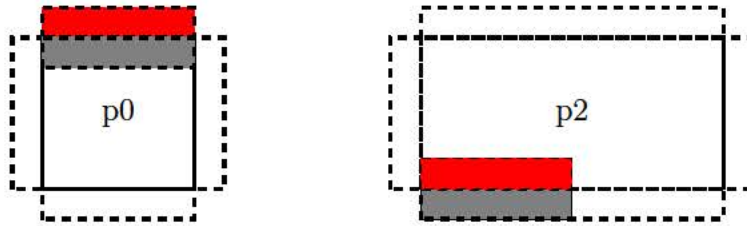


Figure G.2: Domain-to-domain connection example where the red shaded area is a p0 ghost to p2 physical window and the grey shaded area is a p2 ghost to p0 physical window.

window	0	1	2	3	4	5	6	7	8	9
local	0	2	0	1	2	1	2	3	3	1
remote	2	0	1	0	1	2	3	2	1	3

Table G.1: Generic memory window list generated from Figure G.1 domain connections where ‘local’ is the domain sending its physical cell data to the ghost cell of the ‘remote’ domain.

REFERENCES

- [1] K. Ziolkovsky. The investigation of outer space by means of reaction apparatus. *Science Survey*, 1903.
- [2] Robert H. Goddard. A method of reaching extreme altitudes. *The Smithsonian Institute*, 1919.
- [3] P. Hill and C. Peterson. *Mechanics and Thermodynamics of Propulsion*. Addison-Wesley Publishing Company, 2nd edition, 1992.
- [4] Jean-Luc Cambier. A thermodynamic study of MHD ejectors. *AIAA*, 1998.
- [5] Jean-Luc Cambier. MHD augmentation of pulse detonation rocket engines. Technical Report 2001-1782, *AIAA*, 2001.
- [6] D. L. Chapman. On the rate of explosion in gases. *Philos. Mag.*, 47:90104, 1899.
- [7] E. Jouguet. On the propagation of chemical reactions in gases. *J. de mathematiques Pures et Appliquees*, 1:347425, 1905.
- [8] Ja. B. Zel'dovich. On the theory of the propagation of detonation in gaseous systems. *Zh. Eksp. Teor. Fiz.*, 10:542568, 1940.
- [9] J. von Neumann. Theory of detonation waves. *Von Neumann, Collected Works*, 1:347425, 1942.
- [10] W. Döring. On detonation processes in gases. *Ann. Phys.*, 43:421436, 1943.
- [11] John H. S. Lee. *The Detonation Phenomenon*. Cambridge University Press, 2008.
- [12] A. Bourlioux and A. J. Majda. Theoretical and numerical structure for unstable two-dimensional detonations. *Combustion and Flame*, 90:211–229, 1992.
- [13] Peter Hwang, B. Merriman, Ann R. Karagozian, and S. J. Osher. Numerical resolution of pulsating detonation waves. *Combustion Theory & Modeling*, 4(3):217240, 2000.
- [14] Y. Daimon and A. Matsuo. Detailed features of one-dimensional detonations. *Phys. Fluids*, 15:112–122, 2003.

- [15] H. D. Ng, A. J. Higgins, C. B. Kiyanda, M. I. Radulescu, J. H. S. Lee, K. R. Bates, and N. Nikiforakis. Nonlinear dynamics and chaos analysis of one-dimensional pulsating detonations. *Combustion Theory and Modeling*, 9:159170, 2005.
- [16] Jean-Luc Cambier. Development of numerical tools for pulse detonation engine studies. Technical report, Aero. Research Inst. of Sweden, 1996. Flygtekniska Försökstantalten FFA TN 1996-50.
- [17] C. Leung, M. I. Radulescu, and G. J. Sharpe. Characteristics analysis of the one-dimensional detonations. *Phys. Fluids*, 22:126101–1 126101–15, 2010.
- [18] M. Short and G. J. Sharpe. Pulsating instability of detonations with a two-step chain-branching reaction model: Theory and numerics. *Combustion Theory and Modeling*, 7:401–416, 2003.
- [19] M. I. Radulescu, H. D. Ng, J. H. S. Lee, and B. Varatharajan. The effects of argon dilution on the stability of Acetylene/Oxygen detonations. In *Proceedings of the Combustion Institute*, volume 29, page 28252831, 2002.
- [20] C. A. Eckett, J. J. Quirk, and J. E. Shepherd. The role of unsteadiness in direct initiation of gaseous detonations. *Journal of Fluid Mechanics*, 421:147–183, 2000.
- [21] J. E. Shepherd and J. H. S. Lee. On the transition from deflagration to detonation. In *Major topics in Combustion*. Springer-Verlag, 1992.
- [22] E. Schultz, E. Wintenberger, and J. Shepherd. Investigation of deflagration to detonation transition for application to pulse detonation engine ignition systems. In *Proceedings of the 16th JANNAF Propulsion Symposium*, Chemical Propulsion Information Agency, 1999.
- [23] Elaine S. Oran and Vadim N. Gamezo. Origins of the deflagration-to-detonation transition in gas-phase combustion. *Combustion and Flame*, 148:4–47, 2007.
- [24] L. Barr. Pulse detonation engine flies into history. *Air Force Print News Today*, May 2008.
- [25] J. Cole, J. Campbell, and A. Robertson. Rocket induced magnetohydrodynamic ejector - a single-state-to-orbit propulsion concept. Technical Report 95-4079, AIAA, 1995.

- [26] C. Bruno and P. Czysz. An electro-magnetic-chemical hypersonic propulsion system. Technical Report 98-1582, AIAA, 1998.
- [27] N. Krall and A. Trivelpiece. *Principles of Plasma Physics*. McGraw-Hill, New York, 1973.
- [28] R.J. Rosa. *Magnetohydrodynamic Energy Conversion*. Hemisphere Publishing Corporation, Washington, D.C, 1987.
- [29] G. Pollack and D. Stump. *Electromagnetism*. Addison-Wesley Publishing Company, 2002.
- [30] Jean-Luc Cambier. MHD power extraction from a pulse detonation engine. In *34th AIAA/ASME/SAE/ASEE Joint Propulsion Conference and Exhibit*, Albuquerque, New Mexico, June 1998. AIAA.
- [31] Jean-Luc Cambier. Preliminary modeling of pulse detonation rocket engines. Technical Report 99-2659, AIAA, 1999.
- [32] A.C. Kolb. Production of high-energy plasmas by magnetically driven shock-waves. *Physical Review*, 107:345350, 1957.
- [33] Christopher Zeineh. *Numerical Simulations of Pulse Detonation Rocket Engines with Magnetohydrodynamic Thrust Augmentation*. PhD thesis, University of California, Los Angeles, 2010.
- [34] Christopher Zeineh, Lord K. Cole, Timothy Roth, Ann R. Karagozian, and Jean-Luc Cambier. Magnetohydrodynamic augmentation of pulse detonation rocket engines. *Journal of Propulsion and Power*, 28(1):146159, January 2012.
- [35] Jean-Luc Cambier, M. Carroll, and Michael Kapper. Development of a hybrid model for non-equilibrium high-energy plasmas. In *35th AIAA Plasmadynamics and Lasers Conference*, Portland, Oregon, June 2004.
- [36] William C. Gardiner. *Combustion Chemistry*. Springer-Verlag, 1984.
- [37] Casimir J. Jachimowski. An analysis of combustion studies in shock expansion tunnels and reflected shock tunnels. Technical Report NASA TP-3224, 1992.
- [38] M. Short and G. J. Sharpe. Pulsating instability of detonations with a two-step chain-branching reaction model: Theory and numerics. *Combustion Theory and Modeling*, 7:401–416, 2003.

- [39] C. Leung, M. I. Radulescu, and G. J. Sharpe. Characteristics analysis of the one-dimensional detonations. *Phys. Fluids*, 22:126101–1 – 126101–15, 2010.
- [40] Jean-Luc Cambier. Mhd augmentation of pulse detonation rocket engines. Technical Report 2001-1782, AIAA, 2001.
- [41] W. Lotz. Electron-impact ionization cross-sections and ionization rate coefficients for atoms and ions. *The Astrophysical Journal Supplement Series*, 14:207, 1967.
- [42] IUri Petrovich Razer. *Gas discharge physics*. Springer-Verlag, 1991.
- [43] R.J. Rosa. *Magnetohydrodynamic Energy Conversion*. Hemisphere Publishing Corporation, Washington, D.C, 1987.
- [44] J. C. Strikwerda. *Finite Difference Schemes and Partial Differential Equations*. Wadsworth and Brooks, 1989.
- [45] G.-S. Jiang and C.-W. Shu. Efficient implementation of weighted ENO schemes. *Journal of Computational Physics*, 126:202228, 1996.
- [46] P. L Roe. Approximate riemann solvers, parameter vectors, and difference schemes. *Journal of computational physics*, 43(2):357372, 1981.
- [47] B. Einfeldt. On godunov-type methods for gas dynamics. *SIAM Journal on Numerical Analysis*, pages 294–318, 1988.
- [48] X.-D. Liu, S. J. Osher, and T. Chan. Weighted essentially non-oscillatory schemes. *Journal of Computational Physics*, 115:200 – 212, 1994.
- [49] A. Harten, B. Engquist, S. Osher, and S. R Chakravarthy. Uniformly high order accurate essentially non-oscillatory schemes, III. *Journal of Computational Physics*, 71(2):231–303, 1987.
- [50] A. Suresh and H. T. Huynh. Accurate monotonicity-preserving schemes with runge-kutta time stepping. *Journal of Computational Physics*, 136:8399, 1997.
- [51] Dinshaw S. Balsara and Chi-Wang Shu. Monotonicity preserving weighted essentially non-oscillatory schemes with increasingly high order of accuracy. *Journal of Computational Physics*, 160(2):405–452, May 2000.
- [52] V. A. Titarev and E. F. Toro. ADER: arbitrary high order godunov approach. *Journal of Computation Physics*, 17:609–618, 2002.

- [53] Dinshaw S Balsara, Tobias Rumpf, Michael Dumbser, and Claus-Dieter Munz. Efficient, high accuracy ADER-WENO schemes for hydrodynamics and divergence-free magnetohydrodynamics. *arXiv:0811.2200*, November 2008.
- [54] Gary A Sod. A survey of several finite difference methods for systems of nonlinear hyperbolic conservation laws. *Journal of Computational Physics*, 27(1):1–31, April 1978.
- [55] P. Woodward and P. Colella. The numerical simulation of two-dimensional fluid flow with strong shocks. *Journal of Computation Physics*, 54:115–173, 1984.
- [56] C.-W. Shu and S. J. Osher. Efficient implementation of essentially non-oscillatory shock-capturing schemes, II. *Journal of Computational Physics*, 83:3278, 1989.
- [57] Milton Van Dyke. *An Album of Fluid Motion*. The Parabolic Press, Stanford, California, 1982.
- [58] James J. Quirk. A contribution to the great riemann solver debate. *International Journal for Numerical Methods in Fluids*, 18(6):555574, 1994.
- [59] S. Chandrasekhar. *Hydrodynamic and Hydromagnetic Stability*. Oxford University Press, 1961.
- [60] M Brio and C.C Wu. An upwind differencing scheme for the equations of ideal magnetohydrodynamics. *Journal of Computational Physics*, 75(2):400–422, April 1988.
- [61] Guang-Shan Jiang and Cheng-chin Wu. A high-order WENO finite difference scheme for the equations of ideal magnetohydrodynamics. *Journal of Computational Physics*, 150(2):561–594, April 1999.
- [62] Steven A. Orszag and Cha-Mei Tang. Small-scale structure of two-dimensional magnetohydrodynamic turbulence. *Journal of Fluid Mechanics*, 90(01):129–143, 1979.
- [63] Dinshaw S Balsara and Daniel S Spicer. A staggered mesh algorithm using high order godunov fluxes to ensure solenoidal magnetic fields in magnetohydrodynamic simulations. *Journal of Computational Physics*, 149(2):270–292, March 1999.

- [64] J. F. Remacle, J. E. Flaherty, and M. S. Shephard. An adaptive discontinuous galerkin technique with an orthogonal basis applied to compressible flow problems. *SIAM review*, page 5372, 2003.
- [65] Byung-Il Jun, Michael L. Norman, and James M. Stone. A numerical study of rayleigh-taylor instability in magnetic fluids. *The Astrophysical Journal*, 453:332–349, November 1995.
- [66] Gábor Tóth. The $\nabla \cdot B = 0$ constraint in shock-capturing magnetohydrodynamics codes. *Journal of Computational Physics*, 161(2):605–652, July 2000.
- [67] Jean-Luc Cambier. Preliminary Modeling of Pulse Detonation Rocket Engines. Technical Report 99-2659, AIAA, 1999.
- [68] Lord K. Cole, A. R. Karagozian, and J.-L. Cambier. Stability of flame-shock coupling in detonation waves: 1D dynamics. *Combustion Science and Technology*, 184(10-11):1502–1525, 2012.
- [69] J. H. S. Lee. Initiation of gaseous detonations. *Ann. Rev. of Phys. Chem.*, 28:75104, 1977. DOI: 10.1146/annurev.pc.28.100177.000451.
- [70] Xing He and Ann R. Karagozian. Pulse-detonation-engine simulations with alternative geometries and reaction kinetics. *Journal of Propulsion and Power*, 22:852–861, 2006.
- [71] J. H. S. Lee, R. Knystaustas, and N. Yoshikawa. Photochemical initiation of gaseous detonations. *Acta Astronautica*, 5:971–982, 1978.
- [72] Joseph M. Powers and S. Paolucci. Accurate spatial resolution estimates for reactive supersonic flow with detailed chemistry. *AIAA*, 43:10881099, May 2005.
- [73] Elaine S. Oran and J. P. Boris. *Numerical Simulation of Reactive Flow*. Elsevier Science, 1987.
- [74] J. B. McVey and T. Y. Toong. Mechanism of instabilities of exothermic hypersonic blunt-body flows. *Combustion Science and Technology*, 3:63 – 76, 1971.
- [75] J.-L. Cambier. Numerical simulations of a nonequilibrium argon plasma in a shock-tube experiment. *22nd AIAA Fluid Dynamics, Plasma Dynamics and Lasers Conference*, AIAA paper 91-1464, July 1991.
- [76] M. G. Kapper and J.-L. Cambier. Ionizing shocks in argon part i: Collisional-radiative model and steady-state structure. *J. Appl. Phys.*, 109:113308, 2011.

- [77] M. G. Kapper and J.-L. Cambier. Ionizing shocks in argon part II: transient and multi-dimensional effects. *J. Appl. Phys.*, 109:113309, 2011.
- [78] V. N. Gamezo, D. Desbordes, and E. S. Oran. Formation and evolution of two-dimensional cellular detonations. *Combustion and Flame*, 116(1):154165, 1999.
- [79] V. N. Gamezo, D. Desbordes, and E. S. Oran. Two-dimensional reactive flow dynamics in cellular detonation waves. *Shock Waves*, 9(1):1117, 1999.
- [80] D. N. Williams, L. Bauwens, and E. S. Oran. A numerical study of the mechanisms of self-reignition in low-overdrive detonations. *Shock Waves*, 6(2):93110, 1996.
- [81] D. Scott Stewart, Tariq D. Aslam, and Jin Yao. On the evolution of cellular detonation. *Symposium (International) on Combustion*, 26(2):2981–2989, 1996.
- [82] A. Bogaerts, R. Gijbels, and J. Vlcek. Collisional-radiative model for an argon glow discharge. *Journal of applied physics*, 84(1):121136, 1998.
- [83] C. O. Laux, L. Pierrot, and R. J. Gessman. State-to-state modeling of a recombining nitrogen plasma experiment. *Chemical Physics*, 2011.
- [84] Elaine S. Oran, James W. Weber Jr., Eliza I. Stefaniw, Michel H. Lefebvre, and John D. Anderson Jr. A numerical study of a two-dimensional h₂-o₂-ar detonation using a detailed chemical reaction model. *Combustion and Flame*, 113(12):147–163, April 1998.
- [85] K. Inaba, A. Matsuo, and J. E. Shepherd. Soot track formation by shock waves and detonations. In *Proceedings of the 20th International Colloquium of Dynamics of Explosion and Reactive Systems, Montreal*, 2005.
- [86] Y. B. Zel'Dovich and Y. P. Raizer. *Physics of shock waves and high-temperature hydrodynamic phenomena*. Dover Publications, 2002.
- [87] J. Damazo, J. Ziegler, J. Karnesky, and J. E. Shepherd. Investigating shock WaveBoundary layer interaction caused by reflecting detonations. In *Proceedings of the 8th ISPHMIE Conference, Sep*, page 510, September 2010.
- [88] Jean-Luc Cambier. Numerical methods for TVD transport and coupled relaxing processes in gases and plasmas. volume 90-1574, Seattle, WA, June 1990.

AFRL-RQ-ED-TR-2015-0015

Primary Distribution of this Report:

RQR
AFRL R&D Case Files
Completed Interim and Final Tech Reports Repository

AFRL/RQ Technical Library (2 CD + 1 HC)
6 Draco Drive
Edwards AFB, CA 93524-7130

Chemical Propulsion Information Analysis Center
Attn: Tech Lib (Mary Gannaway) (1 CD)
10630 Little Patuxent Parkway, Suite 202
Columbia, MD 21044-3200

Defense Technical Information Center
(1 Electronic Submission via STINT)
Attn: DTIC-ACQS
8725 John J. Kingman Road, Suite 94
Ft. Belvoir, VA 22060-6218